UNIVERSIDAD COMPLUTENSE DE MADRID

FACULTAD DE CIENCIAS FÍSICAS

Departamento de Astrofísica y Ciencias de la Atmósfera

TESIS DOCTORAL

Complejidad molecular en envolturas de estrellas evolucionadas: estudio detallado de la emisión molecular de los objetos IK Tau, OH231.8 + 4,2 e IRC + 10216

Molecular complexity in envelopes of evolved stars : detailed study of the molecular emissión of the objects IK Tau, OH231.8 + 4,2 and IRC + 10216

MEMORIA PARA OPTAR AL GRADO DE DOCTOR

PRESENTADA POR

Luis Velilla Prieto

Directores

Carmen Sánchez Contreras
José Cernicharo Quintanillaa

Madrid, 2018

© **Luis Velilla Prieto, 2017**

UNIVERSIDAD COMPLUTENSE DE MADRID

Departamento de Astrofísica y Ciencias de la Atmósfera

Facultad de Ciencias Físicas

Complejidad molecular en envolturas de estrellas evolucionadas: estudio detallado de la emisión molecular de los objetos IK Tau, OH231.8+4.2 e IRC+10216

Molecular complexity in envelopes of evolved stars: detailed study of the molecular emission of the objects IK Tau, OH231.8+4.2, and IRC+10216

Tesis doctoral presentada por Luis Velilla Prieto para optar al grado de Doctor en Astrofísica por la Universidad Complutense de Madrid

Madrid, Abril de 2017

Dirigida por:

Dra. Carmen Sánchez Contreras
CAB-INTA-CSIC

Prof. José Cernicharo Quintanilla
ICMM-CSIC

A mi familia.

"The Road goes ever on and on
Down from the door where it began.
Now far ahead the Road has gone,
And I must follow, if I can,
Pursuing it with eager feet,
Until it joins some larger way
Where many paths and errands meet.
And whither then? I cannot say."
J.R.R. Tolkien. The Lord Of The Rings.

DECLARACIÓN DE ORIGINALIDAD / DECLARATION OF ORIGINALITY

Yo, Luis Velilla Prieto, declaro que el trabajo que aquí se presenta para la obtención del título de Doctor en Astrofísica en la Universidad Complutense de Madrid, es de mi autoría y que no me consta que haya sido previamente presentado para la obtención de cualquier tipo de grado o calificación profesional en ninguna universidad española o extranjera. Así mismo declaro que no he cometido ningún tipo de plagio, que no he manipulado en algún modo los datos, que he documentado todos los métodos de forma sincera y que la información derivada de trabajos publicados y no publicados por otros ha sido debidamente citada y referenciada. Igualmente, algunas de las imágenes utilizadas a lo largo de esta tesis doctoral han sido tomadas de colecciones de imágenes o publicaciones accesibles a través de Internet. Su uso tiene simplemente carácter ilustrativo y educacional, y dichas imágenes han sido también debidamente referenciadas, dando crédito a su autor o autores. En ningún caso se obtiene ningún tipo de beneficio o crédito personal ni de ningún tipo que derive de su uso y no se pretende violar los derechos de autor o de propiedad intelectual.

I hereby declare that the presented work, which is submitted for the degree of PhD at the Complutense University of Madrid, is from my own and it is to the best of my knowledge original, and neither this, nor any substantial similar dissertation has been submitted for any other degree or professional qualification at any other (foreign or Spanish) University. I declare that I did not make any kind of plagiarism and I did not manipulate data. I also declare that I documented all methods in a sincere way. Where other people's work has been used (either from a printed source, Internet or any other source), this has been properly acknowledged and referenced in the text, including several images which have been used only for illustrative purposes. In no case any personal benefit or credit results from their use and it is not intended to violate copyright or intellectual property rights.

AGRADECIMIENTOS

Sorprende que precisamente estas líneas sean tan complejas de escribir, y es justamente hoy cuando entiendo el porqué. Parece fácil y simple agradecer a todas aquellas personas e instituciones que me han apoyado durante este periodo de doctorando. Personas e instituciones de las que me siento profundamente orgulloso y agradecido de haber conocido. Sin duda alguna son lo más positivo que he obtenido en este precioso viaje. Sorprende porque pronto habrá que soltar amarras rumbo a un nuevo destino en el que no siempre ese apoyo estará tan cerca. Parece fácil pero no lo es... A todos gracias.

En primer lugar a mis directores de tesis, Carmen y Pepe, dos científicos y por supuesto personas fuera de serie. Gracias por vuestra paciencia y apoyo en cada uno de los momentos de este camino, y por haber compartido vuestro conocimiento y haberme hecho crecer tanto profesional como personalmente. Gracias por vuestra confianza y cercanía. Espero y deseo que sigamos compartiendo muchas metas.

Quiero también agradecer especialmente la ayuda y apoyo de otros dos auténticos "cracks", Marce y Javier. A Marce por estar siempre dispuesto para discutir aspectos tanto científicos como otros más mundanos, y sobre todo por haber sido un gran apoyo durante mi estancia en Burdeos. A Javier por su ayuda y preocupación en todos los aspectos prácticos relacionados con la administración, y también por compartir su sabiduría y consejos en lo profesional y lo personal. Os merecéis lo mejor.

No olvidaré tampoco a otra serie de excelentes científicos con los que he tenido la oportunidad de compartir más tiempo y trabajo como Valentín Bujarrabal, Javier Alcolea, Arancha Castro Carrizo, Juan Ramón Pardo y Asunción Fuente. Y también a todos aquellas personas con los que he compartido propuestas, reuniones, artículos y discusiones.

Agradezco enormemente el trabajo de revisión que el Prof. Karl M. Menten y el Dr. Roberto Neri han realizado sobre este manuscrito. Es sinceramente un gran privilegio haber contado con la experiencia y el juicio de dos científicos de su talla.

Mi agradecimiento a todas las instituciones que han apoyado e intervenido en algún modo a la consecución de esta tesis doctoral. Al MINECO y al anterior MICINN, al ERC, al CSIC, al CAB/INTA y al ICMM principalmente, tanto por la financiación obtenida gracias a los proyectos AYA2009-07304, AYA2012-32032, CSD2009-00038 y ERC-610256 (NANOCOSMOS), así como por el apoyo administrativo y fundamental en el desarrollo de mis tareas. También al LAB y la Universidad de Burdeos y al CNRS, por facilitar mi fantástica estancia en Burdeos. Gracias a IRAM, especialmente a todo el personal con el que he podido compartir tiempo, personal de cocina, operadores, AoDs, técnicos, administración y directores.

Agradecer sin duda a la Universidad Complutense de Madrid, a la Facultad de Físicas y todo su personal, y en particular al Departamento de Astrofísica y Ciencias de la Atmósfera, con

especial cariño al Profesor Jaime Zamorano quién me dio la oportunidad de dar mis primeros pasos en el campo de la radioastronomía.

Por supuesto a ti, Sara, por la cantidad de tiempo y el largo trecho que hemos recorrido y compartido, por tu simpatía, tus ánimos y ayuda. Aprecio cada una de esas experiencias, y sólo deseo que en adelante disfrutes de una próspera carrera científica y personal, y que aquí nos tendrás para lo que necesitéis, pues desde hace ya un tiempo tanto tú como Leo formáis parte de nuestra familia. Quiero también transmitir mi especial agradecimiento a Marcelo, por su cercanía, humor, apoyo, ayuda, amistad y *"todo bien"*. Espero que podamos seguir compartiendo esos momentos que siempre guardaré en mi memoria, A Guillermo, Pablo, Nuria, Belén, Miguel, Alicia, Natalia, Sarah, Emeric, Elena y Juan Antonio, gracias por los ratos que hemos compartido y que espero sigamos disfrutando. Aquí siempre tendréis un amigo. A toda la gente de Villafranca, Margie, Sergio, Antonio, Jesús, Albert, Bea, Jorge, Belén, Miguel, Pablo... Y a todos los compañeros de Torrejón.

Por último, a las personas más importantes de mi vida. Quiero agradecer a mis amigos y familia el cariño, ayuda y paciencia que me dais siempre. A mi madre, gracias por el esfuerzo que has realizado para que hoy pueda defender mis ideas y trabajo, enseñarme a ser un poco mejor y por cuidar en todo momento de mí, sobre todo durante los momentos más complicados. A mi mujer, por darme todo aquello que siempre he soñado, por la felicidad y el amor que siento por nosotros, por tener el valor de afrontar la vida conmigo, por el mundo que hemos recorrido, por ser siempre la estrella más brillante del Universo. Tú eres mi teoría del todo. Gracias por las 2 personitas que hoy crecen en tu interior y que traen consigo la mayor felicidad que jamás he conocido y que no podría expresar con unas pocas palabras. No podéis imaginar la emoción que siento y las ganas que tengo de teneros en mis brazos.

Aquellos que me conocen bien sabrán por qué he elegido esa canción de la magnífica obra de Tolkien, "El Señor de los Anillos", que Bilbo entona tras cruzar el umbral de su hogar sin saber bien qué le espera. Das un paso para cruzar la puerta y todo puede ocurrir. Un paso que siempre lleva al cambio, siempre errantes en un vasto Universo por explorar. Los caminos que elegimos no son siempre los más sencillos, cómodos o siquiera están trazados, y probablemente muchos de vosotros no comprenderéis que nos lleva a dar un paso en cierta dirección. Sólo espero que los caminos que tomamos, por muy lejos que nos lleven, nos permitan seguir juntos.

SUMMARY

Evolved stars whose main sequence masses were comprised between approximately 1 and 8 solar masses, for example like our Sun will be after 4.5 billion years from now, are the main contributors to the enrichment of the interstellar medium. These stars create a circumstellar envelope around them during the asymptotic giant branch phase, which is formed due to an intense process of mass loss. Circumstellar envelopes are composed mainly of dust grains and molecules in gas phase, which are efficiently formed in the atmospheres of these stars. These compounds experience different physico-chemical processes in the circumstellar envelopes, that lead to the production of new species. Circumstellar envelopes are excellent laboratories to study the molecular complexity and the chemical evolution of the Universe.

Radiative and collisional processes can modify the quantum state of the molecules present in the circumstellar envelopes of evolved stars. In particular, at the temperatures found in these objects (about 2500 K near the photosphere of the star, down to ∼10 K in the outermost regions), numerous transitions occur due to the change in the rotational state of the molecules, producing emission lines detectable mainly in the millimeter wavelength range. From the analysis of these emission lines we obtain information about the composition and properties of the envelopes. The latest advances in the field of instrumentation are allowing us to observe the circumstellar envelopes of evolved stars in this range of the electromagnetic spectrum with an unprecedented sensitivity, spatial, and spectral resolution. We are in the era of ALMA, Herschel, IRAM-30 m, NOEMA, and many other instruments that are motivating important discoveries, as well as changing our vision of the circumstellar envelopes and the Universe in general.

In this thesis, the results obtained from the study of the molecular emission of three circumstellar envelopes around the evolved stars IKTau, OH231.8+4.2, and IRC+10216, are presented. IKTau and OH231.8+4.2 are oxygen-rich circumstellar envelopes ([C]/[O]<1), whose physical properties are relatively well determined. However, their molecular inventory is not completely known given that they have not been extensively studied up to date, since oxygen chemistry is less rich than carbon chemistry. IRC+10216 is a carbon-rich circumstellar envelope ([C]/[O]>1), in fact, it is the most studied circumstellar envelope of the Universe due to its particular properties and chemical richness. In the case of the two O-rich objects, we carried out two analogous line spectral surveys in the millimeter wavelength range using the IRAM-30 m antenna, and also observations with Herschel-HIFI toward OH231.8+4.2. This work has allowed us to determine the molecular inventory, and also to characterise the physical properties of the molecular emission, and to estimate the abundances of the molecules present in both objects. Concerning IRC+10216, we present the first high spatial resolution observations obtained with ALMA, for molecules such as SiO, SiS, or SiC_2, among other results based on

observations with the IRAM-30 m telescope and ALMA.

The main results obtained show that the chemistry of oxygen-rich objects is not as poor as it was previously thought. We have discovered for the first time emission lines of molecules such as HNCO, HNCS, HC_3N, NO, or SO^+, toward OH231.8+4.2. We also detected for the first time emission lines of H_2CO, NS, or NO toward IKTau. In addition, we detected for the first time and unambiguously emission of warm SO_2 (T$\sim$290 K) in the innermost region of the circumstellar envelope of IKTau, which was not expected according to current chemical models. The analysis of the spectral line surveys of both objects support the idea that the chemistry of OH231.8+4.2 has been probably altered by high-speed shocks caused by the interaction between the slow AGB wind and the fast (few 100 km s^{-1}) highly collimated bipolar winds. In the case of IRC+10216 we have detected emission lines of SiS, from vibrationally excited levels up to v=7, which arise from the innermost ($<$50 R_*) and hottest regions of the envelope. We also determined through ALMA observations, that SiC_2 is the most abundant (in the gas phase) Si-C bond bearing molecule in the dust forming region of IRC+10216. We have also characterised the spatial distribution of the emission of other molecules such as CH_3CN or some metals such as NaCl or KCl.

Thanks to the work done in this thesis, we have obtained satisfactory results for the NOEMA and ALMA time assignment committees, to continue our study of the molecular emission in these objects. Our work will serve as a reference for future studies of the molecular emission in circumstellar envelopes of evolved stars, particularly for the oxygen rich envelopes.

RESUMEN

Las estrellas evolucionadas cuyas masas durante la secuencia principal estaban comprendidas aproximadamente entre 1 y 8 masas solares, es decir, por ejemplo como lo será nuestro Sol dentro de aproximadamente 4500 millones de años, son las principales responsables del enriquecimiento del medio interestelar. En la fase llamada rama asintótica de las gigantes, estas estrellas crean una envoltura a su alrededor, que se forma debido a intensos procesos de pérdida de masa. Dichas envolturas están compuestas principalmente por granos de polvo y moléculas en fase gaseosa, que se forman de manera eficiente en las atmósferas de estos objetos. Estos compuestos experimentan distintos procesos físico-químicos en las envolturas circunestelares, que llevan a la producción de nuevas especies. Las condiciones físicas en las envolturas circunestelares se conocen de manera bastante precisa. Por estas razones estos objetos son excelentes laboratorios para estudiar y comprender la complejidad molecular y la evolución química del Universo.

Los procesos radiativos y colisionales que se dan en las envolturas de las estrellas evolucionadas, pueden modificar el estado cuántico de las moléculas. En particular, a las temperaturas que encontramos en estas envolturas circunestelares (cercanas a 2500 K cerca de la fotosféra de la estrella hasta ∼10 K en las zonas más externas), se producen numerosas transiciones del estado rotacional de las moléculas, que producen líneas de emisión detectables en el rango de longitud de onda milimétrico. Del análisis de estas líneas de emisión obtenemos información sobre la composición y propiedades de las envolturas, para lo que debemos observar este rango de longitud de onda. Los últimos avances en el campo de la instrumentación están permitiendo observar las envolturas circunestelares de estrellas evolucionadas, en esta región del espectro electromagnético, con una sensibilidad, y resolución tanto espacial como espectral, sin precedentes. Nos encontramos en la era de ALMA, Herschel, IRAM-30 m, NOEMA y otros muchos instrumentos que están impulsando importantes descubrimientos y cambiando la visión de las envolturas circunestelares y del Universo en general.

En esta tesis, se presentan los resultados obtenidos del estudio de la emisión molecular de tres envolturas circunestelares alrededor de estrellas evolucionadas: IKTau, OH231.8+4.2, e IRC+10216. IKTau y OH231.8+4.2 son envolturas ricas en oxígeno ([C]/[O]<1) cuyas propiedades físicas están relativamente bien determinadas. Sin embargo, no se conoce el inventario molecular completo de ambas fuentes dado que hasta la fecha no han sido extensivamente estudiadas, debido a que la química del oxígeno es menos rica que la del carbono. IRC+10216 es una envoltura rica en carbono ([C]/[O]>1), en particular, es la envoltura circunestelar más estudiada del Universo por sus propiedades y su riqueza química. En el caso de las envolturas ricas en oxígeno, hemos llevado a cabo dos barridos espectrales en el rango milimétrico utilizando la antena de IRAM-30 m, y también observaciones de OH231.8+4.2 con el instrumento HIFI de Herschel. Este trabajo nos ha permitido obtener el inventario molecular, caracterizar

las propiedades físicas de la emisión molecular, y determinar las abundancias de las moléculas presentes en ambos objetos. Respecto a IRC+10216, presentamos las primeras observaciones de alta resolución espacial obtenidas con ALMA, para moléculas como el SiO, el SiS, o el SiC_2, además de otros resultados obtenidos con IRAM-30 m y ALMA.

Los principales resultados obtenidos muestran que la química de los objetos ricos en oxígeno no es tan pobre como se podía anticipar. Hemos descubierto por primera vez la emisión de moléculas como HNCO, HNCS, HC_3N, NO, o SO^+, en la envoltura de OH231.8+4.2. También hemos detectado por primera vez líneas de emisión de H_2CO, NS, o NO en IKTau, además de haber detectado por primera vez sin ambigüedad emisión de SO_2 caliente (T$\sim$290 K) en la región más interna de la envoltura, lo que no se esperaba de acuerdo a los modelos químicos actuales. Los barridos espectrales de ambos objetos apoyan la idea de que la química de OH231.8+4.2 ha sido probablemente alterada por choques de alta velocidad causados por la interacción entre el viento AGB lento y los vientos rápidos (de unos pocos 100 km s^{-1}) bipolares altamente colimados. En el caso de IRC+10216 hemos detectado líneas de emisión de SiS de niveles vibracionalmente excitados hasta v=7, que provienen de la región más interna ($<50\,R_*$) y caliente de la envoltura. Mediante las observaciones con ALMA, hemos determinado también que el SiC_2 es la molécula portadora de enlaces de Si-C más abundante (en fase gas) en la región de formación de polvo de IRC+10216. Hemos caracterizado también la distribución espacial de la emisión de otras moléculas como el CH_3CN o algunos metales como el NaCl, o el KCl.

Gracias al trabajo realizado en esta tesis, hemos obtenido resultados satisfactorios en los comités de asignación de tiempos de NOEMA y ALMA, para continuar con el estudio de la emisión molecular en estos objetos. Nuestro trabajo servirá como futura referencia para los estudios de envolturas circunestelares de estrellas evolucionadas, especialmente para las envolturas ricas en oxígeno.

CONSTANTS AND UNITS

The constants, units, and conversion factors given in this table are taken from the values provided by the IAU (Wilkins, 1989), the NIST (Mohr et al., 2015), and Tarduno et al. (2014) and references therein. Numbers between parentheses represent the uncertainties (1σ) of the last digits of the corresponding value.

PHYSICAL CONSTANTS AND UNITS OF INTEREST	
Name	Value in CGS units
Speed of light in vacuum	$c = 2.99792458 \times 10^{10}\,\mathrm{cm\,s^{-1}}$
Planck's constant	$h = 6.626070040(81) \times 10^{-27}\,\mathrm{erg\,s}$
Boltzmann's constant	$k,\ k_\mathrm{b} = 1.38064852(79) \times 10^{-16}\,\mathrm{erg\,K^{-1}}$
Gravitational constant	$G = 6.67259(85) \times 10^{-8}\,\mathrm{cm^3\,g^{-1}\,s^{-2}}$
Atomic mass unit	$\mathrm{amu} = 1.660539040(20) \times 10^{-24}\,\mathrm{g}$
Stefan-Boltzmann constant	$\sigma = 5.670367(13) \times 10^{-5}\,\mathrm{erg\,cm^{-2}\,K^{-4}\,s^{-1}}$
Elementary charge	$e = 4.803204671(29) \times 10^{-10}\,\mathrm{statC}$ or esu
Electron mass	$m_\mathrm{e} = 9.10938356(11) \times 10^{-28}\,\mathrm{g}$
Proton mass	$m_\mathrm{p} = 1.672621898(21) \times 10^{-24}\,\mathrm{g}$
Neutron mass	$m_\mathrm{n} = 1.674927471(21) \times 10^{-24}\,\mathrm{g}$
Debye	$1\,\mathrm{D} = 10^{-18}\,\mathrm{statC\,cm}$
Astronomical unit	$1\,\mathrm{AU} = 1.495979 \times 10^{13}\,\mathrm{cm}$
Parsec	$1\,\mathrm{pc} = 3.085678 \times 10^{18}\,\mathrm{cm}$
Solar mass	$M_\odot = 1.98855(24) \times 10^{33}\,\mathrm{g}$
Solar radius	$R_\odot = 6.95660(100) \times 10^{10}\,\mathrm{cm}$
Solar luminosity	$L_\odot = 3.8270(44) \times 10^{33}\,\mathrm{erg\,s^{-1}}$
Effective solar temperature	$T_{\mathrm{eff},\odot} = 5771.8\,\mathrm{K}$
Jansky	$1\,\mathrm{Jy} = 10^{-23}\,\mathrm{erg\,cm^{-2}\,s^{-1}\,Hz^{-1}}$
1 year (in Julian days)	$1\,\mathrm{yr} = 365.25\,\mathrm{d} = 3.15576 \times 10^{6}\,\mathrm{s}$
K to eV†	$8.6173303(50) \times 10^{-5}\,\mathrm{eV\,K^{-1}}$
†eV	$1.6021766208(98) \times 10^{-12}\,\mathrm{erg}$
K to cm^{-1}	$0.69503457(40)\,\mathrm{cm^{-1}\,K^{-1}}$
K to Hz	$2.0836612(12) \times 10^{10}\,\mathrm{Hz\,K^{-1}}$

ACRONYMS

Acronyms are written in their original language, and abbreviations are written both in English and Spanish according to their usage throughout this thesis manuscript.

AAS — American Astronomical Society
ACA — Atacama Compact Array
AFCRL — AirForce Cambridge Research Laboratory
AFGL — AirForce Geophysics Laboratory
AGB — Asymptotic Giant Branch
ALMA — Atacama Large Millimeter Array
APEX — Atacama Pathfinder EXperiment
CAB — Centro de AstroBiología
CARMA — Combined Array for Research in Millimeter Astronomy
CDMS — Cologne Database for Molecular Spectroscopy
CIT — California Institute of Technology
CMBR — Cosmic Microwave Background Radiation
CNRS — Centre National de la Recherche Scientifique
COM — Complex Organic Molecule
CR — Cosmic Ray
CRESU — Cinétique de Réaction en Ecoulement Supersonique Uniforme
CRL — Cambridge Research Laboratory
CSE — CircumStellar Envelope
CSIC — Consejo Superior de Investigaciones Científicas
CSM — CircumStellar Medium
DSB — Double SideBand
E-AGB — Early Asymptotic Giant Branch
EM — ElectroMagnetic
EMIR — Eight MIxer Receiver
ERC — European Research Council
ESA — European Space Agency
ESO — European Southern Observatory
ETL — Equilibrio Termodinámico Local
FOV — Field Of View
FUV — Far UltraViolet
FWHM — Full Width at Half Maximum
FWZI — Full Width at Zero Intensity

GALEX — GALaxy Evolution eXplorer
GCVS — General Catalogue of Variable Stars
HB — Horizontal Branch
HBB — Hot Bottom Burning
HIFI — Heterodyne Instrument for the Far-Infrared
HPBW — Half-Power Beam Width
HR — Herztsprung-Russell
HSO — Herschel Space Observatory
HST — Hubble Space Telescope
IAU — International Astronomical Union
ICMM — Instituto de Ciencia de Materiales de Madrid
IEEE — Institute of Electrical and Electronics Engineers
IF — Intermediate Frequency
INTA — Instituto Nacional de Técnica Aeroespacial
IR — InfraRed
IRAM — Institut de Radioastronomie Millimétrique
IRAS — InfraRed Astronomical Satellite
IRC — InfraRed Compact catalogue
ISM — InterStellar Medium
ISO — Infrared Space Observatory
ISRF — InterStellar Radiation Field
JANAF — Joint Army-Navy-Air Force
JPL — Jet Propulsion Laboratory
KIDA — KInetic Database for Astrochemistry
LAMDA — Leiden Atomic and Molecular DAtabase
LTE — Local Thermodynamical Equilibrium
LO — Local Oscillator
LVG — Large Velocity Gradient
LSR — Local Standard of Rest
MADEX — MADrid molecular spectroscopy EXcitation code
mas — milliarcsecond
MASER — Microwave Amplification by Stimulated Emission of Radiation
MB — Main Beam
MICINN — Ministerio de Ciencia e Innovación
MINECO — Ministerio de Economía y Competitividad
MRS — Maximum Recoverable Scale
NIST — National Institute of Standards and Technology
NAOJ — National Astronomical Observatory of Japan
NASA — National Aeronautics and Spatial Administration
NOEMA — NOrthern Extended Millimeter Array
NRAO — National Radio Astronomy Observatory
ODE — Ordinary Differential Equation
OVRO — Owens Valley Radio Observatory
PACS — Photoconductor Array Camera and Spectrometer
PAH — Polycyclic Aromtic Hydrocarbon
PdBI — Plateau de Bure Interferometer

PDR — PhotoDissociation Region
PES — Potential Energy Surface
PN — Planetary Nebulae
pPN — pre-Planetary Nebula and/or proto-Planetary Nebula
PSF — Point Source Function
RGB — Red Giant Branch
rms — Root Mean Square
SED — Spectral Energy Distribution
SMA — SubMillimeter Array
SOFIA — Stratospheric Observatory For Infrared Astronomy
SPIRE — Spectral and Photometric Imaging REceiver
SSB — Single SideBand
TE — Thermodynamical Equilibrium
TP-AGB — Thermally Pulsing Asymptotic Giant Branch
UDfA — UMIST Database for Astrochemistry
UMIST — University of Manchester Institute of Science and Technology
UV — UltraViolet
VLA — Very Large Array
VLT — Very Large Telescope
VLBI — Very Large Baseline Interferometry
YHG — Yellow HyperGiant
YSO — Young Stellar Object
WFPC2 — Wide Field Planetary Camera 2
ZAHB — Zero Age Horizontal Branch

CONTENTS

Declaración de originalidad / Declaration of originality

Agradecimientos **I**

Summary **III**

Resumen **V**

Constants and units **VII**

Acronyms **IX**

Contents **XI**

List of figures **XV**

List of tables **XIX**

1 Introduction **XXI**

1

1.1 Molecular Astrophysics: historical perspective 1
1.2 Molecular astrophysics presently 5
1.3 Circumstellar envelopes: relevance and present 8
1.4 Motivation and structure of this PhD thesis 9
1.4.1 Studied objects in this thesis 12
1.4.1.1 IK Tau 12
1.4.1.2 OH231.8+4.2 14
1.4.1.3 IRC+10216 16

1 Introducción **19**
1.1 Astrofísica molecular: perspectiva histórica 19
1.2 Actualidad de la astrofísica molecular 23
1.3 Envolturas circunestelares: relevancia y actualidad 26
1.4 Motivación y estructura de esta tesis 28
1.4.1 Objetos estudiados en esta tesis 30
1.4.1.1 IK Tau 31
1.4.1.2 OH231.8+4.2 33

1.4.1.3 IRC+10216 35

2 Tools for this PhD thesis **39**
2.1 Population diagrams 39
2.2 MADEX 41
2.3 Chemical codes 42
2.3.1 Thermodynamical equilibrium: LTEINNER 42
2.3.2 Chemical kinetics: CHEMCLOUD 42

3 Spectral line surveys: IK Tau and OH231.8+4.2 **45**
3.1 Summary 45
3.2 Resumen 49
3.3 Velilla Prieto et al. 2017 53
3.4 Velilla Prieto et al. in prep: OH231 survey 101
3.4.1 Line identification 102
3.4.2 Observational results 114
3.4.3 Rotational diagrams 127
3.4.4 Abundances and isotopic ratios 134

4 New N-bearing species toward OH231.8+4.2 **137**
4.1 Summary 137
4.2 Resumen 141
4.3 Velilla Prieto et al. 2015a 145

5 Molecular ions in the O-rich CSE OH231.8+4.2 **167**
5.1 Summary 167
5.2 Resumen 171
5.3 Sánchez Contreras et al. 2015 175

6 Si-bearing molecules toward IRC+10216 **197**
6.1 Summary 197
6.2 Resumen 200
6.3 Velilla Prieto et al. 2015b 203

7 IRC+10216: further studies **211**
7.1 Time variability of the spectral line emission 211
7.2 Detection of SiCSi toward IRC+10216 211
7.3 Mid-IR observations of SiS isotopologues 213
7.4 The ALMA view of IRC+10216: CH_3CN and metals 214
7.5 First page of publications 217

8 General discussion and conclusions **223**
8.1 General discussion 223
8.2 Conclusions 227

8 Discusión general y conclusiones **231**
8.1 Discusión general 231
8.2 Conclusiones 235

9 Current and future work **239**
9.1 Current work . . . 239
9.2 Future approach to several unsolved problems . . . 240

A Circumstellar envelopes: basic concepts **243**
A.1 Brief description of stellar evolution . . . 243
A.2 Formation, evolution, and properties . . . 246
A.2.1 Formation . . . 246
A.2.2 Evolution . . . 246
A.2.3 Observations . . . 248
A.2.4 Physical properties of CSEs . . . 249
A.3 Circumstellar chemistry . . . 254
A.3.1 Elemental composition: carbon vs oxygen . . . 254
A.3.2 Molecular formation . . . 254
A.3.3 Isotopologues . . . 256

B Theory and methods **257**
B.1 Circumstellar chemistry . . . 257
B.1.1 Types of reactions . . . 258
B.1.2 Equilibrium chemistry . . . 261
B.1.3 Chemical kinetics . . . 262
B.2 Formation of rotational lines . . . 263
B.2.1 Radiation-matter interaction . . . 263
B.2.2 Molecular rotational spectroscopy . . . 276
B.3 Line detection: radiotelescopes . . . 280
B.3.1 Single dish observations . . . 281
B.3.2 Basic concepts of millimeter interferometry . . . 287

C Contribution and list of publications **293**
C.1 Personal contribution . . . 293
C.2 Publications in peer-reviewed journals . . . 294
C.2.1 Pillar papers of this thesis . . . 294
C.2.2 Co-author papers . . . 294
C.3 Non-refereed publications and conference contributions . . . 296

Bibliography **299**

LIST OF FIGURES

1.1 Antennas designed and built by K. G. Jansky and G. Reber 2
1.2 Map of our Galaxy at 160 MHz by G. Reber 3
1.3 Atmospheric transparency for the EM spectrum between 0.1 nm and 1 km 4
1.4 IRAM-30 m, NOEMA, and ALMA radiotelescopes 5
1.5 H_2O image at 179 μm toward the class 0 protostar L1157 6
1.6 CO J=3–2 map toward the CSE of R Sculptoris observed with ALMA 8
1.7 The life-cycle of stars 9
1.8 Image of IK Tau observed with the HST with the F606W filter of WFPC2 and also of the ^{12}CO J=2–1 line with IRAM-PdBI 12
1.9 Images of OH231.8+4.2 observed with the HST and the ^{12}CO J=2–1 line with the IRAM-PdBI 15
1.10 Images of IRC+10216 observed with GALEX and the IRAM-30 m radiotelescope 17

1.1 Antenas construidas y diseñadas por K. G. Jansky y G. Reber 20
1.2 Mapa de La Galaxia tomado por G. Reber a 160 MHz 21
1.3 Esquema de la transparencia atmosférica en el espectro electromagnético entre 0.1 nm y 1 km 23
1.4 Radiotelescopio de IRAM-30 m, NOEMA y ALMA 24
1.5 Imagen de H_2O a 179 μm de la protoestrella de clase 0 L1157 24
1.6 Mapa de la línea CO J=3–2 en la envoltura circunestelar de R Sculptoris observado con ALMA 25
1.7 Ciclo de vida de las estrellas 28
1.8 Imagen de IK Tau con el HST tomada con el filtro F606W de la WFPC2 y con IRAM-PdBI de ^{12}CO J=2–1 31
1.9 Imágenes de OH231.8+4.2 con el HST y con IRAM-PdBI de ^{12}CO J=2–1 34
1.10 Imágenes de IRC+10216 tomadas con GALEX y el radiotelescopio IRAM-30 m . 36

3.1 IRAM-30 m spectral line survey of OH231.8+4.2 102
3.2 Rotational diagram of CO isotopologues toward OH231.8+4.2 127
3.3 Rotational diagram of SiO isotopologues toward OH231.8+4.2 128
3.4 Rotational diagram of SiS toward OH231.8+4.2 128
3.5 Rotational diagram of HCN and HNC isotopologues toward OH231.8+4.2 129
3.6 Rotational diagram of CS isotopologues toward OH231.8+4.2 129
3.7 Rotational diagram of H_2CO isotopologues toward OH231.8+4.2 130
3.8 Rotational diagram of H_2S isotopologues toward OH231.8+4.2 130

3.9 Rotational diagram of OCS isotopologues toward OH231.8+4.2 131
3.10 Rotational diagram of SO isotopologues toward OH231.8+4.2 131
3.11 Rotational diagram of SO_2 isotopologues toward OH231.8+4.2 132
3.12 Rotational diagram of NS isotopologues toward OH231.8+4.2 132
3.13 Rotational diagram of N-bearing species toward OH231.8+4.2 133
3.14 Rotational diagram of ions toward OH231.8+4.2 133

7.1 Time variability of the intensity of CCH lines toward IRC+10216 212
7.2 Circumstellar chemistry model of Si-C bond bearing molecules in IRC+10216 . . 213
7.3 CH_3CN maps observed with ALMA toward IRC+10216 214
7.4 Emission of NaCl as observed with ALMA toward IRC+10216 215

9.1 Sample of the spectrum of IRC+10216 as observed with NOEMA 241

A.1 Evolutionary track of a $2\,M_\odot$ star in the HR diagram 244
A.2 Sketch of the stellar interior of RGB and E-AGB stars 245
A.3 Images of the CSE IRC+10216 247
A.4 Images of several planetary nebulae observed with the HST 247
A.5 Physical properties of a CSE 249
A.6 Thermodynamical equilibrium models for O- and C-rich CSEs 255

B.1 Sketch of the circumstellar chemistry 258
B.2 Radiative transport diagram 266
B.3 Two energy levels system 266
B.4 Radiative transfer in a CSE 274
B.5 Principal moments of inertia of an asymmetric rotor 278
B.6 ALMA in Chajnantor (Chile) 281
B.7 Beam pattern of a single dish antenna 282
B.8 Atmospheric transmission models with ASTRO (ATM85) 284
B.9 Signal delay for a two element interferometer 288
B.10 Sketch of the observation with a two element interferometer 289
B.11 Example of coverage and visibilities with NOEMA 290
B.12 Example of dirty beam and clean image for NOEMA 292

LIST OF TABLES

1.1 Detected molecules in the ISM and the CSM up to June, 2016 7
1.2 Stellar and circumstellar parameters of IK Tau 13
1.3 Stellar and circumstellar parameters of OH231.8+4.2 14
1.4 Stellar and circumstellar parameters of IRC+10216 17
1.5 Molecular inventory of IRC+10216 18

1.1 Moléculas detectadas en el medio interestelar y circunestelar hasta Junio de 2016 27
1.2 Parámetros de la estrella y de la envoltura circunestelar de IK Tau 32
1.3 Parámetros de la estrella y de la componente central de expansión lenta de OH231.8+4.2 33
1.4 Parámetros de la estrella y de la envoltura circunestelar IRC+10216 36
1.5 Inventario molecular de IRC+10216 37

2.1 Elemental abundances used in the TE models of O-rich CSEs 42

3.1 Measured and spectroscopic parameters of the detected lines in the survey of OH231.8+4.2 114
3.2 Results from the rotational diagrams of the molecules in OH231.8+4.2 134
3.3 Isotopic ratios obtained from the survey of OH231.8+4.2 135

8.1 Molecular inventory of IKTau after our work 224
8.2 Molecular inventory of OH231.8+4.2 after our work 225

8.1 Inventario molecular en IKTau tras nuestro trabajo 232
8.2 Inventario molecular en OH231.8+4.2 tras nuestro trabajo 233

B.1 Examples of reaction types in CSEs 260

CHAPTER

1

INTRODUCTION

This chapter introduces and contextualises this thesis within the research field of molecular astrophysics and circumstellar envelopes in particular, reviewing the most relevant and current aspects of their study. The motivation of this PhD thesis as well as the structure of the manuscript are explained. The properties of the three studied circumstellar envelopes, IKTau, OH231.8+4.2, and IRC+10216, are compiled.

1.1 Molecular Astrophysics: historical perspective

Molecular astrophysics is the branch of astrophysics that seeks to understand the Universe through the study of molecules, in particular the study of electromagnetic radiation produced by molecules (either emitted, absorbed or scattered by them), that we receive from those astrophysical environments that contain a molecular component. From the Earth, the Sun and the Solar system, the interstellar medium, exoplanets, clouds, nebulae, stars, and galaxies, molecules are found in all kind of objects. However, molecules require that certain physical conditions (temperature, density, radiation ...) are given in order to be formed. These particular conditions occur only at very specific places in the Universe, which draw our attention given that we are made of molecules.

The first detections of molecules, beyond the Earth and its atmosphere, date back to the second half of the nineteenth century. Simple molecules such as C_2 were detected toward the Donati comet, or CN in the 1881b comet (Donati, 1864, Huggins, 1881). But if we consider molecules in the ISM, first molecules were detected during the twentieth century. CH^+, CH, and CN were detected studying the optical absorption spectrum (4230-4300 Å) of the ISM through observations in the visible wavelength range using the Mount Wilson Observatory (Swings & Rosenfeld, 1937, McKellar, 1940, Douglas & Herzberg, 1941). Nevertheless, the real development of this branch of astrophysics occurred in parallel with the development of radio astronomy. In 1928, Karl G. Jansky, a recent graduate student at the University of Wisconsin, began to work for Bell laboratories with the purpose of investigate the origin of static noise on transatlantic radio communications. Two years later, Jansky decided to build an antenna that tuned to receive signals at 20.5 MHz (Fig. 1.1). After the analysis of the signals he recorded for about two years, Jansky was able to identify two different sources of static noise, whose origin was related to storms, and an additional source of noise of unknown origin. In 1933, Jansky published his results, and he concluded that the data collected proved the existence of EM waves that seemed to come from a fixed direction in space (Jansky, 1933, Brittain, 1984). Jansky noted that he was not able to determine the origin of that signal, although, he

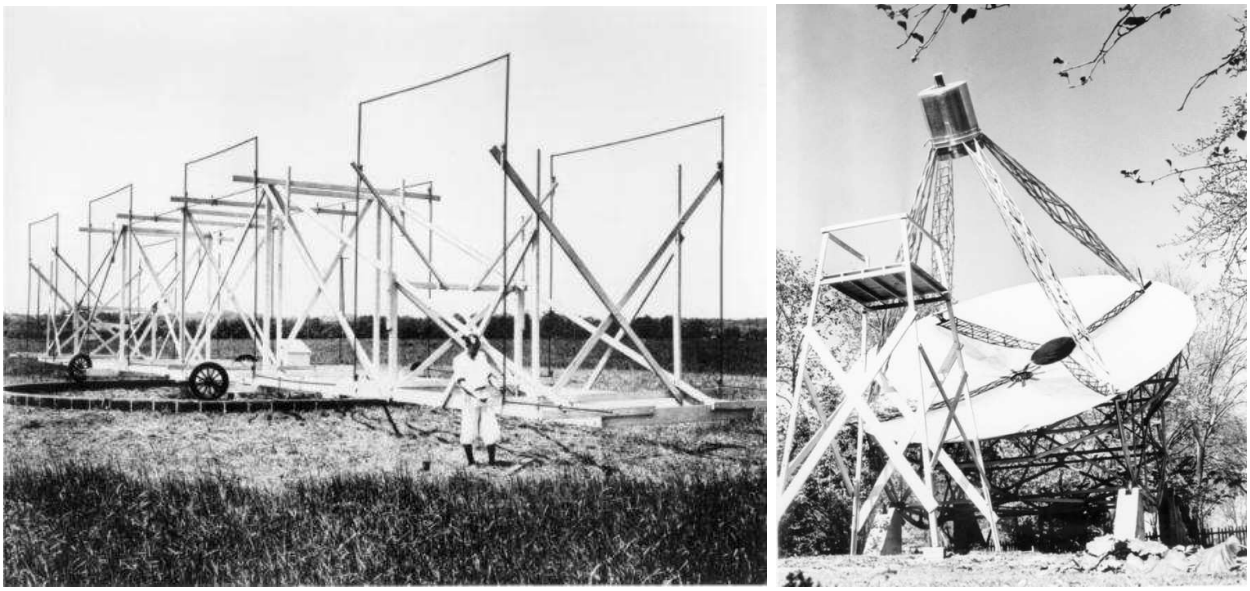

Figure 1.1: Left, picture of the antenna built by K. G. Jansky. Right, radiotelescope built by G. Reber. *(Credits: NRAO)*

mentioned that one of the most fascinating plausible explanation, would point to somewhere in the Milky Way. Jansky proposed to Bell laboratories to continue his research by building a 30 m antenna, without success, due to the economical crisis during "the great depression". In his honour, the unit commonly used to measure flux density in radioastronomy is named Jansky.

In 1937, an engineer from Chicago called Grote Reber, decided to construct his own radiotelescope motivated by Jansky's work. He wondered about the origin of the static noise, and this curiosity lead him to build this radiotelescope by his own means. The radiotelescope consisted of a parabolic reflector of approximately 9 m of diameter, equipped with receivers constructed also by Reber (Fig. 1.1). He carried out his observations by night, since the combustion engines of the epoch produced interferences in the receiver system. Eventually, in 1940, he managed to publish the results of his research showing the first maps of the 160 MHz (λ=1.87 m) EM radiation with his radiotelescope (Reber, 1940, 1944). Reber noted that the noise must be somehow related to the amount of matter in space, because absorption owing to dust should be small at that particular wavelength range. Thus, these maps indicate the amount of matter that lies between us and the edge of our Galaxy, and that the detected maxima would trace the direction of the projections of the Galaxy, which could be similar to the spiral arms observed toward other spiral nebulae. In that case, Reber suggests that the Galaxy centre would be in the direction of Sagittarius, and the spiral arms should be located in the directions of Cygnus, Cassiopeia and Canis Major. Additionally, the minimum in Perseus' direction would indicate that we are near to the Galaxy edge in this direction (Fig. 1.2).

During the following years, due to the Second World War, radio communication systems experienced a great technical development, which promoted the progress of radioastronomy. In 1951, H. I. Ewen and E. M. Purcell published the detection of the neutral hydrogen line at 21 cm toward our Galaxy (Ewen & Purcell, 1951). But it was in 1963, when the first interstellar molecule was detected through observations in the radio wavelength range, OH (Weinreb et al., 1963). Since then, evolution of detection techniques and radiotelescopes (in the whole ra-

Figure 1.2: First (radio) map of the sky as observed by G. Reber at 160 MHz. The directions to the different constellations (Cassiopeia, Cygnus and Sagittarius) are shown in the map. *(Credits: Reber (1944))*

dio wavelength range) led to a cascade of new molecular detections toward the ISM (e.g. Cheung et al., 1969, Wilson et al., 1970, 1971, Townes, 1977). Of course, these technological improvements in radioastronomy led also to great discoveries not only related with the detection of molecules. For example, the measurement of the CMBR temperature by A. A. Penzias and R. W. Wilson, which was awarded in 1978 with the Nobel prize for its implication in the Big Bang theory (Penzias & Wilson, 1965).

Besides radioastronomy, molecular astrophysics as a scientific discipline is closely related to spectroscopy. From a historical point of view, spectroscopy has progressed thanks to the contribution of many great scientist like I. Newton, T. Young, G. Stokes, E. Morley, A. A. Michelson, etcetera. The experiments designed for and carried out by spectroscopists are based on the use of mechanical devices (e.g. vacuum chambers), optical devices (e.g. lasers) and electronic devices (e.g. transistors), and electromagnetism and quantum physics theories. Therefore, analogous to radioastronomy, the twentieth century has been a qualitative leap forward for spectroscopy owing to the progress made in semiconductors and solid state devices. It has to be mentioned one of the most important leading figures in the field of spectroscopy, G. Herzberg (1904-1999), who was awarded with the chemistry Nobel prize in 1971, in recognition of his contribution to the research about molecular structure. His classical trilogy published in the mid-twentieth century is still considered as the "Book" of molecular spectroscopy (Herzberg, 1939, 1945, 1966).

Synergy between these disciplines has allowed to witness important discoveries in the molecular astrophysics field in the latest decades of the twentieth century. Concerning the first molecular detections mentioned before, it is worth noting the detection of CO (Wilson et al., 1970). The Universe is mainly composed of atomic H, and the most abundant molecule in the ISM is H_2. The total H_2 mass in our Galaxy is estimated to be approximately $0.84{\times}10^9\,M_\odot$, which

represents about ∼20 % of the total H, while the remaining ∼80 % is in the form of neutral H (∼60 %) and ionized H (∼20 %) (Draine, 2011). However, H_2 is difficult to detect, since it is a homonuclear molecule,[1] highly symmetric. Thus, its electrical charge is symmetrically arranged and, consequently, it has no electrical permanent dipole moment. This means that in the observable wavelength range from Earth, it is not possible to observe how H_2 is distributed along the ISM at low temperatures (∼10–50 K), given that its electronic or quadrupole transitions would trace warmer regions or cannot be observed from Earth's surface. Nevertheless, CO has an electrical permanent dipole moment and therefore, it has several transitions that are observable from Earth, and it has been extensively used to trace the distribution of cold molecular gas toward different regions of our Galaxy and other galaxies. CO has been proved to be an excellent molecular gas tracer (e.g. Dickman et al., 1986, Heyer & Dame, 2015).

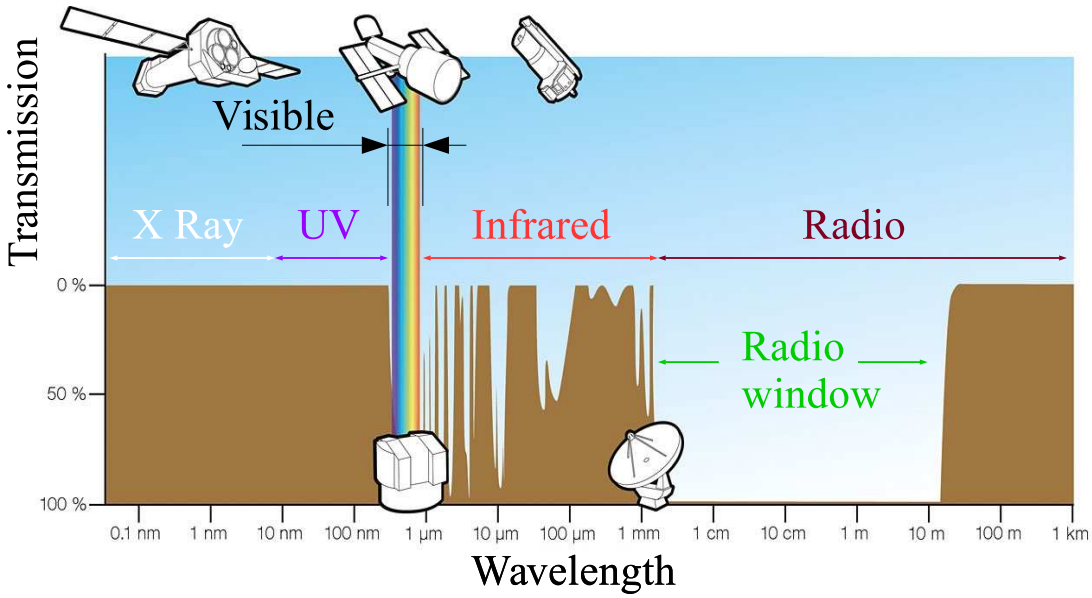

Figure 1.3: Sketch of the atmospheric transparency for the wavelengths between X-rays up to radio. The radio window is shown, as well as several miniatures of the most relevant telescopes, for example: Chandra (X-rays), HST (in the optical/visible wavelength range from space), William Herschel (in the optical/visible form Earth's surface), ISO (in the infrared from space), and IRAM (as a radiotelescope). *(Credits: Adapted from ESA/Hubble F. Granato)*

Finally, another great milestone in molecular astrophysics (and also for all radioastronomy related astrophysical branches) is the application of interferometry for the so-called aperture synthesis. During the last third of the twentieth century and supported by the first discoveries in the radioastronomy field, institutions began to invest in the construction of radiotelescopes of different sizes to cover the whole long-wavelength region of the EM spectrum where the atmosphere is transparent, i.e. the radio window which covers wavelengths between a millimeter up to a few meters (Fig. 1.3). The 40 m antenna of OVRO, the 100 m antenna in Effelsberg or the IRAM-30 m antenna (Fig. 1.4) are some examples of these radiotelescopes. However, spatial resolution of single dish radiotelescopes is limited by the size of the dish (see Sect. B.3.2), given that it is difficult, from the technical point of view, to build huge antennas to obtain high spatial resolutions. Interferometry allows to obtain high spatial resolution by using an array

[1] A molecule composed of equal atoms.

Figure 1.4: Left, IRAM-30 m radiotelescope located near Veleta peak in Granada, Spain. Center, group of several antennas of the NOEMA interferometer, located near the Bure peak in the Alps, France. Right, antenna of ALMA located in the "Alto del Chajnantor", Chile. *(Credits: NOEMA image by C. Lefevre/IRAM and ALMA image by B.Tafreshi/ESO)*

of several antennas, in such a way that it would be like virtually observing with an antenna that has the same diameter as the maximum separation between a pair of the antennas in the array. Interferometers like the VLA, CARMA, or PdBI (now NOEMA) allowed us to increase our knowledge of the Universe up to scales that single dish radioastronomy could not yet.

1.2 Molecular astrophysics presently

The study of the molecular Universe during the latest years has led to different scientific discoveries, which have settled the basis of the field, and have served to carry out important instrumental challenges in the infrared and radio wavelength ranges. Single dishes, whose construction was finished in the last third of the twentieth century, have progressively improved their capabilities thanks to the new generation of Fourier transform spectrometers, and heterodyne and superheterodyne receivers. These devices have allowed to reach better image band attenuation or improve the instantaneous observable bandwidth. These upgrades have been recently installed for example in the IRAM-30 m radiotelescope (EMIR, Carter et al., 2012).

Concerning to space telescopes, it has been successfully carried out one of the most ambitious projects ever conceived, the *Herschel* telescope. This telescope was built by ESA, and it was launched and put into orbit in 2009. This telescope has a 3.5 m diameter, and it observed the Universe in the wavelength range from 55 up to 672 μm until 2013, when the telescope ran out of liquid He (approximately 2000 litres), which is the instrumentation coolant. The scientific community is still working on the analysis of the data collected by the Herschel Space Observatory. Among its accomplishments, it is worth noting for instance, the observation of the distribution of H_2O toward star forming regions (van Dishoeck et al., 2011, and following

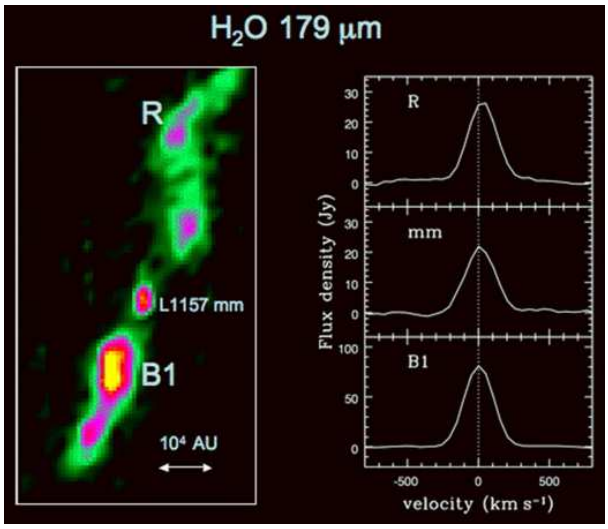

Figure 1.5: H_2O image at 179 μm of the class 0 protostar L1157 observed with PACS instrument (on-board the Herschel Space Observatory) with the corresponding spectra toward the three different positions shown in the image: R, mm, and B1. *(Credits: van Dishoeck et al. (2011))*

articles, see Fig. 1.5), the study of Solar system objects (Küppers et al., 2014), or the detection of H_2O toward the innermost regions of the C-rich CSE IRC+10216 (Decin et al., 2010c).

The latest four years have been undoubtedly influenced by the ALMA interferometer. ALMA is an interferometer composed of 66 antennas (54 of them have a diameter of 12 m, and the remaining 12 antennas have a diameter of 7 m), which is built in the "Alto del Chajnantor" in Chile at approximately 5000 m above sea level. ALMA is equipped with receivers that allow to observe in the 0.32 up to 3.57 mm wavelength range (or equivalently in the frequency range from 950 up to 84 GHz), which is currently conducting its Cycle 4 science observations with ∼50 fully operational antennas. This interferometer has an unprecedented sensitivity and angular resolution, which can reach baselines as long as ∼16 km which will allow (when the observatory becomes completed) to achieve a spatial resolution of a few milliarcsecond. A total of 1571 proposals have been submitted for the latest ALMA Cycle 4 call for proposals, where a third of the total are proposals related to ISM, stellar formation, astrochemistry, stellar evolution and the Sun. ALMA has produced great impact results on molecular astrophysics during its three first years of life. For instance, the CO spiral structure observed toward the AGB star R Sculptoris (Maercker et al., 2012, see Fig. 1.6), or the high spatial resolution image of the protoplanetary disk around the star HL Tau (ALMA Partnership et al., 2015).

Finally, concerning to molecular detections, ∼190 molecules have been detected toward the ISM and the circumstellar medium up-to-date (Table 1.1). Among them, we can find different kind of molecules like radicals[2](e.g. SO), ions (e.g. N_2H^+, HCO^+ o C_6H^-), or complex organic molecules[3](e.g. C_{60}, C_{70}, CH_2CCHCN). As it will be discussed throughout this thesis, each molecule provides information about the regions where they are located, like the morphology, kinematics, dynamics and chemistry of these environments and objects.

[2]Molecules which have at least one unpaired valence electron.

[3]A given organic molecule is considered as a COM if it has six or more than six atoms (Herbst & van Dishoeck, 2009)

Table 1.1: Detected molecules in the ISM and the CSM up to June, 2016.

2-atoms	3-atoms	4-atoms	5-atoms	6-atoms or more	
H_2	C_3	c-C_3H	C_5	C_5H	HC_7N
AlF	C_2H	l-C_3H	C_4H	l-H_2C_4	C_8H
AlCl	C_2O	C_3N	C_4Si	C_2H_4	$CH_3C(O)NH_2$
C_2	C_2S	C_3O	l-C_3H_2	CH_3CN	C_8H^-
CH	CH_2	C_3S	c-C_3H_2	CH_3NC	C_3H_6
CH^+	HCN	C_2H_2	H_2CCN	CH_3OH	CH_3CH_2SH(?)
CN	NCO	H_2CS	CH_4	CH_3SH	CH_3C_5N
CO	HCO^+	H_3O^+	HC_3N	HC_3NH^+	$(CH_3)_2CO$
CO^+	HCS^+	c-SiC_3	HC_2NC	HC_2CHO	$(CH_2OH)_2$
CP	HOC^+	CH_3	HCOOH	NH_2CHO	CH_3CH_2CHO
SiC	H_2O	C_3N^-	H_2CNH	C_5N	CH_3C_4H
HCl	H_2S	PH_3	SiH_4	H_2CCNH(?)	C_6H^-
KCl	HNC	HCNO	H_2COH^+	C_5N^-	CH_3NCO
NH	HNO	HCCN	C_4H^-	HNCHCN	CH_3C_3N
NO	MgCN	$HCNH^+$	HC(O)CN	C_6H	c-C_6H_6
NS	MgNC	HNCO	HNCNH	CH_2CHCN	n-C_3H_7CN
NaCl	N_2H^+	HNCS	CH_3O	CH_3C_2H	i-C_3H_7CN
OH	N_2O	$HOCO^+$	NH_4^+	HC_5N	$C_2H_5OCH_3$(?)
PN	NaCN	H_2CO	H_2NCO^+(?)	CH_3CHO	CH_3CHCH_2O
SO	OCS	H_2CN	$NCCNH^+$	CH_3NH_2	CH_3CH_2OH
SO^+	SO_2	HMgNC	H_2C_2O	c-C_2H_4O	C_{60}
SiN	HCP	HCCO	H_2NCN	$HC(O)OCH_3$	C_{70}
SiO	CCP	HOCN	HNC_3	CH_3COOH	C_{60}^+
SiS	AlOH	HSCN		C_7H	
CS	H_2O^+	H_2O_2		C_6H_2	
HF	H_2Cl^+	C_3H^+		CH_2OHCHO	
HD	KCN	NH_3		l-HC_6H	
FeO(?)	FeCN			CH_2CHCHO(?)	
O_2	c-SiC_2			CH_2CCHCN	
CF^+	CO_2			H_2NCH_2CN	
SiH(?)	NH_2			CH_3CHNH	
PO	H_3^+			H_2CCHOH	
AlO	SiCN			l-HC_4H	
OH^+	AlNC			l-HC_4N	
CN^-	SiNC			c-H_2C_3O	
SH^+	HO_2			CH_3C_6H	
SH	TiO_2			C_2H_5OCHO	
HCl^+	C_2N			$CH_3OC(O)CH_3$	
TiO	Si_2C			HC_9N	
ArH^+				CH_3CH_2CN	
NO^+(?)				$(CH_3)_2O$	

Notes. The formulas tabulated correspond to the main isotopologues of the molecular species detected. Nevertheless, in numerous cases different isotopologues of the same species have been detected. Tentative detections are marked with (?). *(Source: CDMS, http://www.astro.uni-koeln.de/cdms/molecules)*

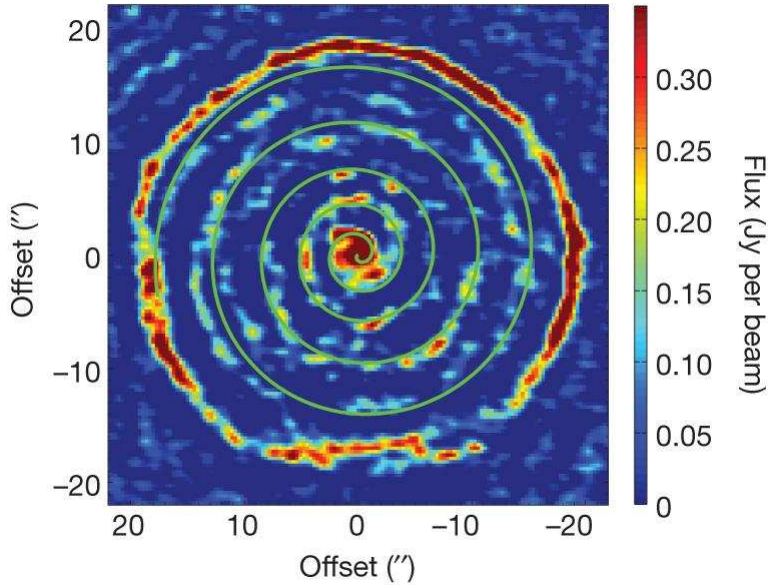

Figure 1.6: Map of the CO J=3–2 emission line toward the CSE of R Sculptoris observed with ALMA. This map corresponds to the emission at the systemic velocity of the source, and the colour scale goes from low flux density (blue) to high flux density (red). The green line represents the fit of the emission maxima observed to a spiral structure. *(Credits: Maercker et al. (2012))*

1.3 Circumstellar envelopes: relevance and present

Part of the molecules listed in Table 1.1 have been detected toward AGB CSEs. These envelopes are formed during the AGB stage of stars with main sequence masses between 0.8-8$M_{\odot}$, as a result to the intense mass loss process, in the form of a slow and dense stellar wind, which takes place during this evolutive stage. These CSEs surround the AGB star and are composed of gas and dust (e.g. Habing & Olofsson, 2003). AGB stars participate in the return to the ISM of a ∼50-80% of the total gaseous material and dust (Gehrz, 1989, Wallerstein & Knapp, 1998). This gas is mainly composed of molecules that are formed under the favourable conditions, i.e. high densities and low temperatures, that are found in the atmospheres of CSEs (see Fig. A.5). Molecular formation occurs due to different physico-chemical processes in these objects, which are considered as factories of molecules and dust grains. (see Sect. A). CSEs play an important role in the life cycle of the Universe, by processing simple material (in chemical terms) and synthesising more complex material (e.g. dust grains of silicates or molecules like NaCl), which will be injected to ISM. This life cycle will lead to a new stage of star-formation (Fig. 1.7). These objects are excellently suited to study the dust and molecular formation processes, the molecular complexity of the Universe, or radiative transfer problems, just to mention some of the most relevant works in the context of this thesis (e.g. Kwok, 1975, Goldreich & Scoville, 1976, Cernicharo & Guelin, 1987, Habing, 1996, Olofsson, 1996b, Agúndez et al., 2010b, Decin et al., 2010c, and references therein).

Presently, there are several research topics that gather the efforts and attention of the scientific community, although, some of them had their origin since the first observations of CSEs. The principal research topics are:

- molecular complexity studies, which address the variety of molecules that can be found toward CSEs (e.g. O-bearing molecules in C-rich CSEs and vice versa), and which are

the physico-chemical processes that form these molecules (e.g. shock induced formation or chemical modelling), and also the characteristics of their emission (e.g. Agúndez et al., 2010b, Decin et al., 2010a, Danilovich et al., 2016, Li et al., 2016),

- studies devoted to understand the dust formation processes, and their link to the formation of AGB winds (e.g. Bladh & Höfner, 2012, Karovicova et al., 2013, Gobrecht et al., 2016),
- observationally unbiased statistical studies, which try to extract general conclusions about CSEs properties. For example, about the HCN emission in different types of AGB stars (Schöier et al., 2013), or about the $^{12}CO/^{13}CO$ isotopic ratio (Ramstedt & Olofsson, 2014).

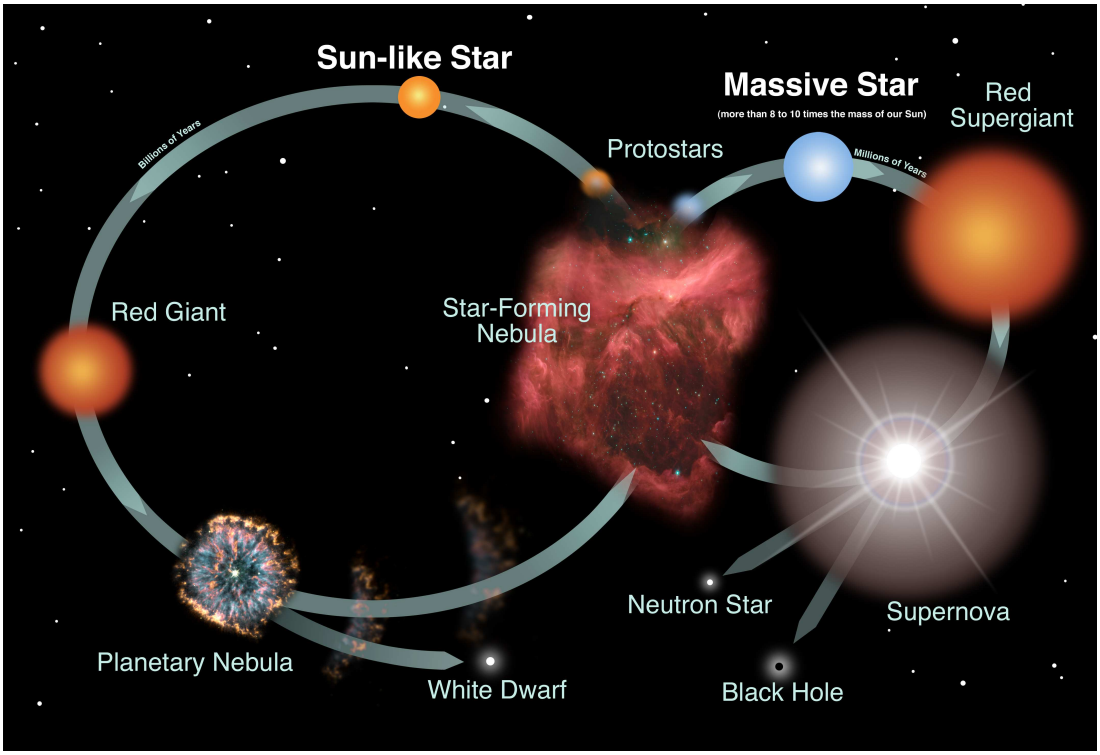

Figure 1.7: Sketch of the life-cycle of low-intermediate mass stars ($0.8M_{\odot} < m < 8M_{\odot}$, left), and massive stars (right path for stars with $m > 8M_{\odot}$), from their birth in star forming regions up to their deaths, and posterior return of material to ISM closing their life-cycle. *(Credits: NASA and Night Sky Network)*

ALMA is motivating an increasing number of observations toward CSEs. ALMA projects are mainly devoted to observe and to study the physico-chemical processes that occur in the innermost regions of CSEs, given the high spatial resolution provided (e.g. Cernicharo et al., 2013).

1.4 Motivation and structure of this PhD thesis

This thesis is framed in the context of molecular astrophysics, and the studies of molecular complexity in the circumstellar envelopes of AGB stars in the era of IRAM-30 m and ALMA. As it is shown throughout this thesis, the study of the emission lines (mainly rotational) of the

molecules in CSEs provide us with information about the mass loss rate of the star, excitation temperature of the gas, column densities, kinematics, chemical composition of gas and dust grains, or abundances. It is important to understand which molecules are formed, and how they are produced in AGB stars, given that these objects are major contributors to the molecular synthesis and processing in the Universe.

Goals

The main objective of this thesis is to characterise the molecular emission in circumstellar envelopes around AGB stars, using the most recent observational techniques (e.g. spectral surveys) and state-of-the-art instruments (e.g. IRAM-30 m or ALMA), as well as chemistry and radiative transfer codes (see Sect. 2.2 and 2.3). In particular, it is intended to characterise two oxygen rich circumstellar envelopes (IK Tau and OH231.8+4.2), whose physical properties are well known and have been studied in detail. Nevertheless, the chemical studies of these two objects previous to our work are based on observational studies limited to a scarce number of lines of the most abundant species. This is in part because carbon is more active than oxygen, therefore, most of the previous characterisation studies of circumstellar envelopes have been focused on C-rich objects. This thesis represents a huge difference compared to previous studies given that we have carried out complete spectral line surveys with the IRAM-30 m telescope instead of a study based on one or two lines of a few species. These studies allow us also to discover new molecular species in the circumstellar medium.

Additionally in this thesis, the emission observed of several molecules toward IRC+10216 is characterised. These observations represent the study of the first high spatial resolution ALMA maps toward this object for the lines observed. Among others, we have studied the emission of silicon bearing molecules, which are relevant for dust grain formation processes in AGB stars. This work aims to observe how these Si-bearing molecules are distributed in IRC+10216, and investigate the relevant physico-chemical processes that would form and destroy these species in the gas phase, and their role in dust grain formation.

Structure

This PhD thesis manuscript is presented as an article thesis or thesis by publications. The manuscript is divided in 9 chapters and 3 appendices. The manuscript is presented in English, given that is most commonly used for scientific communication and also because the thesis will aim for the European PhD recognition. Additionally, we present in Spanish the summary, the introduction and the conclusions (Chapters 1 and 8), as well as the summaries of each of the main articles of the thesis (Chapters 3 to 6). The Chapters 3, 4, 5, and 6 are presented starting from the most general work (i.e. the spectral line surveys) and going through the specific studied matters, without necessarily following the chronological order of the articles. The content is divided as follows:

- in Chapter 1 a general introduction is presented to contextualise the thesis and summarily present the historical perspective of a relatively young discipline such as molecular astrophysics, from its beginnings (Sect. 1.1), up to the most recent progress (Sect. 1.2), following the bibliography provided within the manuscript. There is also a brief introduction to the main topic of this thesis, i.e. the study of circumstellar envelopes. In this chapter, it is

also explained concisely the motivation and goals of the thesis. Finally, the studied objects are described, as well as their most relevant properties,

- in Chapter 2, we describe the specific analysis techniques used in this thesis (i.e. rotational diagrams, the radiative transfer code MADEX, and the chemical codes LTEINNER and CHEMCLOUD), which are complemented with the basic theoretical concepts summarised in Appendix B,
- in Chapter 3, the overall results obtained from the IRAM-30 m millimeter wavelength spectral line surveys toward the O-rich CSEs IKTau and OH231.8+4.2 are presented. The spectral line survey toward IKTau has been published in Velilla Prieto et al. (2017). The complete spectral line survey of OH231, which will be published in Velilla Prieto et al. (in prep.), complements the detailed studies of particularly relevant species presented in Chapters 4 and 5. The line identification, the table with the measured integrated intensities and spectroscopic parameters of the lines, and the rotational diagrams corresponding to this survey are presented in Section 3.4,
- in Chapter 4, the study of nitrogen bearing molecules toward OH231.8+4.2 with the IRAM-30 m telescope is presented, which have been published in Velilla Prieto et al. (2015a),
- in Chapter 5, the work published in Sánchez Contreras et al. (2015) is presented, which has served to characterise the molecular emission of the ions HCO^+, SO^+, N_2H^+, and H_3O^+, toward the O-rich CSE of OH231.8+4.2 observed with the IRAM-30 m telescope,
- in Chapter 6, the work published in Velilla Prieto et al. (2015b) is reported, where the emission of Si-bearing molecules in the C-rich CSE of IRC+10216 observed with ALMA is discussed,
- Chapter 7 gathers in a summarised way the main results obtained in six other published articles in which I have participated, including the first published page of each of them sorted in chronological order,
- in Chapter 8, the conclusions derived from the research work done during the PhD are presented, with a consolidating discussion,
- in Chapter 9 I summarise the activities and projects in which I am currently involved that have arisen from the work carried out during my PhD. Additionally, we comment on several important topics for future research in the field of CSEs of evolved stars,
- Appendix A summarises the basic concepts about circumstellar envelopes, from stellar evolution (Sect. A.1), the formation, evolution and physico-chemical properties (Sect. A.2 and A.3),
- in Appendix B we summarised the fundamental concepts required to describe and understand how electromagnetic radiation is produced due to the changes in the rotational state of molecules found in circumstellar envelopes, as well as the theory that describes the interaction between matter and radiation, chemical processes, basic concepts about radioastronomy and the use of radiotelescopes and interferometers,
- in Appendix C I put on record in a clear and honest way my contribution to this PhD thesis (Sect. C.1), the peer-reviewed publications in international journals in which I participated as author or co-author (Sect. C.2), and other publications (Sect. C.3).

1.4.1 Studied objects in this thesis

The objects studied in this thesis are three circumstellar envelopes around AGB stars: the C-rich CSE IRC+10216, and the O-rich CSEs IK Tauri and OH231.8+4.2. These three objects have been selected according to the goals of this thesis, given that they are excellent candidates to analyse their molecular complexity and to characterise their molecular emission. In the particular case of O-rich objects, this work is mandatory given that their molecular inventory is worst known compared to the inventory of C-rich CSEs. On the other hand, IRC+10216, which is the most observed CSE, is an excellent candidate for interferometric studies of its molecular emission with NOEMA and ALMA, given its chemical wealth and its proximity to us. I describe below the main properties (stellar and circumstellar) of the three objects, required to the development of LVG and chemical models (Sect. 2.2 and 2.3), as well as their known molecular inventory from previous studies.

1.4.1.1 IK Tau

IK Tauri (hereafter IK Tau), which is also known as NML Tau (Fig. 1.8), is a Mira-type variable star with a period of 470 days and a spectral type M9 (Pesch, 1967, Wing & Lockwood, 1973, Alcolea et al., 1999). The central star was discovered by Neugebauer et al. (1965), and it is located at coordinates α(J2000)=$3^{\rm h}53^{\rm m}28\overset{\rm s}{.}87$ and δ(J2000)=$11°24'21\overset{''}{.}7$ (Cutri et al., 2003). The distance to the star from us is 250-265 pc, and its systemic velocity with respect to the LSR is approximately 34 km s^{-1} (Hale et al., 1997, Olofsson et al., 1998, Kim et al., 2010, and references therein). The star has an effective temperature of $\sim$2200 K, and a radius of $R_*\sim2.5\times10^{13}$ cm (Decin et al., 2010a). The most relevant parameters of this object are given in Table 1.2.

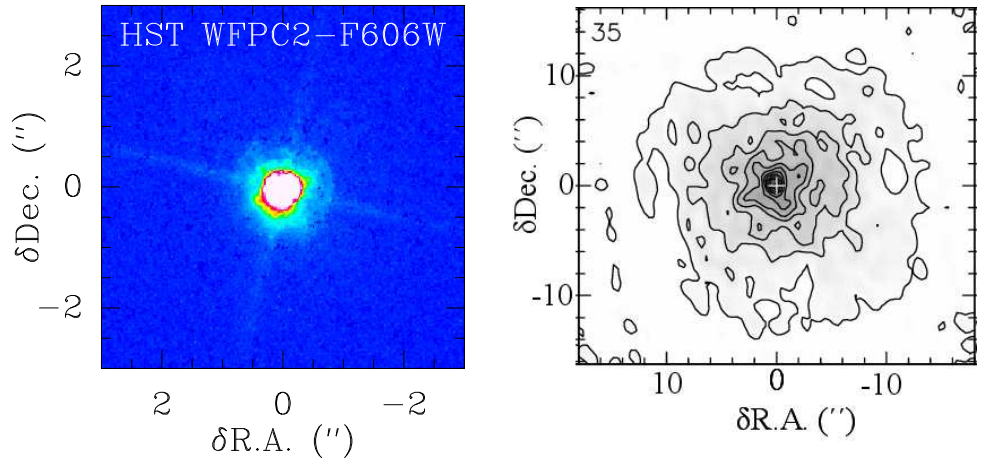

Figure 1.8: Left, IK Tau observed with the F606W filter (which corresponds approximately to the Johnson's V band) of the WFPC2 on-board of the HST. Right, brightness distribution of the emission of the J=2–1 ^{12}CO line at 35 km s^{-1}, which is approximately the systemic velocity of the source (Castro-Carrizo et al., 2010). *(Credits: HST image created from the data of the proposal P10185 (PI: R. Sahai), and Castro-Carrizo et al. (2010))*

The star is surrounded by a CSE composed of gas and dust, which has been formed as a consequence of the mass loss experienced by the star. The mass loss rate of the star has been estimated using different methods. Neri et al. (1998) estimated a mass loss rate of $3.8\times10^{-6}\,M_\odot$ year^{-1} from the observation of the J=1–0 and J=2–1 ^{12}CO lines. A mass loss

Table 1.2: Stellar and circumstellar parameters of IK Tau

Parameter	Value	Reference
α(J2000)	$3^{\rm h}53^{\rm m}28\overset{\rm s}{.}87$	c
δ(J2000)	$11°24'21\overset{''}{.}7$	c
Distance (d)	250-265 pc	f,i
Stellar radius (R_*)	$360\,R_\odot$	d
Effective temperature (T_*)	2200 K	d
Stellar luminosity (L_*)	$\sim 10^4\,L_\odot$	b
Period (P)	470 days	a
LSR systemic velocity of the source (v_{sys})	34 km s^{-1}	g
Terminal expansion velocity (v_∞)	18.5 km s^{-1}	j
Mass loss rate ($\dot{M}$)	$\sim 8\times10^{-6}\,M_\odot$ year^{-1}	e,h,g
Gas kinetic temperature (T_k)	$T_*(r/R_*)^{-0.60}$ K	d

Notes. a: Alcolea et al. (1999), b: Castro-Carrizo et al. (2010), c: Cutri et al. (2003), d: Decin et al. (2010a), e: González Delgado et al. (2003), f: Hale et al. (1997), g : Kim et al. (2010), h : Neri et al. (1998), i : Olofsson et al. (1998), j : Velilla Prieto et al. (2017)

rate of $3.0\times10^{-5}\,M_\odot$ year^{-1} from the fit of the J=1–0, J=2–1, J=3–2, and J=4–3 ^{12}CO lines was estimated by González Delgado et al. (2003). Recently, (Kim et al., 2010) have estimated a mass loss rate of $4.7\times10^{-6}\,M_\odot$ year^{-1} using the J=3–2, J=4–3, and J=7–6 ^{12}CO lines. The terminal expansion velocity of the CSE is $v_\infty\sim$18.5 km s^{-1} De Beck et al. (2013). The size of the CSE depends on the molecule used to evaluate it (see Sect. A.2). Bujarrabal & Alcolea (1991) measured a diameter at half-intensity of $\theta_{1/2}\sim$16-17$''$ using the J=1–0 and J=2–1 ^{12}CO lines observed with the IRAM-30 m. Kim et al. (2010) measured a $\theta_{1/2}\sim20''$ for the J=3–2 ^{12}CO line with the APEX radiotelescope. Recent observations carried out with the PdBI (currently known as NOEMA) showed that the J=1–0 ^{12}CO line has a size of $\theta_{1/2}\sim18''$ (Castro-Carrizo et al., 2010). Also, HCN displays a size of $\theta_{1/2}\sim3\overset{''}{.}85$ which has been observed with the OVRO interferometer by Marvel (2005). The size of the J=2–1 SiO line is $\theta_{1/2}$=$2\overset{''}{.}2\pm0\overset{''}{.}1$ as observed with the PdBI (Lucas et al., 1992). Finally, it has been also measured recently the brightness distribution of different emission lines of PO and PN with the SMA, which display sizes of $\theta_{1/2}\lesssim0\overset{''}{.}65$ (De Beck et al., 2013).

IK Tau is an O-rich CSE. It shows maser emission of the molecules OH, H_2O and SiO (which are commonly found in O-rich CSEs Lane et al., 1987, Bowers et al., 1989, Alcolea & Bujarrabal, 1992, Kim et al., 2010, and references therein). From previous studies, the molecular inventory of this CSE is ^{12}CO, ^{13}CO, SiO, ^{29}SiO, ^{30}SiO, SiS, HCN, HC_3N, H_2S, SO, SO_2, NaCl, H_2O, $H_2{}^{17}O$, $H_2{}^{18}O$, NH_3, CS, CN, PO, PN, AlO, and tentatively HNC (Lindqvist et al., 1988, Omont et al., 1993, Bujarrabal et al., 1994, Milam et al., 2007, Kim et al., 2010, Decin et al., 2010d, Menten et al., 2010, De Beck et al., 2013, 2015). The molecular emission observed up to date has been analysed by using chemical and radiative transfer models (Willacy & Millar, 1997, Duari et al., 1999, Cherchneff, 2006, Kim et al., 2010, Decin et al., 2010a, Danilovich et al., 2016, Gobrecht et al., 2016, Li et al., 2016).

1.4.1.2 OH231.8+4.2

OH231.8+4.2 (hereafter OH231) is the name given to the CSE that surrounds the star QX Pup, which was discovered by Turner (1971b) owing to the OH maser emission of the CSE emitted at 1612 MHz. It is also known as the "Calabash nebula" due to its shape, and also as the "rotten egg nebula" due to its high content of S-bearing molecules, in particular, H_2S which is the main responsible for the characteristic smell of rotten eggs. The central star, QX Pup, is classified as a M9-10 star with a variability consistent with an AGB star with a period of 660-690 days (Cohen, 1981, Feast et al., 1983, Kastner et al., 1992, Sánchez Contreras et al., 2004, and references therein). Additionally, QX Pup has a hot companion star with a spectral type A0 V, which has been indirectly identified through the analysis of the spectrum of the star light reflected by the dust in the nebula (Sánchez Contreras et al., 2004). The object is located at 1500 pc from us, it has a total luminosity of $\sim 10^4 L_{\odot}$, and its LSR systemic velocity is $\sim$34 km s^{-1}(Sánchez Contreras et al., 2000, Alcolea et al., 2001, Choi et al., 2012). The coordinates of the object are α(J2000)=$7^{\rm h}42^{\rm m}16\overset{\rm s}{.}947$ and δ(J2000)=-14°42′50″.20 (Cutri & et al., 2012). OH231 is probably part of the open cluster M 46 (NGC 2437) and should have had a progenitor mass of $\sim 3\,M_{\odot}$ (Jura & Morris, 1985, Alcolea et al., 2001). The nebular properties of this object, that is its marked bipolar structure and the fast expansion, are unusual for a star that is in the AGB stage, which should be surrounded by a slowly expanding spherical envelope (e.g. see Sect. 1.4.1.1). Therefore, this object is believed to be a precursor of a PN which has been caught in the AGB to PN transition stage (post-AGB stage) (e.g. Reipurth, 1987, Alcolea et al., 2001). The most relevant parameters of this object are given in Table 1.3.

Table 1.3: Stellar and circumstellar (AGB CSE component) parameters of OH231.8+4.2

Parameter	Value	Reference
α(J2000)	$7^{\rm h}42^{\rm m}16\overset{\rm s}{.}947$	d
δ(J2000)	-14°42′50″.20	d
Distance (d)	1500 pc	b
Stellar radius (R_*)	$630\,R_{\odot}$	h
Effective temperature (T_*)	2300 K	c,e,i
Stellar luminosity (L_*)	$10^4\,L_{\odot}$	h
Period (P)	$\sim$600 days	e
LSR systemic velocity of the source (v_{sys})	34 km s^{-1}	a
Terminal expansion velocity (v_{∞})	20 km s^{-1}	a
Mass loss rate ($\dot{M}$)	$\sim 10^{-4}\,M_{\odot}$ year^{-1}	a,f,g
Gas kinetic temperature (T_k)	$T_*(r/R_*)^{-0.70}$ K	j

Notes. a: Alcolea et al. (2001), b: Choi et al. (2012), c: Cohen (1981), d: Cutri & et al. (2012), e: Kastner et al. (1992), f: Morris (1987b), g: Sánchez Contreras et al. (1997), h: (Sánchez Contreras et al., 2002), i: Sánchez Contreras et al. (2004), j: Velilla Prieto et al. (2015a)

In Fig. 1.9 is shown that most of the nebular material is mainly gas and dust, which are traced by the scattered star light (in the case of dust), and the CO emission (in the case of gas) (e.g. Sánchez Contreras et al., 1997, Alcolea et al., 2001, Bujarrabal et al., 2002) . The gas distribution displays an elongated an clumpy structure with two main components: (*i*) a central component (I3 in Fig. 1.9), with an angular diameter of $\sim$6-8″, a total mass of $\sim 0.64\,M_{\odot}$, and expansion velocities of $\sim$6-35 km s^{-1}, and (*ii*) a bipolar elongated outflow,

highly collimated (with a size of $6''\times57''$), a total mass of $\sim0.3M_{\odot}$, and expansion velocities that can reach values of $\sim$200 and 430 km s^{-1} at the tip of the South and North lobes, respectively (Sánchez Contreras et al., 1997, Alcolea et al., 2001). This elongated structure clearly evidences the differences that OH231 displays compared to the characteristic spherical symmetric envelopes of AGB stars. Elongated structures are typically found in more evolved objects, with axial symmetry, high expansion velocities, and where shock processes may have occurred. This kind of objects are known as pPNs (Neri et al., 1998, Bujarrabal et al., 2001, Castro-Carrizo et al., 2010, Sánchez Contreras & Sahai, 2012).

The bipolar outflow, which has an elongated shape, observed toward OH231 was probably created as a consequence of the sudden acceleration of the spherical AGB CSE (this AGB CSE was created owing to a mass loss rate of $\sim10^{-4}\,M_{\odot}$ year^{-1}). Probably, such an acceleration occurred as the result from the energetic and violent collision between underlying jets, which most likely emanate from the stellar companion, on the slowly expanding AGB envelope (Sánchez Contreras et al., 2000, Alcolea et al., 2001, Bujarrabal et al., 2002, Sánchez Contreras et al., 2004). This plausible scenario may explain the shaping and acceleration of bipolar pre-PNs and PNs (e.g. Sahai & Trauger, 1998, Balick & Frank, 2002). Relating the observed size of the CO outflow with the expansion velocities (where the velocity gradient along the axial plane is $\nabla v\sim6.5$ km s^{-1} arcsec^{-1}), the material in the lobes was accelerated $\sim$800 years ago, in a short period of time of $\lesssim$150 years (Alcolea et al., 2001). According to this scenario, the low-velocity central core would correspond to the fossil remnant of the AGB CSE.

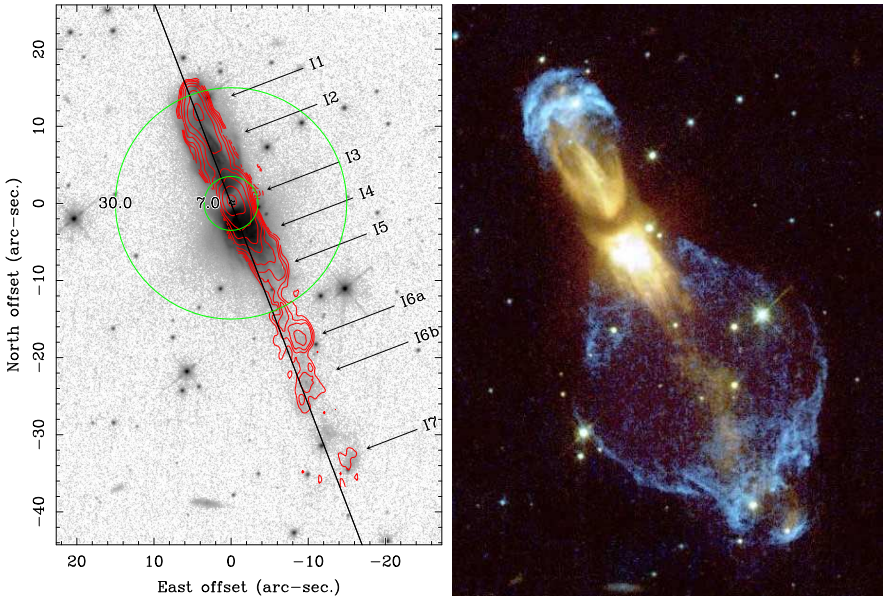

Figure 1.9: Left, the background image corresponds to the F791W filter (approximately Johnson's I band) of the WFPC2 image (Bujarrabal et al., 2002), red contours correspond to the J=2–1 ^{12}CO velocity integrated emission as observed with the PdBI (Alcolea et al., 2001). The different molecular clumps seen are named accordingly to Alcolea et al. (2001), and the green circles represent the HPBW of the IRAM-30 m telescope at 82 GHz (θ_b=30″) and 351 GHz (θ_b=7″). Right, false color image of OH231.8+4.2 (Hα in blue and R-band in yellow) observed with the HST (see Sánchez Contreras et al., 2004). *(Credits: Alcolea et al. (2001), Bujarrabal et al. (2002), ESA/HST V. Bujarrabal)*

Concerning the chemistry of this CSE, OH231 is one of the most rich CSEs of its class, i.e. an O-rich CSE surrounding an AGB star. Besides the typical maser emission of OH/IR objects, i.e. H_2O, OH, or SiO (Bowers & Morris, 1984, Morris et al., 1987a, Zijlstra et al., 2001, Sánchez Contreras et al., 2002, Desmurs et al., 2007), OH231 displays emission of a rich variety of molecules: ^{12}CO, ^{13}CO, SO, SO_2, H_2O, OH, SiO, H_2S, HCN, $H^{13}CN$, HNC, CS, HCO^+, $H^{13}CO^+$,OCS, H_2CO, NH_3, and NS (Ukita & Morris, 1983, Guilloteau et al., 1986, Morris, 1987b, Lindqvist et al., 1992, Omont et al., 1993, Sánchez Contreras et al., 1997, 2000, and references therein). The spectrum of OH231 is unusually rich, even for O-rich CSEs' standards, in lines of C-, S-, and N-bearing molecules, for example, it was the first O-rich CSE in which H_2S, NS, CS, and OCS were detected. Some of these molecules are particularly abundant, like SO_2 and HNC (see references above). A possible scenario that could explain these highly unusual abundances for some molecules in OH231 would be the presence of shocks. These shocks may extract material from the dust grains, or dissociate molecules that were in the former AGB CSE (adding atoms and ions to the gas phase), or may initiate reactions that will result in the formation of these abundant species Morris (1987b). For example, the emission of J=1–0 HCO^+ is found to be abundant in the lobes of the nebula, as well as SiO emission, which is interpreted as a shock-induced enhancement of the abundances of these molecules (Sánchez Contreras et al., 1997, 2000).

1.4.1.3 IRC+10216

IRC+10216 was observed for the first time in 1965 through its IR emission at 2 μm (Becklin et al., 1969, Neugebauer & Leighton, 1969). It is the most studied CSE given its proximity (∼130 pc, Schöier & Olofsson, 2001, and references therein), and its unprecedented molecular richness, which makes this object the archetype of C-rich CSE (Fig. 1.10). The star has an approximated variability period of ∼640 days, an effective temperature of ∼2300 K, and its spectral type is C9 (Cohen, 1979, Ridgway & Keady, 1988, Le Bertre, 1992, and references therein). The stellar radius is estimated to be ∼390-500 $R_\odot$ and its luminosity is measured to be between 5200-13000 $L_\odot$ (Men'shchikov et al., 2001). Coordinates of the object are α=$9^h47^m57\overset{s}{.}4255$ and δ=$13°16'43\overset{''}{.}815$ (J2000), as measured with the VLA, with a spatial resolution of 40 mas (Menten et al., 2012). The most relevant parameters of this object are given in Table 1.4.

The CSE of IRC+10216 displays a spherical symmetry centred toward the star, which has been created as a result of an intense mass loss from the star with $\dot{M}$∼1-5×10^{-5} $M_\odot$ $year^{-1}$ (e.g. Groenewegen & Ludwig, 1998, Skinner et al., 1999). The terminal expansion velocity (v_∞) of the CSE is ∼14.5 km s^{-1} (Cernicharo et al., 2000). The first circumstellar molecule ever detected was CO, detected toward this object (Solomon et al., 1971). Since then, ∼80 molecular species have been discovered in this CSE (see Table 1.5), C-bearing molecules mainly, like C_2H, HCN, C_6H or HC_3N, but also P-bearing molecules (e.g. PN or PH_3), Si-bearing molecules (e.g. SiCN, SiC_2 or SiC), anions (e.g. C_4H^- or C_6H^-), O-bearing molecules (e.g. OH, H_2CO o SiO), and more, which prove the uniqueness of this object (see e.g. Solomon et al., 1971, Cernicharo et al., 1986, Cernicharo & Guelin, 1987, Cernicharo et al., 1987, 2000, Agúndez, 2009). ALMA is playing now a key role in the characterisation of the innermost regions of the CSE (e.g. Agúndez et al., 2010b, 2012, Daniel et al., 2012).

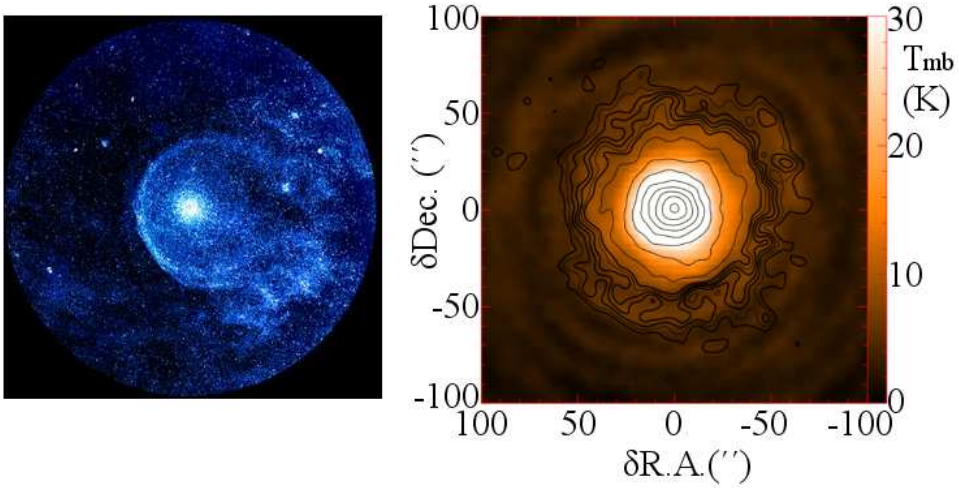

Figure 1.10: Images of IRC+10216. Left, image from GALEX space telescope in the FUV wavelength range, where the interaction between the CSE and the ISM is seen as a $24'$ diameter bubble-like structure (Sahai & Chronopoulos, 2010). Right, combined image of the ^{13}CO J=2–1 integrated emission between the velocities from -28.5 to -24.5 km s^{-1} with respect to the LSR (contours), and the integrated emission for the same velocity range of the ^{12}CO J=2–1 line (colour), observed with the IRAM-30 m radiotelescope (Cernicharo et al., 2015a). *(Credits: Sahai & Chronopoulos (2010) and Cernicharo et al. (2015a))*

Table 1.4: Stellar and circumstellar parameters of IRC+10216

Parameter	Value	Reference
α(J2000)	$9^{h}47^{m}57\overset{s}{.}4255$	e
δ(J2000)	$13°16'43\overset{''}{.}815$	e
Distance (d)	130 pc	g
Stellar radius (R_*)	390-500 $R_\odot$	d
Effective temperature (T_*)	2300 K	f
Stellar luminosity (L_*)	5200-13000 $L_\odot$	d
Period (P)	640 days	c
LSR systemic velocity of the source (v_{sys})	-26.5 km s^{-1}	b
Terminal expansion velocity (v_∞)	14.5 km s^{-1}	b
Mass loss rate ($\dot{M}$)	(1-5)$\times10^{-5}$ $M_\odot$ year^{-1}	a
Gas kinetic temperature (T_k)	$T_*(r/R_*)^{-0.72}$ K	a

Notes. a: Agúndez (2009), b: Cernicharo et al. (2000), c: Le Bertre (1992), d: Men'shchikov et al. (2001), e: Menten et al. (2012), f: Ridgway & Keady (1988), g: Schöier & Olofsson (2001)

Table 1.5: Molecular inventory of IRC+10216

2-atoms	3-atoms	4-atoms	5-atoms	6-atoms	7 or more atoms
CO	HCN	C_2H_2	CH_4	C_5H	HC_5N
CN	C_2H	NH_3	C_4H	CH_3CN	C_6H
C_2	C_3	C_3N	HC_3N	C_2H_4	CH_3C_2H
SiS	SiC_2	l-C_3H	C_5	H_2C_4	C_2H_3CN
CS	H_2O	c-C_3H	SiH_4	C_5N	C_6H^-
SiO	HNC	C_3S	c-C_3H_2	C_5N^-	C_7H
HCl	Si_2C	H_2CS	CH_2CN	HC_4N	H_2C_6
OH	C_2S	PH_3	HCCNC	C_5S	HC_7N
CN^-	HCP	HC_2N	SiC_4	$SiH_3CN^{(t)}$	C_8H
SiC	NaCN	c-SiC_3	H_2C_3		C_8H^-
AlCl	MgNC	C_3O	C_4H^-		HC_9N
CP	H_2S	C_3N^-	HNCCC		
HF	SiCN	HMgNC			
SiN	SiNC	$NCCP^{(t)}$			
AlF	C_2P	$MgCCH^{(t)}$			
PN	AlNC				
NaCl	HCO^+				
KCl	MgCN				
	FeCN				
	KCN				
	C_2N				

Notes. $^{(t)}$Tentative detections.

CAPÍTULO

1

INTRODUCCIÓN

En este capítulo se introduce y contextualiza la tesis dentro de la astrofísica molecular, y en particular el campo de las envolturas circunestelares, revisando los aspectos más relevantes y actuales de su estudio. Se presenta además la motivación de la tesis y la estructura del presente manuscrito. Por último, se presentan de manera concisa las propiedades de las tres envolturas circunestelares estudiadas: IKTau, OH231.8+4.2 e IRC+10216.

1.1 Astrofísica molecular: perspectiva histórica

La astrofísica molecular es la rama de la astrofísica que pretende conocer el Universo a través del estudio de las moléculas, en particular, del estudio de la radiación electromagnética relacionada con las moléculas (bien sea emitida, absorbida o dispersada por éstas) que recibimos de aquellos entornos astrofísicos que contienen una componente molecular. Desde nuestro planeta, La Tierra, pasando por el Sol y el Sistema Solar, el medio interestelar, exoplanetas, nubes y nebulosas, estrellas, galaxias, encontramos moléculas en prácticamente todo tipo de objetos. No obstante, deben darse unas ciertas condiciones físicas (temperatura, densidad, radiación...) para que las moléculas puedan formarse y sobrevivir, unas condiciones particulares que se dan solamente en lugares muy concretos del Universo, y que tanta atención suscitan de la curiosidad del ser humano, pues de ellas estamos formados.

Las primeras detecciones de moléculas más allá de La Tierra y su atmósfera, datan de la segunda mitad del siglo XIX, detecciones de moléculas sencillas como el C_2 detectada en el cometa Donati o el CN en el cometa 1881b (Donati, 1864, Huggins, 1881). Si consideramos las detecciones de moléculas en el medio interestelar, entonces tendríamos que avanzar hasta el siglo XX. Mediante observaciones en el rango de longitud de onda visible desde el observatorio de Monte Wilson, se detectó la presencia de CH^+, CH y CN, estudiando el espectro óptico (4230-4300 Å) de absorción del medio interestelar (Swings & Rosenfeld, 1937, McKellar, 1940, Douglas & Herzberg, 1941). Sin embargo, el verdadero desarrollo de esta rama de la astrofísica ocurre en paralelo con el desarrollo de la radioastronomía. En 1928, Karl G. Jansky, un recién graduado estudiante de la Universidad de Wisconsin, comienza a trabajar para los laboratorios Bell con el propósito de investigar el origen del ruido estático en las radiocomunicaciones transatlánticas. Dos años más tarde, Jansky termina la construcción de una antena diseñada para recibir señales a la frecuencia de 20.5 MHz (Fig. 1.1). Tras analizar las señales registradas durante aproximadamente dos años, Jansky distingue dos fuentes de estática de origen relacionado con tormentas y una fuente adicional de ruido constante de origen desconocido. En 1933,

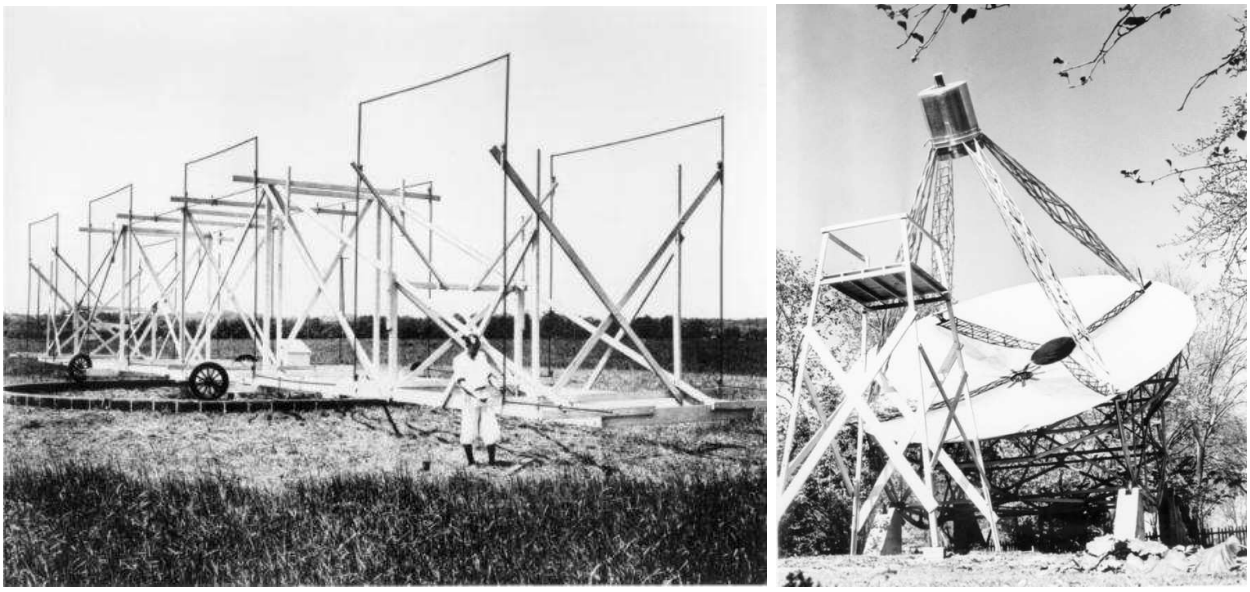

Figura 1.1: A la izquierda, imagen de la antena construida por K. G. Jansky. A la derecha, radiotelescopio construido por G. Reber. *(Créditos: NRAO)*

Jansky publica sus resultados concluyendo que los datos recogidos mostraban la existencia de ondas electromagnéticas que aparentemente parecen venir de una dirección fija en el espacio (Jansky, 1933, Brittain, 1984). Si bien Jansky no es capaz de determinar su origen, menciona que una de las más fascinantes explicaciones posibles apunta a que el origen de la señal estaría en algún punto de la Vía Láctea. Jansky propuso a los laboratorios Bell la construcción de una antena de 30 metros de diámetro para continuar su investigación. Desafortunadamente, el proyecto no pudo ejecutarse dada la situación económica del momento debida a la crisis económica de "la gran depresión". En su honor, se nombra la unidad de medida de densidad de flujo espectral utilizada comúnmente en radioastronomía.

Un ingeniero de Chicago llamado Grote Reber motivado por el trabajo de Jansky, decide construir en 1937 su propio radiotelescopio. La curiosidad sobre el ruido estático que Jansky había detectado y su posible origen en el espacio, llevan a Reber a construir este radiotelescopio por sus propios medios. El radiotelescopio consistía en un reflector parabólico de aproximadamente 9 metros de diámetro, equipado con receptores de radio construidos también por el propio Reber (ver Fig. 1.1). Realizaba sus observaciones de noche, ya que los motores de combustión de la época producían interferencias en el sistema receptor. En 1940, Reber consigue publicar los resultados de su investigación mostrando los primeros mapas de la radiación electromagnética recibida a la frecuencia de 160 MHz (λ=1.87 m) con su radiotelescopio (Reber, 1940, 1944). En dicho trabajo, Reber menciona que el ruido debe estar de algún modo relacionado con la cantidad de materia en el espacio, pues a dicha longitud de onda la absorción debida al polvo sería pequeña. Así que los mapas indicarían la cantidad de materia que se encuentra entre nosotros y el borde de nuestra Galaxia, y que los máximos detectados señalarían en la dirección de las proyecciones de la Galaxia, que podrían ser similares a los brazos que se observan en otras nebulosas espirales. En ese caso, Reber sugiere que el centro estaría en la dirección de Sagitario, y los brazos se encontrarían en las direcciones del Cisne, Casiopea y el Can Mayor, con un mínimo hacia Perseo que indicaría que estaríamos cerca del borde de La Galaxia en esa dirección (Fig. 1.2).

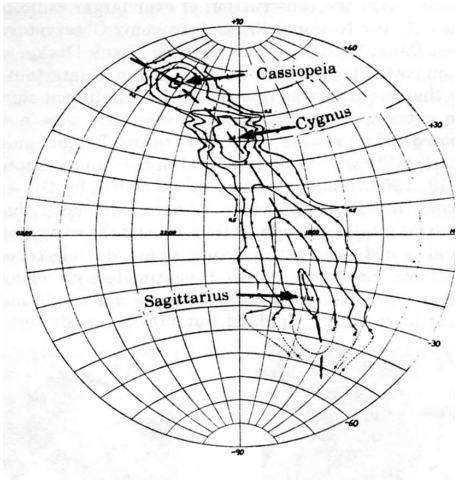

Figura 1.2: Primer mapa (radio) del cielo tomado por G. Reber a la frecuencia de 160 MHz. En la imagen se pueden ver anotadas las direcciones de las constelaciones de Casiopea, Cisne y Sagitario. *(Créditos: Reber (1944))*

Durante los siguientes años, debido en gran medida a la Segunda Guerra Mundial, los sistemas de comunicación de radio experimentaron grandes avances tecnológicos, lo que ayudo al avance de la radioastronomía. En 1951, H. I. Ewen y E. M. Purcell publican la detección de la línea del hidrógeno neutro en la longitud de onda de 21 cm en La Galaxia (Ewen & Purcell, 1951). Pero es en 1963 cuando se publica la primera detección de una molécula en el medio interestelar mediante observaciones en el rango de longitud de onda radio, la molécula OH (Weinreb et al., 1963). A partir de entonces, la evolución de las técnicas de detección y los radiotelescopios no sólo en longitudes de onda centimétricas sino también en el rango milimétrico y sub-milimétrico, derivaron en una cascada de detecciones de moléculas en el medio interestelar (e.g. Cheung et al., 1969, Wilson et al., 1970, 1971, Townes, 1977). Cabe destacar, que gracias también a estos avances en la radioastronomía, se han realizado grandes descubrimientos no sólo relacionados con la detección de moléculas, como podría ser la medida de la temperatura del fondo cósmico de microondas por A. A. Penzias y R. W. Wilson, descubrimiento merecedor del premio Nobel en 1978 por sus implicaciones en la teoría del Big Bang (Penzias & Wilson, 1965).

Además de la radioastronomía, la astrofísica molecular y su avance como disciplina científica, esta íntimamente ligado a la espectroscopía. Desde un punto de vista histórico, la espectroscopía ha evolucionado gracias a la aportación de grandes científicos como I. Newton, T. Young, G. Stokes, E. Morley, A. A. Michelson, y un largo etcétera. En general, la espectroscopía y los experimentos desarrollados para su investigación dependen principalmente de componentes mecánicos (e.g. cámaras de vacío), componentes ópticos (e.g. láser) y componentes electrónicos (e.g. transistores), además de las teorías del electromagnetismo y la física cuántica. Por tanto, el siglo XX ha supuesto un salto cualitativo adelante gracias a la investigación en semiconductores y los componentes de estado sólido. Cabe notar una de las figuras más importantes en el

campo de la espectroscopía molecular, G. Herzberg, que fue galardonado con el premio Nobel de Química en 1971 por su contribución y trabajo en el campo de la estructura molecular. Su clásica trilogía publicada hacia la mitad del siglo XX se considera aún como "el Libro" de espectroscopía molecular (Herzberg, 1939, 1945, 1966).

La sinergia entre estas disciplinas ha permitido que en las últimas décadas del siglo XX hayamos presenciado importantes descubrimientos en el campo de la astrofísica molecular. De las primeras detecciones ya mencionadas, cabe destacar la detección del CO (Wilson et al., 1970). El Universo está principalmente compuesto por H atómico, y la molécula más abundante en el medio interestelar es el H_2. En nuestra Galaxia se estima que la masa de H_2 es de aproximadamente $0.84{\times}10^9\,M_\odot$, lo que representaría un ∼20 % total del hidrógeno, estando el otro ∼80 % restante repartido entre hidrógeno neutro (∼60 %) e hidrógeno ionizado (∼20 %) (Draine, 2011). Sin embargo, el H_2 es complicado de detectar, ya que es una molécula homonuclear[1] altamente simétrica, lo que implica que su carga eléctrica está simétricamente distribuida y por tanto no presenta un momento dipolar eléctrico permanente. Ésto supone que en el rango de longitud observable desde la superficie de La Tierra no tenemos posibilidad de observar cómo se distribuye el gas H_2 a bajas temperaturas (∼10–50 K) en el medio interestelar, ya que sus transiciones electrónicas o cuadrupolares trazarían otro tipo de regiones más calientes o ocurrirían en regiones del espectro electromagnético no observables desde tierra. Sin embargo, el CO sí presenta un momento dipolar eléctrico permanente, por lo que tiene transiciones que son observables desde tierra y ha sido extensamente utilizado para trazar la distribución del gas frío en múltiples regiones de nuestra Galaxia y en otras galaxias dada su probada eficiencia como trazador del gas molecular (e.g. Dickman et al., 1986, Heyer & Dame, 2015).

Finalmente, otro de los grandes hitos en la astrofísica molecular en particular, y para aquellas ramas de las astrofísica relacionadas con la radioastronomía, es la aplicación de la interferometría para la llamada síntesis de apertura. Durante el último tercio del siglo XX y auspiciado por los primeros descubrimientos en el campo de la radioastronomía, las instituciones comenzaron a invertir en la construcción de radiotelescopios de todo tipo y tamaños para cubrir la región del espectro electromagnético de longitudes de onda largas en las que la atmósfera es transparente, la llamada ventana radio (Fig. 1.3) que aproximadamente se extiende desde longitudes de onda del orden del milímetro hasta los pocos metros. Algunos ejemplos de estos radiotelescopios serían la antena de 40 m de OVRO, la antena de Effelsberg de 100 m o la de 30 m de IRAM (Fig. 1.4). Sin embargo, la resolución espacial de los radiotelescopios está limitada por el tamaño de la antena (ver Sec. B.3.2),y por tanto, desde el punto de vista de la construcción, estaríamos limitados en el tamaño de las estructuras que podemos resolver. La interferometría permite alcanzar mejores resoluciones espaciales utilizando un conjunto de antenas de modo que virtualmente sería como observar con una antena de tamaño igual a la máxima separación entre dos antenas del conjunto, si bien esta técnica presenta otras peculiaridades. Interferómetros como el VLA, CARMA o PdBI (actualmente NOEMA) nos han permitido avanzar en el entendimiento del Universo a escalas que la radioastronomía de antena única no ha podido igualar aún.

[1]Se llama homonuclear a la molécula compuesta por átomos iguales.

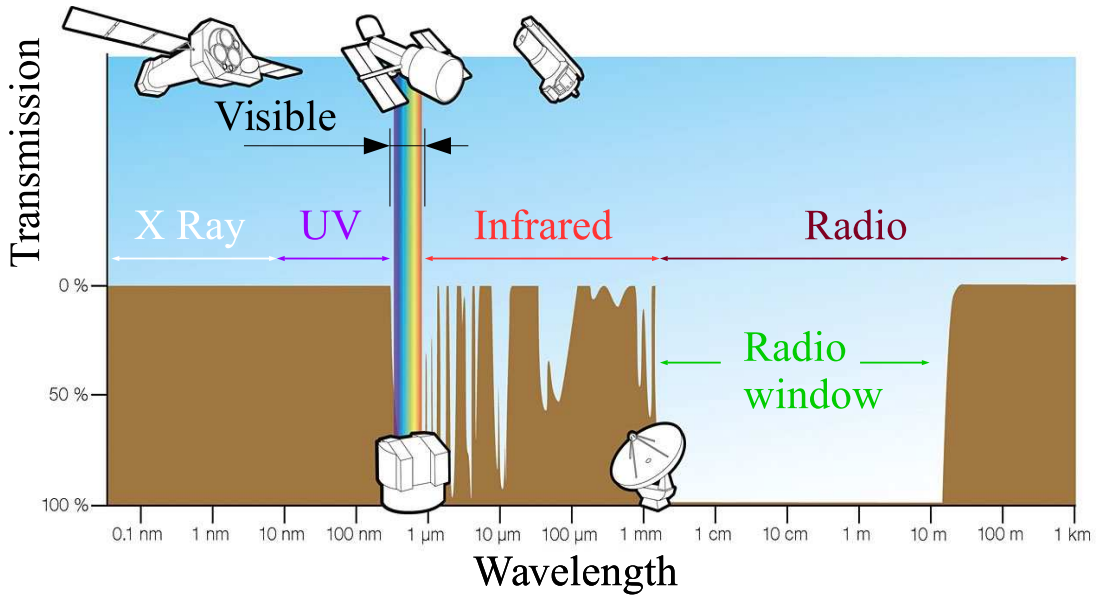

Figura 1.3: Esquema de la transmisión de la atmósfera entre las longitudes de onda correspondientes al rango de los rayos X y radio. Se muestra en la figura la ventana radio, así como unos pequeños dibujos de algunos de los telescopios más importantes, por ejemplo: Chandra (rayos X), HST (desde el espacio en el rango visible/óptico), William Herschel (como telescopio óptico localizado en la superficie terrestre), ISO (desde el espacio en el rango infrarrojo) e IRAM (como radiotelescopio). *(Créditos: Adaptación de ESA/Hubble F. Granato)*

1.2 Actualidad de la astrofísica molecular

El estudio del Universo molecular durante los años más recientes ha derivado en importantes aportaciones científicas, sirviendo esta época para asentar las bases del campo y ejecutar grandes retos instrumentales en el rango de longitud de onda infrarrojo y radio. Las antenas únicas que terminaron de construirse en el último tercio del siglo XX, han ido mejorando sus capacidades gracias sobre todo a las nuevas generaciones de espectrómetros de transformada de Fourier y los receptores heterodinos y superheterodinos que han permitido alcanzar mejores atenuaciones de la banda imagen o mejorar el ancho de banda registrable. Éstos cambios se han introducido recientemente por ejemplo en la antena de IRAM-30 m con EMIR (Carter et al., 2012).

En lo que respecta a los telescopios espaciales, se ha llevado a cabo con éxito uno de los proyectos más ambiciosos de la historia, el telescopio espacial *Herschel*. Con un diámetro de 3.5 m, este telescopio construido por la ESA, fue lanzado y puesto en órbita en 2009 y ha estado observando el Universo en el rango de longitud de onda de 55 a 672 μm hasta 2013, cuando los aproximadamente 2000 litros de He líquido (el refrigerante de la instrumentación) del telescopio se terminaron. En la actualidad, aún se está trabajando en el análisis de los datos recogidos por el observatorio espacial Herschel. Entre sus logros, caben destacar por ejemplo, la observación de la distribución de H_2O en regiones de formación estelar (van Dishoeck et al., 2011, y los artículos subsiguientes, ver Fig. 1.5), el estudio de objetos del Sistema Solar (Küppers et al., 2014) o la detección de H_2O en las zonas más internas de la envoltura rica en carbono IRC+10216 (Decin et al., 2010c).

Los últimos cuatro años han estado marcados, sin lugar a dudas, por el interferómetro ALMA. ALMA es un interferómetro constituido por 66 antenas (54 de 12 m de diámetro y

Figura 1.4: A la izquierda, radiotelescopio de IRAM-30 m situado cerca del Pico Veleta en Granada, España. En el centro, subconjunto de antenas del interferómetro NOEMA, situado cerca del pico Bure en los Alpes, Francia. A la derecha, antena del interferómetro ALMA, situado en el Alto del Chajnantor, Chile. *(Créditos: Imagen de NOEMA por C. Lefevre/IRAM e imagen de ALMA por B.Tafreshi/ESO)*

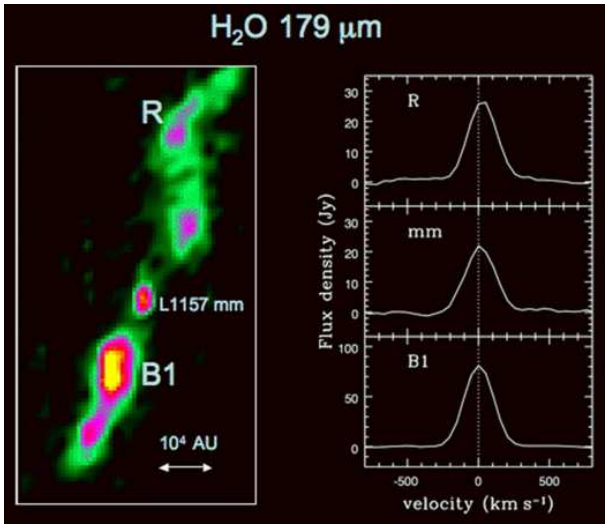

Figura 1.5: Imagen de H_2O a 179 μm de la protoestrella de clase 0 L1157 tomada con el instrumento PACS abordo de Herschel junto con su correspondiente espectro tomado en las tres posiciones mostradas en la imagen: R, mm y B1. *(Créditos: van Dishoeck et al. (2011))*

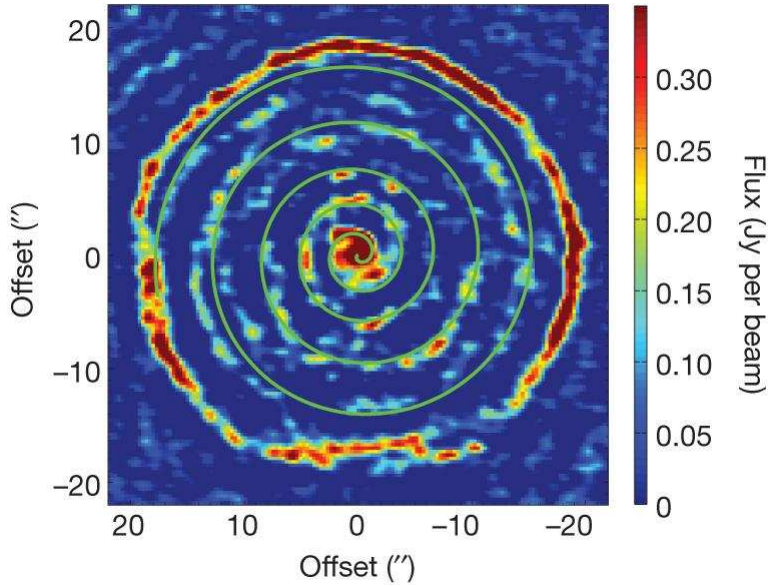

Figura 1.6: Mapa de la emisión de la línea de CO J=3–2 en la envoltura circunestelar de la estrella R Sculptoris tomado con ALMA. El mapa corresponde a la emisión a la velocidad sistémica de la fuente donde el rojo representa mayor densidad de flujo por haz que el azul. La línea en color verde corresponde al ajuste en estructura de espiral de los máximos de emisión que se observan. *(Créditos: Maercker et al. (2012))*

12 de 7 m) construido en el Alto del Chajnantor en Chile a unos 5000 m de altura. ALMA está equipado con receptores que permiten observar en el rango de longitud de onda de 0.32 a 3.57 mm (o en frecuencias de 950 a 84 GHz, respectivamente) y actualmente se encuentra realizando las observaciones de su cuarto ciclo de ciencia con un total de hasta ∼50 antenas operativas. La sensibilidad que se puede alcanzar con este interferómetro así como su resolución angular no tiene precedentes, llegando a desarrollar líneas de base de hasta ∼16 km (cuando se encuentre totalmente operativo) que permiten resoluciones de pocos milisegundos de arco. En los últimos ciclos de propuestas para ALMA, se han enviado un total de 1571 propuestas, de las que aproximadamente un tercio representan propuestas relacionadas con el medio interestelar, la formación estelar, la astroquímica, la evolución estelar y el Sol. Durante sus tres primeros ciclos científicos de vida, ALMA ha producido resultados de gran impacto en el campo de la astrofísica molecular, como por ejemplo la observación de la estructura espiral del CO en la envoltura circunestelar de la estrella AGB R Sculptoris (Maercker et al., 2012, ver Fig. 1.6), y para la astrofísica en general como por ejemplo la imagen de alta resolución espacial del disco protoplanetario alrededor de la estrella HL Tau (ALMA Partnership et al., 2015).

Finalmente, en lo que respecta a la detección de moléculas, hasta la fecha se han detectado, aproximadamente, 190 moléculas en el medio interestelar y circunestelar (Tabla 1.1). Entre ellas encontramos gran variedad de especies, por ejemplo radicales[2] (e.g. SO), iones moleculares (e.g. N_2H^+, HCO^+ o C_6H^-), o moléculas orgánicas complejas[3] (e.g. C_{60}, C_{70}, CH_2CCHCN). Como veremos más adelante, cada molécula ofrece información distinta en relación con las regiones donde se ubican, información sobre la morfología, cinemática, dinámica y química de dichos

[2]Moléculas que contienen al menos un electrón de valencia no apareado.

[3]Se consideran como tal aquellas moléculas orgánicas con 6 o más átomos (véase Herbst & van Dishoeck, 2009).

entornos y objetos.

1.3 Envolturas circunestelares: relevancia y actualidad

Una gran parte de las moléculas listadas en la Tabla 1.1 se han descubierto o encontrado en las envolturas circunestelares de las estrellas AGB. Dichas envolturas se forman durante la fase AGB de las estrellas que han tenido durante la secuencia principal masas comprendidas entre 0.8-8$M_{\odot}$, como resultado de un intenso proceso de perdida de masa, en forma de viento estelar lento y denso, que tiene lugar en estos ultimos estadios evolutivos. Estos vientos AGB crean una envoltura circunestelar que rodea a la estrella, y que están principalmente compuestas por gas y polvo (e.g. Habing & Olofsson, 2003). Las estrellas AGB son responsables del retorno de un ∼50-80 % del material gaseoso y del polvo total al ISM (Gehrz, 1989, Wallerstein & Knapp, 1998). El gas esta principalmente compuesto por moléculas, que ven favorecidas su formación debido a las condiciones de alta densidad y temperaturas bajas (ver Fig. A.5) que encontramos en éstos objetos. La formación molecular ocurre a través de distintos procesos físico-químicos en éstos objetos, que son considerados factorías de síntesis de moléculas y granos de polvo (ver Sec. A). Así, las envolturas circunestelares juegan un papel fundamental en el ciclo vital del Universo, procesando material más simple (en términos químicos, e.g. H o He) y devolviendo al ISM material más complejo (e.g. silicatos en forma de polvo o moléculas como el NaCl), que podrá dar lugar a una nueva etapa de formación estelar (Fig. 1.7). Estos objetos son importantes fuentes de estudio para comprender los procesos de formación de polvo y moléculas, la complejidad molecular del Universo, y los problemas de transferencia radiativa por citar los que más relevancia tienen en el contexto de esta tesis, y los que mayor número de estudios han atraído (e.g. Kwok, 1975, Goldreich & Scoville, 1976, Cernicharo & Guelin, 1987, Habing, 1996, Olofsson, 1996b, Agúndez et al., 2010b, Decin et al., 2010c, y referencias en los artículos).

Actualmente, existen varios temas de investigación que atraen el esfuerzo y la atención de la comunidad científica, aunque muchos de ellos tienen origen ya desde las primeras observaciones de envolturas circunestelares. Entre estos temas encontramos:

- estudios de complejidad molecular, que tratan de identificar la variedad de moléculas que podemos encontrar en las envolturas circunestelares (e.g. moléculas con oxígeno en envolturas ricas en carbono y viceversa), los procesos físico-químicos que las forman (e.g. formación inducida por choques y modelización química), y las características de su emisión (e.g. Agúndez et al., 2010b, Decin et al., 2010a, Danilovich et al., 2016, Li et al., 2016),
- procesos de formación de granos de polvo, y su relación con la formación de vientos en estrellas AGB, (e.g. Bladh & Höfner, 2012, Karovicova et al., 2013, Gobrecht et al., 2016),
- ampliación de las muestras de objetos estudiados, que tratan de aclarar si existe un sesgo observacional para algunas de las conclusiones extraídas sobre las propiedades de las envolturas circunestelares. Por ejemplo, sobre la emisión de HCN (Schöier et al., 2013) o las proporciones isotópicas de ^{12}CO/^{13}CO (Ramstedt & Olofsson, 2014).

Además, y como se ha mencionado anteriormente para el campo de la astrofísica molecular en general, ocurre que la aparición de ALMA está motivando un número elevado de estudios y observaciones en envolturas circunestelares de estrellas evolucionadas. Estos estudios están principalmente dirigidos a comprender los procesos físico-químicos que se dan en las zonas más internas de las envolturas circunestelares, ya que ALMA permite resolver espacialmente dichas regiones (e.g. Cernicharo et al., 2013).

Tabla 1.1: Moléculas detectadas en el medio interestelar y circunestelar hasta Junio de 2016.

2-átomos	3-átomos	4-átomos	5-átomos	6 o más átomos	
H_2	C_3	c-C_3H	C_5	C_5H	HC_7N
AlF	C_2H	l-C_3H	C_4H	l-H_2C_4	C_8H
AlCl	C_2O	C_3N	C_4Si	C_2H_4	$CH_3C(O)NH_2$
C_2	C_2S	C_3O	l-C_3H_2	CH_3CN	C_8H^-
CH	CH_2	C_3S	c-C_3H_2	CH_3NC	C_3H_6
CH^+	HCN	C_2H_2	H_2CCN	CH_3OH	CH_3CH_2SH(?)
CN	NCO	H_2CS	CH_4	CH_3SH	CH_3C_5N
CO	HCO^+	H_3O^+	HC_3N	HC_3NH^+	$(CH_3)_2CO$
CO^+	HCS^+	c-SiC_3	HC_2NC	HC_2CHO	$(CH_2OH)_2$
CP	HOC^+	CH_3	HCOOH	NH_2CHO	CH_3CH_2CHO
SiC	H_2O	C_3N^-	H_2CNH	C_5N	CH_3C_4H
HCl	H_2S	PH_3	SiH_4	H_2CCNH(?)	C_6H^-
KCl	HNC	HCNO	H_2COH^+	C_5N^-	CH_3NCO
NH	HNO	HCCN	C_4H^-	HNCHCN	CH_3C_3N
NO	MgCN	$HCNH^+$	HC(O)CN	C_6H	c-C_6H_6
NS	MgNC	HNCO	HNCNH	CH_2CHCN	n-C_3H_7CN
NaCl	N_2H^+	HNCS	CH_3O	CH_3C_2H	i-C_3H_7CN
OH	N_2O	$HOCO^+$	NH_4^+	HC_5N	$C_2H_5OCH_3$(?)
PN	NaCN	H_2CO	H_2NCO^+(?)	CH_3CHO	CH_3CHCH_2O
SO	OCS	H_2CN	$NCCNH^+$	CH_3NH_2	CH_3CH_2OH
SO^+	SO_2	HMgNC	H_2C_2O	c-C_2H_4O	C_{60}
SiN	HCP	HCCO	H_2NCN	$HC(O)OCH_3$	C_{70}
SiO	CCP	HOCN	HNC_3	CH_3COOH	C_{60}^+
SiS	AlOH	HSCN		C_7H	
CS	H_2O^+	H_2O_2		C_6H_2	
HF	H_2Cl^+	C_3H^+		CH_2OHCHO	
HD	KCN	NH_3		l-HC_6H	
FeO(?)	FeCN			CH_2CHCHO(?)	
O_2	c-SiC_2			CH_2CCHCN	
CF^+	CO_2			H_2NCH_2CN	
SiH(?)	NH_2			CH_3CHNH	
PO	H_3^+			H_2CCHOH	
AlO	SiCN			l-HC_4H	
OH^+	AlNC			l-HC_4N	
CN^-	SiNC			c-H_2C_3O	
SH^+	HO_2			CH_3C_6H	
SH	TiO_2			C_2H_5OCHO	
HCl^+	C_2N			$CH_3OC(O)CH_3$	
TiO	Si_2C			HC_9N	
ArH^+				CH_3CH_2CN	
NO^+(?)				$(CH_3)_2O$	

Notes. Se relacionan en la tabla las fórmulas de los isotopólogos principales de las especies moleculares detectadas, si bien en muchos casos se han detectado diferentes isotopólogos de una misma especie. Las moléculas marcadas con (?) deben considerarse detecciones tentativas. *(Fuente: CDMS, http://www.astro.uni-koeln.de/cdms/molecules)*

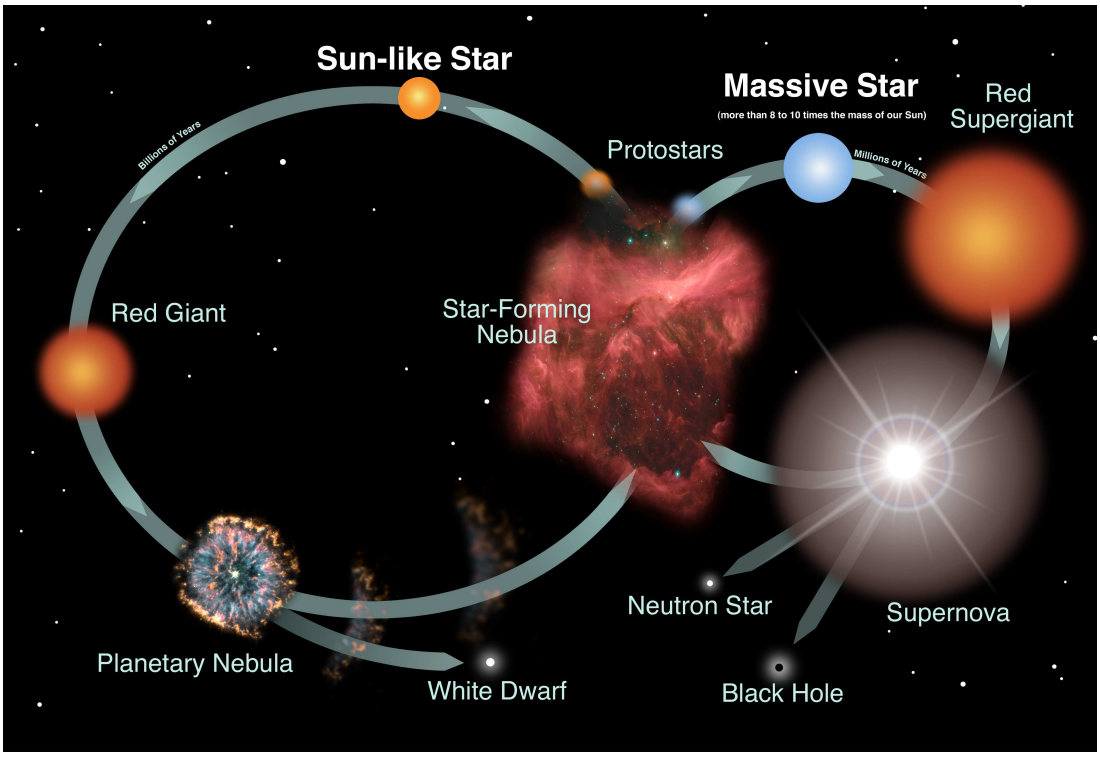

Figura 1.7: Imagen del ciclo vital que experimentan las estrellas poco masivas y de masa intermedia ($0.8M_{\odot}< m <8M_{\odot}$, izquierda) y las más masivas (derecha para $m >8M_{\odot}$), desde su origen en las regiones de formación estelar, hasta su posterior muerte y reintegración en el ISM cerrando el ciclo. *(Créditos: NASA y Night Sky Network)*

1.4 Motivación y estructura de esta tesis

La presente tesis se enmarca en el contexto de la astrofísica molecular, y el estudio de la complejidad molecular en las envolturas circunestelares de las estrellas AGB en la era de IRAM-30 m y ALMA. Como veremos a lo largo de esta tesis, el estudio de las líneas (principalmente rotacionales) de emisión de las moléculas de las envolturas, nos dan información sobre la pérdida de masa de la estrella, la temperatura de excitación del gas, la densidad de columna de una determinada especie, la cinemática de la envoltura, la composición química del gas y los granos de polvo, o las abundancias de las especies, entre otras propiedades. Como se ha mencionado anteriormente, es importante entender qué moléculas se forman, así como los procesos que las forman, dado que las estrellas AGB son las principales responsables de la síntesis y procesamiento molecular en el Universo.

Objetivos

El objetivo principal de esta tesis es caracterizar la emisión molecular en envolturas circunestelares alrededor de estrellas AGB, mediante el uso de las técnicas observacionales (e.g. barridos espectrales) e instrumentos (e.g. IRAM-30 m o ALMA) más recientes, así como los códigos de química y transferencia radiativa más actuales (ver Sec. 2.2 y 2.3).

En particular, se pretende caracterizar dos envolturas circunestelares ricas en oxígeno (IK-Tau y OH231.8+4.2), cuyas propiedades físicas se conocen con bastante detalle y son objetos

bien estudiados. No obstante, los estudios químicos de estos dos objetos hasta la fecha previa a nuestro trabajo están basados en estudios observacionales dedicados a unas pocas líneas de las especies más abundantes. Esto se debe en parte a la mayor capacidad del carbono para formar distintos compuestos, por lo que la mayor parte de estudios de caracterización de envolturas en el pasado se han realizado sobre objetos ricos en carbono. En esta tesis se ha marcado una gran diferencia dado que hemos hecho barridos espectrales completos con el radiotelescopio IRAM-30 m, y no solo estudios centrados en una o dos líneas de unas pocas especies. Este tipo de estudios permite además detectar nuevas especies moleculares en el medio circunestelar.

En esta tesis además, se caracteriza la emisión registrada con ALMA, de distintas moléculas en la envoltura rica en carbono IRC+10216. Estas observaciones suponen el estudio de los primeros mapas de ALMA con alta resolución angular de este objeto para las líneas observadas. Entre otras, se ha estudiado la emisión de moléculas que contienen silicio, y que son relevantes para la formación de granos de polvo en estrellas AGB. Con este trabajo se pretende entender cómo se distribuyen estas moléculas en IRC+10216, e investigar los procesos físico-químicos relevantes que formarían y destruirían estas especies en fase gaseosa, y su relación con los granos de polvo.

Estructura

Esta tesis doctoral se presenta en formato de recopilación de artículos y está subdividida en 9 capítulos y 3 apéndices. El manuscrito se presenta en su totalidad en inglés, entendiendo que éste es el idioma más utilizado para la comunicación científica y dado que la tesis se presentará para optar a la mención de doctorado europea. Adicionalmente, se presentan en español el resumen de la tesis, los capítulos de introducción y conclusiones (Capítulos 1 y 8) así como los resúmenes que preceden a cada uno de los artículos principales en los que se basa la tesis (Capítulos 3 a 6). Los Capítulos 3, 4, 5 y 6 se presentan yendo desde el análisis general de los barridos espectrales, a los aspectos y temas concretos, sin seguir necesariamente el orden cronológico de las publicaciones. El contenido de los distintos capítulos es el siguiente:

- en el Capítulo 1 se desarrolla una introducción general para contextualizar la tesis y presentar, de manera resumida, la perspectiva histórica de una disciplina relativamente joven, como es la astrofísica molecular, desde sus comienzos (Sec. 1.1), hasta los avances más recientes (Sec. 1.2) siguiendo la bibliografía descrita a lo largo del texto. También se encuentra una breve introducción al tema concreto de la tesis, es decir, el estudio de la emisión molecular en las envolturas circunestelares. En este capítulo además, se detalla de manera concisa la motivación y objetivos de la tesis doctoral. Por último, se describen los objetos estudiados en la tesis, así como sus propiedades más relevantes,
- en el Capítulo 2 se describen las técnicas específicas de análisis utilizadas en esta tesis (i.e. los diagramas rotacionales, el código MADEX de transferencia radiativa y los códigos de química LTEINNER y CHEMCLOUD), que se complementan con conceptos más básicos resumidos en el Apéndice B,
- en el Capítulo 3, se presenta y resume el trabajo realizado en los artículos Velilla Prieto et al. (2017) y Velilla Prieto et al. (in prep.), en los que se reportan los resultados generales obtenidos del estudio de las envolturas ricas en oxígeno IK Tau y OH231.8+4.2 mediante los barridos espectrales observados con el radiotelescopio de IRAM-30 m. La identificación de líneas, la tabla con las medidas de las intensidades integradas y parámetros espectroscópicos de dichas líneas, asi como los diagramas rotacionales que corresponden a la totalidad

del barrido espectral de OH231.8+4.2 se presentan en la Sección 3.4. El barrido espectral completo de OH231, que se publicará en Velilla Prieto et al. (in prep.), complementa los estudios mas detallados de especies particularmente relevantes a los que se refieren los Capítulos 4 y 5,

- en el Capítulo 4, se presenta y resume el trabajo realizado en el artículo Velilla Prieto et al. (2015a), donde se estudian las primeras detecciones de determinadas moléculas que contienen nitrógeno (i.e. HNCO, HNCS, HC_3N y NO) en la envoltura circunestelar rica en oxígeno OH231.8+4.2, con el radiotelescopio de IRAM-30 m,
- en el Capítulo 5, se presenta el trabajo realizado en el artículo Sánchez Contreras et al. (2015), que ha servido para caracterizar la emisión molecular de los iones HCO^+, SO^+, N_2H^+ y H_3O^+, en la envoltura circunestelar rica en oxígeno OH231.8+4.2, mediante el radiotelescopio de IRAM-30 m,
- en el Capítulo 6, se reporta el trabajo realizado en el artículo Velilla Prieto et al. (2015b), que trata sobre la emisión de moléculas que contienen silicio en la envoltura circunestelar IRC+10216 y su distribución espacial observada con ALMA,
- en el Capítulo 7, se recoge de manera resumida los resultados principales obtenidos en otros seis artículos en los que he participado, así como la primera página del artículo publicado en la revista correspondiente en orden cronológico,
- en el Capítulo 8, se detallan las conclusiones derivadas de los trabajos de investigación desarrollados a lo largo de la presente tesis, así como una discusión integradora de todos ellos,
- en el Capítulo 9, se señalan las actividades que actualmente desempeño en el campo de la investigación en astrofísica, que han surgido a raíz del trabajo realizado durante la tesis. Además, se apuntan algunas cuestiones importantes para futuras investigaciones en el campo de las envolturas circunestelares,
- en el Apéndice A se describen de manera resumida los conceptos básicos sobre envolturas circunestelares, desde la evolución estelar (Sec. A.1), la formación, evolución y las propiedades físicas (Sec. A.2) y químicas (Sec. A.3),
- en el Apéndice B se resumen los conceptos teóricos básicos para describir y entender cómo se produce radiación electromagnética por los cambios en el estado rotacional de las moléculas encontradas en las envolturas circunestelares, así como la teoría que describe la interacción entre la materia y la radiación, los procesos químicos fundamentales, los conceptos básicos sobre radioastronomía y el uso de radiotelescopios e interferómetros,
- por último, en el Apéndice C he dejado constancia de manera clara y honesta cuál ha sido mi contribución en esta tesis doctoral (Sec. C.1), las publicaciones en revistas internacionales con sistema de arbitraje en las que he participado bien como autor principal o como coautor (Sec. C.2), y otras publicaciones (Sec. C.3).

1.4.1 Objetos estudiados en esta tesis

Los objetos estudiados en esta tesis son tres envolturas circunestelares alrededor de estrellas AGB: la envoltura rica en carbono IRC+10216, y las envolturas ricas en oxígeno IKTau y OH231.8+4.2. En relación al objetivo de la tesis, se han seleccionado estos tres objetos por su interés para analizar su complejidad molecular y caracterización de la emisión molecular. En el caso de las envolturas ricas en oxígeno, este trabajo es necesario dado que el inventario

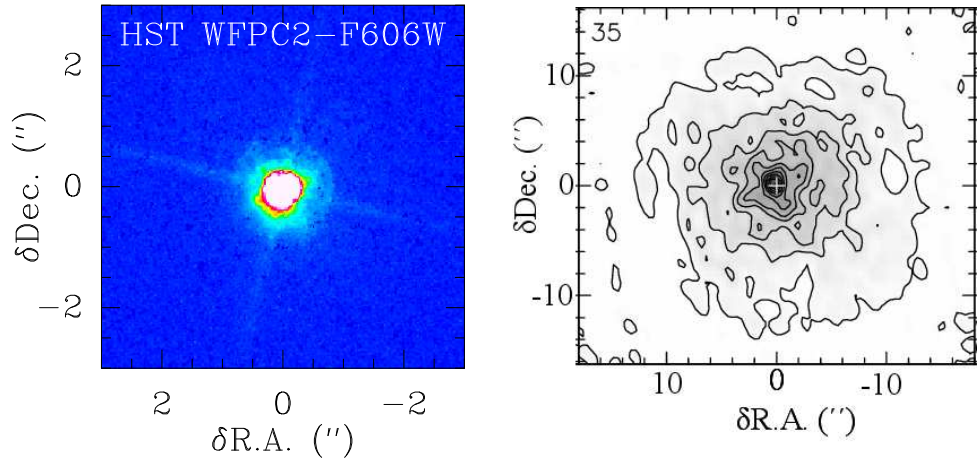

Figura 1.8: Imágenes de IK Tau. A la izquierda, imagen tomada con el filtro F606W (que correspondería aproximadamente a la banda V de Johnson) de la cámara WFPC2 a bordo del HST. A la derecha, distribución de brillo de la línea ^{12}CO J=2–1 para una velocidad de 35 km s^{-1} (aproximadamente la velocidad sistémica de la fuente) tomada de Castro-Carrizo et al. (2010). *(Créditos: Imagen del HST creada a partir de los datos de la propuesta P10185 (PI: R. Sahai) e imagen de Castro-Carrizo et al. (2010))*

de especies químicas es peor conocido que en las envolturas ricas en carbono. En el caso de IRC+10216, que es la envoltura circunestelar más observada, su riqueza química y cercanía la convierten en un candidato excelente para el desarrollo de estudios interferométricos con los nuevos instrumentos NOEMA y ALMA. Describiré a continuación las propiedades principales de los tres objetos (tanto estelares como circunestelares), requeridas para la creación de modelos LVG y químicos (Sec. 2.2 y 2.3), así como el inventario molecular conocido a través de los estudios previos de estas fuentes.

1.4.1.1 IK Tau

IK Tauri (en adelante IK Tau), también conocida como NML Tau (Fig. 1.8), es una estrella variable tipo Mira con un periodo de ∼470 días y tipo espectral M9 (Pesch, 1967, Wing & Lockwood, 1973, Alcolea et al., 1999). La estrella que da nombre a la envoltura fue descubierta por Neugebauer et al. (1965) y se encuentra localizada en las coordenadas α(J2000)=3$^{\rm h}$53$^{\rm m}$28$^{\rm s}$.87 y δ(J2000)=11°24′21″.7 (Cutri et al., 2003). La distancia a la estrella se estima en unos 250-265 pc y su velocidad sistémica respecto al LSR es de aproximadamente unos 34 km s^{-1} (Hale et al., 1997, Olofsson et al., 1998, Kim et al., 2010, y referencias en los artículos). Su temperatura efectiva se estima en aproximadamente unos 2200 K y tiene un radio estelar aproximado de R_*∼2.5×10^{13} cm (Decin et al., 2010a). Los parámetros más importantes de este objeto pueden encontrarse en la Tabla 1.2.

La estrella se encuentra rodeada por una envoltura circunestelar compuesta por gas y polvo, que se ha formado como consecuencia de las pérdidas de masa sufridas por la estrella, y que se han estimado utilizando diferentes métodos. Neri et al. (1998) calcula una tasa de pérdida de masa de 3.8×10^{-6} $M_\odot$ year^{-1} de la observación de las líneas J=1–0 y J=2–1 de ^{12}CO. González Delgado et al. (2003) estima una tasa de 3.0×10^{-5} $M_\odot$ year^{-1} del ajuste de las líneas J=1–0, J=2–1, J=3–2 y J=4–3 de ^{12}CO. Recientemente, se ha establecido un valor de 4.7×10^{-6} $M_\odot$ year^{-1} a través de las observaciones de las líneas J=3–2, J=4–3 y J=7–6

Tabla 1.2: Parámetros de la estrella y de la envoltura circunestelar de IK Tau

Parámetro	Valor	Referencia
α(J2000)	$3^{\rm h}53^{\rm m}28\overset{\rm s}{.}87$	c
δ(J2000)	$11°24'21\overset{''}{.}7$	c
Distancia (d)	250-265 pc	f,i
Radio estelar (R_*)	$360\,R_\odot$	d
Temperatura estelar efectiva (T_*)	2200 K	d
Luminosidad estelar (L_*)	$\sim 10^4\,L_\odot$	b
Periodo (P)	470 días	a
Velocidad LSR sistémica de la fuente (v_{sys})	$34\,{\rm km\ s^{-1}}$	g
Velocidad terminal de expansión (v_∞)	$18.5\,{\rm km\ s^{-1}}$	j
Tasa de pérdida de masa ($\dot{M}$)	$\sim 8\times10^{-6}\,M_\odot\ {\rm year^{-1}}$	e,h,g
Temperatura cinética del gas (T_k)	$T_*(r/R_*)^{-0.60}\,{\rm K}$	d

Notes. a: Alcolea et al. (1999), b: Castro-Carrizo et al. (2010), c: Cutri et al. (2003), d: Decin et al. (2010a), e: González Delgado et al. (2003), f: Hale et al. (1997), g : Kim et al. (2010), h : Neri et al. (1998), i : Olofsson et al. (1998), j : Velilla Prieto et al. (2017)

de ^{12}CO (Kim et al., 2010). La velocidad terminal de expansión del gas de la envoltura es $v_\infty\sim18.5\,{\rm km\ s^{-1}}$ medida según De Beck et al. (2013). El tamaño de la envoltura circunestelar depende de la molécula considerada para evaluarlo (ver Sec. A.2). Bujarrabal & Alcolea (1991) miden un diámetro a mitad de intensidad de $\theta_{1/2}\sim$16-17$''$ a través de observaciones de las líneas J=1–0 y J=2–1 de ^{12}CO con el radiotelescopio de IRAM-30 m. Kim et al. (2010) miden $\theta_{1/2}\sim20''$ para la línea J=3–2 de ^{12}CO con el radiotelescopio APEX. Observaciones recientes realizadas con el PdBI (actualmente conocido como NOEMA) muestran que la línea J=1–0 de ^{12}CO tiene un tamaño de $\theta_{1/2}\sim18''$ (Castro-Carrizo et al., 2010). Por otro lado, la línea HCN J=1–0 muestra un tamaño de $\theta_{1/2}\sim3\overset{''}{.}85$ observada con el interferómetro de OVRO por Marvel (2005). También se conoce el tamaño de la emisión de la línea J=2–1 de SiO, que muestra un tamaño de $\theta_{1/2}$=$2\overset{''}{.}2\pm0\overset{''}{.}1$ observada con el PdBI (Lucas et al., 1992). Por último, también se han medido recientemente los tamaños de la emisión de diferentes líneas de PO y PN mediante el SMA, donde se estiman tamaños de $\theta_{1/2}\lesssim0\overset{''}{.}65$ (De Beck et al., 2013).

IK Tau es una envoltura circunestelar rica en oxígeno. Muestra emisión máser de OH, H_2O y SiO (típica de las envolturas ricas en oxígeno Lane et al., 1987, Bowers et al., 1989, Alcolea & Bujarrabal, 1992, Kim et al., 2010, y referencias en los artículos). En estudios previos del contenido molecular de esta envoltura, se ha detectado la presencia de ^{12}CO, ^{13}CO, SiO, ^{29}SiO, ^{30}SiO, SiS, HCN, HC_3N, H_2S, SO, SO_2, NaCl, H_2O, $H_2{}^{17}O$, $H_2{}^{18}O$, NH_3, CS, CN, PO, PN, OH, AlO y tentativamente HNC (Lindqvist et al., 1988, Omont et al., 1993, Bujarrabal et al., 1994, Milam et al., 2007, Kim et al., 2010, Decin et al., 2010d, Menten et al., 2010, De Beck et al., 2013, 2015). Por último, su contenido se ha comparado con diferentes modelos químicos y la emisión molecular analizada con modelos de transporte radiativo (Willacy & Millar, 1997, Duari et al., 1999, Cherchneff, 2006, Kim et al., 2010, Decin et al., 2010a, Danilovich et al., 2016, Gobrecht et al., 2016, Li et al., 2016).

1.4.1.2 OH231.8+4.2

OH231.8+4.2 (en adelante OH231) es la envoltura circunestelar que rodea a la estrella QX Pup y fue descubierta por Turner (1971b) a través de la emisión máser de OH que presenta el objeto a 1612 MHz. También se la conoce como la *nebulosa de la calabaza*, por su forma, y como *nebulosa del huevo podrido*, por su alto contenido en moléculas con azufre, entre ellas el H_2S que daría ese característico olor a los huevos podridos. La estrella central, QX Pup, es una estrella clasificada como M9-10 que presenta una variabilidad consistente con una estrella AGB con un periodo aproximado de 660-690 días (Cohen, 1981, Feast et al., 1983, Kastner et al., 1992, Sánchez Contreras et al., 2004, y referencias en los artículos). Adicionalmente, parece que QX Pup tiene una estrella compañera cercana más caliente de tipo A0 V, que se ha identificado de manera indirecta a través del análisis del espectro de la luz reflejada por la nebulosa de polvo del objeto (Sánchez Contreras et al., 2004). El sistema se encuentra localizado aproximadamente a 1500 pc, tiene una luminosidad total $\sim 10^4 L_\odot$, y una velocidad sistémica respecto al LSR de $\sim$34 km s^{-1}(Sánchez Contreras et al., 2000, Alcolea et al., 2001, Choi et al., 2012). Las coordenadas del objeto son α(J2000)=$7^{\rm h}42^{\rm m}16\overset{\rm s}{.}947$ y δ(J2000)=-14°42′50″.20 (Cutri & et al., 2012). OH231 probablemente pertenezca al cúmulo abierto M 46 (NGC 2437) y habría tenido una masa progenitora de $\sim 3\,M_\odot$ (Jura & Morris, 1985, Alcolea et al., 2001). Las propiedades nebulares de este objeto (bipolar y en rápida expansión) son muy inusuales para una estrella que aún está en la etapa de AGB que debería estar rodeada de una envoltura lenta y más o menos redonda (e.g. ver Sec. 1.4.1.1). Debido a esta marcada estructura bipolar se cree que este objeto es un precursor de nebulosa planetaria que se encuentra en una fase de transición (etapa post-AGB) (e.g. Reipurth, 1987, Alcolea et al., 2001). Los parámetros más importantes de este objeto pueden encontrarse en la Tabla 1.3.

Tabla 1.3: Parámetros de la estrella y de la componente central de expansión lenta de OH231.8+4.2

Parámetro	Valor	Referencia
α(J2000)	$7^{\rm h}42^{\rm m}16\overset{\rm s}{.}947$	d
δ(J2000)	-14°42′50″.20	d
Distancia (d)	1500 pc	b
Radio estelar (R_*)	$630\,R_\odot$	h
Temperatura estelar efectiva (T_*)	2300 K	c,e,i
Luminosidad estelar (L_*)	$10^4\,L_\odot$	h
Periodo (P)	$\sim$600 días	e
Velocidad LSR sistémica de la fuente (v_{sys})	34 km s^{-1}	a
Velocidad terminal de expansión (v_∞)	20 km s^{-1}	a
Tasa de pérdida de masa ($\dot{M}$)	$\sim 10^{-4}\,M_\odot$ year^{-1}	a,f,g
Temperatura cinética del gas (T_k)	$T_*(r/R_*)^{-0.70}$ K	j

Notes. a: Alcolea et al. (2001), b: Choi et al. (2012), c: Cohen (1981), d: Cutri & et al. (2012), e: Kastner et al. (1992), f: Morris (1987b), g: Sánchez Contreras et al. (1997), h: (Sánchez Contreras et al., 2002), i: Sánchez Contreras et al. (2004), j: Velilla Prieto et al. (2015a)

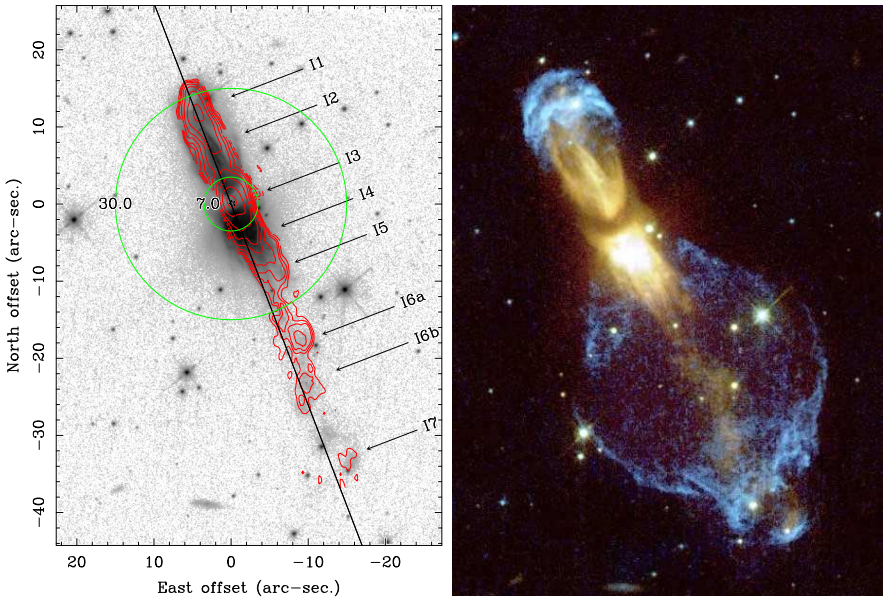

Figura 1.9: A la izquierda, la imagen de fondo es del telescopio HST tomada con la WFPC2 con el filtro F791W que correspondería con la banda I de Johnson (Bujarrabal et al., 2002), los contornos en rojo corresponden con la emisión de la línea J=2–1 de ^{12}CO integrada para todas las velocidades según se observó con el PdBI (Alcolea et al., 2001) donde se marcan los distintos grumos o *clumps* de la emisión molecular de acuerdo a la nomenclatura usada por Alcolea et al. (2001), y los círculos concéntricos en verde, marcan el HPBW del radiotelescopio de IRAM-30 m para las frecuencias de 82 GHz (θ_b=30″) y 351 GHz (θ_b=7″). A la derecha, imagen de OH231.8+4.2 en falso color (Hα en azul y banda R en amarillo) tomada con el HST (ver e.g. Sánchez Contreras et al., 2004). *(Créditos: Alcolea et al. (2001), Bujarrabal et al. (2002), ESA/HST V. Bujarrabal)*

Como puede verse en la Fig. 1.9 la mayor parte del material de la nebulosa está compuesta principalmente por gas y polvo, que son trazados por la luz emitida por la estrella al ser dispersada por el polvo (*scattering*), y en el caso del gas molecular, principalmente por la molécula CO (e.g. Sánchez Contreras et al., 1997, Alcolea et al., 2001, Bujarrabal et al., 2002). La distribución del gas presenta una forma alargada y grumosa con dos componentes principales: (*i*) un núcleo central (I3 en la Fig. 1.9), con un diámetro angular de unos ∼6-8″, una masa total de ∼0.64 $M_\odot$, y unas velocidades de expansión de ∼6-35 km s^{-1}, y (*ii*) una componente bipolar, alargada, y altamente colimada (con un tamaño de 6″×57″) con una masa total de ∼0.3$M_\odot$ y velocidades de expansión que pueden llegar a alcanzar valores de ∼200 y 430 km s^{-1} hacia el final de los lóbulos Sur y Norte, respectivamente (Sánchez Contreras et al., 1997, Alcolea et al., 2001). Esta estructura evidencia claramente las diferencias que esta envoltura presenta (comparada con las envolturas con simetría esférica que suelen mostrar las estrellas AGB), y que son más habituales de objetos más evolucionados, con simetría axial, velocidades de expansión elevadas, y en los que se han dado procesos de choques, y que son las llamadas pre-nebulosas planetarias o pre-PNs (Neri et al., 1998, Bujarrabal et al., 2001, Castro-Carrizo et al., 2010, Sánchez Contreras & Sahai, 2012). La nebulosa bipolar y alargada que observamos en OH231, se creó probablemente como consecuencia de una aceleración súbita de la envoltura esférica de la fase AGB (la envoltura AGB original se habría formado por una pérdida de masa de la estrella de ∼10^{-4} $M_\odot$ year^{-1}). Esta aceleración resultaría, proba-

blemente, de la colisión violenta de chorros o *jets* generados por la estrella compañera con la envoltura AGB previa (Sánchez Contreras et al., 2000, Alcolea et al., 2001, Bujarrabal et al., 2002, Sánchez Contreras et al., 2004). Este mecanismo se ha propuesto como escenario plausible para la formación y aceleración de pre-PNs (e.g. Sahai & Trauger, 1998, Balick & Frank, 2002). Relacionando la distancia observada con las velocidades de expansión que se observan en el flujo de CO (siendo sobre el plano axial este gradiente de velocidad de $\nabla v \sim 6.5\,\mathrm{km\ s^{-1}\ arcsec^{-1}}$), se estima que la aceleración del material que se encuentra en los lóbulos, ocurrió hace ~ 800 años en un periodo de tiempo de $\sim$150 años o inferior (Alcolea et al., 2001). Por otro lado, la componente o núcleo central, de expansión lenta, sería el remanente de la envoltura AGB original.

Respecto a la química de la envoltura, OH231 se muestra como una de las envolturas circunestelares más ricas dentro de su clase, i.e. la envoltura de una estrella AGB rica en oxígeno. Además de la emisión máser típica de los objetos OH/IR, i.e. H_2O, OH, o SiO (Bowers & Morris, 1984, Morris et al., 1987a, Zijlstra et al., 2001, Sánchez Contreras et al., 2002, Desmurs et al., 2007), OH231 muestra emisión de una gran variedad de moléculas. Hasta la fecha previa a las publicaciones en las que se basa esta tesis, las moléculas descubiertas en este objeto son: ^{12}CO, ^{13}CO, SO, SO_2, H_2O, OH, SiO, H_2S, HCN, H^{13}CN, HNC, CS, HCO^+, H^{13}CO$^+$, OCS, H_2CO, NH_3 y NS (Ukita & Morris, 1983, Guilloteau et al., 1986, Morris, 1987b, Lindqvist et al., 1992, Omont et al., 1993, Sánchez Contreras et al., 1997, 2000, y referencias en los artículos). OH231 muestra una riqueza química inusual para el contenido observado típicamente en estrellas ricas en oxígeno, con abundancia de moléculas que contienen carbono, nitrógeno y azufre, siendo la primera envoltura circunestelar en la que se detectaron las moléculas H_2S, NS, CS y OCS. Alguna de estas moléculas son especialmente abundantes, como por ejemplo el SO_2 y el HNC (ver las referencias citadas anteriormente). Un posible escenario que explicaría la abundancia inusual de ciertas moléculas en OH231 sería la presencia de choques, que pueden extraer material de los granos de polvo, disociar moléculas que formaran parte de la envoltura AGB de modo que integraría a la fase gas átomos e iones, o podrían iniciar reacciones que desencadenen la formación de dichas moléculas Morris (1987b). Por ejemplo, la emisión de la línea de HCO^+ J=1–0 es abundante en la región de los lóbulos, al igual que la emisión del SiO parece también destacar en las regiones que han sido o están siendo recientemente chocadas (Sánchez Contreras et al., 1997, 2000).

1.4.1.3 IRC+10216

IRC+10216 se comenzó a observar en 1965 en el IR a longitudes de onda de 2 μm (Becklin et al., 1969, Neugebauer & Leighton, 1969). Es la envoltura circunestelar más estudiada, dada su cercanía ($\sim$130 pc Schöier & Olofsson, 2001, y referencias en los artículos), y su incomparable riqueza molecular, que la convierten en el arquetipo de envoltura circunestelar rica en carbono (Fig. 1.10). La estrella tiene un periodo aproximado de $\sim$640 días, una temperatura efectiva aproximada de 2300-2500 K y su tipo espectral es C9 (Cohen, 1979, Ridgway & Keady, 1988, Le Bertre, 1992, y referencias en los artículos). El radio estelar se estima en $\sim$390-500 $R_\odot$ y su luminosidad en 5200-13000 $L_\odot$ (Men'shchikov et al., 2001). Las coordenadas de la estrella son α=9$^{\mathrm{h}}$47$^{\mathrm{m}}$57$^{\mathrm{s}}$.4255 y δ=13°16′43″.815 (J2000), medidas con el VLA con una resolución de 40 milisegundos de arco (Menten et al., 2012). Los parámetros más importantes de este objeto pueden encontrarse en la Tabla 1.4.

Su envoltura circunestelar presenta una simetría más o menos esférica centrada alrededor de la estrella, que se habría generado a partir de una tasa de pérdida de masa estimada entre 1-5$\times10^{-5}$ $M_\odot$ year^{-1} (e.g. Groenewegen & Ludwig, 1998, Skinner et al., 1999), y cuya velocidad

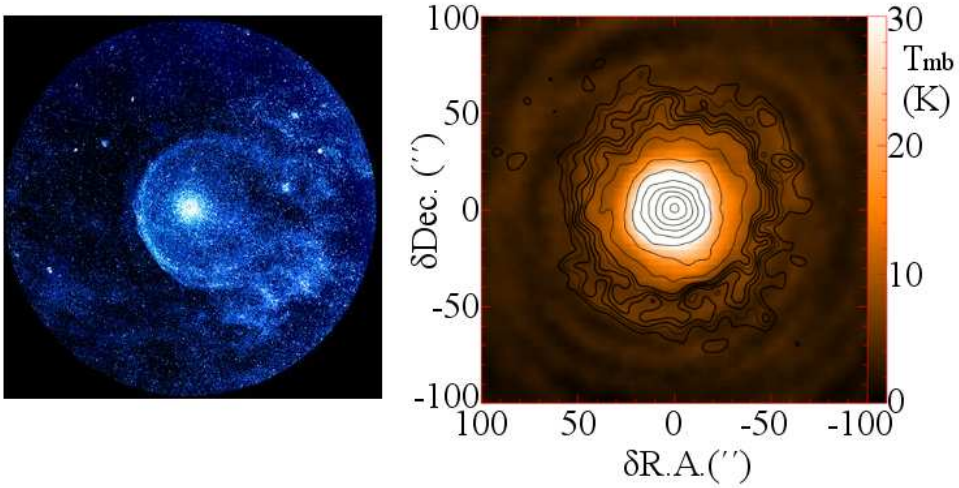

Figura 1.10: Imágenes de IRC+10216. A la izquierda, imagen tomada con el telescopio espacial GALEX en el rango de longitud de onda FUV, donde se observa la interacción entre la envoltura circunestelar y el medio interestelar en forma de burbuja con un tamaño de $24'$ de diámetro (Sahai & Chronopoulos, 2010). A la derecha, imagen combinada de la emisión de ^{13}CO J=2–1 integrada entre las velocidades LSR de -28.5 a -24.5 km s^{-1} (contornos), y la emisión de ^{12}CO J=2–1 integrada para el mismo rango de velocidad, tomadas con IRAM-30 m (Cernicharo et al., 2015a). *(Créditos: Sahai & Chronopoulos (2010) y Cernicharo et al. (2015a))*

Tabla 1.4: Parámetros de la estrella y de la envoltura circunestelar IRC+10216

Parámetro	Valor	Referencia
α(J2000)	$9^h47^m57^s.4255$	e
δ(J2000)	$13°16'43''.815$	e
Distancia (d)	130 pc	g
Radio estelar (R$_*$)	390-500 $R_\odot$	d
Temperatura estelar efectiva (T$_*$)	2300 K	f
Luminosidad estelar (L$_*$)	5200-13000 $L_\odot$	d
Periodo (P)	640 días	c
Velocidad LSR sistémica de la fuente (v$_{sys}$)	-26.5 km s^{-1}	b
Velocidad terminal de expansión (v$_\infty$)	14.5 km s^{-1}	b
Tasa de pérdida de masa ($\dot{M}$)	(1-5)$\times10^{-5}$ $M_\odot$ year^{-1}	a
Temperatura cinética del gas (T$_k$)	$T_*(r/R_*)^{-0.72}$ K	a

Notes. a: Agúndez (2009), b: Cernicharo et al. (2000), c: Le Bertre (1992), d: Men'shchikov et al. (2001), e: Menten et al. (2012), f: Ridgway & Keady (1988), g: Schöier & Olofsson (2001)

Tabla 1.5: Inventario molecular de IRC+10216

2-átomos	3-átomos	4-átomos	5-átomos	6-átomos	7 o más átomos
CO	HCN	C_2H_2	CH_4	C_5H	HC_5N
CN	C_2H	NH_3	C_4H	CH_3CN	C_6H
C_2	C_3	C_3N	HC_3N	C_2H_4	CH_3C_2H
SiS	SiC_2	l-C_3H	C_5	H_2C_4	C_2H_3CN
CS	H_2O	c-C_3H	SiH_4	C_5N	C_6H^-
SiO	HNC	C_3S	c-C_3H_2	C_5N^-	C_7H
HCl	Si_2C	H_2CS	CH_2CN	HC_4N	H_2C_6
OH	C_2S	PH_3	HCCNC	C_5S	HC_7N
CN^-	HCP	HC_2N	SiC_4	$SiH_3CN^{(t)}$	C_8H
SiC	NaCN	c-SiC_3	H_2C_3		C_8H^-
AlCl	MgNC	C_3O	C_4H^-		HC_9N
CP	H_2S	C_3N^-	HNCCC		
HF	SiCN	HMgNC			
SiN	SiNC	$NCCP^{(t)}$			
AlF	C_2P	$MgCCH^{(t)}$			
PN	AlNC				
NaCl	HCO^+				
KCl	MgCN				
	FeCN				
	KCN				
	C_2N				

Notes. $^{(t)}$Detecciones tentativas.

terminal de expansión es de $\sim$14.5 km s^{-1} (Cernicharo et al., 2000). La primera detección de una molécula en el medio circunestelar fue en IRC+10216, la detección del CO (Solomon et al., 1971). Desde entonces, se han descubierto aproximadamente un total de 80 moléculas en esta envoltura, principalmente moléculas que contienen carbono como por ejemplo C_2H, HCN, C_6H o HC_3N, pero también moléculas que contienen fósforo (e.g. PN o PH_3), moléculas con silicio (e.g. SiCN, SiC_2 o SiC), aniones (e.g. C_4H^- o C_6H^-), moléculas con oxígeno (e.g. OH, H_2CO o SiO), y más, convirtiéndola en un objeto único (ver e.g. Solomon et al., 1971, Cernicharo et al., 1986, Cernicharo & Guelin, 1987, Cernicharo et al., 1987, 2000, Agúndez, 2009). Tanto la química como la emisión molecular de este objeto se han estudiado previamente y son relativamente bien conocidas, salvo para la emisión y procesos químicos que ocurren en las regiones más internas de la envoltura, para los cuales ALMA será un instrumento clave (e.g. Agúndez et al., 2010b, 2012, Daniel et al., 2012).

CHAPTER

2

TOOLS FOR THIS PHD THESIS

In this chapter we describe the specific analysis techniques used throughout this PhD thesis. In particular we describe the formalism of the population diagrams, as well as a description of the radiative transfer code MADEX, and the chemical codes LTEINNER and CHEMCLOUD. The basic theoretical concepts that complement these topics are briefly summarised in the Appendix B.

2.1 Population diagrams

Population diagrams are used to obtain the column densities and excitation temperatures of the molecular emission arising from an astronomical source. In the case of this PhD thesis, population diagrams were used to analyse the rotational emission lines arising from the circumstellar gas around evolved stars. This technique can be used under certain approximations, which are explained below.

Let us consider the molecular emission, in particular rotational emission lines, arising from an homogeneous cloud in ISM, observed with a radiotelescope. The observed radiation fulfils the radiative transfer equation (Eq.(B.30)), and the measured antenna temperature is given by Eq.(B.92). In LTE conditions ($\mathcal{S}_\nu = B_\nu(T)$), the solution to the radiative transfer equation is:

$$I_\nu(\tau_\nu) = I_\nu(0)e^{-\tau_\nu} + B_\nu(T)(1 - e^{-\tau_\nu}), \tag{2.1}$$

where the temperature of the cloud is T, and the optical depth is τ. In the case of an emission line ($T > T_{bg}$), where T_{bg} is the temperature that describes the background radiation ($I_\nu(0)$), we can neglect the term that depends on the background intensity.

Additionally, in the Rayleigh-Jeans limit:

$$I_\nu = \frac{h\nu/k}{e^{h\nu/kT} - 1}(1 - e^{-\tau}). \tag{2.2}$$

Under LTE conditions, the populations are described by Boltzmann distributions, then:

$$N_u = \frac{N}{Z} g_u e^{-E_u/kT}, \tag{2.3}$$

where N_u is the *column density* (i.e. the number of molecules per unit area along the line of sight) of molecules within the energy state u, N is the total column density, Z is the partition function at a temperature T, g_u is the degeneration of the energy level, and E_u the upper energy

level. The optical depth of a line can be expressed by using the definition of the optical depth (Eq.(B.26)), and the microscopical description of the Einstein emission coefficient (Eq.(B.38)), for a Gaussian line profile (Eq.(B.55)) as follows:

$$\tau_\nu = \frac{h}{\Delta v} N_u B_{ul} (e^{h\nu/kT} - 1) = \frac{1}{\Delta v} N_u \frac{c^3 A_{ul}}{8\pi\nu^3} (e^{h\nu/kT} - 1), \tag{2.4}$$

where h is the Planck constant, k the Boltzmann constant, Δv is the FWHM of the line, c is the speed of light, ν the frequency of the transition, and A_{ul} and B_{ul} are the Einstein coefficients. The Einstein coefficients as a function of the strength of the line (S_{ul}) and the electric dipole moment (μ) of the molecule can be written as:

$$A_{ul} = \frac{64\pi^4 \nu^3 S_{ul} \mu^2}{3hc^3 g_u}. \tag{2.5}$$

From the measured antenna temperature, the velocity integrated intensity of the line is:

$$W = \int_{line} T_A^* \, dv, \quad [K \, km \, s^{-1}] \tag{2.6}$$

which in practice can be calculated as:

$$W = T_A^* \Delta v, \tag{2.7}$$

or by the sum of the measured antenna temperature for each channel multiplied by the width of the channels.

Using the expression for the main beam temperature (Eq.(B.90)) and the expression for the corrected antenna temperature (Eq.(B.92)), and considering an extended source with a uniform brightness distribution, we can write:

$$N_u = \frac{8\pi k \nu^2 W}{hc^3 A_{ul}} \left(\frac{\tau_\nu}{1 - e^{-\tau_\nu}} \right), \tag{2.8}$$

where W is the velocity integrated intensity of the line. Finally, in the optically thin case, we obtain the expression of the population diagram:

$$\ln \left(\frac{3kW}{8\pi^3 \nu S_{ul} \mu^2} \right) = \ln \left(\frac{N}{Z} \right) - \frac{E_u}{kT}, \tag{2.9}$$

which will be the equation of a straight line with slope $m = -E_u/kT$, and intercept $y_0 = \ln\left(\frac{N}{Z}\right)$, when several lines of the molecular species are observed. Thus, from the velocity integrated intensities of the lines and several spectroscopic parameters, it can be determined the excitation temperature of the lines, which is usually called *rotational temperature*, and the total column density of the molecules (N), which is defined as follows:

$$N = \int_0^d n \, ds, \quad [cm^{-2}] \tag{2.10}$$

where n is the number density of the molecule per unit volume, integrated along the line of sight to an object located at a distance d. It is worth noting, that in the case of LTE conditions, the excitation temperature (i.e. the rotation temperature) corresponds to the kinetic temperature of the gas.

If the observed molecules has hyperfine structure, and this structure is not spectrally resolved, we still may use the rotational diagrams by considering all the hyperfine components that contribute to the spectral line, and the sum of their line strengths (S_{ul}).

Limiting cases

The population diagram technique is valid if the emission is optically thin and under LTE conditions with a homogeneous temperature T. Additionally, if the source does not fill completely the main beam of the telescope, i.e. it is diluted, the emission must be corrected (Eq.(B.100)).

If the emission is optically thick, the following approximation ($\tau/(1-e^{-\tau}) \rightarrow 1$) is no longer valid, which was used in Eq.(2.8). In this case, Eq.(2.9) is written as follows:

$$\ln\left(\frac{3kW}{8\pi^3\nu S_{ul}\mu^2}\right) + \ln C_\tau = \ln\left(\frac{N}{Z}\right) - \frac{E_u}{kT}, \tag{2.11}$$

where C_τ is equal to

$$C_\tau = \frac{\tau_{\rm ul}}{1-e^{-\tau_{\rm ul}}}, \tag{2.12}$$

and each line must be corrected by using an estimation of the optical depth (Eq.(2.4)). A priori, if we do not know anything about the optical depth of the observed emission, the usage of the rotational diagram may result in a wrong determination of the rotational temperature and the column density. The error will depend on the number of lines observed, and the optical depths of these lines. Therefore, each diagram must be considered in detail (e.g. Goldsmith & Langer, 1999, Velilla Prieto et al., 2017).

If the LTE approximation is not valid, the population of the levels are not given by a Boltzmann distribution, given that the density is not high enough to thermalise the rotational transitions of the molecules. However, we can make use of the definition of the excitation temperature (Eq.(B.40)) as well as the rotational diagram technique, but in this case the derived rotational temperature is not equal to the kinetic temperature of the gas. If the density of the system is well below the critical density, the lines will be sub-thermally excited, and the derived T_{ex} from the diagram is lower than the kinetic temperature.

It can be concluded that the use of the rotational diagrams is justified in the cases where the gas is close to LTE conditions, and the emission is optically thin. However, if the analysis takes into account the impact of deviations from LTE conditions, from optically thin emission, and temperature inhomogeneities, we can still extract conclusions from the rotational diagrams if the number of observed transitions is large enough and cover a wide range of energies.

2.2 MADEX

MADEX is a code written by Prof. J. Cernicharo (Cernicharo, 2012), which solves the molecular line excitation and the radiative transfer problem with the LVG formalism described in Goldreich & Kwan (1974), for a multi-shell circumstellar envelope as described in Sect. B.2.1. MADEX contains also spectroscopic information (frequencies, energies, Einstein coefficients, collisional coefficients...) for more than 5000 different species, atoms and molecules, including isotopologues and vibrationally excited states. This catalogue has been built by using and gathering the available information in the literature and extensive laboratory works, such as the collisional coefficients of SO_2 used in Velilla Prieto et al. (2017). MADEX allows to study the excitation conditions of an astronomical source and predict its emergent spectrum (synthetic spectrum) through the physical conditions and parameters of the cloud or CSE.

Throughout this PhD thesis MADEX has been used to identify the rotational lines detected toward the studied CSEs. It has been used to model the emission under LTE conditions as well

Table 2.1: Elemental abundances used in the TE models of O-rich CSEs. *(Source: Asplund et al. (2009))*

Element	Abundance
H	12.00
He	10.93
C	8.43
O	8.69
N	7.83
S	7.12
Si	7.51
Fe	7.50
Mg	7.60
...	

Notes. Abundances are reported in the usual logarithmic scale, where the elemental H abundance (ϵ(H)) is defined as $\log \epsilon(\mathrm{H})=12.00$, and $\log \epsilon(\mathrm{X})=\log (N_\mathrm{X}/N_\mathrm{H})+12$, where N_X and N_H are the number densities of the elements X and H, respectively.

as under the LVG approximation, and for the case of a multi-shell spherical CSE. Examples of its usage can be seen in the Appendix A in Velilla Prieto et al. (2015a), where we used MADEX to evaluate the LTE deviations of the emission of HNCO, HNCS, HC_3N, and NO toward OH231, and also to model the emission of SO_2 toward IKTau (Velilla Prieto et al., 2017).

2.3 Chemical codes

2.3.1 Thermodynamical equilibrium: LTEINNER

In this thesis, we used the thermodynamical equilibrium code written by J. Tejero and Prof. J. Cernicharo in order to predict the abundances in the innermost regions (1-5R_*) of the CSEs. This code is called *LTEINNER* (Tejero & Cernicharo, 1991), and it is based on the formalism of Tsuji (1973). A complete description on how the code calculates the thermodynamical equilibrium abundances of the species considered in our system can be found in Section B.1.2. This software requires several stellar parameters such as the photosphere temperature of the star (T_*), the stellar radius (R_*), the mass loss rate ($\dot{M}$), the radial dependence of the density ($n(H_2) = f(r)$), the radial dependence of the kinetic temperature ($n(T_k) = f(r)$), the expansion velocity of the envelope (v_{exp}), thermodynamical information about the species considered (Gibbs energy, standard formation enthalpy and entropy), and the initial elemental abundances, like those shown in Table 2.1.

An example of its usage for the case of an O-rich star can be seen in the Sect. 5.2 of Velilla Prieto et al. (2015a).

2.3.2 Chemical kinetics: CHEMCLOUD

The chemical kinetics code, which is called *CHEMCLOUD*, used throughout this thesis was written by Prof. J. Cernicharo (Cernicharo, 2004). The code has been gradually updated to

cover a large number of cases, i.e. it is not exclusively adapted for CSEs, and also updated to incorporate the most recent rate constants (e.g. Agúndez et al., 2010b). The code operates by solving the ODEs system for the chemical network considered as explained in Sect. B.1.3 to obtain the fractional abundances of molecules as a function of radius (or time) for the studied CSE. The code requires as input the photosphere temperature of the star (T_*), the stellar radius (R_*), the mass loss rate ($\dot{M}$), the radial dependence of the density ($n(H_2) = f(r)$), the radial dependence of the kinetic temperature ($n(T_k) = f(r)$), the expansion velocity of the envelope (v_{exp}), the initial and final radius for the calculation (r_{in} and r_{out}), the reaction network and constant rates (e.g. Woodall et al., 2007), the UV ISRF intensity (e.g. Draine, 1978), the H_2 cosmic ray photodissociation rate (e.g. Dalgarno, 2006), and the initial abundances for the most abundant species (*parent* species) at the initial radius, which are taken from observations or from thermodynamical calculations. An example of the application of this code for the CSE oh OH231 can be seen in the Sect. 5.3 in Velilla Prieto et al. (2015a).

CHAPTER

3

MILLIMETER WAVELENGTH SPECTRAL LINE SURVEYS: IK TAU AND OH231.8+4.2

In this chapter the overall results derived from the IRAM-30 m millimeter wavelength spectral line surveys of the oxygen rich circumstellar envelopes IKTau and OH231.8+4.2 are presented. Their molecular inventory has been updated thanks to these surveys, proving that oxygen rich circumstellar envelopes are active sources of molecular formation. The IRAM-30 m millimeter wavelength survey of IKTau has been published in Velilla Prieto et al. (2017). Concerning OH231.8+4.2, the most important results from the line survey are presented in Chapters 4 and 5, that includes our comprehensive study of the new discovered species, which have been published in Velilla Prieto et al. (2015a) and Sánchez Contreras et al. (2015). In this chapter, the complete spectral line survey of OH231.8+4.2 and the most general results derived are discussed by analogy with IKTau. The full line identification list, the table of the measured line fluxes, and the rotational diagrams are presented in Section 3.4. This survey will be published in Velilla Prieto et al. (in prep.).

3.1 Summary

Spectral line surveys are wide frequency coverages of the same source. This technique allows to sample simultaneously a huge number of spectral lines, depending on the chemical richness of the source. Thus, we can determine the composition of the object by identifying the spectral lines detected. Also, we can estimate the excitation conditions, the distribution, and the abundance of a particular species if several of its lines are detected, which is the main objective of spectral line surveys (see Sect. 2). In particular, lines produced by the change of the rotational state of the molecules in the source lie in the millimeter wavelength range (see Sect. B.2.2). Previous to our study, only a few partial millimeter wavelength spectral line surveys have been carried out toward CSEs (e.g. Cernicharo et al., 2000, Kim et al., 2010). Our study represents the first sensitive millimeter wavelength surveys, for the whole frequency range covered by the IRAM-30 m telescope, toward two oxygen rich CSEs of AGB stars (Velilla Prieto et al. (2017) and Velilla Prieto et al. (in prep.)). The results from our detailed study of the new discoveries in OH231 are presented in Chapters 4 and 5, while general results are discussed here and we also present the full line identification list, the table of measured line fluxes, and the rotational diagrams in Section 3.4.

We carried out observations with the IRAM-30 m telescope using the state-of-the-art receiver EMIR (Carter et al., 2012), during several observational runs between 2009 and 2014, toward the objects IKTau and OH231 (see Sect. 1.4.1.1 and 1.4.1.2). The data reduction, analysis, and also most of the graphic representation were done using the GILDAS software package. The standard procedure followed to reduce the data and obtain the final spectra consists of the flagging of bad channels, flagging of low-quality scans, baseline subtraction, and averaging of individual scans. The spectra were obtained in the antenna temperature scale and must be corrected due to the efficiency of the antenna to the main beam temperature scale (see Sect. B.3.1).

➢ We have done the following analysis:

- identification of the spectral lines detected by using the CDMS (Müller et al., 2005) and JPL (Pickett et al., 1998) databases, as well as the the private spectroscopic catalogue compiled from extensive laboratory and theoretical works MADEX (Cernicharo, 2012),
- study of the line profiles, and measure of the main parameters of the lines such as their velocity integrated intensity or the linewidths,
- study of the time variability of the intensity of spectral lines detected,
- rotational diagram analysis to derive the rotational temperatures and column densities of the detected molecules, and the abundances averaged in the emitting region (by estimating the source dilution in the beam of the telescope),
- radiative transfer analysis with MADEX (see Sect. 2.2) of selected molecules, when needed, in particular to model the emission of SO_2 toward IKTau.

➢ From the analysis we derive the following main results:

IKTau:

- we detected spectral lines corresponding to 34 different species, including isotopologues. In particular, we detected for the first time, lines of HCO^+, H_2CO, NO, and NS, as well as lines of different isotopologues of species previously detected,
- we derived bulk gas expansion velocities consistent with the terminal expansion velocity of the CSE (v_∞∼18.5 km s^{-1}) for most species. However, NaCl, SO_2, H_2O, PO, and the lines of vibrationally excited species (e.g. SiO ν=1) display line profiles consistent with $v_{\rm exp}<v_\infty$. These narrow profiles indicate emission of gas arising from the acceleration region, i.e. the dust grain formation and growth region,
- most of the species display rotational temperatures in the range between 15 and 40 K. The most extreme values are given for CN, with a rotational temperature of 9 K, and for the warm component of SO_2, with 290 K. The column densities, averaged in the emitting region of each species, range between $\gtrsim$1.3×10^{17} cm^{-2} (in the case of ^{12}CO), and 2.6×10^{13} cm^{-2} (in the case of NS),
- the radiative transfer analysis of the SO_2 emission indicates that this molecule is present in the innermost regions of the CSE (r <8R_*), with f(SO_2)∼10^{-6}, and also with a similar abundance in the intermediate and outer parts of the CSE.

OH231:

- we observed emission lines corresponding to 45 different species, including isotopologues. Besides the molecules presented in the Chapters 4 and 5, that is HNCO, HNCS, HC_3N, NO, HCO^+, N_2H^+, SO^+, and H_3O^+, we discovered for the first time emission lines of SiS, CN, and lines of several isotopologues of other species previously detected,

- the line profiles are varied. Some species display lines compatible with emission that arises from the central slow region of the CSE ($v_{\rm exp}$∼15 km s^{-1}) and also from the fast lobes (such as CO or SO_2), lines of other species (such as SiS) are consistent with emission arising only from the central component. There is also emission of some molecules that seems to be enhanced toward the fast lobes (e.g. HCO^+ or SO^+),

- we estimated bulk gas rotational temperatures between 10 and 40 K, in general, and column densities ranging between 2.1×10^{18} cm^{-2} for ^{12}CO, down to 2.4×10^{12} cm^{-2} for Si^{17}O.

➢ From these results, we can extract the main following conclusions:

IKTau:

- the molecular content of the source evidences that it is not so chemically poor than it was assumed for O-rich AGB stars. In this object we detected emission lines of a list of H-, O-, C-, N-, S-, Si- and P-bearing molecules,

- we did not observe, a significant variability of the intensity of emission lines in the ground vibrational state observed at different epochs. However, we observed intensity variations of >25% for lines corresponding to vibrationally excited states,

- according to our analysis, the presence of SO_2 in the innermost parts of the CSE of IKTau is unexpected as predicted by the standard chemical models, even for those models that take into account shock processes in this region. TE models do not predict an efficient formation of SO_2 in the atmospheres of O-rich AGB stars, as well as for standard chemical kinetic models. Photoinduced chemistry may enhance the formation of SO_2 through the reaction between SO and OH. This could occur in an efficient way in the innermost parts of the CSE, if the envelope is clumpy enough to allow UV ISM photons penetrate deep from the outermost parts of the CSE. The surface chemistry in dust grains should be also considered for future modelling,

- the derived isotopic ratios from our analysis (see Table 6 in Sect. 3.3, which are published in Velilla Prieto et al., 2017) indicate that the post-main sequence evolution of the object has been the expected evolution for a Sun-like star.

OH231:

- in this case we detected emission lines of H-, O-, C-, N-, S-, and Si-bearing molecules. OH231 displays a particularly rich chemistry of N-bearing species (e.g. HNCO, HC_3N or NO) and cations (e.g. HCO^+, SO^+, o N_2H^+),

- the abundances observed for several species are not predicted by current chemical models, as discussed for the specific case of N-bearing molecules and the ions presented in Chapters 4 and 5, respectively,

- we observed intensity variations >25% for emission lines corresponding to vibrationally excited states,
- the derived isotopic ratios (see Table 3.3 in Sect. 3.4) also indicate a post-main sequence evolution compatible with the evolution of a Sun-like star.

3.2 Resumen

Los barridos de líneas espectrales son observaciones que cubren un amplio rango de frecuencia, lo que nos permite registrar simultáneamente un gran número de líneas espectrales, dependiendo de la riqueza química de la fuente observada. Así podemos determinar la composición del objeto observado mediante la identificación de las líneas registradas. Además, si se detectan varias líneas pertenecientes a una misma especie, que es el objetivo de los barridos, podemos estimar las condiciones de excitación, la distribución y la abundancia de dicha especie en el objeto observado (ver Sec. 2). En particular, como se muestra en la Sección B.2.2, en el rango de longitud de onda milimétrico podemos observar las líneas espectrales que se producen debido al cambio de estado rotacional de las moléculas que componen el objeto. En el caso concreto de envolturas circunestelares, anteriormente a nuestro estudio se han realizado barridos espectrales parciales en el rango milimétrico (e.g. Cernicharo et al., 2000, Kim et al., 2010). Nuestro trabajo supone los primeros barridos espectrales de alta sensibilidad para todo el rango observable con el radiotelescopio de IRAM-30 m (∼79–356 GHz), de dos envolturas circunestelares ricas en oxígeno alrededor de estrellas AGB (Velilla Prieto et al. (2017) y Velilla Prieto et al. (in prep.)). Los resultados correspondientes al estudio detallado de los nuevos descubrimientos en OH231 se presentan en los Capítulos 4 y 5, mientras que los resultados generales se discuten en el presente capítulo. En la Sección 3.4 presentamos la lista completa de líneas identificadas y la tabla con las medidas de sus flujos pertenecientes al barrido de OH231, así como los diagramas rotacionales correspondientes.

Durante distintas campañas observacionales entre los años 2009 y 2014, hemos realizado observaciones con el radiotelescopio de IRAM-30 m de los objetos IKTau y OH231.8+4.2 (ver Sec. 1.4.1.1 y 1.4.1.2) utilizando el receptor EMIR (Carter et al., 2012). La reducción de datos ha consistido en la identificación y marcado de canales y espectros malos, sustracción de línea de base, y promediado de los espectros individuales, utilizando el paquete de programas de GILDAS. Los espectros obtenidos en temperatura de antena deben corregirse de la eficiencia del telescopio a la escala de temperatura del haz principal (ver Sec. B.3.1).

➢ El análisis realizado ha consistido en:

- identificación de las líneas espectrales detectadas, utilizando las bases de datos disponibles de CDMS (Müller et al., 2005) y JPL (Pickett et al., 1998), junto con el catálogo espectroscópico privado de MADEX que compila un extenso número de trabajos teóricos y de laboratorio (Cernicharo, 2012),

- estudio de los perfiles de las líneas, junto con la medida de sus parámetros principales como sus intensidades integradas en velocidad o sus anchuras,

- estudio de la variabilidad temporal de la intensidad de las líneas observadas,

- análisis de los diagramas rotacionales para obtener las temperaturas rotacionales y densidades de columna de las moléculas detectadas, y abundancias promediadas dentro de la región emisora (estimando la dilución de la fuente en el haz del telescopio),

- análisis de transferencia radiativa con MADEX (ver Sec. 2.2) para modelizar la emisión molecular de ciertas moléculas seleccionadas, en particular para SO_2 en IKTau.

➢ Los resultados extraídos del análisis son los siguientes:

IKTau:

- se han detectado líneas espectrales correspondientes a 34 especies distintas, incluyendo isotopólogos. En particular, se han detectado por primera vez las moléculas HCO^+, H_2CO, NO y NS, además de distintos isotopólogos de especies previamente detectadas,
- de los perfiles de líneas se derivan velocidades de expansión para el grueso del gas trazado consistentes con la velocidad terminal del gas de la envoltura ($v_\infty \sim 18.5\,\mathrm{km\ s^{-1}}$) para la mayor parte de especies. Se observan perfiles estrechos que indicarían $v_{\rm exp} < v_\infty$ para líneas de especies como NaCl, SO_2, H_2O, PO y las líneas de especies en estados vibracionales excitados (e.g. SiO ν=1), que correspondería con emisión de gas en la zona de aceleración (zona de formación y crecimiento del polvo),
- la mayor parte de las especies detectadas muestran temperaturas rotacionales comprendidas entre 15 y 40 K. Los valores más extremos se dan para el CN, con una temperatura de 9 K, y para la componente caliente de SO_2, con 290 K. Las densidades de columna promediadas para la región emisora que estimamos, varían entre $\gtrsim 1.3\times10^{17}\,\mathrm{cm^{-2}}$ para ^{12}CO y $2.6\times10^{13}\,\mathrm{cm^{-2}}$ para NS,
- el análisis de transferencia radiativa de la emisión del SO_2 indica que esta especie debe estar presente en las regiones internas de la envoltura ($r < 8R_*$) con una abundancia $f(SO_2) \sim 10^{-6}$, y en la región intermedia y externa también con una abundancia similar.

OH231:

- hemos observado líneas de emisión que corresponden a 45 especies distintas, incluyendo isotopólogos. Además de las moléculas presentadas en los Capítulos 4 y 5, HNCO, HNCS, HC_3N, NO, HCO^+, N_2H^+, SO^+, y H_3O^+ se han detectado por primera vez líneas de emisión de SiS, CN, y algunos isotopólogos de otras especies previamente detectadas,
- se observan distintos perfiles dependiendo de la especie considerada. Algunas especies muestran perfiles que indicarían que la emisión proviene de la región central de expansión lenta ($v_{\rm exp} \sim 15\,\mathrm{km\ s^{-1}}$) de la envoltura, y también con los lóbulos de expansión rápida (como por ejemplo CO o SO_2), otras sólo muestran emisión en la zona central (e.g. SiS), y otras parecen estar favorecidas en los lóbulos (e.g. HCO^+ o SO^+),
- encontramos temperaturas comprendidas entre 10 y 40 K para el grueso del gas en general, y densidades de columna comprendidas entre $2.1\times10^{18}\,\mathrm{cm^{-2}}$ para ^{12}CO y $2.4\times10^{12}\,\mathrm{cm^{-2}}$ para $Si^{17}O$.

➢ De estos resultados podemos concluir que:

IKTau:

- el contenido molecular de la fuente demuestra que no es tan químicamente pobres como se asumía para estrellas AGB ricas en oxígeno. En este objeto hemos detectado líneas de emisión de especies que contienen H, O, C, N, S, Si y P,
- no se ha observado, en general, una variabilidad significativa en la intensidad de las líneas de emisión correspondientes al nivel vibracional fundamental y que han sido observadas en distintas épocas. Sólo para aquellas líneas que corresponden a especies en estados de vibración excitados, se han detectado variaciones de intensidad que alcanzan valores >25 %,

- la presencia de SO_2 con una abundancia de $\sim 10^{-6}$ en la región interna de la envoltura de IKTau, de acuerdo a nuestro análisis, es inesperada de acuerdo a los modelos de química estándar, incluso aquellos que tienen en cuenta los procesos de choque. Los modelos de química en ET no predicen la formación eficiente de SO_2 en las atmósferas de estrellas AGB ricas en oxígeno, y tampoco la química estándar predice su formación. La química fotoinducida podría favorecer la formación de SO_2 mediante la reacción del SO con el OH. Para que esto ocurriera de manera eficiente en las regiones internas, la envoltura debería estar distribuido de manera grumosa para permitir la penetración de fotones UV del medio interestelar desde las zonas externas. Otro factor adicional que habrá que considerar para modelos futuros es la química de granos de polvo,

- las razones isotópicas derivadas de nuestro análisis (ver Tabla 6 en la Sec. 3.3, publicada en Velilla Prieto et al., 2017) indicarían que la evolución del objeto tras la secuencia principal ha sido la esperada para una estrella de masa similar a la del Sol.

OH231:

- en el caso de OH231, encontramos líneas de emisión de especies con H, O, C, N, S y Si. OH231 muestra una química peculiar, particularmente rica en especies con nitrógeno (e.g. HNCO, HC_3N o NO), y algunos cationes moleculares (e.g. HCO^+, SO^+, o N_2H^+),

- las abundancias que determinamos para muchas especies no son predichas por los modelos químicos actuales, como discutimos para el caso específico de las moléculas con nitrógeno y los iones de los Capítulos 4 y 5, respectivamente,

- hemos observado variaciones de intensidad $>25\,\%$ correspondientes a las líneas de emisión de niveles vibracionalmente excitados,

- para OH231, las razones isotópicas (ver Tabla 3.3 en la Sec. 3.4) también indicarían una evolución post-secuencia principal compatible con la evolución de una estrella de tipo solar.

3.3 Velilla Prieto et al. 2017[1]

A&A 597, A25 (2017)
DOI: 10.1051/0004-6361/201628776
© ESO 2016

Astronomy & Astrophysics

The millimeter IRAM-30 m line survey toward IK Tauri[⋆,⋆⋆]

L. Velilla Prieto[1,2], C. Sánchez Contreras[2], J. Cernicharo[1], M. Agúndez[1], G. Quintana-Lacaci[1], V. Bujarrabal[3], J. Alcolea[4], C. Balança[5], F. Herpin[6,7], K. M. Menten[8], and F. Wyrowski[8]

[1] Instituto de Ciencia de Materiales de Madrid, CSIC, c/ Sor Juana Inés de la Cruz 3, 28049 Cantoblanco, Madrid, Spain
e-mail: lvelilla@icmm.csic.es
[2] Centro de Astrobiología, INTA-CSIC, 28691 Villanueva de la Cañada, Madrid, Spain
[3] Observatorio Astronómico Nacional (IGN), Ap 112, 28803 Alcalá de Henares, Madrid, Spain
[4] Observatorio Astronómico Nacional (IGN), Alfonso XII No 3, 28014 Madrid, Spain
[5] LERMA, Observatoire de Paris, Sorbonne Université, UPMC, UMR 8112, 92195 Meudon, France
[6] Université de Bordeaux, LAB, UMR 5804, 33270 Floirac, France
[7] CNRS, LAB, UMR 5804, 33270 Floirac, France
[8] Max-Planck-Institut für Radioastronomie, Auf dem Hügel 69, 53121 Bonn, Germany

Received 22 April 2016 / Accepted 24 August 2016

ABSTRACT

Aims. We aim to investigate the physical and chemical properties of the molecular envelope of the oxygen-rich AGB star IK Tau.
Methods. We carried out a millimeter wavelength line survey between ~79 and 356 GHz with the IRAM-30 m telescope. We analysed the molecular lines detected in IK Tau using the population diagram technique to derive rotational temperatures and column densities. We conducted a radiative transfer analysis of the SO_2 lines, which also helped us to verify the validity of the approximated method of the population diagram for the rest of the molecules.
Results. For the first time in this source we detected rotational lines in the ground vibrational state of HCO^+, NS, NO, and H_2CO, as well as several isotopologues of molecules previously identified, namely, $C^{18}O$, $Si^{17}O$, $Si^{18}O$, ^{29}SiS, ^{30}SiS, $Si^{34}S$, $H^{13}CN$, ^{13}CS, $C^{34}S$, $H_2{}^{34}S$, ^{34}SO, and $^{34}SO_2$. We also detected several rotational lines in vibrationally excited states of SiS and SiO isotopologues, as well as rotational lines of H_2O in the vibrationally excited state $\nu_2 = 2$. We have also increased the number of rotational lines detected of molecules that were previously identified toward IK Tau, including vibrationally excited states, enabling a detailed study of the molecular abundances and excitation temperatures. In particular, we highlight the detection of NS and H_2CO with fractional abundances of $f(\mathrm{NS}) \sim 10^{-8}$ and $f(\mathrm{H_2CO}) \sim [10^{-7}$–$10^{-8}]$. Most of the molecules display rotational temperatures between 15 and 40 K. NaCl and SiS isotopologues display rotational temperatures higher than the average (~65 K). In the case of SO_2 a warm component with $T_{\rm rot} \sim 290$ K is also detected.
Conclusions. With a total of ~350 lines detected of 34 different molecular species (including different isotopologues), IK Tau displays a rich chemistry for an oxygen-rich circumstellar envelope. The detection of carbon bearing molecules like H_2CO, as well as the discrepancies found between our derived abundances and the predictions from chemical models for some molecules, highlight the need for a revision of standard chemical models. We were able to identify at least two different emission components in terms of rotational temperatures. The warm component, which is mainly traced out by SO_2, is probably arising from the inner regions of the envelope (at $\lesssim 8\ R_*$) where SO_2 has a fractional abundance of $f(\mathrm{SO_2}) \sim 10^{-6}$. This result should be considered for future investigation of the main formation channels of this, and other, parent species in the inner winds of O-rich AGB stars, which at present are not well reproduced by current chemistry models.

Key words. astrochemistry – line: identification – stars: abundances – stars: AGB and post-AGB – circumstellar matter

1. Introduction

Asymptotic giant branch (AGB) stars are the main contributors to the interstellar medium (ISM) chemical enrichment. The physical conditions, that is, the high densities ($\gtrsim 10^{12}$ cm^{-3}) and temperatures (~2000–3000 K), in their atmospheres allow the formation of stable molecules. All this molecular material is driven by the slow AGB wind creating a circumstellar envelope (CSE) that surrounds the star, up to regions where the interstellar UV field photodissociates the molecules. Carbon and oxygen are the two most abundant and reactive elements in the atmospheres and winds of AGB stars, after hydrogen. All the possible carbon monoxide, which is a very stable molecule, is formed and then depending on which element (carbon or oxygen) is in excess, other molecules will be formed. Hence, the chemistry in these objects mainly depends on the elemental carbon to oxygen ratio, being O-rich ([C]/[O] < 1), C-rich ([C]/[O] > 1) or S-type stars ([C]/[O] ~ 1) (e.g. Olofsson 1996).

Since the first detection of CO in the millimeter wavelength range toward the CSE of an AGB star (Solomon et al. 1971), the observations of the molecular emission of CSEs in that wavelength domain have increased (e.g. Morris et al. 1975; Bujarrabal & Alcolea 1991; Cernicharo et al. 2015). These studies have been mostly focused on C-rich CSEs given that carbon is more chemically active than oxygen and, therefore, C-rich envelopes are expected and observed to display a large

⋆ Based on observations carried out with the IRAM-30 m Telescope. The Institut de Radioastronomie Millimétrique (IRAM) is supported by INSU/CNRS (France), MPG (Germany) and IGN (Spain).
⋆⋆ Full Tables E.1 and E.2 and the reduced spectrum (FITS file) are only available at the CDS via anonymous ftp to cdsarc.u-strasbg.fr (130.79.128.5) or via http://cdsarc.u-strasbg.fr/viz-bin/qcat?J/A+A/597/A25

[1] A&A, 597, A25, 2017, reproduced with permission © ESO

A&A 597, A25 (2017)

variety of different molecular species (e.g. Cernicharo et al. 2000; Smith et al. 2015). However, the number of studies in the millimeter wavelength range has increased in the last years, and these studies have evidenced that O-rich CSEs do also host a rich variety of molecules (Ziurys et al. 2007; Kim et al. 2010; De Beck et al. 2013; Sánchez Contreras et al. 2015, and references therein).

Our motivation is to observe and to study the molecular content of the oxygen-rich CSE IK Tauri which is one of the most studied O-rich CSEs, and is considered a reference of its class.

1.1. IK Tauri

IK Tauri (hereafter IK Tau), also known as NML Tau, is a Mira-type variable star with a period of 470 days and a spectral type ~M9 (Pesch 1967; Wing & Lockwood 1973; Alcolea et al. 1999). This star was discovered by Neugebauer et al. (1965) and it is located at α(J2000) = $3^h53^m28\overset{s}{.}87$ and δ(J2000) = 11°24′21.″7 (Cutri et al. 2003). The distance to IK Tau was estimated to be 250–265 pc (Hale et al. 1997; Olofsson et al. 1998). The systemic velocity of the star with respect to the local standard of rest is $V_{\rm sys}^{\rm LSR} \sim 34$ km s^{-1} (Kim et al. 2010, and references therein). Its effective temperature is $T_{\rm eff} \sim 2200$ K and the stellar radius is $R_* \sim 2.5 \times 10^{13}$ cm (Decin et al. 2010a).

The star is surrounded by a an O-rich CSE, composed of dust and gas, which is the result of mass loss at a rate that has been estimated by different methods. Neri et al. (1998) estimated $\dot{M} \sim 3.8{\times}10^{-6}\ M_\odot$ yr^{-1} from the model of ^{12}CO J = 1–0 and J = 2–1 lines. González Delgado et al. (2003) estimated $\dot{M} \sim 3.0 \times 10^{-5}\ M_\odot$ yr^{-1} from the model of ^{12}CO J = 1–0, J = 2–1, J = 3–2, and J = 4–3 lines. Recent modelling of the J = 3–2, J = 4–3, and J = 7–6 lines of ^{12}CO yielded $\dot{M} \sim 4.7 \times 10^{-6}\ M_\odot$ yr^{-1} (Kim et al. 2010). The terminal expansion velocity of the CSE is $v_\infty \sim 18.5$ km s^{-1} as measured from De Beck et al. (2013) and references therein. The size of the CSE depends on the molecule used to trace it out. Bujarrabal & Alcolea (1991) gave a half-intensity diameter of $\theta_{1/2} \sim$ 16–17″ measured for ^{12}CO J = 1–0 and ^{12}CO J = 2–1 emission detected with the IRAM-30 m telescope. Kim et al. (2010) measured a $\theta_{1/2} \sim 20''$ for ^{12}CO J = 3–2 with the Atacama Pathfinder EXperiment (APEX) telescope. Recent observations with the Plateau de Bure Interferometer (PdBI), showed that ^{12}CO (J = 1–0) displays a $\theta_{1/2} \sim 18''$ (Castro-Carrizo et al. 2010). Also, HCN J = 1–0 was observed with the Owens Valley millimeter-array by Marvel (2005), displaying a size of $\theta_{1/2} \sim 3\overset{''}{.}85$. The size of the SiO v = 0 J = 2–1 emission is $\theta_{1/2} = 2\overset{''}{.}2 \pm 0\overset{''}{.}1$ as determined with PdBI (Lucas et al. 1992). Finally, the emission of several lines of PN and PO has been mapped with the SubMillimeter Array (SMA), with $\theta_{1/2} \lesssim 0\overset{''}{.}65$ (De Beck et al. 2013).

The O-rich CSE around IK Tau displays maser emission of OH, H_2O, and SiO (Lane et al. 1987; Bowers et al. 1989; Alcolea & Bujarrabal 1992; Kim et al. 2010, and references therein). It also shows thermal molecular emission of ^{12}CO, ^{13}CO, SiO, ^{29}SiO, ^{30}SiO, OH, SiS, HCN, HC_3N, H_2S, SO, SO_2, NaCl, H_2O, $H_2{}^{17}O$, $H_2{}^{18}O$, NH_3, CS, CN, PO, PN, AlO, and tentatively, HNC (Lindqvist et al. 1988; Omont et al. 1993; Bujarrabal et al. 1994; Milam et al. 2007; Kim et al. 2010; Decin et al. 2010b; Menten et al. 2010; Justtanont et al. 2012; De Beck et al. 2013, 2015, and references therein). Some of the molecules observed up to date in IK Tau have been compared with chemical models and their line emission analysed with radiative transfer models (Willacy & Millar 1997; Duari et al. 1999; Cherchneff 2006; Kim et al. 2010; Decin et al. 2010a; Danilovich et al. 2016; Gobrecht et al. 2016; Li et al. 2016). Nevertheless, most of the reported abundances in previous studies were derived from the analysis of a moderated number of lines (e.g. Milam et al. 2007; De Beck et al. 2013). Additionally, discrepancies remain between the predicted abundances and the observations, for example for SO_2 (Decin et al. 2010a; Gobrecht et al. 2016).

1.2. This paper

In this article we report the millimeter wavelength survey between ~79 and ~356 GHz carried out with the IRAM-30 m telescope toward IK Tau, which allowed us to detect rotational lines of 34 different species (including isotopologues). We detected for the first time in this source HCO^+, NS, H_2CO, and NO, as well as several isotopologues of previously identified molecules, such as $C^{18}O$, $Si^{17}O$, $Si^{18}O$, ^{29}SiS, ^{30}SiS, $Si^{34}S$, $H^{13}CN$, ^{13}CS, $C^{34}S$, $H_2{}^{34}S$, ^{34}SO, and $^{34}SO_2$. For molecules with previous detections reported in the literature, we increased significantly the number of transitions observed, which is needed for a robust estimate of the excitation conditions and molecular abundances. We report the results of our analysis based on population diagrams, used to derive rotational temperatures and column densities. We also estimated fractional abundances which have been compared with values derived from previous observations and with predictions by chemical models. In the particular case of SO_2, we performed a radiative transfer calculation to study the excitation conditions of the ~90 lines detected with more detail. This suggests that this molecule is rather abundant not only in the intermediate and outer envelope but also in the inner, hotter and more dense regions of the CSE, where we estimate an average fractional abundance of $\sim 10^{-6}$ (with respect to H_2). This radiative transfer model also allowed us to verify the validity of the population diagram analysis for the rest of the species detected.

2. Observations

The observations presented in this paper correspond to a sensitive millimeter-wavelength (~79–356 GHz) survey carried out with the IRAM-30 m telescope toward the CSEs of two O-rich evolved stars, IK Tau and OH231.8+4.2, during several observing runs from 2009 to 2014. Partial results from the survey toward OH 231.8+4.2 are reported in Sánchez Contreras et al. (2014, 2015) and Velilla Prieto et al. (2013, 2015).

We used the heterodyne Eight MIxer Receiver (EMIR) working at four different wavelengths bands: E090 = 3 mm, E150 = 2 mm, E230 = 1.3 mm, and E330 = 0.9 mm (Carter et al. 2012). This receiver system was operated in single-sideband (SSB) mode for the E150 band and in dual sideband (2SB) mode for bands E090, E230, and E330. Two polarizations – horizontal and vertical – were available per sideband. The typical EMIR value image band rejection is approximately −14 dB or better, this implies that the peak intensity of a line entering through the image band is only $\lesssim$4% of its real value. We verified this value for the image band rejection measuring the relative intensities of strong lines that appear both in the signal and image bands.

Four different backends or spectrometers were connected to each receiver depending on their availability: the WIde Lineband Multiple Autocorrelator (WILMA), the fast Fourier Transform Spectrometer (FTS), the VErsatile SPectrometer Array (VESPA) and the 4 MHz spectrometer. The capabilities of these spectrometers and their usage are summarised in Table 1.

The observational technique used was the wobbler switching with a single pointing toward the position of the source (see

Table 1. Specifications for the spectrometers used.

Name	SR	VR	IBWEP	Usage
–	(MHz)	(km s^{-1})	(GHz)	–
WILMA	2.000	1.7–7.6	3.7	E090, E150, E230, E330
FTS	0.195	0.2–0.7	4.0	E230, E330
VESPA	1.250	1.0–4.7	0.4	E090, E150, E230, E330
4 MHz	4.000	3.4–15.2	4.0	E150, E230, E330

Notes. Column 2: spectral resolution; Col. 3: spectral resolution in velocity units, the highest velocity resolution (the first number of the range) corresponds to 356 GHz and the lowest resolution to 79 GHz; Col. 4: instantaneous bandwidth in each polarization; Col. 5: EMIR bands observed with the corresponding spectrometer.

Sect. 1.1) and a wobbler throw of 120″ in azimuth. We configured different setups (tuning steps) to observe both polarizations simultaneously until we covered the total frequency range available for each EMIR band. We selected a small overlap between adjacent setups to ensure a uniform calibration across the bands. During the observations we checked regularly the pointing and focus of the antenna every ∼1.5 and ∼4 h, respectively, on strong nearby sources. On-source integration times per setup were ∼1 h. Calibration scans on the standard two loads + sky system were taken every ∼18 min using the atmospheric transmission model (ATM) adopted by IRAM-30 m (Cernicharo et al. 1985; Pardo et al. 2001). Errors in the absolute flux calibration are expected to be ≲25%.

The data reduction, analysis and also most of the graphic representation were done using the GILDAS[1] software package. The standard procedure followed to reduce the data and obtain the final spectra consists of the flagging of bad channels, the flagging of low-quality scans, the baseline substracting, and finally, the averaging of individual scans.

The output spectra obtained from the antenna are calibrated in antenna temperature ($T_A{}^*$), which can be converted to main beam temperature (T_{mb}) and brightness temperature (T_B) according to:

$$T_B = T_A^* \, \eta^{-1} \, bff^{-1}, \quad (1)$$

$$\eta^{-1} = F_{eff}/B_{eff}, \quad (2)$$

$$bff^{-1} = (\theta_b^2 + \theta_s^2)/\theta_s^2, \quad (3)$$

where η is the main beam efficiency, bff is the beam-filling factor, B_{eff} is the main-beam efficiency of the antenna, F_{eff} is the forward efficiency of the antenna, θ_s is the size (diameter) of the emitting region of the source, and θ_b is the half power beamwidth (HPBW) of the main beam of the antenna. See Table 2 for a summary of the relevant telescope parameters.

The half power width of the main beam can be approximated, using the values in Table 2, to a good accuracy by the expression:

$$\theta_b\,('') = 2460/\nu\,(\mathrm{GHz}), \quad (4)$$

and the inverse of the main beam efficiency can be fitted (see Fig. 1) using the parameters in Table 2, to obtain:

$$\eta^{-1} \equiv F_{eff}/B_{eff} = 1.114 \, \exp\{(\nu\,(\mathrm{GHz})/399.5)^2\}. \quad (5)$$

[1] GILDAS is a world-wide software to process, reduce and analyse astronomical single-dish and interferometric observations mainly. It is maintained by the Institut de Radioastronomie Millimétrique (IRAM). See http://www.iram.fr/IRAMFR/GILDAS

Table 2. Main parameters of the IRAM-30 m antenna measured with EMIR between 2009 and 2013 at representative frequencies.

Frequency	B_{eff}	F_{eff}	HPBW	S/T_A^*
(GHz)	(%)	(%)	(″)	(Jy/K)
86	81	95	29†	5.9†
115	78	94	–	–
145	73	93	16†	6.4†
210	63	94	11†	7.5†
230	59	92	10.7‡	–
280	49	87	–	–
340	35	81	7.5†	10.9†
345	34	80	–	–

Notes. Column 1: representative frequency; Col. 2: beam efficiency; Col. 3: forward efficiency; Col. 4: half power beam width; Col. 5: flux density to antenna temperature conversion factor in Jansky per Kelvin for a point-like source. $^{(\dagger)}$ 2009 values. $^{(\ddagger)}$ 2012 value. The values without symbols were reported on 2013. Source: http://www.iram.es/IRAMES/mainWiki/Iram30mEfficiencies

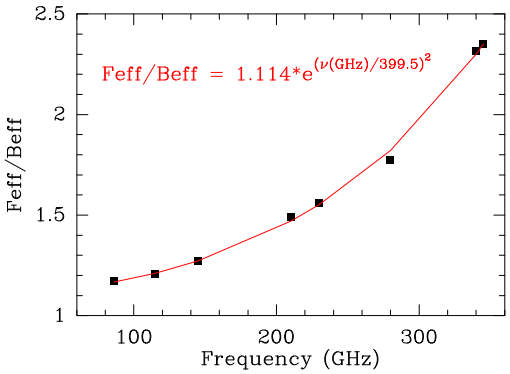

Fig. 1. Fit of the inverse of the main beam efficiency for the IRAM-30 m with EMIR.

2.1. Observational results

Our results are based mainly on the spectra obtained with WILMA and FTS given their better spectral resolution and bandwidth. The data obtained with the 4 MHz spectrometer were used to check the edges of the setups that were only observed with WILMA, given that the 4 MHz bandwidth is slightly larger than the bandwidth of WILMA, but it has the same bandwidth than that of the FTS (see Table 1). VESPA data were used only to check certain line profiles. However, only WILMA was available to cover the full EMIR wavelength range. For example, FTS was not avaliable in the E150 band at the epoch of the observations and also some technical issues prevented us from use the FTS with the E090 band.

The spectra of the full mm-wavelength survey carried out with IRAM-30 m toward IK Tau with the WILMA and the FTS spectrometers can be seen in Fig. 2 and also in more detail in Fig. C.1. The ^{12}CO, ^{13}CO, and C^{18}O line profiles are shown in Fig. 3. In Table 3 we show a summary of the observational results.

A&A 597, A25 (2017)

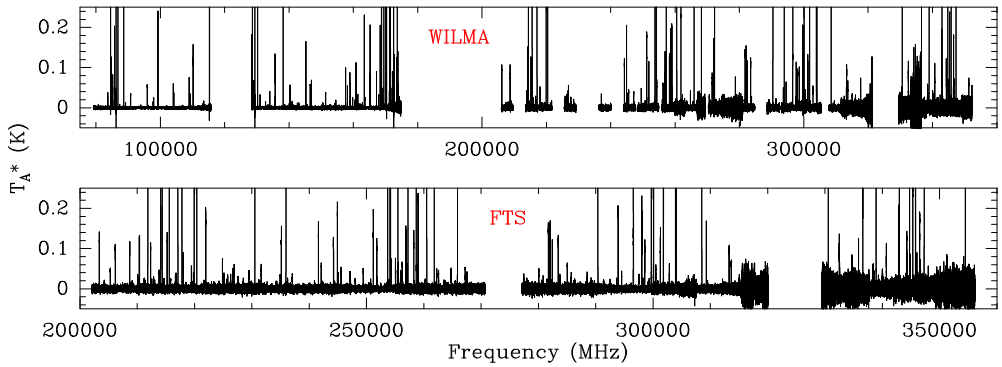

Fig. 2. Overall view of the survey observed with WILMA (*top*) and FTS (*bottom*). The spectral resolution is $\Delta\nu = 2$ MHz.

Table 3. Summary of the observational results.

Band	SP	ν_{obs}	rms	Opacity
–	–	(GHz)	(mK)	–
E090	WILMA	79.3–115.7	1.5 (0.5)	0.12 (0.05)
E150	WILMA	128.4–174.8	2.7 (1.3)	0.19 (0.11)
E230	FTS	202.1–270.7†	4.7 (0.6)	0.18 (0.03)
E330	FTS	277.1–356.2‡	12.8 (10.4)	0.26 (0.16)

Notes. Values given between parentheses represent 1σ of the value. Col. 1 EMIR band; Col. 2 spectrometer; Col. 3 observed frequency windows in GHz; Col. 4 root mean square (rms) noise in units of T_a^* for a spectral resolution of 2 MHz; Col. 5 zenith atmospheric opacity at the observed frequency. $^{(\dagger)}$ 217.5–217.8 gap. $^{(\ddagger)}$ 325.0–329.5 gap.

3. Line identification

For the line identification, we used the public line catalogues from the Cologne Database for Molecular Spectroscopy (CDMS, Müller et al. 2005) and the Jet Propulsion Laboratory (JPL, Pickett et al. 1998), together with a private spectroscopic catalogue that assembles information for more than five thousand spectral entries (atoms and molecules, including vibrationally excited states), compiled from extensive laboratory and theoretical works (the MADEX code, Cernicharo 2012).

Given the wavelength range covered in our observations, we detected, mainly, rotational transitions in the ground vibrational state, but also, rotational transitions in higher vibrational states (i.e. SiO $v = 1$, SiO $v = 2$, SiO $v = 3$, ^{29}SiO $v = 1$, ^{29}SiO $v = 2$, ^{29}SiO $v = 3$, ^{30}SiO $v = 1$, ^{30}SiO $v = 2$, H_2O $\nu_2 = 1$, and H_2O $\nu_2 = 2$). We established the detection limit at $\geq 5\sigma$ with respect to the integrated intensity for well detected features, and between 3σ and 5σ for tentative detections, although, these tentative detections may be more reliable when they belong to well-known species that have been identified through other stronger lines.

We detected ~450 spectral features in the spectra of IK Tau, ~90 % of which are lines in the signal side band of the receivers. Of the ~400 signal band features, ~350 lines have been unambiguously identified with rotational transitions of 34 different species (including vibrationally excited states), which are reported in Tables A.1 and A.2, along with some of their spectroscopic parameters and their fitted parameters. The rest of the lines (~35) remain unidentified, although, we proposed a tentative identification for some of them (see Table B.1).

There were several lines that we assigned to spurious features produced in the receivers in the range 167 475–174 800 MHz (Table B.2). These spurious features are symmetrical replicas at both sides of certain strong real emission lines, with the intensities of the replicas decreasing with the frequency distance to the real feature. We show in Fig. B.1 an example of this problem.

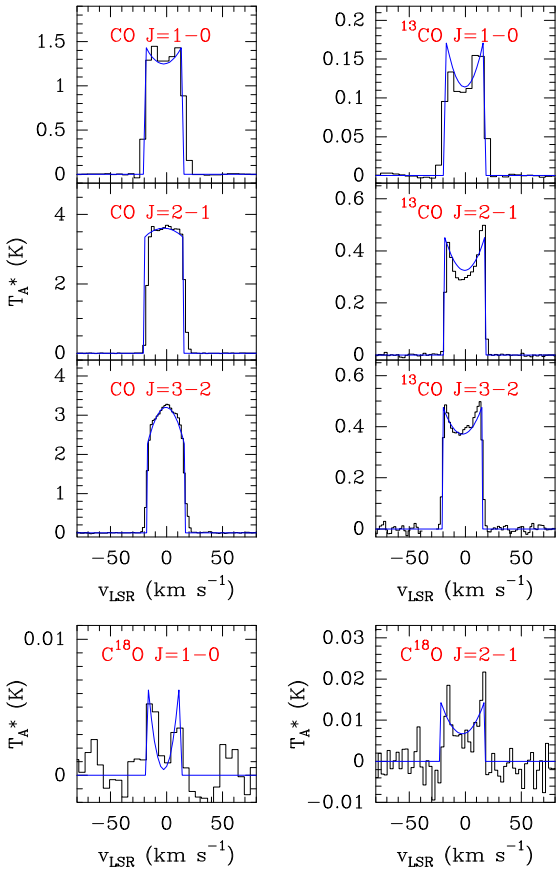

Fig. 3. ^{12}CO, ^{13}CO, and C^{18}O lines detected with our millimeter wavelength survey with a spectral resolution of $\Delta\nu = 2$ MHz. The fit of each line to a function of the type given by Eq. (6) is shown in blue.

The features of the image band and the spurious features were blanked in the final data.

We identified for the first time toward IK Tau, rotational lines of: HCO^+, NO, H_2CO, NS, $C^{18}O$, SiO v = 2, ^{29}SiO v = 2, ^{29}SiO v = 3, ^{30}SiO v = 2, $Si^{17}O$, $Si^{18}O$, ^{29}SiS, ^{30}SiS, $Si^{34}S$, SiS v = 1, $H^{13}CN$, ^{13}CS, $C^{34}S$, $H_2{}^{34}S$, ^{34}SO, $^{34}SO_2$, and H_2O ν_2 = 2. We also detected rotational lines of: ^{12}CO, ^{13}CO, SiO, SiO v = 1, SiO v = 3, ^{29}SiO, ^{29}SiO v = 1, ^{30}SiO v = 1, SiS, HCN, HNC, CS, NaCl, H_2S, SO, SO_2, PN, PO, CN, H_2O, and H_2O ν_2 = 1. The result of the identification can be seen in Fig. C.1.

4. Data analysis

4.1. Line profiles

Most of the lines show profiles that can be reasonably well fitted with the so-called shell profile provided by the software CLASS[2]:

$$f(\nu) = \frac{A}{\Delta\nu}\frac{1 + 4H[(\nu - \nu_o)/\Delta\nu]^2}{1 + H/3}, \quad (6)$$

where A is the area under the profile, ν_o is the central frequency, $\Delta\nu$ is the full width at zero intensity, and H is the horn to centre ratio. The expansion velocity (v_{exp}) can be related to the $\Delta\nu$ of a line through the expression:

$$v_{exp} = c\frac{\Delta\nu/2}{\nu_o}, \quad (7)$$

where c is the speed of light.

In the case of a spherical CSE, there are several typical line profiles which are commonly found: U-shaped, parabolic, flat-topped, Gaussian-like or triangular. Each type of profile has a particular interpretation in terms of the size of the emitting region compared to the θ_b of the telescope, the optical thickness of the line, and the kinematical properties of the gas responsible of the spectroscopic feature (e.g. Zuckerman 1987; Habing & Olofsson 2004). All these profiles are described to a good accuracy by the shell function described before in Eq. (6).

In Fig. 4 we show a sample of the line profiles observed. Most of the lines display profiles that match one of the types mentioned before, although, some profiles are complex and have to be considered carefully in the analysis. We also observed lines that are significatively narrower and more intense than the average, that is, they show maser like spectral profiles (see Fig. 4 bottom-right panel). For the sake of consistency we used the shell profile described in Eq. (6) to fit all the lines detected, even for the narrow lines since that should give us an approximated idea of the characteristic velocity in the regions of the wind acceleration. The aim of the fit is to estimate the centroids and linewidths, however, the velocity integrated intensities given in Tables A.1, A.2, and B.1 were obtained integrating the whole line profiles. The line profiles observed are discussed in detail for each detected molecule in Sect. 6.

4.2. Population diagrams and fractional abundances

Using the population diagram technique (Goldsmith & Langer 1999), we derived rotational temperatures and column densities averaged in the emitting region of the molecules detected. These values were derived using the following equation:

$$\ln\left(\frac{N_u}{g_u}\right) = \ln\left(\frac{3k_B W}{8\pi^3\,\nu\,S_{ul}\,\mu^2}\right) = \ln\left(\frac{N}{Z}\right) - \frac{E_u}{k_B T_{rot}}, \quad (8)$$

[2] See http://www.iram.fr/IRAMFR/GILDAS

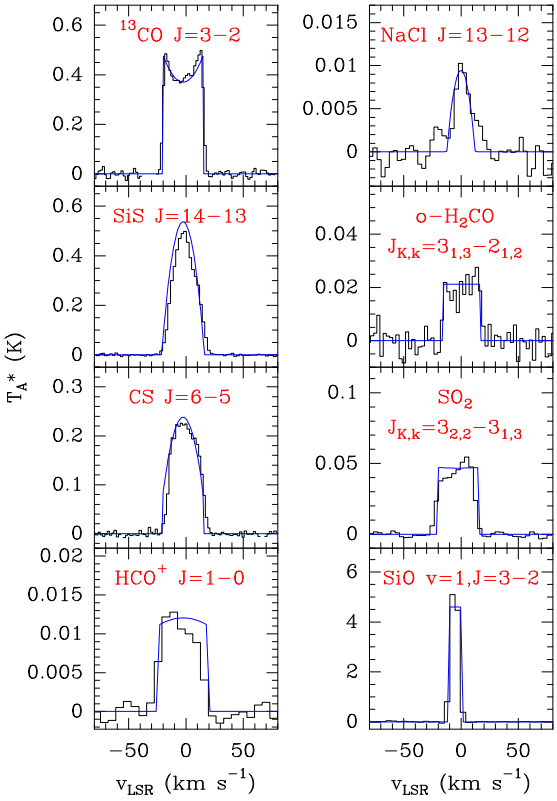

Fig. 4. Representative profiles of the lines observed. From *top-left to bottom-right*: U-shaped, Gaussian-like, triangular, flat-topped, parabolic, complex, flat-topped, and a narrow maser-like line. The spectral resolution is $\Delta\nu$ = 2 MHz. The fit of each line to a function of the type given by Eq. (6) is shown in blue.

where N_u is the column density of the upper level, g_u is the degeneracy of the upper level, W is the velocity-integrated intensity of the line, k_B is the Boltzmann constant, ν is the rest frequency of the transition, S_{ul} is the line strength, μ is the dipole moment of the molecule, N is the total column density, Z is the partition function, E_u is the upper level energy of the transition, and T_{rot} is the rotational temperature. The results of the populations diagrams are reported in Sect. 5.2 and Appendix D.

This method relies on local thermodynamical equilibrium (LTE), optically thin emission, as well as an uniform rotational temperature for the gas shell, and it permits the analysis of all the molecules using a homogeneus criteria. Also, the size of the emitting region for each molecule has to be known to account for the proper dilution of the emission. We have adopted approximate sizes of the emitting regions of $\theta_s(^{12}CO,^{13}CO)$ = 18″ which is a representative value for the sizes measured in Bujarrabal & Alcolea (1991), Castro-Carrizo et al. (2010), and Kim et al. (2010). We also adopted the sizes θ_s(HCN, $H^{13}CN$) = 4″ (Marvel 2005), θ_s = 2″ for SiO isotopologues (Lucas et al. 1992), and $\theta_s \lesssim$ 0.″7 for PO and PN (De Beck et al. 2013). Similar values have been also used for these molecules by Kim et al. (2010). For the rest of the molecules, which have not been mapped, we assumed emitting

A&A 597, A25 (2017)

region sizes according to observational constraints, previous estimations, or predictions by radiative transfer and chemical models. These values are given in Table 5 and discussed in Sect. 6. We note that the adopted sizes are uncertain for some molecules and also that the emitting region size may vary for each transition of a given molecule. In general, an underestimation of the size of any emitting region will cause an underestimation of the beam filling factor (see Eq. (3)) and, thus, an overestimation of the abundance, and vice versa.

There are additional sources of uncertainty in the values derived from the population diagrams. In particular, the kinetic temperature ($T_{\rm kin}$) throughout the CSE is not expected to be constant. This effect is less important for the molecules whose emission arises from regions with very uniform physical conditions (inner layers, photodissociation layers, etc.), and it must be more important for species whose emission extends through the whole envelope, such as probably SO_2, for which we did a more detailed radiative transfer analysis (see Sect. 4.3).

In the population diagrams, we have included lines (unambigously identified and unblended) with fluxes above 5σ. For those molecules well known to be present in the envelope of IK Tau, we have also included lines with 3–5σ detections. In the case of molecules with a hyperfine structure that cannot be spectrally resolved with the spectral resolution achieved, that is, CN, NS, and NO, we measured the total integrated intensity of the blend of the hyperfine components and we calculated the sum of the strength of the hyperfine components to compute their population diagrams. In the case of H_2S we fitted together the lines of the ortho and para species due to the scarce number of lines detected for each species individually.

We have not calculated population diagrams for the molecules SiO $v = 1$, SiO $v = 2$, SiO $v = 3$, ^{29}SiO $v = 1$, ^{29}SiO $v = 2$, ^{29}SiO $v = 3$, ^{30}SiO $v = 1$, ^{30}SiO $v = 2$, H_2O, H_2O $\nu_2 = 1$ or H_2O $\nu_2 = 2$. Some of these lines are masers and their populations are expected to strongly deviate from a Boltzmann distribution. Also, the intensity of the lines of these molecules may vary with the stellar pulsation phase and, given that the observations spread over a period of time of approximately five years, the excitation conditions may have changed along the observational runs (see Sect. 6.1).

The fractional abundances averaged in the emitting region for the molecules detected are calculated using the following equation:

$$f(X) = N(X)\frac{f(^{13}\mathrm{CO})}{N(^{13}\mathrm{CO})}, \quad (9)$$

where f(X) and N(X) represent the fractional abundance (with respect to H_2) and column density of the molecule analysed, respectively. $N(^{13}\mathrm{CO})$ is the column density that we derived from the ^{13}CO population diagram, and $f(^{13}\mathrm{CO}) = 1.4 \times 10^{-5}$ (Decin et al. 2010a).

4.3. Radiative transfer model: MADEX

MADEX (Cernicharo 2012) is a radiative transfer code which is able to operate under LTE and large velocity gradient (LVG) approximation (Goldreich & Kwan 1974). It solves the radiative transfer problem coupled with statistical equilibrium equations to derive the radiation field and populations of the levels on each point of a gas cloud. Then, the emergent profile of the lines is obtained through ray-tracing.

We used MADEX to calculate line opacities, excitation temperatures, and critical densities for the physical conditions expected at a given distance from the star, that is, $n(r)$ and $T_{\rm kin}(r)$ (see Table 4), along with the column densities derived from the population diagrams (given in Table 5), and the $v_{\rm exp}$ derived from the line fitting (given in Table A.1) for all the molecules detected. We systematically used this procedure to compare the line opacities obtained from the interpretation of the line profiles and to verify if a given molecule could be sub-thermally excited or not. These calculations are detailed in each subsection of the Sect 6. The sets of the collisional coefficients used for these calculations (when available) are: CO (Yang et al. 2010), SiO (Dayou & Balança 2006), H_2O (Daniel et al. 2011), HCN (Ben Abdallah et al. 2012), CS (Lique & Spielfiedel 2007), SiS (Toboła et al. 2008), NaCl (Quintana-Lacaci et al. 2016), SO (Lique et al. 2007), PN (Toboła et al. 2007), CN (Lique & Kłos 2011), HCO^+ (Flower 1999), and H_2CO (Schöier et al. 2005, and references therein). We also obtained synthetic spectra that helped us to correctly identify the spectral features.

Table 4. Parameters of the central Mira-type star and the CSE of IK Tau.

Parameter	Value	Reference
Distance (d)	265 pc	a
Stellar radius (R_*)	2.5×10^{13} cm	c
Stellar effective temperature (T_*)	2200 K	c
Terminal expansion velocity (v_∞)	18.5 km s^{-1}	e
AGB mass loss rate ($\dot{M}$)	$8 \times 10^{-6}\ M_\odot$ yr^{-1}	c
Gas kinetic temperature ($T_{\rm kin}$)	$T_*(r/R_*)^{-0.6}$	c
Dust temperature ($T_{\rm d}$)	$T_*(2r/R_*)^{-0.4}$	b
Dust condensation radius ($R_{\rm c}$)	$8\,R_*$	d
Density of particles (n)	$\dot{M}/(4\pi r^2 \langle m_{\rm g}\rangle v_{\rm exp})$	–

Notes. The density of particles is calculated with the law of conservation of mass, where $\langle m_{\rm g}\rangle$ is the mean mass of gas particles (2.3 amu, after considering H_2, He, and CO). (a): Hale et al. (1997); (b): Decin et al. (2006); (c): Decin et al. (2010a); (d): Gobrecht et al. (2016); (e): this work (see Sect. 5.1).

As it is shown in Sect 5.2, the detected SO_2 transitions have a large span in energies (i.e. from 7.7 up to 733.4 K). The population diagram analysis of this molecule indicates that it is possibly tracing out an inner region of the CSE, with a $T_{\rm kin} \gtrsim 290$ K which is not observed for other molecules, and also a more external region with $T_{\rm rot} \sim 40$ K from where most of the emission of the rest of the molecules arises. To investigate more precisely the excitation conditions of SO_2 and to confirm or not the temperature stratification inferred from the population diagrams, we have performed a detailed radiative transfer calculation for SO_2. Our main goal is to investigate the presence of SO_2 in the innermost regions of the CSE.

The physical model consists on a spherical expanding envelope of dust and gas with a constant mass loss rate, similar to the model presented in Agúndez et al. (2012) but corrected for IK Tau (see Table 4). The radius of the star is 2.5×10^{13} cm (Decin et al. 2010a). The density of particles is calculated with the law of conservation of mass, that is, $n \propto r^{-2}$ (valid for a CSE expanding at constant velocity). In terms of $v_{\rm exp}$, the envelope is divided in three regions: (*i*) from 1 to 5 R_* where $v_{\rm exp} = 5$ km s^{-1} as an average value in this region (Decin et al. 2010b), (*ii*) from 5 to 8 R_* where $v_{\rm exp} = 10$ km s^{-1} according to the dust condensation radius (Gobrecht et al. 2016), and (*iii*) from 8 R_* to the end of the CSE where $v_{\rm exp} = 18.5$ km s^{-1}(see Sect. 5.1). Concerning dust, we adopted a dust-to-gas ratio of 1.3×10^{-4} for the region (*i*), a value of 1.2×10^{-3} for region (*ii*) and a value of 2.3×10^{-3} for the region (*iii*), according to the values given by Gobrecht et al. (2016) for silicates. The dust temperature has been taken from Decin et al. (2006; see Table 4). The optical

Table 5. Results from the population diagrams, sorted according to the molecular fractional abundance (relative to H_2) in descending order.

Molecule	T_{rot} (K)	Column density (cm^{-2})	Abundance –	θ_s $''$	Lit. observational $f(X)$ –	Ref. –	Lit. chemical model $f(X)$ –	Ref. –
CO	18 (4)	$\gtrsim 1.3\,(0.3)\times10^{17}$	$\gtrsim 1.1\times10^{-4}$	18	$[2–3]\times10^{-4}$	d, f	7×10^{-4}–1×10^{-3}	γ
^{13}CO	21 (8)	$1.6\,(0.6)\times10^{16}$	1.4×10^{-5}[†]	18	$[1–3]\times10^{-5}$	d, f	–	–
SO_2 cold	40 (2)	$>1.1\,(0.1)\times10^{16}$[‡]	$>9.6\times10^{-6}$[‡]	2[‡]	2×10^{-6}–1×10^{-5}	b, f	2×10^{-7}	ϵ
SiO	17 (2)	$>9.1\,(3.3)\times10^{15}$	$>8.0\times10^{-6}$	2	4×10^{-7}–2×10^{-5}	e, d	2×10^{-5}–9×10^{-5}	γ
SO	17 (1)	$\gtrsim 8.9\,(1.6)\times10^{15}$	$\gtrsim 7.8\times10^{-6}$	2	3×10^{-7}–3×10^{-6}	f, a	2×10^{-12}–9×10^{-7}	γ, ϵ
SiS	64 (5)	$5.2\,(0.6)\times10^{15}$	4.6×10^{-6}	2	8×10^{-9}–1×10^{-5}	d	8×10^{-10}–3×10^{-6}	β, ϵ
SO_2 warm	290 (60)	$>3.1\,(1.0)\times10^{15}$[‡]	$>2.7\times10^{-6}$[‡]	2[‡]	–	–	2×10^{-14}–4×10^{-9}	γ
^{29}SiO	17 (2)	$\gtrsim 2.1\,(0.6)\times10^{15}$	$\gtrsim 1.8\times10^{-6}$	2	–	–	–	–
PO	17 (2)	$2.0\,(0.4)\times10^{15}$	1.7×10^{-6}	0.7	5×10^{-8}–6×10^{-7}	c	2×10^{-10}–1×10^{-7}	γ
^{30}SiO	17 (2)	$\gtrsim 1.5\,(0.5)\times10^{15}$	$\gtrsim 1.3\times10^{-6}$	2	–	–	–	–
H_2S	39 (3)	$1.4\,(0.3)\times10^{15}$	1.2×10^{-6}	2	–	–	6×10^{-13}–3×10^{-5}	β, γ
$^{34}SO_2$	35 (6)	$1.1\,(0.3)\times10^{15}$	9.6×10^{-7}	2	–	–	–	–
CS	25 (2)	$9.2\,(1.0)\times10^{14}$	8.0×10^{-7}	2	8×10^{-8}–3×10^{-7}	f, g	2×10^{-11}–2×10^{-5}	γ, β
^{34}SO	14 (1)	$8.9\,(2.4)\times10^{14}$	7.8×10^{-7}	2	–	–	–	–
PN	18 (2)	$8.3\,(1.7)\times10^{14}$	7.3×10^{-7}	0.7	3×10^{-7}	c	4×10^{-10}–6×10^{-7}	γ
HCN	10 (1)	$>7.6\,(2.9)\times10^{14}$	$>6.6\times10^{-7}$	4	4×10^{-7}–1×10^{-6}	i, f	6×10^{-12}–3×10^{-4}	γ, β
^{29}SiS	78 (5)	$4.9\,(0.4)\times10^{14}$	4.3×10^{-7}	2	–	–	–	–
$Si^{34}S$	70 (10)	$4.5\,(0.8)\times10^{14}$	3.9×10^{-7}	2	–	–	–	–
NaCl	67 (7)	$3.5\,(0.6)\times10^{14}$	3.1×10^{-7}	0.3	4×10^{-9}	h	4×10^{-12}–1×10^{-8}	γ
^{30}SiS	83 (9)	$3.5\,(0.5)\times10^{14}$	3.1×10^{-7}	2	–	–	–	–
H_2CO	10 (2)	$2.8\,(0.5)\times10^{14}$	2.4×10^{-7}	2	–	–	1×10^{-9}–5×10^{-7}	α, ϵ
CN	9 (2)	$1.5\,(0.7)\times10^{14}$	1.3×10^{-7}	6	2×10^{-10}–2×10^{-7}	d, f	3×10^{-13}–3×10^{-7}	β, δ
$Si^{18}O$	24 (8)	$1.5\,(0.8)\times10^{14}$	1.3×10^{-7}	2	–	–	–	–
$Si^{17}O$	12 (2)	$1.0\,(0.4)\times10^{14}$	8.7×10^{-8}	2	–	–	–	–
^{13}CS	34 (3)	$9.6\,(0.8)\times10^{13}$	8.4×10^{-8}	2	–	–	–	–
$H^{13}CN$	11 (2)	$9.2\,(2.5)\times10^{13}$	8.0×10^{-8}	4	–	–	–	–
$C^{34}S$	24 (1)	$6.9\,(0.6)\times10^{13}$	6.0×10^{-8}	2	–	–	–	–
NS	18 (2)	$2.6\,(0.5)\times10^{13}$	2.3×10^{-8}	6	–	–	7×10^{-13}–8×10^{-9}	β, δ

Notes. We give the formal uncertainties derived from the population diagram fits within parentheses. Column 5: size adopted for the emitting region. Columns 6 and 7: range of the fractional abundances given in the literature, derived from the following works based on observations: (a): Bujarrabal et al. (1994); (b): Danilovich et al. (2016); (c): De Beck et al. (2013); (d): Decin et al. (2010a); (e): González Delgado et al. (2003); (f): Kim et al. (2010); (g): Lindqvist et al. (1988); (h): Milam et al. (2007); (i): Schöier et al. (2013). Columns 8 and 9: range of the fractional abundances given in the literature, which were derived from the following chemical and shocks models: (α): Agúndez et al. (2010); (β): Duari et al. (1999); (γ): Gobrecht et al. (2016); (δ): Li et al. (2016); (ϵ): Willacy & Millar (1997). [(†)] Value given in Table 6 in Decin et al. (2010a). [(‡)] See Sect. 6.5.1.

properties of the silicate dust and the size of the grains (0.1 μm) have been adopted from Suh (1999). For the microturbulence velocity we adopted the values given in Agúndez et al. (2012) for the C-rich CSE IRC+10216. We used different SO_2 abundance profiles (see Fig. 5) in order to investigate the presence of warm SO_2 in the inner regions of the CSE. For the calculations we used a set of collisional coefficients which are described in Appendix E. The results of the radiative transfer model are shown in Fig. 11 and discussed in Sect. 6.5.1.

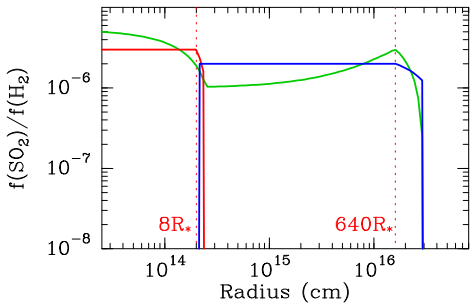

Fig. 5. Radial profiles of the abundance adopted for the radiative transfer model of the lines of SO_2. We tested three different radial profiles: (i) an inner distribution of SO_2 with $f(SO_2) = 3\times10^{-6}$ between 1–8 R_* (red line); (ii) a constant radial profile with $f(SO_2) = 2\times10^{-6}$ between 8–640 R_* (blue line); and (iii) a two component profile (green line) which includes an inner warm component plus an extended component of SO_2. The results of the different models are shown in Fig. 11.

5. Results

Here we present the general results from the analysis, which are summarised in Table 5 and Fig. 6.

5.1. Expansion velocity

The terminal expansion velocity of the CSE (v_∞) can be estimated from the linewidths of the spectral features that arise from the outer ($r > 8\ R_*$, Gobrecht et al. 2016) envelope regions where the gas has been fully accelerated to this maximal velocity. We estimated the v_∞ from the ^{13}CO linewidths (see Table A.1) given that ^{13}CO emission certainly extends beyond the wind acceleration region, and the line profiles display a clear U-shaped profile (see Fig. 3) and, thus, no significant opacity broadening is expected (Phillips et al. 1979). Assuming a mean density of $n(H_2) = 10^5\ cm^{-3}$, and the temperature and column density given in Table 5, the highest opacity measured

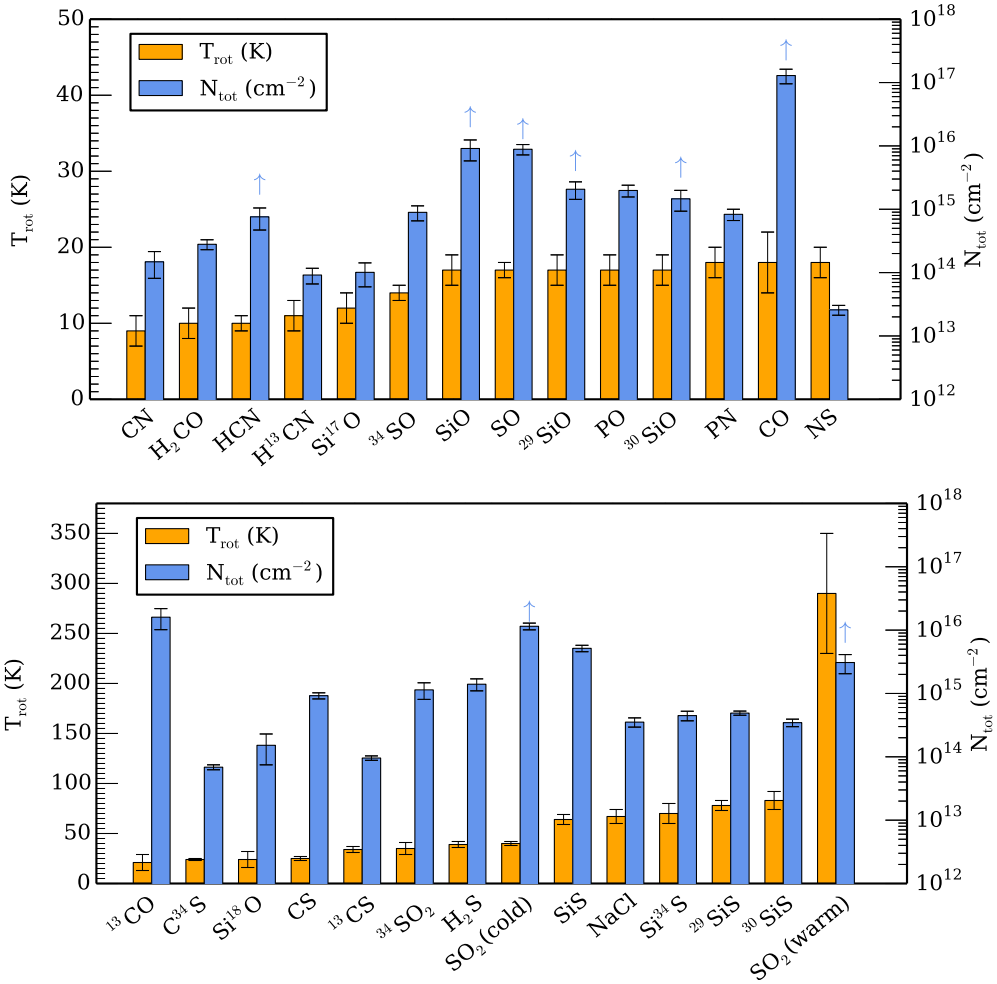

Fig. 6. Graph of the rotational temperatures (orange bars) and column densities (blue bars), with their formal uncertainties (black lines), derived from the population diagrams. Vertical blue arrows are plotted to indicate column density lower limits over each corresponding molecule. The temperature scale is represented on the left vertical axis, and the column density logarithmic scale is represented on the right vertical axis. The limits of the temperature scale are different in both boxes to improve the visual aspect of the figures. The values represented are tabulated in Table 5.

with MADEX is $\tau = 0.13$ for the ^{13}CO $J = 3$–2 line. We derived $v_\infty = 18.6 \pm 1.2$ km s^{-1} which is in good agreement with previous measurements (e.g. De Beck et al. 2013).

Most of the rest of the lines detected display linewidths consistent with v_∞ like for example SiS (see Tables A.1, A.2 and Fig. 7). In the particular case of H_2CO, we stacked the lines with $K = 0$, $K = 1$, and $K = 2$ to confirm that H_2CO linewidths are consistent with $v_{exp} = v_\infty$ (Fig. 8). There are also several lines with linewidths larger than v_∞, due to a blend of several hyperfine components (as occurs for NO and NS), or a poor fitting for lines detected below 5σ.

Additionally, the lines with $E_u \gtrsim 160$ K, that is, the lines of vibrationally excited states (Table A.2), H_2O, PO, NaCl, and several high-E_u SO_2lines, have line profiles indicative of $v_{exp} \lesssim 10$ km s^{-1}, consistent with emission from the inner regions of the CSE where the gas is still being accelerated ($r < 8\ R_*$, i.e. $\sim 2 \times 10^{14}$ cm^{-2}, Decin et al. 2010b; Gobrecht et al. 2016). In order to obtain a more reliable estimate of the NaCl linewidths, we stacked the lines with E_u = [22.5–56.9] K (group 1), E_u = [85.0–118.7] K (group 2), and E_u = [131.2–187.4] K (group 3) (see Fig. 8). The linewidths measured are consistent with $v_{exp} = 14.8 \pm 2.2$ km s^{-1} (group 1), $v_{exp} = 20.1 \pm 1.1$ km s^{-1} (group 2), and $v_{exp} = 11.8 \pm 1.1$ km s^{-1} (group 3). Therefore, it seems that $v_{exp} < v_\infty$ at least for the lines of the group 3, that is to say, the high-E_u lines.

There are also some lines with low E_u (<200 K) which appear to have expansion velocities of $\sim$10 km s^{-1} (e.g. SO_2, see Fig. 7). Such low values of the v_{exp} were measured for weak SO_2 lines with low S/N, thus, the linewidths observed in their profiles are uncertain.

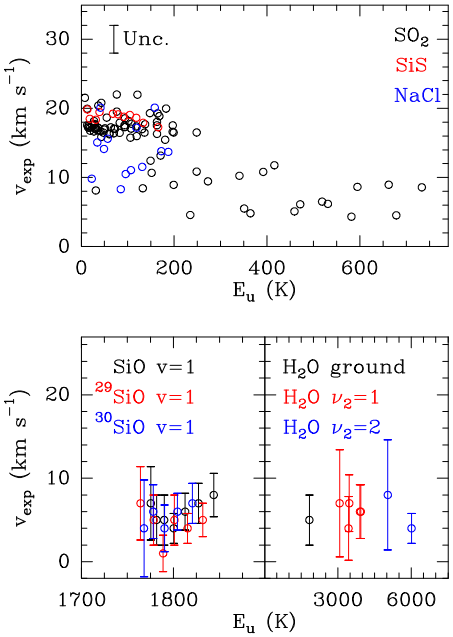

Fig. 7. Plot of the v_{exp} derived from the fit of the lines as a function of the E_u of the corresponding transition for several molecules. In the *top*, we did not represent each error bar to improve the visualization of the figure. A typical error bar of 4 km s^{-1} is plotted in the top left corner of the box. The values and uncertainties of the *bottom* correspond to the values given in Table A.2. For those lines that were observed in different epochs, we adopted an average value of the different measurements for the v_{exp} and its uncertainty.

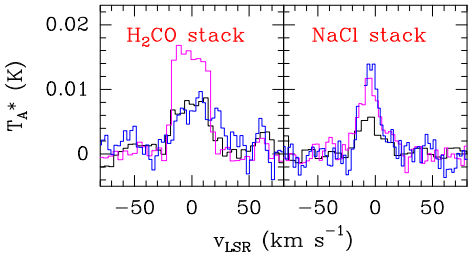

Fig. 8. Line stacking of the H_2CO (*left*) and the NaCl (*right*) lines detected, with a spectral resolution of 2 MHz. Black spectrum correspond to the H_2CO K_a = 0 lines and the NaCl lines with E_u = [22.5–56.9] K, pink spectrum correspond to the H_2CO K_a = 1 lines and the NaCl lines with E_u = [85.0–118.7] K, and blue spectrum correspond to the H_2CO K_a = 2 lines and the NaCl lines with E_u = [131.2–187.4] K.

5.2. Rotational temperatures, column densities and fractional abundances

The population diagrams for all the molecules detected are shown in Appendix D, in Figs. D.1–D.13. Most diagrams display a linear trend, however, the population diagrams of, for example, SiO, ^{29}SiO, or SO, display departures from a linear behaviour, which are more notable for low J transitions (see e.g. Fig. D.2). These departures are discussed in detail in Sect. 6

Table 6. Isotopic ratios obtained from the abundances derived with the population diagrams.

Ratio	Value	From
^{12}C/^{13}C	>8 (~10)	CO
^{12}C/^{13}C	10	CS
^{12}C/^{13}C	>8 (~15)	HCN
^{16}O/^{18}O	≫61	SiO
^{16}O/^{17}O	≫91	SiO
^{28}Si/^{29}Si	>4 (~18)	SiO
^{28}Si/^{29}Si	11	SiS
^{28}Si/^{30}Si	>6 (~34)	SiO
^{28}Si/^{30}Si	16	SiS
^{32}S/^{34}S	>8 (~15)	SO
^{32}S/^{34}S	13	CS
^{32}S/^{34}S	12	SiS
^{32}S/^{34}S	>10 (~13)†	SO_2

Notes. Opacity corrected values are given between parentheses (see Sect. 6.10). $^{(\dagger)}$ This value was computed using only the cold SO_2 component in Table 5.

and they reflect the effect of optically thick emission and/or subthermal excitation. For SO_2 we see two different trends for lines below and above E_u = 160 K. We fitted both separately and their implications are explained in Sect. 6.5.1.

The rotational temperatures derived range from 9 K (for CN) to 290 K (for the warm component of SO_2), with most of the molecules displaying rotational temperatures between 15 K and 40 K (see Fig. 6). The column densities range from $\gtrsim$1.3 × 10^{17} cm^{-2} for ^{12}CO, down to 2.6 × 10^{13} cm^{-2} for NS. We obtained averaged fractional abundances using the Eq. (9), which range between >1.1×10^{-4} for ^{12}CO, down to 2.3×10^{-8} for NS. We calculated the isotopic ratios of the molecules for which several isotopologues were detected. Results are presented in Table 6 and discussed in Sect. 6.10.

6. Discussion: an overall picture of the whole envelope

6.1. Variability

The excitation mechanisms of the lines are a mix of collisional and radiative procceses, where the radiation emitted by the central star has an impact on the population of the rotational levels (e.g. H_2O Agúndez & Cernicharo 2006). Since AGB stars are variable with periods of one to two years, the net excitation mechanism for those molecules is variable and the results obtained from the analysis of the molecular lines of AGB CSEs could be affected by this variability. In the case of O-rich stars, the impact of radiative pumping effects on masers is well-known (e.g. Nakashima & Deguchi 2007). Thermal line observations of CSEs have also to be considered carefully in the sub-millimeter and far-IR domain, while for the millimeter wavelength range, specially for low-J lines, the variation of the stellar light has not a major impact (Cernicharo et al. 2014). Given that our observations spread over a period of approximately five years, we observed a few spectral ranges at different epochs and here we discuss the results observed.

For the spectra observed at different epochs we observed intensity variations of less than 25% for the rotational lines of the

A&A 597, A25 (2017)

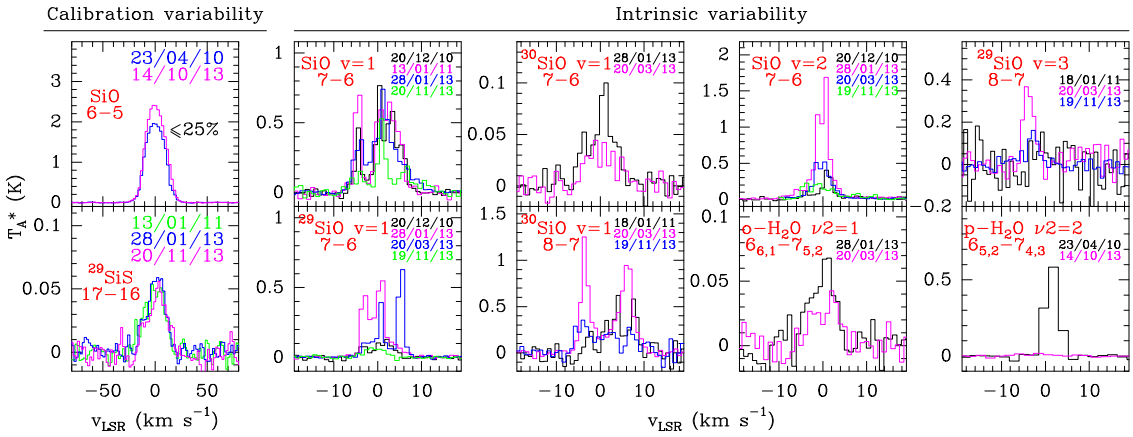

Fig. 9. Variability of some of the lines observed. The observation dates which correspond to the spectra are shown in the top right corner of each box with its corresponding colour. The spectral resolution is 2 MHz. As discussed in Sect. 6.1, variations of up to a 25% are within the uncertainties of the calibration, pointing and baseline substraction (i.e. *left boxes*). Variations of intensity higher than a 25% are observed in vibrationally excited lines or masers (i.e. *right boxes*).

ground vibrational levels. This value (i.e. 25%) was taken as the calibration uncertainty (see Sect. 2), and considered in the results presented throughout this work (Fig. 9 left). However, we observed strong intensity variations (>25%) for several lines, like for example the SiO $v = 1$ $J = 7$–6, (see Table A.2 and Fig. 9). These strongly variable lines correspond to rotational transitions of vibrationally excited states with $v_{\rm exp} \lesssim 10$ km s^{-1}, which arise from very inner regions of the CSE. The excitation mechanism of these lines may be correlated with the stellar phase, thus, it is not possible to extract any information of their abundances. In Table A.2 we present the fit parameters for these vibrationally excited and maser lines, where we included the mean Julian date of the observation and, in case that the feature was observed in different epochs, multiple measurements of that spectral feature.

6.2. O-bearing molecules

CO is the most abundant molecule in IK Tau (after H_2). It is distributed along the whole CSE with a size of ∼[7–8] × 10^{16} cm (see Sect. 1.1). The ^{12}CO $J = 2$–1 and ^{12}CO $J = 3$–2 lines display parabolic profiles typical of optically thick lines, while the ^{12}CO $J = 1$–0 line, all the ^{13}CO lines, and the C^{18}O lines show U-shaped profiles typical of optically thin lines (Fig. 3). The emission of all the CO isotopologues is probably spatially resolved considering the typical beam size (Table 2) and the shape of the line profiles. The population diagrams of ^{12}CO and ^{13}CO hint small departures from a linear trend, owing to high optical depth and/or sub-thermal excitation (Fig. D.1). The results can be seen in Table 5 and Fig. 6. We derived a fractional abundance $f(^{12}\mathrm{CO}) \gtrsim 1.1 \times 10^{-4}$ (with respect to H_2) in agreement with previous estimates. For C^{18}O, we estimated $f(\mathrm{C}^{18}\mathrm{O}) \sim 4 \times 10^{-8}$, assuming the same excitation temperature (20 K) and emitting size as for ^{13}CO.

We used MADEX to estimate the opacities of the CO lines (using the $T_{\rm kin}$, the $v_{\rm exp}$ derived from the linewidhts, the column density derived from the population diagram, and the $n(H_2)$ density at the outer radius of the shell according to the equation given in Table 4). With these input parameters, MADEX predicts that the ^{12}CO $J = 2$–1 and the $J = 3$–2 lines are moderately thick ($\tau \lesssim 1.4$), while the $J = 1$–0 line is optically thin ($\tau \sim 0.2$). This is consistent with CO tracing the coolest, outermost layers of the CSE and ^{13}CO probing also regions deeper inside.

For SiO isotopologues we have adopted an emitting size equivalent to 7.9×10^{15} cm (2″) at a distance of 265 pc (Sect. 1.1). All the line profiles of the different SiO isotopologues are parabolic, consistent with optically thick emission. The rotational diagrams of all the SiO isotopologues display small departures from a linear trend, except perhaps for Si^{17}O (Fig. D.2). We found similar $T_{\rm rot}$ for all the isotopologues, that is, $T_{\rm rot} \sim 20$ K, which are much lower than the $T_{\rm kin}$ expected at a distance of 1″ from the star (i.e. $T_{\rm kin} \sim 105$ K). Hence, sub-thermal excitation may have an impact on the values derived from the population diagrams of SiO isotopologues.

MADEX (see Sect. 4.3) predicted τ>1 for all of the SiO, ^{29}SiO and ^{30}SiO lines (except for the $J = 2$–1 lines of ^{29}SiO and ^{30}SiO, for which MADEX predicted $\tau \lesssim 0.6$.) These values are consistent with the observed line profiles. For Si^{18}O and Si^{17}O lines, MADEX predicted $\tau < 0.5$. Therefore, except for Si^{18}O and Si^{17}O, the column densities and the abundances derived for the SiO isotopologues, given in Table 5, should be considered lower limits. The lower limit obtained, $f(\mathrm{SiO}) > 8.0 \times 10^{-6}$, is in good agreement with previous measures (Decin et al. 2010a, and references therein), and, in principle, is also consistent with the low SiO abundances predicted by the model by Gobrecht et al. (2016) that proposes the formation of SiO in abundance under thermodynamical equilibrium (TE) in the stellar photosphere, and a significant abundace decay (to 1.5×10^{-5}) already at 6 R_* mainly due to dust condensation.

6.3. C-bearing molecules

We detected emission of molecules, like CS, HCN and HNC, that are typically found in C-rich CSEs (e.g. Bujarrabal et al. 1994; Cernicharo et al. 2000; Zhang et al. 2009).

According to Marvel (2005), the HCN emission arises from a compact region with $\theta_s \sim 4''$, which we adopted in this work.

For CS, there are no observational constraints on the size of the emission, therefore, we adopted a size of $\theta_s = 2''$ which is the same size used for SiO and it is consistent with the extent of the CSE emission predicted by chemical models (Li et al. 2016). Adopting these sizes we obtained T_{rot}(HCN) ~ 10 K and T_{rot}(CS) ~ 25 K, and N_{tot}(HCN) $\gtrsim 8 \times 10^{14}$ cm^{-2} and N_{tot}(CS) ~ 9×10^{14} cm^{-2} (Figs. D.3 and D.4).

Using MADEX, we found optically thick lines ($\tau \gtrsim 1.5$) for HCN, and moderately thick lines ($\tau \lesssim 1.2$) for H^{13}CN. Therefore, the column density and the abundance of HCN should be considered as lower limits. In the case of CS isotopologues, with the physical conditions expected at $r \sim 1''$, MADEX predicted optically thin lines ($\tau \lesssim 1.0$). Finally, given that $T_{kin}(r \lesssim 1'') \gtrsim 100$ K, the lines of HCN and CS isotopologues are most likely sub-thermally excited.

The rotational temperatures and abundances derived for HCN and CS isotopologues (see Table 5) are consistent with previous measurements in IK Tau (Lindqvist et al. 1988; Kim et al. 2010). The HCN abundance is in the high end of the abundance range deduced by Schöier et al. (2013) in a sample of M-type AGB stars. The TE models for O-rich CSEs do not account for the HCN and CS abundances observed in O-rich CSEs, predicting values of f(HCN) ~ 10^{-11} and f(CS) ~ 10^{-10} (Duari et al. 1999; Gobrecht et al. 2016). The inclusion of shocks can contribute to enhance the formation of HCN in O-rich stars (Duari et al. 1999; Cherchneff 2006; Gobrecht et al. 2016), but it also brings up a theoretical homogeinity on the expected HCN abundances among different chemical types of stars that it is not observed, as noted by Schöier et al. (2013). Other authors invoked the photochemistry to try to explain the abundances of C-bearing molecules observed in O-rich CSEs (Nercessian et al. 1989; Ziurys et al. 2009). In particular, the chemical model of Willacy & Millar (1997) predicts peak abundances of f(HCN) ~ 1×10^{-7} and f(CS) ~ 3×10^{-7}, although the carbon source proposed by these authors is CH_4 which has been later on refuted (Marvel 2005). Additionally, it has been also proposed that CSEs could be clumpy, hence, photochemistry could be important also in the inner layers of the envelopes (Agúndez et al. 2010). Our results do not conclude clearly which is the most likely scenario, although, our derived abundances are more similar to those predicted by the models of Gobrecht et al. (2016).

Finally, we detected two HNC lines, in particular, the J = 1–0, and the J = 3–2 line, which is blended with the image of the SiO J = 6–5 line. We estimated $f \sim 8 \times 10^{-9}$, assuming an excitation temperature of ~30 K and a size of 2″ for the emitting region, which are average values for these parameters.

6.4. Refractory species

We confirmed the presence of two important refractory molecules which are mainly found in C-rich envelopes: SiS and NaCl. The emission of these molecules has not been mapped in previous studies and, therefore, the size of the emitting region is unknown. The NaCl line profiles, with v_{exp} ~ 14 km s^{-1}, are narrower than those of SiS, consistent with v_{exp} ~ 18.5 km s^{-1}, which suggests a more inner distribution of NaCl around the star (see Fig. 7). This molecule may condense onto the dust grains beyond the dust condensation radius, as proposed by Milam et al. (2007). The profiles of the lines of NaCl and SiS isotopologues indicate spatially unresolved emission, which is compatible with the Gaussian-like profiles observed in the case of NaCl, and the triangular or parabolic profiles observed for the SiS isotopologues. Moreover, the Gaussian-like profiles observed for NaCl may support that the emission of this molecule arises from the innermost regions of the CSE, where the gas has not been fully accelerated.

We adopted a size of $\theta_s = 2''$ for SiS isotopologues, as a first guess considering the emission size of SiO ($\theta_s = 2''$). This size is also consistent with the size predicted by recent chemical model of IK Tau (Li et al. 2016). For NaCl we adopted a size of θ_s(NaCl) = 0.″3 (Milam et al. 2007). We derived similar rotational temperatures for SiS and NaCl (i.e. T_{rot} ~ 65 K) even higher for ^{29}SiS, ^{30}SiS, and Si^{34}S (see Figs. D.5 and D.6). According to the size adopted for SiS (i.e. $r \lesssim 4 \times 10^{15}$ cm), we estimated $T_{kin} \gtrsim 105$ K, and $n(H_2) \gtrsim 3.5 \times 10^5$ cm^{-3}. For the size adopted for NaCl (i.e. $r \lesssim 6 \times 10^{14}$ cm), we estimated $T_{kin} \gtrsim 330$ K. Hence, SiS and NaCl are most likely sub-thermally excited. We estimated critical densities for the SiS lines of n_{crit} ~ [10^4–10^6] cm^{-3} for a temperature of ~105 K, therefore, $n \lesssim n_{crit}$ for several lines of SiS confirming sub-thermal excitation. For NaCl the critical densities expected are even higher, $n_{crit} \gtrsim 5 \times 10^7$ cm^{-3}, due to the high dipole moment of NaCl. MADEX predicted optically thin lines for both SiS ($\tau < 0.6$) and NaCl ($\tau < 0.3$).

We derived f(SiS) ~ 5×10^{-6}. This value is in good agreement with the estimations by Kim et al. (2010). The chemical model by Gobrecht et al. (2016) predicts a SiS abundance of 4×10^{-8} under TE and up to ~3×10^{-7} including dust condensation and shocks due to the pulsation of the star, which is at least one order of magnitude lower than our results. Willacy & Millar (1997) used SiS in their chemical models as a parent molecule with an abundance consistent with our observations (see Table 5).

Concerning NaCl, Milam et al. (2007) derived a rotational temperature and a column density consistent with our results. However, Milam et al. (2007) derived a fractional abundance ~80 times lower than ours, through the population diagram of two low S/N NaCl emission lines, and also a radiative transfer calculation using the code by Bieging & Tafalla (1993), with a set of SiO-corrected collisional coefficients. We detected 13 NaCl lines which cover a wide range in E_u and have better S/N, from which we derived an average fractional abundance of f(NaCl) = 3×10^{-7} (see Table 5 and Fig. D.6). We cannot rule out uncertainties in our estimation due to the emitting size, and the ^{13}CO column density adopted, which could not be representative in the region of NaCl emission. Moreover, NaCl line profiles are not incompatible with θ_s(NaCl) $\gtrsim$ 0.″3, in particular, if θ_s(NaCl) = 1″ we would derive f(NaCl) = 3×10^{-8}. TE calculations predict abundances of 10^{-11} up to 10^{-7} (Tsuji 1973; Milam et al. 2007), while Gobrecht et al. (2016) models (TE and shocks) predicts NaCl abundances between 4×10^{-12} up to 1×10^{-8}. It would be necessary to obtain maps of the NaCl spatial distribution in order to clarify these discrepancies.

6.5. S-bearing molecules

Here we discuss the detected emission of H_2S, SO, and SO_2. The first detection of these molecules toward IK Tau and their chemistry in O-rich CSEs was presented in Omont et al. (1993) and references therein. Omont et al. (1993) only detected one line of H_2S, and they were not able to estimate its abundance toward IK Tau. The emission of SO and SO_2 molecules in O-rich CSEs, including IK Tau, has been recently reviewed and modelled by Danilovich et al. (2016).

We detected three ortho and one para lines of H_2S as well as one line of o-$H_2{}^{34}S$, which point out $v_{exp} \sim v_\infty$. The profiles of the

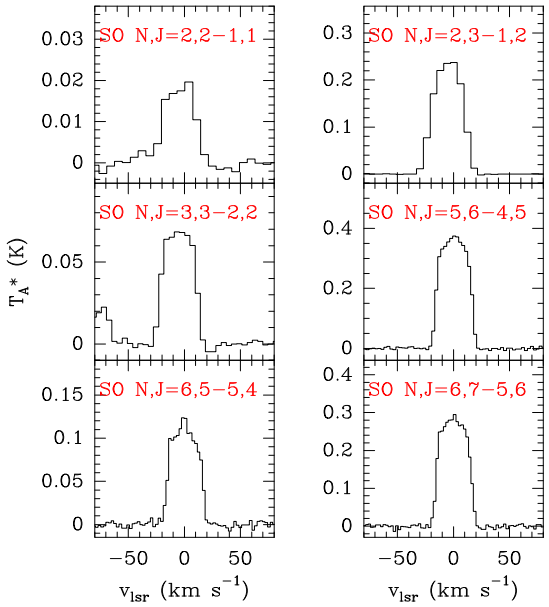

Fig. 10. Line profiles of some of the SO lines identified. The quantum numbers of each transition are plotted in red in each box.The spectral resolution is 2 MHz for all the spectra shown.

lines indicate spatially unresolved emission. Since there are not maps of the H_2S emission, we adopted a size of $\theta_s(H_2S) = 2''$ which is consistent with the size predicted by chemical models (Li et al. 2016). Given that we only detected two lines of o-H_2S with $S/N > 5$, we calculated the population diagram (Fig. D.7) of ortho and para species together adopting an ortho-to-para ratio of 3:1 which is the value that could be expected from the formation processes of H_2S. We derived $T_{rot} \sim 40$ K and $f(H_2S) \sim 1 \times 10^{-6}$. This value is consistent with the chemical models presented by Gobrecht et al. (2016) at a few stellar radii. We found that the lines of H_2S are likely to be sub-thermally excited at the distances adopted for the H_2S emission ($r \lesssim 1''$). However, we did not made further non-LTE calculations due to the lack of a set of collisional coefficients for H_2S. Under LTE conditions, MADEX predicts optically thin lines ($\tau < 0.6$).

The profiles of the SO lines observed are varied (see Fig. 10). Most of them are flat-topped (optically thin and spatially unresolved emission), some of them display parabolic profiles (optically thick or moderately thick emission) and a few SO lines display profiles which seem to be composed of two components, at least: one dominant flat-topped or parabolic component with linewidths consistent with v_∞, and an additional narrow feature which may indicate SO gas inside the gas acceleration region. These two components are more clearly seen in several SO_2 lines (Fig. 11) which display a broad component plus a bulge-like centred narrow component, which we interpreted as SO_2 emission arising from $r < 8\ R_*$ (see Sect. 6.5.1). Nevertheless, we have not detected high-E_u SO narrow lines or two different trends in the SO population diagram (see below) which could prove a very inner component of warm SO gas (contrary to SO_2 as discussed in Sect. 6.5.1). Thus we have no firm evidence that could prove the presence of warm SO gas in the innermost regions of the CSE with a noticeable abundance. Finally, the ^{34}SO flat-topped (optically thin emission) profiles yield also $v_{exp} \sim v_\infty$.

The brightness distribution of SO has not been mapped before, thus, we adopted a size of $\theta_s(SO) = 2''$ as well as for ^{34}SO, according to the models by Li et al. (2016). The population diagrams (Fig. D.8) display departures from a linear trend for SO. We obtained $T_{rot}(SO) \sim T_{rot}(^{34}SO) \sim 15$ K, $N_{tot}(SO) \gtrsim 9 \times 10^{15}$ cm^{-2} and $N_{tot}(^{34}SO) \sim 9 \times 10^{14}$ cm^{-2}. We verified with MADEX (see Sect. 4.3) that SO lines would be moderatelly thick ($\tau \lesssim 1.5$) with a $T_{kin} = 105$ K and $n \sim 4 \times 10^5$ cm^{-3} at $r = 1''$. MADEX predicted optically thin lines for ^{34}SO ($\tau \lesssim 0.2$). Furthermore, we estimated $n_{crit}(SO) \sim [10^5$–$10^7]$ cm^{-3} and similar values for ^{34}SO, which suggests sub-thermal excitation of several transitions.

We derived abundances of $f(SO) \gtrsim 8 \times 10^{-6}$ and $f(^{34}SO) \sim 8 \times 10^{-7}$. The abundance measured of SO is at least a factor three higher compared to previous observational works toward IK Tau (Omont et al. 1993; Bujarrabal et al. 1994; Kim et al. 2010). On the other hand, TE models predict abundances of $f(SO) \sim [2$–$4] \times 10^{-8}$ (Duari et al. 1999; Gobrecht et al. 2016). Willacy & Millar (1997) derived peak abundances up to $f(SO) \sim 9 \times 10^{-7}$ with a chemical model for an O-rich CSE that used only H_2S and SiS as parent S-bearing molecules. Compared to these models, our derived abundance is at least nine times higher than the highest value obtained from the models. Our analysis seems to overestimate the SO abundance compared to previous measurements and chemical models. These dicrepancies may be explained given the uncertainty on the size of the SO emitting region adopted, and the $f(^{13}CO)$ adopted (see Eq. (9)). In particular, a size of $\theta_s(SO) \sim 5''$ would fix this discrepancy.

6.5.1. SO_2 and $^{34}SO_2$

We detected ~90 lines of SO_2 displaying complex profiles which can be grouped according to their v_{exp}: (i) ~60 lines with $v_{exp} \sim 18$ km s^{-1} consistent with the v_∞ of the CSE; and (ii) ~30 lines with $v_{exp} < v_\infty$, with velocities as low as ~5 km s^{-1} (see Fig. 7). The lines of SO_2 display parabolic profiles, flat-topped profiles, and complex profiles. Several lines display a self-absorption in the blue side of the line (see Fig. 11). This self-absorption may be explained considering that part of the SO_2 emission arising from the inner and warm shells of the CSE, is absorbed by the external and cold shells of the CSE, which are located (within the line of sight) between us and the warm gas. The narrow lines seem to be spatially unresolved, although, for the lines that have $v_{exp} \sim v_\infty$ it is not clear whether they are spatially resolved or not. Most of the $^{34}SO_2$ lines show flat-topped profiles with indicative of spatially unresolved emission.

The rotational diagram of SO_2 was done adopting an emission size of $\theta_s(SO_2) = 2''$, which should be considered as an educated guess derived from the chemical models by Li et al. (2016). From the population diagram of SO_2 (Fig. D.9) we observed also two components, a cold component with $T_{rot} \sim 40$ K traced out by ~60 lines with $E_u \lesssim 160$ K and a warm component with $T_{rot} \sim 290$ K traced out by ~30 lines with $E_u > 160$ K. The cold component displays a slight change in the trend for the lines with $E_u \lesssim 50$ K which may be explained as a result of moderate optically thick emission for those lines and/or sub-thermal excitation. Using Eq. (9) we derived $f(SO_2, cold) \gtrsim 9.6 \times 10^{-6}$ and $f(SO_2, warm) \gtrsim 2.7 \times 10^{-6}$. For $^{34}SO_2$ we derived a $T_{rot} \sim 35$ K and $f(^{34}SO_2) \sim 9.6 \times 10^{-7}$.

As we said in Sect. 4.3, the SO_2 lines detected span over a wide range of energies, thus, the parameters derived from the population diagram may be unreliable given that the

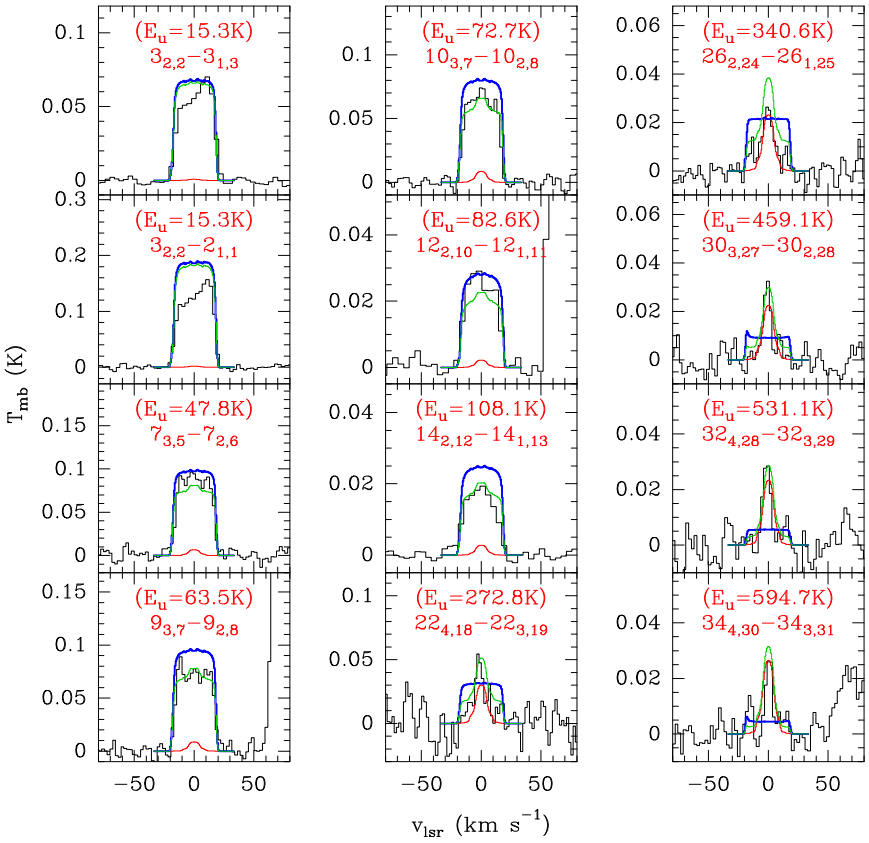

Fig. 11. Results of the radiative transfer models of SO_2 explained in Sects. 4.3 and 6.5.1. The coloured curves correspond to the models adopting the abundance profiles shown in Fig. 5. The spectral resolution is 2 MHz. The temperature scale is in main beam temperature.

homogenous temperature assumption may turn out to be a very crude approximation. We carried out several LVG models adopting different radial abundance profiles (see Sect. 4.3 and Fig. 5). As it is discussed below, the different abundance profiles were adopted mainly to illustrate the need of the presence of warm SO_2 at $r < 8\ R_*$ in order to reproduce the profiles of the high-E_u lines. The results of the radiative transfer models are shown in Fig. 11 for several lines of SO_2.

The first model (red line in Figs. 5 and 11) reproduces to a good accuracy the profiles of the narrow high-E_u (i.e. $E_u > 160$ K) lines observed. However, it is unable to reproduce the line profiles of the low-E_u (i.e. $E_u < 160$ K) lines, underestimating their emission completely. We created a second model (blue line in Figs. 5 and 11) which reproduces, within a factor two in intensity, most of the low-E_u SO_2 lines observed. However, this model is unable to explain the narrow profiles of the high-E_u SO_2 lines, predicting wide flat-topped lines or even no emission for these high energy lines. We may note, that the fractional abundance adopted for this second model is approximately a factor five lower than the abundance derived from the population diagram of the SO_2 cold component. If the abundance is increased up to a value consistent with the population diagram results for the cold component (i.e. $f(SO_2) = 9.6 \times 10^{-6}$), the model highly overestimates the line profiles observed. This discrepancy may arise from the lack of precise information about the spatial distribution of SO_2 toward the CSE.

Finally, we tested the possibility of SO_2 being distributed as a sum of two components, in particular, the sum of a compact inner component plus an extended component with a shell-like enhancement in the outermost part of the CSE, in order to reproduce the whole set of SO_2 lines observed with a single radial abundance profile. This last model (green line in Figs. 5 and 11) is able to approximately reproduce both the low- and high-E_u SO_2 lines observed, although, it does not reproduces perfectly all the line profiles. The discrepancies found between this best model and the observations are within a factor two or three in intensity for most of the lines observed. This disagreement emerges probably from the lack of precise information about the spatial distribution of SO_2. The radial abundance profile adopted for the model is consistent, within a factor two or three in intensity, with the results obtained from the population diagram for the SO_2 warm and cold components. Additionally, the best model predicts both optically thin and optically thick lines which is consistent with the variety of profiles observed.

Hence, we can conclude that SO_2 is distributed along the CSE with an average fractional abundance of $f(SO_2) \sim 10^{-6}$.

A&A 597, A25 (2017)

Our models evidenced the presence of an inner (1–8 R_*) warm ($\gtrsim$290 K) component of SO_2 with fractional abundances $\sim 10^{-6}$, which produces most of the emission from SO_2 lines with $E_u \gtrsim 160$ K. This is also consistent with the narrow profiles of the high-E_u SO_2 lines. Nevertheless, our model is not able to reproduce the complexity observed in the profiles, which probably indicates the simplicity of the approximated physical model. In particular, the outer radius of the SO_2 cold component is critical to control the expected intensities of the low-E_u lines, which we adopted from the chemical model by Li et al. (2016). Therefore, it would be necessary to map the brightness distribution of this molecule in order to constrain the outer radius of SO_2 emission. High angular resolution observations are also required to map the innermost regions of the CSE, since the distribution of SO_2 in the region between 1–20 R_* would improve the results obtained not only for the high-E_u lines but also for those lines that display a narrow core component (e.g. SO_2 $7_{3,5}$–$7_{2,6}$ in Fig. 11).

Previous works toward IK Tau pointed out SO_2 abundances in the intermediate and outer envelope consistent with our results (Omont et al. 1993; Kim et al. 2010; Decin et al. 2010a). Decin et al. (2010a) hinted the presence of SO_2 in the inner wind, since they were not able to reproduce with their radiative transfer model simultaneously the emission of a few lines with $E_u \sim 140$ K detected with APEX and the low-E_u transitions observed with the IRAM-30 m telescope. Given the limited number of high-E_u lines detected by Decin et al. (2010a), these authors were unable to reach conclusive results on the presence of SO_2 in the inner wind of IK Tau and its abundance. Recent research was conducted to investigate one SO_2 line with $E_u \sim 600$ K detected with *Herschel*/HIFI as well as other SO_2 lines reported in the literature toward IK Tau with a radiative transfer model by Danilovich et al. (2016). Their best-fit model has a peak abundance of $f(SO_2) = 2 \times 10^{-6}$ and an *e*-folding radius $R_e = 10^{16}$ cm, although, it is unable to reproduce all the SO_2 observed line profiles as indicated by these authors.

TE models predict the formation of SO_2 in the photosphere of the star with abundances of $f(SO_2) \sim 10^{-11}$ (Tsuji 1973; Gobrecht et al. 2016), which is approximately five orders of magnitude lower than our results. Willacy & Millar (1997) predicted a peak abundance of $f(SO_2) \sim 2{\times}10^{-7}$ in the intermediate and outer parts of the CSE, at $r \sim 10^{16}$ cm (i.e. $\sim$500 R_*), and $f(r \lesssim 3 \times 10^{15}\,\mathrm{cm}) \lesssim 10^{-10}$, where they used H_2S and SiS as the S-bearing parent molecules of the model. This chemical model is also inconsistent with our results given that they do not predict the formation of SO_2 in the inner parts of the CSE and the abundance in the intermediate and outer parts is aprroximately two orders of magnitude lower than our measures. In the recent chemical model presented by Li et al. (2016), the authors explore the effect of including SO_2 as a parent molecule. In the absence of a reliable observational estimate of the SO_2 abundance in the inner envelope, these authors adopt $f(SO_2) = 2 \times 10^{-6}$, which is the value estimated from low-E_u SO_2 transitions arising in the outer envelope regions (Decin et al. 2010a). In the innermost parts of the envelope ($r < 8$ R_*) the SO_2 abundance can be enhanced up to $f(SO_2) = 4 \times 10^{-9}$ including the effect of shocks and dust grains (Gobrecht et al. 2016). These authors suggest that the production of SO triggers the formation of SO_2 at $\sim$4 R_* in the gas phase through the reaction with OH. Although, the SO_2 abundance obtained with the inclussion of shocks is approximately two or three orders of magnitude lower than our estimates. Photochemistry may also enhance the formation of SO_2 in the inner layers of the CSE, which would require an additional source of UV radiation to dissociate H_2O providing OH to react with the SO formed leading to the enhancement of SO_2. This could be plausible if the envelope of IK Tau is clumpy, as proposed for other objects (Agúndez et al. 2010).

6.6. N-bearing molecules

Besides HCN, HNC and PN, which are discussed in other sections, we detected CN, NS, and NO. The CN lines with unblended hyperfine components have widths consistent with $v_{exp} = v_\infty$ within errors. The spatial distribution of CN in IK Tau is unknown. CN has been observed in the outer shells of the C-rich CSE IRC+10216 (Lucas et al. 1995), and chemical models predict that it is formed as a result of the photodissociation of HCN and HNC in these outer shells (e.g. Nejad & Millar 1988). Given that the HCN size is θ_s(HCN) = 3.″85, CN would be expected to be in a shell external to the HCN. According to the chemical model by Li et al. (2016), the CN peak abundance occurs at $r \sim 1.5 \times 10^{16}$ cm. We converted the area between the HCN outer shell and the CN abundance peak to an equivalent emitting size, obtaining θ_s(CN) $\sim$ 6″. With this size, we calculated the population diagram of CN (Fig. D.10). We estimated $T_{rot} = 9 \pm 2$ and $N_{tot} \sim 1 \times 10^{14}$ cm^{-2}. At $r \sim 1.5 \times 10^{16}$ cm, T_{kin} is $\sim$50 K and $n(H_2) \sim 2 \times 10^4$ cm^{-3}, thus, CN lines are probably sub-thermally excited ($n_{crit} \gtrsim 10^6$ cm^{-3}). With these physical conditions MADEX predicted optically thin lines. We estimated $f(CN) \sim 1 \times 10^{-7}$ which is consistent with previous estimations (Kim et al. 2010). Chemical models predict abundances up to 3×10^{-7} (Willacy & Millar 1997; Li et al. 2016), which are also in good agreement with our observations.

As far as we know, our discovery of NS emission toward IK Tau is the first detection of this molecule in this source. Given that we did not resolve its hyperfine structure we cannot extract information on the line profiles observed. There are not observational constraints on the emission size of this molecule. According to the chemical model by Li et al. (2016), which predicts that NS would be formed through the neutral-neutral reaction of NH and S in an external shell of the envelope, similar to the CN shell, we adopted a θ_s(NS) $\sim$ 6″. With this size, from its population diagram (Fig. D.11), we derive a $T_{rot} = 18 \pm 2$ K and a column density of $(2.6 \pm 0.5) \times 10^{13}$ cm. As for CN, the lines of NS may be sub-thermally excited. Since, we have not a set of collisional coefficients for NS we could neither estimate the opacities of the lines nor their critical densities. A rough estimation under LTE conditions with MADEX yields optically thin lines ($\tau < 0.1$). We derived an abundance of $f(NS) \sim 2 \times 10^{-8}$. The chemistry of NS in O-rich CSEs was discussed in Willacy & Millar (1997), although, these authors did not give a value for the predicted NS abundance. Recently, chemical models by Li et al. (2016) predicted $f(NS) \sim 8 \times 10^{-9}$, which is (within uncertainties) consistent with our results.

For NO, we only detected two lines with low S/N. One of them is a blend of several hyperfine components. For the NO hyperfine component spectrally resolved we derived $v_{exp} = v_\infty$. We estimated a rough value of the NO abundance adopting $\theta_s \sim 6''$ (like for CN and NS), and an excitation temperature of 30 K, which is representative of the T_{kin} in the outer shells of the CSE ($r \sim [2\text{–}5] \times 10^{16}$ cm). With these considerations, we obtained $f(NO) \sim 2 \times 10^{-6}$, in agreement with the predictions of the chemical model by Li et al. (2016).

6.7. P-bearing molecules

PN and PO were detected for the first time toward IK Tau by De Beck et al. (2013), and we detected one additional line of

PN, and seven additional lines of PO. Concerning PO, which has hyperfine structure, we observed several spectrally resolved (as well as unresolved) lines with linewidths consistent with $v_{exp} \sim 9$ km s^{-1}. This suggests that PO emission lines arise from $r < 8\ R_*$. De Beck et al. (2013) mapped the brightness distribution of both PN and PO toward IK Tau, and found $\theta_s \lesssim 0\farcs7$. With this size we calculated the rotational diagram of both molecules (Fig. D.12), and we derived low rotational temperatures ($T_{rot} \sim 20$ K), N_{tot}(PN) $\sim 8 \times 10^{14}$ cm^{-2} and N_{tot}(PO) $\sim 2 \times 10^{15}$ cm^{-2}. The low T_{rot} deduced for PN and PO is probably indicative of sub-thermal excitation since at the inner wind layers (<0.7″) where the emission is produced, the gas kinetic temperature is expected to be well above 200 K. We used our radiative transfer code (see Sect. 4.3) to confirm our results. MADEX predicted optically thin ($\tau \lesssim 0.4$) and sub-thermally excited lines for PN. In the case of PO, MADEX predicted optically thin ($\tau < 0.1$) PO lines, under LTE approximation given that there is not a set of PO collisional coefficients available. We derived f(PN) $\sim 7 \times 10^{-7}$ and f(PO) $\sim 2 \times 10^{-6}$, which are consistent with previous estimates considering uncertainties (De Beck et al. 2013).

Concerning chemical models, these P-bearing molecules are adopted as parent molecules and their abundances are assumed from observations of the inner region of the CSE (De Beck et al. 2013; Li et al. 2016). TE calculations predict abundances for PN compatible with our results, and one order of magnitude lower than our measurements for PO (Tsuji 1973; Agúndez et al. 2007; Milam et al. 2008).

6.8. HCO^+

We detected the $J = 1$–0 line of the HCO^+ ion. The $J = 3$–2 line was not detected probably due to an unsufficient sensitivity. The $J = 2$–1 and the $J = 4$–3 lines lie in wavelength ranges that were not observed. The flat-topped profile of the HCO^+ $J = 1$–0 line indicates $v_{exp} \sim v_\infty$, optically thin, and spatially unresolved emission. We estimated a very rough value of the $f(HCO^+)$ adopting an emission region and an excitation temperature equal to those adopted for NO (see Sect. 6.6) since both molecules are expected to be formed in the outer shells of the CSE. With these values, we obtained $f(HCO^+) \sim 10^{-8}$.

According to chemical models, this molecule is formed efficiently in the outer layers of O-rich CSEs as a result of reactions that involve CO, H_2O, and their photodissociation products, with abundances consistent with our results (Willacy & Millar 1997; Sánchez Contreras et al. 2015, and references therein).

6.9. The organic precursor missing link to carbon chemistry: H_2CO

This is the first detection of the organic precursor molecule H_2CO toward IK Tau. We detected ortho and para lines with flat-topped profiles, indicating optically thin and spatially unresolved emission, even for the lines at high frequencies with $\theta_b \sim 8''$ (see Eq. (4)). We adopted a size of $\theta_s(H_2CO) = 2''$, which is an educated guess, taking into account that most of the molecules detected are expected to emit in that region of the CSE.

In the population diagram of H_2CO (see Fig. D.13), the $K_a = 0$, $K_a = 1$, and $K_a = 2$ ladders were fitted separately. For $K_a = 2$ only two data were collected. The average rotational temperature indicated by the fits of the different K_a ladders is ∼10 K. For the $K_a = 3$ ladder we only detected two lines with the same upper energy level, therefore, we adopted an average excitation temperature of ∼10 K to derive a rough value of the $K_a = 3$ column density. Formaldehyde is an asymmetric rotor with its dipolar moment oriented along the a axis. Therefore, transitions between different K_a levels are weakly connected through radiative processes. This explains why each of the K_a ladders appears as separated lines in the rotational diagram. The column densities derived result in an ortho-to-para ratio of ∼3:1, which has been computed dividing the sum of the $K_a = 1$ and 3 (ortho transitions) by the sum of the $K_a = 0$ and 2 (para transitions) column densities (see Fig. D.13). The total column density is $N_{tot}(H_2CO) \sim 3 \times 10^{14}$ cm^{-2}. Adding both o-H_2CO and p-H_2CO, we obtained a fractional abundance of $f(H_2CO) \sim 2 \times 10^{-7}$. In this case, MADEX predicted optically thin lines ($\tau < 0.3$) and sub-thermal excitation which is consistent with $T_{kin}(r = 1'') > T_{rot}$.

The origin of formaldehyde, as well as other C-bearing species, in O-rich envelopes has puzzled the scientific community since H_2CO was first detected in the O-rich CSE OH231.8+4.2, with a fractional abundance of 4×10^{-8} (Lindqvist et al. 1992; Charnley et al. 1995). Millar & Olofsson (1993) proposed a formation route which requires methane to produce formaldehyde in the external envelope with abundances up to 10^{-7} depending on the mass loss rate of the star. Methane is a highly symmetric molecule with no permanent dipole, thus, indirect evidence for the presence of methane can be provided by the search of expected products of CH_4 chemistry, such as C_2H and CH_3OH. A previous search for these molecules toward IK Tau and other O-rich CSEs has resulted in non-detections of C_2H ($f(C_2H) < 9.7 \times 10^{-9}$) and methanol ($f(CH_3OH) < 3.2 \times 10^{-8}$; Charnley & Latter 1997; Marvel 2005). We also did not detect emission of these molecules consistent with the upper limits provided by Marvel (2005). If the correct scenario were that H_2CO is formed in the outer envelope, the size adopted for the calculation of the population diagram would result in an abundance overestimate. In that case, assuming $\theta_s = 6''$, like for CN, NS, or NO, we derive an abundance of $f(H_2CO) \sim 2 \times 10^{-8}$. Furthermore, a clumpy envelope may lead to an enhanced photochemistry in the inner layers of the CSE, which result in the formation of carbon molecules in the inner and intermediate layers of O-rich CSEs, and in particular formaldehyde with $f(H_2CO) \sim 10^{-9}$ (Agúndez et al. 2010).

6.10. Isotopic ratios

Isotopic ratios of different species can be measured from the column densities derived in the rotational diagrams (see Table 6). However, these ratios have to be considered as lower limits when the molecule used to calculate the ratio has optically thick lines. In case that the opacities are moderately high, the isotopic ratio can be corrected using the approach by Goldsmith & Langer (1999).

For $^{12}C/^{13}C$ ratio, we measured values of eight to ten depending on the molecule used (i.e. CO, CS or HCN). The opacity correction yielded a $^{12}C/^{13}C$ ratio of ∼10 from CO. This value is in good agreement with that obtained by Ramstedt & Olofsson (2014) from their radiative transfer model of the ^{12}CO and ^{13}CO emission in IK Tau. This ratio is also compatible with other estimates in M-type stars like TX Cam or W Hya, consistent with a standard evolution for an M-type star (Ramstedt & Olofsson 2014, and references therein).

For the $^{16}O/^{17}O$ and $^{16}O/^{18}O$ ratios, we estimated lower limits of 90 and 60, respectively. MADEX predicted opacities as high as $\tau \sim 10$ for a few SiO lines that would result in opacity

A&A 597, A25 (2017)

corrected values of one order of magnitude higher, in agreement with previous estimates (Decin et al. 2010b).

The opacity corrected isotopic ratios of ^{28}Si/^{29}Si and ^{28}Si/^{30}Si are ∼18 and ∼34, respectively. Both isotopic ratios are (within uncertainties) in reasonable agreement with previous estimations toward IK Tau (Decin et al. 2010a), and also with the solar ratios ([^{28}Si/^{29}Si] ∼ 20 and [^{28}Si/^{30}Si] ∼ 30, Asplund et al. 2009). Therefore, it seems that in the case of IK Tau, Si isotopic ratios do not indicate significant alterations in the post-main sequence evolution.

Finally, we measured the isotopic ratio of ^{32}S/^{34}S using SO, SiS, SO_2, and CS obtaining values between 10 and 13. We corrected the effect of optically thick emission and we estimated a ^{32}S/^{34}S ratio of ∼15. As far as we know, there are no previous observational constraints to this isotopic ratio toward IK Tau. The solar ^{32}S/^{34}S ratio is ∼22 (Asplund et al. 2009). Recently, Danilovich et al. (2016) reported [^{32}S/^{34}S] ∼ 32 toward the O-rich CSE of R Dor. Both, Sun and R Dor isotopic ratios are, within uncertainties, compatible with our estimations.

6.11. Qualitative comparison with other O-rich objects

The molecular content of only a few O-rich CSEs has been studied so far. In particular, the best studied objects are the AGB CSE IK Tau, the CSE of the hypergiant VY CMa and the peculiar object OH231.8+4.2 (Alcolea et al. 2013; De Beck et al. 2013; Matsuura et al. 2014; Sánchez Contreras et al. 2015; Ziurys et al. 2007, and references therein).

IK Tau has, in terms of chemical composition, more similarities with VY CMa. AlOH and H_3O^+ are the only molecules present in the CSE of VY CMa that are not found in the CSE of IK Tau. Formaldehyde is found in the CSE of IK Tau but it is not found in the CSE of VY CMa. Regardless of the possible chemical processes at work in the CSE of IK Tau, the presence of CO, CN, CS, HCN, HNC, HCO^+, and H_2CO in IK Tau indicates that the emission of C-bearing molecules in VY CMa is not so unique (Ziurys et al. 2009).

OH231.8+4.2 displays emission of several molecules that are not found toward IK Tau: HNCO, HNCS, OCS, $H^{13}CO^+$, SO^+, N_2H^+, and H_3O^+. The remarkable chemistry of OH231.8+4.2 probably reflects the molecular regeneration process within its envelope after the passage of fast (∼100 km s^{-1}) shocks that accelerated and dissociated molecules in the AGB wind ∼800 yr ago (Sánchez Contreras et al. 2015). In IK Tau there is no evidence of a similar molecular destruction process by fast (∼100 km s^{-1}) velocity shocks. Instead, slower shocks due to stellar pulsation may have an impact on the chemistry of AGB CSEs (Gobrecht et al. 2016). However, the fact that these molecules are not observed toward IK Tau point out that slow shocks are not able to enhance the formation of these particular species, which are unexpectedly abundant in OH231.8+4.2 (Velilla Prieto et al. 2015). Nevertheless, slow shocks could enhance the formation of molecules like HCN or CS (see Sect. 6.3). Another difference with respect to OH231.8+4.2 is that IK Tau displays emission of NaCl and more intense lines of vibrationally excited SiO (Velilla Prieto et al., in prep.). The emission of these lines arises from very warm and inner regions of the CSE. The absence of NaCl and the weakness of the vibrationally excited SiO lines toward OH231.8+4.2, probably indicates that the mass loss rate of OH231.8+4.2 is decreasing at present (as suggested by Sánchez Contreras et al. 2002), which results in the progressive growth of a central cavity around the star.

7. Conclusion

In this work we present the detection toward IK Tau of ∼350 rotational lines corresponding to a list of H-, O-, C-, N-, S-, Si- and P-bearing molecules, which evidences an active chemistry for an O-rich AGB CSE.

We detected for first time in this source emission of HCO^+, NO, H_2CO, and NS. We also detected for the first time toward IK Tau rotational lines of $C^{18}O$, $Si^{17}O$, $Si^{18}O$, ^{29}SiS, ^{30}SiS, $Si^{34}S$, $H^{13}CN$, ^{13}CS, $C^{34}S$, $H_2{}^{34}S$, ^{34}SO, $^{34}SO_2$, and H_2O $v_2 = 2$, as well as several rotational lines of SiO isotopologues in vibrationally excited states. In addition, we significantly increased the number of lines detected for those molecules that were previously identified toward IK Tau. This has allowed us to deduce characteristic values of the rotational temperatures, column densities, and ultimately fractional abundances of the molecules present in its envelope. From our work we extract the following conclusions:

- The intensity of the rotational lines of molecules in the ground vibrational state do not show a significant variability as a function of time, for the spectral ranges that we could observe in different epochs. The small variations found for these lines can be explained owing to calibration or pointing uncertainties within a a 25%. We confirmed the time variability of the intensity of the lines of molecules in vibrationally excited states (e.g. SiO $v = 1$) by an average factor of 60%.
- Most of the molecules display rotational temperatures between 15 and 40 K. NaCl and SiS isotopologues display rotational temperatures of ∼65 K.
- We detected a warm component of SO_2 traced out by lines with upper energy levels between 160 and 730 K which display $v_{exp} < v_\infty$. This points out that SO_2 is present close to the stellar surface ($\lesssim 8\,R_*$) with an abundance of $f(SO_2) \sim 10^{-6}$.
- Among the species detected, we highlight the detection of H_2CO and NS for the first time in this source with abundances of $f(H_2CO) \sim [10^{-7}$–$10^{-8}]$ and $f(NS) \sim 10^{-8}$. We also estimated fractional abundances for the first time detected (toward IK Tau) molecules HCO^+ and NO obtaining $f(HCO^+) \sim 10^{-8}$ and $f(NO) \sim 10^{-6}$.
- The detection of several C-bearing species like HCN, CS, H_2CO or CN with abundances of $\sim 10^{-7}$ indicates an active carbon chemistry which is not expected given that most of the available carbon should be locked up into CO.
- The greatest discrepancies between our results and previous chemical models are found for PO, NaCl, and SO_2.

It would be necessary to obtain very high angular resolution observations to characterise the molecular emission in the inner parts of the CSE and the abundances and distribution of the molecules formed in this region. Further investigation is required to understand the nature of the discrepancies found between our derived values and chemical models, in particular, the discrepancies for S-bearing molecules and C-bearing molecules. The inclusion of photo-induced or shock-induced chemistry or maybe other processes is necessary to enhance the formation of these molecules up to values comparable to the abundances observed. Additionally, there are ∼40 lines that still remain unidentified. We expect that future observations, supported by improvements in the molecular catalogues and chemical models, lead to fully understand the envelope of IK Tau and, more generally, in O-rich AGB envelopes.

Acknowledgements. We acknowledge the IRAM staff for the support and help offered during all the observational runs. We acknowledge the Spanish MICINN/MINECO for funding support through grants AYA2009-07304,

AYA2012-32032, the ASTROMOL Consolider project CSD2009-00038 and also the European Research Council funding support (ERC grant 610256: NANOCOSMOS). L.V.P. also acknowledges the support of the Universidad Complutense de Madrid Ph.D. programme. This research has made use of the The JPL Molecular Spectroscopy catalog, The Cologne Database for Molecular Spectroscopy, the SIMBAD database operated at CDS (Strasbourg, France), the NASA's Astrophysics Data System, the IRAM GILDAS software, and Aladin.

References

Alcolea, J., & Bujarrabal, V. 1992, A&A, 253, 475
Alcolea, J., Pardo, J. R., Bujarrabal, V., et al. 1999, A&AS, 139, 461
Alcolea, J., Bujarrabal, V., Planesas, P., et al. 2013, A&A, 559, A93
Asplund, M., Grevesse, N., Sauval, A. J., & Scott, P. 2009, ARA&A, 47, 481
Agúndez, M., & Cernicharo, J. 2006, ApJ, 650, 374
Agúndez, M., Cernicharo, J., & Guélin, M. 2007, ApJ, 662, L91
Agúndez, M., Cernicharo, J., & Guélin, M. 2010, ApJ, 724, L133
Agúndez, M., Fonfría, J. P., Cernicharo, J., et al. 2012, A&A, 543, A48
Ben Abdallah, D., Najar, F., Jaidane, N., Dumouchel, F., & Lique, F. 2012, MNRAS, 419, 2441
Bieging, J. H., & Tafalla, M. 1993, AJ, 105, 576
Bowers, P. F., Johnston, K. J., & de Vegt, C. 1989, ApJ, 340, 479
Bujarrabal, V., & Alcolea, J. 1991, A&A, 251, 536
Bujarrabal, V., Fuente, A., & Omont, A. 1994, A&A, 285, 247
Carter, M., Lazareff, B., Maier, D., et al. 2012, A&A, 538, A89
Castro-Carrizo, A., Quintana-Lacaci, G., Neri, R., et al. 2010, A&A, 523, A59
Cernicharo, J. 1985, Internal IRAM report (Granada: IRAM)
Cernicharo, J. 2012, EAS Pub. Ser., 58, 251
Cernicharo, J., Guélin, M., & Kahane, C. 2000, A&AS, 142, 181
Cernicharo, J., Spielfiedel, A., Balança, C., et al. 2011, A&A, 531, A103
Cernicharo, J., Teyssier, D., Quintana-Lacaci, G., et al. 2014, ApJ, 796, L21
Cernicharo, J., McCarthy, M. C., Gottlieb, C. A., et al. 2015, ApJ, 806, L3
Charnley, S. B., & Latter, W. B. 1997, MNRAS, 287, 538
Charnley, S. B., Tielens, A. G. G. M., & Kress, M. E. 1995, MNRAS, 274, L53
Cherchneff, I. 2006, A&A, 456, 1001
Cutri, R. M., Skrutskie, M. F., van Dyk, S., et al. 2003, VizieR Online Data Catalog: II/246
Daniel, F., Dubernet, M.-L., & Grosjean, A. 2011, A&A, 536, A76
Danilovich, T., De Beck, E., Black, J. H., Olofsson, H., & Justtanont, K. 2016, A&A, 588, A119
Dayou, F., & Balança, C. 2006, A&A, 459, 297
De Beck, E., Kamiński, T., Patel, N. A., et al. 2013, A&A, 558, A132
De Beck, E., Kamiński, T., Menten, K. M., et al. 2015, Why Galaxies Care about AGB Stars III: A Closer Look in Space and Time, 497, 73
Decin, L., Hony, S., de Koter, A., et al. 2006, A&A, 456, 549
Decin, L., De Beck, E., Brünken, S., et al. 2010a, A&A, 516, A69
Decin, L., Justtanont, K., De Beck, E., et al. 2010b, A&A, 521, L4
Duari, D., Cherchneff, I., & Willacy, K. 1999, A&A, 341, L47
Flower, D. R. 1999, MNRAS, 305, 651
Gobrecht, D., Cherchneff, I., Sarangi, A., Plane, J. M. C., & Bromley, S. T. 2016, A&A, 585, A6
Goldreich, P., & Kwan, J. 1974, ApJ, 189, 441
Goldsmith, P. F., & Langer, W. D. 1999, ApJ, 517, 209
González Delgado, D., Olofsson, H., Kerschbaum, F., et al. 2003, A&A, 411, 123
Green, S. 1976, J. Chem. Phys., 64, 3463
Green, S. 1979, J. Chem. Phys., 70, 816
Habing, H.J., & Olofsson, H. 2004, AGB Stars, A&A Library (Berlin: Springer)
Hale, D. D. S., Bester, M., Danchi, W. C., et al. 1997, ApJ, 490, 407
Justtanont, K., Khouri, T., Maercker, M., et al. 2012, A&A, 537, A144
Kim, H., Wyrowski, F., Menten, K. M., & Decin, L. 2010, A&A, 516, A68
Lane, A. P., Johnston, K. J., Bowers, P. F., Spencer, J. H., & Diamond, P. J. 1987, ApJ, 323, 756
Li, X., Millar, T. J., Heays, A. N., et al. 2016, A&A, 588, A4
Lindqvist, M., Nyman, L.-A., Olofsson, H., & Winnberg, A. 1988, A&A, 205, L15
Lindqvist, M., Olofsson, H., Winnberg, A., & Nyman, L. A. 1992, A&A, 263, 183
Lique, F., & Kłos, J. 2011, MNRAS, 413, L20
Lique, F., & Spielfiedel, A. 2007, A&A, 462, 1179
Lique, F., Senent, M.-L., Spielfiedel, A., & Feautrier, N. 2007, J. Chem. Phys., 126, 164312
Lucas, R., Bujarrabal, V., Guilloteau, S., et al. 1992, A&A, 262, 491
Lucas, R., Guélin, M., Kahane, C., Audinos, P., & Cernicharo, J. 1995, Ap&SS, 224, 293
Marvel, K. B. 2005, AJ, 130, 261
Matsuura, M., Yates, J. A., Barlow, M. J., et al. 2014, MNRAS, 437, 532
Menten, K. M., Wyrowski, F., Alcolea, J., et al. 2010, A&A, 521, L7
Milam, S. N., Apponi, A. J., Woolf, N. J., & Ziurys, L. M. 2007, ApJ, 668, L131
Milam, S. N., Halfen, D. T., Tenenbaum, E. D., et al. 2008, ApJ, 684, 618-625
Millar, T. J., & Olofsson, H. 1993, MNRAS, 262, L55
Morris, M., Gilmore, W., Palmer, P., Turner, B. E., & Zuckerman, B. 1975, ApJ, 199, L47
Müller, H. S. P., Schlöder, F., Stutzki, J., & Winnewisser, G. 2005, J. Mol. Struct., 742, 215
Nakashima, J.-I., & Deguchi, S. 2007, ApJ, 669, 446
Nejad, L. A. M., & Millar, T. J. 1988, MNRAS, 230, 79
Nercessian, E., Omont, A., Benayoun, J. J., & Guilloteau, S. 1989, A&A, 210, 225
Neri, R., Kahane, C., Lucas, R., Bujarrabal, V., & Loup, C. 1998, A&AS, 130, 1
Neugebauer, G., Martz, D. E., & Leighton, R. B. 1965, ApJ, 142, 399
Olofsson, H. 1996, Ap&SS, 245, 169
Olofsson, H., Lindqvist, M., Nyman, L.-A., & Winnberg, A. 1998, A&A, 329, 1059
Omont, A., Lucas, R., Morris, M., & Guilloteau, S. 1993, A&A, 267, 490
Pardo, J. R., Cernicharo, J., & Serabyn, E. 2001, IEEE Trans. Antennas and Propagation, 49, 1683
Pesch, P. 1967, ApJ, 147, 381
Phillips, T. G., Huggins, P. J., Wannier, P. G., & Scoville, N. Z. 1979, ApJ, 231, 720
Pickett, H. M., Poynter, R. L., Cohen, E. A., et al. 1998, J. Quant. Spectr. Rad. Trans. 60, 883
Quintana-Lacaci, G., Cernicharo, J., Agúndez, M., et al. 2016, ApJ, 818, 192
Ramstedt, S., & Olofsson, H. 2014, A&A, 566, A145
Sánchez Contreras, C., Desmurs, J. F., Bujarrabal, V., Alcolea, J., & Colomer, F. 2002, A&A, 385, L1
Sánchez Contreras, C., Velilla, L., Alcolea, J., et al. 2014, Asymmetrical Planetary Nebulae VI Conference, 88
Sánchez Contreras, C., Velilla Prieto, L., Agúndez, M., et al. 2015, A&A, 577, A52
Schöier, F. L., van der Tak, F. F. S., van Dishoeck, E. F., & Black, J. H. 2005, A&A, 432, 369
Schöier, F. L., Ramstedt, S., Olofsson, H., et al. 2013, A&A, 550, A78
Smith, C. L., Zijlstra, A. A., & Fuller, G. A. 2015, MNRAS, 454, 177
Solomon, P., Jefferts, K. B., Penzias, A. A., & Wilson, R. W. 1971, ApJ, 163, L53
Spielfiedel, A., Senent, M.-L., Dayou, F., et al. 2009, J. Chem. Phys., 131, 014305
Suh, K.-W. 1999, MNRAS, 304, 389
Toboła, R., Kłos, J., Lique, F., Chałasiński, G., & Alexander, M. H. 2007, A&A, 468, 1123
Toboła, R., Lique, F., Kłos, J., & Chałasiński, G. 2008, J. Phys. B At. Mol. Phys., 41, 155702
Tsuji, T. 1973, A&A, 23, 411
Velilla Prieto, L., Sánchez Contreras, C., Cernicharo, J., et al. 2013, Highlights of Spanish Astrophysics VII, 676
Velilla Prieto, L., Sánchez Contreras, C., Cernicharo, J., et al. 2015, A&A, 575, A84
Willacy, K., & Millar, T. J. 1997, A&A, 324, 237
Wing, R. F., & Lockwood, G. W. 1973, ApJ, 184, 873
Yang, B., Stancil, P. C., Balakrishnan, N., & Forrey, R. C. 2010, ApJ, 718, 1062
Zhang, Y., Kwok, S., & Nakashima, J.-I. 2009, ApJ, 700, 1262
Ziurys, L. M., Milam, S. N., Apponi, A. J., & Woolf, N. J. 2007, Nature, 447, 1094
Ziurys, L. M., Tenenbaum, E. D., Pulliam, R. L., Woolf, N. J., & Milam, S. N. 2009, ApJ, 695, 1604
Zuckerman, B. 1987, Astrochemistry, 120, 345

A&A 597, A25 (2017)

Appendix A: Table of measured lines

Table A.1. Measured and spectroscopic parameters of the detected lines.

Molecule	Transition QNs	$\nu_{\rm rest}$ (MHz)	$E_{\rm u}$ (K)	$A_{\rm ul}$ (s^{-1})	$\int T_{\rm ant}^{*}\,{\rm d}v$ (K km s^{-1})	$v_{\rm exp}$ (km s^{-1})
CO	1–0	115 271.202	5.5	7.205×10^{-8}	49.14 (0.04)	18 (3)
CO	2–1	230 538.000	16.6	6.916×10^{-7}	121.61 (0.06)	16.7 (1.3)
CO	3–2	345 795.990	33.2	2.501×10^{-6}	103.38 (0.07)	16.7 (1.0)
^{13}CO	1–0	110 201.354	5.3	6.336×10^{-8}	5.08 (0.02)	19 (3)
^{13}CO	2–1	220 398.684	15.9	6.082×10^{-7}	13.11 (0.05)	18.6 (1.4)
^{13}CO	3–2	330 587.964	31.7	2.199×10^{-6}	15.37 (0.12)	18.1 (1.0)
C^{18}O	1–0	109 782.176	5.3	6.263×10^{-8}	0.07 (0.02)	14 (6)
C^{18}O	2–1	219 560.358	15.8	6.013×10^{-7}	0.39 (0.03)	19.8 (1.4)
SiO	2–1	86 846.986	6.3	2.927×10^{-5}	31.16 (0.03)	17 (3)
SiO	3–2	130 268.687	12.5	1.059×10^{-4}	50.51 (0.03)	18 (2)
SiO	4–3	173 688.237	20.8	2.602×10^{-4}	48.63 (0.06)	18 (2)
SiO	5–4	217 104.920	31.3	5.197×10^{-4}	59.86 (0.04)	17.0 (1.4)
SiO	6–5	260 518.018	43.8	9.117×10^{-4}	56.51 (0.07)	14.4 (1.2)
SiO	7–6	303 926.814	58.4	1.464×10^{-3}	56.96 (0.06)	17.6 (1.0)
SiO	8–7	347 330.592	75.0	2.203×10^{-3}	40.76 (0.15)	17.3 (1.0)
^{29}SiO	2–1	85 759.194	6.2	2.819×10^{-5}	5.85 (0.03)	17 (3)
^{29}SiO	3–2	128 637.044	12.3	1.019×10^{-4}	10.71 (0.03)	15 (2)
^{29}SiO	4–3	171 512.796	20.6	2.505×10^{-4}	13.05 (0.05)	18 (2)
^{29}SiO	5–4	214 385.752	30.9	5.004×10^{-4}	14.82 (0.04)	17.8 (1.4)
^{29}SiO	6–5	257 255.213	43.2	8.779×10^{-4}	12.88 (0.05)	17.9 (1.2)
^{29}SiO	7–6	300 120.480	57.6	1.409×10^{-3}	10.60 (0.08)	17.1 (1.0)
^{29}SiO	8–7	342 980.854	74.1	2.121×10^{-3}	10.27 (0.09)	16.7 (1.0)
^{30}SiO	2–1	84 746.165	6.1	2.720×10^{-5}	3.74 (0.03)	18 (3)
^{30}SiO	4–3	169 486.869	20.3	2.418×10^{-4}	8.72 (0.03)	19 (2)
^{30}SiO	5–4	211 853.467	30.5	4.829×10^{-4}	11.78 (0.06)	16.1 (1.4)
^{30}SiO	6–5	254 216.652	42.7	8.472×10^{-4}	8.96 (0.03)	17.0 (1.2)
^{30}SiO	7–6	296 575.741	56.9	1.360×10^{-3}	10.39 (0.03)	20.0 (1.0)
^{30}SiO	8–7	338 930.052	73.2	2.047×10^{-3}	6.78 (0.15)	16.8 (1.1)
Si^{18}O	2–1	80 704.922	5.8	2.349×10^{-5}	0.21 (0.03)	19 (4)
Si^{18}O	4–3	161 404.893	19.4	2.088×10^{-4}	0.82 (0.02)	16 (2)
Si^{18}O	6–5	242 094.961	40.7	7.317×10^{-4}	1.34 (0.05)	16.9 (1.3)
Si^{18}O	7–6	282 434.735	54.2	1.175×10^{-3}	2.56 (0.04)	16.8 (1.1)
Si^{17}O	4–3	167 171.991	20.1	2.320×10^{-4}	0.89 (0.02)	11 (3)
Si^{17}O	5–4	208 960.009	30.1	4.634×10^{-4}	0.52 (0.04)	21.9 (1.4)
Si^{17}O	6–5	250 744.706	42.1	8.129×10^{-4}	0.43 (0.05)	18 (3)
Si^{17}O	7–6	292 525.420	56.2	1.305×10^{-3}	0.27 (0.04)	9 (2)
SiS	5–4	90 771.566	13.1	1.191×10^{-5}	1.02 (0.02)	20 (3)
SiS	6–5	108 924.303	18.3	2.090×10^{-5}	2.04 (0.03)	18 (3)
SiS	8–7	145 227.054	31.4	5.050×10^{-5}	4.23 (0.02)	18 (2)
SiS	9–8	163 376.782	39.2	7.238×10^{-5}	5.88 (0.02)	19 (2)
SiS	12–11	217 817.656	68.0	1.738×10^{-4}	9.36 (0.05)	19.2 (1.4)
SiS	13–12	235 961.366	79.3	2.216×10^{-4}	11.13 (0.06)	19.1 (1.3)
SiS	14–13	254 103.213	91.5	2.775×10^{-4}	11.68 (0.04)	18.8 (1.2)
SiS	15–14	272 243.055	104.5	3.421×10^{-4}	7.50 (0.07)	19.0 (1.1)
SiS	16–15	290 380.747	118.5	4.159×10^{-4}	13.18 (0.04)	18.6 (1.0)
SiS	17–16	308 516.147	133.3	4.997×10^{-4}	10.28 (0.05)	17.9 (1.0)
SiS	19–18	344 779.495	165.5	6.996×10^{-4}	11.87 (0.10)	17.3 (1.0)

Notes. Column 2: quantum numbers; Col. 6: integrated intensity (in antenna temperature) of the line with its formal uncertainty; Col. 7: expansion velocity derived from the linewidth with its uncertainty which includes the width of half a channel (1 MHz) except for the lines with a low S/N where a full channel (2 MHz) is included. The uncertainties given (within parentheses) do not include additional uncertainties derived from the absolute flux calibration. (HB) Hard blend, thus, we cannot estimate the contribution of the line to the spectral feature observed. (BF) Bad fit.

Table A.1. continued.

Molecule	Transition QNs	$\nu_{\rm rest}$ (MHz)	$E_{\rm u}$ (K)	$A_{\rm ul}$ (s^{-1})	$\int T_{\rm ant}^{*}\,{\rm d}v$ (K km s^{-1})	$v_{\rm exp}$ (km s^{-1})
^{29}SiS	6–5	106 922.982	18.0	1.977×10^{-5}	0.14 (0.02)	17 (4)
^{29}SiS	8–7	142 558.821	30.8	4.777×10^{-5}	0.29 (0.03)	18 (3)
^{29}SiS	9–8	160 375.153	38.5	6.846×10^{-5}	0.50 (0.02)	17 (2)
^{29}SiS	12–11	213 816.142	66.7	1.644×10^{-4}	1.02 (0.04)	18 (2)
^{29}SiS	13–12	231 626.676	77.8	2.096×10^{-4}	1.22 (0.06)	18.8 (1.5)
^{29}SiS	14–13	249 435.415	89.8	2.625×10^{-4}	1.10 (0.05)	17.6 (1.3)
^{29}SiS	15–14	267 242.221	102.6	3.236×10^{-4}	1.15 (0.05)	16 (2)
^{29}SiS	16–15	285 046.956	116.3	3.934×10^{-4}	1.28 (0.06)	14.5 (1.2)
^{29}SiS	17–16	302 849.482	130.8	4.727×10^{-4}	1.23 (0.03)	17.7 (1.1)
^{29}SiS	18–17	320 649.661	146.2	5.619×10^{-4}	0.99 (0.11)	15 (2)
^{29}SiS	19–18	338 447.355	162.5	6.617×10^{-4}	1.17 (0.12)	16 (2)
^{30}SiS	8–7	140 073.964	30.3	4.532×10^{-5}	0.26 (0.02)	20 (2)
^{30}SiS	9–8	157 579.811	37.8	6.494×10^{-5}	0.27 (0.02)	19 (2)
^{30}SiS	12–11	210 089.621	65.5	1.560×10^{-4}	0.67 (0.05)	12 (2)
^{30}SiS	13–12	227 589.870	76.5	1.989×10^{-4}	0.62 (0.04)	17 (2)
^{30}SiS	14–13	245 088.386	88.2	2.490×10^{-4}	0.67 (0.04)	16.7 (1.5)
^{30}SiS	15–14	262 585.036	100.8	3.070×10^{-4}	0.86 (0.06)	17.6 (1.2)
^{30}SiS	16–15	280 079.687	114.3	3.732×10^{-4}	1.17 (0.04)	20.3 (1.3)
^{30}SiS	17–16	297 572.206	128.6	4.484×10^{-4}	0.88 (0.05)	13.6 (1.0)
^{30}SiS	18–17	315 062.459	143.7	5.331×10^{-4}	0.71 (0.06)	17 (2)
^{30}SiS	19–18	332 550.312	159.6	6.278×10^{-4}	0.85 (0.09)	15 (2)
Si^{34}S	5–4	88 285.830	12.7	1.096×10^{-5}	0.09 (0.02)	7 (7)
Si^{34}S	6–5	105 941.505	17.8	1.923×10^{-5}	0.18 (0.02)	24 (5)
Si^{34}S	8–7	141 250.280	30.5	4.647×10^{-5}	0.18 (0.02)	15 (2)
Si^{34}S	9–8	158 903.109	38.1	6.659×10^{-5}	0.44 (0.02)	20 (2)
Si^{34}S	13–12	229 500.871	77.1	2.039×10^{-4}	0.96 (0.05)	15.2 (1.5)
Si^{34}S	14–13	247 146.245	89.0	2.553×10^{-4}	0.96 (0.03)	17.1 (1.3)
Si^{34}S	15–14	264 789.722	101.7	3.147×10^{-4}	0.97 (0.05)	17.2 (1.3)
Si^{34}S	17–16	300 070.442	129.6	4.598×10^{-4}	1.01 (0.11)	16 (2)
Si^{34}S	18–17	317 707.414	144.9	5.466×10^{-4}	1.07 (0.13)	13 (2)
HCO^{+}	1–0	89 188.526	4.3	4.234×10^{-5}	0.45 (0.03)	20 (3)
HNC	1–0	90 663.563	4.4	2.690×10^{-5}	0.13 (0.02)	20 (7)
HNC	3–2	271 981.107	26.1	9.336×10^{-4}	HB	HB
HCN	1–0	88 631.602	4.3	2.406×10^{-5}	8.09 (0.02)	18 (3)
HCN	3–2	265 886.433	25.5	8.352×10^{-4}	33.02 (0.04)	18.2 (1.1)
HCN	4–3	354 505.476	42.5	2.053×10^{-3}	20.5 (0.2)	17.6 (1.0)
H^{13}CN	1–0	86 339.921	4.1	2.224×10^{-5}	0.85 (0.04)	18 (4)
H^{13}CN	2–1	172 677.851	12.4	2.135×10^{-4}	3.90 (0.09)	16 (2)
H^{13}CN	3–2	259 011.798	24.9	7.721×10^{-4}	6.43 (0.05)	16.4 (1.2)
H^{13}CN	4–3	345 339.769	41.4	1.898×10^{-3}	HB	HB
NaCl	8–7	104 189.669	22.5	5.020×10^{-4}	0.05 (0.01)	10 (8)
NaCl	10–9	130 223.637	34.4	9.919×10^{-4}	0.10 (0.01)	15 (5)
NaCl	11–10	143 237.371	41.3	1.326×10^{-3}	0.18 (0.02)	20 (4)
NaCl	12–11	156 248.639	48.8	1.727×10^{-3}	0.21 (0.02)	14 (4)
NaCl	13–12	169 257.217	56.9	2.202×10^{-3}	0.27 (0.02)	16 (2)
NaCl	16–15	208 264.570	85.0	4.131×10^{-3}	0.15 (0.02)	8 (3)
NaCl	17–16	221 260.147	95.6	4.962×10^{-3}	0.24 (0.03)	10 (4)
NaCl	18–17	234 251.912	106.9	5.898×10^{-3}	0.27 (0.04)	11 (3)
NaCl	19–18	247 239.643	118.7	6.945×10^{-3}	0.40 (0.03)	17 (2)
NaCl	20–19	260 223.113	131.2	8.108×10^{-3}	0.27 (0.06)	11 (3)
NaCl	22–21	286 176.379	158.1	1.081×10^{-2}	0.28 (0.05)	20 (3)
NaCl	23–22	299 145.726	172.4	1.236×10^{-2}	0.25 (0.02)	13.8 (1.5)
NaCl	24–23	312 109.915	187.4	1.405×10^{-2}	0.28 (0.06)	14 (2)

A&A 597, A25 (2017)

Table A.1. continued.

Molecule	Transition QNs	$\nu_{\rm rest}$ (MHz)	$E_{\rm u}$ (K)	$A_{\rm ul}$ (s^{-1})	$\int T_{\rm ant}^{*}\,{\rm d}v$ (K km s^{-1})	$v_{\rm exp}$ (km s^{-1})
CS	2–1	97 980.953	7.1	1.679×10^{-5}	0.79 (0.01)	22 (3)
CS	3–2	146 969.026	14.1	6.071×10^{-5}	2.11 (0.02)	17 (2)
CS	5–4	244 935.555	35.3	2.981×10^{-4}	5.77 (0.04)	16.1 (1.2)
CS	6–5	293 912.089	49.4	5.229×10^{-4}	5.87 (0.04)	17.4 (1.0)
CS	7–6	342 882.854	65.8	8.395×10^{-4}	5.30 (0.07)	19.6 (1.0)
^{13}CS	3–2	138 739.264	13.3	5.107×10^{-5}	0.17 (0.01)	13 (3)
^{13}CS	5–4	231 220.684	33.3	2.507×10^{-4}	0.63 (0.05)	23 (3)
^{13}CS	6–5	277 455.398	46.6	4.399×10^{-4}	0.70 (0.06)	15.4 (1.1)
C^{34}S	3–2	144 617.101	13.9	5.784×10^{-5}	0.18 (0.02)	18 (4)
C^{34}S	5–4	241 016.089	34.7	2.840×10^{-4}	0.41 (0.04)	22 (4)
C^{34}S	6–5	289 209.067	48.6	4.982×10^{-4}	0.43 (0.03)	19 (2)
o-H_2S	$1_{1,0}$–$1_{0,1}$	168 762.754	8.1	2.677×10^{-5}	6.35 (0.02)	18 (2)
o-H_2S	$4_{1,4}$–$3_{2,1}$	204 140.204	144.5	3.006×10^{-8}	0.14 (0.03)	BF
o-H_2S	$3_{3,0}$–$3_{2,1}$	300 505.524	149.1	1.024×10^{-4}	1.05 (0.07)	17.3 (1.1)
p-H_2S	$2_{2,0}$–$2_{1,1}$	216 710.444	84.0	4.870×10^{-5}	0.66 (0.05)	18.3 (1.4)
o-$^{34}H_2S$	$1_{1,0}$–$1_{0,1}$	167 910.516	8.1	2.616×10^{-5}	0.89 (0.02)	22 (2)
SO	(2, 2)–(1, 1)	86 093.959	19.3	5.250×10^{-6}	0.70 (0.03)	17 (3)
SO	(2, 3)–(1, 2)	99 299.891	9.2	1.125×10^{-5}	7.50 (0.02)	16 (3)
SO	(3, 2)–(2, 1)	109 252.184	21.1	1.080×10^{-5}	1.11 (0.02)	17 (3)
SO	(3, 3)–(2, 2)	129 138.904	25.5	2.250×10^{-5}	2.19 (0.03)	17 (2)
SO	(3, 4)–(2, 3)	138 178.659	15.9	3.166×10^{-5}	12.43 (0.02)	17 (2)
SO	(4, 3)–(3, 2)	158 971.816	28.7	4.233×10^{-5}	2.79 (0.02)	17 (2)
SO	(4, 4)–(3, 3)	172 181.407	33.8	5.833×10^{-5}	2.77 (0.05)	17 (2)
SO	(5, 4)–(4, 3)	206 176.019	38.6	1.010×10^{-4}	3.23 (0.04)	17.4 (1.5)
SO	(5, 5)–(4, 4)	215 220.653	44.1	1.193×10^{-4}	3.76 (0.04)	16.9 (1.4)
SO	(5, 6)–(4, 5)	219 949.396	35.0	1.335×10^{-4}	10.68 (0.03)	17.7 (1.4)
SO	(6, 5)–(5, 4)	251 825.767	50.7	1.925×10^{-4}	3.15 (0.04)	16.1 (1.2)
SO	(6, 6)–(5, 5)	258 255.830	56.5	2.120×10^{-4}	3.44 (0.05)	17.4 (1.2)
SO	(6, 7)–(5, 6)	261 843.713	47.6	2.282×10^{-4}	7.54 (0.07)	16.2 (1.1)
SO	(1, 1)–(0, 1)	286 340.151	15.2	1.403×10^{-5}	0.54 (0.05)	19 (2)
SO	(7, 6)–(6, 5)	296 550.061	64.9	3.230×10^{-4}	2.31 (0.03)	16.7 (1.2)
SO	(7, 7)–(6, 6)	301 286.123	71.0	3.429×10^{-4}	3.38 (0.04)	19.2 (1.0)
SO	(7, 8)–(6, 7)	304 077.867	62.1	3.609×10^{-4}	7.23 (0.05)	16.2 (1.0)
SO	(2, 2)–(1, 2)	309 502.443	19.3	1.419×10^{-5}	0.46 (0.03)	17.6 (1.0)
SO	(3, 3)–(2, 3)	339 341.457	25.5	1.455×10^{-5}	0.45 (0.06)	16 (2)
SO	(8, 7)–(7, 6)	340 714.295	81.2	4.985×10^{-4}	2.46 (0.06)	18.1 (1.0)
SO	(8, 8)–(7, 7)	344 310.717	87.5	5.186×10^{-4}	2.72 (0.08)	18.2 (1.0)
SO	(8, 9)–(7, 8)	346 528.537	78.8	5.382×10^{-4}	HB	HB
^{34}SO	(2, 3)–(1, 2)	97 715.405	9.1	1.073×10^{-5}	0.51 (0.02)	18 (3)
^{34}SO	(3, 2)–(2, 1)	106 743.368	20.9	1.007×10^{-5}	0.07 (0.01)	6 (9)
^{34}SO	(3, 4)–(2, 3)	135 775.651	15.6	3.004×10^{-5}	0.93 (0.02)	18 (2)
^{34}SO	(4, 3)–(3, 2)	155 506.808	28.4	3.961×10^{-5}	0.16 (0.02)	17 (4)
^{34}SO	(4, 4)–(3, 3)	168 815.114	33.4	5.498×10^{-5}	0.17 (0.02)	20 (4)
^{34}SO	(5, 5)–(4, 4)	211 013.024	43.5	1.124×10^{-4}	0.34 (0.05)	21 (5)
^{34}SO	(5, 6)–(4, 5)	215 839.917	34.4	1.262×10^{-4}	0.74 (0.04)	17.6 (1.4)
^{34}SO	(6, 5)–(5, 4)	246 663.403	49.9	1.809×10^{-4}	0.26 (0.03)	19 (2)
^{34}SO	(6, 6)–(5, 5)	253 207.022	55.7	1.998×10^{-4}	0.28 (0.04)	21 (3)
^{34}SO	(7, 6)–(6, 5)	290 562.257	63.8	3.037×10^{-4}	0.27 (0.03)	22 (4)
^{34}SO	(7, 8)–(6, 7)	298 257.973	61.0	3.406×10^{-4}	0.50 (0.03)	15.6 (1.4)

Table A.1. continued.

Molecule	Transition QNs	$\nu_{\rm rest}$ (MHz)	$E_{\rm u}$ (K)	$A_{\rm ul}$ (s^{-1})	$\int T_{\rm ant}^{*}\,{\rm d}v$ (K km s^{-1})	$v_{\rm exp}$ (km s^{-1})
SO_2	$8_{1,7}$–$8_{0,8}$	83 688.092	36.7	6.825×10^{-6}	1.32 (0.03)	20 (4)
SO_2	$2_{2,0}$–$3_{1,3}$	100 878.107	12.6	1.026×10^{-6}	0.11 (0.01)	20 (6)
SO_2	$3_{1,3}$–$2_{0,2}$	104 029.420	7.7	1.006×10^{-5}	1.73 (0.03)	21 (3)
SO_2	$10_{1,9}$–$10_{0,10}$	104 239.299	54.7	1.122×10^{-5}	1.12 (0.02)	19 (3)
SO_2	$12_{2,10}$–$12_{1,11}$	128 605.111	82.6	2.615×10^{-5}	0.64 (0.02)	16 (2)
SO_2	$12_{1,11}$–$11_{2,10}$	129 105.786	76.4	9.029×10^{-6}	0.64 (0.02)	19 (2)
SO_2	$10_{2,8}$–$10_{1,9}$	129 514.799	60.9	2.502×10^{-5}	0.92 (0.03)	16 (2)
SO_2	$12_{1,11}$–$12_{0,12}$	131 014.841	76.4	1.856×10^{-5}	1.00 (0.01)	22 (2)
SO_2	$14_{2,12}$–$14_{1,13}$	132 744.832	108.1	2.933×10^{-5}	0.47 (0.03)	18 (2)
SO_2	$8_{2,6}$–$8_{1,7}$	134 004.812	43.1	2.501×10^{-5}	1.28 (0.02)	16 (2)
SO_2	$5_{1,5}$–$4_{0,4}$	135 696.017	15.7	2.208×10^{-5}	3.78 (0.03)	17 (2)
SO_2	$6_{2,4}$–$6_{1,5}$	140 306.166	29.2	2.528×10^{-5}	1.76 (0.02)	17 (2)
SO_2	$16_{2,14}$–$16_{1,15}$	143 057.080	137.5	3.572×10^{-5}	0.31 (0.02)	18 (3)
SO_2	$4_{2,2}$–$4_{1,3}$	146 605.520	19.0	2.470×10^{-5}	1.81 (0.03)	17 (2)
SO_2	$2_{2,0}$–$2_{1,1}$	151 378.663	12.6	1.875×10^{-5}	1.11 (0.03)	18 (2)
SO_2	$3_{2,2}$–$3_{1,3}$	158 199.781	15.3	2.532×10^{-5}	1.58 (0.02)	17 (2)
SO_2	$18_{2,16}$–$18_{1,17}$	160 342.971	170.8	4.692×10^{-5}	0.33 (0.02)	13 (2)
SO_2	$4_{3,1}$–$5_{2,4}$	160 543.024	31.3	4.321×10^{-6}	0.06 (0.01)	8 (4)
SO_2	$10_{0,10}$–$9_{1,9}$	160 827.841	49.7	3.954×10^{-5}	3.37 (0.02)	17 (2)
SO_2	$14_{1,13}$–$14_{0,14}$	163 605.533	101.8	3.006×10^{-5}	1.33 (0.03)	18 (2)
SO_2	$5_{2,4}$–$5_{1,5}$	165 144.652	23.6	3.122×10^{-5}	2.47 (0.02)	18 (2)
SO_2	$7_{1,7}$–$6_{0,6}$	165 225.452	27.1	4.135×10^{-5}	6.14 (0.02)	17 (2)
SO_2	$12_{0,12}$–$11_{1,11}$	203 391.484	70.1	8.805×10^{-5}	4.04 (0.06)	16.4 (1.5)
SO_2	$18_{3,15}$–$18_{2,16}$	204 246.762	180.6	9.267×10^{-5}	0.38 (0.05)	15 (3)
SO_2	$11_{2,10}$–$11_{1,11}$	205 300.539	70.2	5.318×10^{-5}	1.54 (0.06)	17.1 (1.5)
SO_2	$3_{2,2}$–$2_{1,1}$	208 700.337	15.3	6.719×10^{-5}	3.08 (0.03)	17.2 (1.4)
SO_2	$26_{3,23}$–$26_{2,24}$	213 068.427	350.8	1.156×10^{-4}	0.19 (0.04)	5 (3)
SO_2	$16_{3,13}$–$16_{2,14}$	214 689.395	147.8	9.902×10^{-5}	0.32 (0.03)	19 (2)
SO_2	$22_{2,20}$–$22_{1,21}$	216 643.304	248.5	9.271×10^{-5}	0.40 (0.04)	11 (2)
SO_2	$11_{1,11}$–$10_{0,10}$	221 965.221	60.4	1.138×10^{-4}	5.81 (0.06)	16.2 (1.4)
SO_2	$13_{2,12}$–$13_{1,13}$	225 153.705	93.0	6.523×10^{-5}	0.94 (0.07)	17.3 (1.4)
SO_2	$14_{3,11}$–$14_{2,12}$	226 300.028	119.0	1.068×10^{-4}	HB	HB
SO_2	$4_{2,2}$–$3_{1,3}$	235 151.721	19.0	7.691×10^{-5}	4.41 (0.05)	17.2 (1.3)
SO_2	$16_{1,15}$–$15_{2,14}$	236 216.688	130.7	7.505×10^{-5}	0.66 (0.05)	17.0 (1.4)
SO_2	$12_{3,9}$–$12_{2,10}$	237 068.834	94.0	1.141×10^{-4}	0.85 (0.04)	18.6 (1.4)
SO_2	$18_{1,17}$–$18_{0,18}$	240 942.792	163.1	7.024×10^{-5}	0.47 (0.04)	18 (3)
SO_2	$5_{2,4}$–$4_{1,3}$	241 615.798	23.6	8.455×10^{-5}	4.74 (0.06)	17.6 (1.2)
SO_2	$14_{0,14}$–$13_{1,13}$	244 254.220	93.9	1.639×10^{-4}	3.71 (0.04)	17.3 (1.2)
SO_2	$10_{3,7}$–$10_{2,8}$	245 563.423	72.7	1.191×10^{-4}	1.31 (0.04)	17.0 (1.2)
SO_2	$15_{2,14}$–$15_{1,15}$	248 057.403	119.3	8.056×10^{-5}	0.66 (0.05)	16.0 (1.3)
SO_2	$13_{1,13}$–$12_{0,12}$	251 199.676	82.2	1.756×10^{-4}	HB	HB
SO_2	$8_{3,5}$–$8_{2,6}$	251 210.586	55.2	1.198×10^{-4}	HB	HB
SO_2	$6_{3,3}$–$6_{2,4}$	254 280.537	41.4	1.136×10^{-4}	2.02 (0.03)	16.7 (1.2)
SO_2	$4_{3,1}$–$4_{2,2}$	255 553.303	31.3	9.284×10^{-5}	1.62 (0.06)	17.2 (1.2)
SO_2	$3_{3,1}$–$3_{2,2}$	255 958.045	27.6	6.626×10^{-5}	1.09 (0.06)	17.6 (1.2)
SO_2	$5_{3,3}$–$5_{2,4}$	256 246.946	35.9	1.074×10^{-4}	1.94 (0.04)	17.2 (1.2)
SO_2	$7_{3,5}$–$7_{2,6}$	257 099.967	47.8	1.223×10^{-4}	1.78 (0.04)	16.5 (1.2)
SO_2	$32_{4,28}$–$32_{3,29}$	258 388.714	531.1	2.102×10^{-4}	0.19 (0.03)	6.2 (1.4)
SO_2	$9_{3,7}$–$9_{2,8}$	258 942.200	63.5	1.318×10^{-4}	1.53 (0.04)	17.2 (1.2)
SO_2	$30_{4,26}$–$30_{3,27}$	259 599.446	471.5	2.072×10^{-4}	0.16 (0.02)	6 (2)
SO_2	$11_{3,9}$–$11_{2,10}$	262 256.907	82.8	1.408×10^{-4}	0.88 (0.09)	18 (2)
SO_2	$30_{3,27}$–$30_{2,28}$	263 543.954	459.1	1.894×10^{-4}	0.21 (0.02)	5.1 (1.4)
SO_2	$34_{4,30}$–$34_{3,31}$	265 481.970	594.7	2.277×10^{-4}	0.12 (0.02)	8.6 (1.2)

A&A 597, A25 (2017)

Table A.1. continued.

Molecule	Transition QNs	$\nu_{\rm rest}$ (MHz)	$E_{\rm u}$ (K)	$A_{\rm ul}$ (s^{-1})	$\int T_{\rm ant}^{*}\,{\rm d}v$ (K km s^{-1})	$v_{\rm exp}$ (km s^{-1})
SO_2	$13_{3,11}$–$13_{2,12}$	267 537.453	105.8	1.513×10^{-4}	0.88 (0.05)	15.8 (1.2)
SO_2	$28_{4,24}$–$28_{3,25}$	267 719.839	415.9	2.157×10^{-4}	0.11 (0.04)	12 (2)
SO_2	$7_{2,6}$–$6_{1,5}$	271 529.016	35.5	1.107×10^{-4}	2.53 (0.07)	16.8 (1.1)
SO_2	$17_{2,16}$–$17_{1,17}$	273 752.962	149.2	9.966×10^{-5}	0.29 (0.06)	12 (2)
SO_2	$15_{3,13}$–$15_{2,14}$	275 240.185	132.5	1.645×10^{-4}	0.64 (0.08)	8 (4)
SO_2	$26_{4,22}$–$26_{3,23}$	280 807.246	364.3	2.329×10^{-4}	0.22 (0.05)	4.8 (1.3)
SO_2	$36_{4,32}$–$36_{3,33}$	281 688.930	662.1	2.636×10^{-4}	0.22 (0.03)	9 (2)
SO_2	$15_{1,15}$–$14_{0,14}$	281 762.602	107.4	2.609×10^{-4}	4.64 (0.05)	17.1 (1.1)
SO_2	$6_{2,4}$–$5_{1,5}$	282 036.568	29.2	1.003×10^{-4}	4.33 (0.05)	17.7 (1.1)
SO_2	$20_{1,19}$–$20_{0,20}$	282 292.806	198.9	1.002×10^{-4}	0.40 (0.05)	16 (2)
SO_2	$16_{0,16}$–$15_{1,15}$	283 464.770	121.0	2.700×10^{-4}	3.80 (0.03)	22.0 (1.1)
SO_2	$17_{3,15}$–$17_{2,16}$	285 743.589	162.9	1.816×10^{-4}	0.78 (0.06)	17.5 (1.0)
SO_2	$22_{2,20}$–$21_{3,19}$	286 416.272	248.5	9.293×10^{-5}	0.30 (0.06)	16 (2)
SO_2	$18_{1,17}$–$17_{2,16}$	288 519.997	163.1	1.570×10^{-4}	1.00 (0.06)	16.3 (1.1)
SO_2	$26_{2,24}$–$26_{1,25}$	296 168.675	340.6	1.873×10^{-4}	0.21 (0.02)	10.2 (1.4)
SO_2	$9_{2,8}$–$8_{1,7}$	298 576.309	51.0	1.442×10^{-4}	3.35 (0.04)	17.1 (1.0)
SO_2	$19_{3,17}$–$19_{2,18}$	299 316.820	197.0	2.037×10^{-4}	0.55 (0.06)	17 (2)
SO_2	$32_{3,29}$–$32_{2,30}$	300 273.420	518.7	2.547×10^{-4}	0.13 (0.03)	6 (2)
SO_2	$19_{2,18}$–$19_{1,19}$	301 896.629	182.6	1.229×10^{-4}	0.35 (0.06)	20 (3)
SO_2	$38_{4,34}$–$38_{3,35}$	307 185.315	733.4	3.228×10^{-4}	0.41 (0.06)	9 (2)
SO_2	$22_{4,18}$–$22_{3,19}$	312 542.520	272.8	2.819×10^{-4}	0.27 (0.03)	9 (2)
SO_2	$3_{3,1}$–$2_{2,0}$	313 279.719	27.6	3.396×10^{-4}	3.77 (0.07)	18.2 (1.0)
SO_2	$17_{1,17}$–$16_{0,16}$	313 660.853	136.1	3.747×10^{-4}	1.87 (0.05)	16.5 (1.0)
SO_2	$21_{3,19}$–$21_{2,20}$	316 098.875	234.7	2.319×10^{-4}	0.35 (0.04)	5 (2)
SO_2	$18_{0,18}$–$17_{1,17}$	321 330.168	151.5	4.087×10^{-4}	1.5 (0.2)	11 (2)
SO_2	$4_{3,1}$–$3_{2,2}$	332 505.243	31.3	3.290×10^{-4}	3.01 (0.09)	17.0 (1.0)
SO_2	$8_{2,6}$–$7_{1,7}$	334 673.355	43.1	1.270×10^{-4}	2.5 (0.2)	21 (2)
SO_2	$18_{4,14}$–$18_{3,15}$	338 305.994	196.8	3.266×10^{-4}	0.44 (0.06)	17 (2)
SO_2	$20_{1,19}$–$19_{2,18}$	338 611.811	198.9	2.868×10^{-4}	0.48 (0.06)	9 (2)
SO_2	$28_{2,26}$–$28_{1,27}$	340 316.406	391.8	2.580×10^{-4}	0.36 (0.04)	10.8 (1.0)
SO_2	$36_{5,31}$–$36_{4,32}$	341 673.955	678.5	4.344×10^{-4}	0.18 (0.03)	4 (2)
SO_2	$34_{3,31}$–$34_{2,32}$	342 761.629	581.9	3.447×10^{-4}	0.18 (0.03)	4 (2)
SO_2	$13_{2,12}$–$12_{1,11}$	345 338.540	93.0	2.381×10^{-4}	HB	HB
SO_2	$16_{4,12}$–$16_{3,13}$	346 523.879	164.5	3.390×10^{-4}	HB	HB
SO_2	$19_{1,19}$–$18_{0,18}$	346 652.171	168.1	5.219×10^{-4}	1.43 (0.12)	19 (3)
SO_2	$5_{3,3}$–$4_{2,2}$	351 257.225	35.9	3.357×10^{-4}	2.05 (0.12)	17.2 (1.0)
$^{34}SO_2$	$3_{1,3}$–$2_{0,2}$	102 031.880	7.6	9.495×10^{-6}	0.17 (0.02)	24 (6)
$^{34}SO_2$	$8_{2,6}$–$8_{1,7}$	128 668.791	42.8	2.245×10^{-5}	0.054 (0.015)	10 (6)
$^{34}SO_2$	$5_{1,5}$–$4_{0,4}$	133 471.429	15.5	2.107×10^{-5}	0.19 (0.02)	16 (6)
$^{34}SO_2$	$4_{3,1}$–$5_{2,4}$	151 917.559	30.5	3.663×10^{-6}	0.07 (0.02)	13 (5)
$^{34}SO_2$	$3_{2,2}$–$3_{1,3}$	153 015.053	15.0	2.290×10^{-5}	0.11 (0.02)	12 (5)
$^{34}SO_2$	$18_{2,16}$–$18_{1,17}$	160 802.573	170.3	4.611×10^{-5}	0.04 (0.01)	4 (4)
$^{34}SO_2$	$10_{0,10}$–$9_{1,9}$	162 020.378	49.5	4.100×10^{-5}	0.24 (0.02)	17 (2)
$^{34}SO_2$	$7_{1,7}$–$6_{0,6}$	162 775.882	26.9	3.976×10^{-5}	0.35 (0.02)	17 (2)
$^{34}SO_2$	$11_{1,11}$–$10_{0,10}$	219 355.012	60.1	1.110×10^{-4}	0.32 (0.02)	15.2 (1.4)
$^{34}SO_2$	$13_{1,13}$–$12_{0,12}$	248 698.698	81.8	1.721×10^{-4}	0.26 (0.04)	18 (2)
$^{34}SO_2$	$7_{2,6}$–$6_{1,5}$	265 554.053	35.1	1.038×10^{-4}	0.52 (0.04)	27 (2)
PN	2–1	93 979.768	6.8	2.916×10^{-5}	0.18 (0.02)	16 (3)
PN	3–2	140 967.690	13.5	1.054×10^{-4}	0.48 (0.02)	17 (2)
PN	5–4	234 935.691	33.8	5.177×10^{-4}	0.82 (0.05)	14.2 (1.4)
PN	6–5	281 914.200	47.4	9.083×10^{-4}	0.99 (0.06)	18.6 (1.1)

Table A.1. continued.

Molecule	Transition QNs	$\nu_{\rm rest}$ (MHz)	$E_{\rm u}$ (K)	$A_{\rm ul}$ (s^{-1})	$\int T_{\rm ant}^{*}\,{\rm d}v$ (K km s^{-1})	$v_{\rm exp}$ (km s^{-1})
PO	Ω = 1/2,e,(5/2,3)–(3/2,2)	108 998.445	8.4	2.132×10^{-5}	0.08 (0.02)	6 (3)
PO	Ω = 1/2,f,(5/2,3)–(3/2,2)	109 206.200	8.4	2.143×10^{-5}	0.07 (0.02)	7 (3)
PO	Ω = 1/2,e,(7/2,4)–(5/2,3)	152 656.979	15.7	6.274×10^{-5}	0.28 (0.03)	BF
PO	Ω = 1/2,e,(7/2,3)–(5/2,2)	152 680.282	15.7	5.975×10^{-5}	0.14 (0.02)	BF
PO	Ω = 1/2,f,(7/2,4)–(5/2,3)	152 855.454	15.8	6.296×10^{-5}	0.14 (0.02)	13 (4)
PO	Ω = 1/2,f,(7/2,3)–(5/2,2)	152 888.128	15.7	5.998×10^{-5}	0.16 (0.02)	15 (4)
PO	Ω = 1/2,e,(11/2,5)–(9/2,5)	239 704.364	36.7	4.699×10^{-6}	0.06 (0.02)	5 (3)
PO	Ω = 1/2,f,(11/2,6)–(9/2,5)	239 948.978	36.7	2.583×10^{-4}	0.33 (0.04)	HB
PO	Ω = 1/2,f,(11/2,5)–(9/2,4)	239 958.096	36.7	2.536×10^{-4}		
PO	Ω = 1/2,e,(11/2,6)–(9/2,5)	240 141.054	36.7	2.590×10^{-4}	0.25 (0.04)	HB
PO	Ω = 1/2,e,(11/2,5)–(9/2,4)	240 152.530	36.7	2.543×10^{-4}		
PO	Ω = 1/2,f,(13/2,7)–(11/2,6)	283 586.816	50.3	4.330×10^{-4}	0.44 (0.03)	HB
PO	Ω = 1/2,f,(13/2,6)–(11/2,5)	283 593.166	50.3	4.274×10^{-4}		
PO	Ω = 1/2,e,(13/2,7)–(11/2,6)	283 777.587	50.3	4.339×10^{-4}	0.44 (0.03)	HB
PO	Ω = 1/2,e,(13/2,6)–(11/2,5)	283 785.404	50.3	4.283×10^{-4}		
NO	Ω = 1/2,e,(5/2,7/2)–(3/2,5/2)	250 436.842	19.2	1.841×10^{-6}	0.47 (0.05)	HB
NO	Ω = 1/2,e,(5/2,5/2)–(3/2,3/2)	250 440.653	19.2	1.547×10^{-6}		
NO	Ω = 1/2,e,(5/2,3/2)–(3/2,1/2)	250 448.526	19.2	1.381×10^{-6}		
NO	Ω = 1/2,e,(5/2,3/2)–(3/2,5/2)	250 517.704	19.2	1.841×10^{-8}	0.17 (0.04)	20 (2)
o-H_2CO	$2_{1,2}$–$1_{1,1}$	140 839.516	6.8	5.296×10^{-5}	0.41 (0.02)	20 (2)
o-H_2CO	$2_{1,1}$–$1_{1,0}$	150 498.335	7.5	6.462×10^{-5}	0.43 (0.03)	13 (2)
o-H_2CO	$3_{1,3}$–$2_{1,2}$	211 211.449	16.9	2.268×10^{-4}	0.71 (0.05)	16.6 (1.5)
o-H_2CO	$3_{1,2}$–$2_{1,1}$	225 697.772	18.3	2.767×10^{-4}	0.61 (0.06)	18 (3)
o-H_2CO	$4_{1,4}$–$3_{1,3}$	281 526.919	30.4	5.874×10^{-4}	0.75 (0.06)	25 (2)
o-H_2CO	$4_{3,2}$–$3_{3,1}$	291 380.441	125.8	3.040×10^{-4}	0.19 (0.02)	BF
o-H_2CO	$4_{3,1}$–$3_{3,0}$	291 384.360	125.8	3.040×10^{-4}	0.29 (0.02)	BF
o-H_2CO	$4_{1,3}$–$3_{1,2}$	300 836.630	32.7	7.168×10^{-4}	0.63 (0.11)	15.1 (1.0)
p-H_2CO	$2_{0,2}$–$1_{0,1}$	145 602.951	10.5	7.802×10^{-5}	0.28 (0.02)	25 (3)
p-H_2CO	$3_{0,3}$–$2_{0,2}$	218 222.187	21.0	2.814×10^{-4}	0.26 (0.03)	24 (3)
p-H_2CO	$3_{2,2}$–$2_{2,1}$	218 475.634	68.1	1.569×10^{-4}	0.41 (0.04)	17 (2)
p-H_2CO	$4_{0,4}$–$3_{0,3}$	290 623.412	34.9	6.891×10^{-4}	0.31 (0.03)	24 (2)
p-H_2CO	$4_{2,2}$–$3_{2,1}$	291 948.066	82.1	5.241×10^{-4}	0.15 (0.03)	14 (2)
CN	(1, 1/2, 1/2)–(0, 1/2, 3/2)	113 144.157	5.4	1.053×10^{-6}	0.19 (0.03)	11 (3)
CN	(1, 1/2, 3/2)–(0, 1/2, 1/2)	113 170.492	5.4	5.145×10^{-6}	0.18 (0.03)	15 (3)
CN	(1, 1/2, 3/2)–(0, 1/2, 3/2)	113 191.279	5.4	6.682×10^{-6}	0.20 (0.03)	18 (4)
CN	(1, 3/2, 3/2)–(0, 1/2, 1/2)	113 488.120	5.4	6.736×10^{-6}	0.47 (0.03)	HB
CN	(1, 3/2, 5/2)–(0, 1/2, 3/2)	113 490.970	5.4	1.192×10^{-5}		
CN	(2, 3/2, 1/2)–(1, 3/2, 3/2)	226 298.943	16.3	8.227×10^{-6}	HB	HB
CN	(2, 3/2, 3/2)–(1, 3/2, 1/2)	226 303.037	16.3	4.169×10^{-6}		
CN	(2, 3/2, 1/2)–(1, 1/2, 3/2)	226 616.571	16.3	1.073×10^{-5}	0.21 (0.03)	20.9 (1.5)
CN	(2, 3/2, 3/2)–(1, 1/2, 3/2)	226 632.190	16.3	4.259×10^{-5}	0.28 (0.02)	11 (3)
CN	(2, 3/2, 5/2)–(1, 1/2, 3/2)	226 659.558	16.3	9.467×10^{-5}	1.32 (0.04)	HB
CN	(2, 3/2, 1/2)–(1, 1/2, 1/2)	226 663.693	16.3	8.465×10^{-5}		
CN	(2, 3/2, 3/2)–(1, 1/2, 1/2)	226 679.311	16.3	5.268×10^{-5}	0.26 (0.03)	10.9 (1.1)
CN	(2, 5/2, 5/2)–(1, 3/2, 3/2)	226 874.191	16.3	9.621×10^{-5}	1.60 (0.04)	HB
CN	(2, 5/2, 7/2)–(1, 3/2, 5/2)	226 874.781	16.3	1.143×10^{-4}		
CN	(2, 5/2, 3/2)–(1, 3/2, 1/2)	226 875.896	16.3	8.587×10^{-5}		
CN	(2, 5/2, 3/2)–(1, 3/2, 3/2)	226 887.420	16.3	2.731×10^{-5}		
CN	(3, 5/2, 7/2)–(2, 5/2, 7/2)	339 516.635	32.6	2.535×10^{-5}	0.13 (0.03)	4.4 (0.4)
CN	(3, 5/2, 3/2)–(2, 3/2, 3/2)	340 019.626	32.6	9.270×10^{-5}	1.31 (0.05)	HB
CN	(3, 5/2, 7/2)–(2, 3/2, 5/2)	340 031.549	32.6	3.845×10^{-4}		
CN	(3, 5/2, 3/2)–(2, 3/2, 1/2)	340 035.408	32.6	2.887×10^{-4}		
CN	(3, 5/2, 5/2)–(2, 3/2, 3/2)	340 035.408	32.6	3.231×10^{-4}		

A&A 597, A25 (2017)

Table A.1. continued.

Molecule	Transition QNs	$\nu_{\rm rest}$ (MHz)	$E_{\rm u}$ (K)	$A_{\rm ul}$ (s^{-1})	$\int T_{\rm ant}^{*}\,{\rm d}v$ (K km s^{-1})	$v_{\rm exp}$ (km s^{-1})
CN	(3, 7/2, 7/2)–(2, 5/2, 5/2)	340 247.770	32.7	3.796×10^{-4}		
CN	(3, 7/2, 9/2)–(2, 5/2, 7/2)	340 247.770	32.7	4.131×10^{-4}		
CN	(3, 7/2, 5/2)–(2, 5/2, 3/2)	340 248.544	32.7	3.674×10^{-4}	0.83 (0.05)	HB
CN	(3, 7/2, 5/2)–(2, 5/2, 5/2)	340 261.773	32.7	4.479×10^{-5}		
CN	(3, 7/2, 7/2)–(2, 5/2, 7/2)	340 264.949	32.7	3.350×10^{-5}		
NS	Ω = 1/2,e,(7/2, 9/2)–(5/2, 7/2)	161 297.246	16.6	6.865×10^{-5}		
NS	Ω = 1/2,e,(7/2, 7/2)–(5/2, 5/2)	161 298.411	16.6	6.301×10^{-5}	0.35 (0.02)	HB
NS	Ω = 1/2,e,(7/2, 5/2)–(5/2, 3/2)	161 301.747	16.6	6.108×10^{-5}		
NS	Ω = 1/2,f,(7/2, 9/2)–(5/2, 7/2)	161 697.257	16.7	6.916×10^{-5}		
NS	Ω = 1/2,f,(7/2, 7/2)–(5/2, 5/2)	161 703.404	16.7	6.348×10^{-5}	0.31 (0.02)	HB
NS	Ω = 1/2,f,(7/2, 5/2)–(5/2, 3/2)	161 703.987	16.7	6.154×10^{-5}		
NS	Ω = 1/2,e,(9/2, 11/2)–(7/2, 9/2)	207 436.051	26.5	1.512×10^{-4}		
NS	Ω = 1/2,e,(9/2, 9/2)–(7/2, 7/2)	207 436.636	26.5	1.436×10^{-4}	0.31 (0.03)	HB
NS	Ω = 1/2,e,(9/2, 7/2)–(7/2, 5/2)	207 438.692	26.5	1.417×10^{-4}		
NS	Ω = 1/2,f,(9/2, 11/2)–(7/2, 9/2)	207 834.866	26.6	1.521×10^{-4}		
NS	Ω = 1/2,f,(9/2, 9/2)–(7/2, 7/2)	207 838.365	26.6	1.445×10^{-4}	0.35 (0.03)	HB
NS	Ω = 1/2,f,(9/2, 7/2)–(7/2, 5/2)	207 838.365	26.6	1.425×10^{-4}		
NS	Ω = 1/2,e,(11/2, 13/2)–(9/2, 11/2)	253 570.476	38.7	2.824×10^{-4}		
NS	Ω = 1/2,e,(11/2, 11/2)–(9/2, 9/2)	253 570.476	38.7	2.730×10^{-4}	0.47 (0.03)	HB
NS	Ω = 1/2,e,(11/2, 9/2)–(9/2, 7/2)	253 572.148	38.7	2.711×10^{-4}		
NS	Ω = 1/2,f,(11/2, 13/2)–(9/2, 11/2)	253 968.393	38.8	2.838×10^{-4}		
NS	Ω = 1/2,f,(11/2, 11/2)–(9/2, 9/2)	253 970.581	38.8	2.743×10^{-4}	0.42 (0.03)	HB
NS	Ω = 1/2,f,(11/2, 9/2)–(9/2, 7/2)	253 970.581	38.8	2.723×10^{-4}		
NS	Ω = 1/2,f,(15/2, 17/2)–(13/2, 15/2)	346 220.137	69.8	7.385×10^{-4}		
NS	Ω = 1/2,f,(15/2, 15/2)–(13/2, 13/2)	346 221.163	69.8	7.250×10^{-4}	0.15 (0.05)	HB
NS	Ω = 1/2,f,(15/2, 13/2)–(13/2, 11/2)	346 221.163	69.8	7.234×10^{-4}		

Table A.2. Line parameters for transitions that may present variability.

Molecule	Transition QNs	$\nu_{\rm rest}$ (MHz)	$E_{\rm u}$ (K)	$A_{\rm ul}$ (s^{-1})	$\int T_{\rm ant}^{*}\,{\rm d}v$ (K km s^{-1})	$v_{\rm exp}$ (km s^{-1})	Julian date
SiO $v = 1$	2–1	86 243.429	1775.4	2.903×10^{-5}	154.73 (0.04)	7 (3)	2 455 018.5
SiO $v = 1$	3–2	129 363.350	1781.6	1.050×10^{-4}	50.01 (0.02)	5 (2)	2 455 018.5
SiO $v = 1$	4–3	172 481.120	1789.9	2.580×10^{-4}	12.98 (0.02)	5 (2)	2 455 578.5
SiO $v = 1$	5–4	215 596.021	1800.3	5.154×10^{-4}	7.52 (0.03)	4 (1)	2 456 579.5
SiO $v = 1$	6–5	258 707.335	1812.7	9.042×10^{-4}	1.04 (0.07)	8 (1)	2 455 309.5
...	...	...	...	...	1.99 (0.05)	4 (1)	2 456 579.5
SiO $v = 1$	7–6	301 814.346	1827.2	1.452×10^{-3}	4.40 (0.08)	6 (1)	2 455 550.5
...	...	...	...	...	5.35 (0.10)	6 (1)	2 455 574.5
...	...	...	...	...	4.88 (0.05)	8 (1)	2 456 320.5
...	...	...	...	...	2.33 (0.12)	10 (1)	2 456 616.5
SiO $v = 1$	8–7	344 916.336	1843.7	2.185×10^{-3}	0.74 (0.08)	8 (1)	2 455 576.5
SiO $v = 2$	2–1	85 640.455	3527.5	2.879×10^{-5}	0.77 (0.02)	7 (3)	2 455 018.5
SiO $v = 2$	3–2	128 458.888	3533.6	1.041×10^{-4}	1.63 (0.01)	4.70 (2)	2 455 018.5
SiO $v = 2$	4–3	171 275.169	3541.9	2.559×10^{-4}	6.62 (0.04)	8 (2)	2 455 578.5
SiO $v = 2$	5–4	214 088.579	3552.1	5.110×10^{-4}	1.94 (0.03)	7 (1)	2 456 579.5
SiO $v = 2$	6–5	256 898.401	3564.5	8.966×10^{-4}	2.03 (0.05)	7 (1)	2 456 579.5
SiO $v = 2$	7–6	299 703.918	3578.9	1.439×10^{-3}	1.63 (0.09)	2 (1)	2 455 550.5
...	...	...	...	...	6.29 (0.06)	3 (1)	2 456 320.5
SiO $v = 2$	8-7	342 504.411	3595.3	2.166×10^{-3}	0.34 (0.07)	5,(1)	2 455 576.5
SiO $v = 3$	4–3	170 070.353	5276.8	2.536×10^{-4}	2.78 (0.02)	4 (2)	2 455 576.5
SiO $v = 3$	5–4	212 582.557	5287.0	5.066×10^{-4}	0.12 (0.03)	3 (1)	2 456 579.5
SiO $v = 3$	6–5	255 091.170	5299.2	8.888×10^{-4}	0.78 (0.03)	8 (1)	2 456 579.5
SiO $v = 3$	7–6	297 595.476	5313.5	1.427×10^{-3}	1.46 (0.03)	2 (3)	2 456 371.5
...	...	...	...	...	0.01 (0.02)	3 (1)	2 456 615.5
SiO $v = 3$	8–7	340 094.756	5329.8	2.148×10^{-3}	0.36 (0.05)	5 (1)	2 455 575.5
...	...	...	...	...	0.37 (0.10)	3 (1)	2 456 615.5
^{29}SiO $v = 1$	2–1	85 166.957	1764.3	2.796×10^{-5}	1.50 (0.03)	7 (3)	2 455 018.5
^{29}SiO $v = 1$	4–3	170 328.320	1778.6	2.485×10^{-4}	9.34 (0.02)	5 (2)	2 455 576.5
^{29}SiO $v = 1$	5–4	212 905.155	1788.8	4.963×10^{-4}	0.15 (0.03)	1 (2)	2 456 579.5
^{29}SiO $v = 1$	6–5	255 478.493	1801.1	8.707×10^{-4}	11.18 (0.04)	5 (2)	2 456 579.5
^{29}SiO $v = 1$	7–6	298 047.635	1815.4	1.398×10^{-3}	0.80 (0.06)	5 (1)	2 455 550.5
...	...	...	...	...	2.91 (0.04)	4 (1)	2 456 320.5
...	...	...	...	...	2.21 (0.04)	5 (1)	2 456 371.5
...	...	...	...	...	0.35 (0.03)	4 (1)	2 456 615.5
^{29}SiO $v = 1$	8–7	340 611.882	1831.8	2.104×10^{-3}	0.21 (0.06)	5 (1)	2 455 575.5
^{29}SiO $v = 2$	2–1	84 575.290	3505.6	2.773×10^{-5}	12.64 (0.02)	10 (3)	2 455 018.5
^{29}SiO $v = 2$	4–3	169 144.982	3519.8	2.464×10^{-4}	0.66 (0.02)	6 (2)	2 455 576.5
^{29}SiO $v = 2$	5–4	211 425.980	3529.9	4.922×10^{-4}	0.16 (0.02)	2 (2)	2 456 579.5
^{29}SiO $v = 2$	6–5	253 703.479	3542.1	8.635×10^{-4}	9.61 (0.03)	1 (2)	2 456 579.5
^{29}SiO $v = 3$	8–7	335 880.698	5296.5	2.069×10^{-3}	0.3 (0.3)	8 (2)	2 455 579.5
...	...	...	...	...	1.0 (0.2)	2 (2)	2 456 371.5
...	...	...	...	...	0.57 (0.10)	2 (2)	2 456 615.5
^{30}SiO $v = 1$	4–3	168 323.349	1768.0	2.398×10^{-4}	2.00 (0.02)	4 (5)	2 455 576.5
^{30}SiO $v = 1$	5–4	210 399.065	1778.1	4.790×10^{-4}	1.11 (0.04)	6 (2)	2 456 579.5
^{30}SiO $v = 1$	6–5	252 471.366	1790.3	8.403×10^{-4}	0.15 (0.04)	4 (2)	2 456 579.5
...	...	...	...	...	0.08 (0.03)	4 (2)	2 456 579.5
^{30}SiO $v = 1$	7–6	294 539.570	1804.4	1.349×10^{-3}	0.59 (0.04)	6 (2)	2 456 320.5
...	...	...	...	...	0.35 (0.04)	5 (1)	2 456 371.5
...	...	...	...	...	0.23 (0.03)	6 (1)	2 456 615.5

Notes. Column 2: quantum numbers of the corresponding line; Col. 6: integrated intensity (in antenna temperature) of the line with its formal uncertainty; Col. 7: expansion velocity derived from the linewidth with its uncertainty which includes the width of half a channel (1 MHz) except for the lines with a low S/N where a full channel (2 MHz) is included. Column 8: Julian date. The uncertainties given (within parentheses) do not include additional uncertainties derived from the absolute flux calibration and baseline subtraction. The ellipsis symbol indicate that the field is equal to the same field of the previous row.

A&A 597, A25 (2017)

Table A.2. continued.

Molecule	Transition QNs	$\nu_{\rm rest}$ (MHz)	$E_{\rm u}$ (K)	$A_{\rm ul}$ (s^{-1})	$\int T_{\rm ant}^{*}\,{\rm d}v$ (K km s^{-1})	$v_{\rm exp}$ (km s^{-1})	Julian date
^{30}SiO $v = 1$	8–7	336 602.993	1820.6	2.031×10^{-3}	2.8 (0.3)	9 (1)	2 456 371.5
...	...	...	...	...	3.3 (0.3)	8 (1)	2 456 371.5
...	...	...	...	...	7.14 (0.11)	6 (1)	2 456 615.5
...	...	...	...	...	7.77 (0.13)	6 (1)	2 456 615.5
...	...	...	...	...	3.5 (0.3)	6 (1)	2 455 579.5
^{30}SiO $v = 2$	2–1	83 583.203	3485.0	2.676×10^{-5}	0.45 (0.02)	7 (7)	2 455 018.5
^{30}SiO $v = 2$	4–3	167 160.941	3499.1	2.379×10^{-4}	0.68 (0.01)	4 (3)	2 455 575.5
SiS $v = 1$	8–7	144 520.367	1102.4	5.034×10^{-5}	0.04 (0.01)	19 (5)	2 455 018.5
SiS $v = 1$	9–8	162 581.756	1110.2	7.215×10^{-5}	0.13 (0.01)	16 (4)	2 455 550.5
SiS $v = 1$	12–11	216 757.603	1138.8	1.733×10^{-4}	0.10 (0.03)	4 (3)	2 456 579.5
SiS $v = 1$	13–12	234 812.968	1150.1	2.209×10^{-4}	0.16 (0.03)	7 (3)	2 456 579.5
SiS $v = 1$	14–13	252 866.469	1162.2	2.766×10^{-4}	0.14 (0.03)	7 (3)	2 456 579.5
...	...	...	...	...	0.14 (0.02)	5 (2)	2 456 579.5
SiS $v = 1$	15–14	270 917.961	1175.2	3.410×10^{-4}	0.13 (0.04)	4 (3)	2 455 309.5
SiS $v = 1$	17–16	307 014.349	1203.8	4.982×10^{-4}	0.32 (0.06)	5 (2)	2 456 320.5
SiS $v = 1$	19–18	343 100.984	1235.9	6.974×10^{-4}	0.30 (0.05)	9 (2)	2 455 576.5
o-H_2O	$10_{2,9}$–$9_{3,6}$	321 225.640	1827.1	6.124×10^{-6}	1.0 (0.2)	5 (2)	2 455 574.5
o-H_2O $\nu_2 = 1$	$5_{5,0}$–$6_{4,3}$	232 686.700	3427.8	4.630×10^{-6}	0.18 (0.03)	4 (3)	2 456 579.5
o-H_2O $\nu_2 = 1$	$6_{6,1}$–$7_{5,2}$	293 664.442	3899.5	7.018×10^{-6}	0.48 (0.04)	5 (1)	2 456 320.5
...	...	...	...	...	0.26 (0.04)	4 (2)	2 456 371.5
...	...	...	...	...	0.22 (0.04)	8 (2)	2 456 615.5
p-H_2O $\nu_2 = 1$	$4_{4,0}$–$5_{3,3}$	96 259.644	3064.2	4.608×10^{-7}	0.10 (0.01)	7 (5)	2 455 019.5
p-H_2O $\nu_2 = 1$	$5_{5,1}$–$6_{4,2}$	209 118.370	3462.1	3.369×10^{-6}	0.21 (0.03)	7 (2)	2 456 372.5
...	...	...	...	...	0.06 (0.06)	8 (2)	2 456 579.5
p-H_2O $\nu_2 = 1$	$6_{6,0}$–$7_{5,3}$	297 439.107	3933.7	7.289×10^{-6}	0.12 (0.04)	5 (2)	2 456 320.5
...	...	...	...	...	0.17 (0.03)	7 (2)	2 456 371.5
...	...	...	...	...	0.08 (0.03)	5 (2)	2 456 615.5
o-H_2O $\nu_2 = 2$	$6_{5,2}$–$7_{4,3}$	268 149.175	6005.0	1.471×10^{-5}	2.38 (0.07)	2 (1)	2 455 309.5
...	...	...	...	...	0.12 (0.03)	7 (1)	2 456 579.5
p-H_2O $\nu_2 = 2$	$3_{3,1}$–$4_{2,2}$	137 048.521	5036.7	2.096×10^{-6}	0.03 (0.01)	8 (5)	2 455 019.5

Appendix B: Unidentified lines

Table B.1. Unidentified features and, in some cases, tentative line identification.

$\nu_{\rm rest}$ (MHz)	Tentative assignment –	$\int T_{\rm ant}^{*}\,{\rm d}v$ (K km s^{-1})	$v_{\rm exp}$ (km s^{-1})
81 166	–	0.08 (0.03)	16 (7)
83 825	SiO v = 5 J = 2–1	0.30 (0.03)	35 (5)
84 478	–	0.06 (0.02)	7 (7)
86 190	OH v = 1 J, Ω, p, F = 8/2,3/2,1,9–8/2,3/2,–1,9	0.71 (0.02)	7 (3)
87 385	–	0.23 (0.02)	17 (3)
108 892	–	0.09 (0.01)	11 (4)
128 883	TiO_2 $J_{K,k}$=$19_{10,10}$–$20_{9,11}$	0.10 (0.02)	13 (4)
131 195	SiN N, J, F = 3,7/2,7/2-2,5/2,7/2	0.05 (0.01)	7 (4)
136 946	–	0.15 (0.01)	27 (4)
139 065	–	0.05 (0.01)	13 (4)
143 997	–	0.05 (0.01)	7 (4)
145 101	$N^{17}O$ J = 3/2–1/2 hfs blend	0.11 (0.02)	18 (4)
149 968	–	0.12 (0.02)	18 (4)
150 165	–	0.13 (0.03)	20 (4)
158 409	$^{29}Si^{18}O$ J = 4–3	0.04 (0.01)	10 (4)
159 227	^{29}SiS v = 1 J = 9–8	0.08 (0.01)	13 (4)
159 607	–	0.08 (0.01)	4 (3)
161 197	–	0.06 (0.02)	8 (4)
165 641	$Na^{37}Cl$ J = 13–12	0.09 (0.01)	11 (4)
169 652	–	0.12 (0.02)	16 (3)
172 925	–	0.47 (0.04)	28 (3)
208 612	TiO_2 $J_{K,k}$ = $43_{10,34}$–$42_{11,31}$	0.09 (0.02)	3 (3)
209 295	–	0.22 (0.03)	17 (2)
216 602	^{13}CN J = 2–1 hfs blend	0.26 (0.03)	8 (2)
218 065	–	0.41 (0.02)	3 (3)
218 575	–	0.43 (0.03)	24 (2)
219 840	$^{34}SO_2$ $J_{K,k}$ = $6_{4,2}$–$7_{3,5}$	0.35 (0.04)	3 (2)
221 614	–	0.48 (0.04)	18 (2)
223 370	$SO^{18}O$ $J_{K,k}$ = $6_{4,2}$–$7_{3,5}$	0.35 (0.05)	22 (3)
224 876	–	1.98 (0.06)	17 (2)
250 807	–	0.15 (0.02)	8 (3)
252 256	–	0.20 (0.02)	19 (3)
252 531	–	0.45 (0.04)	15 (3)
254 677	–	0.34 (0.03)	25 (3)
263 452	–	0.12 (0.03)	4 (2)
271 968	–	0.44 (0.05)	7 (2)
306 192	AlO N, J, F = 8,15/2,8–7,15/2,7	0.64 (0.08)	22 (2)

Notes. Column 3: integrated intensity (in antenna temperature) of the line with its formal uncertainty; Col. 4: expansion velocity derived from the linewidth with its uncertainty which includes the width of half a channel (1 MHz) except for the lines with a low S/N where a full channel (2 MHz) is included. The uncertainties given (within parentheses) do not include additional uncertainties derived from the absolute flux calibration and baseline subtraction.

A&A 597, A25 (2017)

Table B.2. Artifacts identified in the spectra between 167 475–174 800 MHz.

$\nu_{\rm rest}$ (MHz)	$\int T_{\rm ant}^{*}\,{\rm d}v$ (K km s^{-1})	$v_{\rm exp}$ (km s^{-1})
168 422	0.007 (0.002)	9 (1)
169 104	0.008 (0.002)	23 (2)
169 729	0.012 (0.002)	6.1 (0.9)
170 407	0.008 (0.002)	4.0 (0.9)
171 000	0.005 (0.002)	22.8 (0.6)
171 145	0.037 (0.002)	10.9 (0.7)
171 174	0.010 (0.002)	20 (1)
171 393	0.032 (0.002)	26.0 (0.4)
171 591	0.009 (0.002)	13 (2)
171 638	0.044 (0.003)	17.8 (0.8)
171 758	0.016 (0.003)	23 (2)
171 874	0.013 (0.003)	4.6 (0.4)
172 605	0.063 (0.004)	8.13 (0.08)
172 725	0.049 (0.003)	3.9 (0.2)
172 799	0.010 (0.003)	21 (1)
173 242	0.015 (0.003)	3 (31)
173 444	0.048 (0.004)	24.9 (0.7)
173 562	0.122 (0.004)	18.7 (0.3)
173 812	0.135 (0.006)	18.8 (0.3)
173 933	0.051 (0.005)	22 (1)
174 267	0.014 (0.004)	7 (2)

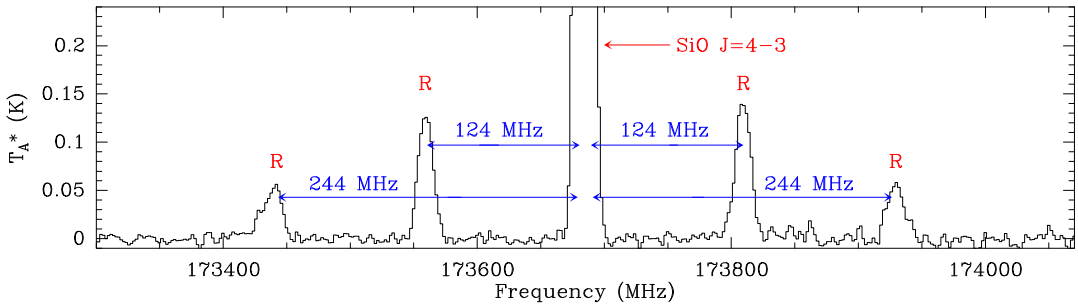

Fig. B.1. Example of the artifacts (*R*) produced by the receivers (see Table B.2). Several symmetrical spurious replicas of the real SiO J = 4–3 line appear at both sides of it (equidistant). The intensities of the replicas decrease with the frequency distance to the real feature.

Appendix C: IRAM-30 m survey of IK Tau

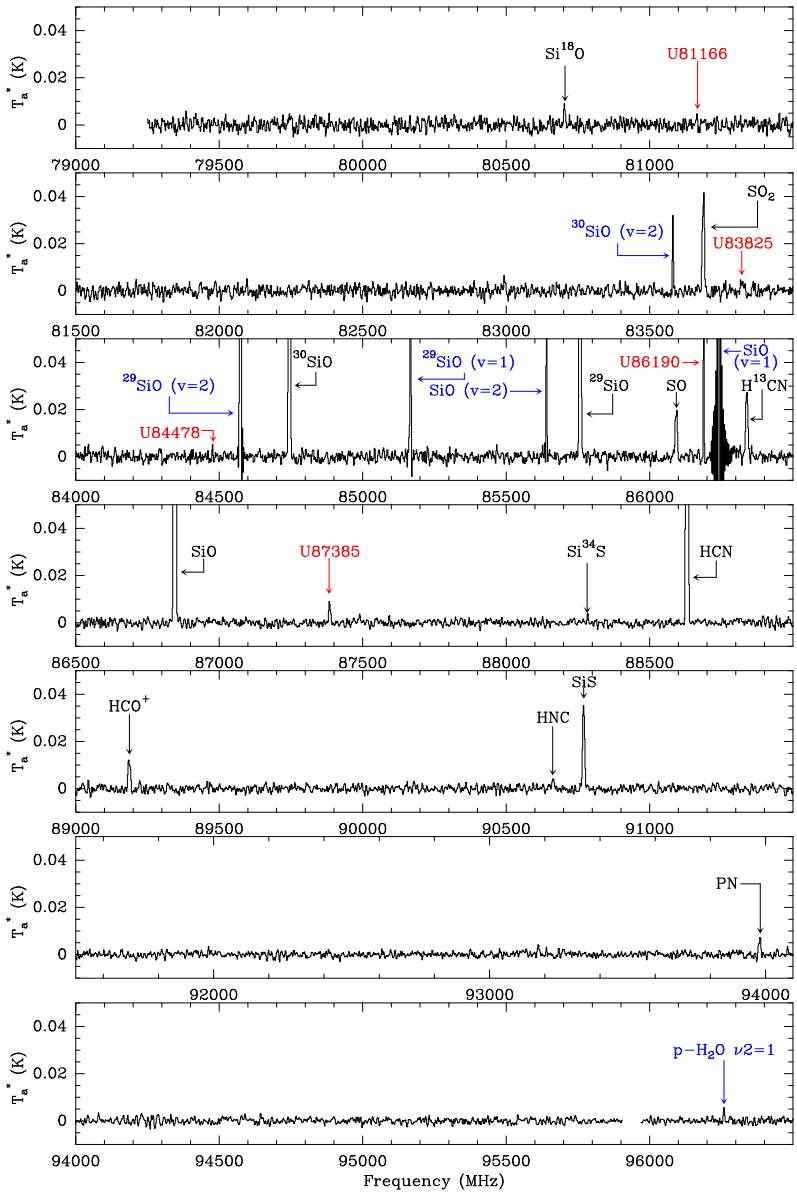

Fig. C.1. Line identification of the IRAM-30 m line survey of IK Tau. We marked in red the unidentified lines (UIs) with the central frequency of the line. The lines which display time variability of their intensity are marked in blue. Image band and spurious feaures/artifacts have been blanked off (see Table B.2 and Fig. B.1)

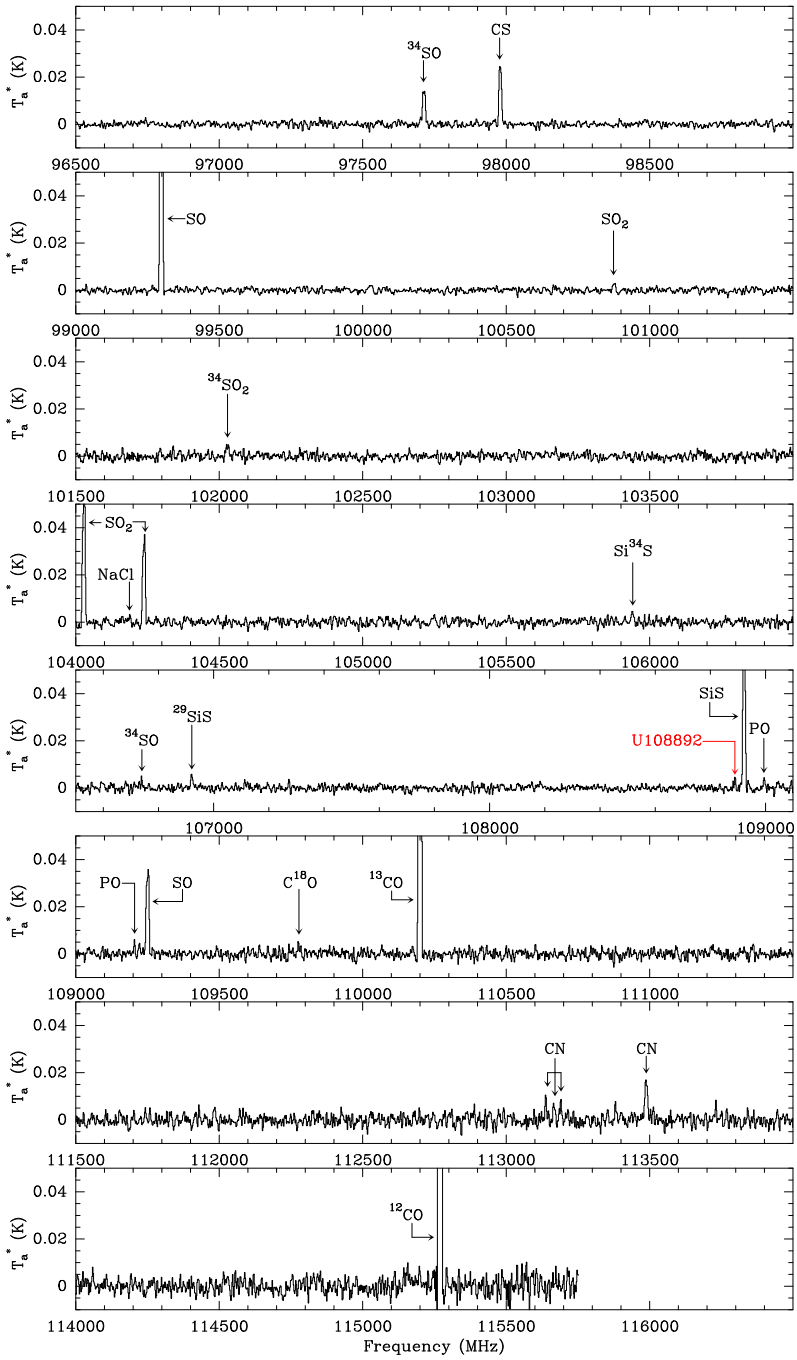

Fig. C.1. continued.

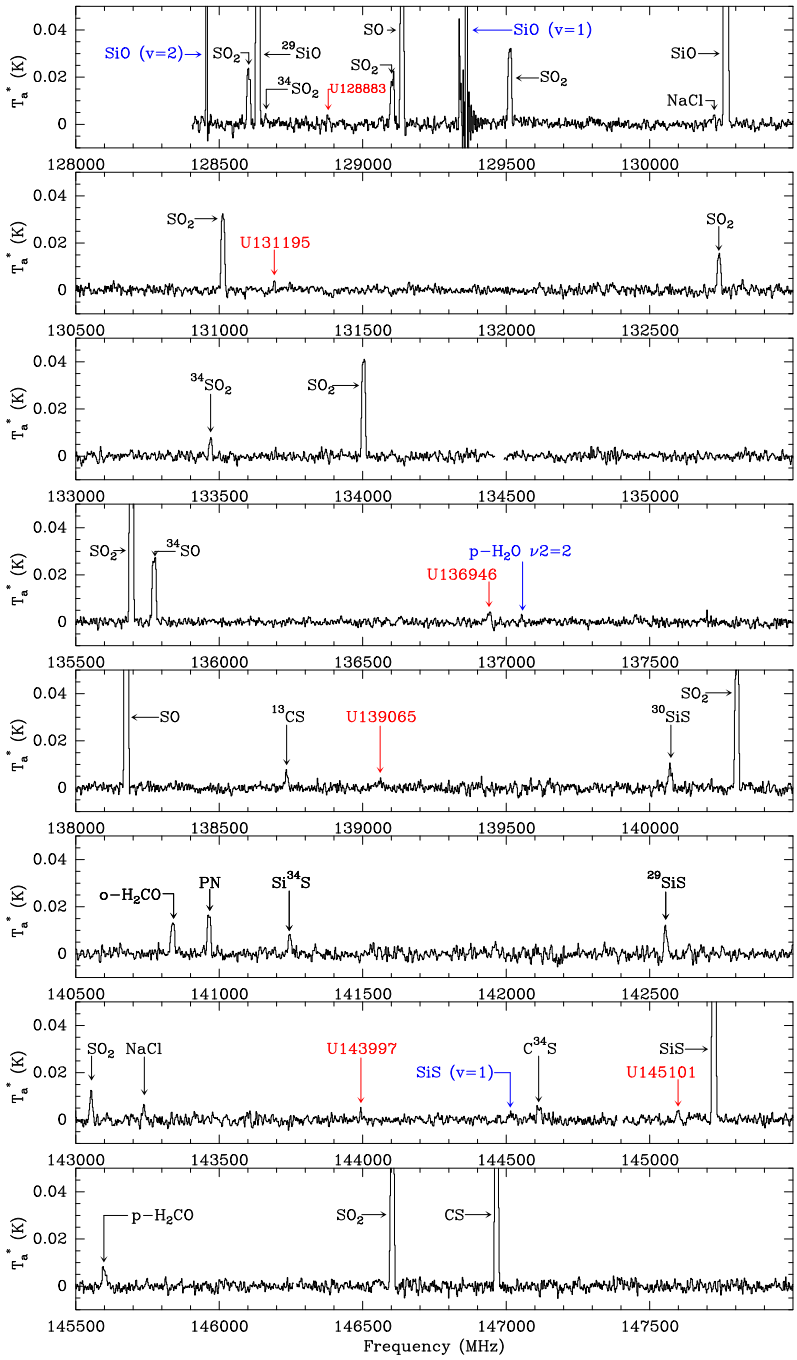

Fig. C.1. continued.

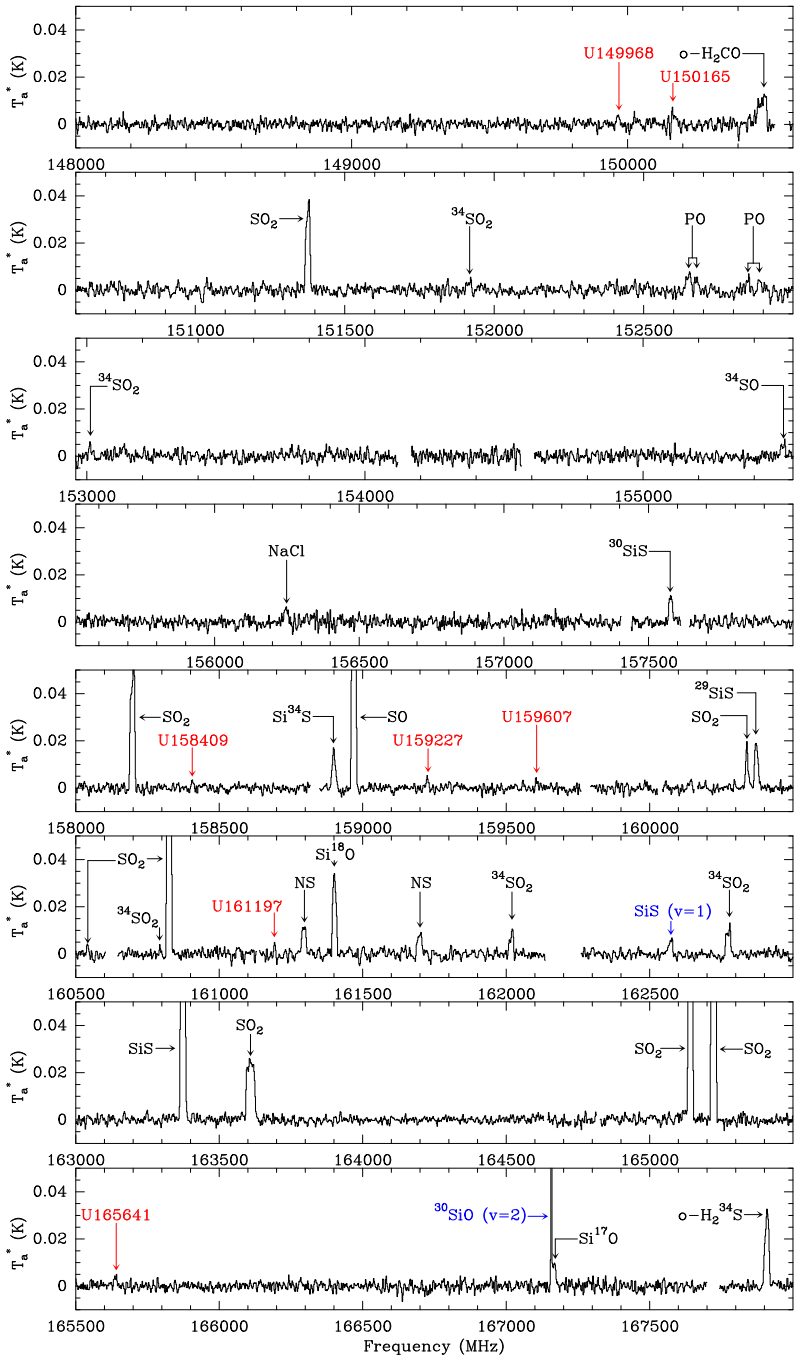

Fig. C.1. continued.

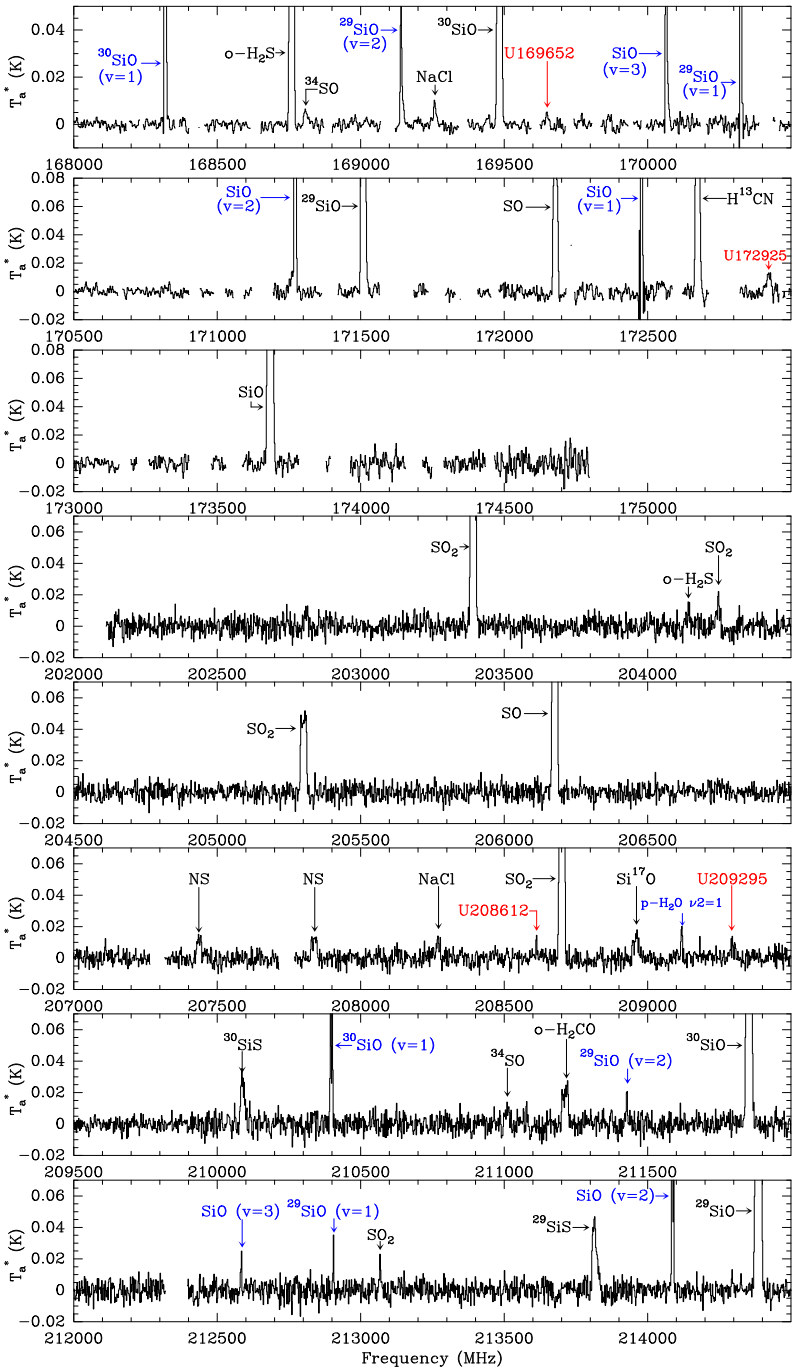

Fig. C.1. continued.

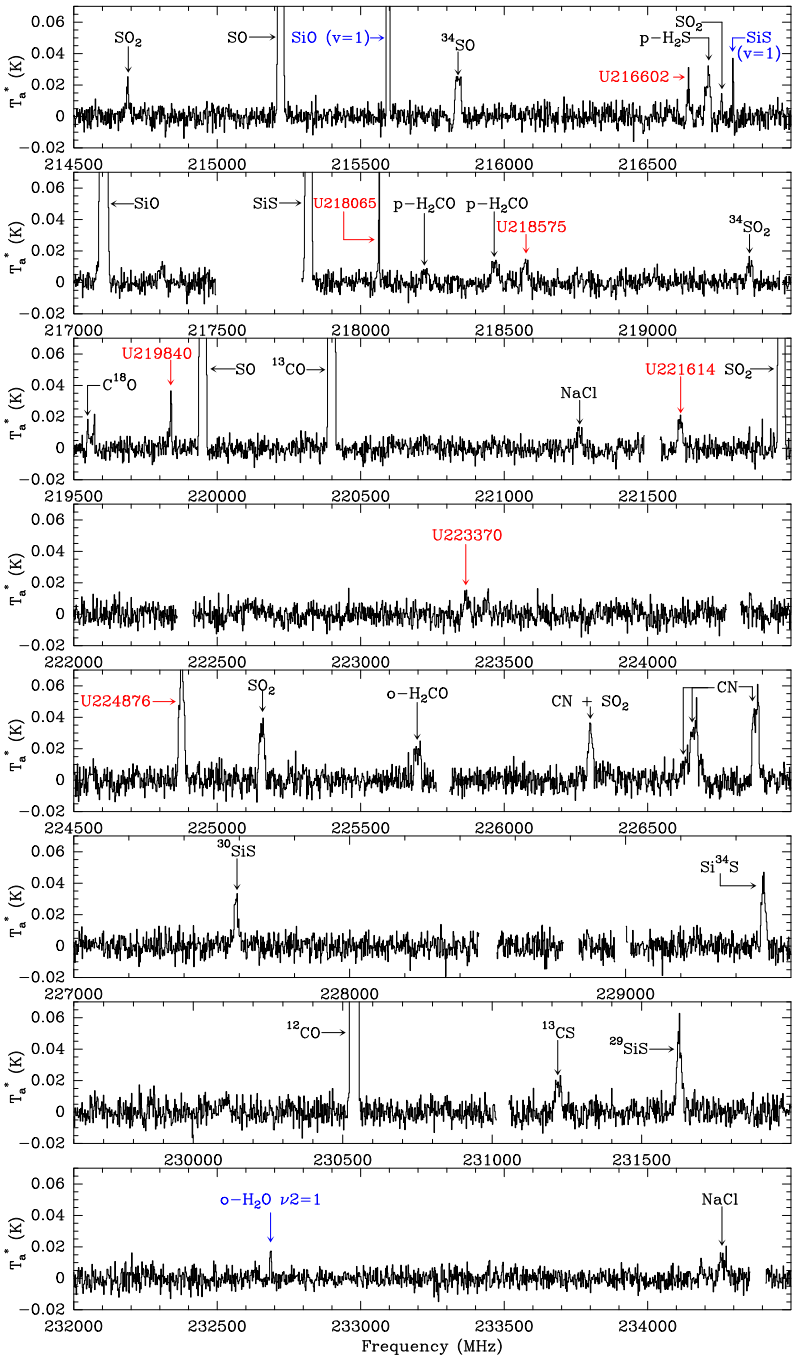

Fig. C.1. continued.

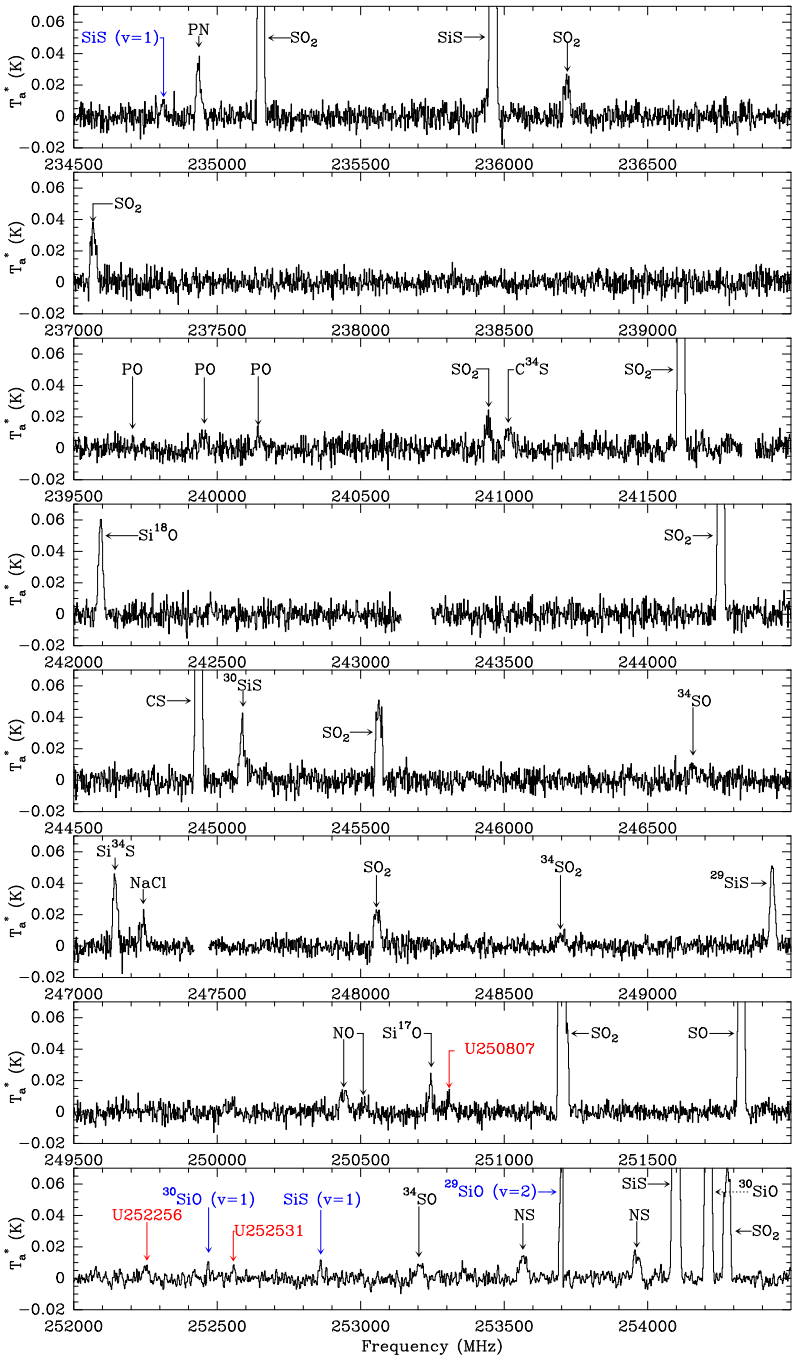

Fig. C.1. continued.

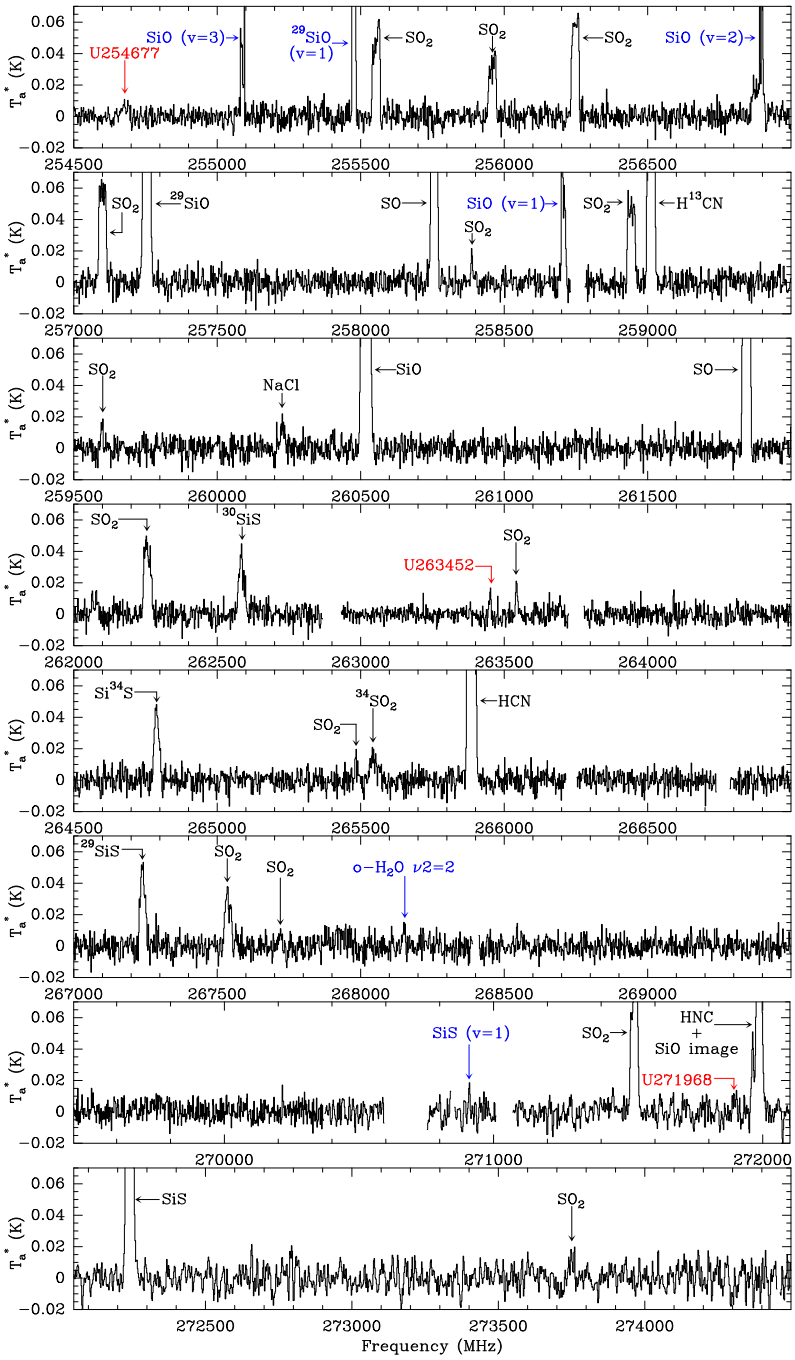

Fig. C.1. continued.

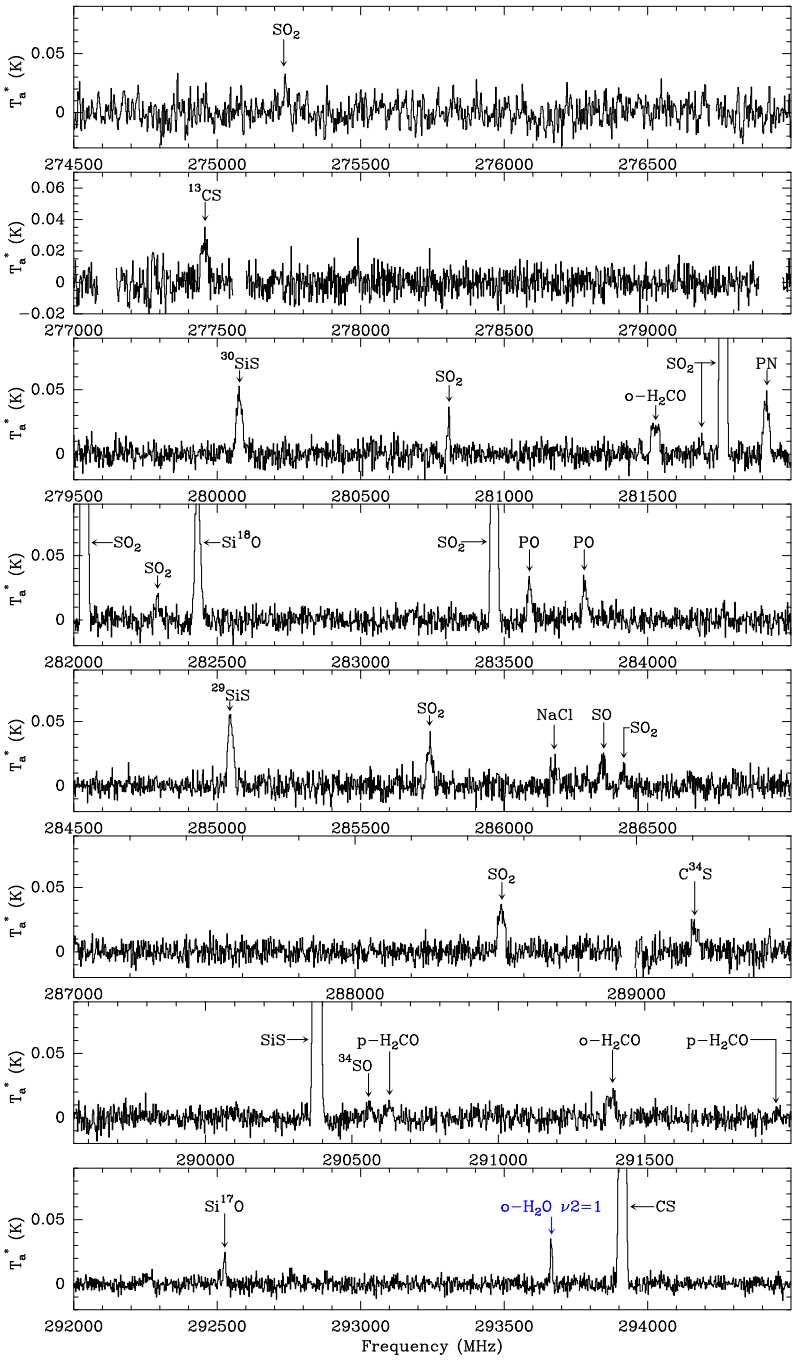

Fig. C.1. continued.

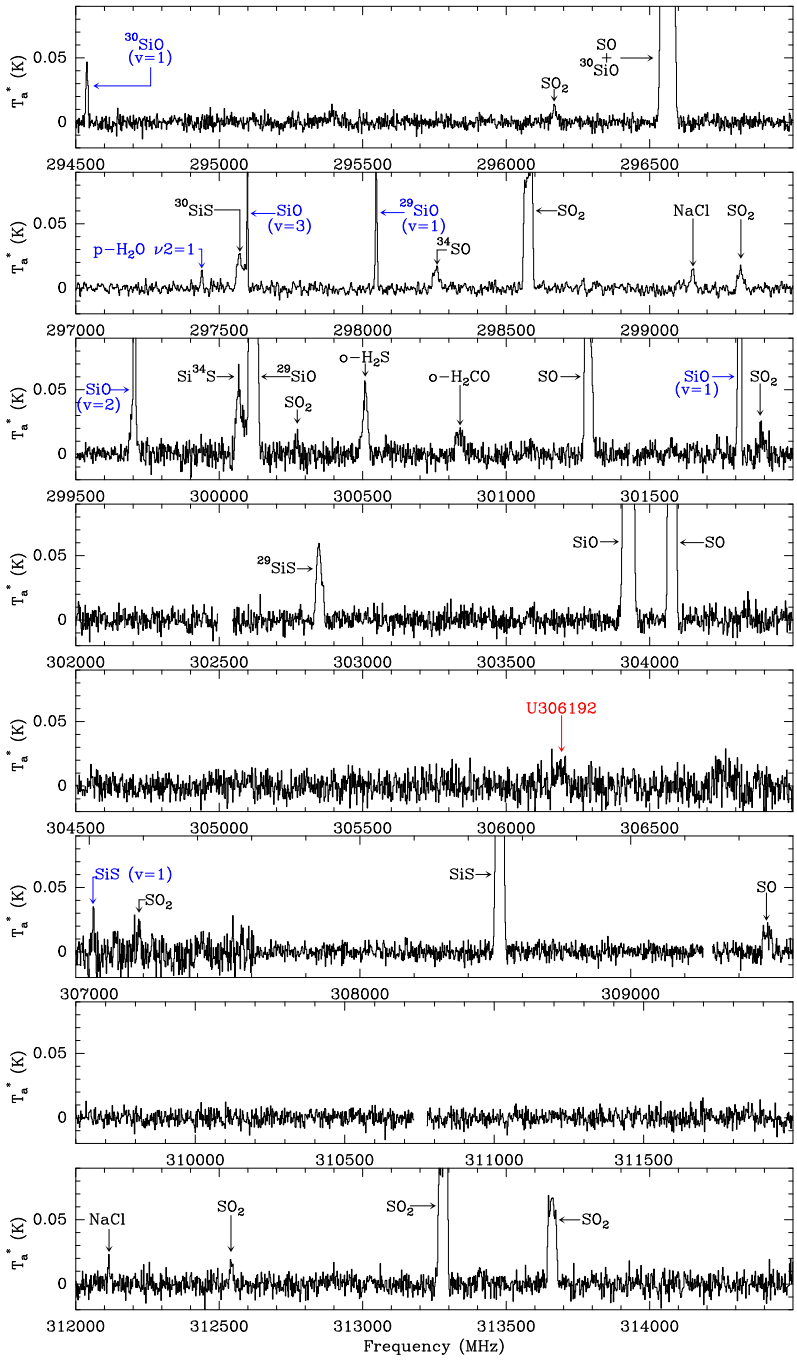

Fig. C.1. continued.

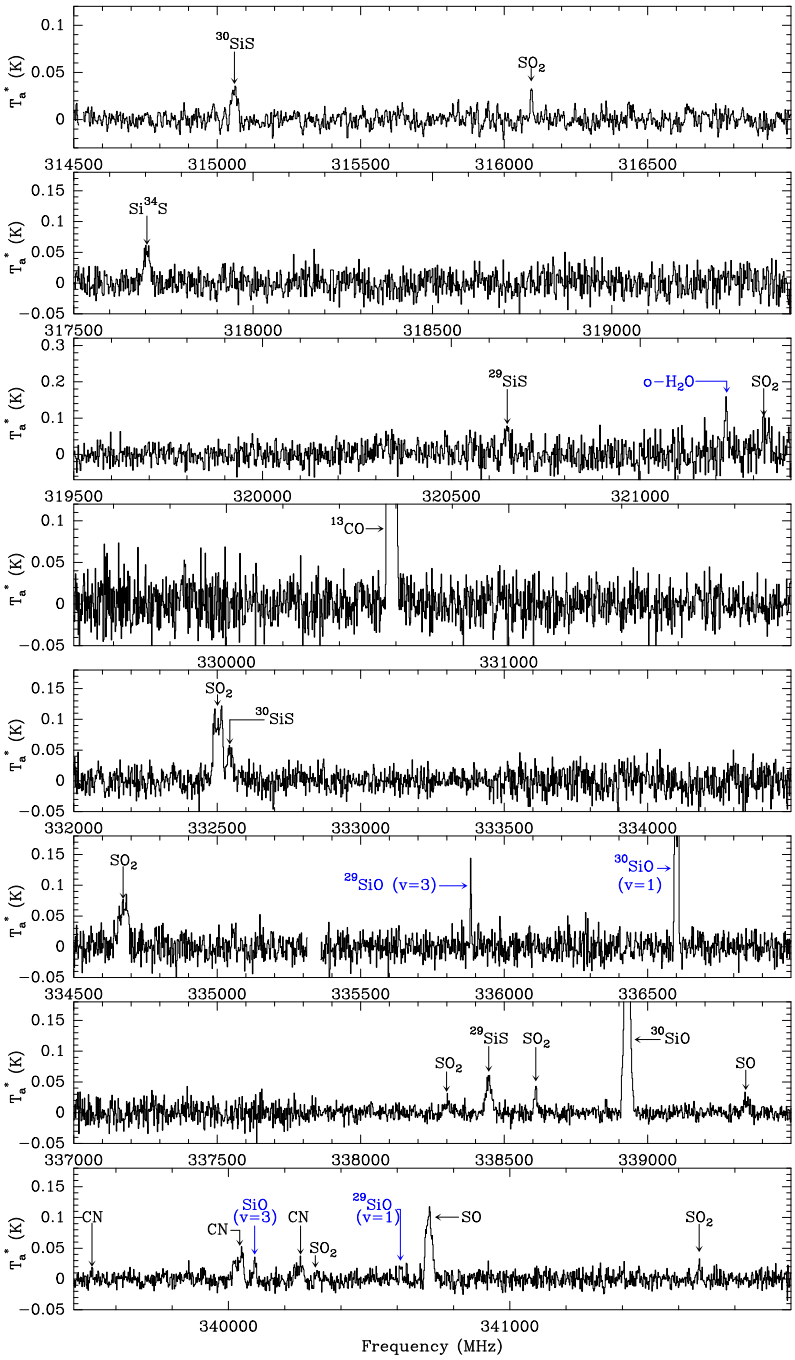

Fig. C.1. continued.

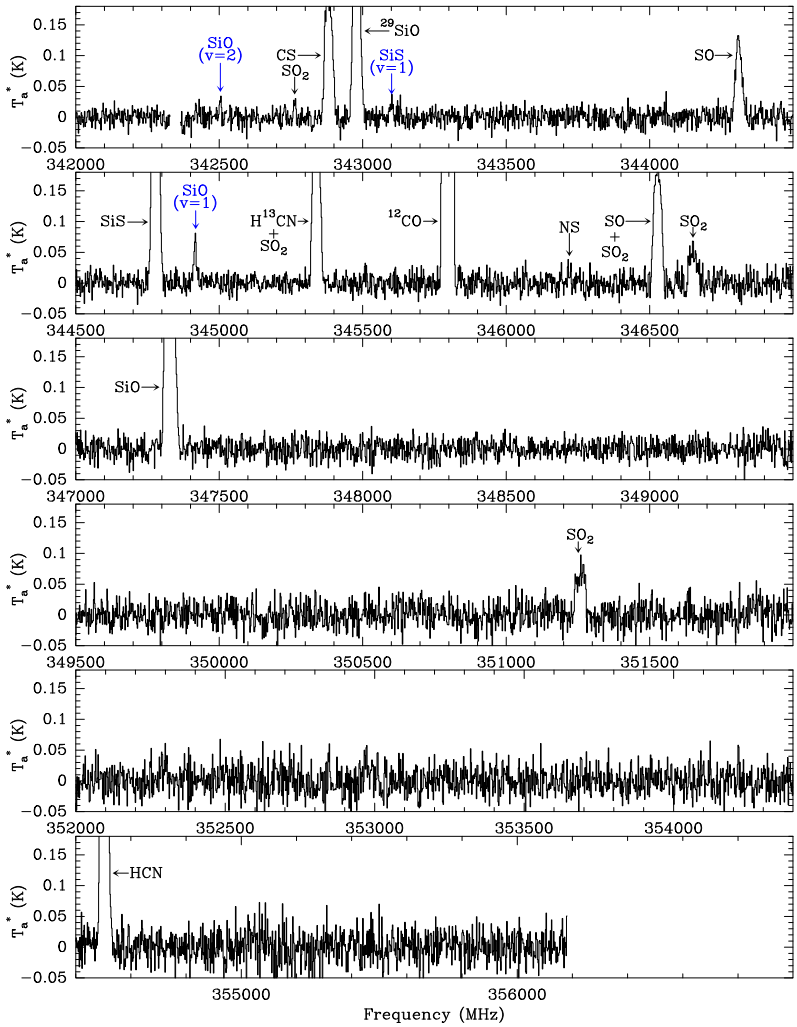

Fig. C.1. continued.

Appendix D: Population diagrams

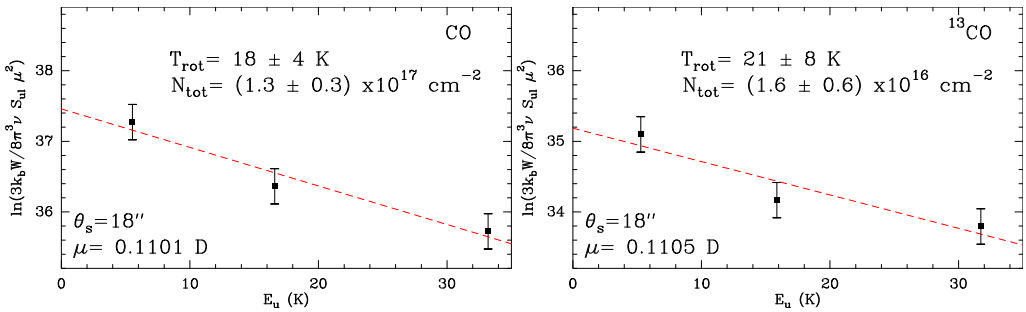

Fig. D.1. Population diagrams for CO and ^{13}CO. The results from the fit (red dashed line) are shown in each box. The emission size adopted and the dipole moment of the molecule are shown in the bottom-left corner of each box. Error bars include the formal uncertainty of the measurement and a 25% uncertainty due to flux calibration or poor baseline substraction.

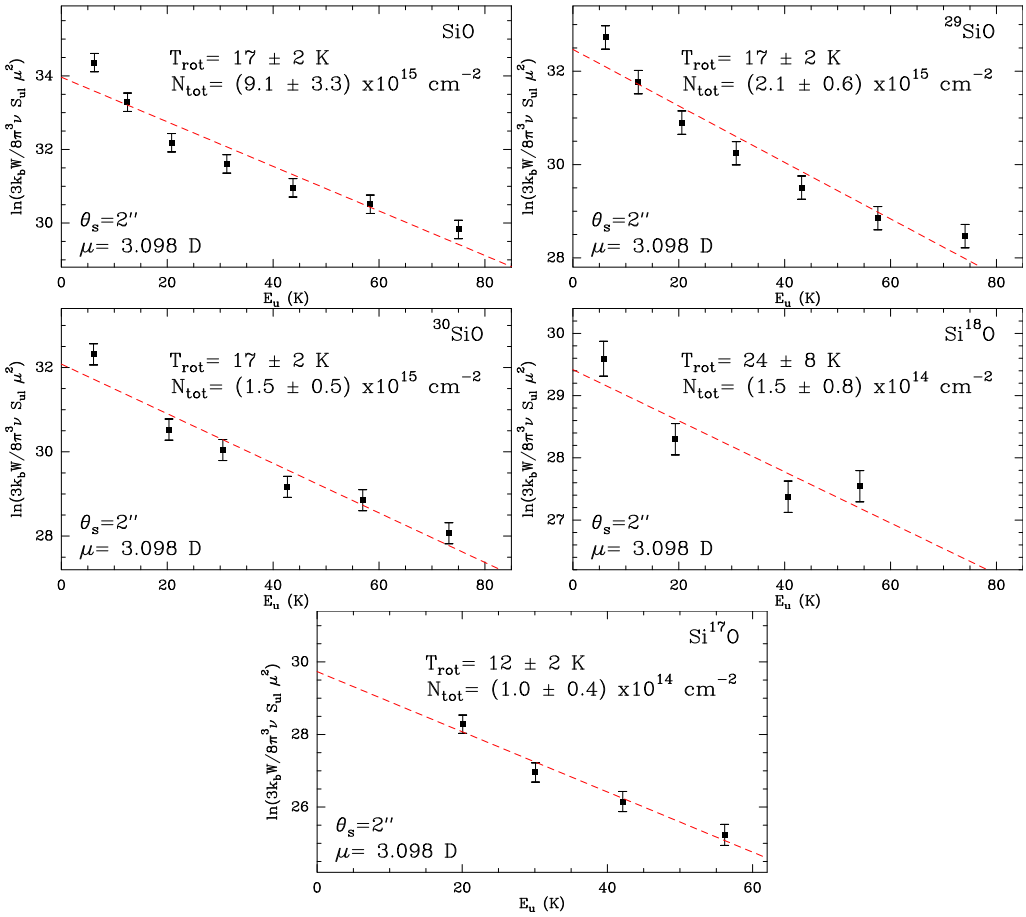

Fig. D.2. As in Fig. D.1 but for SiO isotopologues.

A&A 597, A25 (2017)

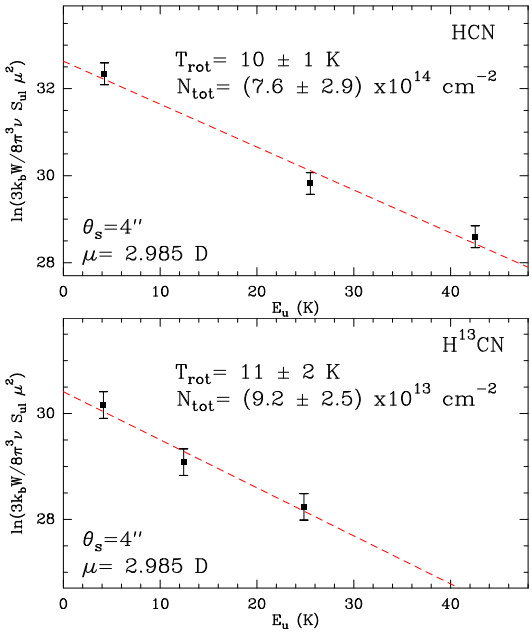

Fig. D.3. As in Fig. D.1 but for HCN isotopologues.

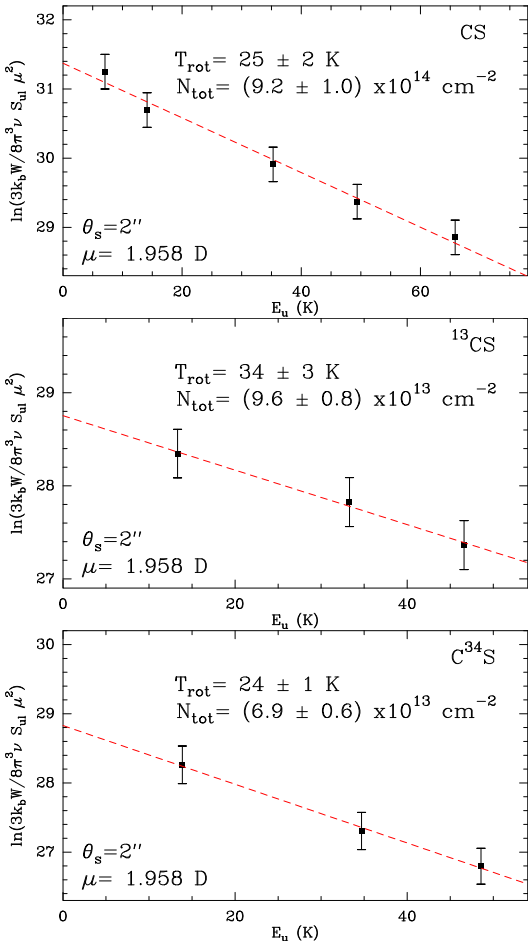

Fig. D.4. As in Fig. D.1 but for CS isotopologues.

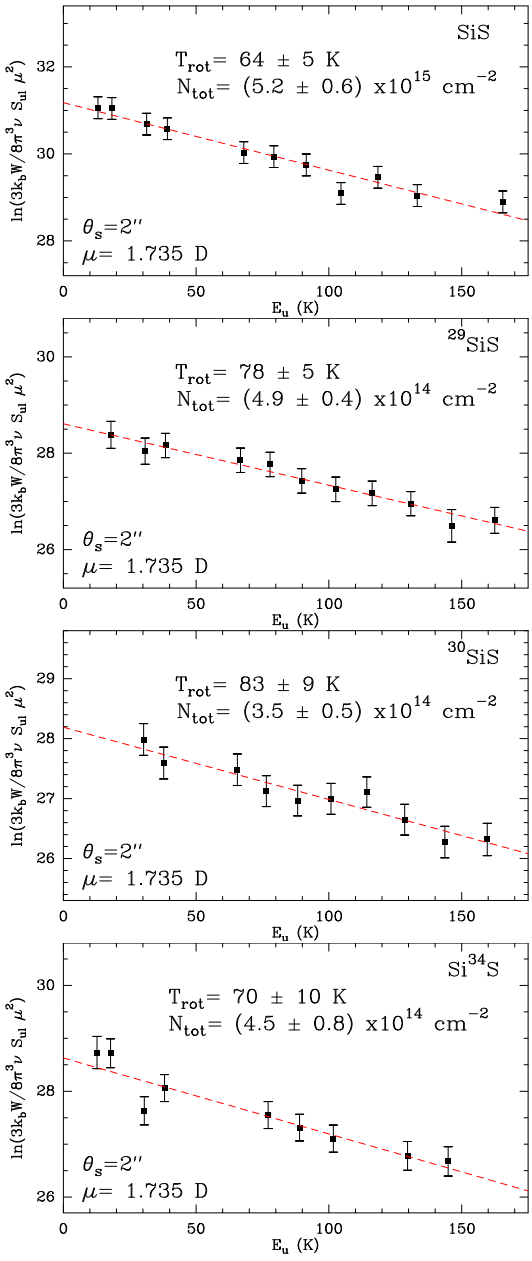

Fig. D.5. As in Fig. D.1 but for SiS isotopologues.

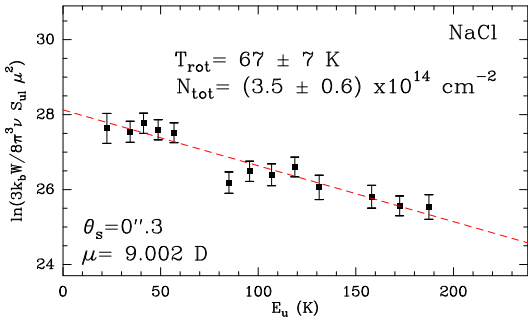

Fig. D.6. As in Fig. D.1 but for NaCl.

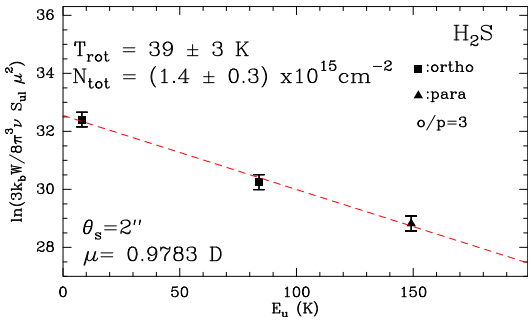

Fig. D.7. As in Fig. D.1 but for H_2S. We fitted simultaneously the ortho and para species adopting an ortho-to-para ratio of 3:1 (Decin et al. 2010a). The line o-H_2S $J, K_a, k = 4_{1,4}$–$3_{2,1}$ significantly outlies the fit probably owing to its low S/N, therefore, it has been excluded from the diagram.

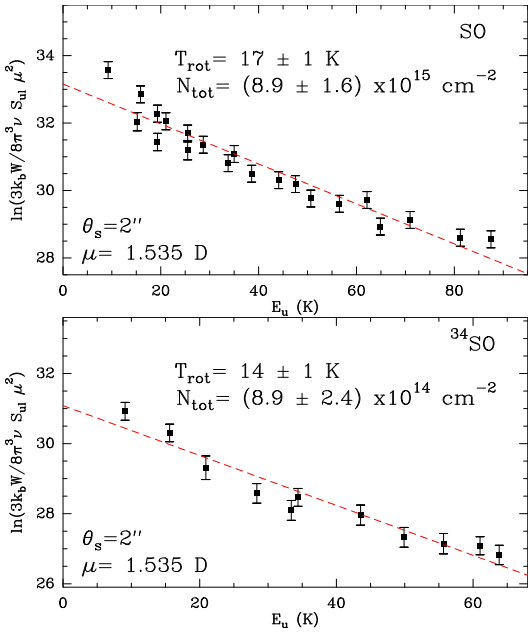

Fig. D.8. As in Fig. D.1 but for SO isotopologues.

A&A 597, A25 (2017)

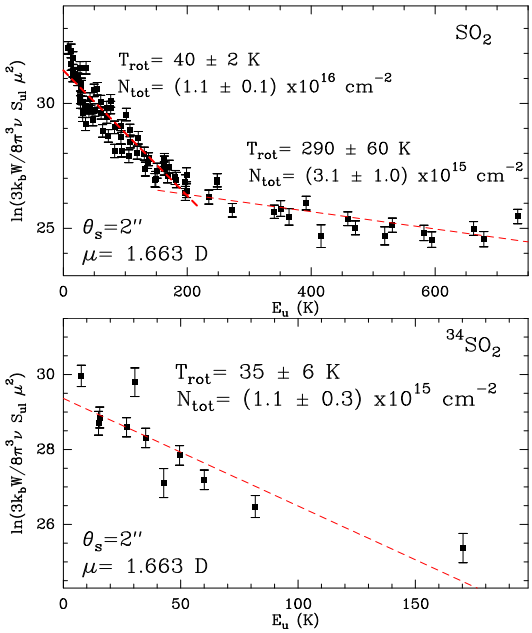

Fig. D.9. As in Fig. D.1 but for SO_2 isotopologues. The rotational diagram of SO_2 was separated in two different trends (see Sect. 5.2).

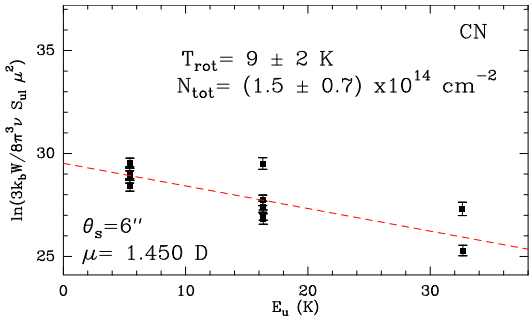

Fig. D.10. As in Fig. D.1 but for CN.

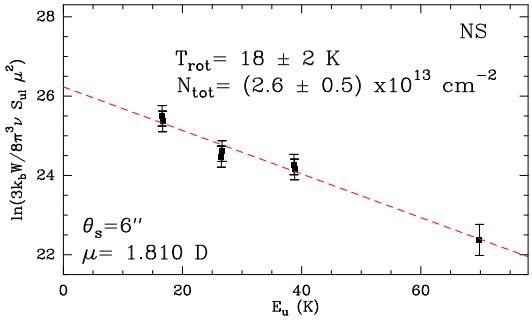

Fig. D.11. As in Fig. D.1 but for NS.

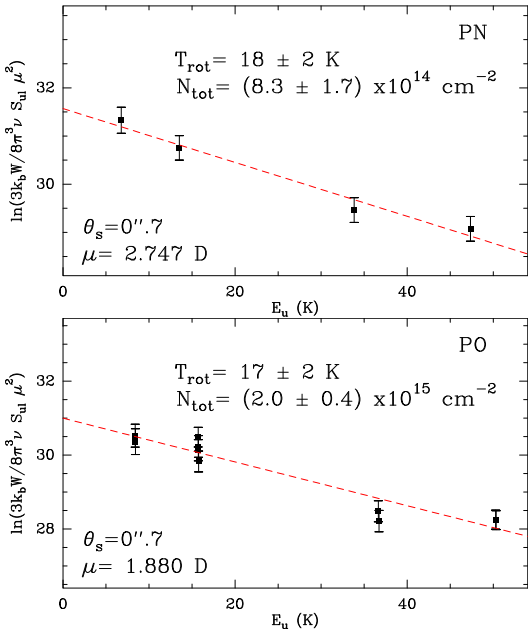

Fig. D.12. As in Fig. D.1 but for P-bearing molecules. The PO line $\Omega = 1/2$, e, $J, F = (11/2, 5)$–$(9/2, 5)$ significantly outlies the fit probably owing to its low S/N, therefore, it has been excluded from the diagram.

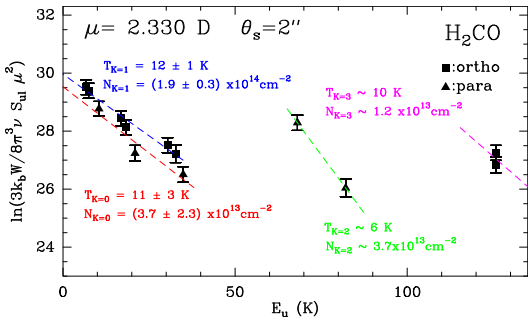

Fig. D.13. Population diagram for H_2CO. We show the results from the fits of the rotational ladders $K_a = 0$ (red), $K_a = 1$ (blue), and $K_a = 2$ (green). For the $K_a = 3$ (pink) we adopted as rotational temperature the average of the rotational temperatures of the $K_a = 0$, 1, and 2 ladders to estimate a rough value for the $K_a = 3$ column density.

Appendix E: SO_2 IOS calculations

Close coupling (CC) calculations based on a state-of-the-art potential-energy surface (PES) (Spielfiedel et al. 2009) have provided collisional para- and ortho-H_2 rate coefficients for temperatures ranging from 5 to 30 K for the 31 lowest SO_2 rotational levels (Cernicharo et al. 2011). However, an extension of these full CC calculations to a large number of SO_2 rotational levels and high temperatures would be prohibitive in terms of memory and CPU time, so the use of different approximate methods (coupled states (CS) and infinite order sudden (IOS)) is needed (Green 1976, 1979). Considering the high-J SO_2 levels observed in the present work, we used the IOS approximation which is expected to give reliable estimates of rate coefficients, except for low energies. State-to-state de-excitation rate coefficients between the 410 lowest levels (with energy up to 743.9 K) were calculated for energies up to 9000 cm^{-1} (value limited by the validity domain of the PES) giving data for temperatures up to 1000 K Balança et al. (in prep.). The SO_2 energy levels and wave functions were obtained from spectroscopic constants describing the SO_2 Hamiltonian up to the fourth order and provided by the MADEX code (Cernicharo 2012). The results show a relatively flat temperature variation of the rates.

The accuracy of these data was studied by comparing the resulting rate coefficients with CC and CS values obtained for collisions with para and ortho-H_2 and all transitions involving the 31 lowest levels. Compared to CC and CS data, it is found that the IOS approach leads a systematic underestimation of para-H_2 rates, within a factor better than 50% in average, the agreement being better at high temperatures. However, the situation is not as good for collisions with ortho-H_2 as the IOS approximation describes collisions with para-H_2 (j_{H_2} = 0) and does take into account all the angular couplings involved in collisions with ortho-H_2. The comparison between ortho- and para-H_2 CS rate coefficients shows that ortho-H_2 rates are systematically larger than para-H_2 rates by a factor two in average, with larger differences (up to a factor eight) for a number of transitions mainly identified as $\Delta K_a = 1$ transitions.

Table E.1. Parameters of the energy levels used for SO_2 modelling.

Identifier	J	K_a	K_c	E	g
–	–	–	–	K	–
1	0	0	0	0.000000	1
2	2	0	2	2.751006	5
3	1	1	1	3.339254	3
4	2	1	1	5.320091	5
5	3	1	3	7.743834	7
6	4	0	4	9.151093	9
...					

Notes. Table E.1, available at the CDS, contains the following information: Col. 1: identifier for the energy level used in Table E.2; Col. 2: quantum number J; Col. 3: quantum number K_a; Col. 4: quantum number K_c; Col. 5: energy of the level in Kelvin; Col. 6: degeneracy of the level.

The rate coefficients were implemented in MADEX fitting the logarithm of the rate coefficients to a sixth order polynomial as:

$$P(x) = \sum_{i=0}^{6} a_i x^i, \tag{E.1}$$

where

$$x = T^{3/2}, \tag{E.2}$$

which reproduces practically all the rates with a relative error below 30% for temperatures between 20 and 1000 K, 410 energy levels and a maximum E_u = 744 K. We provide the energy levels involved in the calculations in Table E.1, as well as the polynomial coefficients of the fit in Table E.2. The level identifier used in Table E.2 can be consulted in Table E.1 to find the corresponding level.

A&A 597, A25 (2017)

Table E.2. Polynomial coefficients of the fit to the rate coefficients.

Upper level id	Lower level id	a_0	a_1	a_2	a_3	a_4	a_5	a_6
–	–	–	–	–	–	–	–	–
2	1	−9.48415	−29.3454	350.453	−2071.21	6590.82	−11012.6	7610.91
3	1	−9.58292	−35.9159	406.891	−2385.77	7513.84	−12378.6	8410.64
3	2	−9.99698	−14.3352	120.467	−442.266	635.155	52.7172	−657.401
4	1	0.00000	0.00000	0.00000	0.00000	0.00000	0.00000	0.00000
4	2	−9.53669	−26.9597	289.292	−1598.36	4761.52	−7413.75	4772.86
4	3	−9.09926	−29.6351	346.972	−2025.33	6401.05	−10614.5	7267.38
...								

Notes. Table E.2, available at the CDS, contains the following information: Col. 1: identifier for the upper energy level described in Table E.1; Col. 2: identifier for the lower energy level described in Table E.1; Cols. 3–9: coefficients of the 6th order polynomial fit to the rate coefficients.

Table E.2: Polynomial coefficients of the fit to the rate coefficients.

Upper level id	Lower level id	a_0	a_1	a_2	a_3	a_4	a_5	a_6
-	-	-	-	-	-	-	-	-
2	1	-9.48415	-29.3454	350.453	-2071.21	6590.82	-11012.6	7610.91
3	1	-9.58292	-35.9159	406.891	-2385.77	7513.84	-12378.6	8410.64
3	2	-9.99698	-14.3352	120.467	-442.266	635.155	52.7172	-657.401
4	1	0.00000	0.00000	0.00000	0.00000	0.00000	0.00000	0.00000
4	2	-9.53669	-26.9597	289.292	-1598.36	4761.52	-7413.75	4772.86
4	3	-9.09926	-29.6351	346.972	-2025.33	6401.05	-10614.5	7267.38
...								

Notes. Table E.2, available at the CDS, contains the following information: (Col. 1) identifier for the upper energy level described in Table E.1; (Col. 2) identifier for the lower energy level described in Table E.1; (Col. 3) to (Col. 9) coefficients of the 6th order polynomial fit to the rate coefficients.

3.4 Velilla Prieto et al. in prep: OH231 survey

In this section we present the overall results from the IRAM-30 m spectral line survey of OH231, which complements the detailed studies of particularly relevant species presented in Chapters 4 and 5. These results have been obtained analogously to the work done in IKTau, in terms of observations, line identification (Sect. 3.4.1), line parameters determination (Sect. 3.4.2), and analysis methods (Sect. 3.4.3) as described at the beginning of this Chapter (see also e.g. Velilla Prieto et al., 2015a).

The rotational diagrams have been calculated by using the main beam corrected integrated intensities of the lines and the formalism described in Section 2.1. We assumed a uniform elliptical source with major and minor axes $\theta_{\rm a}$ and $\theta_{\rm b}$. In this case, the beam-filling factor is given by (see e.g. Kramer, 1997):

$$\delta = 1 - e^{-\ln 2 \frac{\theta_{\rm a} \times \theta_{\rm b}}{HPBW^2}} \tag{3.1}$$

where $HPBW$ is the half power beam width of an elliptical Gaussian beam. Based on previous maps of CO and other molecules, we adopt an angular source size of $\theta_{\rm a} \times \theta_{\rm b}$=12″×4″ for all the species.

The results obtained from the rotational diagrams of the species in OH231 are summarised in Table 3.2 with an estimation of the source-averaged fractional abundance (relative to H_2) calculated as:

$$\frac{f(m)}{f(^{13}CO)} = \frac{N_{\rm tot}(m)}{N_{\rm tot}(^{13}CO)}, \tag{3.2}$$

where m represents the name of the analysed molecule, f is the fractional abundance of the species relative to H_2, and $N_{\rm tot}$ the total column density. As a reference, we have used the fractional abundance of ^{13}CO, for which we adopt $f(^{13}{\rm CO})=5\times10^{-5}$ as calculated by Morris et al. (1987a). The ^{13}CO abundance adopted is in the high end of the typical range of values for O-rich stars; in the case of OH 231.8+4.2, it reflects the particularly low $^{12}{\rm C}/^{13}{\rm C}$ isotopic ratio, ∼5-10, measured in this object (and other O-rich CSEs; Sánchez Contreras et al., 2000, Teyssier et al., 2006, Milam et al., 2009, Ramstedt & Olofsson, 2014, and references therein).

We also present the isotopic ratios in Table 3.3, which have been derived by dividing the corresponding fractional abundances.

3.4.1 Line identification

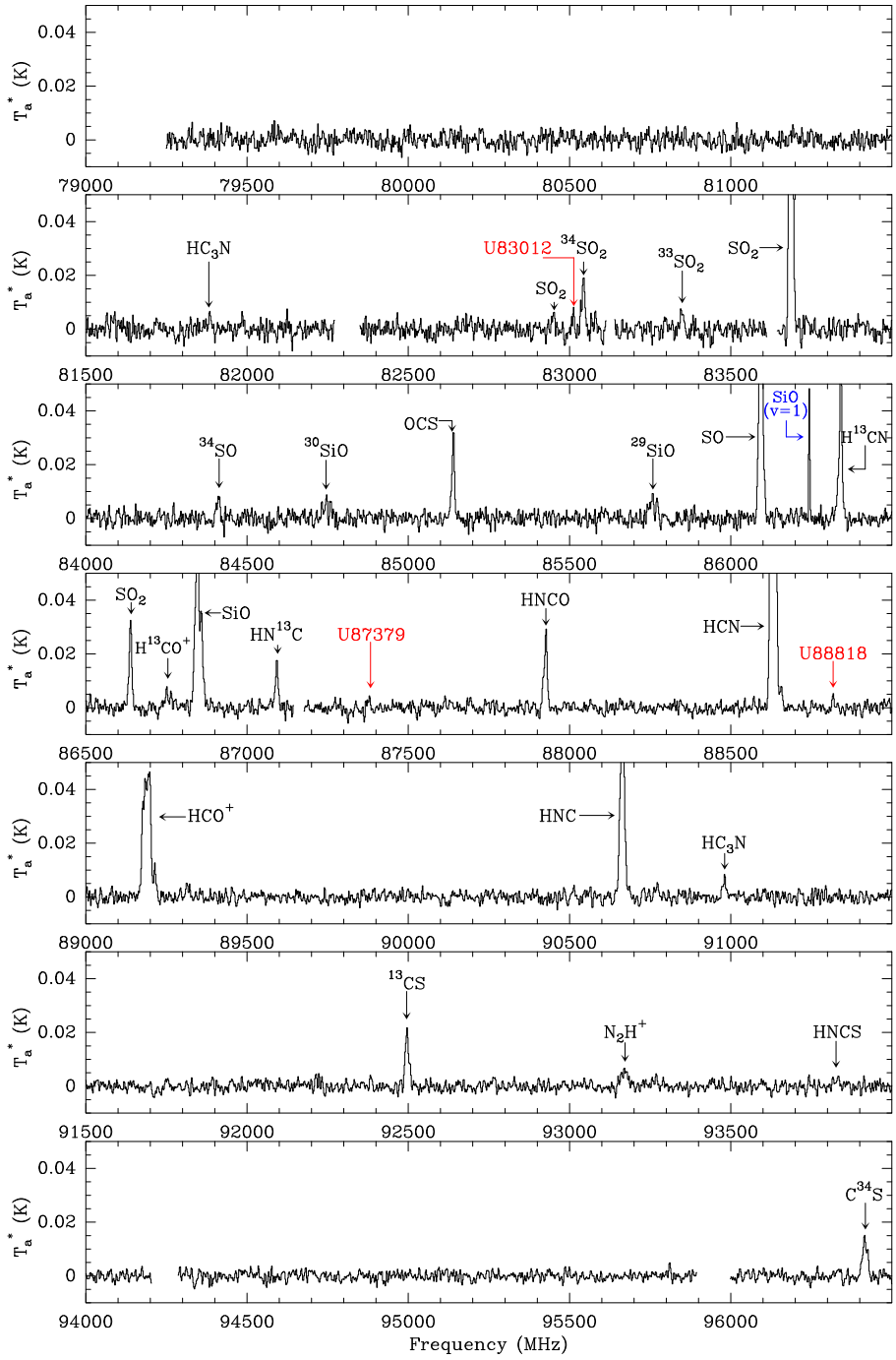

Figure 3.1: Line identification of the IRAM-30 m line survey of OH231.8+4.2. We marked in red the unidentified lines (UIs) with the central frequency of the line. The lines that may display time variability of their intensity are marked in blue. Image band and spurious features/artifacts have been blanked off.

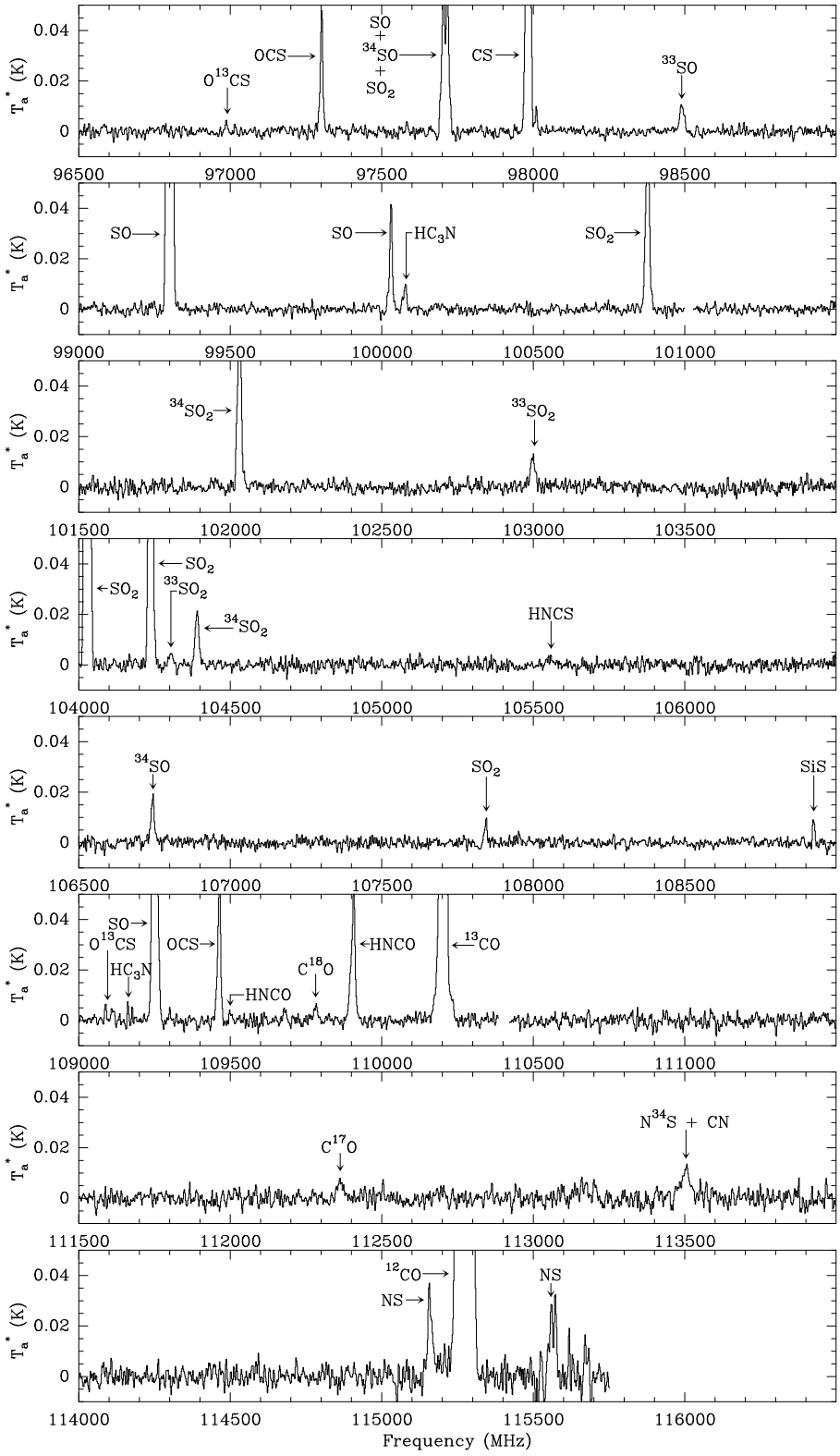

Figure 3.1: (Continued)

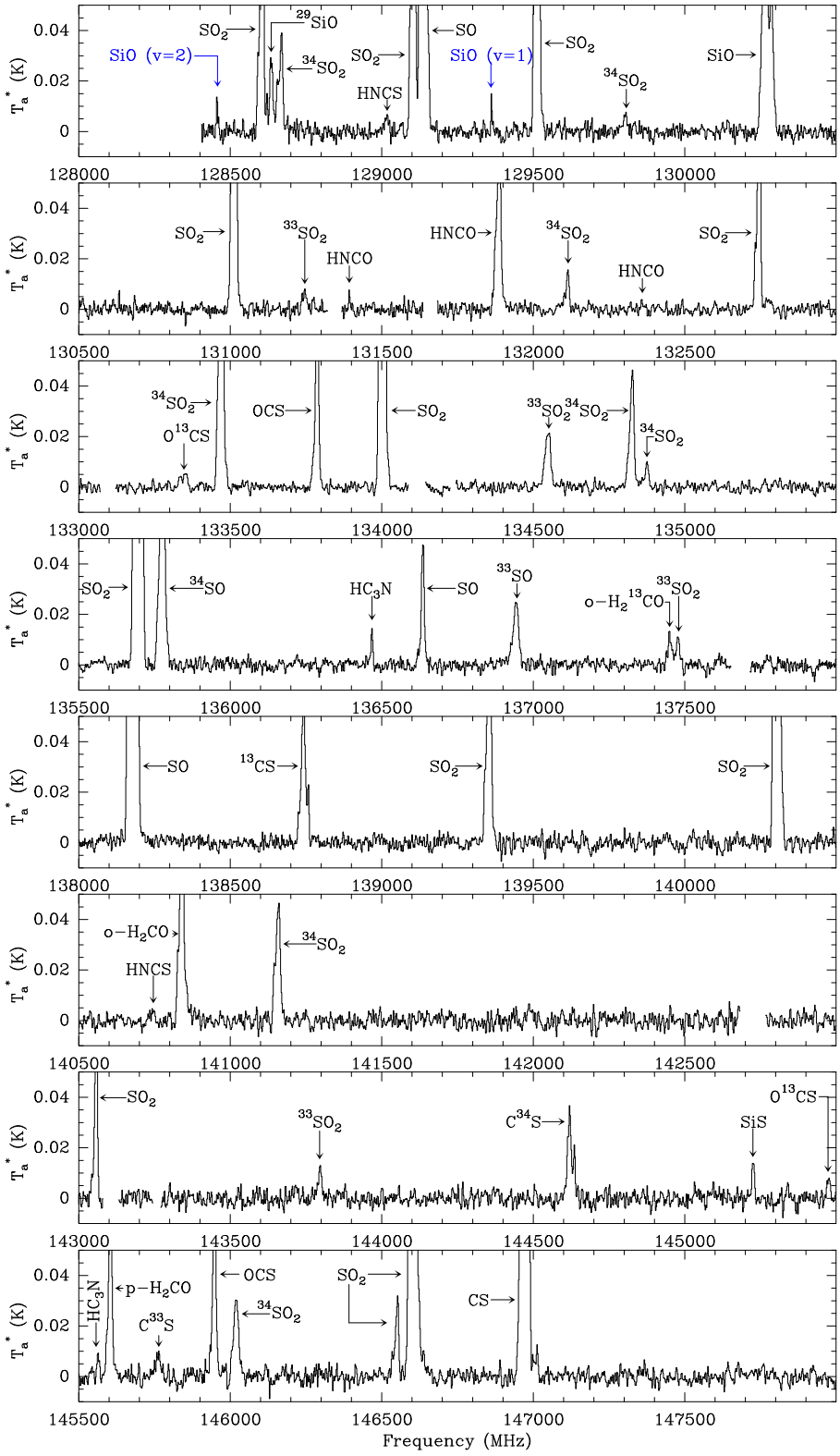

Figure 3.1: (Continued)

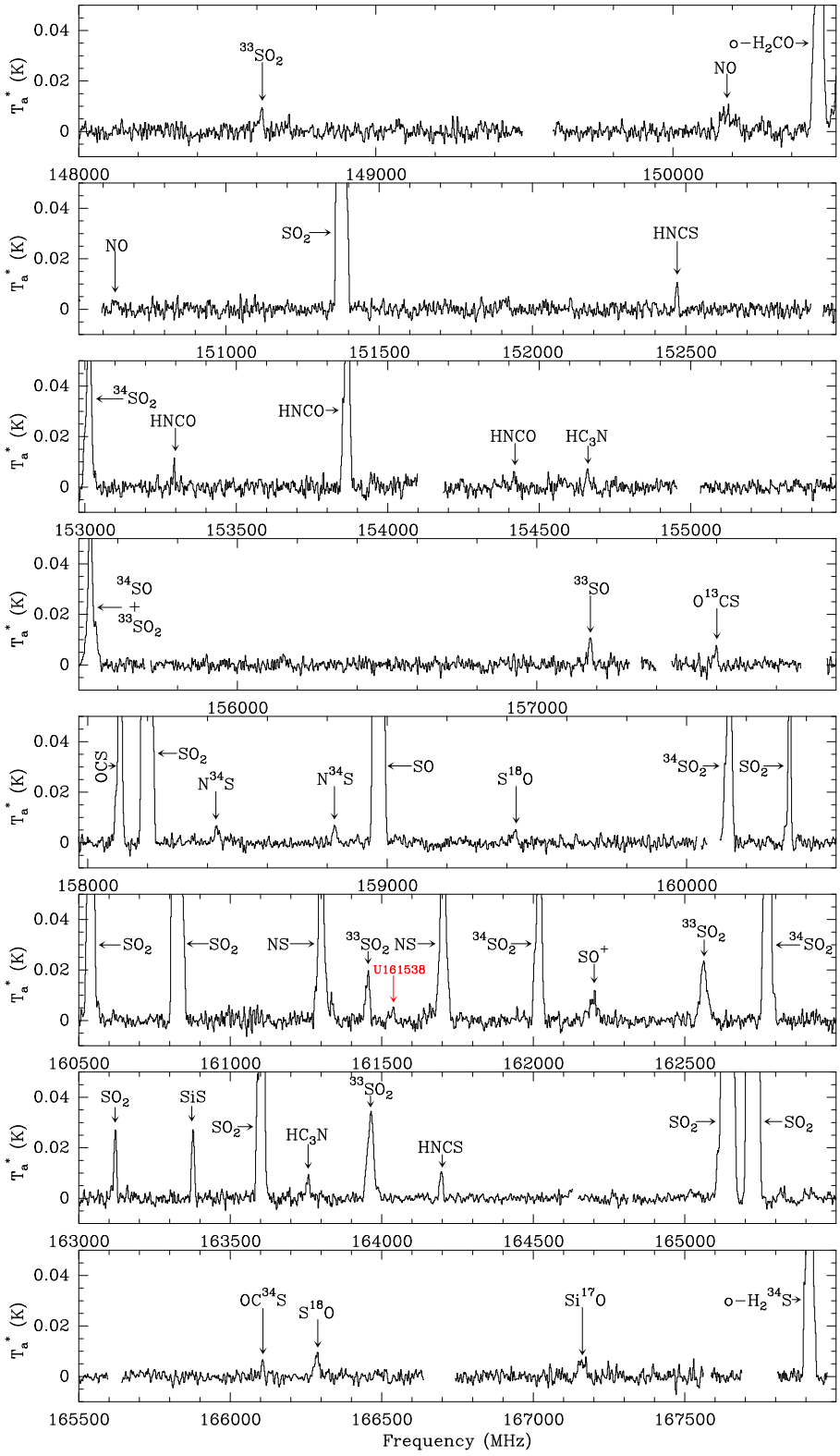

Figure 3.1: (Continued)

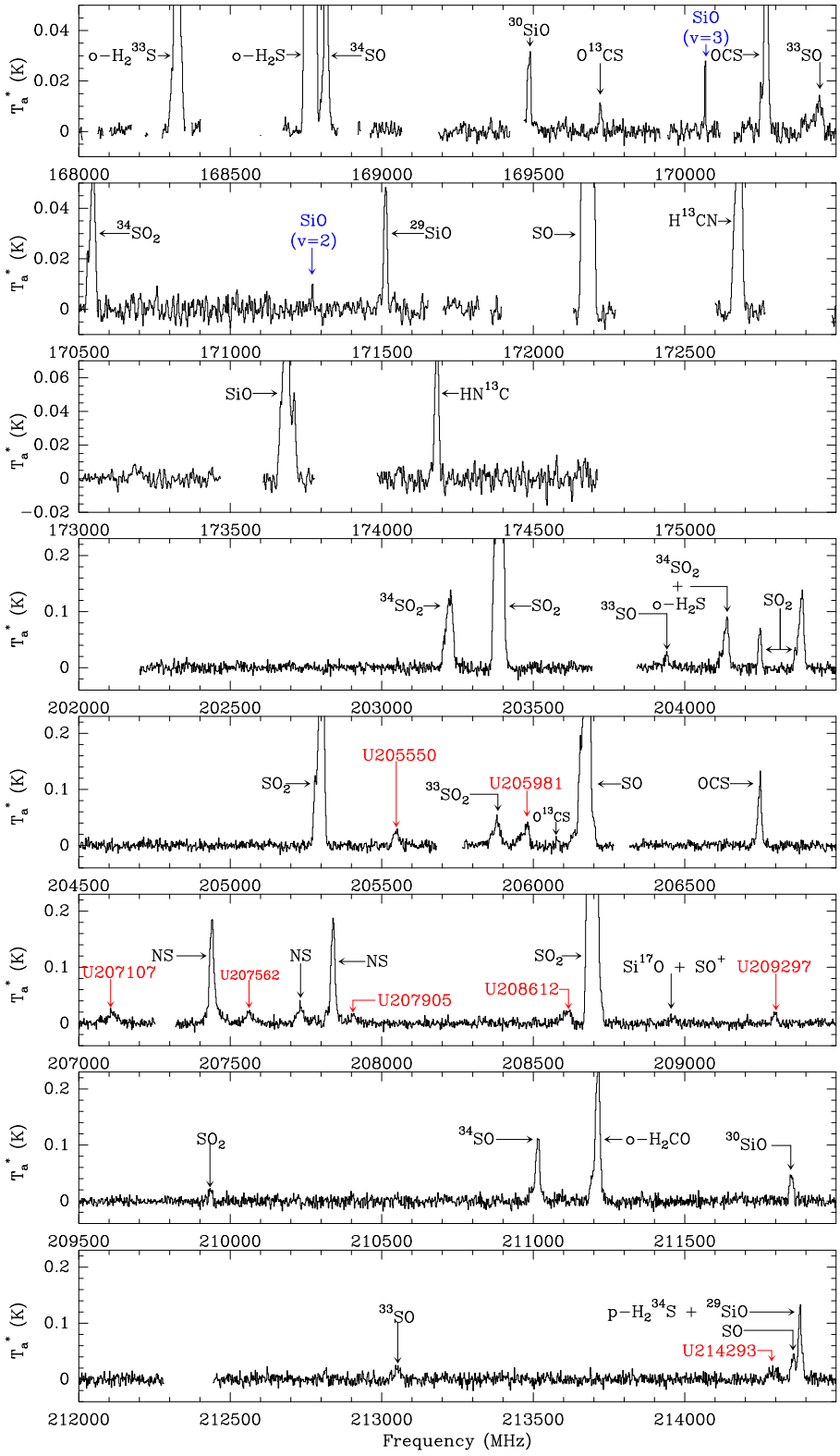

Figure 3.1: (Continued)

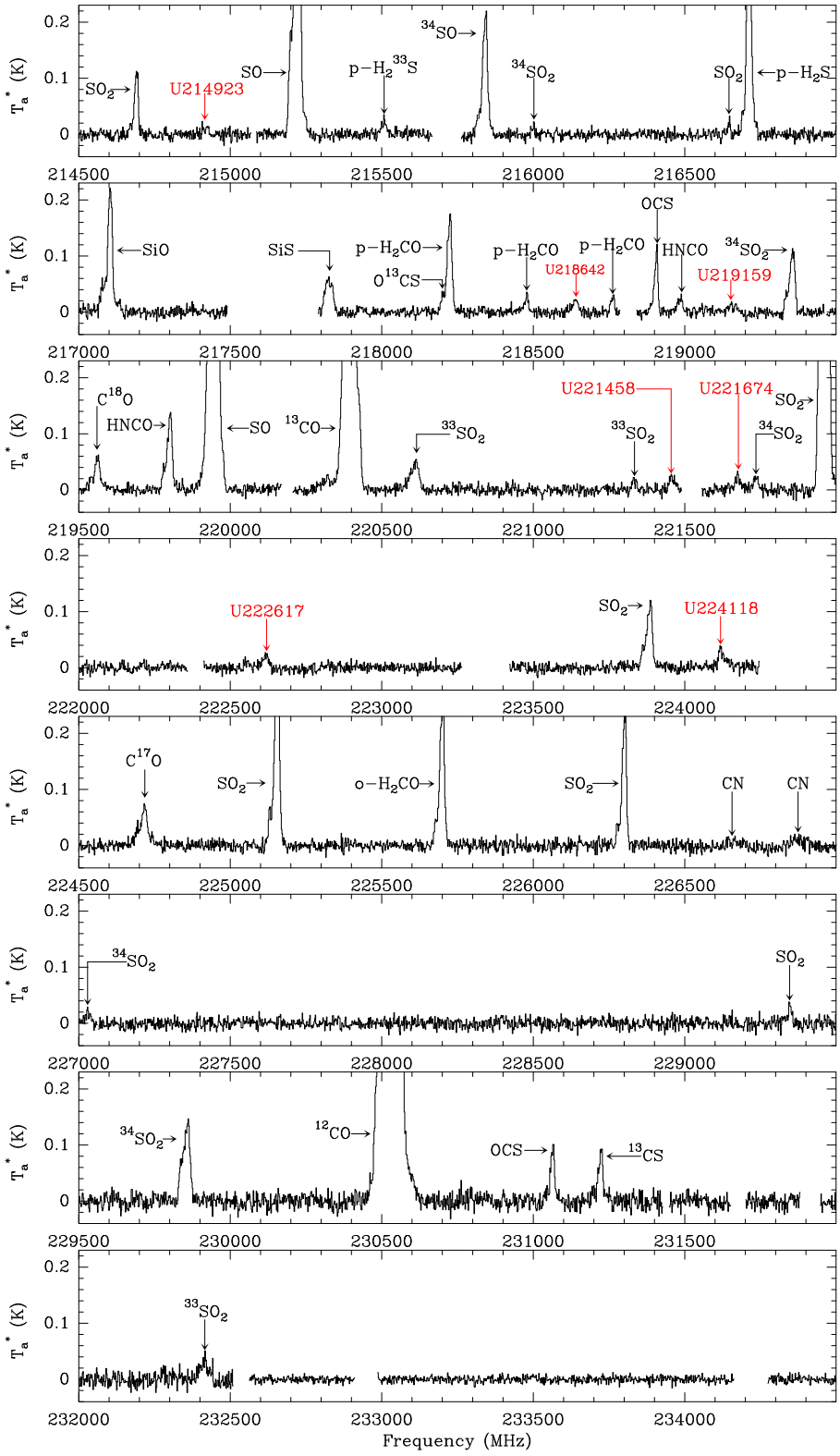

Figure 3.1: (Continued)

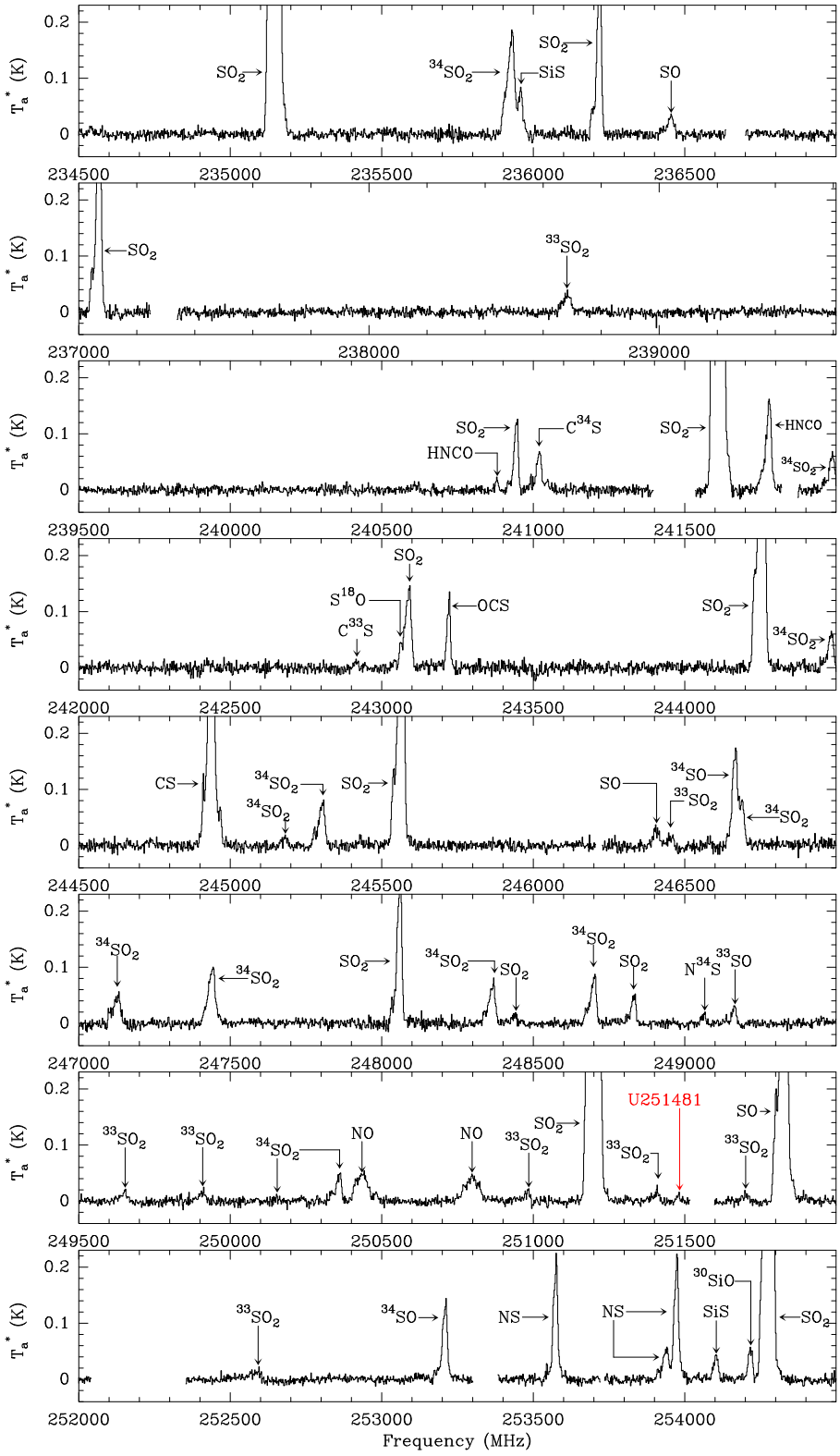

Figure 3.1: (Continued)

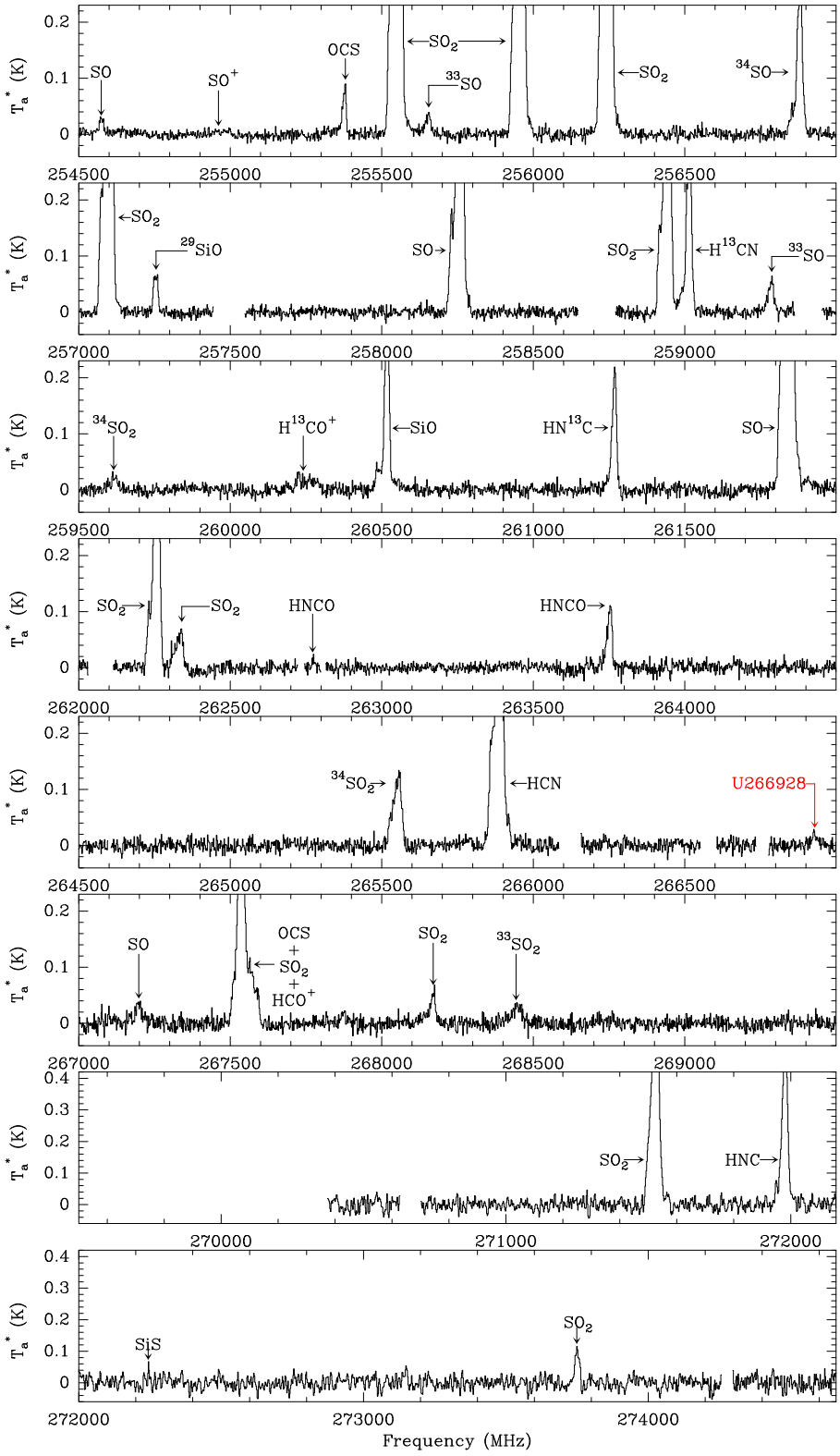

Figure 3.1: (Continued)

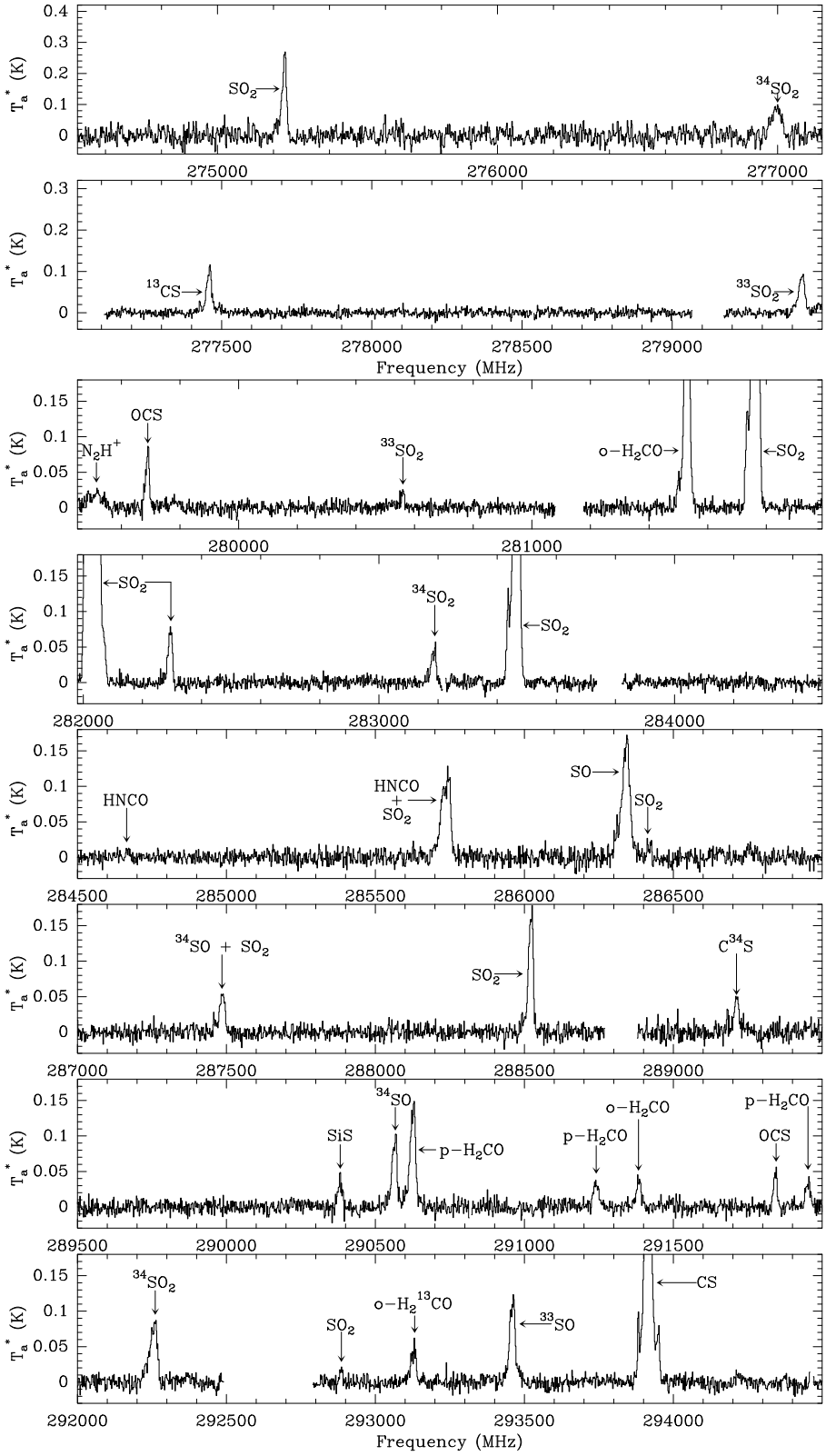

Figure 3.1: (Continued)

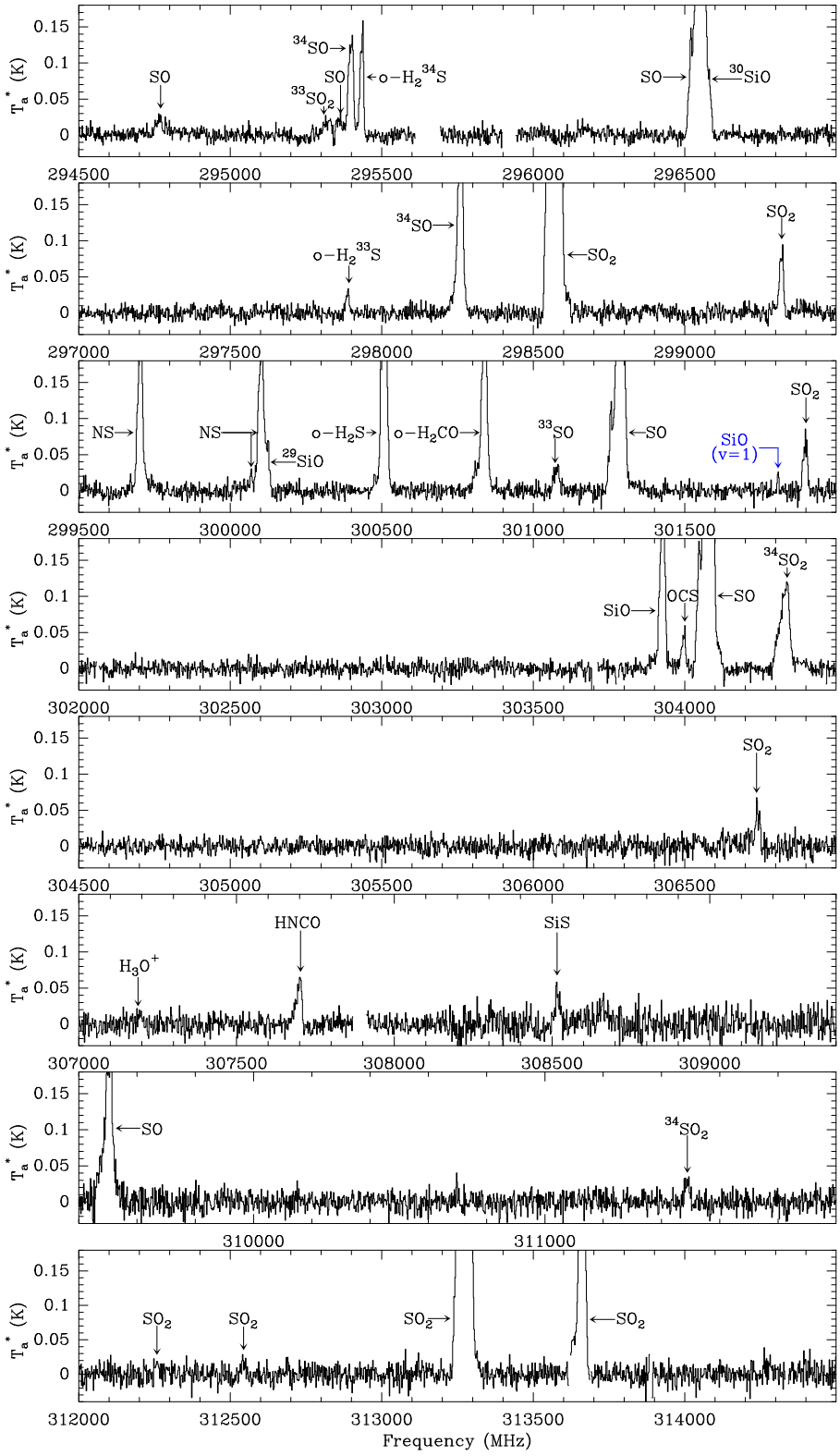

Figure 3.1: (Continued)

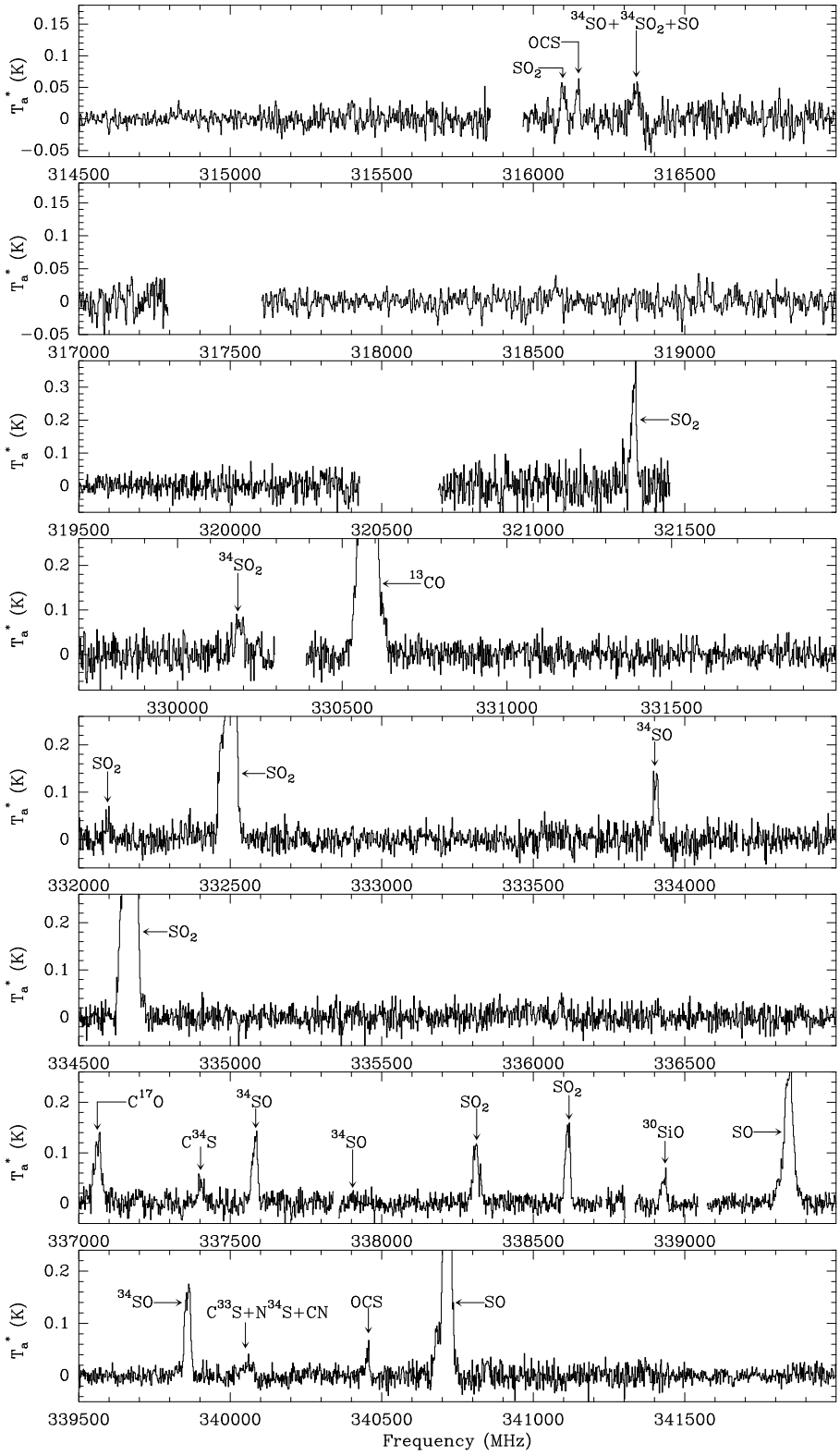

Figure 3.1: (Continued)

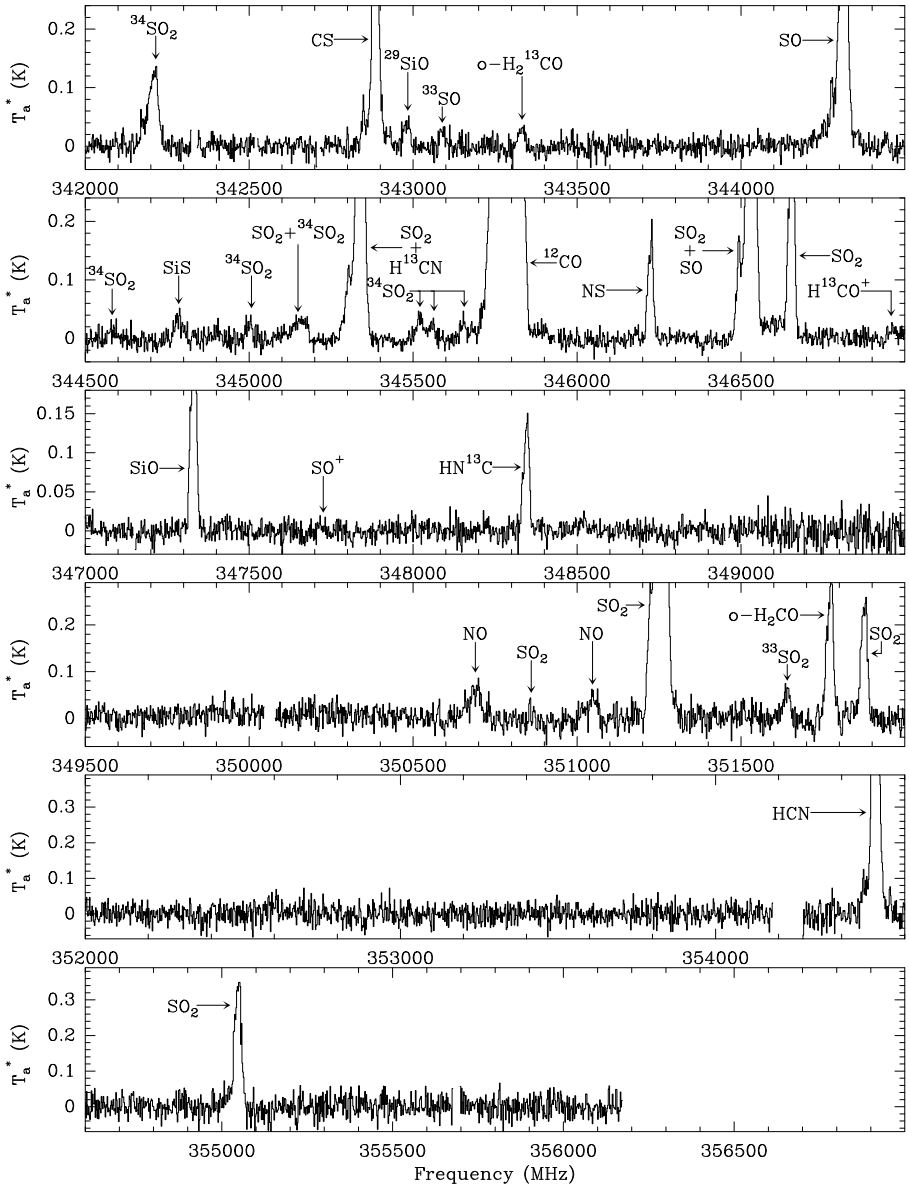

Figure 3.1: (Continued)

3.4.2 Observational results

Table 3.1: Measured and spectroscopic parameters of the detected lines.

Molecule	Transition QNs	$\nu_{\rm rest}$ (MHz)	$E_{\rm u}$ (K)	$A_{\rm ul}$ $\rm s^{-1}$	$\int T_{\rm ant}^{*}\,dv$ (K km $\rm s^{-1}$)
CO	1–0	115271.202	5.5	7.205×10^{-8}	52.68 (0.11)
CO	2–1	230538.000	16.6	6.916×10^{-7}	151.6 (0.2)
CO	3–2	345795.990	33.2	2.501×10^{-6}	133.7 (0.2)
^{13}CO	1–0	110201.354	5.3	6.336×10^{-8}	13.45 (0.06)
^{13}CO	2–1	220398.684	15.9	6.082×10^{-7}	51.50 (0.13)
^{13}CO	3–2	330587.964	31.7	2.199×10^{-6}	42.0 (0.3)
C^{18}O	1–0	109782.176	5.3	6.263×10^{-8}	0.20 (0.03)
C^{18}O	2–1	219560.358	15.8	6.013×10^{-7}	2.02 (0.06)
C^{17}O	1–0	112359.285	5.4	6.715×10^{-8}	0.32 (0.04)
C^{17}O	2–1	224714.385	16.2	6.446×10^{-7}	3.00 (0.09)
C^{17}O	3–2	337061.118	32.3	2.331×10^{-6}	3.91 (0.11)
SiO	2–1	86846.986	6.3	2.927×10^{-5}	4.68 (0.06)
SiO	3–2	130268.687	12.5	1.059×10^{-4}	7.36 (0.06)
SiO	4–3	173688.237	20.8	2.602×10^{-4}	7.65 (0.10)
SiO	5–4	217104.920	31.3	5.197×10^{-4}	6.82 (0.09)
SiO	6–5	260518.018	43.8	9.117×10^{-4}	7.49 (0.09)
SiO	7–6	303926.814	58.4	1.464×10^{-3}	4.45 (0.05)
SiO	8–7	347330.592	75.0	2.203×10^{-3}	4.56 (0.09)
^{29}SiO	2–1	85759.194	6.2	2.819×10^{-5}	0.58 (0.05)
^{29}SiO	3–2	128637.044	12.3	1.019×10^{-4}	1.05 (0.04)
^{29}SiO	4–3	171512.796	20.6	2.505×10^{-4}	1.21 (0.04)
^{29}SiO	5–4	214385.752	30.9	5.004×10^{-4}	2.41 (0.05)
^{29}SiO	6–5	257255.213	43.2	8.779×10^{-4}	1.48 (0.05)
^{29}SiO	7–6	300120.480	57.6	1.409×10^{-3}	0.85 (0.04)
^{29}SiO	8–7	342980.854	74.1	2.121×10^{-3}	0.90 (0.06)
^{30}SiO	2–1	84746.165	6.1	2.720×10^{-5}	0.39 (0.04)
^{30}SiO	4–3	169486.869	20.3	2.418×10^{-4}	0.73 (0.02)
^{30}SiO	5–4	211853.467	30.5	4.829×10^{-4}	0.86 (0.08)
^{30}SiO	6–5	254216.652	42.7	8.472×10^{-4}	1.09 (0.04)
^{30}SiO	7–6	296575.741	56.9	1.360×10^{-3}	1.35 (0.03)
^{30}SiO	8–7	338930.052	73.2	2.047×10^{-3}	0.92 (0.06)
Si^{17}O	4–3	167171.991	20.1	2.320×10^{-4}	0.12 (0.02)
Si^{17}O	5–4	208960.009	30.1	4.634×10^{-4}	0.26 (0.03)
SiS	6–5	108924.303	18.3	2.090×10^{-5}	0.19 (0.02)
SiS	8–7	145227.054	31.4	5.050×10^{-5}	0.33 (0.03)
SiS	9–8	163376.782	39.2	7.238×10^{-5}	0.55 (0.02)
SiS	12–11	217817.656	68.0	1.738×10^{-4}	2.35 (0.08)
SiS	13–12	235961.366	79.3	2.216×10^{-4}	1.81 (0.07)
SiS	14–13	254103.213	91.5	2.775×10^{-4}	0.75 (0.04)
SiS	15–14	272243.055	104.5	3.421×10^{-4}	0.4 (0.2)

Table 3.1: Continued.

Molecule	Transition QNs	$\nu_{\rm rest}$ (MHz)	$E_{\rm u}$ (K)	$A_{\rm ul}$ $\rm s^{-1}$	$\int T_{\rm ant}^{*}\, dv$ (K km $\rm s^{-1}$)
SiS	16–15	290380.747	118.5	4.159×10^{-4}	0.68 (0.04)
SiS	17–16	308516.147	133.3	4.997×10^{-4}	0.83 (0.13)
SiS	19–18	344779.495	165.5	6.996×10^{-4}	1.33 (0.08)
HCN	1–0	88631.602	4.3	2.406×10^{-5}	12.96 (0.04)
HCN	3–2	265886.433	25.5	8.352×10^{-4}	22.55 (0.07)
HCN	4–3	354505.476	42.5	2.053×10^{-3}	23.9 (0.3)
$H^{13}CN$	1–0	86339.921	4.1	2.224×10^{-5}	2.43 (0.04)
$H^{13}CN$	2–1	172677.851	12.4	2.135×10^{-4}	7.07 (0.05)
$H^{13}CN$	3–2	259011.798	24.9	7.721×10^{-4}	8.15 (0.06)
$H^{13}CN$	4–3	345339.769	41.4	1.898×10^{-3}	—[b]
HNC	1–0	90663.563	4.4	2.690×10^{-5}	5.08 (0.05)
HNC	3–2	271981.107	26.1	9.336×10^{-4}	15.10 (0.24)
$HN^{13}C$	1–0	87090.860	4.2	2.384×10^{-5}	0.57 (0.05)
$HN^{13}C$	2–1	174179.444	12.5	2.289×10^{-4}	2.53 (0.08)
$HN^{13}C$	3–2	261263.473	25.1	8.275×10^{-4}	4.40 (0.08)
$HN^{13}C$	4–3	348340.672	41.8	2.034×10^{-3}	2.50 (0.07)
NS	Ω=1/2,f,(5/2,7/2)–(3/2,5/2)	115153.935	8.8	2.329×10^{-5}	1.50 (0.10)
NS	Ω=1/2,f,(5/2,5/2)–(3/2,3/2)	115156.812	8.8	1.960×10^{-5}	
NS	Ω=1/2,f,(5/2,3/2)–(3/2,1/2)	115162.982	8.8	1.747×10^{-5}	
NS	Ω=1/2,e,(5/2,7/2)–(3/2,5/2)	115556.253	8.9	2.354×10^{-5}	1.05 (0.10)
NS	Ω=1/2,e,(5/2,5/2)–(3/2,3/2)	115570.763	8.9	1.982×10^{-5}	0.73 (0.07)
NS	Ω=1/2,e,(5/2,3/2)–(3/2,1/2)	115571.954	8.9	1.766×10^{-5}	
NS	Ω=1/2,e,(7/2,9/2)–(5/2,7/2)	161297.246	16.6	6.865×10^{-5}	4.05 (0.03)
NS	Ω=1/2,e,(7/2,7/2)–(5/2,5/2)	161298.411	16.6	6.301×10^{-5}	
NS	Ω=1/2,e,(7/2,5/2)–(5/2,3/2)	161301.747	16.6	6.108×10^{-5}	
NS	Ω=1/2,e,(7/2,5/2)–(5/2,5/2)	161330.290	16.6	7.472×10^{-6}	0.17 (0.02)
NS	Ω=1/2,e,(7/2,7/2)–(5/2,7/2)	161335.952	16.6	5.605×10^{-6}	
NS	Ω=1/2,e,(7/2,5/2)–(5/2,7/2)	161367.831	16.6	1.557×10^{-7}	
NS	Ω=1/2,f,(7/2,9/2)–(5/2,7/2)	161697.257	16.7	6.916×10^{-5}	4.18 (0.04)
NS	Ω=1/2,f,(7/2,7/2)–(5/2,5/2)	161703.404	16.7	6.348×10^{-5}	
NS	Ω=1/2,f,(7/2,5/2)–(5/2,3/2)	161703.987	16.7	6.154×10^{-5}	
NS	Ω=1/2,e,(9/2,11/2)–(7/2,9/2)	207436.051	26.5	1.512×10^{-4}	5.53 (0.05)
NS	Ω=1/2,e,(9/2,9/2)–(7/2,7/2)	207436.636	26.5	1.436×10^{-4}	
NS	Ω=1/2,e,(9/2,7/2)–(7/2,5/2)	207438.692	26.5	1.417×10^{-4}	
NS	Ω=1/2,f,(9/2,7/2)–(7/2,7/2)	207470.606	26.5	9.322×10^{-6}	0.43 (0.03)
NS	Ω=1/2,f,(9/2,9/2)–(7/2,9/2)	207475.341	26.5	7.458×10^{-6}	
NS	Ω=1/2,f,(9/2,11/2)–(7/2,9/2)	207834.866	26.6	1.521×10^{-4}	4.55 (0.06)
NS	Ω=1/2,f,(9/2,9/2)–(7/2,7/2)	207838.365	26.6	1.445×10^{-4}	
NS	Ω=1/2,f,(9/2,7/2)–(7/2,5/2)	207838.365	26.6	1.425×10^{-4}	
NS	Ω=1/2,e,(11/2,13/2)–(9/2,11/2)	253570.476	38.7	2.824×10^{-4}	4.83 (0.06)
NS	Ω=1/2,e,(11/2,11/2)–(9/2,9/2)	253570.476	38.7	2.730×10^{-4}	
NS	Ω=1/2,e,(11/2,9/2)–(9/2,7/2)	253572.148	38.7	2.711×10^{-4}	

Table 3.1: Continued.

Molecule	Transition QNs	$\nu_{\rm rest}$ (MHz)	$E_{\rm u}$ (K)	$A_{\rm ul}$ s^{-1}	$\int T_{\rm ant}^{*}\,dv$ (K km s^{-1})
NS	Ω=1/2,f,(11/2,11/2)–(9/2,11/2)	253913.173	38.8	9.363×10^{-6}	0.21 (0.03)
NS	Ω=1/2,f,(11/2,9/2)–(9/2,9/2)	253925.462	38.8	1.124×10^{-5}	
NS	Ω=1/2,f,(11/2,13/2)–(9/2,11/2)	253968.393	38.8	2.838×10^{-4}	4.44 (0.05)
NS	Ω=1/2,f,(11/2,11/2)–(9/2,9/2)	253970.581	38.8	2.743×10^{-4}	
NS	Ω=1/2,f,(11/2,9/2)–(9/2,7/2)	253970.581	38.8	2.723×10^{-4}	
NS	Ω=1/2,f,(13/2,15/2)–(11/2,13/2)	299699.781	53.1	4.735×10^{-4}	4.43 (0.08)
NS	Ω=1/2,f,(13/2,13/2)–(11/2,11/2)	299699.781	53.1	4.626×10^{-4}	
NS	Ω=1/2,f,(13/2,11/2)–(11/2,9/2)	299700.901	53.1	4.602×10^{-4}	
NS	Ω=1/2,e,(13/2,15/2)–(11/2,13/2)	300097.098	53.2	4.753×10^{-4}	4.30 (0.06)
NS	Ω=1/2,e,(13/2,13/2)–(11/2,11/2)	300098.611	53.2	4.645×10^{-4}	
NS	Ω=1/2,e,(13/2,11/2)–(11/2,9/2)	300098.611	53.2	4.620×10^{-4}	
NS	Ω=1/2,f,(15/2,17/2)–(13/2,15/2)	346220.137	69.8	7.385×10^{-4}	2.78 (0.05)
NS	Ω=1/2,f,(15/2,15/2)–(13/2,13/2)	346221.163	69.8	7.250×10^{-4}	
NS	Ω=1/2,f,(15/2,13/2)–(13/2,11/2)	346221.163	69.8	7.234×10^{-4}	
$N^{34}S$	Ω=1/2,e,(5/2,7/2)–(3/2,5/2)	113499.980	8.7	2.230×10^{-5}	—[b]
$N^{34}S$	Ω=1/2,e,(5/2,5/2)–(3/2,3/2)	113514.550	8.7	1.878×10^{-5}	
$N^{34}S$	Ω=1/2,e,(5/2,3/2)–(3/2,1/2)	113515.670	8.7	1.673×10^{-5}	
$N^{34}S$	Ω=1/2,e,(7/2,9/2)–(5/2,7/2)	158426.983	16.3	6.505×10^{-5}	0.18 (0.02)
$N^{34}S$	Ω=1/2,e,(7/2,7/2)–(5/2,5/2)	158428.161	16.3	5.970×10^{-5}	
$N^{34}S$	Ω=1/2,e,(7/2,5/2)–(5/2,3/2)	158431.459	16.3	5.788×10^{-5}	
$N^{34}S$	Ω=1/2,f,(7/2,9/2)–(5/2,7/2)	158820.003	16.4	6.553×10^{-5}	0.18 (0.02)
$N^{34}S$	Ω=1/2,f,(7/2,7/2)–(5/2,5/2)	158826.180	16.4	6.016×10^{-5}	
$N^{34}S$	Ω=1/2,f,(7/2,5/2)–(5/2,3/2)	158826.670	16.4	5.831×10^{-5}	
$N^{34}S$	Ω=1/2,e,(11/2,13/2)–(9/2,11/2)	249058.630	38.0	2.676×10^{-4}	0.32 (0.04)
$N^{34}S$	Ω=1/2,e,(11/2,11/2)–(9/2,9/2)	249058.630	38.0	2.587×10^{-4}	
$N^{34}S$	Ω=1/2,e,(11/2,9/2)–(9/2,7/2)	249060.203	38.0	2.569×10^{-4}	
$N^{34}S$	Ω=1/2,f,(15/2,17/2)–(3/2,15/2)	340060.050	68.6	6.998×10^{-4}	—[b]
$N^{34}S$	Ω=1/2,f,(15/2,15/2)–(3/2,13/2)	340061.137	68.6	6.870×10^{-4}	
$N^{34}S$	Ω=1/2,f,(15/2,13/2)–(3/2,11/2)	340061.137	68.6	6.855×10^{-4}	
CS	2–1	97980.953	7.1	1.679×10^{-5}	8.27 (0.04)
CS	3–2	146969.026	14.1	6.071×10^{-5}	13.69 (0.04)
CS	5–4	244935.555	35.3	2.981×10^{-4}	20.26 (0.07)
CS	6–5	293912.089	49.4	5.229×10^{-4}	16.65 (0.07)
CS	7–6	342882.854	65.8	8.395×10^{-4}	10.80 (0.10)
^{13}CS	2–1	92494.271	6.7	1.412×10^{-5}	1.00 (0.04)
^{13}CS	3–2	138739.264	13.3	5.107×10^{-5}	2.32 (0.04)
^{13}CS	5–4	231220.684	33.3	2.507×10^{-4}	2.64 (0.15)
^{13}CS	6–5	277455.398	46.6	4.399×10^{-4}	2.4 (0.2)
$C^{34}S$	2–1	96412.952	6.9	1.600×10^{-5}	0.80 (0.04)
$C^{34}S$	3–2	144617.101	13.9	5.784×10^{-5}	1.42 (0.05)
$C^{34}S$	5–4	241016.089	34.7	2.840×10^{-4}	2.17 (0.08)
$C^{34}S$	6–5	289209.067	48.6	4.982×10^{-4}	1.19 (0.07)

Table 3.1: Continued.

Molecule	Transition QNs	$\nu_{\rm rest}$ (MHz)	$E_{\rm u}$ (K)	$A_{\rm ul}$ $\rm s^{-1}$	$\int T_{\rm ant}^{*}\,dv$ (K km $\rm s^{-1}$)
$C^{34}S$	7–6	337396.459	64.8	7.998×10^{-4}	0.86 (0.09)
$C^{33}S$	3–2	145755.731	14.0	5.922×10^{-5}	0.27 (0.03)
$C^{33}S$	5–4	242913.610	35.0	2.907×10^{-4}	0.27 (0.06)
$C^{33}S$	7–6	340052.574	65.3	8.188×10^{-4}	—[b]
CN	(1,3/2,3/2)–(0,1/2,1/2)	113488.120	5.4	6.736×10^{-6}	
CN	(1,3/2,5/2)–(0,1/2,3/2)	113490.970	5.4	1.192×10^{-5}	—[b]
CN	(1,3/2,1/2)–(0,1/2,1/2)	113499.644	5.4	1.063×10^{-5}	
CN	(1,3/2,3/2)–(0,1/2,3/2)	113508.907	5.4	5.190×10^{-6}	
CN	(2,3/2,5/2)–(1,1/2,3/2)	226659.558	16.3	9.467×10^{-5}	
CN	(2,3/2,1/2)–(1,1/2,1/2)	226663.693	16.3	8.465×10^{-5}	0.68 (0.05)
CN	(2,3/2,3/2)–(1,1/2,1/2)	226679.311	16.3	5.268×10^{-5}	
CN	(2,5/2,5/2)–(1,3/2,3/2)	226874.191	16.3	9.621×10^{-5}	
CN	(2,5/2,7/2)–(1,3/2,5/2)	226874.781	16.3	1.143×10^{-4}	
CN	(2,5/2,3/2)–(1,3/2,1/2)	226875.896	16.3	8.587×10^{-5}	0.61 (0.05)
CN	(2,5/2,3/2)–(1,3/2,3/2)	226887.420	16.3	2.731×10^{-5}	
CN	(2,5/2,5/2)–(1,3/2,5/2)	226892.128	16.3	1.810×10^{-5}	
CN	(3,5/2,3/2)–(2,3/2,3/2)	340008.126	32.6	6.197×10^{-5}	
CN	(3,5/2,3/2)–(2,3/2,3/2)	340019.626	32.6	9.270×10^{-5}	
CN	(3,5/2,7/2)–(2,3/2,5/2)	340031.549	32.6	3.845×10^{-4}	—[b]
CN	(3,5/2,3/2)–(2,3/2,1/2)	340035.408	32.6	2.887×10^{-4}	
CN	(3,5/2,5/2)–(2,3/2,3/2)	340035.408	32.6	3.231×10^{-4}	
o-H_2CO	$2_{1,2}$–$1_{1,1}$	140839.516	6.8	5.296×10^{-5}	3.57 (0.06)
o-H_2CO	$2_{1,1}$–$1_{1,0}$	150498.335	7.5	6.462×10^{-5}	4.47 (0.03)
o-H_2CO	$3_{1,3}$–$2_{1,2}$	211211.449	16.9	2.268×10^{-4}	7.35 (0.11)
o-H_2CO	$3_{1,2}$–$2_{1,1}$	225697.772	18.3	2.767×10^{-4}	6.28 (0.08)
o-H_2CO	$4_{1,4}$–$3_{1,3}$	281526.919	30.4	5.874×10^{-4}	8.86 (0.05)
o-H_2CO	$4_{3,2}$–$3_{3,1}$	291380.441	125.8	3.040×10^{-4}	0.26 (0.03)
o-H_2CO	$4_{3,1}$–$3_{3,0}$	291384.360	125.8	3.040×10^{-4}	0.33 (0.03)
o-H_2CO	$4_{1,3}$–$3_{1,2}$	300836.630	32.7	7.168×10^{-4}	5.53 (0.06)
o-H_2CO	$5_{1,5}$–$4_{1,4}$	351768.637	47.3	1.200×10^{-3}	6.4 (0.2)
p-H_2CO	$2_{0,2}$–$1_{0,1}$	145602.951	10.5	7.802×10^{-5}	2.13 (0.03)
p-H_2CO	$3_{0,3}$–$2_{0,2}$	218222.187	21.0	2.814×10^{-4}	4.68 (0.06)
p-H_2CO	$3_{2,2}$–$2_{2,1}$	218475.634	68.1	1.569×10^{-4}	0.80 (0.04)
p-H_2CO	$3_{2,1}$–$2_{2,0}$	218760.062	68.1	1.575×10^{-4}	0.67 (0.04)
p-H_2CO	$4_{0,4}$–$3_{0,3}$	290623.412	34.9	6.891×10^{-4}	3.35 (0.07)
p-H_2CO	$4_{2,3}$–$3_{2,2}$	291237.765	82.1	5.203×10^{-4}	0.60 (0.06)
p-H_2CO	$4_{2,2}$–$3_{2,1}$	291948.066	82.1	5.241×10^{-4}	0.73 (0.05)
o-$H_2{}^{13}CO$	$2_{1,2}$–$1_{1,1}$	137449.954	6.6	4.923×10^{-5}	0.40 (0.03)
o-$H_2{}^{13}CO$	$4_{1,3}$–$3_{1,2}$	293126.495	31.9	6.631×10^{-4}	0.83 (0.05)
o-$H_2{}^{13}CO$	$5_{1,5}$–$4_{1,4}$	343325.654	46.2	1.116×10^{-3}	0.49 (0.10)
o-H_2S	$1_{1,0}$–$1_{0,1}$	168762.754	8.1	2.677×10^{-5}	32.61 (0.04)
o-H_2S	$4_{1,4}$–$3_{2,1}$	204140.204	144.5	3.006×10^{-8}	—[b]

Table 3.1: Continued.

Molecule	Transition QNs	$\nu_{\rm rest}$ (MHz)	$E_{\rm u}$ (K)	$A_{\rm ul}$ s^{-1}	$\int T_{\rm ant}^{*}\,dv$ (K km s^{-1})
o-H_2S	$3_{3,0}$–$3_{2,1}$	300505.524	149.1	1.024×10^{-4}	10.57 (0.07)
p-H_2S	$2_{2,0}$–$2_{1,1}$	216710.444	84.0	4.870×10^{-5}	12.58 (0.08)
o-$H_2{}^{34}S$	$1_{1,0}$–$1_{0,1}$	167910.516	8.1	2.616×10^{-5}	12.93 (0.03)
o-$H_2{}^{34}S$	$3_{3,0}$–$3_{2,1}$	295431.052	148.7	9.755×10^{-5}	2.07 (0.04)
p-$H_2{}^{34}S$	$2_{2,0}$–$2_{1,1}$	214376.924	83.8	4.697×10^{-5}	2.13 (0.05)
o-$H_2{}^{33}S$	$1_{1,0}$–$1_{0,1}$	168322.972	8.1	2.636×10^{-5}	6.58 (0.03)
o-$H_2{}^{33}S$	$3_{3,0}$–$3_{2,1}$	297884.271	148.9	9.951×10^{-5}	0.41 (0.05)
p-$H_2{}^{33}S$	$2_{2,0}$–$2_{1,1}$	215505.334	83.9	4.762×10^{-5}	0.61 (0.06)
OCS	7–6	85139.104	12.3	1.715×10^{-6}	1.15 (0.04)
OCS	8–7	97301.208	16.3	2.581×10^{-6}	1.56 (0.04)
OCS	9–8	109463.063	21.0	3.699×10^{-6}	1.86 (0.04)
OCS	11–10	133785.898	32.1	6.818×10^{-6}	2.48 (0.03)
OCS	12–11	145946.815	38.5	8.884×10^{-6}	2.02 (0.04)
OCS	13–12	158107.358	45.5	1.133×10^{-5}	3.40 (0.03)
OCS	14–13	170267.494	53.1	1.419×10^{-5}	2.78 (0.05)
OCS	17–16	206745.155	79.4	2.555×10^{-5}	2.62 (0.06)
OCS	18–17	218903.355	89.3	3.038×10^{-5}	2.07 (0.05)
OCS	19–18	231060.993	99.8	3.578×10^{-5}	2.39 (0.15)
OCS	20–19	243218.037	110.9	4.178×10^{-5}	2.01 (0.08)
OCS	21–20	255374.457	122.6	4.842×10^{-5}	1.48 (0.07)
OCS	22–21	267530.220	134.8	5.573×10^{-5}	—[b]
OCS	23–22	279685.296	147.7	6.374×10^{-5}	1.24 (0.07)
OCS	24–23	291839.653	161.1	7.248×10^{-5}	0.62 (0.05)
OCS	25–24	303993.261	175.1	8.199×10^{-5}	0.69 (0.03)
OCS	26–25	316146.088	189.7	9.229×10^{-5}	0.68 (0.11)
OCS	28–27	340449.273	220.6	1.154×10^{-4}	0.74 (0.06)
$O^{13}CS$	8–7	96988.121	21.0	2.557×10^{-6}	0.12 (0.02)
$O^{13}CS$	9–8	109110.845	26.2	3.665×10^{-6}	0.13 (0.03)
$O^{13}CS$	11–10	133355.416	38.4	6.756×10^{-6}	0.19 (0.02)
$O^{13}CS$	12–11	145477.197	45.4	8.803×10^{-6}	0.23 (0.03)
$O^{13}CS$	13–12	157598.625	53.0	1.123×10^{-5}	0.20 (0.02)
$O^{13}CS$	14–13	169719.648	61.1	1.406×10^{-5}	0.19 (0.02)
$O^{13}CS$	17–16	206079.955	89.0	2.532×10^{-5}	0.22 (0.05)
$O^{13}CS$	18–17	218198.998	99.5	3.010×10^{-5}	—[b]
$OC^{34}S$	14–13	166105.721	59.8	1.318×10^{-5}	0.13 (0.02)
SO	(2,2)–(1,1)	86093.959	19.3	5.250×10^{-6}	6.12 (0.06)
SO	(2,3)–(1,2)	97715.405	9.2	1.125×10^{-5}	—[b]
SO	(2,3)–(1,2)	99299.891	9.2	1.125×10^{-5}	23.83 (0.05)
SO	(5,4)–(4,4)	100029.558	38.6	1.082×10^{-6}	1.28 (0.03)
SO	(3,2)–(2,1)	109252.184	21.1	1.080×10^{-5}	9.91 (0.05)
SO	(3,3)–(2,2)	129138.904	25.5	2.250×10^{-5}	16.54 (0.04)
SO	(6,5)–(5,5)	136634.672	50.7	1.749×10^{-6}	1.44 (0.04)

Table 3.1: Continued.

Molecule	Transition QNs	$\nu_{\rm rest}$ (MHz)	$E_{\rm u}$ (K)	$A_{\rm ul}$ $\rm s^{-1}$	$\int T_{\rm ant}^{*}\, dv$ (K km $\rm s^{-1}$)
SO	(3,4)–(2,3)	138178.659	15.9	3.166×10^{-5}	37.72 (0.04)
SO	(4,3)–(3,2)	158971.816	28.7	4.233×10^{-5}	27.14 (0.03)
SO	(4,4)–(3,3)	172181.407	33.8	5.833×10^{-5}	25.87 (0.05)
SO	(5,4)–(4,3)	206176.019	38.6	1.010×10^{-4}	27.21 (0.08)
SO	(8,7)–(7,7)	214357.075	81.3	3.351×10^{-6}	0.87 (0.06)
SO	(5,5)–(4,4)	215220.653	44.1	1.193×10^{-4}	27.01 (0.08)
SO	(5,6)–(4,5)	219949.396	35.0	1.335×10^{-4}	43.50 (0.09)
SO	(2,1)–(1,2)	236452.292	15.8	1.417×10^{-6}	1.18 (0.07)
SO	(3,2)–(2,3)	246404.586	21.1	1.008×10^{-6}	1.18 (0.05)
SO	(6,5)–(5,4)	251825.767	50.7	1.925×10^{-4}	29.10 (0.08)
SO	(9,8)–(8,8)	254573.653	99.7	4.240×10^{-6}	0.61 (0.04)
SO	(6,6)–(5,5)	258255.830	56.5	2.120×10^{-4}	28.43 (0.08)
SO	(6,7)–(5,6)	261843.713	47.6	2.282×10^{-4}	41.66 (0.13)
SO	(4,3)–(3,4)	267197.743	28.7	7.118×10^{-7}	1.26 (0.12)
SO	(1,1)–(0,1)	286340.151	15.2	1.403×10^{-5}	6.17 (0.13)
SO	(5,4)–(4,5)	294768.391	38.6	5.326×10^{-7}	0.56 (0.05)
SO	(10,9)–(9,9)	295355.609	120.3	5.167×10^{-6}	0.53 (0.04)
SO	(7,6)–(6,5)	296550.061	64.9	3.230×10^{-4}	28.43 (0.07)
SO	(7,7)–(6,6)	301286.123	71.0	3.429×10^{-4}	18.47 (0.06)
SO	(7,8)–(6,7)	304077.867	62.2	3.609×10^{-4}	27.80 (0.05)
SO	(2,2)–(1,2)	309502.443	19.3	1.419×10^{-5}	7.3 (0.2)
SO	(1,1)–(1,0)	316341.695	15.2	8.451×10^{-8}	—[b]
SO	(3,3)–(2,3)	339341.457	25.5	1.455×10^{-5}	8.96 (0.10)
SO	(8,7)–(7,6)	340714.295	81.3	4.985×10^{-4}	19.83 (0.13)
SO	(8,8)–(7,7)	344310.717	87.5	5.186×10^{-4}	20.08 (0.12)
SO	(8,9)–(7,8)	346528.537	78.8	5.382×10^{-4}	—[b]
^{34}SO	(2,2)–(1,1)	84410.686	19.2	4.948×10^{-6}	0.32 (0.04)
^{34}SO	(2,3)–(1,2)	97715.405	9.1	1.073×10^{-5}	—[b]
^{34}SO	(3,2)–(2,1)	106743.368	20.9	1.007×10^{-5}	0.62 (0.04)
^{34}SO	(3,4)–(2,3)	135775.651	15.6	3.004×10^{-5}	5.20 (0.04)
^{34}SO	(4,3)–(3,2)	155506.808	28.4	3.961×10^{-5}	2.59 (0.04)
^{34}SO	(4,4)–(3,3)	168815.114	33.4	5.498×10^{-5}	2.41 (0.03)
^{34}SO	(5,5)–(4,4)	211013.024	43.5	1.124×10^{-4}	3.25 (0.10)
^{34}SO	(5,6)–(4,5)	215839.918	34.4	1.262×10^{-4}	6.14 (0.07)
^{34}SO	(6,5)–(5,4)	246663.403	49.9	1.809×10^{-4}	4.23 (0.06)
^{34}SO	(6,6)–(5,5)	253207.022	55.7	1.998×10^{-4}	3.25 (0.06)
^{34}SO	(6,7)–(5,6)	256877.811	46.7	2.155×10^{-4}	7.00 (0.07)
^{34}SO	(10,9)–(9,9)	287481.110	18.1	4.789×10^{-6}	—[b]
^{34}SO	(7,6)–(6,5)	290562.257	63.8	3.037×10^{-4}	2.13 (0.08)
^{34}SO	(7,7)–(6,6)	295396.326	69.9	3.232×10^{-4}	3.36 (0.06)
^{34}SO	(7,8)–(6,7)	298257.974	61.0	3.406×10^{-4}	5.02 (0.07)
^{34}SO	(1,1)–(1,0)	316335.872	15.2	8.450×10^{-8}	—[b]

Table 3.1: Continued.

Molecule	Transition QNs	$\nu_{\rm rest}$ (MHz)	$E_{\rm u}$ (K)	$A_{\rm ul}$ $\rm s^{-1}$	$\int T_{\rm ant}^{*}\,dv$ (K km $\rm s^{-1}$)
^{34}SO	(8,7)–(7,6)	333900.992	79.9	4.692×10^{-4}	2.4 (0.2)
^{34}SO	(8,8)–(7,7)	337580.153	86.1	4.887×10^{-4}	2.62 (0.12)
^{34}SO	(3,3)–(2,3)	337892.294	25.3	1.399×10^{-5}	0.25 (0.06)
^{34}SO	(8,9)–(7,8)	339857.271	77.3	5.077×10^{-4}	3.80 (0.08)
^{33}SO	(2,3)–(1,2)	98483.146	9.2	1.098×10^{-5}	0.56 (0.03)
^{33}SO	(3,4)–(2,3)	136939.183	15.7	3.082×10^{-5}	1.20 (0.04)
^{33}SO	(4,3)–(3,2)	157183.672	28.5	4.091×10^{-5}	0.29 (0.03)
^{33}SO	(4,4)–(3,3)	170444.833	33.6	5.658×10^{-5}	0.51 (0.03)
^{33}SO	(5,4)–(4,3)	203942.464	38.3	9.772×10^{-5}	0.43 (0.07)
^{33}SO	(5,5)–(4,4)	213050.060	43.8	1.157×10^{-4}	0.82 (0.10)
^{33}SO	(6,5)–(5,4)	249162.732	50.3	1.865×10^{-4}	0.76 (0.04)
^{33}SO	(6,6)–(5,5)	255651.298	56.1	2.056×10^{-4}	0.91 (0.08)
^{33}SO	(6,7)–(5,6)	259281.740	47.1	2.216×10^{-4}	1.32 (0.05)
^{33}SO	(7,6)–(6,5)	293461.308	64.4	3.129×10^{-4}	2.74 (0.07)
^{33}SO	(7,8)–(6,7)	301075.347	61.6	3.503×10^{-4}	0.70 (0.04)
^{33}SO	(8,9)–(7,8)	343086.834	78.0	5.223×10^{-4}	0.59 (0.09)
$S^{18}O$	(4,4)–(3,3)	159428.312	32.4	4.631×10^{-5}	0.16 (0.02)
$S^{18}O$	(4,5)–(3,4)	166285.321	22.9	5.670×10^{-5}	0.30 (0.02)
$S^{18}O$	(6,7)–(5,6)	243039.314	44.4	1.825×10^{-4}	0.24 (0.06)
SO_2	$13_{4,10}$–$14_{3,11}$	82951.936	123.0	1.265×10^{-6}	0.29 (0.05)
SO_2	$8_{1,7}$–$8_{0,8}$	83688.092	36.7	6.825×10^{-6}	10.29 (0.08)
SO_2	$8_{3,5}$–$9_{2,8}$	86639.090	55.2	1.343×10^{-6}	1.18 (0.04)
SO_2	$7_{3,5}$–$8_{2,6}$	97702.334	47.8	1.815×10^{-6}	—[b]
SO_2	$2_{2,0}$–$3_{1,3}$	100878.107	12.6	1.026×10^{-6}	3.19 (0.04)
SO_2	$3_{1,3}$–$2_{0,2}$	104029.420	7.7	1.006×10^{-5}	24.29 (0.04)
SO_2	$10_{1,9}$–$10_{0,10}$	104239.299	54.7	1.122×10^{-5}	10.35 (0.05)
SO_2	$12_{4,8}$–$13_{3,11}$	107843.470	111.0	2.649×10^{-6}	0.23 (0.03)
SO_2	$12_{2,10}$–$12_{1,11}$	128605.111	82.6	2.615×10^{-5}	5.55 (0.05)
SO_2	$12_{1,11}$–$11_{2,10}$	129105.786	76.4	9.029×10^{-6}	5.86 (0.04)
SO_2	$10_{2,8}$–$10_{1,9}$	129514.799	60.9	2.502×10^{-5}	8.75 (0.05)
SO_2	$12_{1,11}$–$12_{0,12}$	131014.841	76.4	1.856×10^{-5}	8.28 (0.04)
SO_2	$14_{2,12}$–$14_{1,13}$	132744.832	108.1	2.933×10^{-5}	3.43 (0.04)
SO_2	$8_{2,6}$–$8_{1,7}$	134004.812	43.1	2.501×10^{-5}	12.53 (0.03)
SO_2	$5_{1,5}$–$4_{0,4}$	135696.017	15.7	2.208×10^{-5}	34.64 (0.04)
SO_2	$5_{3,3}$–$6_{2,4}$	139355.030	35.9	3.855×10^{-6}	3.53 (0.06)
SO_2	$6_{2,4}$–$6_{1,5}$	140306.166	29.2	2.528×10^{-5}	14.79 (0.05)
SO_2	$16_{2,14}$–$16_{1,15}$	143057.080	137.5	3.572×10^{-5}	1.71 (0.03)
SO_2	$10_{4,6}$–$11_{3,9}$	146550.044	89.8	5.897×10^{-6}	0.90 (0.05)
SO_2	$4_{2,2}$–$4_{1,3}$	146605.520	19.0	2.470×10^{-5}	19.92 (0.05)
SO_2	$2_{2,0}$–$2_{1,1}$	151378.663	12.6	1.875×10^{-5}	20.53 (0.04)
SO_2	$3_{2,2}$–$3_{1,3}$	158199.781	15.3	2.532×10^{-5}	29.54 (0.04)
SO_2	$18_{2,16}$–$18_{1,17}$	160342.971	170.8	4.692×10^{-5}	1.52 (0.03)

Table 3.1: Continued.

Molecule	Transition QNs	$\nu_{\rm rest}$ (MHz)	$E_{\rm u}$ (K)	$A_{\rm ul}$ s^{-1}	$\int T_{\rm ant}^{*}\, dv$ (K km s^{-1})
SO_2	$4_{3,1}$–$5_{2,4}$	160543.024	31.3	4.321×10^{-6}	6.14 (0.03)
SO_2	$10_{0,10}$–$9_{1,9}$	160827.841	49.7	3.954×10^{-5}	29.49 (0.04)
SO_2	$18_{2,16}$–$17_{3,15}$	163119.379	170.8	1.354×10^{-5}	0.60 (0.02)
SO_2	$14_{1,13}$–$14_{0,14}$	163605.533	101.8	3.006×10^{-5}	7.06 (0.03)
SO_2	$5_{2,4}$–$5_{1,5}$	165144.652	23.6	3.122×10^{-5}	35.33 (0.04)
SO_2	$7_{1,7}$–$6_{0,6}$	165225.452	27.1	4.135×10^{-5}	52.41 (0.04)
SO_2	$12_{0,12}$–$11_{1,11}$	203391.484	70.1	8.805×10^{-5}	28.18 (0.12)
SO_2	$18_{3,15}$–$18_{2,16}$	204246.762	180.6	9.267×10^{-5}	1.21 (0.08)
SO_2	$7_{4,4}$–$8_{3,5}$	204384.191	65.0	1.114×10^{-5}	4.17 (0.09)
SO_2	$11_{2,10}$–$11_{1,11}$	205300.539	70.2	5.318×10^{-5}	16.09 (0.08)
SO_2	$3_{2,2}$–$2_{1,1}$	208700.337	15.3	6.719×10^{-5}	39.52 (0.10)
SO_2	$12_{5,7}$–$13_{4,10}$	209936.041	133.0	1.593×10^{-5}	0.54 (0.09)
SO_2	$16_{3,13}$–$16_{2,14}$	214689.395	147.8	9.902×10^{-5}	2.41 (0.08)
SO_2	$22_{2,20}$–$22_{1,21}$	216643.304	248.5	9.271×10^{-5}	0.35 (0.04)
SO_2	$11_{1,11}$–$10_{0,10}$	221965.221	60.4	1.138×10^{-4}	41.47 (0.11)
SO_2	$6_{4,2}$–$7_{3,5}$	223883.568	58.6	1.161×10^{-5}	3.67 (0.09)
SO_2	$13_{2,12}$–$13_{1,13}$	225153.705	93.0	6.523×10^{-5}	9.96 (0.10)
SO_2	$14_{3,11}$–$14_{2,12}$	226300.028	119.0	1.068×10^{-4}	5.38 (0.08)
SO_2	$11_{5,7}$–$12_{4,8}$	229347.627	122.0	1.908×10^{-5}	0.94 (0.08)
SO_2	$4_{2,2}$–$3_{1,3}$	235151.721	19.0	7.691×10^{-5}	53.69 (0.09)
SO_2	$16_{1,15}$–$15_{2,14}$	236216.688	130.7	7.505×10^{-5}	6.74 (0.08)
SO_2	$12_{3,9}$–$12_{2,10}$	237068.834	94.0	1.141×10^{-4}	11.39 (0.07)
SO_2	$18_{1,17}$–$18_{0,18}$	240942.792	163.1	7.024×10^{-5}	2.76 (0.06)
SO_2	$5_{2,4}$–$4_{1,3}$	241615.798	23.6	8.455×10^{-5}	56.30 (0.09)
SO_2	$5_{4,2}$–$6_{3,3}$	243087.646	53.1	1.027×10^{-5}	4.62 (0.09)
SO_2	$14_{0,14}$–$13_{1,13}$	244254.220	93.9	1.639×10^{-4}	24.54 (0.08)
SO_2	$10_{3,7}$–$10_{2,8}$	245563.423	72.7	1.191×10^{-4}	19.01 (0.06)
SO_2	$15_{2,14}$–$15_{1,15}$	248057.403	119.3	8.056×10^{-5}	6.30 (0.10)
SO_2	$13_{3,11}$–$14_{0,14}$	248436.938	105.8	1.303×10^{-6}	0.29 (0.04)
SO_2	$10_{5,5}$–$11_{4,8}$	248830.822	111.9	2.190×10^{-5}	1.16 (0.04)
SO_2	$13_{1,13}$–$12_{0,12}$	251199.676	82.2	1.756×10^{-4}	50.10 (0.06)
SO_2	$6_{3,3}$–$6_{2,4}$	254280.537	41.4	1.136×10^{-4}	29.70 (0.07)
SO_2	$4_{3,1}$–$4_{2,2}$	255553.303	31.3	9.284×10^{-5}	33.67 (0.10)
SO_2	$3_{3,1}$–$3_{2,2}$	255958.045	27.6	6.626×10^{-5}	28.29 (0.10)
SO_2	$5_{3,3}$–$5_{2,4}$	256246.946	35.9	1.074×10^{-4}	33.79 (0.09)
SO_2	$7_{3,5}$–$7_{2,6}$	257099.967	47.8	1.223×10^{-4}	28.71 (0.07)
SO_2	$9_{3,7}$–$9_{2,8}$	258942.200	63.5	1.318×10^{-4}	22.24 (0.06)
SO_2	$11_{3,9}$–$11_{2,10}$	262256.907	82.8	1.408×10^{-4}	15.66 (0.10)
SO_2	$4_{4,0}$–$5_{3,3}$	262333.965	48.5	6.317×10^{-6}	2.45 (0.10)
SO_2	$13_{3,11}$–$13_{2,12}$	267537.453	105.8	1.513×10^{-4}	—[b]
SO_2	$9_{5,5}$–$10_{4,6}$	268168.331	102.7	2.386×10^{-5}	1.78 (0.11)
SO_2	$7_{2,6}$–$6_{1,5}$	271529.016	35.5	1.107×10^{-4}	26.5 (0.3)

Table 3.1: Continued.

Molecule	Transition QNs	$\nu_{\rm rest}$ (MHz)	$E_{\rm u}$ (K)	$A_{\rm ul}$ s^{-1}	$\int T_{\rm ant}^{*}\,dv$ (K km s^{-1})
SO_2	$17_{2,16}$–$17_{1,17}$	273752.962	149.2	9.966×10^{-5}	1.7 (0.2)
SO_2	$15_{3,13}$–$15_{2,14}$	275240.185	132.5	1.645×10^{-4}	6.1 (0.2)
SO_2	$15_{1,15}$–$14_{0,14}$	281762.602	107.4	2.609×10^{-4}	23.12 (0.06)
SO_2	$6_{2,4}$–$5_{1,5}$	282036.568	29.2	1.003×10^{-4}	49.93 (0.07)
SO_2	$20_{1,19}$–$20_{0,20}$	282292.806	198.9	1.002×10^{-4}	1.46 (0.05)
SO_2	$16_{0,16}$–$15_{1,15}$	283464.770	121.0	2.700×10^{-4}	17.11 (0.07)
SO_2	$17_{3,15}$–$17_{2,16}$	285743.589	163.0	1.816×10^{-4}	2.46 (0.07)[b]
SO_2	$22_{2,20}$–$21_{3,19}$	286416.272	248.4	9.293×10^{-5}	0.30 (0.07)
SO_2	$8_{5,3}$–$9_{4,6}$	287485.506	94.4	2.438×10^{-5}	—[b]
SO_2	$18_{1,17}$–$17_{2,16}$	288519.997	163.1	1.570×10^{-4}	3.75 (0.10)
SO_2	$13_{6,8}$–$14_{5,9}$	292882.580	171.9	3.737×10^{-5}	0.32 (0.05)
SO_2	$9_{2,8}$–$8_{1,7}$	298576.309	51.0	1.442×10^{-4}	34.61 (0.09)
SO_2	$19_{3,17}$–$19_{2,18}$	299316.820	197.0	2.037×10^{-4}	1.32 (0.08)
SO_2	$19_{2,18}$–$19_{1,19}$	301896.629	182.6	1.229×10^{-4}	1.14 (0.04)
SO_2	$7_{5,3}$–$8_{4,4}$	306738.847	87.1	2.269×10^{-5}	1.06 (0.09)
SO_2	$12_{6,6}$–$13_{5,9}$	312258.415	160.0	4.105×10^{-5}	0.34 (0.05)
SO_2	$22_{4,18}$–$22_{3,19}$	312542.520	272.8	2.819×10^{-4}	0.33 (0.06)
SO_2	$3_{3,1}$–$2_{2,0}$	313279.719	27.6	3.396×10^{-4}	29.08 (0.11)
SO_2	$17_{1,17}$–$16_{0,16}$	313660.853	136.1	3.747×10^{-4}	10.22 (0.10)
SO_2	$21_{3,19}$–$21_{2,20}$	316098.875	234.7	2.319×10^{-4}	0.86 (0.11)
SO_2	$18_{0,18}$–$17_{1,17}$	321330.168	151.5	4.087×10^{-4}	6.3 (0.5)
SO_2	$21_{2,20}$–$21_{1,21}$	332091.430	219.5	1.507×10^{-4}	0.77 (0.10)
SO_2	$4_{3,1}$–$3_{2,2}$	332505.243	31.3	3.290×10^{-4}	25.3 (0.2)
SO_2	$8_{2,6}$–$7_{1,7}$	334673.355	43.1	1.270×10^{-4}	38.2 (0.2)
SO_2	$18_{4,14}$–$18_{3,15}$	338305.994	196.8	3.266×10^{-4}	2.55 (0.09)
SO_2	$20_{1,19}$–$19_{2,18}$	338611.811	198.9	2.868×10^{-4}	2.56 (0.09)
SO_2	$5_{5,1}$–$6_{4,2}$	345148.967	75.1	9.811×10^{-6}	0.95 (0.07)
SO_2	$13_{2,12}$–$12_{1,11}$	345338.540	93.0	2.381×10^{-4}	—[b]
SO_2	$16_{4,12}$–$16_{3,13}$	346523.879	164.5	3.390×10^{-4}	—[b]
SO_2	$19_{1,19}$–$18_{0,18}$	346652.171	168.1	5.219×10^{-4}	6.71 (0.10)
SO_2	$10_{6,4}$–$11_{5,7}$	350862.746	138.9	4.403×10^{-5}	0.30 (0.10)
SO_2	$5_{3,3}$–$4_{2,2}$	351257.225	35.9	3.357×10^{-4}	39.8 (0.2)
SO_2	$14_{4,10}$–$14_{3,11}$	351873.874	135.9	3.432×10^{-4}	6.1 (0.2)
SO_2	$12_{4,8}$–$12_{3,9}$	355045.518	111.0	3.396×10^{-4}	7.7 (0.3)
$^{34}SO_2$	$8_{1,7}$–$8_{0,8}$	83043.824	36.6	6.544×10^{-6}	1.06 (0.06)
$^{34}SO_2$	$3_{1,3}$–$2_{0,2}$	102031.878	7.6	9.495×10^{-6}	2.82 (0.04)
$^{34}SO_2$	$10_{1,9}$–$10_{0,10}$	104391.706	54.6	1.096×10^{-5}	0.86 (0.03)
$^{34}SO_2$	$8_{2,6}$–$8_{1,7}$	128668.790	42.8	2.245×10^{-5}	1.47 (0.05)
$^{34}SO_2$	$14_{2,12}$–$14_{1,13}$	129803.360	107.7	2.737×10^{-5}	0.26 (0.03)
$^{34}SO_2$	$12_{1,11}$–$12_{0,12}$	132114.040	76.2	1.837×10^{-5}	0.44 (0.03)
$^{34}SO_2$	$5_{1,5}$–$4_{0,4}$	133471.470	15.5	2.107×10^{-5}	4.35 (0.03)
$^{34}SO_2$	$6_{2,4}$–$6_{1,5}$	134826.120	28.8	2.268×10^{-5}	1.74 (0.03)

Table 3.1: Continued.

Molecule	Transition QNs	$\nu_{\rm rest}$ (MHz)	$E_{\rm u}$ (K)	$A_{\rm ul}$ s^{-1}	$\int T_{\rm ant}^{*}\,dv$ (K km s^{-1})
$^{34}SO_2$	$12_{1,11}$–$11_{2,10}$	134873.840	76.2	1.054×10^{-5}	0.32 (0.02)
$^{34}SO_2$	$4_{2,2}$–$4_{1,3}$	141158.760	18.7	2.219×10^{-5}	1.86 (0.05)
$^{34}SO_2$	$2_{2,0}$–$2_{1,1}$	146020.420	12.2	1.687×10^{-5}	1.21 (0.04)
$^{34}SO_2$	$3_{2,2}$–$3_{1,3}$	153015.053	15.0	2.290×10^{-5}	2.46 (0.04)
$^{34}SO_2$	$5_{2,4}$–$5_{1,5}$	160143.612	23.2	2.839×10^{-5}	3.11 (0.03)
$^{34}SO_2$	$10_{0,10}$–$9_{1,9}$	162020.376	49.6	4.100×10^{-5}	3.14 (0.03)
$^{34}SO_2$	$7_{1,7}$–$6_{0,6}$	162775.880	26.9	3.976×10^{-5}	6.00 (0.04)
$^{34}SO_2$	$7_{2,6}$–$7_{1,7}$	170546.952	35.1	3.373×10^{-5}	2.07 (0.05)
$^{34}SO_2$	$3_{2,2}$–$2_{1,1}$	203225.140	15.0	6.204×10^{-5}	5.49 (0.10)
$^{34}SO_2$	$12_{0,12}$–$11_{1,11}$	204136.228	69.9	9.021×10^{-5}	—[b]
$^{34}SO_2$	$14_{3,11}$–$14_{2,12}$	215999.655	118.1	9.440×10^{-5}	0.32 (0.04)
$^{34}SO_2$	$11_{1,11}$–$10_{0,10}$	219355.009	60.1	1.110×10^{-4}	3.18 (0.07)
$^{34}SO_2$	$13_{2,12}$–$13_{1,13}$	221735.715	92.5	6.131×10^{-5}	0.70 (0.07)
$^{34}SO_2$	$12_{3,9}$–$12_{2,10}$	227031.881	93.1	1.014×10^{-4}	0.79 (0.07)
$^{34}SO_2$	$4_{2,2}$–$3_{1,3}$	229857.628	18.7	7.141×10^{-5}	5.39 (0.15)
$^{34}SO_2$	$5_{2,4}$–$4_{1,3}$	235927.500	23.2	7.878×10^{-5}	6.87 (0.09)
$^{34}SO_2$	$8_{3,5}$–$8_{2,6}$	241985.449	54.4	1.075×10^{-4}	1.90 (0.07)
$^{34}SO_2$	$14_{0,14}$–$13_{1,13}$	244481.517	93.5	1.662×10^{-4}	1.49 (0.05)
$^{34}SO_2$	$15_{2,14}$–$15_{1,15}$	245178.728	118.7	7.629×10^{-5}	0.40 (0.05)
$^{34}SO_2$	$6_{3,3}$–$6_{2,4}$	245302.239	40.6	1.023×10^{-4}	2.54 (0.07)
$^{34}SO_2$	$4_{3,1}$–$4_{2,2}$	246686.119	30.5	8.363×10^{-5}	1.48 (0.04)
$^{34}SO_2$	$3_{3,1}$–$3_{2,2}$	247127.390	26.8	5.971×10^{-5}	1.85 (0.05)
$^{34}SO_2$	$5_{3,3}$–$5_{2,4}$	247440.298	35.1	9.682×10^{-5}	3.56 (0.06)
$^{34}SO_2$	$7_{3,5}$–$7_{2,6}$	248364.763	47.0	1.105×10^{-4}	2.35 (0.07)
$^{34}SO_2$	$13_{1,13}$–$12_{0,12}$	248698.698	81.8	1.721×10^{-4}	2.30 (0.05)
$^{34}SO_2$	$4_{4,0}$–$5_{3,3}$	250156.049	47.1	5.482×10^{-6}	0.16 (0.03)
$^{34}SO_2$	$9_{3,7}$–$9_{2,8}$	250358.493	62.6	1.194×10^{-4}	1.27 (0.05)
$^{34}SO_2$	$13_{3,11}$–$13_{2,12}$	259617.206	104.9	1.381×10^{-4}	0.60 (0.06)
$^{34}SO_2$	$7_{2,6}$–$6_{1,5}$	265554.051	35.1	1.038×10^{-4}	4.65 (0.07)
$^{34}SO_2$	$6_{2,4}$–$5_{1,5}$	276999.605	28.8	9.365×10^{-5}	4.5 (0.2)
$^{34}SO_2$	$16_{0,16}$–$15_{1,15}$	283183.556	120.5	2.717×10^{-4}	1.07 (0.05)
$^{34}SO_2$	$9_{2,8}$–$8_{1,7}$	292257.222	50.6	1.360×10^{-4}	2.59 (0.06)
$^{34}SO_2$	$3_{3,1}$–$2_{2,0}$	304332.030	26.8	3.113×10^{-4}	4.58 (0.06)
$^{34}SO_2$	$17_{1,17}$–$16_{0,16}$	311485.378	135.5	3.700×10^{-4}	0.48 (0.06)
$^{34}SO_2$	$11_{2,10}$–$10_{1,9}$	316339.787	69.7	1.763×10^{-4}	—[b]
$^{34}SO_2$	$8_{2,6}$–$7_{1,7}$	330191.103	42.8	1.186×10^{-4}	2.2 (0.2)
$^{34}SO_2$	$5_{3,3}$–$4_{2,2}$	342208.857	35.1	3.101×10^{-4}	4.36 (0.09)
$^{34}SO_2$	$19_{1,19}$–$18_{0,18}$	344581.045	167.4	5.162×10^{-4}	0.45 (0.06)
$^{34}SO_2$	$11_{4,8}$–$11_{3,9}$	344998.160	98.5	3.051×10^{-4}	0.84 (0.09)
$^{34}SO_2$	$8_{4,4}$–$8_{3,5}$	345168.664	70.9	2.754×10^{-4}	0.81 (0.06)
$^{34}SO_2$	$7_{4,4}$–$7_{3,5}$	345519.656	63.6	2.591×10^{-4}	1.12 (0.09)
$^{34}SO_2$	$6_{4,2}$–$6_{3,3}$	345553.093	57.2	2.346×10^{-4}	0.52 (0.06)

Table 3.1: Continued.

Molecule	Transition QNs	$\nu_{\rm rest}$ (MHz)	$E_{\rm u}$ (K)	$A_{\rm ul}$ $\rm s^{-1}$	$\int T_{\rm ant}^{*}\,dv$ (K km $\rm s^{-1}$)
$^{34}SO_2$	$5_{4,2}$–$5_{3,3}$	345651.293	51.7	1.965×10^{-4}	0.57 (0.07)
$^{33}SO_2$	$8_{1,7}$–$8_{0,8}$	83345.818	36.7	6.678×10^{-6}	0.32 (0.05)
$^{33}SO_2$	$3_{1,3}$–$2_{0,2}$	103000.258	7.7	9.766×10^{-6}	0.58 (0.04)
$^{33}SO_2$	$10_{1,9}$–$10_{0,10}$	104301.966	54.6	1.108×10^{-5}	0.22 (0.03)
$^{33}SO_2$	$8_{2,6}$–$8_{1,7}$	131247.049	43.0	2.367×10^{-5}	0.30 (0.02)
$^{33}SO_2$	$5_{1,5}$–$4_{0,4}$	134550.979	15.6	2.156×10^{-5}	1.03 (0.03)
$^{33}SO_2$	$6_{2,4}$–$6_{1,5}$	137478.134	29.0	2.392×10^{-5}	0.36 (0.03)
$^{33}SO_2$	$4_{2,2}$–$4_{1,3}$	143795.870	18.8	2.338×10^{-5}	0.34 (0.04)
$^{33}SO_2$	$2_{2,0}$–$2_{1,1}$	148614.406	12.4	1.777×10^{-5}	0.24 (0.03)
$^{33}SO_2$	$3_{2,2}$–$3_{1,3}$	155523.945	15.2	2.405×10^{-5}	0.41 (0.02)
$^{33}SO_2$	$10_{0,10}$–$9_{1,9}$	161452.956	49.6	4.029×10^{-5}	0.58 (0.03)
$^{33}SO_2$	$5_{2,4}$–$5_{1,5}$	162562.342	23.4	2.974×10^{-5}	1.11 (0.03)
$^{33}SO_2$	$7_{1,7}$–$6_{0,6}$	163964.985	27.0	4.053×10^{-5}	1.57 (0.02)
$^{33}SO_2$	$3_{2,2}$–$2_{1,1}$	205876.481	15.2	6.450×10^{-5}	1.96 (0.08)
$^{33}SO_2$	$11_{1,11}$–$10_{0,10}$	220619.072	60.2	1.123×10^{-4}	2.01 (0.07)
$^{33}SO_2$	$11_{5,7}$–$12_{4,8}$	221328.839	120.9	1.715×10^{-5}	0.22 (0.04)
$^{33}SO_2$	$4_{2,2}$–$3_{1,3}$	232419.835	18.8	7.404×10^{-5}	1.4 (0.2)
$^{33}SO_2$	$5_{2,4}$–$4_{1,3}$	238683.410	23.4	8.154×10^{-5}	1.33 (0.06)
$^{33}SO_2$	$8_{3,5}$–$8_{2,6}$	246455.769	54.8	1.133×10^{-4}	0.47 (0.04)
$^{33}SO_2$	$6_{3,3}$–$6_{2,4}$	249650.188	41.0	1.077×10^{-4}	0.54 (0.05)
$^{33}SO_2$	$13_{1,13}$–$12_{0,12}$	249907.904	82.0	1.738×10^{-4}	0.73 (0.04)
$^{33}SO_2$	$4_{3,1}$–$4_{2,2}$	250978.790	30.9	8.801×10^{-5}	0.40 (0.04)
$^{33}SO_2$	$3_{3,1}$–$3_{2,2}$	251401.862	27.2	6.282×10^{-5}	0.51 (0.03)
$^{33}SO_2$	$5_{3,3}$–$5_{2,4}$	251702.803	35.5	1.018×10^{-4}	0.37 (0.04)
$^{33}SO_2$	$7_{3,5}$–$7_{2,6}$	252591.694	47.4	1.161×10^{-4}	0.63 (0.05)
$^{33}SO_2$	$7_{2,6}$–$6_{1,5}$	268450.516	35.3	1.071×10^{-4}	1.56 (0.12)
$^{33}SO_2$	$6_{2,4}$–$5_{1,5}$	279434.518	29.0	9.686×10^{-5}	2.66 (0.08)
$^{33}SO_2$	$15_{1,15}$–$14_{0,14}$	280557.119	107.2	2.588×10^{-4}	0.35 (0.05)
$^{33}SO_2$	$9_{2,8}$–$8_{1,7}$	295322.165	50.8	1.400×10^{-4}	0.68 (0.05)
$^{33}SO_2$	$5_{4,2}$–$5_{3,3}$	351635.237	52.4	2.067×10^{-4}	1.77 (0.14)
HNCO	$4_{0,4}$–$3_{0,3}$	87925.237	10.5	9.025×10^{-6}	1.11 (0.04)
HNCO	$5_{1,5}$–$4_{1,4}$	109495.996	59.0	1.692×10^{-5}	0.07 (0.03)
HNCO	$5_{0,5}$–$4_{0,4}$	109905.749	15.8	1.802×10^{-5}	2.10 (0.05)
HNCO	$6_{1,6}$–$5_{1,5}$	131394.230	65.3	3.006×10^{-5}	0.18 (0.02)
HNCO	$6_{0,6}$–$5_{0,5}$	131885.734	22.2	3.163×10^{-5}	2.90 (0.04)
HNCO	$6_{1,5}$–$5_{1,4}$	132356.701	65.5	3.072×10^{-5}	0.13 (0.03)
HNCO	$7_{1,7}$–$6_{1,6}$	153291.935	72.7	4.863×10^{-5}	0.19 (0.03)
HNCO	$7_{0,7}$–$6_{0,6}$	153865.086	29.5	5.078×10^{-5}	3.71 (0.05)
HNCO	$7_{1,6}$–$6_{1,5}$	154414.765	72.9	4.971×10^{-5}	0.21 (0.03)
HNCO	$10_{0,10}$–$9_{0,9}$	219798.274	58.0	1.510×10^{-4}	4.39 (0.09)
HNCO	$11_{1,11}$–$10_{1,10}$	240875.727	112.6	1.957×10^{-4}	0.22 (0.06)
HNCO	$11_{0,11}$–$10_{0,10}$	241774.032	69.6	2.019×10^{-4}	4.52 (0.09)

Table 3.1: Continued.

Molecule	Transition QNs	$\nu_{\rm rest}$ (MHz)	$E_{\rm u}$ (K)	$A_{\rm ul}$ s^{-1}	$\int T_{\rm ant}^{*}\, dv$ (K km s^{-1})
HNCO	$12_{1,12}$–$11_{1,11}$	262769.477	125.3	2.554×10^{-4}	0.18 (0.05)
HNCO	$12_{0,12}$–$11_{0,11}$	263748.625	82.3	2.630×10^{-4}	2.72 (0.13)
HNCO	$13_{1,13}$–$12_{1,12}$	284662.172	138.9	3.261×10^{-4}	0.15 (0.04)
HNCO	$13_{0,13}$–$12_{0,12}$	285721.951	96.0	3.355×10^{-4}	3.36 (0.12)[b]
HNCO	$14_{0,14}$–$13_{0,13}$	307693.905	110.8	4.200×10^{-4}	1.22 (0.10)
HNCS	$8_{0,8}$–$7_{0,7}$	93830.070	20.3	1.217×10^{-5}	0.16 (0.03)
HNCS	$9_{0,8}$–$8_{0,7}$	105558.076	25.3	1.744×10^{-5}	0.19 (0.03)
HNCS	$11_{0,8}$–$10_{0,7}$	129013.259	37.2	3.215×10^{-5}	0.26 (0.03)
HNCS	$12_{0,8}$–$11_{0,7}$	140740.378	43.9	4.189×10^{-5}	0.21 (0.03)
HNCS	$13_{0,8}$–$12_{0,7}$	152467.142	51.2	5.342×10^{-5}	0.23 (0.03)
HNCS	$14_{0,8}$–$13_{0,7}$	164193.523	59.1	6.690×10^{-5}	0.25 (0.02)
HC_3N	9–8	81881.46210	19.6	4.215×10^{-5}	0.25 (0.05)
HC_3N	10–9	90978.98877	24.0	5.812×10^{-5}	0.32 (0.03)
HC_3N	11–10	100076.38486	28.8	7.770×10^{-5}	0.37 (0.03)
HC_3N	12–11	109173.63729	34.1	1.012×10^{-4}	-
HC_3N	15–14	136464.40210	52.4	1.993×10^{-4}	0.28 (0.03)
HC_3N	16–15	145560.94935	59.4	2.424×10^{-4}	0.23 (0.04)
HC_3N	17–16	154657.28766	66.8	2.912×10^{-4}	0.16 (0.03)
HC_3N	18–17	163753.40398	74.7	3.463×10^{-4}	0.19 (0.02)
NO	$\Pi^{+}(3/2,5/2) \rightarrow (1/2,3/2)$	150176.457	7.2	3.310×10^{-7}	
NO	$\Pi^{+}(3/2,3/2) \rightarrow (1/2,1/2)$	150198.757	7.2	1.839×10^{-7}	
NO	$\Pi^{+}(3/2,3/2) \rightarrow (1/2,3/2)$	150218.742	7.2	1.471×10^{-7}	0.89 (0.06)
NO	$\Pi^{+}(3/2,1/2) \rightarrow (1/2,1/2)$	150225.650	7.2	2.943×10^{-7}	
NO	$\Pi^{+}(3/2,1/2) \rightarrow (1/2,3/2)$	150245.635	7.2	3.679×10^{-8}	
NO	$\Pi^{-}(3/2,3/2) \rightarrow (1/2,1/2)$	150644.349	7.2	1.853×10^{-7}	0.16 (0.03)
NO	$\Pi^{+}(5/2,7/2) \rightarrow (3/2,5/2)$	250436.841	19.2	1.841×10^{-6}	
NO	$\Pi^{+}(5/2,5/2) \rightarrow (3/2,3/2)$	250440.653	19.2	1.547×10^{-6}	
NO	$\Pi^{+}(5/2,3/2) \rightarrow (3/2,1/2)$	250448.526	19.2	1.381×10^{-6}	3.06 (0.10)
NO	$\Pi^{+}(5/2,3/2) \rightarrow (3/2,3/2)$	250475.419	19.2	4.420×10^{-7}	
NO	$\Pi^{+}(5/2,5/2) \rightarrow (3/2,5/2)$	250482.939	19.2	2.947×10^{-7}	
NO	$\Pi^{-}(5/2,7/2) \rightarrow (3/2,5/2)$	250796.423	19.3	1.849×10^{-6}	
NO	$\Pi^{-}(5/2,5/2) \rightarrow (3/2,3/2)$	250815.610	19.3	1.554×10^{-6}	2.86 (0.09)
NO	$\Pi^{-}(5/2,3/2) \rightarrow (3/2,1/2)$	250816.930	19.3	1.387×10^{-6}	
NO	$\Pi^{+}(7/2,9/2) \rightarrow (5/2,7/2)$	350689.526	36.1	5.418×10^{-6}	
NO	$\Pi^{+}(7/2,7/2) \rightarrow (5/2,5/2)$	350690.687	36.1	4.976×10^{-6}	
NO	$\Pi^{+}(7/2,5/2) \rightarrow (5/2,3/2)$	350694.797	36.1	4.815×10^{-6}	3.0 (0.2)
NO	$\Pi^{+}(7/2,5/2) \rightarrow (5/2,5/2)$	350729.583	36.1	5.897×10^{-7}	
NO	$\Pi^{+}(7/2,7/2) \rightarrow (5/2,7/2)$	350736.778	36.1	4.423×10^{-7}	
NO	$\Pi^{-}(7/2,9/2) \rightarrow (5/2,7/2)$	351043.518	36.1	5.433×10^{-6}	
NO	$\Pi^{-}(7/2,7/2) \rightarrow (5/2,5/2)$	351051.517	36.1	4.990×10^{-6}	2.1 (0.2)
NO	$\Pi^{-}(7/2,5/2) \rightarrow (5/2,3/2)$	351051.962	36.1	4.830×10^{-6}	
HCO^{+}	1–0	89188.526	4.3	4.234×10^{-5}	4.56 (0.05)

Table 3.1: Continued.

Molecule	Transition QNs	$\nu_{\rm rest}$ (MHz)	$E_{\rm u}$ (K)	$A_{\rm ul}$ s^{-1}	$\int T_{\rm ant}^{*}\,dv$ (K km s^{-1})
HCO^+	3–2	267557.626	25.7	1.470×10^{-3}	9.1 (0.3)^b
$H^{13}CO^+$	1–0	86754.288	4.2	3.897×10^{-5}	0.50 (0.05)
$H^{13}CO^+$	3–2	260255.338	25.0	1.353×10^{-3}	1.85 (0.11)
$H^{13}CO^+$	4–3	346998.336	41.6	3.325×10^{-3}	0.76 (0.10)
SO^+	Ω=1/2,e,(7/2)–(5/2)	162198.598	16.7	1.108×10^{-4}	0.64 (0.04)
SO^+	Ω=1/2,f,(9/2)–(7/2)	208965.420	26.8	2.457×10^{-4}	0.50 (0.08)
SO^+	Ω=1/2,e,(11/2)–(9/2)	254977.935	38.9	4.566×10^{-4}	0.55 (0.15)
SO^+	Ω=1/2,e,(15/2)–(13/2)	347740.011	70.1	1.189×10^{-3}	0.25 (0.15)^t
N_2H^+	1–0	93173.399	4.5	3.628×10^{-5}	0.54 (0.04)
N_2H^+	3–2	279511.752	26.8	1.259×10^{-3}	1.17 (0.10)
H_3O^+	1_1^-–2_1^+	307192.410	79.5	3.498×10^{-4}	0.28 (0.09)

Notes. (Col. 2) Quantum numbers of the corresponding line; (Col. 6) Integrated intensity (in antenna temperature) of the line with its formal uncertainty; (Col. 7) Expansion velocity derived from the linewidth with its uncertainty which includes the width of half a channel (1 MHz) except for the lines with a low S/N where a full channel (2 MHz) is included. The uncertainties given (within parentheses) do not include additional uncertainties derived from the absolute flux calibration and baseline subtraction. (b) Blended. (t) Tentative .

3.4.3 Rotational diagrams

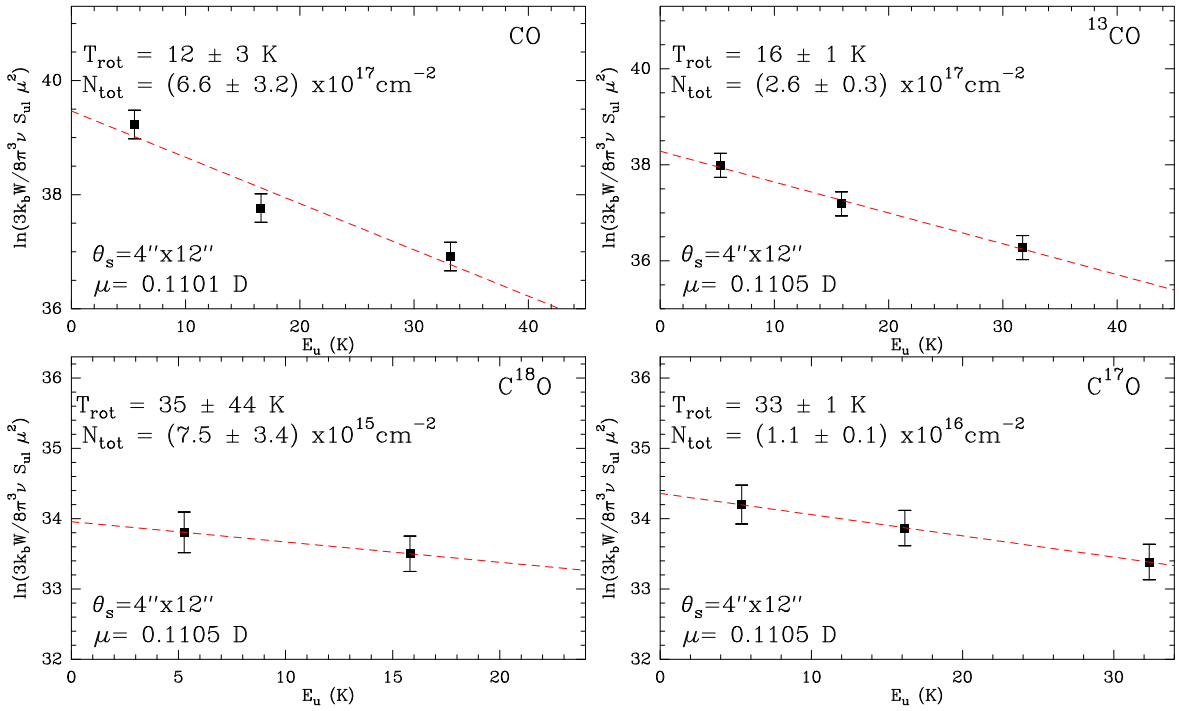

Figure 3.2: Population diagrams for CO isotopologues. The results from the fit (red dashed line) are shown in each box. The emission size adopted and the dipole moment of the molecule are shown in the bottom-left corner of each box. Error bars include the formal uncertainty of the measurement and a 25% uncertainty due to flux calibration or poor baseline subtraction.

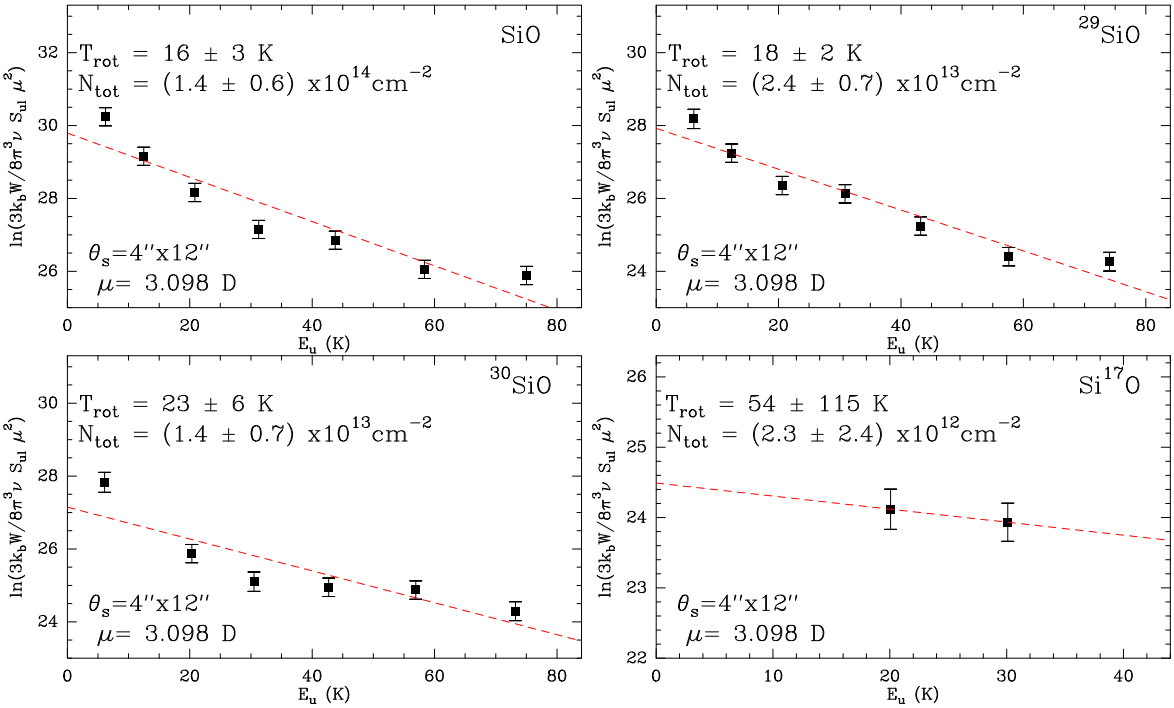

Figure 3.3: As in Fig. 3.2 but for SiO isotopologues.

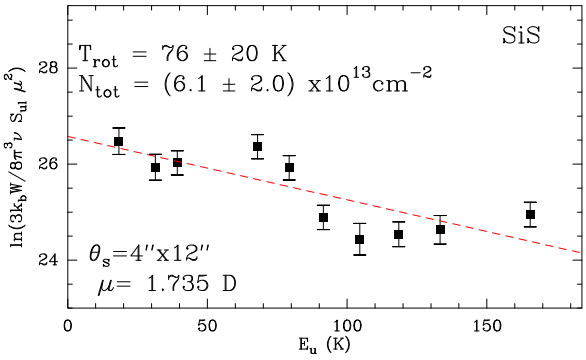

Figure 3.4: As in Fig. 3.2 but for SiS.

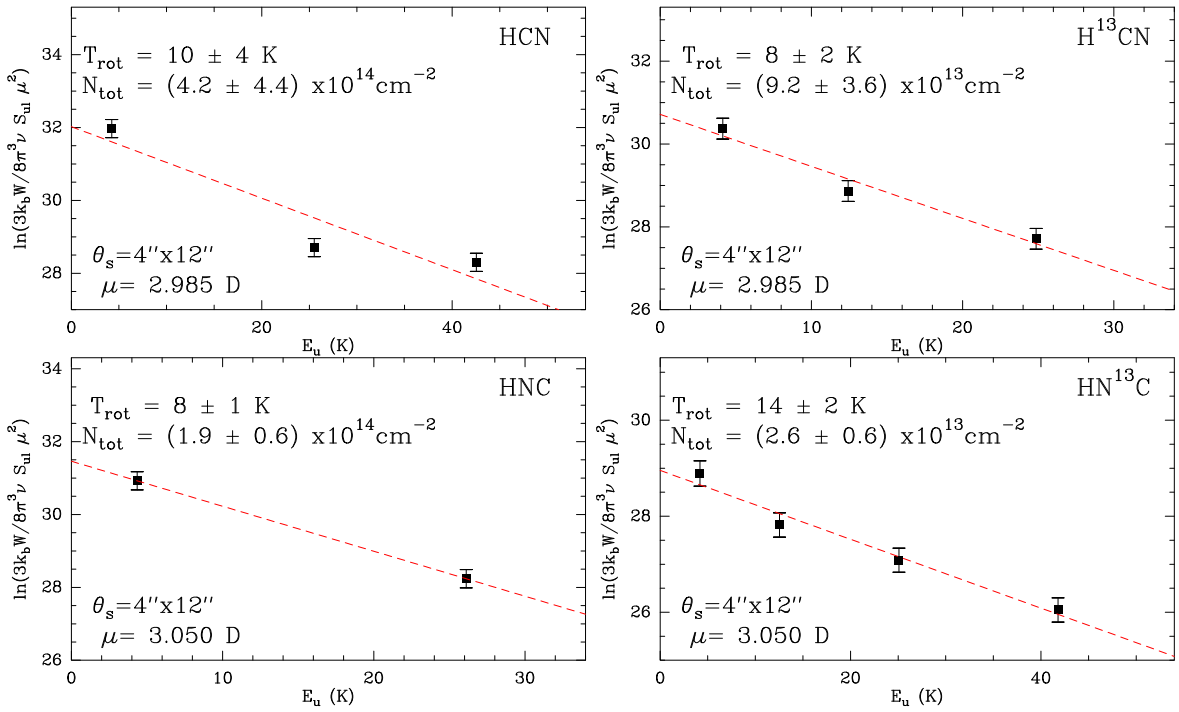

Figure 3.5: As in Fig. 3.2 but for HCN and HNC isotopologues.

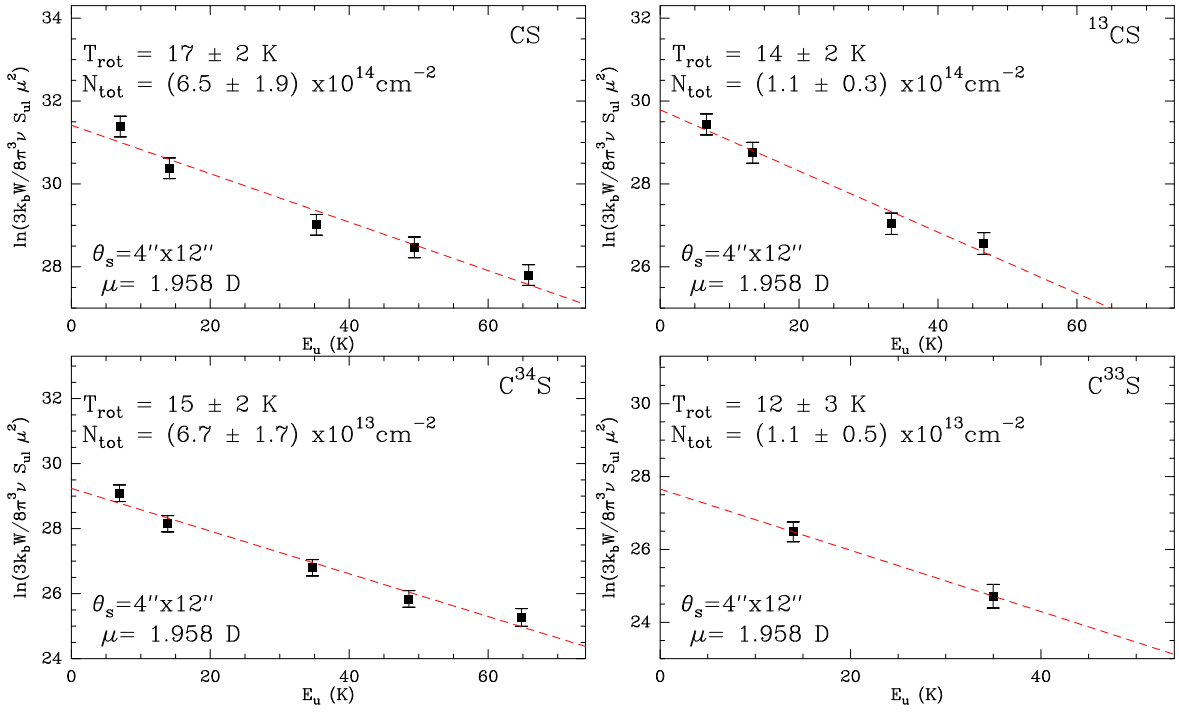

Figure 3.6: As in Fig. 3.2 but for CS isotopologues.

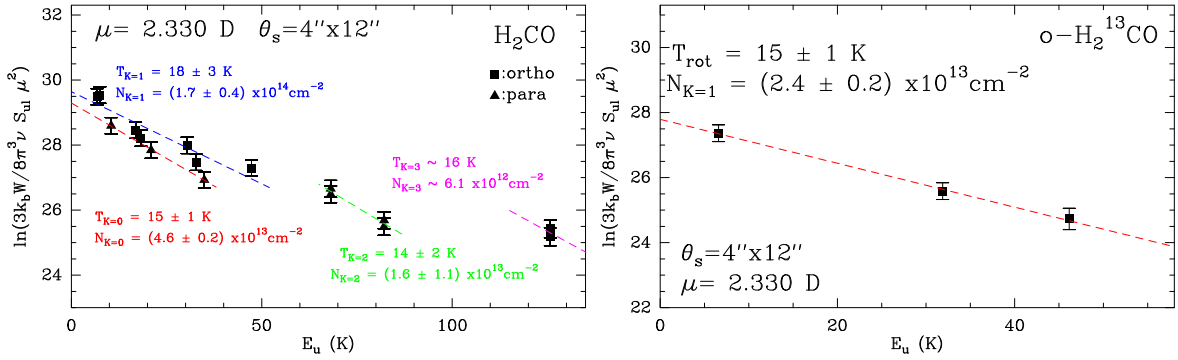

Figure 3.7: Population diagram for H_2CO and o-$H_2^{13}CO$. For H_2CO we show the results from the fits of the rotational ladders K_a=0 (red) and K_a=1 (blue), and K_a=2 (green). For the K_a=3 (pink) we adopted as rotational temperature the average of the rotational temperatures of the K_a=0, 1, and 2 ladders to estimate a rough value for the K_a=3 column density.

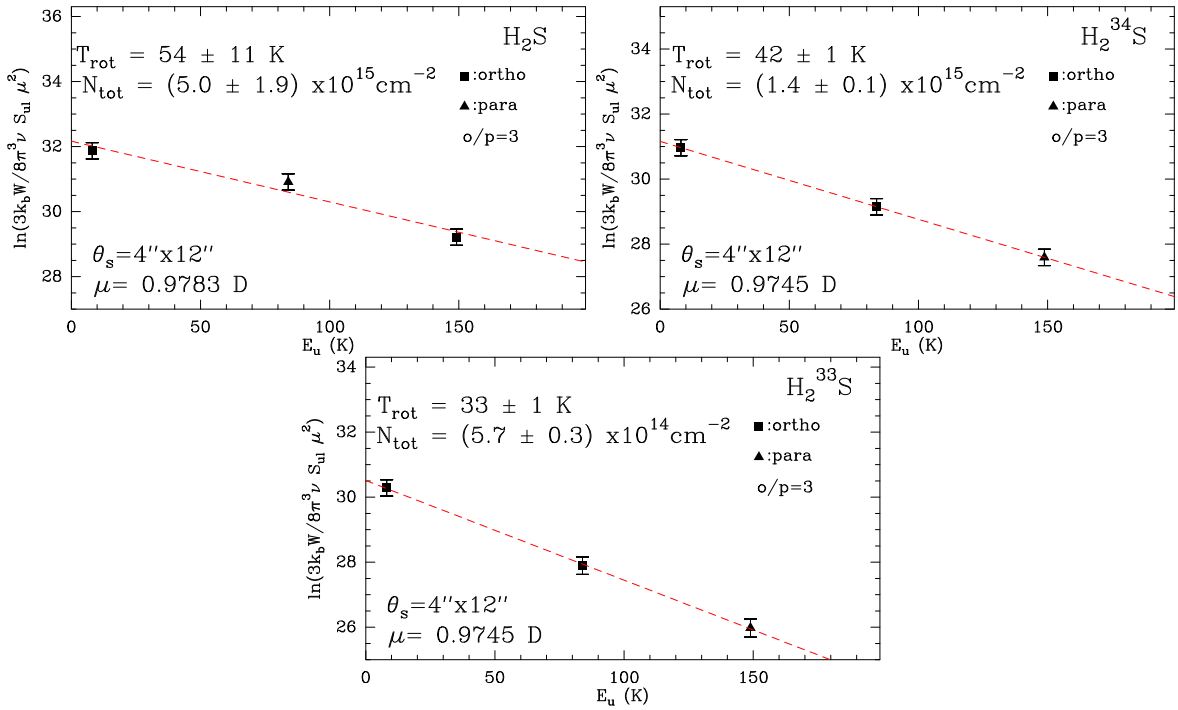

Figure 3.8: As in Fig. 3.2 but for H_2S. We fitted simultaneously the ortho and para species adopting an ortho-to-para ratio of 3:1.

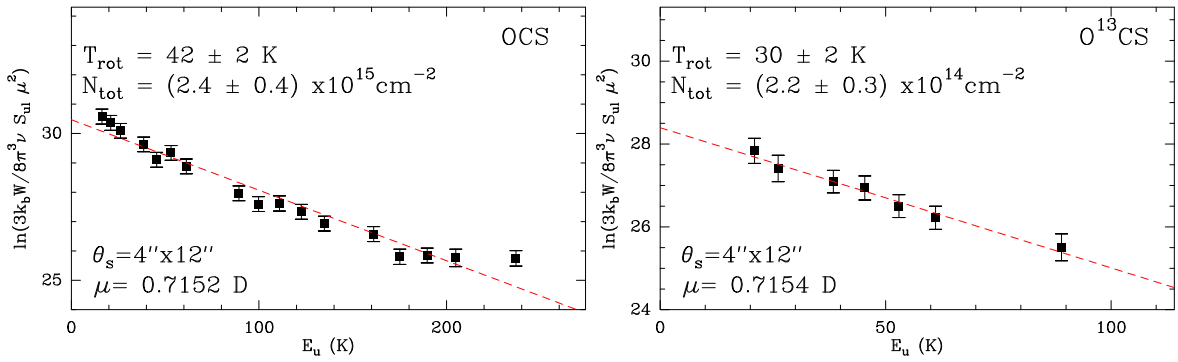

Figure 3.9: As in Fig. 3.2 but for OCS isotopologues.

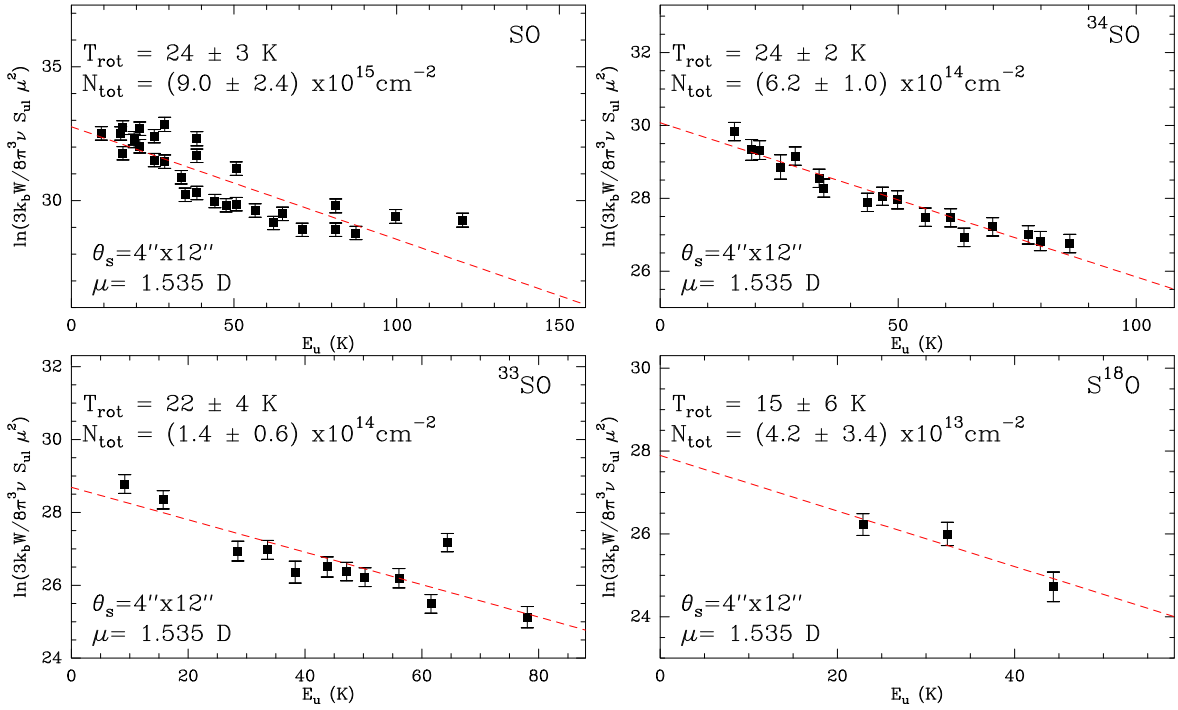

Figure 3.10: As in Fig. 3.2 but for SO isotopologues.

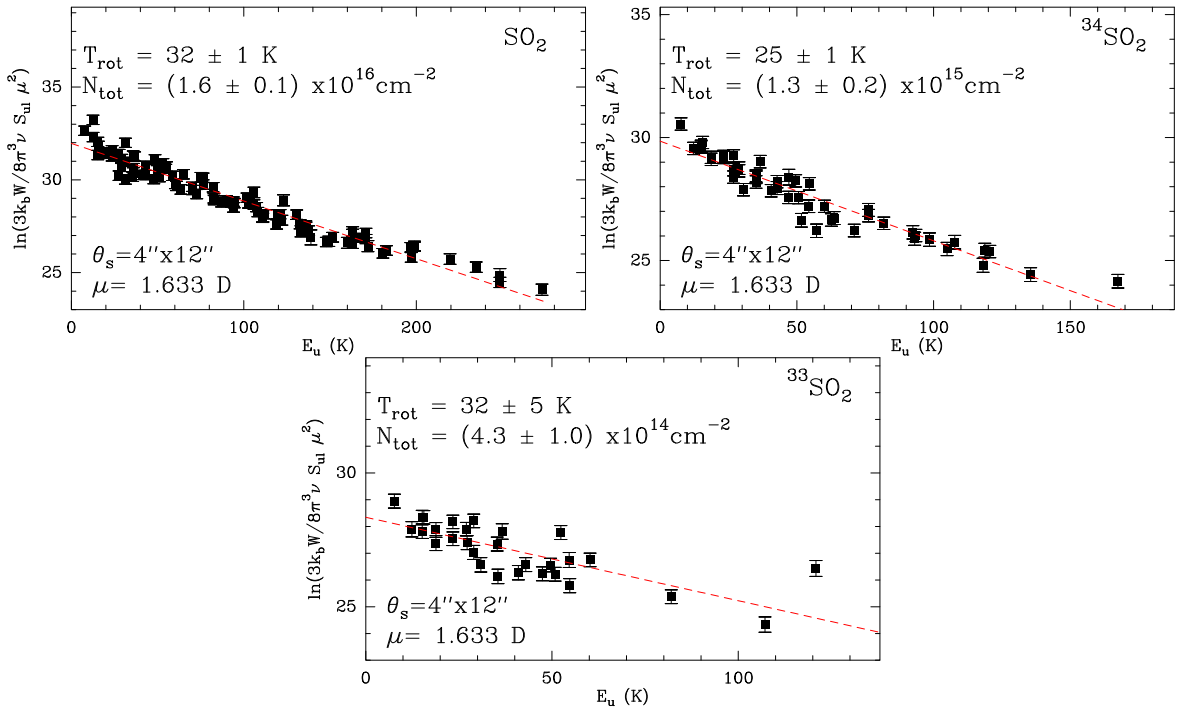

Figure 3.11: As in Fig. 3.2 but for SO_2 isotopologues.

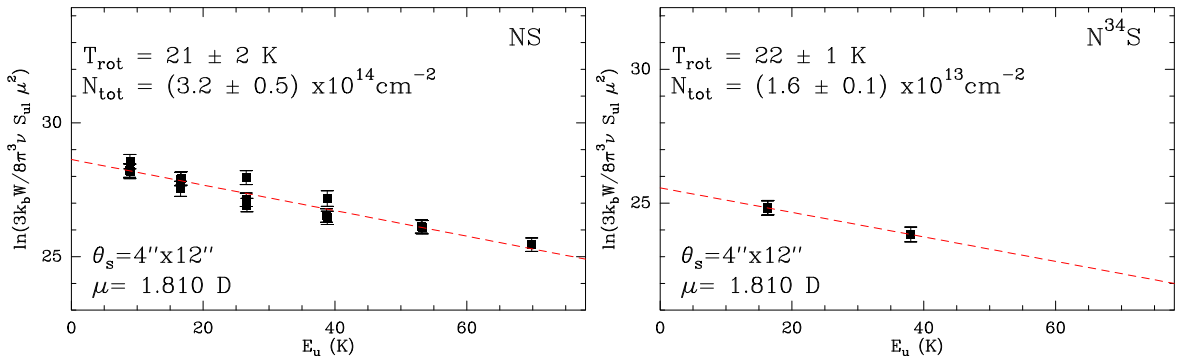

Figure 3.12: As in Fig. 3.2 but for NS isotopologues.

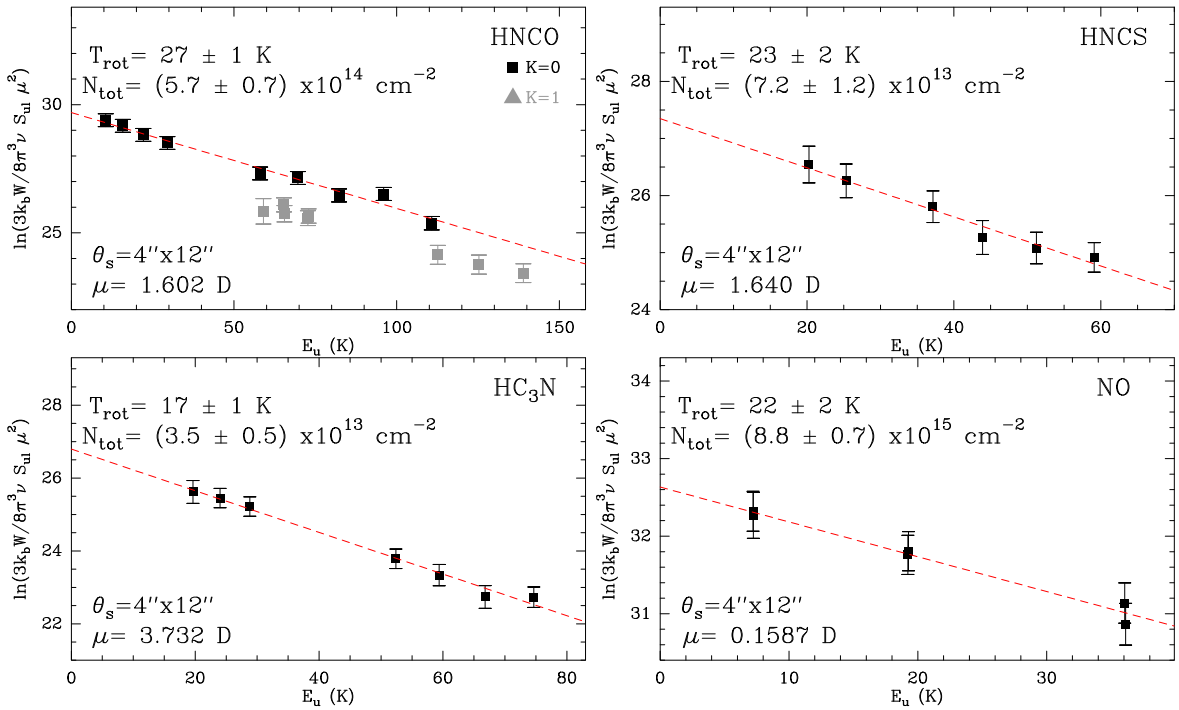

Figure 3.13: As in Fig. 3.2 but for previously reported N-bearing molecules (Velilla Prieto et al., 2015a).

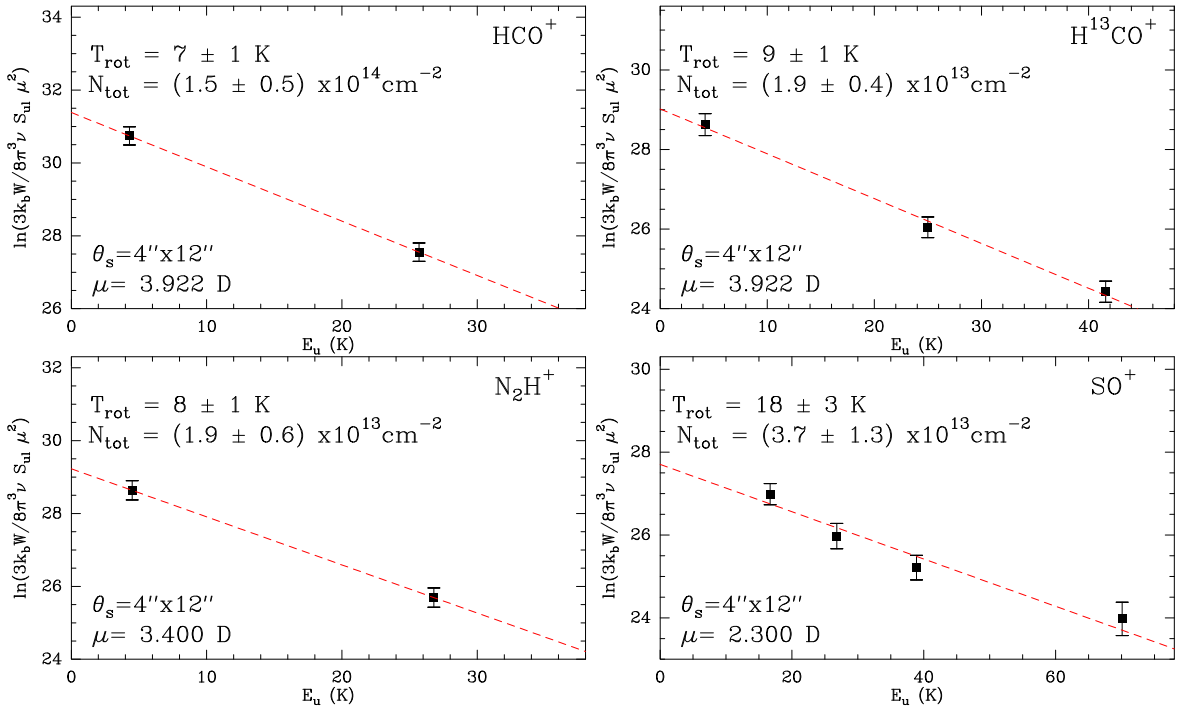

Figure 3.14: As in Fig. 3.2 but for previously reported ions (Sánchez Contreras et al., 2015).

3.4.4 Abundances and isotopic ratios

Table 3.2: Results from the rotational diagrams, sorted according to the molecular fractional abundance (relative to H_2) in descending order.

Molecule	T_{rot}	Column density	Abundance
-	(K)	(cm^{-2})	-
CO	12 (3)	$\gtrsim$6.6 (3.2)×10^{17}	$\gtrsim$1.3×10^{-4}
^{13}CO	16 (1)	2.6 (0.3)×10^{17}	5.0×$10^{-5\dagger}$
SO_2	32 (1)	1.6 (0.1)×10^{16}	3.1×10^{-6}
C^{17}O	33 (1)	1.1 (0.1)×10^{16}	2.1×10^{-6}
NO	22 (2)	8.8 (0.7)×10^{15}	1.7×10^{-6}
SO	24 (3)	9.0 (2.4)×10^{15}	1.7×10^{-6}
C^{18}O	35 (44)	7.5 (3.4)×10^{15}	1.4×10^{-6}
H_2S	54 (11)	5.0 (1.9)×10^{15}	9.6×10^{-7}
OCS	42 (2)	2.4 (0.4)×10^{15}	4.6×10^{-7}
$H_2{}^{34}S$	42 (1)	1.4 (0.1)×10^{15}	2.7×10^{-7}
$^{34}SO_2$	25 (1)	1.3 (0.2)×10^{15}	2.5×10^{-7}
CS	17 (2)	6.5 (1.9)×10^{14}	1.2×10^{-7}
^{34}SO	24 (2)	6.2 (1.0)×10^{14}	1.2×10^{-7}
$H_2{}^{33}S$	33 (1)	5.7 (0.3)×10^{14}	1.1×10^{-7}
HNCO	27 (1)	5.7 (0.7)×10^{14}	1.1×10^{-7}
$^{33}SO_2$	32 (5)	4.3 (1.0)×10^{14}	8.3×10^{-8}
HCN	10 (4)	4.2 (4.4)×10^{14}	8.1×10^{-8}
NS	21 (2)	3.2 (0.5)×10^{14}	6.2×10^{-8}
H_2CO	16 (2)	2.4 (0.6)×10^{14}	4.6×10^{-8}
O^{13}CS	30 (2)	2.2 (0.3)×10^{14}	4.2×10^{-8}
HNC	8 (1)	1.9 (0.6)×10^{14}	3.6×10^{-8}
HCO^+	7 (1)	1.5 (0.5)×10^{14}	2.9×10^{-8}
SiO	16 (3)	$\gtrsim$1.4 (0.6)×10^{14}	$\gtrsim$2.7×10^{-8}
^{33}SO	22 (4)	1.4 (0.6)×10^{14}	2.7×10^{-8}
^{13}CS	14 (2)	1.1 (0.3)×10^{14}	2.1×10^{-8}
H^{13}CN	8 (2)	9.2 (3.6)×10^{13}	1.8×10^{-8}
HNCS	23 (2)	7.2 (1.2)×10^{13}	1.4×10^{-8}
C^{34}S	15 (2)	6.7 (1.7)×10^{13}	1.3×10^{-8}
SiS	76 (20)	6.1 (2.0)×10^{13}	1.2×10^{-8}
S^{18}O	15 (6)	4.2 (3.4)×10^{13}	8.1×10^{-9}
SO^+	18 (3)	3.7 (1.3)×10^{13}	7.1×10^{-9}
HC_3N	17 (1)	3.5 (0.5)×10^{13}	6.7×10^{-9}
HN^{13}C	14 (2)	2.6 (0.6)×10^{13}	5.0×10^{-9}
^{29}SiO	18 (2)	$\gtrsim$2.4 (0.7)×10^{13}	$\gtrsim$4.6×10^{-9}
o-$H_2{}^{13}$CO	15 (1)	2.4 (0.2)×10^{13}	4.6×10^{-9}
N_2H^+	8 (1)	1.9 (0.6)×10^{13}	3.7×10^{-9}
H^{13}CO$^+$	9 (1)	1.9 (0.4)×10^{13}	3.7×10^{-9}
N^{34}S	22 (1)	1.6 (0.1)×10^{13}	3.1×10^{-9}
^{30}SiO	23 (6)	1.4 (0.7)×10^{13}	2.7×10^{-9}

Table 3.2: Continued.

Molecule	T_{rot}	Column density	Abundance
-	(K)	(cm^{-2})	-
$C^{33}S$	12 (3)	1.1 (0.5)$\times10^{13}$	2.1×10^{-9}
$Si^{17}O$	54 (115)	2.3 (2.4)$\times10^{12}$	4.4×10^{-10}

†Reference value from Morris et al. (1987a).

Table 3.3: Isotopic ratios obtained from the population diagrams.

Ratio	Value	From
$^{12}C/^{13}C$	$\gtrsim$3	CO
$^{12}C/^{13}C$	5	HCN
$^{12}C/^{13}C$	7	HNC
$^{12}C/^{13}C$	6	CS
$^{12}C/^{13}C$	11	OCS
$^{12}C/^{13}C$	8	HCO^+
$^{16}O/^{18}O$	>88	CO
$^{16}O/^{18}O$	214	SO
$^{16}O/^{17}O$	>60	CO
$^{16}O/^{17}O$	>61	SiO
$^{28}Si/^{29}Si$	$\gtrsim$6	SiO
$^{28}Si/^{30}Si$	$\gtrsim$10	SiO
$^{32}S/^{34}S$	10	CS
$^{32}S/^{34}S$	15	SO
$^{32}S/^{34}S$	12	SO_2
$^{32}S/^{34}S$	4	H_2S
$^{32}S/^{34}S$	20	NS
$^{32}S/^{33}S$	59	CS
$^{32}S/^{33}S$	64	SO
$^{32}S/^{33}S$	37	SO_2
$^{32}S/^{33}S$	9	H_2S

CHAPTER

4

NEW N-BEARING SPECIES TOWARD OH231.8+4.2

In this chapter we present the comprehensive study of the new discovered nitrogen bearing species HNCO, HNCS, HC_3N, and NO toward OH231.8+4.2. This work is based on the IRAM-30 m line survey of the source briefly introduced in Chapter 3. We analysed the excitation conditions and abundances by using the population diagram technique, as well as the non-LTE deviations with MADEX. We also modelled the chemistry of these species. The N-chemistry enhancement in O-rich circumstellar envelopes cannot be explained as a result of standard chemical processes. This enhancement is probably a consequence of the shocks that the source has experienced. This work has been published in Velilla Prieto et al. (2015a).

4.1 Summary

The CSE of OH231 (Sect. 1.4.1.2) shows an exceptionally rich chemistry compared to other objects of its class (O-rich CSEs of evolved stars), displaying emission of molecules like HCN, HCO^+ or CN (Morris et al., 1987a, Sánchez Contreras et al., 1997, Ziurys et al., 2009). The chemical processes that lead the formation of these and other molecules in O-rich CSEs are not well understood yet. In this article, we analyse the detection of HNCO, HNCS, HC_3N, and NO toward OH231, as a part of the millimeter wavelength survey carried out with the IRAM-30 m radiotelescope (see Chapter 3).

HNCO was previously detected in different astrophysical environments as Sgr B2, TMC-1, the shocked outflow of the YSO L1157, hot cores, and other objects (e.g. Snyder & Buhl, 1972, Brown, 1981, Rodríguez-Fernández et al., 2010, Martín et al., 2008). This molecule has been used as a dense gas tracer, and more recently, as a shock tracer (Jackson et al., 1984, Rodríguez-Fernández et al., 2010). HNCS was detected toward Sgr B2 by (Frerking et al., 1979), and recently in TMC-1 by Adande et al. (2010), where the authors also reviewed its gas phase chemistry. HC_3N was detected toward several astrophysical environments that include Sgr B2, dark clouds, protoplanetary disks, the CSE IRC+10216, and more (e.g. Turner, 1971a, Morris et al., 1976, Cernicharo et al., 1984, 2000). This molecule is considered as a dense gas tracer (Morris et al., 1976), and particularly in the CSE of IRC+10216, it seems to be efficiently formed through chemical reactions that involve the photodissociation products of HCN (Audinos et al., 1994). Finally, NO was also detected toward different sources (e.g. Gerin et al., 1992, Halfen et al., 2001, Akyilmaz et al., 2007), including the circumstellar envelope of the massive YHG star IRC+10420 ($\sim 50 M_\odot$) (Quintana-Lacaci et al., 2013). Chem-

ical models predict that this molecule is efficiently formed in the outer parts of the envelopes through the reaction between N and OH.

Our work represents the first time that emission lines of HNCO and HNCS are detected in a CSE, i.e. OH231, and also this is the first time that HC_3N is detected toward an O-rich CSE.

➢ We made the following analysis:

- measurement of the velocity integrated intensities of the spectral lines detected, and study of their profiles (linewidths and temperatures). For the particular case of NO, we compared the line profiles observed with a synthetic model created with MADEX (see Sec 2.2), to analyse the origin and characteristics of its emission,

- calculation of the rotational diagrams (see Sect. 2.1) of the detected molecules, in order to estimate their excitation temperatures and column densities, which allowed us to obtain their abundances averaged in the emitting region,

- analysis of possible non-LTE excitation effects. We created LVG models with MADEX for a range of kinetic temperatures, column densities, and H_2 densities, which were compared with the derived results from the LTE rotational diagrams for a number of molecules,

- chemical modelling of the CSE of OH231 in order to reproduce the observed abundances (for the detected molecules) using two different models: *i*) TE models (which are valid close to the photosphere of the star, see Sect. 2.3), and *ii*) a chemical kinetics model applied from the dust condensation region ($\sim 10^{15}$ cm) up to the end of the CSE ($\sim 10^{17}$ cm), where only gas phase processes, UV ISRF photodissociation, and cosmic rays are taken into account (see Sect. 2.3). Gas-grain interactions and shock-induced processes are not considered. HNCS has not been included in these models since there are neither thermodynamical information nor kinetic coefficients of the molecule. Nevertheless, we scaled its abundance with the predicted abundance for HNCO (as a rough approximation) using the O/S ratio in the Sun, ∼37 (Asplund et al., 2009). We incorporated the reactions and kinetic constants of HNCO to our chemical code according to Quan et al. (2010),

- the chemical kinetic models have been calculated for two different physical models: *i*) one for the central component, which corresponds to the slowly expanding AGB CSE, and *ii*) a second model for the extended fast lobes,

- we evaluated the effect that could cause the increase of the ionising/dissociating radiation (UV) in the chemical kinetic models, which could be caused due to the presence of the T_{eff} ∼10000 K stellar companion (see Sect. 1.4.1.2),

- we also evaluated the effect of a N-abundance enhancement of the initial abundances (possibly caused by HBB) on the chemical models.

➢ We obtained the following results:

- HNCO K_a=0 lines seem to arise not only from the central component (with FWHM∼25-30 km s^{-1}), but also from the South lobe of the object; HNCO K_a=1 lines (with FWHM∼10-15 km s^{-1}) seem to arise only from the central component; HNCS K_a=0 lines are narrower (FWHM$\lesssim$25 km s^{-1}) and less intense than HNCO K_a=0 lines, and they arise from the central component of the CSE; HC_3N lines have linewidths of FWHM∼20 km s^{-1} and they seem to

arise from the central component of the CSE, although, there is tentative emission at velocities of v_{LSR}∼60-65 km s^{-1}, which indicates that it is also present at the South lobe of the source; finally, the NO lines (which have hyperfine structure), display larger linewidths than the rest of the analysed molecules, and they seem to be redshifted. The broadening of the NO lines detected cannot be only explained due to its hyperfine structure. Hence, the redshift (∼+10 or 15 km s^{-1}) of the lines may indicate that this molecule is particularly abundant in the OH231's South lobe,

- rotational diagrams (under LTE approximation) show low rotational temperatures (∼15-30 K) and abundances (obtained with the column densities) of 2×10^{-6} for NO, 1×10^{-7} for HNCO, 1×10^{-8} for HNCS, and 7×10^{-9} for HC_3N. In particular for the rotational diagram of HNCO, a separation between the HNCO K_a=0 trend and the K_a=1 trend is observed,

- the rotational temperatures and column densities derived for HNCO, HNCS, and NO through the non-LTE analysis (measured for a wide range of n_{H_2} values, from 10^4 cm^{-3} up to LTE values), are similar to the results obtained under LTE approximation, except for HC_3N. HC_3N rotational temperature may be consistent with a higher value (T_{rot}∼50 K). We also observed that the separation between the fit of the HNCO K_a=0 lines and the fit of the K_a=1 lines (in the rotational diagram), varies with the H_2 density. In particular, both fits coincide in a single line under LTE conditions, and they separate progressively into two parallel lines as the H_2 density decreases,

- TE chemical models predict lower abundances than those derived from rotational diagrams. Chemical kinetic models only reproduce the abundances observed for NO, which should be efficiently formed in the outermost parts of the AGB CSE, and also in the lobes of the nebula after characteristic times consistent with the dynamical age of the fast lobes (or shock-accelerated lobes),

- the effect caused by the extra UV photons emitted by the A0 V companion star would be comparable or inferior than the effect caused by UV ISRF, thus, its inclusion in the chemical models is unable to explain the differences between the observed abundances and the abundances predicted by the models,

- the discrepancies found between the abundances derived from the rotational diagram and the abundances predicted by the TE chemical model cannot be explained even when the N abundance is enhanced, being the predictions much lower than the rotational diagram results. For the case of chemical kinetic models, HNCO and HNCS abundances are still predicted lower than the abundances derived from the rotational diagrams, while the NO abundance is predicted one order of magnitude higher than the values derived by the rotational diagrams.

➢ After the interpretation of these results, we can extract the following conclusions:

- we found that HNCO, HNCS, HC_3N, and NO are present and abundant in the envelope of OH231. All these molecules have been detected for the first time in this source and, particularly, HNCO and HNCS represent first detections in CSEs,

- HNCO K_a=1 and HNCS emission lines seem to arise only from the central and dense regions of the nebula, while HNCO K_a=0, NO, and probably HC_3N, seem to arise from the central dense region but also from the South lobe of the nebula,

- derived rotational temperatures (∼15-30 K) are consistent with previous estimations in the CO outflow,
- the abundance derived for NO is very high and comparable to the abundances of molecules like SO or SO_2 ($\sim 10^{-6}$); the abundance derived for HNCO ($\sim 10^{-7}$) is also remarkable, being comparable to other molecules like the C-bearing molecules H_2CO, CS, or HCN,
- from the observed separation between the fit of the K_a=0 and K_a=1 HNCO lines in the rotational diagram, we derived $n(H_2) \sim 4 \times 10^7$ cm^{-3}. For this value of H_2 density, the excitation of the detected molecules may be considered as LTE or conditions close to LTE, which is also indicated by the critical densities of the lines, except perhaps for HC_3N. In the case of HC_3N we cannot rule out subthermal excitation,
- standard chemical models are unable to reproduce the abundances derived from the rotational diagrams (except probably for NO in the case of chemical kinetic models in the outer parts of the CSE). Additionally, there are not other detections of HNCO, HNCS, and HC_3N toward different O-rich CSEs. Therefore, we conclude that probably the interaction between the high speed jets (∼400 km s^{-1}) and the standard AGB CSE caused the chemical changes observed in this object. Shock-induced processes may alter the standard chemistry observed for example in IK Tau (Chapter 3), i.e. shocks may dissociate the slow expanding AGB CSE material or extract material from the dust grains, and after the passage of shocks new molecules are formed.

4.2 Resumen

La envoltura circunestelar de OH231.8+4.2 (ver Sec. 1.4.1.2) muestra una química excepcionalmente rica comparada con otros objetos de su clase (envolturas de estrellas evolucionadas ricas en oxígeno), detectándose en ella por ejemplo moléculas como HCN, HCO^+ o CN (Morris et al., 1987a, Sánchez Contreras et al., 1997, Ziurys et al., 2009). Aún no se conocen bien los procesos químicos que conducen a la formación de éstas y otras moléculas en envolturas ricas en oxígeno. En este artículo, tratamos la detección de las moléculas HNCO, HNCS, HC_3N y NO en OH231, como parte del barrido espectral en el rango de longitud de onda milimétrico llevado a cabo con el radiotelescopio IRAM-30 m (ver Capítulo 3).

HNCO ha sido detectado en diferentes entornos astrofísicos como Sgr B2, TMC-1, en el flujo chocado del YSO L1157, hot cores, y otros objetos (e.g. Snyder & Buhl, 1972, Brown, 1981, Rodríguez-Fernández et al., 2010, Martín et al., 2008). Esta molécula ha sido utilizada como trazador de gas denso, y más recientemente, como trazador de choques (Jackson et al., 1984, Rodríguez-Fernández et al., 2010). HNCS, ha sido detectada en Sgr B2 (Frerking et al., 1979) y recientemente en TMC-1, donde además se ha revisado su química en fase gas (Adande et al., 2010). HC_3N también ha sido detectada en distintos entornos astrofísicos que incluyen Sgr B2, nubes oscuras, discos protoplanetarios, en la envoltura circunestelar de IRC+10216, etc (e.g. Turner, 1971a, Morris et al., 1976, Cernicharo et al., 1984, 2000). Esta molécula se considera un trazador de gas denso (Morris et al., 1976), y en particular para IRC+10216, parece formarse como consecuencia de la reacción de los productos de fotodisociación del HCN (Audinos et al., 1994). Por último, NO también ha sido detectada en diferentes entornos (e.g. Gerin et al., 1992, Halfen et al., 2001, Akyilmaz et al., 2007), incluyendo la envoltura circunestelar de la estrella masiva YHG IRC+10420 ($\sim 50 M_\odot$) (Quintana-Lacaci et al., 2013). Los modelos químicos predicen que esta molécula se forma eficientemente en las zonas externas de las envolturas a través de la reacción entre el N y el OH.

Nuestro trabajo representa la primera vez que se detectan líneas de HNCO y HNCS en una envoltura circunestelar, i.e. OH231, y también es la primera vez que se detecta HC_3N en una envoltura rica en oxígeno.

➢ El análisis que hemos llevado acabo se divide en los siguientes pasos:

- medida de las intensidades integradas en velocidad de las líneas espectrales y estudio de sus perfiles (anchuras y temperaturas). En el caso particular de NO, hemos comparado los perfiles observados con un modelo sintético creado con MADEX (ver Sec 2.2) para analizar el origen y características de la emisión de esta molécula,

- cálculo de los diagramas de rotación (ver Sec. 2.1) de las moléculas detectadas, para estimar sus temperaturas de excitación y densidades de columna (que nos permite obtener sus abundancias) promediadas para la región emisora,

- estudio de los posibles efectos de excitación en condiciones de no-ETL, para lo cual, hemos creado modelos LVG para un rango de temperaturas cinéticas, densidades de columna y densidades de H_2, con MADEX (ver Sec 2.2), que han sido comparados con los resultados derivados de los diagramas de rotación en aproximación ETL para un determinado número de moléculas,

- modelización química de la envoltura de OH231.8+4.2 para explicar las abundancias observadas de las moléculas detectadas, mediante dos modelos distintos: *i*) en condiciones de equili-

brio termodinámico (válido en las zonas más cercanas a la fotosfera estelar, ver Sec. 2.3), y *ii*) un modelo de cinética química aplicado desde la zona de condensación de polvo ($\sim 10^{15}$ cm) hasta el final de la envoltura ($\sim 10^{17}$ cm), donde sólo se tienen en cuenta los procesos en fase gas, la fotodisociación por el UV ISRF y por rayos cósmicos (ver Sec. 2.3), y no se considera la interacción gas-grano ni los procesos de choque. Al no existir datos termodinámicos para el HNCS, ni coeficientes cinéticos, no ha sido incluido en nuestros modelos, no obstante podemos escalar la abundancia predicha de HNCS con la de HNCO (como aproximación grosera) teniendo en cuenta que O/S$\sim$37 (Asplund et al., 2009). Las reacciones de HNCO y sus constantes cinéticas se han incorporado en nuestro modelo según el trabajo realizado por Quan et al. (2010),

- los modelos de cinética química se han subdividido en dos modelos físicos: *i*) uno para la componente central del objeto, que correspondería con la envoltura circunestelar AGB de expansión lenta, y *ii*) otro para los lóbulos extensos de alta velocidad,

- se ha evaluado el efecto del incremento de la radiación ionizante/disociante (UV) en los modelos de cinética química, que podría generar la presencia de una estrella compañera de T_{eff} $\sim$10000 K (ver Sec. 1.4.1.2),

- hemos evaluado el efecto de un incremento de N (que podría explicarse por procesos de HBB) en las abundancias iniciales utilizadas en los modelos químicos.

➢ Los principales resultados extraídos del análisis son los siguientes:

- las líneas de HNCO K_a=0 parecen proceder no sólo de la parte central de la nebulosa (con FWHM$\sim$25-30 km s^{-1}), sino que además detectamos emisión de HNCO en el lóbulo Sur del objeto, mientras que las líneas de K_a=1 (con FWHM$\sim$10-15 km s^{-1}) sólo aparecen en la componente central; las líneas de HNCS K_a=0 son menos intensas y más estrechas (con FWHM$\lesssim$25 km s^{-1}) y parecen provenir sólo de la componente central, y no detectamos líneas de HNCS K_a=1; las líneas de HC_3N tienen anchuras típicas de FWHM$\sim$20 km s^{-1} y parecen proceder de la componente central de la envoltura, si bien se detecta emisión tentativa a velocidades de $v_{LSR}\sim$60-65 km s^{-1} lo que indicaría que también se observa en el lóbulo Sur; por último, las líneas de NO, que tienen estructura hiperfina, muestran perfiles más anchos que el resto de moléculas analizadas, y además parecen estar ligeramente desplazadas al rojo. Estos resultados de NO, parece que no pueden ser explicados como consecuencia de un simple ensanchamiento por la estructura hiperfina de la molécula, y que el desplazamiento al rojo (de unos $\sim$+10 ó 15 km s^{-1}) de las líneas es real, lo que podría indicar que la emisión de esta molécula es particularmente importante en el lóbulo Sur de OH231,

- los diagramas de rotación (bajo la aproximación de ETL) muestran temperaturas rotacionales bajas ($\sim$15-30 K) y abundancias (obtenidas a través de las densidades de columna de los diagramas) de 2×10^{-6} para NO, 1×10^{-7} para HNCO, 1×10^{-8} para HNCS y de 7×10^{-9} para HC_3N. En particular, se observa una separación en el diagrama de rotación de HNCO entre la tendencia marcada por las líneas de K_a=0 y las líneas de K_a=1,

- en condiciones fuera del ETL (medidas para un rango amplio de valores de n_{H_2}, desde 10^4 cm^{-3} hasta valores de ETL), los resultados de temperatura de rotación y densidad de columna obtenidos para HNCO, HNCS y NO son similares a los obtenidos bajo la aproximación ETL, sólo la emisión de HC_3N podría ser compatible con una temperatura de rotación

algo más elevada ($T_{\rm rot}$∼50 K). Además se observa que la separación entre los ajustes a los diagramas de rotación de las líneas de las escaleras rotacionales $K_{\rm a}$=0 y $K_{\rm a}$=1 de HNCO, varía con la densidad de H_2 considerada. En particular, en condiciones de ETL ambos ajustes coinciden en una única recta y se van separando en dos rectas paralelas conforme disminuimos la densidad, siendo cada vez mayor la distancia de separación,

- los modelos químicos de equilibrio termodinámico predicen abundancias muy inferiores a las que se derivan de los diagramas rotacionales. Los modelos de cinética química sólo predicen abundancias compatibles con las observadas para NO, que se formaría eficientemente en la parte externa de la envoltura circunestelar AGB, y también en los lóbulos del objeto tras tiempos característicos compatibles con la edad dinámica de dichos lóbulos de alta velocidad,

- el efecto producido en la química debido al flujo de fotones UV que emitiría una estrella compañera A0 V sería comparable o inferior al efecto producido por el UV ISRF, por lo que su inclusión en los modelos es incapaz de explicar las diferencias entre las abundancias observadas y las abundancias que predicen los modelos,

- en el caso del enriquecimiento de N, las discrepancias entre las abundancias obtenidas por los diagramas de rotación y las que predice el modelo en equilibrio termodinámico no pueden explicarse incluso aumentando la abundancia inicial de N, siendo aún las predicciones muy bajas. En el caso de aplicarlo al modelo de cinética química, las abundancias de HNCO y HNCS se predicen todavía inferiores comparadas con los resultados de los diagramas, mientras que la abundancia del NO aumentaría hasta f(NO)∼10^{-5} que sería un orden de magnitud superior a la abundancia determinada mediante los diagramas de rotación.

➢ Después de interpretar estos resultados, podemos concluir que:

- encontramos que las moléculas HNCO, HNCS, HC_3N y NO están presentes de manera abundante en la envoltura de OH231. Todas estas moléculas han sido descubiertas por primera vez en este objeto, y en particular, HNCO y HNCS representan primeras detecciones en envolturas circunestelares,

- detectamos por primera vez en este objeto líneas de emisión de HNCO, HNCS, HC_3N y NO, además, es la primera vez que se detecta HNCO y HNCS en una envoltura circunestelar,

- la emisión de las líneas de HNCO $K_{\rm a}$=1 y de HNCS parece provenir únicamente de la región más densa y central de la nebulosa, mientras que para HNCO $K_{\rm a}$=0, NO, y en menor medida HC_3N, además de la componente central densa, detectamos emisión que proviene del lóbulo Sur de la nebulosa,

- las temperaturas rotacionales derivadas (∼15-30 K) son compatibles con estimaciones previas en el flujo de CO,

- la abundancia determinada para NO es alta y comparable con las abundancias de moléculas muy abundantes en este objeto como SO y SO_2 (∼10^{-6}); la abundancia determinada para HNCO (∼10^{-7}) también es destacable, siendo equiparable a las de otras moléculas que contienen carbono como H_2CO, CS o HCN,

- de la separación observada entre los ajustes de las líneas con K_a=0 y K_a=1 de HNCO en el diagrama de rotación, se infiere que la emisión de HNCO sería compatible con $n(H_2)\sim4\times10^7\,cm^{-3}$. Para esa densidad, la emisión de las moléculas detectadas puede considerarse en ETL o en condiciones muy cercanas al ETL como indican las densidades críticas de las líneas, excepto quizá para HC_3N, para el cual no puede descartarse excitación sub-térmica,

- los modelos químicos estándar son incapaces de reproducir las abundancias estimadas mediante los diagramas rotacionales (excepto quizá para NO por cinética química en la parte externa de la envoltura). Adicionalmente, no se ha detectado emisión de HNCO, HNCS, y HC_3N en otras envolturas estándar ricas en oxígeno. Por tanto, concluimos que probablemente la interacción previa entre los chorros de alta velocidad ($\sim$400 km s^{-1}) y la envoltura AGB estándar, es responsable de la alteración química observada en este objeto. Los procesos de choque y, probablemente, de interacción con los granos de polvo, alterarían la química estándar como la que se observa en IK Tau (Capítulo 3), i.e. el choque disociaría el material de la envoltura AGB central de expansión lenta, y tras el paso del choque se formarían éstas y otras moléculas.

4.3 Velilla Prieto et al. 2015a[1]

A&A 575, A84 (2015)
DOI: 10.1051/0004-6361/201424768
© ESO 2015

Astronomy & Astrophysics

New N-bearing species towards OH 231.8+4.2

HNCO, HNCS, HC_3N, and NO⋆,⋆⋆

L. Velilla Prieto[1,2], C. Sánchez Contreras[2], J. Cernicharo[1,3], M. Agúndez[1,3,4], G. Quintana-Lacaci[1,3], J. Alcolea[5], V. Bujarrabal[6], F. Herpin[4], K. M. Menten[7], and F. Wyrowski[7]

[1] Grupo de Astrofísica Molecular. Instituto de Ciencia de Materiales de Madrid, CSIC, c/ Sor Juana Inés de la Cruz 3, 28049 Cantoblanco, Madrid, Spain
e-mail: lvelilla@icmm.csic.es
[2] Centro de Astrobiología, INTA-CSIC, 28691 Villanueva de la Cañada, Madrid, Spain
[3] Centro de Astrobiología, INTA-CSIC, Ctra. de Torrejón a Ajalvir km 4, 28850 Torrejón de Ardoz, Madrid, Spain
[4] Université de Bordeaux, LAB, UMR 5804, 33270 Floirac, France
[5] Observatorio Astronómico Nacional (IGN), Alfonso XII No 3, 28014 Madrid, Spain
[6] Observatorio Astronómico Nacional (IGN), Ap 112, 28803 Alcalá de Henares, Madrid, Spain
[7] Max-Planck-Institut für Radioastronomie, Auf dem Hügel 69, 53121 Bonn, Germany

Received 7 August 2014 / Accepted 4 December 2014

ABSTRACT

Circumstellar envelopes (CSEs) around asymptotic giant branch (AGB) stars are the main sites of molecular formation. OH 231.8+4.2 is a well studied oxygen-rich CSE around an intermediate-mass evolved star that, in dramatic contrast to most AGB CSEs, displays bipolar molecular outflows accelerated up to ∼400 km s^{-1}. OH 231.8+4.2 also presents an exceptional molecular richness probably due to shock-induced chemical processes. We report the first detection in this source of four nitrogen-bearing species, HNCO, HNCS, HC_3N, and NO, which have been observed with the IRAM-30 m radiotelescope in a sensitive mm-wavelength survey towards this target. HNCO and HNCS are also first detections in CSEs. The observed line profiles show that the emission arises in the massive (∼0.6 $M_\odot$) central component of the envelope, expanding with low velocities of V_{exp} ∼ 15–30 km s^{-1}, and at the base of the fast lobes. The NO profiles (with *FWHM* ∼ 40–50 km s^{-1}) are broader than those of HNCO, HNCS, and HC_3N and, most importantly, broader than the line profiles of ^{13}CO, which is a good mass tracer. This indicates that the NO abundance is enhanced in the fast lobes relative to the slow, central parts. From LTE and non-LTE excitation analysis, we estimate beam-average rotational temperatures of T_{rot} ∼ 15–30 K (and, maybe, up to ∼55 K for HC_3N) and fractional abundances relative to H_2 of X(HNCO) ∼ [0.8–1] × 10^{-7}, X(HNCS) ∼ [0.9–1] × 10^{-8}, X(HC_3N) ∼ [5–7] × 10^{-9}, and X(NO) ∼ [1–2] × 10^{-6}. NO is, therefore, amongst the most abundant N-bearing species in OH 231.8+4.2. We performed thermodynamical chemical equilibrium and chemical kinetics models to investigate the formation of these N-bearing species in OH 231.8+4.2. The model underestimates the observed abundances for HNCO, HNCS, and HC_3N by several orders of magnitude, which indicates that these molecules can hardly be products of standard UV-photon and/or cosmic-ray induced chemistry in OH 231.8+4.2 and that other processes (e.g. shocks) play a major role in their formation. For NO, the model abundance, ≈10^{-6}, is compatible with the observed average value; however, the model fails to reproduce the NO abundance enhancement in the high-velocity lobes (relative to the slow core) inferred from the broad NO profiles. The new detections presented in this work corroborate the particularly rich chemistry of OH 231.8+4.2, which is likely to be profoundly influenced by shock-induced processes, as proposed in earlier works.

Key words. astrochemistry – line: identification – molecular processes – stars: AGB and post-AGB – circumstellar matter

1. Introduction

For about 40 years, circumstellar chemistry has been a fertile field as a source of new molecular discoveries and the development of physical and chemical models. Circumstellar envelopes (CSEs) around asymptotic giant branch (AGB) stars are formed as the result of the intense mass loss process undergone by these objects. AGB CSEs are composed of molecular gas and dust, standing among the most complex chemical environments in space (Cernicharo et al. 2000; Ziurys 2006, and references therein).

Circumstellar envelopes are classified according to their elemental [C]/[O] ratio, which are carbon-rich or oxygen-rich if the ratio is >1 or <1, respectively (objects with [C]/[O] ∼ 1 are designed as S-type stars). The chemistry of CSEs is very dependent on the relative abundances of oxygen and carbon. In the case of oxygen-rich CSEs, carbon plays the role of "limiting reactant" and is supposed to be almost fully locked up in CO, which is a very abundant and stable species, while the remaining oxygen is free to react with other atoms, thereby forming additional oxygen-bearing molecules. This is why O-rich envelopes are relatively poor in C-bearing molecules other than CO, while C-rich ones show low abundances of O-bearing species (e.g. Bujarrabal et al. 1994).

To date, most of the observational efforts to detect new circumstellar molecules have focused on C-rich sources, which are believed to have a more complex and rich chemistry than

⋆ Based on observations carried out with the IRAM-30 m Telescope. IRAM is supported by INSU/CNRS (France), MPG (Germany), and IGN (Spain).
⋆⋆ Appendices are available in electronic form at http://www.aanda.org

[1] A&A, 575, A84, 2015, reproduced with permission © ESO

A&A 575, A84 (2015)

their oxygen counterparts. The most studied object of this kind is the carbon-rich evolved star IRC+10216 in whose envelope ~80 molecules have been discovered (e.g. Solomon et al. 1971; Morris et al. 1975; Cernicharo & Guelin 1987; Cernicharo et al. 2000; Cabezas et al. 2013). Recent works suggest, however, that O-rich shells may be more chemically diverse than originally thought. For example, some unexpected chemical compounds (e.g. HNC, HCO^+, CS, CN) have been identified in a number of O-rich late-type stars, including the object OH 231.8+4.2 studied in this work (Sánchez Contreras et al. 1997; Ziurys et al. 2009). The chemical processes that lead to the formation of these and other species in O-rich CSEs remain poorly known.

In this paper, we present our recent results for the study of OH 231.8+4.2: an O-rich CSE around an intermediate-mass evolved star that, to date, displays the richest chemistry amongst the objects in its class. We report the detection of HNCO, HNCS, HC_3N, and NO as part of a sensitive molecular line survey of this object in the mm-wavelength range with the IRAM-30 m telescope (Velilla Prieto et al. 2013, full survey data to be published soon by Velilla et al., in prep.). We have detected hundreds of molecular transitions, discovering >30 new species (including different isotopologues) and enlarging the sequence of rotational transitions detected for many others, in this source. This has led to very detailed information on the physico-chemical global structure of this envelope.

OH 231.8+4.2 (Fig. 1), discovered by Turner (1971), is a well-studied bipolar nebula around an OH/IR source[1]. Although its evolutionary stage is not clear owing to its many unusual properties, it is believed to be a planetary nebula (PN) precursor probably caught in a short-lived transitional phase. The obscured central star, named QX Pup, is classified as M9-10 III and has a Mira-like variability consistent with an evolved AGB star (Cohen 1981; Feast et al. 1983; Kastner et al. 1992; Sánchez Contreras et al. 2004). The late evolution of this object may have been complex since it has a binary companion star (of type A0 V) that has been indirectly identified from analysis of the spectrum of the hidden central source reflected by the nebular dust (Cohen et al. 1985; Sánchez Contreras et al. 2004). The system, located at ~1500 pc (Choi et al. 2012), has a total luminosity of $\sim 10^4\ L_\odot$, and its systemic velocity relative to the Local Standard of Rest is $V_{\rm LSR} \sim 34$ km s^{-1}. OH 231.8+4.2 is very likely a member of the open cluster M 46 with a progenitor mass of $\sim 3\ M_\odot$ (Jura & Morris 1985).

Most of the nebular material of OH 231.8+4.2 is in the form of dust and molecular gas, which are best traced by scattered starlight and by the emission from rotational transitions of CO, respectively (see e.g. Sánchez Contreras et al. 1997; Alcolea et al. 2001; Bujarrabal et al. 2002). The molecular gas is cool (~10–40 K over the bulk of the nebula) and massive ($\sim 1\ M_\odot$). With a spatial distribution similar to that of dust, this gas is located in a very elongated and clumpy structure with two major components (Fig. 1): (i) a central core (clump I3) with an angular diameter of ~6–8″, a total mass of $\sim 0.64\ M_\odot$, and low expansion velocity (~6–35 km s^{-1}); and (ii) a highly collimated $\lesssim$6″ × 57″ bipolar outflow, with a total mass of $\sim 0.3\ M_\odot$ and expansion velocities that increase linearly with the distance from the centre, reaching values of up to ~200 and 430 km s^{-1} at the tip of the northern and southern lobes, respectively. The temperature in the lobes is notably low, ~10–20 K (Sánchez Contreras et al. 1997; Alcolea et al. 2001).

[1] OH/IR objects are infrared-bright evolved stellar objects with a dense envelope showing prominent OH maser emission.

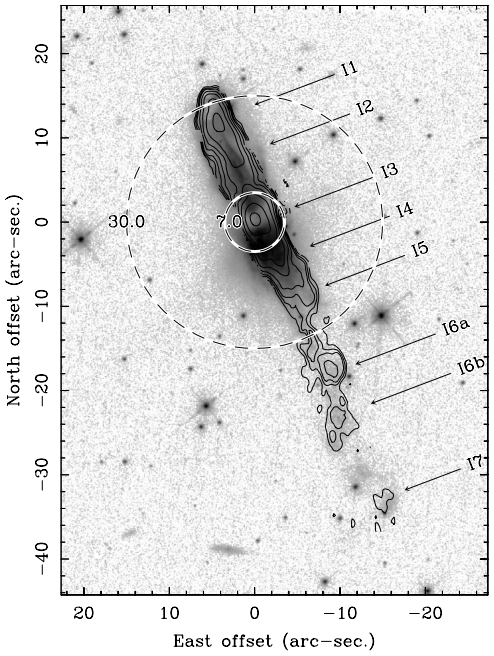

Fig. 1. Composite image of OH 231.8+4.2 displaying: (grey scale) the dust distribution as observed with HST/WFPC2 and the broad-band *F791W* filter (Bujarrabal et al. 2002); (contours) the molecular outflow as traced by the ^{12}CO (2–1) emission (velocity integrated) mapped with 1.″5 × 0.″7-resolution (see Fig. 4 in Alcolea et al. 2001). The dashed circles show the area covered by the largest and smallest telescope beams (HPBW) of the IRAM-30 m observations presented in this work. The different emitting clumps, I1-I7, are labelled as in Alcolea et al. (2001). The $V_{\rm LSR}$ range (in km s^{-1}) of each clump is I1) [−80:−30], I2) [−30:+10], I3) [+10:+55], I4) [+55:+80], I5) [+80:+150], I6a) [+150:+205], I6b) [+205:+230], and I7) [+230:+285] (see Table 2 in Alcolea et al. 2001, for more details on the physical properies of the clumps).

A shock-excited atomic/ionized gas nebulosity, hotter (~10 000 K) but far less massive ($\sim 2 \times 10^{-3}\ M_\odot$), surrounds the front edges of the molecular outflow delineating two inflated bubble-like, asymmetric lobes (not shown in Fig. 1; see Reipurth 1987; Sánchez Contreras et al. 2000a; Bujarrabal et al. 2002; Sánchez Contreras et al. 2004).

The molecular envelope of OH 231.8+4.2 is remarkably different from the slow, roughly round winds of most AGB stars; however, its pronounced axial symmetry, high expansion velocities, and the presence of shocks are common in objects that have left the AGB phase and are evolving to the PN stage, so-called pre-PNs (Neri et al. 1998; Bujarrabal et al. 2001; Castro-Carrizo et al. 2010; Sánchez Contreras & Sahai 2012). It is believed that the nebula of OH 231.8+4.2 was created as the result of a huge mass loss that occurred during the late-AGB evolution of the primary at a rate of $\dot{M} \approx 10^{-4}\ M_\odot$ yr^{-1}. With a total linear momentum of $\sim 27\ M_\odot$ km s^{-1}, the bipolar flow is interpreted as the result of a sudden axial acceleration of the envelope. It is probable that such an acceleration resulted from the violent collision between underlying jets (probably emanating from the stellar companion) on the slowly expanding AGB envelope (Sánchez Contreras et al. 2000b, 2004; Alcolea et al. 2001; Bujarrabal et al. 2002); this is one plausible scenario that

has been proposed to explain the shaping and acceleration of bipolar pre-PNs and PNs (e.g. Sahai & Trauger 1998; Balick & Frank 2002). Recently, Sabin et al. (2014) have found indications of a well-organized magnetic field parallel to the major axis of the CO-outflow that could point to a magnetic-outflow launching mechanism. As mentioned by these authors, the magnetic field could have, alternatively, been dragged by the fast outflow, which may have been launched by a different mechanism. The linear distance-velocity relation observed in the CO-outflow (with a projected velocity gradient of $\nabla V \sim 6.5$ km s^{-1} arcsec^{-1}) suggests that the acceleration of the lobes took place ∼800 yr ago in less than ∼150 yr. The low-velocity central core is thought to be the fossil remnant of the AGB CSE.

OH 231.8+4.2 is the chemically richest CSE around an O-rich low/intermediate mass evolved star. In addition to the typical oxygen-rich content, with molecules such as H_2O, OH, or SiO (Bowers & Morris 1984; Morris et al. 1987; Zijlstra et al. 2001; Sánchez Contreras et al. 2002; Desmurs et al. 2007), it displays strong lines of many different molecular species, including many containing carbon. The full inventory of the molecules reported in OH 231.8+4.2 prior to our survey are ^{12}CO, ^{13}CO, SO, SO_2, H_2O, OH, SiO, H_2S, HCN, H^{13}CN, HNC, CS, HCO$^+$, H^{13}CO$^+$,OCS, H_2CO, NH_3, and NS (Ukita & Morris 1983; Guilloteau et al. 1986; Morris et al. 1987; Omont et al. 1993; Sánchez Contreras et al. 1997, 2000b; Lindqvist et al. 1992, and references therein). High-angular resolution mapping of the HCO$^+$ (J = 1–0) emission indicates that this ion is present in abundance in the fast lobes (Sánchez Contreras et al. 2000b). Based on single-dish maps of the SiO (J = 5–4) emission, the abundance of this molecule could also be enhanced in the lobes (Sánchez Contreras et al. 1997). The spectrum of OH 231.8+4.2 is unusually rich, even for O-rich CSEs' standards, in lines from S- and N-bearing molecules (for example, it was the first O-rich CSE in which H_2S, NS, CS, and OCS were detected.) Some of these S- and N-compounds are present in the envelope at relatively high levels, for example, SO_2 and HNC (see references above). It is believed that extra Si and S are released into the gas phase from dust grains by shocks. Shocks might also initiate (endothermic) reactions that trigger the N and S chemistry and could also be additional suppliers of free atoms and ions (Morris et al. 1987).

2. Observations

The observations presented in this paper are part of a sensitive mm-wavelength (∼79–356 GHz) survey carried out with the IRAM-30 m telescope (Pico Veleta, Granada, Spain) towards the CSEs of two O-rich evolved stars: OH 231.8+4.2 and IK Tau. Preliminary results from this survey are reported in Sánchez Contreras et al. (2011) and Velilla Prieto et al. (2013).

We used the new-generation heterodyne Eight MIxer Receiver (EMIR)[2], which works at four different mm-wavelength bands, E090 = 3 mm, E150 = 2 mm, E230 = 1 mm, and E330 = 0.9 mm (Carter et al. 2012). EMIR was operated in single-sideband (SSB) mode for band E150 and in dual sideband (2SB) mode for bands E090, E230, and E330. E090 and E150 were observed simultaneously providing 8 GHz and 4 GHz instantaneous bandwidths, respectively. E330 was also observed simultaneously with E150, providing 16 GHz of instantaneous bandwidth, and E230 was observed alone, providing 16 GHz of instantaneous bandwidth.

[2] http://www.iram.es/IRAMES/mainWiki/EmirforAstronomers

Table 1. Main parameters of the IRAM-30 m EMIR receiver at representative frequencies.

Frequency (GHz)	Beam eff. (%)	Forward eff. (%)	*HPBW* (″)	S/T_a^* (Jy/K)
86	81	95	29	5.9
145	74	93	17	6.4
210	63	94	12	7.5
340	35	81	7	10.9

Notes. Column 1: representative frequency; Col. 2: beam efficiency; Col. 3: forward efficiency; Col. 4: half power beam width; Col. 5: flux to antenna temperature conversion factor in Jansky per Kelvin.

Table 2. Relevant observational information.

Band	Mode	*IBW* (GHz)	ν_{obs} (GHz)	rms (mK)	Opacity
E090	2SB	8	79.3–115.7	1–3	0.07–0.38
E150	SSB	4	128.4–174.8	2–8	0.03–0.39
E230	2SB	16	202.1–270.7	5–10	0.12–0.30
E330	2SB	16	258.4–356.2	6–24	0.07–0.76

Notes. Column 1: EMIR receiver band; Col. 2: observing mode single sideband (SSB) or dual sideband (2SB); Col. 3: instantaneous bandwidth (IBW); Col. 4: observed frequency windows in GHz, Col. 5: root mean square (rms): noise in units of T_a^* for a spectral resolution of 2 MHz; Col. 6: zenith atmospheric opacities at the observed frequency.

Each receiver band was connected to different spectrometers; here we report data observed with the WILMA autocorrelator, which provides a spectral resolution of 2 MHz (i.e. 7.5–1.7 km s^{-1} in the observed frequency range, 79–356 GHz), and the fast Fourier transform spectrometer (FTS) in its 195 kHz spectral resolution mode (i.e. 0.7–0.2 km s^{-1}). Both spectrometers provide full coverage of the instantaneously available frequencies.

For each band, the two orthogonal polarizations were observed simultaneously for a series of tuning steps until we covered the total frequency range accessible to each band. The central frequencies of the different tuning steps were chosen to provide a small frequency overlap between adjacent tunings. The average rejection of the image band signal was measured to be ∼14 dB, in agreement with the typical values for EMIR; this implies that the peak intensity of a line entering through the image band is only ∼4% of its real value.

Observations were performed towards the centre of the nebula (RA2000 = 07^{h}42^{m}16^s.93, Dec2000 = −14°42′50″.20). We used the wobbler switching mode, with a wobbler throw of 120″ in azimuth. The beamwidth of the antenna is in the range ∼30″–7″ at the observed frequencies (Table 1). These observations thus provide spectra that are spatially integrated over the slow central core of OH 231.8+4.2 (clump I3, from which the bulk of the molecular emission arises), and more or less depending on the observed frequency, from the fast bipolar outflows, always leaving out the emission from the most distant and, thus, fastest and most tenuous clumps (I6–I7) in the southern lobe (see Fig. 1).

Pointing and focus were checked regularly (every ∼1.5 and ∼4 h, respectively) on strong nearby sources. On-source integration times per tuning step were ∼1 h. Additional information on the observations is provided in Table 2.

Calibration scans on the standard two load + sky system were taken every ∼18 min; the atmospheric transmission is

modelled at IRAM-30 m using ATM (Cernicharo et al. 1985; Pardo et al. 2001). All spectra have been calibrated on the antenna temperature (T_A^*) scale, which is related to the mean brightness temperature of the source (T_B) via the equation

$$T_B = T_A^* \frac{F_{eff}}{B_{eff}} \delta^{-1} = T_{mb}\, \delta^{-1} \quad (1)$$

where T_{mb} is the main-beam temperature, F_{eff} and B_{eff} are the forward efficiency and the main-beam efficiency of the telescope, respectively, and δ is the beam-filling factor. The ratio between F_{eff} and B_{eff} is described by the equation

$$\frac{F_{eff}}{B_{eff}} = 1.1e^{(\nu(\mathrm{GHz})/398.5)^2}. \quad (2)$$

The molecular outflow of OH 231.8+4.2 has been assumed to be a uniform elliptical source with major and minor axes θ_a and θ_b. In this case, the beam-filling factor is given by (see e.g. Kramer 1997):

$$\delta = 1 - e^{-\ln 2 \frac{\theta_a \times \theta_b}{HPBW^2}} \quad (3)$$

where HPBW is the half power beam width of an elliptical Gaussian beam. Based on previous maps of CO and other molecules, we adopt an angular source size of $\theta_a \times \theta_b = 4'' \times 12''$.

We have checked the relative calibration between adjacent frequency tunings by comparing the intensities of the lines in the overlap regions and in frequency tunings that were observed in different epochs. An extra check of the calibration has been made by comparing the intensities of the ^{12}CO and ^{13}CO lines from this survey with those measured in previous observations (Morris et al. 1987; Sánchez Contreras et al. 1997). Errors in the absolute flux calibration are expected to be $\lesssim$25%.

Data were reduced using CLASS[3] to obtain the final spectra. We followed the standard procedure, which includes flagging of bad channels, flagging of low-quality scans, baseline substracting, averaging individual scans, and channel smoothing to a typical spectral resolution of (~2 MHz).

3. Observational results

Line identification over the full frequency range covered in this survey was done using the public line catalogues from the Cologne Database for Molecular Spectroscopy (CDMS, Müller et al. 2005) and the Jet Propulsion Laboratory (JPL, Pickett et al. 1998), together with a private spectroscopic catalogue that assembles information for almost five thousand spectral entries (molecules and atoms), including isotopologues and vibrationally excited states, compiled from extensive laboratory and theoretical works by independent teams (Cernicharo 2012).

We have identified hundreds of transitions from more than 50 different molecular species including their main isotopologues (^{13}C-, ^{18}O-, ^{17}O-, ^{33}S-, ^{34}S-, ^{30}Si, and ^{29}Si) in OH 231.8+4.2, confirming the chemical richness of this source, which is unprecedented amongst O-rich AGB and post-AGB stars.

First detections from this survey include the N-bearing species HNCO, HNCS, HC_3N, and NO, which are the focus of this paper. Together with these, we present the spectra of the ^{13}CO J = 1–0, J = 2–1, and J = 3–2 transitions, which are excellent tracers of the mass distribution and dynamics in OH 231.8+4.2: ^{13}CO lines are optically thin (or, at most, moderately opaque towards the nebula centre) and are expected to be thermalized over the bulk of the outflow and, certainly, in the regions that lie within the telescope beam in these observations, characterized by average densities always above 10^4 cm^{-3} (Sánchez Contreras et al. 1997; Alcolea et al. 2001). Spectra of different rotational transitions from the ground vibrational state (v = 0) of ^{13}CO, HNCO, HNCS, HC_3N, and NO are shown in Figs. 2–7, and main line parameters are reported in Table 3.

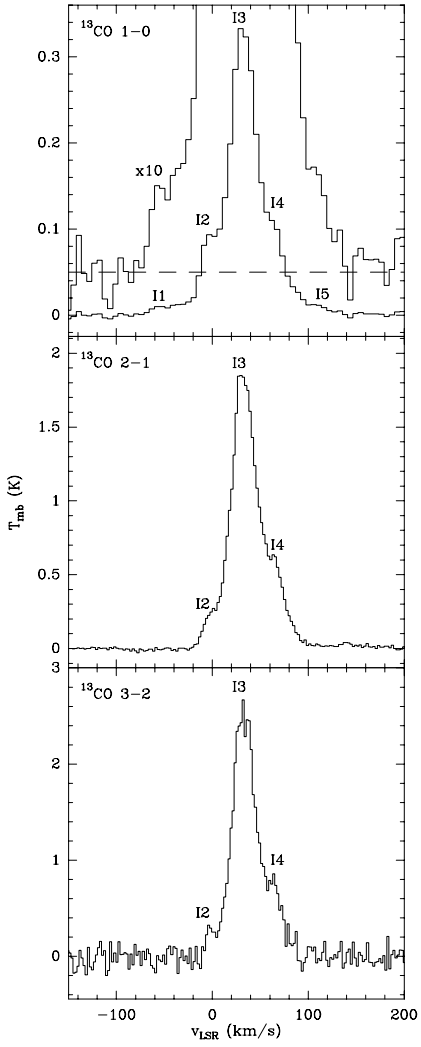

Fig. 2. ^{13}CO mm-wavelength transitions in OH 231.8+4.2. We labelled the different spectral features in the ^{13}CO profiles as I1–I5 to identify them with the corresponding regions/clumps of CO-outflow where the emission features mainly arise (see Fig. 1). *Top panel*: ^{13}CO J = 1–0 spectrum is also plotted using a larger T_{mb} scale for an improved view of the weak broad wings.

[3] CLASS is a world-wide software to process, reduce, and analyse heterodyne line observations maintained by the Institut de Radioastronomie Millimétrique (IRAM) and distributed with the GILDAS software, see http://www.iram.fr/IRAMFR/GILDAS

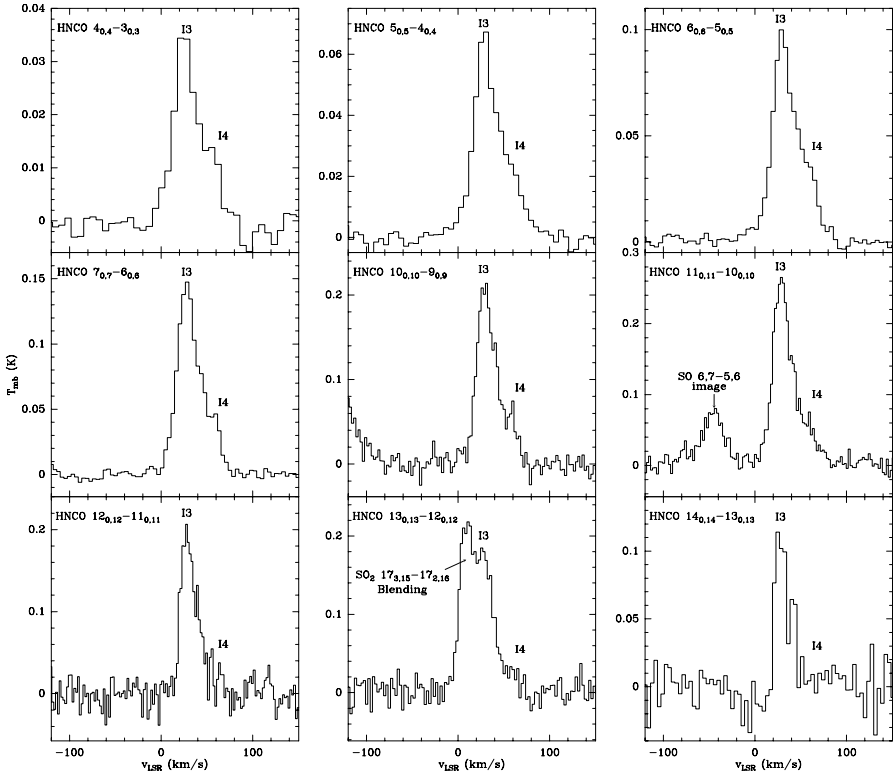

Fig. 3. HNCO transitions of the $K_a = 0$ ladder detected in OH 231.8+4.2. Spectral features have been labelled as in Fig. 2. The HNCO $13_{0,13}-12_{0,12}$ transition is blended with the SO_2 $17_{3,15}-17_{2,16}$ line (central, *bottom panel*).

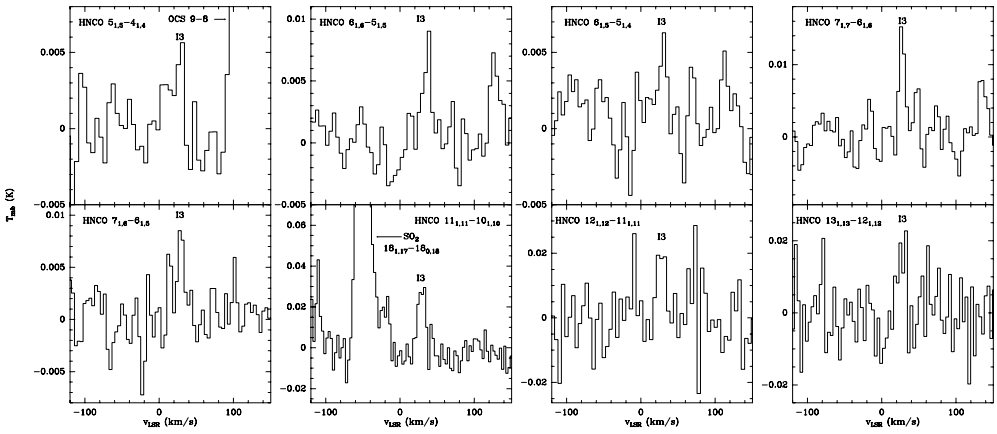

Fig. 4. Same as in Fig. 3 but for the $K_a = 1$ ladder. The S/N of some of these transitions is low, so they may be considered as tentative detections; however, in spite of the large errobars, the intensity, centroid V_{LSR}, and FWHM of the tentative lines are consistent with the trend and values deduced for transitions detected with higher S/N.

3.1. ^{13}CO spectra

The ^{13}CO lines (Fig. 2) show broad, structured profiles with two main components: (1) the intense, relatively narrow (*FWHM* ∼ 30−35 km s^{-1}) core centred at V_{LSR} = 33.4 ± 0.9 km s^{-1}, which arises in the slow, dense central parts of the nebula (clump I3); and (2) weak broad wings, with full widths of up to ∼220 km s^{-1} in the J = 1–0 line, which originate in the fast bipolar lobes clumps I1–I2 and I4–I5). The most intense spectral component in the ^{13}CO wings

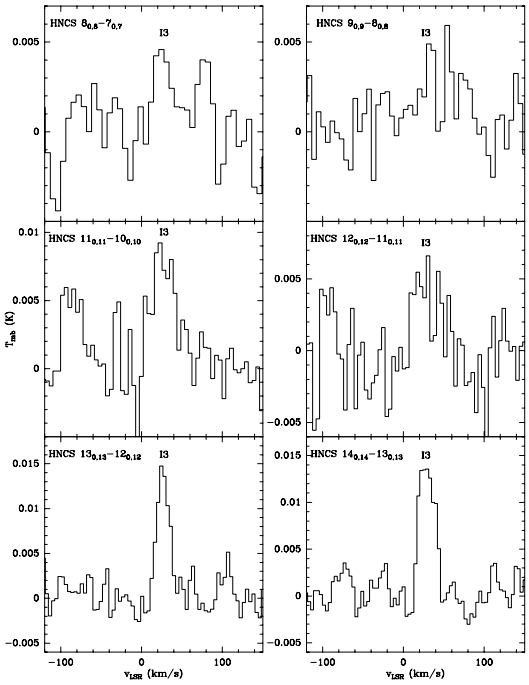

Fig. 5. Same as in Fig. 3 but for HNCS.

arises at clump I4, i.e. the base of the southern lobe, and the I4/I3 feature peak-intensity ratio is I4/I3 ∼ 0.3. The single-dish profiles of the J = 1–0 and 2–1 lines are already known from previous observations (Morris et al. 1987; Sánchez Contreras et al. 1997) and, within the expected calibration errors, are consistent with those observed in this survey.

The full width of the wings is largest for the ^{13}CO (J = 1–0) transition, which is observed over a velocity range of V_{LSR} = [−80:+140] km s^{-1}, and decreases for higher-J transitions down to V_{LSR} = [−10:+90] km s^{-1} for the J = 3–2 line. The different width of the wings is partially explained by the increase in the expansion velocity with the distance to the centre along the CO outflow and the smaller beam for higher frequencies. Also, as can be observed (Fig. 2 and Table 3), the FWHM of the ^{13}CO transitions decrease as the upper energy level increases. This suggests that the envelope layers with higher excitation conditions (i.e. warmer and, thus, presumably closer to the central star) are characterized by lower expansion velocities. This trend is confirmed by higher frequency transitions of ^{13}CO (and of most molecules) observed with *Herschel* with a larger telescope beam (e.g. Bujarrabal et al. 2012; Sánchez Contreras et al. 2014).

3.2. New N-bearing molecules

Isocyanic acid (HNCO) is a quasi-linear asymmetric rotor whose structure was first determined by Jones et al. (1950). It contains a nitrogen atom that has a nuclear spin (I = 1) leading to a splitting of each rotational level. This hyperfine (hpf) structure is not resolved since the maximum separation in velocity of the hpf components from the most intense one is ≲2 km s^{-1}, that is, much less than the expansion velocity of the envelope (and, in some cases, even smaller than the spectral resolution of our observations). The rotational levels of HNCO are expressed in terms of three quantum numbers: J the rotational quantum number, K_a and K_c, which are the projections of J onto the A and C molecular axes, respectively. We have detected several a-type transitions (i.e. with $\Delta K_a = 0$ and $\Delta K_c = \pm 1$) in the $K_a = 0$ and $K_a = 1$ ladders (Figs. 3, 4); the difference between the $K_a = 0$ zero level and the $1_{1,1}$ level is ΔE = 44.33 K. The profiles of the HNCO transitions detected of the $K_a = 0$ and $K_a = 1$ ladders show notable differences: the $K_a = 0$ transitions, which are stronger than the $K_a = 1$ ones, show an intense central core component centred at V_{LSR} = 29.5 ± 1.5 km s^{-1} and with a linewidth of $FWHM$ ∼ 20–33 km s^{-1}; as for ^{13}CO, the linewidth decreases as the transition upper level energy increases. In addition to the line core (arising in the central parts of the nebula, clump I3), the HNCO $K_a = 0$ profiles show red-wing emission from the base of the southern lobe, clump I4; the I4/I3 feature peak-intensity ratio is ∼0.3. The HNCO $K_a = 1$ transitions, centred on V_{LSR} = 29.5 ± 1.1 km s^{-1}, are not only weaker but narrower ($FWHM$ ∼ 13 km s^{-1}) than the $K_a = 0$ lines.

Isothiocyanic acid (HNCS) presents a structure similar to HNCO; i.e., it is a slightly asymmetric rotor (Jones & Badger 1950). Its hpf structure due to the nitrogen nuclear spin is not spectrally resolved in our data. We have detected several a-type (i.e. with $\Delta K_a = 0$ and $\Delta K_c = \pm 1$) transitions of the $K_a = 0$ ladder (Fig. 5). These lines are weak and narrow, with a median $FWHM$ ∼ 25 km s^{-1}, and are centred at V_{LSR} = 28.2 ± 0.4 km s^{-1}, indicating that the emission observed arises mainly in the slow central parts of the nebula. HNCS wing emission from the fast flow (if present) is below the noise level. We have not detected any of the $K_a = 1$ transitions of HNCS in the frequency range covered by us. These transitions have upper-level state energies $E_u \gtrsim 78$ K and expected intensities well below our detection limit.

Cyanoacetylene (HC_3N) is a linear molecule that belongs to the nitriles family. We do not resolve its hpf structure spectrally (which is due to the nitrogen nuclear spin), so its rotational levels are described only by the rotational number J (Westenberg & Wilson 1950). The spectra of the HC_3N transitions detected in OH 231.8+4.2 are shown in Fig. 6. The line profiles are centred at V_{LSR} = 28.0 ± 0.9 km s^{-1} and are relatively narrow, with typical line widths of $FWHM$ ∼ 22 km s^{-1}. Tentative emission from clump I4 (at V_{LSR} ∼ 60–65 km s^{-1}) is observed in most profiles, with a I4/I3 feature peak-intensity ratio of ∼0.2–0.4.

Nitric oxide (NO) is a radical with a $^2\Pi$ ground state that splits into two different ladders, $\Omega = 1/2$ ($^2\Pi_{1/2}$) and $\Omega = 3/2$ ($^2\Pi_{3/2}$), owing to the unpaired electron by spin-orbit coupling. Additionally, Λ-doubling means that each transition is split into two different bands of opposite parity Π^+ and Π^-. NO also presents hpf structure owing to the nitrogen nuclear spin that interacts with the total angular momentum, thereby splitting each single rotational level into $2(I, J)_{min}+1$ levels described by the quantum number F (for a complete description of the structure and spectroscopy of the NO rotational transitions see Lique et al. 2009, and references therein). We have detected several transitions of the $^2\Pi_{1/2}$ ladder around 150, 250, and 350 GHz (see Fig. 7). Transitions of the $^2\Pi_{3/2}$ ladder, with upper level state energies above 180 K, are not detected. As shown in Fig. 7, each of the Λ-doublets (Π^+ and Π^-) of NO is composed of several hpf components that are blended in our spectra, except for the Π^- (3/2, 3/2)–(1/2, 1/2) line at 150.644 GHz, which is isolated.

The NO blends appear on average redshifted by a few km s^{-1} from the source systemic velocity and are broader than the profiles of the other N-bearing species discussed in this work. The broadening is partially (but not only) due to the hpf structure of

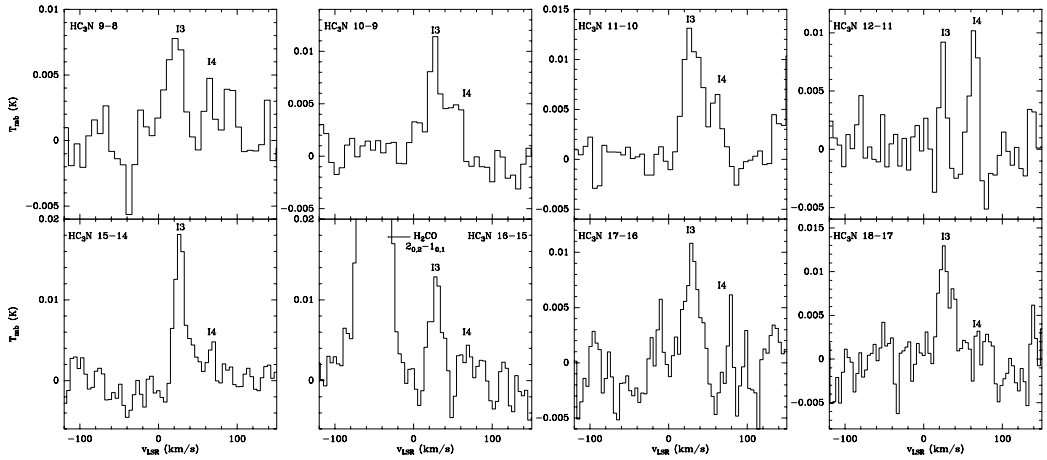

Fig. 6. Same as in Fig. 3 but for HC_3N. The poor baseline in the spectrum of the J = 12–11 line makes the detection of this transition tentative.

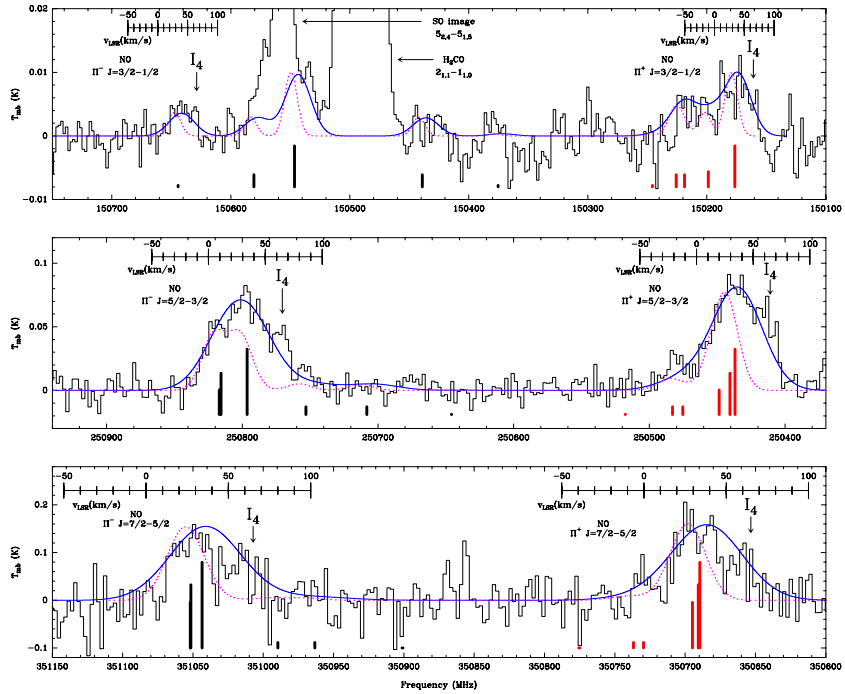

Fig. 7. Spectra of the NO transitions detected in OH 231.8+4.2. The quantum numbers indicated in this plot for NO are Π and J (Table 3). Vertical thick segments indicate the rest frequency and relative strength of the individual hyperfine (hpf) components within each Π^+ and Π^- blend (red and black, respectively). The LSR velocity scale is shown on top of the NO transitions that have been detected (the velocity scale refers to the strongest hpf component in each case). The LSR velocity of the emission feature associated to clump I4, at the base of the southern lobe, is indicated. The dotted line is the model spectrum (Sect. 3.2 and Table 4) assuming that the individual hpf components are centred at V_{LSR} = 28 km s^{-1}, and have an intrinsic width of $FWHM$ = 25 km s^{-1}, similar to the dominant narrow component of the HNCO, HNCS, and HC_3N profiles (Figs. 3–6). These line parameters cannot explain the broad profiles and the apparent overall redshift of the NO blends, which are reproduced better by adopting larger FWHM and V_{LSR} (solid blue line: representative model with $FWHM$ = 50 km s^{-1} and V_{LSR} = 40 km s^{-1}).

the NO transitions. To constrain the intrinsic linewidth and centroid of the individual hpf components contributing to the observed profile, we have calculated and added together the emergent spectrum of the hpf components. The synthetic spectrum was calculated using our code MADEX (Cernicharo 2012, see also Appendix A) and also the task MODSOURCE of CLASS, both giving similar results at LTE (non-LTE calculations are available in MADEX but not in MODSOURCE). We adopted

A&A 575, A84 (2015)

Table 3. Parameters of the lines detected in OH 231.8+4.2 reported in this work.

Molecule	Transition quantum numbers	$\nu_{\rm rest}$ (MHz)	$E_{\rm u}$ (K)	$A_{\rm ul}$ s^{-1}	$\int T_{\rm mb}^{*}\,{\rm d}v$ (K km s^{-1})	*FWHM* (km s^{-1})	$T_{\rm mb,peak}$ (mK)
^{13}CO	$1 \rightarrow 0$	110 201.35	5.3	6.336×10^{-8}	12.81(0.05)	36.1(0.4)	324(2)
J	$2 \rightarrow 1$	220 398.68	15.9	6.082×10^{-7}	69.63(0.13)	32.4(0.4)	1818(9)
	$3 \rightarrow 2$	330 587.96	31.7	2.199×10^{-6}	87.6(0.6)	29.5(0.4)	2420(50)
HNCO	$4_{0,4} \rightarrow 3_{0,3}$	87 925.24	10.5	9.025×10^{-6}	1.31(0.05)	32.0(1.3)	32.8(1.6)
J_{K_a,K_c}	$5_{0,5} \rightarrow 4_{0,4}$	109 905.75	15.8	1.802×10^{-5}	2.54(0.06)	33.2(0.7)	61.3(1.8)
	$6_{0,6} \rightarrow 5_{0,5}$	131 885.73	22.2	3.163×10^{-5}	3.64(0.05)	29.4(0.5)	93.7(2.1)
	$7_{0,7} \rightarrow 6_{0,6}$	153 865.09	29.5	5.078×10^{-5}	4.83(0.06)	28.6(0.4)	140(3)
	$10_{0,10} \rightarrow 9_{0,9}$	219 798.27	58.0	1.510×10^{-4}	6.67(0.14)	24.5(0.9)	200(9)
	$11_{0,11} \rightarrow 10_{0,10}$	241 774.03	69.6	2.019×10^{-4}	7.32(0.14)	21.5(0.5)	260(8)
	$12_{0,12} \rightarrow 11_{0,11}$	263 748.62	82.3	2.630×10^{-4}	4.73(0.22)	21.3(1.0)	179(14)
	$13_{0,13} \rightarrow 12_{0,12}$	285 721.95	96.0	3.355×10^{-4}	6.3(0.4)†	*	*
	$14_{0,14} \rightarrow 13_{0,13}$	307 693.90	110.8	4.200×10^{-4}	2.48(0.20)	19.9(1.6)	114(16)
	$5_{1,5} \rightarrow 4_{1,4}$	109 495.99	59.0	1.692×10^{-5}	0.08(0.04)	13(6)	4.8(2.1)
	$6_{1,6} \rightarrow 5_{1,5}$	131 394.23	65.3	3.006×10^{-5}	0.22(0.02)	14(4)	7.6(1.4)
	$6_{1,5} \rightarrow 5_{1,4}$	132 356.70	65.5	3.072×10^{-5}	0.16(0.03)	14(9)	5.5(1.8)
	$7_{1,7} \rightarrow 6_{1,6}$	153 291.94	72.7	4.863×10^{-5}	0.25(0.04)	9(4)	15.8(2.2)
	$7_{1,6} \rightarrow 6_{1,5}$	154 414.76	72.9	4.971×10^{-5}	0.28(0.03)	18(7)	6.5(2.1)
	$11_{1,11} \rightarrow 10_{1,10}$	240 875.73	112.6	1.957×10^{-4}	0.35(0.10)	12(2)	34(8)
	$12_{1,12} \rightarrow 11_{1,11}$	262 769.48	125.3	2.554×10^{-4}	0.31(0.09)	12(3)	22(11)
	$13_{1,13} \rightarrow 12_{1,12}$	284 662.17	138.9	3.261×10^{-4}	0.28(0.07)	14(3)	20(10)
HNCS	$8_{0,8} \rightarrow 7_{0,7}$	93 830.07	20.3	1.217×10^{-5}	0.19(0.04)	27(9)	4.4(2.0)
J_{K_a,K_c}	$9_{0,9} \rightarrow 8_{0,8}$	105 558.08	25.3	1.744×10^{-5}	0.23(0.04)	*	4.0(1.6)
	$11_{0,11} \rightarrow 10_{0,10}$	129 013.26	37.2	3.215×10^{-5}	0.32(0.04)	33(5)	8.5(2.2)
	$12_{0,12} \rightarrow 11_{0,11}$	140 740.38	43.9	4.189×10^{-5}	0.26(0.04)	34(9)	4.7(2.3)
	$13_{0,13} \rightarrow 12_{0,12}$	152 467.14	51.2	5.342×10^{-5}	0.30(0.04)	18(2)	14.8(2.1)
	$14_{0,14} \rightarrow 13_{0,13}$	164 193.52	59.1	6.690×10^{-5}	0.34(0.02)	21(1)	15.1(1.4)
HC_3N	$9 \rightarrow 8$	81 881.46	19.6	4.215×10^{-5}	0.30(0.06)	27(6)	7.5(2.3)
J	$10 \rightarrow 9$	90 978.99	24.0	5.812×10^{-5}	0.38(0.03)	26(5)	8.5(1.5)
	$11 \rightarrow 10$	100 076.38	28.8	7.770×10^{-5}	0.44(0.04)	28(3)	12.4(1.7)
	$12 \rightarrow 11$	109 173.64	34.1	1.012×10^{-4}	0.15(0.03)	*	*
	$15 \rightarrow 14$	136 464.40	52.4	1.993×10^{-4}	0.35(0.03)	16(2)	17.8(1.9)
	$16 \rightarrow 15$	145 560.95	59.4	2.424×10^{-4}	0.29(0.04)	17(3)	12(3)
	$17 \rightarrow 16$	154 657.29	66.8	2.912×10^{-4}	0.20(0.04)	20(4)	9.6(2.3)
	$18 \rightarrow 17$	163 753.40	74.7	3.463×10^{-4}	0.25(0.03)	22(5)	10.7(2.1)
NO	$\Pi^{+}(3/2,5/2) \rightarrow (1/2,3/2)$	150 176.48	7.2	3.310×10^{-7}			
$\Pi^{\rm band}(J,F)$	$\Pi^{+}(3/2,3/2) \rightarrow (1/2,1/2)$	150 198.76	7.2	1.839×10^{-7}			
	$\Pi^{+}(3/2,3/2) \rightarrow (1/2,3/2)$	150 218.73	7.2	1.471×10^{-7}	1.15(0.08)‡	55(10)‡	9(3)‡
	$\Pi^{+}(3/2,1/2) \rightarrow (1/2,1/2)$	150 225.66	7.2	2.943×10^{-7}			
	$\Pi^{+}(3/2,1/2) \rightarrow (1/2,3/2)$	150 245.64	7.2	3.679×10^{-8}			
	$\Pi^{-}(3/2,3/2) \rightarrow (1/2,1/2)$	150 644.34	7.2	1.853×10^{-7}	0.20(0.03)	39(9)	4.9(2.1)

Notes. For each transition: Col. 1: name of the molecule and set of quantum numbers used; Col. 2: specific quantum numbers; Col. 3: rest frequency; Col. 4: upper level energy; Col. 5: Einstein spontaneus emission coefficient; Col. 6: line flux obtained integrating the area below the profile in main-beam temperature scale; Col. 7: line full width at half maximum (FWHM); Col. 8: main-beam peak temperature and rms for a spectral resolution of ~2 MHz (in parentheses). Columns 7 and 8: were obtained by fitting a Gaussian function to the line core profile, masking the wings. The formal errors given (within parentheses) do not include absolute flux calibration and baseline subtraction uncertainties. $^{(\dagger)}$ Line blend with SO_2 $17_{3,15}-17_{2,16}$; the value of the flux provided here accounts only for the HNCO line flux, which represents a 75% of the total flux of the blend. $^{(\ddagger)}$ The individual hyperfine components of NO are spectrally unresolved, therefore, one single value for the line blend is provided. $^{(*)}$ Unreliable and, thus, not measured value due to line blending, low signal-to-noise ratio, and/or poor baseline subtraction.

Table 3. continued.

Molecule	Transition quantum numbers	ν_{rest} (MHz)	E_u (K)	A_{ul} s^{-1}	$\int T_{mb}^{*}\,dv$ (K km s^{-1})	$FWHM$ (km s^{-1})	$T_{mb,peak}$ (mK)
NO	$\Pi^+(5/2,7/2) \rightarrow (3/2,5/2)$	250 436.85	19.2	1.841×10^{-6}			
$\Pi^{band}(J,F)$	$\Pi^+(5/2,5/2) \rightarrow (3/2,3/2)$	250 440.66	19.2	1.547×10^{-6}			
	$\Pi^+(5/2,3/2) \rightarrow (3/2,1/2)$	250 448.53	19.2	1.381×10^{-6}	5.08(0.16)‡	54(2)‡	82(9)‡
	$\Pi^+(5/2,3/2) \rightarrow (3/2,3/2)$	250 475.41	19.2	4.420×10^{-7}			
	$\Pi^+(5/2,5/2) \rightarrow (3/2,5/2)$	250 482.94	19.2	2.947×10^{-7}			
	$\Pi^-(5/2,7/2) \rightarrow (3/2,5/2)$	250 796.44	19.3	1.849×10^{-6}			
	$\Pi^-(5/2,5/2) \rightarrow (3/2,3/2)$	250 815.59	19.3	1.554×10^{-6}	4.77(0.15)‡	64(2)‡	68(9)‡
	$\Pi^-(5/2,3/2) \rightarrow (3/2,1/2)$	250 816.95	19.3	1.387×10^{-6}			
	$\Pi^+(7/2,9/2) \rightarrow (5/2,7/2)$	350 689.49	36.1	5.418×10^{-6}			
	$\Pi^+(7/2,7/2) \rightarrow (5/2,5/2)$	350 690.77	36.1	4.976×10^{-6}			
	$\Pi^+(7/2,5/2) \rightarrow (5/2,3/2)$	350 694.77	36.1	4.815×10^{-6}	7.2(0.5)‡	40(4)‡	149(40)‡
	$\Pi^+(7/2,5/2) \rightarrow (5/2,5/2)$	350 729.58	36.1	5.897×10^{-7}			
	$\Pi^+(7/2,7/2) \rightarrow (5/2,7/2)$	350 736.78	36.1	4.423×10^{-7}			
	$\Pi^-(7/2,9/2) \rightarrow (5/2,7/2)$	351 043.52	36.1	5.433×10^{-6}			
	$\Pi^-(7/2,7/2) \rightarrow (5/2,5/2)$	351 051.47	36.1	4.990×10^{-6}	5.2(0.5)‡	41(5)‡	122(40)‡
	$\Pi^-(7/2,5/2) \rightarrow (5/2,3/2)$	351 051.70	36.1	4.830×10^{-6}			

a Gaussian profile for the hpf lines. We find that, first, the shape of the NO blends cannot be reproduced by adopting sharply centrally peaked profiles such as those of HNCO, HNCS, and HC_3N, with line centroids at $V_{LSR} \sim 28$–29 km s^{-1} and widths of $FWHM \sim 15$–30 km s^{-1} (dotted line in Fig. 7). In order to match the profiles of the NO blends, the individual hpf components must have a larger width of $FWHM \sim 40$–50 km s^{-1} and must be centered at $V_{LSR} \sim 35$–40 km s^{-1} (Fig. 7). In support of this conclusion, a Gaussian fit to the Π^- (3/2, 3/2)–(1/2, 1/2) line at 150.644 GHz, which is unblended, also indicates a broad profile, with a $FWHM = 40 \pm 8$ km s^{-1}, centred at $V_{LSR} = 41 \pm 4$ km s^{-1}. Although the intrinsic linewidth is uncertain, the broad profiles of NO indicate that this molecule is present in abundance in the high-velocity lobes and that the wing-to-core emission contribution is greater for NO than for HNCO, HNCS, and HC_3N. In particular, an important part of the NO emission profile arises at clump I4. The emission from feature I4 is indeed comparable to that of the narrow core (I3), with an estimated I4/I3 feature peak-intensity ratio of ∼1 at 150 GHz, ∼0.6–0.8 at 250 GHz, and ∼0.5–0.6 at 350 GHz. This significant NO emission contribution from clump I4 to the total profile is one explanation for the apparent overall redshift of the NO lines to an intermediate velocity between that of I3 and I4.

4. Data analysis: molecular abundances

In the following sections, beam-averaged column densities (N_{tot}) and rotational temperatures (T_{rot}) are obtained from the population diagram method (Sect. 4.1) and from non-LTE excitation calculations (Sect. 4.2). We derive fractional abundances (X) relative to molecular hydrogen (H_2) for the different molecular species detected in OH 231.8+4.2. As a reference, we have used the fractional abundance of ^{13}CO, for which we adopt $X(^{13}CO) = 5 \times 10^{-5}$ as calculated by Morris et al. (1987). The ^{13}CO abundance adopted is in the high end of the typical range of values for O-rich stars; in the case of OH 231.8+4.2, it reflects the particularly low $^{12}C/^{13}C$ isotopic ratio, ∼5–10, measured in this object (and other O-rich CSEs; Sánchez Contreras et al. 2000b; Teyssier et al. 2006; Milam et al. 2009; Ramstedt & Olofsson 2014, and references therein).

The fractional abundances of the N-bearing species reported in this work have been calculated as

$$\frac{X(m)}{X(^{13}CO)} = \frac{N_{tot}(m)}{N_{tot}(^{13}CO)}, \quad (4)$$

where m represents the name of the analysed molecule.

4.1. Population diagram analysis

Population (or rotation) diagrams are used to obtain first-order, beam-averaged column densities (N_{tot}) and rotational temperatures (T_{rot}) from the integrated intensities of multiple rotational transitions of a given molecule in the same vibrational state. This method, which is described in detail and extensively discussed by Goldsmith & Langer (1999), among others, relies on two main assumptions: i) lines are optically thin; and ii) all levels involved in the transitions used are under local thermodynamical equilibrium (LTE) conditions. This assumption implies that the level populations are described by the Boltzmann distribution with a single rotational temperature, T_{rot}, which is equal to the kinetic temperature of the gas ($T_{kin} = T_{rot}$). Under these assumptions, the line integrated intensity or line flux (W) is related to N_{tot} and T_{rot} by the following expression:

$$\ln\left(\frac{N_u}{g_u}\right) = \ln\left(\frac{3k_B W}{8\pi^3 \nu S_{ul} \mu^2}\right) = \ln\left(\frac{N}{Z}\right) - \frac{E_u}{k_B T_{rot}} \quad (5)$$

where N_u is the column density of the upper level, g_u the degeneracy of the upper level, W the velocity-integrated intensity of the transition, k_B the Boltzmann constant, ν the rest frequency of the line, S_{ul} the line strength of the transition, μ the dipole moment of the corresponding transition, Z the partition function, and E_u is the upper level energy of the transition.

The partition function, Z_{rot} has been computed for each molecule by explicit summation of

$$Z_{rot} = \sum_{i=0}^{\infty} g_i e^{\frac{-E_i}{kT}}, \quad (6)$$

for enough levels to obtain accurate values, using the code MADEX (Appendix A). At low temperatures (≲50 K), this

A&A 575, A84 (2015)

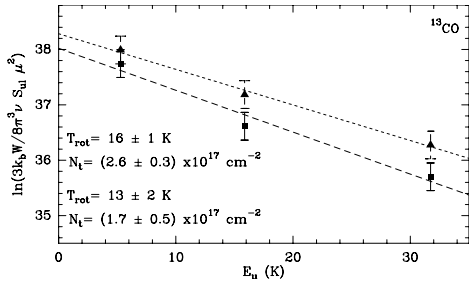

Fig. 8. Population diagram for ^{13}CO and best linear fit (dashed line) to the data (filled symbols). Triangles and squares represent data points with and without the opacity correction C_τ applied, respectively (Sect. 4.1). The values of T_{rot} and N_{tot} derived from the fits are indicated in the bottom left corner of the box for the optically thin (*lower*) and optical depth corrected (*upper*) approximations. The error bars of the data points include flux uncertainties due to the rms of the spectra and absolute flux calibration, up to ∼25% (Sect. 2).

ensures moderate uncertainties in the column density (<5%) as derived from the low-E_u transitions detected, since the contribution of high-energy levels to the partition function is negligible.

The line flux (W) has been obtained by integrating the area below the emission profile, typically within the range V_{LSR} ∼ [0−100] km s^{-1}, and is given in a source brightness temperature scale ($W = \int T_b dv$), obtained from T_a^* via Eq. (1). In the case of ^{13}CO, W does not include the weak emission from the wings beyond V_{LSR} ± 70 km s^{-1} since this high-velocity component is not detected in the other molecules. The values for W used to build the population diagrams are given in Table 3.

The beam-filling factor (δ; see Eq. (3)) has been computed by adopting a characteristic size for the emitting region of $\Omega_s = 4'' \times 12''$ for all molecules. This size is comparable to but slightly less than the angular size (at half intensity) of the CO-outflow measured by Alcolea et al. (2001) – see Fig. 1. In any case, we have checked that the parameters derived from the population diagram do not vary significantly for a range of reasonable values of $\theta_a \times \theta_b$ ∼ (3−6)″ × (10−18)″.

The population diagrams for the molecules reported in this work and the derived results are shown in Figs. 8, 9 and Table 4. For ^{13}CO we obtain T_{rot} ∼ 13 K and $N_{tot}(^{13}CO) \sim 2 \times 10^{17}$ cm^{-2}. For these values of T_{rot} and N_{tot}, we expect moderate optical depths at the line centre ($\tau_{110\ GHz} \sim 0.5$, $\tau_{220\ GHz} \sim 1.1$, and $\tau_{330\ GHz} \sim 0.9$, for a typical linewidth of $FWHM$ ∼ 35 km s^{-1}), which would lead to underestimating both T_{rot} and N_{tot}. According to this, an opacity correction factor $C_\tau = \ln(\tau/(1-e^{-\tau}))$, as defined by, for instance, Goldsmith & Langer (1999), has been introduced in the population diagram, and a new best fit was obtained. This process (of fitting opacity corrected data points and re-computing C_τ) was performed iteratively until convergence was reached. The opacity-corrected values derived are $T_{rot} \sim 16$ K and $N_{tot}(^{13}CO) \sim 3 \times 10^{17}$ cm^{-2}.

In the rotational diagram of HNCO (top panel in Fig. 9), we can clearly see that the transitions of the $K_a = 0$ and $K_a = 1$ ladders follow two different trends. Both trends have similar slopes; that is, the $K_a = 0$ and $K_a = 1$ data points are arranged in two almost parallel straight lines representing similar rotational temperatures. As we show in Sect. 4.2 and Appendix A, the y-offset between both lines can be explained by non-LTE excitation effects, which are most prominent in the $K_a = 1$ transitions. Using only the HNCO transitions of the $K_a = 0$ ladder, we derive $T_{rot} \sim 27$ K and $N_{tot}(HNCO) \sim 6 \times 10^{14}$ cm^{-2}. Following the

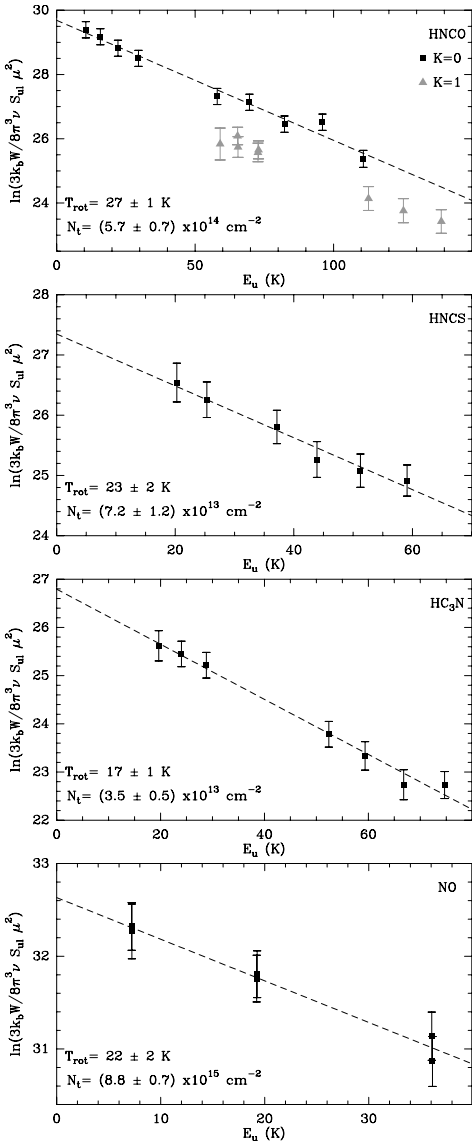

Fig. 9. Population diagrams of HNCO, HNCS, HC_3N, and NO (*from top to bottom*) and best linear fit (dashed line) to the data points (filled symbols; from Table 3). In the case of HNCO, black squares represent transitions with $K_a = 0$ and grey triangles the $K_a = 1$ transitions. The values of T_{rot} and N_{tot} derived from the fit are indicated in the bottom left corner of each box. An opacity correction is not applied in these cases because all the transitions are optically thin. Error bars as in Fig. 8.

Eq. (4) and using the ^{13}CO opacity corrected column density, we derive a fractional abundance of $X(HNCO) \sim 1 \times 10^{-7}$.

The rotational diagrams of HNCS, HC_3N, and NO (Fig. 9) show a linear trend, which is consistent with a unique temperature component of T_{rot} ∼ 15–25 K, in agreement with the relatively low value obtained from ^{13}CO. There is also good agreement with estimates of T_{rot} from other molecules such

Table 4. Column densities (N_{tot}), rotational temperatures (T_{rot}), and fractional abundances relative to H_2 (X) for the molecules detected in OH 231.8+4.2 as derived using the population diagram method (Sect. 4.1) and from non-LTE excitation analysis (Sect. 4.2).

Molecule	N_{tot} (cm^{-2})	T_{rot} (K)	X
	(*i*) LTE RESULTS		
^{13}CO	$2.6(0.3) \times 10^{17}$	16(1)	5×10^{-5} [†]
HNCO	$5.7(0.7) \times 10^{14}$	27(1)	1×10^{-7}
HNCS	$7.2(1.2) \times 10^{13}$	23(2)	1×10^{-8}
HC_3N	$3.5(0.5) \times 10^{13}$	17(1)	7×10^{-9}
NO	$8.8(0.7) \times 10^{15}$	22(2)	2×10^{-6}
	(*ii*) NON-LTE RESULTS[‡]		
HNCO	$[4.0–5.2] \times 10^{14}$	[26–28]	$[0.8–1] \times 10^{-7}$
HNCS	$[4.9–7.4] \times 10^{13}$	[23–28]	$[0.9–1] \times 10^{-8}$
HC_3N	$[2.4–3.3] \times 10^{13}$	[45–55]	$[5–6] \times 10^{-9}$
NO	$[7.5–8.9] \times 10^{15}$	[28–33]	$[1–2] \times 10^{-6}$

Notes. The characteristic angular size for the emitting region adopted is $\Omega_s = 4'' \times 12''$. [(†)] Adopted based on the estimate of $X(^{13}CO)$ by Morris et al. (1987). [(‡)] In this case, we provide ranges of column densities, abundances, and kinetic temperatures consistent with the observations obtained from our non-LTE excitation analysis adopting $n(H_2) = 10^5$ cm^{-3}, for HNCS, HC_3N and NO, and $n(H_2) = 4 \times 10^7$ cm^{-3}, for HNCO (see Sect. 4.2 and Appendix A).

as SO_2 and NH_3 from earlier works (Guilloteau et al. 1986; Morris et al. 1987; Sánchez Contreras et al. 1997). The column densities and fractional abundances derived range between $N_{tot} = 3 \times 10^{13}$ cm^{-2} and 9×10^{15} and $X = 7 \times 10^{-9}$ and 2×10^{-6}, respectively (see Table 4).

Given the relatively low column densities obtained for HNCO, HNCS, HC_3N, and NO, all the transitions detected are optically thin, so no opacity correction is needed. We note that the high abundance of NO inferred from our data ($\approx 10^{-6}$) is comparable to that of SO_2 and SO, standing amongst the most abundant molecules detected to date in this object (see e.g. Morris et al. 1987; Sánchez Contreras et al. 2000b, 2014). The second-most abundant molecule reported in this work is HNCO, which is a factor ~20 less abundant than NO and comparable in abundance to HCN and HNC (Morris et al. 1987; Sánchez Contreras et al. 1997, 2000b). The abundance of HNCO is a factor ~10 larger than that of its sulfur analogue, HNCS.

4.2. Non-LTE excitation

When the local density of molecular hydrogen (n_{H_2}) is insufficient to thermalize the transitions of a given molecule, departures from a linear relation in the population diagram are expected. For example, different values of T_{rot} may be deduced from different transitions, leading to a curvature (or multiple slopes) in the distribution of the data points in the population diagram, which also affects the total column density inferred. Non-LTE excitation effects on the population diagrams of the N-bearing molecules detected in OH 231.8+4.2 are investigated and discussed in Appendix A. The high nebular densities in the dominant emitting regions of the outflow (~10^5–10^6 cm^{-3}) indicate that the ^{13}CO lines are thermalized over the bulk of the outflow; however, the transitions observed from HNCO, HNCS, HC_3N, and NO, have critical densities of up to ~10^6 cm^{-3} and, therefore, some LTE deviations may occur. In these cases, the level populations of the different species are numerically computed (for given input values of T_{kin}, N_{tot}, and n_{H_2}) considering both collisional and radiative proceses and the well known *LVG* approximation – see Appendix A.

In this section, we investigate whether the observations could also be reproduced by values of T_{kin} and N_{tot} that are different from those deduced from LTE calculations using moderate n_{H_2} for which LTE does not apply. The results from our non-LTE excitation models have been represented in a population diagram (i.e. N_u/g_u vs. E_u) together with the observed data-points. The best data-model fits are shown in Fig. 10, and the range of input values for T_{kin} and N_{tot} consistent with the observations are given in Table 4.

Except for HNCO (see below), in our non-LTE models we have adopted a mean characteristic density in the emitting regions of the outflow of $n_{H_2} \sim 10^5$ cm^{-3}. The lowest densities in OH 231.8+4.2, $n_{H_2} \sim 10^3$–10^4 cm^{-3}, are only found at large distances from the star in the southern lobe (clumps I5 and beyond) that do not contribute to the emission observed from these N-bearing species (Alcolea et al. 2001).

In the case of HNCO, one notable effect of non-LTE conditions is the split of the $K_a = 0$ and $K_a = 1$ ladders into two almost paralell straight lines in the population diagram (Appendix A). The separation between the $K_a = 0$ and $K_a = 1$ ladders, which is indeed observed in OH 231.8+4.2 (e.g. Fig. 10, top panel), progressively reduces as the density increases; when densities $\gtrsim 10^8$ cm^{-3} are reached, all transitions reported here are very close to thermalization, and both the $K_a = 0$ and $K_a = 1$ ladders merge into one single straight line. The non-LTE excitation analysis of HNCO indicates that the observed separation between the $K_a = 0$ and $K_a = 1$ ladders in the population diagram of OH 231.8+4.2 requires nebular densities of $n_{H_2} \sim 4 \times 10^7$ cm^{-3}. This suggests that most of the observed HNCO emission probably arises at relatively dense regions in the envelope. Adopting $n_{H_2} \sim 4 \times 10^7$ cm^{-3}, therefore, we find that the observations are reproduced well for a range of values of $N_{tot}(HNCO) \sim [4.0–5.2] \times 10^{14}$ cm^{-2} and $T_{kin} \sim 26$–28 K, that is, very similar to those obtained under the LTE approximation.

Several authors have pointed out the importance of infrared pumping to explain the excitation of HNCO under certain conditions (e.g. Churchwell et al. 1986; Li et al. 2013). We have not taken the effect of IR pumping into account given the complexity of the problem, which is beyond the scope of this paper. This effect adds additional uncertainties to the HNCO abundance, which could be larger or smaller than the value quoted in Table 4, but probably by a factor not greater than ~2–5. Additional discussion about this topic is given in the Appendix A.

For HNCO and the rest of the molecules, HNCS, HC_3N, and NO, one major effect of non-LTE excitation on the population diagram is a modification of the slope of the straight line defined by the data points (N_u/g_u vs. E_u) with respect to the correct value entered as input in the model as T_{kin}. In particular, as can be seen in Fig. 10, for $n_{H_2} \sim 10^5$ cm^{-3}, the rotational temperature that one would deduce from the population diagram is lower than the input kinetic temperature ($T_{rot} < T_{kin}$, sub-thermal excitation). The largest difference between T_{kin} and T_{rot} in our models is found for HC_3N; in this case, values of T_{kin} of up to ~55 K in the emitting regions cannot be ruled out. On the other hand, in general for all species, the column densities derived from the non-LTE excitation analysis are systematically lower than those deduced assuming LTE conditions. We note, however, that these differences are typically $\lesssim 30\%$.

Finally, as shown in the Appendix A, for densities of $n_{H_2} \leq 10^4$ cm^{-3}, non-LTE level populations of HNCO, HNCS, HC_3N, and NO would result in a double slope in their population diagrams. (This effect would be most prominent for HC_3N.)

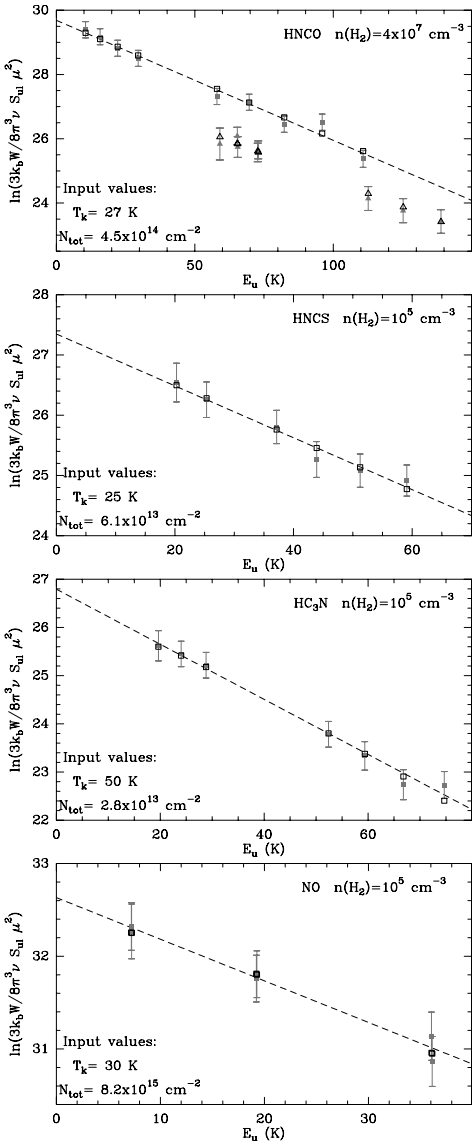

Fig. 10. Population diagrams of HNCO, HNCS, HC_3N, and NO including observational data points (filled symbols) and points from representative non-LTE models (empty symbols; Sect. 4.2). The main input parameters (n_{H_2}, T_{kin}, and N_{tot}) of the non-LTE models are indicated within the boxes, along with the linear fit to the data points (dashed line; same as in Fig. 9). For HNCO, squares and triangles represent the $K_a = 0$ and $K_a = 1$ transitions, respectively (as in Fig. 9).

That this is not observed in our data, described well by a unique value of T_{rot}, corroborates that the typical densities in the emitting regions are above 10^4 cm^{-3}.

5. Chemical modelling

In this section, we present thermodynamical chemical equilibrium (TE) and chemical kinetics models to investigate the formation of HNCO, HNCS, HC_3N, and NO in O-rich CSEs with characteristics similar to those in OH 231.8+4.2. The TE calculations should provide a good estimation of the molecular abundances near the stellar photosphere, up to ~4–5 R_*, given the high densities (≈10^{14}–10^9 cm^{-3}) and high temperatures (~2000 K) expected in these innermost regions (e.g. Tsuji 1973). As the gas or dust in the stellar wind expands, the temperature and the density gradually decrease, and the chemical timescale increases, making chemical kinetics dominate in determining the molecular abundances. Eventually, the dispersion of the envelope allows the interstellar UV photons to penetrate through the outermost layers, leading to the onset of a productive photo-induced chemistry.

For many important molecules, the abundances established by the equilibrium chemistry in the dense, hot photosphere are expected to be greatly modified by various processes (not all understood well) that operate in the deep envelope layers. First, the inner wind regions at a few $R_\star$ are dominated by non-equilibrium reactions triggered by low-velocity shocks generated by the stellar pulsation. Second, the formation of dust particles, which begins farther out at ~5–15$R_\star$, well affects the chemistry a lot in different ways, for example, depleting refractory species from the gas phase (owing to grain adsorption) and powering the production of other compounds through grain surface reactions. Because of all this, the molecules produced by these processes in the deep envelope layers, named "parent", are injected to the intermediate envelope with initial abundances that might differ significantly from values predicted by TE chemical calculations (e.g. Cherchneff 2006).

5.1. Physical model of the envelope

We used two different physical structures as input in our chemical kinetics models: a) a spherical stellar wind with characteristics similar to those of the slow central nebular component of OH 231.8+4.2; and b) a slab of gas (plane-parallel geometry) with characteristics similar to those of the walls of the hollow lobes of OH 231.8+4.2. For the TE calculations, only the physical model *a* has been considered since the conditions for thermodynamical chemical equilibrium are not met in the lobes ($n_{H_2} \sim 10^5$ cm^{-3} and $T_{kin} \sim 20$ K).

The physical model *a* consists of a spherical envelope of gas (and dust) expanding around the central AGB star of OH 231.8+4.2. This has been taken as a representation of the slow central component of the outflow, which has been interpreted as the fossil remnant of the old AGB CSE (Sect. 1). We separately modelled i) the innermost envelope regions (within ~5 $R_\star$), where TE conditions apply; and ii) the intermediate/outer envelope (from ~20 $R_\star$ to its end), where chemistry is driven by chemical kinetics. The density, temperature, and velocity are expected to vary across these two components as a function of the radial distance to the centre (r).

The intermediate/outer envelope is characterized well observationally (Sect. 1) and its main physical parameters are summarized in Table 5. For modelling purposes, the intermediate/outer envelope has been chosen to begin at ~20 $R_\star$, that is to say, well beyond the dust condensation radius (R_c) where the full expansion velocity of the gas (by radiation pressure onto dust) has been reached. Throughout this slow central component, we adopt a characteristic constant expansion velocity of V_{exp} = 20 km s^{-1}. The gas kinetic temperature has been approximated by a power law that varies with the radius as $r^{-0.7}$ (typical of AGB CSEs, e.g. Cherchneff et al. 1992). The density in the intermediate/outer envelope is given by the law of conservation of mass, which

Table 5. Parameters of the central Mira-type star and slow core envelope component of OH 231.8+4.2 used for the chemical models (Sect. 5.)

Parameter	Value	Reference
Distance (d)	1500 pc	b
Stellar radius (R_*)	4.4×10^{13} cm	g
Stellar effective temperature (T_*)	2300 K	c, d, h
Stellar luminosity (L_*)	$10^4\ L_\odot$	g
Stellar mass (M_*)	$1\ M_\odot$	g
AGB CSE expansion velocity ($V_{\rm exp}$)	20 km s^{-1}	a, e, f, g, i
AGB mass loss rate ($\dot{M}$)	$10^{-4}\ M_\odot$ yr^{-1}	e, a, f
Gas kinetic temperature ($T_{\rm k}$)	$T_*(r/R_*)^{-0.70}$ K	i

References. a) Alcolea et al. (2001); b) Choi et al. (2012); c) Cohen (1981); d) Kastner et al. (1992); e) Morris et al. (1987); f) Sánchez Contreras et al. (1997); g) (Sánchez Contreras et al. 2002); h) Sánchez Contreras et al. (2004); i) this work.

results in a density profile varying as $\propto r^{-2}\dot{M}/V_{\rm exp}$. The outer radius of the slow central component of the molecular outflow of OH 231.8+4.2 is $\sim 7 \times 10^{16}$ cm ($3''$ at d = 1500 pc; see Sect. 1), which has been adopted in our model. This value is a factor ∼10 lower than the CO photodissociation radius given the AGB mass-loss rate and expansion velocities measured in this object and adopting $X({\rm CO}) = 3 \times 10^{-4}$, following Mamon et al. (1988) and Planesas et al. (1990). This indicates that the outer radius of the envelope in the equatorial direction represents a real density cut-off in the AGB wind marked by the beginning of the heavy AGB mass loss.

The inner envelope, where the TE calculations were done, begins at the stellar photosphere and ends at the dust condensation radius ($R_{\rm c} = 5\ R_\star$), i.e. before dust acceleration takes place. For these regions we use $V_{\rm exp} = 5$ km s^{-1}, in agreement with the line widths of vibrationally excited H_2O emission lines in the far-IR in this object (Sánchez Contreras et al. 2014) and typical values in other AGB stars (Agúndez et al. 2012, and references therein). For the gas kinetic temperature, we use the same power law as in the intermediate/outer envelope. The densities in these innermost regions near the stellar photosphere were calculated based on theoretical arguments considering hydrostatic equilibrium (in the static stellar atmosphere, up to ∼1.2 $R_\star$) and pulsation induced, low-velocity shocks (in the dynamic atmosphere, from ∼1.2 $R_\star$ and up to $R_{\rm c} \sim 5\ R_\star$ – see e.g. Agúndez et al. 2012, and references therein for a complete formulation and discussion). According to this, in our model, the density steeply varies from $\sim 10^{14}$ cm^{-3} at $R_\star$ to $\sim 10^{12}$ cm^{-3} at 1.2 $R_\star$; beyond this point, it decreases to $\sim 10^9$ cm^{-3} at ∼5 $R_\star$. Although the density and temperature in the innermost nebular regions of OH 231.8+4.2 are not as well constrained observationally as in the intermediate/outer envelope, the laws adopted reproduce the physical conditions in the SiO maser emitting regions well ($\approx 10^{9-10}$ cm^{-3} and ∼1000–1500 K at ∼2–3 $R_\star$; Sánchez Contreras et al. 2002).

The walls of the lobes, where the molecular abundances have also been predicted using our chemical kinetics model, have been approximated by a slab of gas (with a plane-parallel geometry; model b above). We used a wall thickness of ∼1″, and characteristic H_2 number density and kinetic temperature of $n_{\rm H_2} \sim 10^5$ cm^{-2} and $T_{\rm kin} = 20$ K constant in the slab, which is representative of the clumps (I2 and I4) at the base of the lobes (Alcolea et al. 2001). Within the slab, we consider the gas to be static, since the expansion velocity gradient across the lobe walls must be small. The sources of ionization and dissociation adopted in our model are cosmic rays and the interstellar ultraviolet radiation field (see Appendix C for more details on the ionization/dissociation sources adopted in our model).

Table 6. Elemental abundances used in the TE model (Sect. 5.2) taken from Asplund et al. (2009).

Element	Abundance
H	12.00
He	10.93
C	8.43
O	8.69
N	7.83
S	7.12

Notes. The abundances are given in the usual logarithmic astronomical scale where H is defined to be $\log H = 12.00$ and $\log X = \log(N_{\rm X}/N_{\rm H}) + 12$, where $N_{\rm X}$ and $N_{\rm H}$ are the number densities of elements X and H, respectively.

5.2. Thermodynamical chemical equilibrium (TE) model

Although the innermost envelope regions where TE conditions hold are not directly probed by the mm-wavelength data presented in this paper, it is useful to investigate if the new N-bearing molecules detected in OH 231.8+4.2 could form in substantial amounts in these regions or if, alternatively, they need to be produced farther out in the stellar wind. Our TE code is described in Tejero & Cernicharo (1991) and used, for example, in Agúndez et al. (2007). The computations are performed for more than 600 different species (electron, atoms, and molecules) following the method described in Tsuji (1973), and see also Agúndez (2009). The code requires thermochemical information of each molecule (Chase 1998[4]; McBride et al. 2002 and Burcat & Rucsic 2005), as well as the initial elemental abundances (given in Table 6) and the physical conditions in the inner layers of the envelope, as described in the beginning of Sect. 5.

For HNCS, thermochemical information is not available, so this molecule has not been modelled. A rough guess of the HNCS abundance can be obtained scaling from the abundance of its O-bearing analogue, HNCO, by a factor similar to the oxygen-to-sulphur ratio, O/S ∼ 37 (Asplund et al. 2009). Excluding HNCS from our chemical network may, in principle, result in an overestimate of the HNCO, HC_3N, and NO abundances in our model since some of the elements that would have gone into HNCS are now in other N-, C-, and S-bearing compounds. Given that HNCS is neither a major carrier of these atoms nor a key molecule of the gas-phase chemistry, we expect this effect to be weak.

The spatial distribution of the molecular abundances near the star predicted by our TE chemistry model is shown in Fig. 11. In all cases, the model abundances are several orders of magnitude lower than those derived from the observations (Table 4). The largest model-data discrepancy is found for HC_3N, which is formed with an extremely marginal peak fractional abundance of $X(HC_3N) < 10^{-32}$. NO is (after N_2) the most abundant N-compound in the hot photosphere, although the TE peak abundance is two orders of magnitude lower than observed in OH 231.8+4.2. We may safely conclude that the high abundances derived from the observations for these molecules cannot be explained as a result of equilibrium processes at the

[4] NIST-JANAF thermochemical tables http://kinetics.nist.gov/janaf/

A&A 575, A84 (2015)

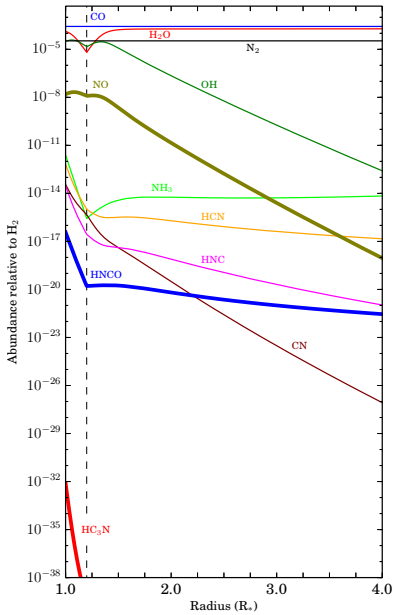

Fig. 11. Thermodynamical chemical equilibrium model predictions for the innermost layers of an O-rich AGB CSE with characteristics presumably similar to those in OH 231.8+4.2 (Sect. 5). The spatial distribution of the N-bearing molecules detected in this work and other relevant species are plotted. The dashed vertical line denotes the boundary between the static and the dynamic atmosphere, at ∼1.2 $R_\star$.

innermost parts of the envelope where, in contrast, abundant parent molecules, such as CO, N_2, and H_2O, are efficiently formed.

5.3. Chemical kinetics model

Our chemical kinetics model is based on that of Agúndez & Cernicharo (2006), which has been widely used to model the chemistry across the different envelope layers of the prototype C-rich star IRC 10216 (see also Agúndez et al. 2007, 2008, 2010) and, most recently, the O-rich YHG IRC+10420 (Quintana-Lacaci et al. 2013). The chemical network in our code includes gas-phase reactions, cosmic rays, and photoreactions with interstellar UV photons, but it does not incorporate reactions involving dust grains, X-rays, or shocks. Chemical reactions considered in this network are mainly obtained from the UMIST database (Woodall et al. 2007). The network has been updated with the latest kinetic rates and coefficients for HNCO (Quan et al. 2010). As mentioned in Sect. 5.2, HNCS has not been modelled because thermochemical parameters or reaction kinetic rates are not available for this molecule. Considering that oxygen is more abundant than sulphur (by a factor O/S ∼ 37; Table 6), we expect the HNCS abundance to be lower than that of its O-analogue, HNCO.

There are two major inputs to our chemical kinetics model, namely, the physical model of the envelope (models *a* and *b*, respectively in Sect. 5.1) and the initial abundances of the "parent" species, formed in deeper layers, which are injected into the envelope. Once incorporated into the outflowing wind, these parent species become the basic ingredients for the formation of new ("daughter") molecules. The initial abundances of the parent species used in our model are given in Table 7. These abundances come from thermodynamical chemical equilibrium calculations and observations in the inner regions of O-rich envelopes (references are provided in this table). In the case of NH_3, which is a basic parent molecule for the formation of N-bearing species, we have adopted the value at the high end of the range of abundances observationally determined for a few O-rich CSEs, $X(NH_3) \sim [0.2–3] \times 10^{-6}$ (Menten et al. 2010). We note that, as also pointed out by these authors, the formation of circumstellar NH_3 is particularly enigmatic since the observed abundances exceed the predictions from conventional chemical models by many orders of magnitude.

Table 7. Initial abundances relative to H_2 for representative elements and parent molecules used as input for the chemical kinetics models.

Species	Abundance	Reference
He	0.17	a
H_2O	3.0×10^{-4}	b, TE
CO	3.0×10^{-4}	c, TE
CO_2	3.0×10^{-7}	d
NH_3	3.0×10^{-6}	e
N_2	4.0×10^{-5}	TE
HCN	2.0×10^{-7}	f, g
H_2S	7.0×10^{-8}	h
SO	9.3×10^{-7}	f
SiO	1.0×10^{-6}	i
SiS	2.7×10^{-7}	j

References. a) Asplund et al. (2009); b) Maercker et al. (2008); c) Teyssier et al. (2006); d) Tsuji et al. (1997); e) Menten & Alcolea (1995); f) Bujarrabal et al. (1994); g) Schöier et al. (2013); h) Ziurys et al. (2007); i) González Delgado et al. (2003); j) Schöier et al. (2007). TE: From thermodynamical chemical equilibrium calculations (Sect. 5.2).

Our chemical kinetics model has been used first to investigate the formation of HNCO, HNCS, HC_3N, and NO in the intermediate/outer envelope of an O-rich AGB star similar to the slow central component of OH 231.8+4.2 (model *a* described in Sect. 5.1, see also Table 5). The spatial distribution of the model molecular abundances as a function of the distance to the centre are shown in Fig. 12. As the gas in the envelope expands, parent molecules start to be exposed to the interstellar UV radiation and photochemistry drives the formation of new species. Penetration of photons through deeper layers is gradually blocked by the dust extinction[5]. At the very inner layers of the intermediate/outer envelope, parent species are preserved with their initial abundances, and at the very outermost layers, all molecules are finally fully dissociated (destroyed).

As seen in Fig. 12, the peak abundances of all the N-molecules detected in this work are significantly lower than observed, except for NO (by 3–4 orders of magnitude). The peak fractional abundance for NO predicted by the model, $X(NO) \sim 3 \times 10^{-6}$, is in principle consistent with the average value measured in OH 231.8+4.2. According to our calculations, this molecule is expected to form rather efficiently in the winds of O-rich CSEs mainly via the gas-phase reaction

$$N + OH \longrightarrow NO + H \quad (7)$$

and, therefore, NO should be common amongst O-rich evolved stars. Detection of NO emission lines is, however, hampered by the low dipole moment of this molecule ($\mu = 0.16$ Debyes).

[5] The visual optical extinction in magnitudes (A_V) is related to the H column density by $N_H = 1.87 \times 10^{21} \times A_V$ cm^{-2}, when adopting the standard conversion from Bohlin et al. (1978).

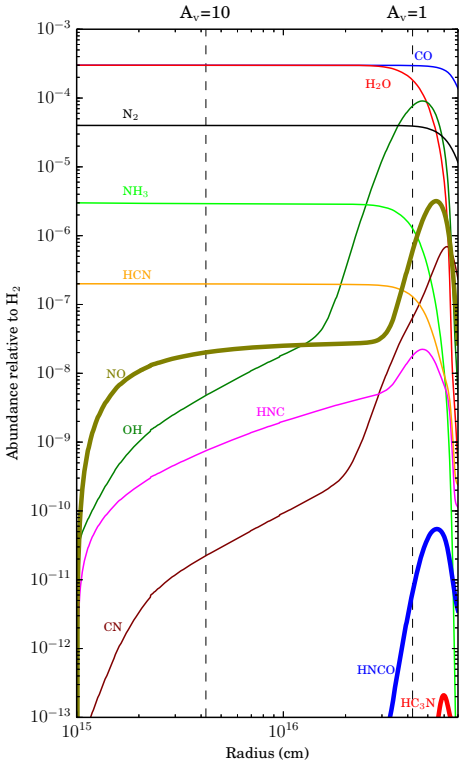

Fig. 12. Chemical kinetics model predictions for the intermediate/outer layers of an O-rich AGB CSE with physical properties similar to those of the slow central parts of OH 231.8+4.2 (model input *a*, Sect. 5 and Table 7). The species represented are as in Fig. 11.

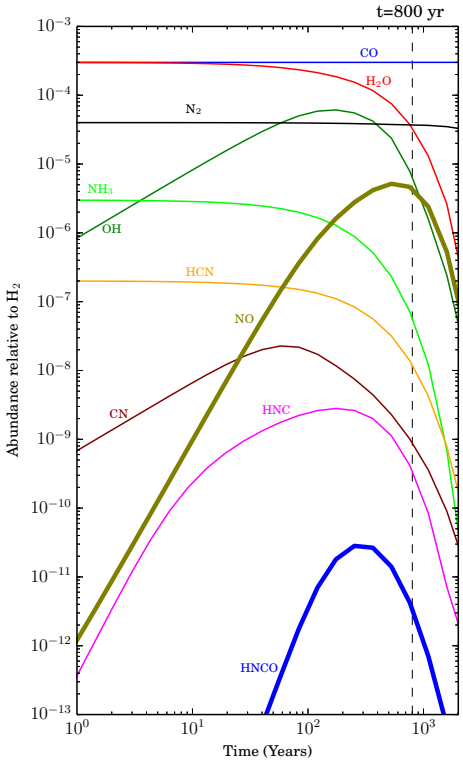

Fig. 13. Evolution with time of the molecular fractional abundances predicted by our chemical kinetics model for a rectangular slab of gas (plane-parallel geometry) with physical properties similar to those of the walls of the hollow lobes of the molecular outflow of OH 231.8+4.2 (model input *b*, Sect. 5). The model presented is for a representative gas cell in the middle of the lobe walls (A_V = 1 mag). The species represented are as in Figs. 11 and 12, except for HC_3N, which has a predicted maximum abundance ($\approx 10^{-19}$) well below the lower limit of the *y*-axis.

As derived from our model, the main chemical routes that would form HNCO and HC_3N in an O-rich CSE are

$$CN + OH \longrightarrow NCO + H \quad (8)$$
$$H_3^+ + NCO \longrightarrow HNCO^+ + H_2 \quad (9)$$
$$HNCO^+ + H_2 \longrightarrow HNCOH^+ + H \quad (10)$$
$$HNCOH^+ + e^- \longrightarrow HNCO + H \quad (11)$$

and

$$CN + C_2H_2 \longrightarrow HC_3N + H. \quad (12)$$

However, the standard processes considered here are not sufficient to reproduce the abundances observed in the particular case of OH 231.8+4.2.

We have investigated whether deeper penetration of interstellar UV radiation through the lobe walls of OH 231.8+4.2, which are on average more tenous than the central regions, can result in a significant production of HNCO and HC_3N, which could explain the observations. The input physical model for the lobe walls (a rectangular gas slab, model *b*) is described in Sect. 5.1. The total extinction through the lobe walls is $A_V \sim 2.3$ mag, taking their thickness, mean H_2 number density, and the standard n_{H_2}/A_v conversion into account (Bohlin et al. 1978). The variation with time of the fractional abundances predicted by the model for a representative cell in the middle of the lobe walls ($A_V \sim 1$ mag) are shown in Fig. 13.

As in the central nebular regions (model *a*), the abundances of HNCO (and probably HNCS) and HC_3N in the lobes never reach values comparable to those observationally determined. Except for NO, the abundances predicted in the lobes after ~800 yr, which is the dynamical age of the molecular flow of OH 231.8+4.2, are lower than those expected in the slow central parts. We find that NO reaches a fractional abundance of $\sim 4 \times 10^{-6}$ in ~800 yr. This value is comparable to the average NO abundance deduced from the observations and to the value found in the slow central component (model *a*, Fig. 12).

5.4. Enhanced N elemental abundance

We have considered whether an overabundance of the elemental nitrogen could result in fractional abundances of N-bearing compounds in better agreement with the observations. Such an elemental N-enrichment could result from hot bottom burning (HBB) process for stars with masses $\gtrsim 3\,M_\odot$ and it has been proposed to explain the high abundance of NO deduced in the molecular envelope of the yellow hypergiant (YHG)

A&A 575, A84 (2015)

star IRC+10420 (Quintana-Lacaci et al. 2013, and references therein).

As a first step, we ran our TE model again, increasing the elemental nitrogen abundance by a factor 40 – a larger enrichment factor is not expected (Boothroyd et al. 1993). In the inner layers of the envelope, our TE model shows that the N_2 fractional abundance increases proportionally, i.e. also by a factor 40. Other N-bearing molecules, such as NH_3, HCN, NO, HNCO, and HC_3N, are less sensitive to the initial N-abundance, and they increase their abundances by a smaller factor, ∼5–10. As expected, given the very large discrepancy between TE model and data abundances, this factor is insufficient to explain the observations in OH 231.8+4.2.

As a second step, we ran our chemical kinetics model (case *a*) again but modified the initial abundances of relevant parent species (N_2, NH_3, and HCN) according to the TE predictions: N_2 is increased by a factor 40 and NH_3 and HCN by a factor 7 relative to the values in Table 7. Our TE calculations also show that these are the N-containing molecules that are most sensitive to the initial abundance of N. From our chemical kinetics model, we find that neither HNCO (and presumably HNCS) nor HC_3N experiment a significant variation, maximum abundance of HNCO is $\sim 8 \times 10^{-10}$ and $\sim 8 \times 10^{-13}$ for HC_3N, which are still low compared to the values derived from the observations. As NO concerns, we find a model peak abundance of $\sim 3 \times 10^{-5}$ in the outer layers of the slow central component, which would be in excess of the value derived from the observations in OH 231.8+4.2. We therefore believe that a resonable enhancement of the elemental abundance of nitrogen, if it exists, would not reproduce the abundances of the N-molecules discussed by us satisfactorily. On the one hand, HNCO, HNCS, and HC_3N are underestimated, and on the other, NO (and maybe others, such as NH_3) would be significantly overestimated.

6. Discussion

Except maybe for NO, the relatively large abundances of the N-molecules detected in this work cannot be explained as thermodynamical chemical equilibrium or photodissociation products in the outflow of OH 231.8+4.2, even in the case of HNCO after considering IR pumping effects (Sect. 4.2, Appendix A). In principle, the inability of the model to reproduce the observed abundances of HNCO, HNCS, and HC_3N could be attributed to the simplicity of the physico-chemical scenario adopted, for example, to the lack of certain molecule formation routes (e.g. involving dust grains). However, if these were the main reasons for the model-data discrepancies in OH 231.8+4.2 (and provided that these unknown chemical routes prove to be an efficient way of producing HNCO, HNCS, and HC_3N in O-rich environments, which remains to be seen), then these molecules should be present with comparable abundances in other O-rich envelopes of similar characteristics.

These molecules have been searched for but not detected by our team (and others) in two of the strongest molecular emitters and best studied O-rich envelopes: the AGB star IK Tau (Velilla et al., in prep.) and the red supergiant VY CMa (Quintana-Lacaci et al., in prep.). In these objects, NO is detected with a fractional abundance of $X(\mathrm{NO}) \approx 10^{-7}$, in agreement with the model predictions, but only upper limits are obtained for the rest of the N molecules discussed here, $\lesssim 10^{-9}$–$\lesssim 10^{-10}$. The upper limits estimated for IK Tau and VY CMa are consistent with the low abundances predicted by the models, which suggests that the physico-chemical scenario used by us is an acceptable representation of a standard O-rich AGB CSE. We recall that the notable chemical differences between OH 231.8+4.2 and other O-rich AGB CSE are widely recognized and are not restricted to the N-molecules detected here but affect most of the species identified in this object, including C-, N-, and S-containing ones such as HCN, H_2CO, H_2S, SO, SO_2, which are undetected or detected with much lower abundances in "normal" O-rich AGB CSE, as pointed out by previous works (Sect. 1).

In principle, there is no reason to suspect a particularly intense interstellar UV radiation field or peculiar dust properties or content that could (or not) account for the unique, rich chemistry of OH 231.8+4.2 compared to its O-rich relatives. The main difference between OH 231.8+4.2 and "normal" O-rich AGB CSEs is the presence of a fast (∼400 km s^{-1}) accelerated outflow in the former. Given the formation history of such an outflow, possibly as the result of a sudden jet+"AGB CSE" interaction ∼800 yr ago (Sect. 1), fast shocks have probably played a major role not only in the physics but also in the chemistry of OH 231.8+4.2. Molecules are expected to be initially destroyed by the high-speed axial shocks produced in the jet+"AGB CSE" interaction (e.g. Neufeld 1990). At present, the shocked material has cooled down sufficiently to allow molecule reformation, which probably happened very quickly, in less than ∼150 yr, under non-equilibrium conditions. Moreover, additional atoms (Si, S, etc.) may have been extracted by the shocks from the dust grains and released into the gas phase (Morris et al. 1987; Lindqvist et al. 1992), altering the proportions of the different elements available for molecule regeneration in the post-shocked gas. Both non-equlibrium conditions and non-standard elemental proportions in the post-shocked gas are crucial factors determining the abundances of the second-generation molecules in OH 231.8+4.2.

Shocks could also have been decisive in defining the chemistry of the slow central parts of the envelope around OH 231.8+4.2. As already pointed by, for example, Lindqvist et al. (1992), the maximum expansion velocities measured towards the central nebular regions, $V_{\mathrm{exp}} \sim 35$ km s^{-1}, are higher than for normal OH/IR stars, which indicates that some acceleration is likely to have occurred. In fact, it may be possible for shocks developed in the jet+AGB CSE interaction to move sideways and backward (with moderate velocities lower than those reached along the jet axis) compressing the gas in the equatorial plane and shaping the central, torus-like structure of OH 231.8+4.2. Although these moderate-velocity ($\lesssim$40 km s^{-1}) shocks are not expected to destroy molecules (at least not fully), the compression and heating of these equatorial regions would result in a profound chemical mutation with respect to normal unperturbed AGB CSEs (for example, activating certain endothermic reactions, or exothermic reactions with barriers, otherwise forbidden).

7. Summary and conclusions

We have reported the first detection of the N-bearing molecules HNCO, HNCS, HC_3N, and NO in the CSE of the O-rich evolved star OH 231.8+4.2 based on single-dish observations with the IRAM-30 m telescope. HNCO and HNCS are first detections in CSEs; HC_3N is a first detection in an O-rich environment; NO is a first detection in a CSE around a low-to-intermediate-mass, evolved star. From the observed profiles, we deduce the presence of these species in the slow central parts of the nebula, as well as at the base of the fast bipolar lobes.

The intense, low-velocity components of the HNCO $K_a = 0$, HNCS, and HC_3N profiles have similar widths ($FWHM \sim 20$–30 km s^{-1}) and velocity peaks ($V_{\mathrm{LSR}} \sim 28$–29 km s^{-1}). Previous SO emission mapping

(Sánchez Contreras et al. 2000b) shows the presence of an equatorial expanding disk or torus around the central star that produces double-peaked (at $V_{\rm LSR}$ = 28 and 40 km s^{-1}) spectral profiles in many SO transitions (and also in other molecules). The coincident peak velocity of HNCO, HNCS, and HC_3N transitions with the blue peak of the disk/torus feature suggests that part of the low-velocity emission from these molecules may arise at this equatorial structure. The HNCO K_a=1 transitions are narrower, with $FWHM \sim 13$ km s^{-1}, and may arise in regions closer in to the central source.

The profiles of the NO lines are broader ($FWHM \sim$ 40–50 km s^{-1}) and are centred on somewhat redder velocities $V_{\rm LSR} \sim 40$ km s^{-1}. As explained in Sect. 3, this is not only due to the hyperfine structure of the NO transitions, but it also indicates that a significant part of the NO emission is produced in regions with high expansion velocities; in particular, the contribution to the emission from clump I4 at the base of the southern lobe is notable. Broad profiles ($FWHM \sim$ 40–90 km s^{-1}) are also found for mm-wave transitions of HCO^+ (Sánchez Contreras et al. 2000b) and other molecular ions recently discovered by us in OH 231.8+4.2 (Sánchez Contreras et al., in prep.). This suggests a similar spatial distribution of these species with enhanced abundances in the high-velocity gas relative to the low-velocity nebular component at the centre.

We derived typical rotational temperatures of ∼15–30 K, in agreement with previous estimates of the kinetic temperature in the CO flow (Alcolea et al. 2001). Non-LTE effects are expected to be moderate, given the relatively high densities of the dominant emitting regions ($\gtrsim 10^5$ cm^{-3}). Nevertheless, in the case of HC_3N, moderate sub-thermal excitation is possible in the most tenuous parts of the outflow, and somewhat higher temperatures of ∼45 to 55 K cannot be ruled out. Adopting a characteristic size of the emitting nebula of $\sim 4'' \times 12''$, we obtained column densities of $N_{\rm tot}(^{13}CO) \sim 3\times10^{17}$ cm^{-2}, $N_{\rm tot}$(HNCO) $\sim 6\times10^{14}$ cm^{-2}, $N_{\rm tot}$(HNCS) $\sim 7\times10^{13}$ cm^{-2}, $N_{\rm tot}(HC_3N) \sim 3\times10^{13}$ cm^{-2}, and $N_{\rm tot}$(NO) $\sim 9\times10^{15}$ cm^{-2}.

The beam-averaged fractional abundances in OH 231.8+4.2 obtained are (in decreasing order) X(NO) ∼ [1–2] × 10^{-6}, X(HNCO) ∼ [0.8–1] × 10^{-7}, X(HNCS) = [0.9–1] × 10^{-8}, and $X(HC_3N)$ = [5–7] × 10^{-9}. We note the large abundance of NO, which is comparable to that of, e.g., SO and SO_2 (already known to be dominant in OH 231.8+4.2). Our measurement implies that NO is one of the most abundant N-containing molecule in this object. Also remarkable is the relatively large abundance of HNCO, closely following that of major carriers of carbon in OH 231.8+4.2, apart from CO and ^{13}CO, such as HCN, H_2CO, and CS, and comparable to and even larger than that of HNC and HCO^+ (Morris et al. 1987; Lindqvist et al. 1992; Sánchez Contreras et al. 1997, 2000b, 2014; Velilla Prieto et al. 2013).

We modelled thermodynamical equilibrium and non-equilibrium kinetically driven chemistry to investigate the production of HNCO, HC_3N, and NO in OH 231.8+4.2. HNCS cannot be modelled because of the lack of thermochemical parameters and reactions rates. We modelled the slow central component and the lobe walls separately.

We found that none of the molecules HNCO, HC_3N, or NO are formed in significant amounts in the vicinity of the AGB star (up to $\sim 4R_\star$), where thermodynamical equilibrium conditions prevail (Fig. 11). In these regions, the vast majority of N atoms are locked in N_2, followed by NO.

In the intermediate/outer layers of the slow central component of the envelope (from $\sim 10^{15}$ to $\sim 10^{17}$ cm^{-}), the model fails to reproduce the large abundances observed in OH 231.8+4.2, except for NO (Fig. 12). The model-data discrepancies cannot be explained by a reasonable enhancement of the elemental nitrogen abundance (as a result of HBB processes).

In the lobes, our chemistry model indicates that the only molecule that reaches fractional abundances comparable to the values observationally determined is NO. For HNCO (and probably HNCS) and HC_3N, the model abundances in the lobes are more than five orders of magnitude lower than the observed average values.

Based on this and previous works, the rich chemistry of OH 231.8+4.2, which is unparalleled amongst AGB and post-AGB envelopes, is corroborated. New detection of HNCO, HNCS, HC_3N, and NO add to the list of N-bearing molecules present in its molecular outflow with high abundances. This could be the best example of a shocked environment around an evolved star, and OH 231.8+4.2 therefore stands out as a reference target for studying non-equilibrium, shock-induced chemical processes in oxygen-rich environments.

Acknowledgements. We acknowledge the IRAM-30 m staff for the support and help kindly given during the observations presented in this article, in particular to M. González. We also acknowledge the help provided by J. R. Pardo during the different observational runs in which he took part. This work was done at the Astrophysics Department of the Centro de Astrobiología (CAB-INTA/CSIC) and the Molecular Astrophysics Department of the Instituto de Ciencias de Materiales de Madrid (ICMM-CSIC). We acknowledge the Spanish MICINN/MINECO for funding support through grants AYA2009-07304, AYA2012-32032, and the ASTROMOL Consolider project CSD2009-00038. L.V. acknowledges the Spanish MINECO for funding support through FPI2012 short stay programme (ref. EEBB-I-13-06211) and the Laboratoire D'Astrophysique de Bordeaux (LAB-CNRS) for hosting this stay under the supervision of Dr. Marcelino Agúndez. L.V. also acknowledges the support of the Universidad Complutense de Madrid through the Ph.D. programme. M.A. acknowledges the support from the European Research Council (ERC Grant 209622: E_3 ARTHS). This research made use of the IRAM GILDAS software, the JPL Molecular Spectroscopy catalogue, the Cologne Database for Molecular Spectroscopy, the SIMBAD database, operated at the CDS, Strasbourg, France, NASA's Astrophysics Data System, and Aladin.

References

Adande, G. R., Halfen, D. T., Ziurys, L. M., Quan, D., & Herbst, E. 2010, ApJ, 725, 561
Agundez, M. 2009, Ph.D. Thesis, Universidad Autónoma de Madrid
Agúndez, M., & Cernicharo, J. 2006, ApJ, 650, 374
Agúndez, M., Cernicharo, J., & Guélin, M. 2007, ApJ, 662, L91
Agúndez, M., Fonfría, J. P., Cernicharo, J., Pardo, J. R., & Guélin, M. 2008, A&A, 479, 493
Agúndez, M., Cernicharo, J., & Guélin, M. 2010, ApJ, 724, L133
Agúndez, M., Fonfría, J. P., Cernicharo, J., et al. 2012, A&A, 543, A48
Akyilmaz, M., Flower, D. R., Hily-Blant, P., Pineau Des Forêts, G., & Walmsley, C. M. 2007, A&A, 462, 221
Alcolea, J., Bujarrabal, V., Sánchez Contreras, C., Neri, R., & Zweigle, J. 2001, A&A, 373, 932
Asplund, M., Grevesse, N., Sauval, A. J., & Scott, P. 2009, ARA&A, 47, 481
Audinos, P., Kahane, C., & Lucas, R. 1994, A&A, 287, L5
Bachiller, R., & Cernicharo, J. 1986, A&A, 168, 262
Balick, B., & Frank, A. 2002, ARA&A, 40, 439
Bohlin, R. C., Savage, B. D., & Drake, J. F. 1978, ApJ, 224, 132
Boothroyd, A. I., Sackmann, I.-J., & Ahern, S. C. 1993, ApJ, 416, 762
Bowers, P. F., & Morris, M. 1984, ApJ, 276, 646
Brown, R. L. 1981, ApJ, 248, L119
Bujarrabal, V., Fuente, A., & Omont, A. 1994, A&A, 285, 247
Bujarrabal, V., Castro-Carrizo, A., Alcolea, J., & Sánchez Contreras, C. 2001, A&A, 377, 868
Bujarrabal, V., Alcolea, J., Sánchez Contreras, C., & Sahai, R. 2002, A&A, 389, 271
Bujarrabal, V., Alcolea, J., Soria-Ruiz, R., et al. 2012, A&A, 537, A8
Burcat, A., & Ruscic, B. 2005, Third millenium ideal gas and condensed phase thermochemical database for combustion with updates from active thermochemical tables, ANL-05/20 and TAE 960 Technion-IIT, Aerospace Engineering, and Argonne National Laboratory, Chemistry Division, September 2005

Cabezas, C., Cernicharo, J., Alonso, J. L., et al. 2013, ApJ, 775, 133
Carter, M., Lazareff, B., Maier, D., et al. 2012, A&A, 538, A89
Castro-Carrizo, A., Quintana-Lacaci, G., Neri, R., et al. 2010, A&A, 523, A59
Cernicharo, J. 1985, Internal IRAM report (Granada: IRAM)
Cernicharo, J. 2012, EAS Pub. Ser., 58, 251
Cernicharo, J., & Guelin, M. 1987, A&A, 183, L10
Cernicharo, J., Guelin, M., & Askne, J. 1984, A&A, 138, 371
Cernicharo, J., Guélin, M., & Kahane, C. 2000, A&AS, 142, 181
Cernicharo, J., Teyssier, D., Quintana-Lacaci, G., et al. 2014, ApJ, 796, L21
Cohen, M. 1981, PASP, 93, 288
Cohen, M., Dopita, M. A., Schwartz, R. D., & Tielens, A. G. G. M. 1985, ApJ, 297, 702
Chapillon, E., Dutrey, A., Guilloteau, S., et al. 2012, ApJ, 756, 58
Chase, M. W. 1998, NIST-JANAF Thermochemical Tables, J. Phys. Chem. Ref. Data, Monograph. 9, 4th edn., Melville: AIP
Cherchneff, I. 2006, A&A, 456, 1001
Cherchneff, I., Barker, J. R., & Tielens, A. G. G. M. 1992, ApJ, 401, 269
Choi, Y. K., Brunthaler, A., Menten, K. M., & Reid, M. J. 2012, IAU Symp., 287, 407
Churchwell, E., Wood, D., Myers, P. C., & Myers, R. V. 1986, ApJ, 305, 405
Dalgarno, A. 2006, Proc. the National Academy of Science, 103, 12269
Desmurs, J.-F., Alcolea, J., Bujarrabal, V., Sánchez Contreras, C., & Colomer, F. 2007, A&A, 468, 189
Dopita, M. A., & Sutherland, R. S. 1995, ApJ, 455, 468
Draine, B. T., & Salpeter, E. E. 1978, Nature, 271, 730
Feast, M. W., Catchpole, R. M., Whitelock, P. A., et al. 1983, MNRAS, 203, 1207
Frerking, M. A., Linke, R. A., & Thaddeus, P. 1979, ApJ, 234, L143
Garrod, R. T., Weaver, S. L. W., & Herbst, E. 2008, ApJ, 682, 283
Gerin, M., Viala, Y., Pauzat, F., & Ellinger, Y. 1992, A&A, 266, 463
Goldsmith, P. F., & Langer, W. D. 1999, ApJ, 517, 209
Goldsmith, P. F., Snell, R. L., Deguchi, S., Krotkov, R., & Linke, R. A. 1982, ApJ, 260, 147
González Delgado, D., Olofsson, H., Kerschbaum, F., et al. 2003, A&A, 411, 123
Guilloteau, S., Lucas, R., Omont, A., & Nguyen-Q-Rieu 1986, A&A, 165, L1
Habing, H. J. 1968, Bull. Astron. Inst. Netherlands, 19, 421
Halfen, D. T., Apponi, A. J., & Ziurys, L. M. 2001, ApJ, 561, 244
Iglesias, E. 1977, ApJ, 218, 697
Jackson, J. M., Armstrong, J. T., & Barrett, A. H. 1984, ApJ, 280, 608
Jones, L. H., & Badger, R. M. 1950, J. Chem. Phys., 18, 1511
Jones, L. H., Shoolery, J. N., Shulman, R. G., & Yost, D. M. 1950, J. Chem. Phys., 18, 990
Jura, M., & Morris, M. 1985, ApJ, 292, 487
Kastner, J. H., Weintraub, D. A., Zuckerman, B., et al. 1992, ApJ, 398, 552
Kłos, J., Lique, F., & Alexander, M. H. 2008, Chem. Phys. Lett., 455, 1
Kramer, C. 1997, Internal IRAM report (Granada: IRAM)
Kuan, Y.-J., & Snyder, L. E. 1996, ApJ, 470, 981
Li, J., Wang, J. Z., Gu, Q. S., & Zheng, X. W. 2013, A&A, 555, A18
Lindqvist, M., Olofsson, H., Winnberg, A., & Nyman, L. A. 1992, A&A, 263, 183
Lique, F., van der Tak, F. F. S., Kłos, J., Bulthuis, J., & Alexander, M. H. 2009, A&A, 493, 557
Maercker, M., Schöier, F. L., Olofsson, H., Bergman, P., & Ramstedt, S. 2008, A&A, 479, 779
Mamon, G. A., Glassgold, A. E., & Huggins, P. J. 1988, ApJ, 328, 797
Marcelino, N., Brünken, S., Cernicharo, J., et al. 2010, A&A, 516, A105
Martín, S., Requena-Torres, M. A., Martín-Pintado, J., & Mauersberger, R. 2008, ApJ, 678, 245
McBride, B. J., Zehe, M. J., & Gordon, S. 2002, NASA Glenn coefficients for calculating thermodynamic properties of individual species, NASA report TP-2002-211556
Menten, K. M., & Alcolea, J. 1995, ApJ, 448, 416
Menten, K. M., Wyrowski, F., Alcolea, J., et al. 2010, A&A, 521, L7
Milam, S. N., Woolf, N. J., & Ziurys, L. M. 2009, ApJ, 690, 837
Morris, M., Gilmore, W., Palmer, P., Turner, B. E., & Zuckerman, B. 1975, ApJ, 199, L47
Morris, M., Turner, B. E., Palmer, P., & Zuckerman, B. 1976, ApJ, 205, 82
Morris, M., Guilloteau, S., Lucas, R., & Omont, A. 1987, ApJ, 321, 888
Müller, H. S. P., Schlöder, F., Stutzki, J., & Winnewisser, G. 2005, J. Mol. Struct., 742, 215
Neri, R., Kahane, C., Lucas, R., Bujarrabal, V., & Loup, C. 1998, A&AS, 130, 1
Neufeld, D. A. 1990, Mol. Astrophys., 374
Nguyen-Q-Rieu, Henkel, C., Jackson, J. M., & Mauersberger, R. 1991, A&A, 241, L33
Omont, A., Lucas, R., Morris, M., & Guilloteau, S. 1993, A&A, 267, 490
Pardo, J.R., Cernicharo, J. & Serabyn, E. 2001, IEEE Tras. Antennas and Propagation, 49, 12
Pardo, J. R., Cernicharo, J., Goicoechea, J. R., & Phillips, T. G. 2004, ApJ, 615, 495
Pickett, H. M., Poynter, R. L., Cohen, E. A., et al. 1998, J. Quant. Spectr. Rad. Transf. 60, 883
Planesas, P., Bachiller, R., Martin-Pintado, J., & Bujarrabal, V. 1990, ApJ, 351, 263
Quan, D., Herbst, E., Osamura, Y., & Roueff, E. 2010, ApJ, 725, 2101
Quintana-Lacaci, G., Agúndez, M., Cernicharo, J., et al. 2013, A&A, 560, L2
Ramstedt, S., & Olofsson, H. 2014, A&A, 566, A145
Reipurth, B. 1987, Nature, 325, 787
Rodríguez-Fernández, N. J., Tafalla, M., Gueth, F., & Bachiller, R. 2010, A&A, 516, A98
Sabin, L., Zhang, Q., Zijlstra, A. A., et al. 2014, MNRAS, 438, 1794
Sahai, R., & Trauger, J. T. 1998, AJ, 116, 1357
Sánchez Contreras, C., & Sahai, R. 2012, ApJS, 203, 16
Sánchez Contreras, C., Bujarrabal, V., & Alcolea, J. 1997, A&A, 327, 689
Sánchez Contreras, C., Bujarrabal, V., Miranda, L. F., & Fernández-Figueroa, M. J. 2000a, A&A, 355, 1103
Sánchez Contreras, C., Bujarrabal, V., Neri, R., & Alcolea, J. 2000b, A&A, 357, 651
Sánchez Contreras, C., Desmurs, J. F., Bujarrabal, V., Alcolea, J., & Colomer, F. 2002, A&A, 385, L1
Sánchez Contreras, C., Gil de Paz, A., & Sahai, R. 2004, ApJ, 616, 519
Sánchez Contreras, C., Velilla Prieto, L., Cernicharo, J., et al. 2011, IAU Symp., 280, 327
Sánchez Contreras, C., Velilla, L., Alcolea, J., et al. 2014, Asymmetrical Planetary Nebulae VI conference, Proc. the conference held 4–8 November, 2013, eds. C. Morisset, G. Delgado-Inglada, & S. Torres-Peimbert, online at http://www.astroscu.unam.mx/apn6/PROCEEDINGS/, 88
Schöier, F. L., Bast, J., Olofsson, H., & Lindqvist, M. 2007, A&A, 473, 871
Schöier, F. L., Ramstedt, S., Olofsson, H., et al. 2013, A&A, 550, A78
Snyder, L. E., & Buhl, D. 1972, ApJ, 177, 619
Solomon, P., Jefferts, K. B., Penzias, A. A., & Wilson, R. W. 1971, ApJ, 163, L53
Tejero, M., & Cernicharo, J. 1991, Modelos de equilibrio termodinámico aplicados a envolturas circunestelares de estrellas evolucionadas (Madrid: IGN)
Teyssier, D., Hernandez, R., Bujarrabal, V., Yoshida, H., & Phillips, T. G. 2006, A&A, 450, 167
Tsuji, T. 1973, A&A, 23, 411
Tsuji, T., Ohnaka, K., Aoki, W., & Yamamura, I. 1997, A&A, 320, L1
Turner, B. E. 1971, ApJ, 163, L35
Turner, B. E., Terzieva, R., & Herbst, E. 1999, ApJ, 518, 699
Ukita, N., & Morris, M. 1983, A&A, 121, 15
Velilla Prieto, L., Sánchez Contreras, C., Cernicharo, J., et al. 2013, Highlights of Spanish Astrophysics VII, 676
Wernli, M., Wiesenfeld, L., Faure, A., & Valiron, P. 2007, A&A, 464, 1147
Westenberg, A. A., & Wilson, E. B. 1950, J. Am. Chem. Soc., 72, 1, 199
Woodall, J., Agúndez, M., Markwick-Kemper, A. J., & Millar, T. J. 2007, A&A, 466, 1197
Zijlstra, A. A., Chapman, J. M., te Lintel Hekkert, P., et al. 2001, MNRAS, 322, 280
Zinchenko, I., Henkel, C., & Mao, R. Q. 2000, A&A, 361, 1079
Ziurys, L. M. 2006, Proc. the National Academy of Science, 103, 12274
Ziurys, L. M., Milam, S. N., Apponi, A. J., & Woolf, N. J. 2007, Nature, 447, 1094
Ziurys, L. M., Tenenbaum, E. D., Pulliam, R. L., Woolf, N. J., & Milam, S. N. 2009, ApJ, 695, 1604

Pages 19 to 22 are available in the electronic edition of the journal at http://www.aanda.org

Appendix A: Non-LTE effects on the population diagrams of HNCO, HNCS, HC_3N, and NO

The population diagram method is a common tool for deriving physical gas conditions from molecular line observations (see Goldsmith & Langer 1999, for a classic reference). It relies on two major assumptions: i) optically thin emission and ii) LTE conditions. The latter assumption (LTE) implies that the populations of all levels are described by the Boltzmann distribution with a unique rotational temperature, $T_{\rm rot}$[6], which is equal to the kinetic temperature of the gas ($T_{\rm kin} = T_{\rm rot}$). In this case, for a given molecule and a series of transitions $u \rightarrow l$, a plot of the natural logarithm of the upper state column density per statistical weight ($N_{\rm u}/g_{\rm u}$) versus the energy above the ground ($E_{\rm u}$), the so-called population diagram, will yield a straight line with a slope $1/T_{\rm rot}$.

Goldsmith & Langer (1999) have numerically investigated how the optical depth and deviations from LTE affect the temperature and column density derived using the population diagram technique for two molecules: HC_3N and CH_3OH. In this appendix, we perform a similar analysis for HNCO, HNCS, HC_3N, and NO, but in this case, we focus on non-LTE excitation effects since the lines detected in OH 231.8+4.2 are optically thin. (For HC_3N we compared our results, analysing both optical depth and non-LTE excitation effects, with those by Goldsmith & Langer 1999 and found an excellent agreement.)

In low-density regions[7], LTE may not be a valid approximation, and therefore, the level populations, which may not longer be described well by the Boltzmann distribution, have to be numerically computed by solving the statistical equilibrium and radiation transport equations. The excitation analysis presented in this Appendix has been done using MADEX (Molecular and Atomic Database and EXcitation code, Cernicharo 2012). This is a code that solves the molecular excitation (including collisional and radiative excitation mechanisms) and radiation transfer problem under the large velocity gradient (LVG) formalism. It contains up-to-date spectroscopy (rest frequencies, level energies, line strength/Einstein coefficients, etc.) and collisional rates available from the literature for more than 5000 different molecular and atomic entries including isotopologues and vibrationally excited states. MADEX computes molecule-H_2 collisional rates from those available in the literature by adopting other collision partners, such as He or para-H_2. MADEX also evaluates the partition function of the molecule (using a large enough number of levels to obtain accurate values of the partition function even at high temperatures) and predicts the emergent spectra.

To examine what happens if some or all of the transitions of HNCO, HNCS, HC_3N, and NO are not thermalized, we computed the level populations for a range of densities, $n_{\rm H_2}$, and a given input value of $T_{\rm kin}$ and $N_{\rm tot}$ for each molecule. The adopted values of $T_{\rm kin}$ and $N_{\rm tot}$ are similar to those obtained from the LTE analysis (Sect. 4.1). We assumed a linear velocity gradient $\mathrm{d}(\ln V)/\mathrm{d}(\ln r) = 1$ and typical line widths of $FWHM$ = 20–40 km s^{-1}, as observed towards OH 231.8+4.2 (Sects. 1 and 3). The resulting population diagrams based on our non-LTE excitation calculations, including the LTE theoretical points, are shown in Fig. A.1.

For HNCO we used collisional rates from Green (1986)[8], computed for the lowest 164 levels at temperatures from 30 to 350 K. For the non-LTE analysis, we considered rotational levels in the ground vibrational state ($v = 0$) up to $J_{\rm max} = 18$ for both the $K_{\rm a} = 0$ and $K_{\rm a} = 1$ ladder transitions (and also up to $K_{\rm a} = 4$, which has been included in the calculations). This implies a maximum upper state energy of 830 K. As shown in Fig. A.1 (top left box), for the lowest density models ($n_{\rm H_2} = 10^5$ cm^{-3}), there is a notable separation between the $K_{\rm a} = 0$ and $K_{\rm a} = 1$ ladders, which follow two straight lines with different slopes. The slope of the $K_{\rm a} = 0$ ladder implies a rotational temperature of $T_{\rm rot} \sim 16$ K, which is lower than the real input kinetic temperature (sub-thermal excitation), while the slope of the $K_{\rm a} = 1$ ladder implies a rotational temperature of $T_{\rm rot} \sim 30$ K. The y-offset between the two $K_{\rm a}$ ladders decreases as the density increases, until they merge in a single line at densities $n_{\rm H_2} \gtrsim 10^8$ cm^{-3}, with $T_{\rm rot} = T_{\rm kin}$.

Collisional rates are not available for HNCS, therefore we used those of HNCO after applying the standard reduced mass correction. As for HNCO, we included rotational levels of up to $J_{\rm max} = 18$ (within the $K_{\rm a} = 0$, 1, and 2 ladders), which implies maximum upper state energies of $E_{\rm u} \sim 355$ K. As expected, deviations from LTE affect the population diagram of HNCS similarly to HNCO. In the case of HNCS, only the $K_{\rm a} = 0$ ladder has been plotted since these are the only ones detected. For the lowest density model, $n_{\rm H_2} = 10^4$ cm^{-3}, the inferred values of $T_{\rm rot} \sim$ 10–12 K deviate significantly from the real input values ($T_{\rm kin} = 25$ K).

Collisional rates for HC_3N are from Wernli et al. (2007), which include 51 levels and are computed for temperatures between 5 K and 100 K. Collisional rates for NO are adopted from Kłos et al. (2008), computed for 98 rotational levels and temperatures between 10 and 500 K. The highest rotational levels included in our non-LTE excitation calculations for HC_3N an NO are $J_{\rm max} = 30$ ($E_{\rm u}^{\rm max} \sim 200$ K) and $J_{\rm max} = 13/2$ ($E_{\rm u}^{\rm max} \sim 300$ K), respectively. The resulting non-LTE models for HC_3N and NO (Fig. A.1), as for the other species, clearly show steeper slopes ($T_{\rm rot} < T_{\rm kin}$) for the lowest density models. Another effect of non-LTE excitation is that the different level populations cannot be described by a unique rotational temperature, which translates into a different slope for the low-J and high-J levels in the population diagram. This effect is most notable for HC_3N: the temperatures implied are $T_{\rm rot} \sim 5$ K for the three lowest-J levels and $T_{\rm rot} \sim 7$ K for the four highest-J levels. The HC_3N column densities that one would derive using low-J or high-J levels are also different, in particular, $N_{\rm tot}$(low-J) = 3.3×10^{13} cm^{-3} > $N_{\rm tot} = 3.0 \times 10^{13}$ cm^{-3} > $N_{\rm tot}$(high-J) = 7.2×10^{12} cm^{-3}. In the lowest density model of NO, the implied $T_{\rm rot}$ (<$T_{\rm kin} = 26$ K) does not vary appreciably across the different levels (less than 6%).

For all molecules, at the highest densities considered, the populations of the levels considered are thermalized or very close to thermalization, and the non-LTE and LTE predictions converge. In both cases, the data points in the population diagram can be satisfactorily fit by a straight line with $T_{\rm rot} = T_{\rm kin}$. We consider of interest to provide a summary with the range of critical densities for the transitions analysed in this work. These are for a representative temperature of 25 K, which is common in the dominant emitting components of AGB CSEs and PPNs (Bujarrabal et al. 2001). For HNCO the critical densities are in

[6] Since we are dealing with pure rotational transitions in the ground vibrational state, we use the term rotational temperature, $T_{\rm rot}$, instead of the more general designation as excitation temperature, $T_{\rm ex}$.

[7] Both collisional and radiative processes can excite molecules, and for each transition a critical density can be defined where the two processes are equally important ($n_{\rm crit} = A_{\rm ul}/\gamma_{\rm ul}$). At lower densities radiation dominates, while at higher densities collisions drive the level populations to thermodynamic equilibrium.

[8] http://data.giss.nasa.gov/mcrates/

A&A 575, A84 (2015)

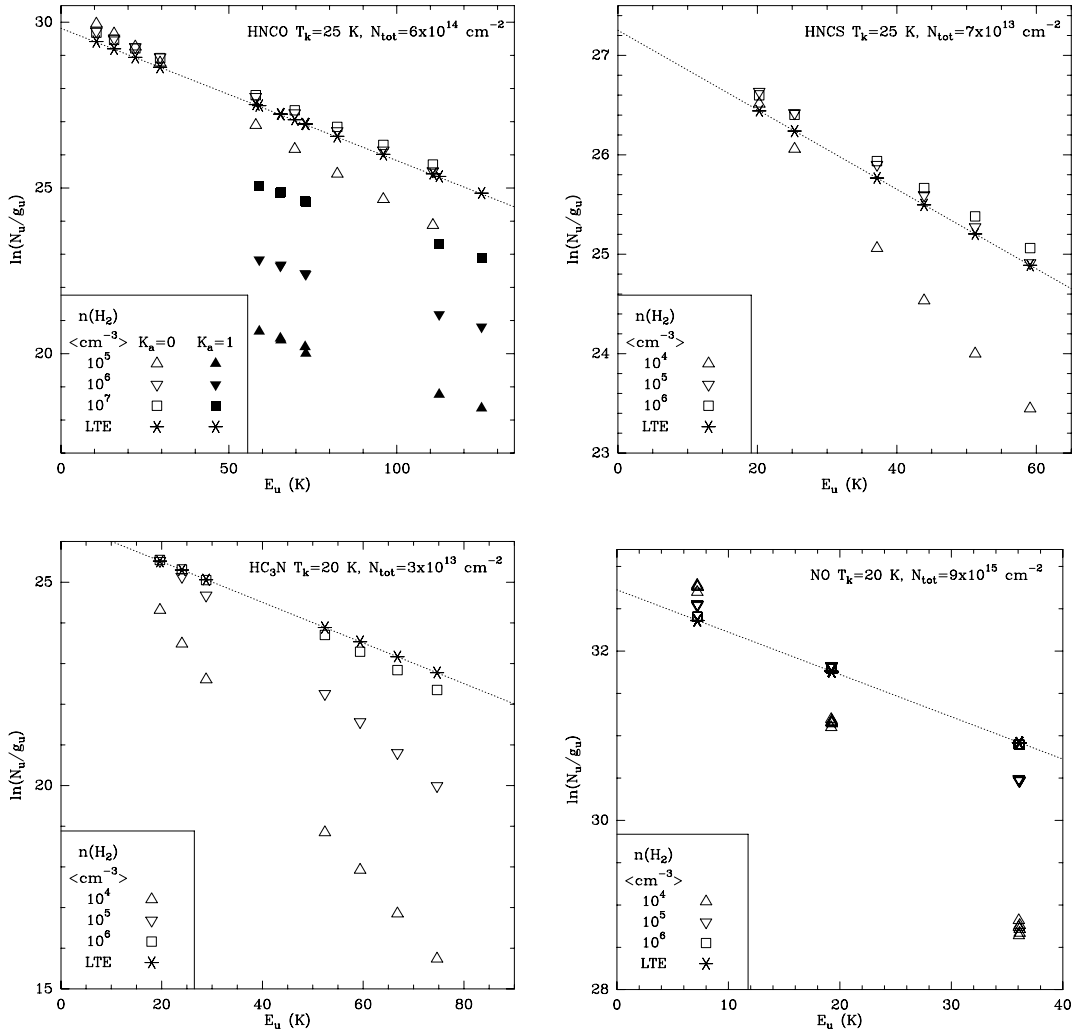

Fig. A.1. Population diagrams of HNCO, HNCS, HC_3N, and NO for a range of molecular hydrogen densities (n_{H_2}, bottom left corner) and a given input value for the kinetic temperature and total column density (T_{kin} and N_{tot}; top right corner); the dotted line connects the LTE points. Only the transitions detected in this work are represented in this diagram (Table 3). For HNCO, the transitions within the $K_a = 0$ and $K_a = 1$ ladders are indicated by empty and filled symbols, respectively. For NO, we plot the three hyperfine components with the highest values of the Einstein coefficient (A_{ul}) for each of the Π^- and Π^+ doublets at 250 and 350 GHz (i.e. at E_u = 19.2 and 36.1 K), the three hyperfine components with the largest A_{ul} of the Π^+ band at 150 GHz (i.e. at E_u = 7.2 K) and the $\Pi^-(3/2,3/2)$–$(1/2,1/2)$ line, which is spectrally isolated in our data, at 150 GHz (E_u = 7.2 K). These calculations have been done with a LVG radiative transfer code (MADEX) – see text in this appendix.

the range of $n_{crit} = [4 \times 10^5$–$1 \times 10^7]\,cm^{-3}$ for the $K_a = 0$ transitions, and $n_{crit} = [1 \times 10^6$–$1 \times 10^7]\,cm^{-3}$ for the $K_a = 1$ transitions. For HNCS, HC_3N, and NO, the critical densities are $n_{crit} = [5 \times 10^5$–$2 \times 10^6]\,cm^{-3}$, $n_{crit} = [1 \times 10^6$–$3 \times 10^6]\,cm^{-3}$, and $n_{crit} = [2 \times 10^4$–$2 \times 10^6]$, respectively. In all these cases, the lowest value of n_{crit} in the ranges given above corresponds to the lowest-J and/or lowest-E_u transition.

Finally, we briefly comment on the possible effect of the pumping of the rotational levels of HNCO by the infrared (IR) photons emitted by the star and the central dust region (see e.g. Kuan & Snyder 1996). This IR emission would cause the radiative pumping of levels inside the ground vibrational state and the vibrationally excited states of HNCO. The latter would eventually produce a fluorescence effect between the ground state and the six vibrational modes of HNCO. The radiative pumping inside the rotational levels of the ground state alone was found to be dominant in the HNCO excitation in Sgr B2 (Churchwell et al. 1986). In this region, the typical densities are relatively low, $n(H_2) \sim 10^4\,cm^{-3}$, but the central source is optically thick at 100 μm and extended. The IR pumping through vibrationally excited states, has also noticeable effects in the emerging intensities of some rotational lines for certain molecules like H_2O in IRC+10216 (Agúndez & Cernicharo 2006). Recently, it has been pointed out that the time variability of the IR pumping

can produce intensity variations in the high rotational lines of abundant molecules in the envelopes of Mira-type stars, such as CCH towards IRC+10216 (Cernicharo et al. 2014). Thus, to summarize, transitions with high upper level energies or those that are severely underexcited by collisions could be more sensitive to IR pumping. When HNCO levels were populated mainly by IR radiation, the column density implied by the rotational diagram method could be different than the true value; the rotational temperature would also be different than the gas kinetic temperature (but see next paragraph).

Our previous discussion of the excitation state of the observed lines of HNCO shows that they are practically thermalized to the temperatures expected in the studied nebula. The population diagram of HNCO (Fig. 9) covers a wide range of upper energies, and it clearly shows a single slope for both the $K_a = 0$ and $K_a = 1$ transitions. This should imply that the line intensities are described well by one rotational temperaure, so that the column density and the derived abundance should be close to the true value. Also, the range of derived kinetic temperatures is consistent with previous estimations of the rotational temperatures and the kinetic temperature in the CO flow (see e.g. Guilloteau et al. 1986; Morris et al. 1987; Alcolea et al. 2001). Finally, the bulk of the emission of HNCO (Sect. 3) arises from the central dense region of the CSE (I3) and the base of the southern lobe (I4). These regions are characterized by densities of $n(H_2) \geq 10^6$–10^7 cm^{-3} in the central region and $n(H_2) \geq 10^5$ cm^{-3} in the lobes (Alcolea et al. 2001; Bujarrabal et al. 2002). This leads to densities close or higher than the critical densities for HNCO $K_a = 0$ and $K_a = 1$ transitions. Therefore, the effects of vibrational cascades should be minor in our case, but we cannot rule out uncertainties in the abundance of HNCO less than a factor 2–5. On the other hand, we have seen that the excitation via the various vibrational states is extremely complex for these relatively heavy molecules. A detailed study of these intricate phenomena is obviously beyond the scope of this paper.

Appendix B: Comparison with other astrophysical environments

B.1. HNCO

Isocyanic acid has been detected in different environments with a variety of physical conditions, including SgrB2 (Snyder & Buhl 1972), the Taurus Molecular Cloud TMC-1 (Brown 1981), external galaxies (Nguyen-Q-Rieu et al. 1991), the shocked-outflow of the young stellar object L1157 (Rodríguez-Fernández et al. 2010), hot cores (Churchwell et al. 1986; Martín et al. 2008), translucent clouds (Turner et al. 1999), etc. Nevertheless, prior to this work, HNCO was not detected in any CSE around evolved stars, either oxygen or carbon rich.

Formation of HNCO through gas-phase and grain surface chemistry from different chemical pathways has been studied by several authors (Iglesias 1977; Turner et al. 1999; Zinchenko et al. 2000; Garrod et al. 2008; Marcelino et al. 2010; Quan et al. 2010). This molecule was first proposed as a high density tracer (Jackson et al. 1984) and, more recently, a shock tracer (Rodríguez-Fernández et al. 2010, and references therein).

The fractional abundance of HNCO varies somewhat in different sources, typically within the range $\approx 10^{-10}$–10^{-9}. The highest fractional abundance (relative to H_2) of HNCO has been measured towards the shocked region of the L1157 outflow, L1157-B2, where $X(\mathrm{HNCO}) \sim 9.6 \times 10^{-8}$ (Rodríguez-Fernández et al. 2010). Interestingly, this value of the abundance is comparable to what is estimated towards OH 231.8+4.2.

B.2. HNCS

Isothiocyanic acid was first detected in SgrB2 (Frerking et al. 1979) and has been recently observed in TMC-1 (Adande et al. 2010). Detection of HNCS in a CSE has not been reported previously to this work.

The formation of HNCS in the cold core TMC-1 and the hot core in SgrB2 has been studied theoretically through gas-phase, ion-molecule chemistry and grain surface reactions (Adande et al. 2010). Prior to this work, the highest abundance of HNCS had been found towards SgrB2 and TMC-1, with a value of $\approx 10^{-11}$. In OH 231.8+4.2 we derive a fractional abundance of HNCS that is about 1000 times higher.

B.3. HC_3N

Cyanoacetylene is detected in assorted environments, including SgrB2 (Turner 1971), H II regions, dark clouds (Morris et al. 1976), the Orion molecular cloud (Goldsmith et al. 1982), the Perseus globules (Bachiller & Cernicharo 1986), in the Taurus molecular clouds (Cernicharo et al. 1984), protoplanetary disks (Chapillon et al. 2012), etc. HC_3N is also detected in several C-rich CSEs, including the well-known AGB star IRC+10216 and the protoplanetary nebula CRL 618 (e.g. Morris et al. 1975; Bujarrabal et al. 1994; Audinos et al. 1994; Cernicharo et al. 2000; Pardo et al. 2004); however, this molecule has not been identified before in an O-rich CSE.

HC_3N is considered to be a high density tracer (Morris et al. 1976) and in CSEs, particularly in IRC+10216, it is distributed in a hollow spherical shell around the central star, which is a major product of photodissociation in the outer parts of the envelope (Audinos et al. 1994). The observed abundance in IRC+10216 is $X(HC_3N) \sim 1 \times 10^{-6}$ agrees with theoretical predictions in C-rich CSEs (Agúndez et al. 2010). We infer $X(HC_3N) \sim 7 \times 10^{-9}$ towards OH 231.8+4.2. This value is much lower than in IRC+10216 by virtue of the O-rich vs. C-rich nature of both sources.

B.4. NO

Nitric oxide has been previously detected in several astrophysical environments, including molecular clouds (Gerin et al. 1992), SgrB2 (Halfen et al. 2001), and pre-protostellar cores (Akyilmaz et al. 2007). Recently, NO has been detected for the first time in the CSE around the yellow hypergiant (YHG) IRC+10420, which is a massive ($\sim 50\,M_\odot$) evolved star with a N-rich chemistry (Quintana-Lacaci et al. 2013), with a fractional abundance of $X(\mathrm{NO}) \approx 10^{-5}$.

Chemical models presented by Quintana-Lacaci et al. (2013) in IRC+10420 predict that indeed NO forms very efficiently by photochemistry (mainly through the reaction N + OH $\longrightarrow$ NO + H) in the outer circumstellar layers, where it reaches a maximum abundance of $\approx 10^{-6}$. In the case of IRC+10240, nitrogen enrichment due to hot bottom burning has been proposed to explain the NO abundance observed, which is larger by a factor 10 than predicted by these models adopting the solar nitrogen abundance.

Appendix C: Ionization and dissociation sources in our chemistry models

The sources of ionization and dissociation adopted in our model are cosmic rays and the interstellar ultraviolet radiation

A&A 575, A84 (2015)

field. The cosmic-ray ionization rate adopted is 1.2×10^{-17} s^{-1} (Dalgarno 2006). The intensity of the UV field assumed is the Draine field (X) or Go = 1.7 in units of the Habing field (Go = 1.6×10^3 erg s^{-1} cm^{-2}; Habing 1968; Draine & Salpeter 1978). The ISM UV field illuminates the nebula externally.

We also evaluated two possible additional sources of internal ionization and dissociation in OH 231.8+4.2: 1) the UV radiation by the A0 main sequence companion of the primary AGB star (QX Pup) at the nucleus of the nebula; and 2) the high-energy radiation generated by the cooling of hot gas behind the fast shock fronts ahead of the lobe tips (Sect. 1). In both cases, the effect on the chemistry is not expected to be predominant and has not been considered in our model.

First, the UV radiation field emitted by the ~10 000 K main-sequence companion cannot penetrate very deep through the dense dusty wind of the AGB mass-losing star except, maybe, along the direction of the lobes owing to the lower extinction by dust along the outflow cavities (of the order of $A_V \sim 1$ mag; Sánchez Contreras et al. 2004). However, there is observational evidence against the presence of a substantial amount of ionized or atomic gas in the stellar vicinity, hence against the existence of an intense stellar UV field that could have a noticeable effect on the chemistry in the inner regions of the lobes: (i) the lack of H_α emission (or any other recombination or forbidden lines in the optical) from the nucleus of OH 231.8+4.2 rules out an emergent ionized region around the star (Cohen et al. 1985; Reipurth 1987; Sánchez Contreras et al. 2000a, 2004); and (ii) the lack of low-excitation atomic emission lines in the far-infrared, e.g. [O I] emission at 63.2 and 145.5 μm (unpublished *Herschel* archive data) indicates the absence of a photodissociation region (PDR) in the nebula centre. Moreover, considering the temperature and luminosity of the warm companion (~10 000 K and ~5–30 $L_\odot$; Sánchez Contreras et al. 2004), it can be demonstrated that the stellar UV flux that reaches to a point located at the inner edges of the lobes (~4″ from the star) with a visual extinction of $A_V = 1.0$ mag, would be smaller than, or at most comparable to, the ISM UV field. Therefore, including the stellar UV radiation as a source of internal illumination of the lobe walls in the model will yield very similar results (and even smaller molecular abundances for "daughter" species) to those obtained assuming external illumination by the ISM UV field.

Second, the shocks that are currently active in OH 231.8+4.2 are those traced by H_α emission, which arises in two bubble-like structures of shock-excited gas surrounding the molecular outflow (Reipurth 1987; Sánchez Contreras et al. 2000a; Bujarrabal et al. 2002). These fast shocks may have been generated by interaction between the dense, fast molecular outflow and the tenuous ambient material. The characteristics of the exciting shocks have been studied in detail by Sánchez Contreras et al. (2000a). In particular, these authors compare the relative intensities of the different optical lines observed with the diagnostic diagrams by Dopita & Sutherland (1995), which can distinguish between shocks with or without a photoionized preshock region. These diagrams not only confirm the shock nature of the emission but also indicate that the emission from a photoionized precursor region is either weak or absent. We note, moreover, that even in the improbable case that sufficiently intense UV radiation from the current shocks is produced, its effect on the chemistry will be almost exclusively limited to the outflow regions immediately behind the shock fronts, that is, the molecular clumps at the very end of the lobes of OH 231.8+4.2. However, given the beam size of our observations (Fig. 1), the contribution of these molecular clumps to the total emission by the N-bearing molecules reported in this work is insignificant.

CHAPTER

5

MOLECULAR IONS IN THE O-RICH CSE OH231.8+4.2

In this chapter we present the results from our comprehensive study of the molecular ions HCO^+, $H^{13}CO^+$, N_2H^+, SO^+, and H_3O^+ detected toward OH231.8+4.2. This work is based on observations with the IRAM-30 m telescope and the Herschel Space Observatory-HIFI. We analysed the excitation conditions and abundances of these ions detected by using the population diagram technique and MADEX to constrain the non-LTE effects. We also modelled the chemistry of these species. The first detection of several molecular ions toward this CSE increases the molecular inventory and the chemical complexity of the source, which is unusually rich compared to standard oxygen rich circumstellar envelopes. This work has been published in Sánchez Contreras et al. (2015).

5.1 Summary

Molecular ions are significant contributors to the molecular formation process in circumstellar environments, which are active sites of molecular synthesis. In the ISM more than 30 molecular ions have been discovered, however, in the envelopes around low-to-intermediate mass evolved stars detections still remain scarce. Only toward few objects in the post-AGB or PN phase, positive ions have been detected, namely, CO^+ , N_2H^+, CH^+, OH^+ , and (tentatively) HCS^+. Except for OH^+, these ions have been identified only in C-rich objects, which display a more active chemistry than their O-rich analogues. In particular, cations have been detected toward the young PN NGC 7027, i.e. HCO^+ , $H^{13}CO^+$, CO^+, N_2H^+, CH^+, and, tentatively, HCS^+ (Cernicharo et al., 1997, Hasegawa & Kwok, 2001, Zhang et al., 2008, and references therein), toward the pre-PN CRL618, where HCO^+ and N_2H^+ were detected (Bujarrabal et al., 1988, Pardo et al., 2007), and also HCO^+ toward OH231.8+4.2 (Morris et al., 1987a). Recently, the ion OH^+ has been discovered with the Herschel Space Observatory in five PNs (Etxaluze et al., 2014, Aleman et al., 2014). To our knowledge, in the circumstellar medium, emission lines of molecular anions have been only observed toward the C-rich AGB star IRC+10216 (e.g. McCarthy et al., 2006, Cernicharo et al., 2007, Agúndez et al., 2010a).

In this article we present the detection of the molecular ions HCO^+, $H^{13}CO^+$, N_2H^+, SO^+, and tentatively H_3O^+, toward OH231. These molecules have been detected thanks to our millimeter, sub-millimeter, and fIR wavelength range observations (from 80 to 355 GHz with the IRAM-30 m and from 479 to 1244 GHz with Herschel Space Observatory-HIFI). This work represents the first detection of SO^+ and, tentatively, H_3O^+ toward a CSE of an evolved stars, i.e. OH231.

➢ In this work, we did the following analysis:

- study of the line profiles detected, in addition to the measurement of their velocity integrated intensities and other parameters,
- rotational diagram analysis under LTE approximation, in order to obtain the rotational temperatures and column densities averaged for the emitting region (we estimated the dilution of the source in the main beam of the telescope) of the molecular ions detected,
- we estimated the upper limits of the column densities for different not detected ions (e.g. CO^+, CS^+, CN^- or NO^+),
- study of the possible LTE deviations for HCO^+ and N_2H^+ emission, using LVG models created with MADEX (Sect. 2.2). We did not include SO^+ or H_3O^+ given that their collisional coefficients are not available,
- chemical modelling of OH231, using two different models: *i*) a first model to predict the abundances expected in the central slowly expanding AGB CSE remnant, and *ii*) a second model to predict the abundances in the extended outflow lobes, which were previously shocked, and following the time evolution of the abundances in a gas cell located at a distance from the outflow wall that corresponds to a A_v=1,
- we analysed the abundance variation of the molecular ions as a function of the depth inside the walls of the lobes, for the dynamical age of the outflow (∼800 years),
- we have modelled the effect of a N-enhancement of the initial abundances for the models, which may occur in the case of HBB, to try to reproduce the N_2H^+ abundances observed. We have also studied the effect of a decrease in the H_2O initial abundance, which plays a major role in the chemistry of O-rich CSEs, in the final predicted abundances of the ions.

➢ After the analysis of the data, we obtained the following results:

- the line profiles observed display FWHM∼50-90 km s^{-1} for all the ions except for H_3O^+ whose profile is narrow (FWHM∼14 km s^{-1}),
- the rotational temperatures derived are $T_{\rm rot}$∼10-20 K, except for H_3O^+ which shows a temperature of ∼100 K,
- the derived abundances from our observations are f(HCO^+)∼10^{-8}, f($H^{13}CO^+$)∼2×10^{-9}, f(SO^+)∼4×10^{-9}, f(N_2H^+)∼2×10^{-9}, and f(H_3O^+)∼7×10^{-9},
- the LVG models created with MADEX predict excitation temperatures and column densities similar (or slightly lower) than those derived through LTE rotational diagrams, with discrepancies lower than a 15%,
- the chemical model created to reproduce the compact and denser region, which corresponds to the AGB CSE remnant, predicts abundances consistent with the abundances derived from the rotational diagram for all the ions (which will be efficiently formed in the outer parts of the CSE) except for N_2H^+ (the predicted abundance is two orders of magnitude lower). These results are consistent with previous theoretical estimations of the models by Mamon et al. (1987),

- the abundances predicted by the chemical model of the lobes, are consistent with those derived from the diagrams for SO^+ and H_3O^+. However, the chemical models do not reproduce the observations of HCO^+ and N_2H^+, where discrepancies of ∼2 orders of magnitude are found (the predicted abundances are lower than the derived abundances),

- the chemical models predict that all ions should be more abundant in the central dense slowly expanding AGB CSE compared with the lobes, which is contrary to the observations as we indicate in the conclusions,

- as indicated previously, we have tested the effect produced in the chemical models that results from a decrease of the initial H_2O abundance (from 3×10^{-4} to 3×10^{-5}). With the decreased abundance the AGB CSE model predicts abundance variations for all the ions. The most notable case is N_2H^+, whose abundance is enhanced in the inner regions of the CSE. The model applied to the lobe including the decrease of the initial H_2O abundance, predicts similar abundances in the outermost region of the wall of the lobes compared to the high-H_2O abundance case. However, if we penetrate into the wall of the lobes all the ion abundances increase, and particularly, for HCO^+ and N_2H^+ their abundances are increased of a factor ∼20-40,

- the N-enhancement only affects significantly to N_2H^+, although, its abundance is still predicted (at least) one order of magnitude lower than the abundance derived from the rotational diagrams.

➢ From these results, we can extract the following conclusions:

- the observed line profiles indicate that the molecular ions are present in the high speed outflow of the nebula, except probably for H_3O^+, which displays a line profile consistent with emission arising from the the slowly expanding central AGB CSE,

- the rotational temperatures obtained are also consistent with this previous interpretation given that they correspond to the low temperatures found in the CO outflow (Alcolea et al., 2001), except for H_3O^+ whose rotational temperature (∼100 K) would be also consistent with emission arising from the slowly expanding central AGB CSE. This scenario is also plausible taking into account the observations of H_2O emission in this object, which is closely related (through chemical formation routes) with the emission of H_3O^+ (Sánchez Contreras et al., 2014),

- the derived abundance for HCO^+ is consistent with previous estimations in this source (Morris, 1987b, Sánchez Contreras et al., 1997, 2000). For the rest of the ions, our estimations represent the first values obtained in O-rich CSEs,

- non-LTE models indicate that the values derived from the rotational diagrams (under LTE approximation) should be strictly considered as lower limits. Nevertheless, the discrepancies found are only approximately a 15% of their values, therefore, we do not expect great deviations from LTE values,

- the discrepancies in the abundances found between the chemical models and the rotational diagrams (except maybe for SO^+, whose abundance is consistent with the results of the rotational diagram, and it is also consistent with the emitting region predicted by its linewidths)

suggest that the interaction between the jets and the slowly expanding AGB CSE have resulted in shock-induced processes that have altered the chemical composition of the CSE. The molecules that were previously distributed in the standard AGB CSE would be dissociated by high-speed ($>$100 km s^{-1}) shocks (Hollenbach & McKee, 1980). After the passage of shocks, the gas would progressively have cooled down, allowing that the dissociated and ionised material, which should be relatively dense ($\sim$10^5-10^6 cm^{-3}), reacted to form new molecules (Glassgold et al., 1989, Neufeld & Dalgarno, 1989). This process would lead to the chemical alteration observed toward OH231, whose chemical richness is not observed in standard O-rich CSEs (see Chapter 3).

5.2 Resumen

Los iones moleculares son muy importantes en los procesos de formación de moléculas en envolturas circunestelares, que son entornos activos de síntesis molecular. En el ISM se han descubierto más de 30 iones moleculares distintos, sin embargo, las detecciones en envolturas circunestelares de estrellas evolucionadas de poca masa o intermedia ($\sim$0.8-8$M_{\odot}$) aún son escasas. En particular, se han detectado los cationes HCO^+, $H^{13}CO^+$, CO^+, N_2H^+, CH^+ y tentativamente el HCS^+, en la nebulosa planetaria NGC 7027 (Cernicharo et al., 1997, Hasegawa & Kwok, 2001, Zhang et al., 2008), y también el HCO^+ y N_2H^+ en la pre-PN CRL 618 (Bujarrabal et al., 1988, Pardo et al., 2007), y HCO^+ en OH231.8+4.2 (Morris et al., 1987a). Recientemente se ha observado emisión del catión OH^+ con Herschel en cinco nebulosas planetarias (Etxaluze et al., 2014, Aleman et al., 2014). Excepto el OH^+, estos cationes han sido exclusivamente detectados en envolturas ricas en carbono, que muestran en general una química más rica que sus análogos ricas en oxígeno. En lo referente a iones negativos (aniones) moleculares, sólo nos consta que hayan sido observadas líneas de emisión en la envoltura rica en carbono IRC+10216 (e.g. McCarthy et al., 2006, Cernicharo et al., 2007, Agúndez et al., 2010a).

En este artículo se presenta la detección de los iones moleculares HCO^+, $H^{13}CO^+$, N_2H^+, SO^+ y tentativamente H_3O^+, en la nebulosa OH231, mediante la observación del espectro de emisión de estas moléculas en el rango de longitud de onda milimétrico, sub-milimétrico, e IR lejano (desde 80 a 355 GHz con IRAM-30 m y de 479 a 1244 GHz con HIFI del observatorio espacial Herschel). Esta supone la primera detección de SO^+ y de H_3O^+ (tentativamente) en envolturas circunestelares de estrellas evolucionadas.

➢ En este trabajo hemos realizado el siguiente análisis:

- estudio de los perfiles de las líneas detectadas, junto con la medida de las intensidades integradas en velocidad y otros parámetros, en el espectro observado,

- análisis de los diagramas rotacionales en aproximación de ETL para obtener las temperaturas rotacionales y densidades de columna de los iones moleculares detectados, promediadas para la región emisora (estimando la dilución de la fuente en el haz del telescopio),

- estimación de límites superiores para las densidades de columna de otros iones no detectados (e.g. CO^+, CS^+, CN^- o NO^+),

- estudio de las posibles desviaciones del ETL a través de los diagramas de rotación para distintos modelos LVG creados con MADEX (ver Sec. 2.2) para HCO^+ y N_2H^+ (para SO^+ y H_3O^+ no existen estimaciones de los coeficientes colisionales),

- modelización de la química en OH231, mediante dos modelos distintos: *i*) uno para reproducir las abundancias que se esperarían en la componente central de expansión lenta, que representaría el remanente de la envoltura AGB, y *ii*) otro modelo para reproducir los lóbulos del flujo de material extendido y previamente chocado, siguiendo la evolución temporal de las abundancias en una celda de gas situada a una distancia de la pared del flujo chocado donde la extinción visual sería de A_v=1,

- adicionalmente, hemos analizado, para la edad dinámica del flujo ($\sim$800 años), la variación de las abundancias de los iones moleculares en función de la profundidad con respecto a la pared del lóbulo,

- hemos evaluado el efecto de incrementar las abundancias iniciales de N en los modelos (producido por HBB, para tratar de reproducir los resultados de N_2H^+), y también el efecto del decremento en la abundancia inicial de agua (cuyo papel es muy importante en la química de las envolturas ricas en oxígeno), en las abundancias finales predichas por nuestros modelos para los iones.

➢ Tras analizar los datos, obtenemos los siguientes resultados principales:

- los perfiles observados muestran FWHM∼50-90 km s^{-1} para todos los iones excepto para H_3O^+ cuyo perfil es más estrecho (FWHM∼14 km s^{-1}),

- las temperaturas de rotación derivadas de los diagramas son compatibles con $T_{\rm rot}$∼10-20 K, excepto para H_3O^+ que mostraría una temperatura de ∼100 K,

- las abundancias calculadas mediante los diagramas de población y considerando la dilución de la emisión en el haz del telescopio serían de f(HCO^+)∼10^{-8}, f($H^{13}CO^+$)∼2×10^{-9}, f(SO^+)∼4×10^{-9}, f(N_2H^+)∼2×10^{-9} y f(H_3O^+)∼7×10^{-9},

- los modelos LVG realizados con MADEX, predicen temperaturas de excitación y densidades de columna similares (o algo más bajas) que las derivadas a través del ajuste de los diagramas rotacionales en ETL, encontrado discrepancias menores de un 15 %,

- el modelo químico utilizado para reproducir la zona compacta densa que correspondería con la envoltura remanente de la fase AGB, predice abundancias compatibles con las obtenidas por los diagramas para todos los iones (que se formarían eficientemente en las zonas externas de la envoltura) excepto para N_2H^+ (predice una abundancia 2 órdenes de magnitud por debajo). Los resultados son además consistentes con las estimaciones de los modelos teóricos creados por Mamon et al. (1987),

- las abundancias predichas por el modelo químico adaptado para los lóbulos son consistentes con las derivadas de los diagramas para SO^+ y H_3O^+, pero no reproducen las observaciones de HCO^+ y N_2H^+, con discrepancias de ∼2 órdenes de magnitud (siendo las predicciones inferiores),

- los modelos predicen que los iones serían más abundantes en la zona central densa de expansión lenta (envoltura AGB) comparados con el modelo para los lóbulos de la nebulosa, que como se indica en las conclusiones, es contrario a lo que observamos,

- como se indicaba anteriormente, hemos evaluado el efecto que produce disminuir la abundancia inicial de agua de 3×10^{-4} a 3×10^{-5} en los modelos químicos. Para el modelo de la envoltura AGB de expansión lenta, el decremento produce variaciones en las abundancias de todos los iones. El caso más notable es el de N_2H^+, que aumenta su abundancia sobre todo en las regiones más internas de la envoltura. Este efecto de disminuir la abundancia inicial de agua aplicado al modelo de los lóbulos, predice abundancias similares en la región externa de la pared del lóbulo comparado con el caso de abundancia normal de agua. Sin embargo, cuando penetramos en la pared del lóbulo las abundancias de todos los iones aumentan, siendo particularmente elevado este aumento para HCO^+ y N_2H^+ (con un factor ∼20-40),

- el efecto del enriquecimiento de N aplicado a los modelos, sólo afecta significativamente al N_2H^+, pero su abundancia aún se seguiría prediciendo un orden de magnitud más bajo que la abundancia derivada de los diagramas, en el mejor de los escenarios.

➢ De la valoración de los resultados obtenidos, podemos extraer las siguientes conclusiones:

- los perfiles de las líneas indican que los iones están presentes en el flujo de alta velocidad de la nebulosa, excepto para el H_3O^+, que muestra un perfil compatible con emisión en la envoltura central de la estrella AGB de expansión lenta,

- las temperaturas obtenidas serían también compatibles con la interpretación de los perfiles de las líneas, dado que corresponderían con las bajas temperaturas encontradas en el flujo de CO (e.g. Alcolea et al., 2001), excepto para el H_3O^+ cuya temperatura ($\sim$100 K) también sería compatible con emisión que vendría de la envoltura interna AGB de expansión lenta. Este escenario también sería consistente con las observaciones realizadas sobre la emisión de H_2O en este objeto y que están relacionadas (por su ruta de formación) con la emisión del H_3O^+ (Sánchez Contreras et al., 2014),

- la abundancia determinada para HCO^+ es consistente con estimaciones previas (Morris, 1987b, Sánchez Contreras et al., 1997, 2000). Para el resto de iones, nuestras estimaciones representan las primeras medidas en envolturas circunestelares ricas en oxígeno,

- los modelos no-ETL indicarían que los valores derivados de los diagramas rotacionales en aproximación ETL deberían ser considerados de modo estricto como límites inferiores, no obstante, las diferencias son del orden del $\sim$15 %, por lo que no se esperan grandes desviaciones respecto de los valores ETL,

- las discrepancias encontradas entre los modelos químicos y las abundancias que se derivan del análisis de los diagramas de rotación (salvo quizá para el SO^+ cuya abundancia es consistente con los resultados del diagrama rotacional, y la región de emisión predicha coincide con la anchura de sus líneas), sugieren que la interacción entre los posibles chorros de material y la envoltura en expansión lenta de la fase AGB, daría lugar a procesos inducidos por choques que alterarían la química del objeto. Las moléculas presentes en la envoltura AGB original, serían disociadas por choques de alta velocidad ($>$100 km s^{-1}) (e.g. Hollenbach & McKee, 1980). Tras el paso del choque, el gas se iría enfriando progresivamente, permitiendo que el material ionizado y disociado, y que sería relativamente denso ($\sim10^5$-10^6 cm^{-3}), reaccionara para reformar moléculas (e.g. Glassgold et al., 1989, Neufeld & Dalgarno, 1989). Este proceso podría dar lugar a la alteración química que se observa en OH231, cuya riqueza no se observa en envolturas de estrellas AGB estándar ricas en oxígeno (ver Capítulo 3).

5.3 Sánchez Contreras et al. 2015[1]

A&A 577, A52 (2015)
DOI: 10.1051/0004-6361/201525652
© ESO 2015

Astronomy & Astrophysics

Molecular ions in the O-rich evolved star OH231.8+4.2: HCO^+, $H^{13}CO^+$ and first detection of SO^+, N_2H^+, and H_3O^+⋆

C. Sánchez Contreras[1], L. Velilla Prieto[1,2], M. Agúndez[2,5], J. Cernicharo[2], G. Quintana-Lacaci[2], V. Bujarrabal[3], J. Alcolea[4], J. R. Goicoechea[2], F. Herpin[5], K. M. Menten[6], and F. Wyrowski[6]

[1] Department of Astrophysics, Astrobiology Center (CSIC-INTA), ESAC campus, PO Box 78, 28691 Villanueva de la Cañada, Madrid, Spain
e-mail: csanchez@cab.inta-csic.es
[2] Instituto de Ciencia de Materiales de Madrid, CSIC, c/ Sor Juana Inés de la Cruz 3, 28049 Cantoblanco, Madrid, Spain
[3] Observatorio Astronómico Nacional (IGN), Ap 112, 28803 Alcalá de Henares, Madrid, Spain
[4] Observatorio Astronómico Nacional (IGN), Alfonso XII No 3, 28014 Madrid, Spain
[5] Université de Bordeaux, LAB, UMR 5804, 33270 Floirac, France
[6] Max-Planck-Institut für Radioastronomie, Auf dem Hügel 69, 53121 Bonn, Germany

Received 13 January 2015 / Accepted 20 February 2015

ABSTRACT

OH 231.8+4.2, a bipolar outflow around a Mira-type variable star, displays a unique molecular richness amongst circumstellar envelopes (CSEs) around O-rich AGB and post-AGB stars. We report line observations of the HCO^+ and $H^{13}CO^+$ molecular ions and the first detection of SO^+, N_2H^+, and (tentatively) H_3O^+ in this source. SO^+ and H_3O^+ have not been detected before in CSEs around evolved stars. These data have been obtained as part of a full mm-wave and far-IR spectral line survey carried out with the IRAM 30 m radio telescope and with *Herschel*/HIFI. Except for H_3O^+, all the molecular ions detected in this work display emission lines with broad profiles (*FWHM* ∼ 50−90 km s^{-1}), which indicates that these ions are abundant in the fast bipolar outflow of OH 231.8. The narrow profile (*FWHM* ∼ 14 km s^{-1}) and high critical densities (>10^6 cm^{-3}) of the H_3O^+ transitions observed are consistent with this ion arising from denser, inner (and presumably warmer) layers of the fossil remnant of the slow AGB CSE at the core of the nebula. From rotational diagram analysis, we deduce excitation temperatures of T_{ex} ∼ 10−20 K for all ions except for H_3O^+, which is most consistent with T_{ex} ≈ 100 K. Although uncertain, the higher excitation temperature suspected for H_3O^+ is similar to that recently found for H_2O and a few other molecules, which selectively trace a previously unidentified, warm nebular component. The column densities of the molecular ions reported here are in the range $N_{tot} \approx [1-8] \times 10^{13}$ cm^{-2}, leading to beam-averaged fractional abundances relative to H_2 of $X(HCO^+) \approx 10^{-8}$, $X(H^{13}CO^+) \approx 2 \times 10^{-9}$, $X(SO^+) \approx 4 \times 10^{-9}$, $X(N_2H^+) \approx 2 \times 10^{-9}$, and $X(H_3O^+) \approx 7 \times 10^{-9}$ cm^{-2}. We have performed chemical kinetics models to investigate the formation of these ions in OH 231.8 as the result of standard gas phase reactions initiated by cosmic-ray and UV-photon ionization. The model predicts that HCO^+, SO^+, and H_3O^+ can form with abundances comparable to the observed average values in the external layers of the slow central core (at ∼[3−8] × 10^{16} cm); H_3O^+ would also form quite abundantly in regions closer to the center ($X(H_3O^+) \sim 10^{-9}$ at ∼10^{16} cm). For N_2H^+, the model abundance is lower than the observed value by more than two orders of magnitude. The model fails to reproduce the abundance enrichment of HCO^+, SO^+, and N_2H^+ in the lobes, which is directly inferred from the broad emission profiles of these ions. Also, in disagreement with the narrow H_3O^+ spectra, the model predicts that this ion should form in relatively large, detectable amounts (≈10^{-9}) in the external layers of the slow central core and in the high-velocity lobes. Some of the model-data discrepancies are reduced, but not suppressed, by lowering the water content and enhancing the elemental nitrogen abundance in the envelope. The remarkable chemistry of OH 231.8 probably reflects the molecular regeneration process within its envelope after the passage of fast shocks that accelerated and dissociated molecules in the AGB wind ∼800 yr ago.

Key words. stars: AGB and post-AGB – stars: late-type – stars: winds, outflows – radio lines: stars – stars: mass-loss – astrochemistry

1. Introduction

OH 231.8+4.2 (hereafter, OH 231.8) is a well-studied bipolar nebula around an OH/IR source[1]. Although its evolutionary stage is not clear because of its many unusual properties, it is believed to be a planetary nebula (PN) precursor probably caught in a short-lived transitional phase. The obscured central star, named QX Pup, is classified as M9-10 III and has a Mira-like variability consistent with an evolved asymptotic giant branch (AGB) star (Cohen 1981; Feast et al. 1983; Kastner et al. 1992; Sánchez Contreras et al. 2004). The evolution of this object may have been complex since it has a binary companion star (of type A0 V), which has been indirectly identified from the analysis of the stellar spectrum reflected by the nebular dust (Cohen et al. 1985; Sánchez Contreras et al. 2004). The system, located at ∼1500 pc (Choi et al. 2012), has a total luminosity of ∼10^4 $L_\odot$ and its systemic velocity relative to the Local Standard of Rest (LSR) is V_{sys}^{LSR} ∼ 34 km s^{-1}. OH 231.8 is likely a member of the open cluster M 46 with a progenitor mass of ∼3 $M_\odot$ (Jura & Morris 1985).

OH 231.8 is surrounded by a massive (∼1 $M_\odot$) and predominantly cold (∼10−40 K) molecular envelope well characterized

⋆ Appendices are available in electronic form at http://www.aanda.org
[1] OH/IR objects are infrared-bright evolved stellar objects with a dense envelope showing prominent OH maser emission.

[1]A&A, 577, A52, 2015, reproduced with permission © ESO

A&A 577, A52 (2015)

by mm-wavelength emission from CO and other molecules (Fig. 1). The molecular gas is located in a very elongated and clumpy structure with two major components: (i) a central core (referred to as *clump I3*) with an angular diameter of ∼6−8″, a total mass of ∼0.64 $M_\odot$, and low expansion velocity of $V_{\rm exp}$ ∼ 6−35 km s^{-1}; and (ii) a highly collimated $\lesssim$6″ × 57″ bipolar outflow, with a mass of ∼0.3 $M_\odot$ and expansion velocities that increase linearly with the distance from the center, reaching values of up to ∼200 and 430 km s^{-1} at the tip of the north and south lobe, respectively. The temperature in the lobes is notably low, ∼10−20 K (Sánchez Contreras et al. 1997; Alcolea et al. 2001).

The molecular envelope of OH 231.8 is markedly different from the slow, roughly round expanding circumstellar envelopes (CSEs) of most AGB stars; its pronounced axial symmetry, large expansion velocities, and the presence of shocks are common in objects that have left the AGB phase and are evolving to the PN stage, the so-called pre-PNe (Neri et al. 1998; Bujarrabal et al. 2001; Castro-Carrizo et al. 2010; Sánchez Contreras & Sahai 2012). It is believed that the nebula of OH 231.8 was created as the result of a huge mass-loss event that occurred during the late-AGB evolution of the primary at a rate of $\dot{M} \approx 10^{-4}\,M_\odot$ yr^{-1}. With a total linear momentum of ∼27 $M_\odot$ km s^{-1}, the bipolar flow is interpreted as the result of a sudden axial acceleration of the envelope. The linear distance-velocity relation observed in the CO-outflow (with a projected velocity gradient of $\nabla\upsilon \sim 6.5$ km s^{-1} arcsec^{-1}) suggests that such an acceleration took place ∼800 yr ago in less than ∼150 yr. The low-velocity, low-latitude central core of the outflow is thought to be the fossil remnant of the AGB star's CSE.

It is probable that the acceleration of the bipolar lobes resulted from the violent collision of underlying jets (emanating from the stellar companion) and the slowly expanding AGB envelope (Sánchez Contreras et al. 2000; Alcolea et al. 2001; Bujarrabal et al. 2002; Sánchez Contreras et al. 2004); this is one plausible scenario that has been proposed to explain the shaping and acceleration of bipolar pre-PNe and PNe (e.g., Sahai & Trauger 1998; Balick & Frank 2002). Recently, Sabin et al. (2014) have found indications of a well-organized magnetic field parallel to the major axis of the CO-outflow of OH 231.8 that could point to a magnetic outflow launching mechanism. Alternatively, as noticed by these authors, the magnetic field could have been dragged by the fast outflow, which may have been driven by a different mechanism. For example, the underlying jets could have been launched by the main-sequence companion powered by mass accretion from the mass-losing AGB star through an FU Ori type outburst (Sánchez Contreras et al. 2004) or a much more violent ($\lesssim$100 days) intermediate-luminosity optical transient (ILOT) like event (Soker & Kashi 2012).

OH 231.8 has a remarkably rich and unusual chemistry amongst CSEs around O-rich low-to-intermediate-mass evolved stars. In addition to the typical oxygen-rich content, with molecules such as H_2O, OH or SiO (Bowers & Morris 1984; Morris et al. 1987; Zijlstra et al. 2001; Sánchez Contreras et al. 2002; Desmurs et al. 2007), OH 231.8 displays strong lines of many different molecular species, including many containing carbon. High-angular-resolution mapping of the HCO^+ (J = 1−0) emission (Fig. 1) indicates that this ion is comparatively more abundant in the fast lobes that in the slow central core (Sánchez Contreras et al. 2000). Single-dish maps of the SiO (J = 5−4) emission show that the abundance of this molecule could also be enhanced in the lobes (Sánchez Contreras et al. 1997). The spectrum of OH 231.8 is unusually rich in lines from S- and N-bearing molecules. For example, it was the first O-rich CSE in which H_2S, NS, CS, and OCS were detected, and we have recently reported the first detection of HNCO, HNCS, HC_3N, and NO (Velilla Prieto et al. 2015). Some of these S- and N-compounds are present in the envelope at levels not expected in O-rich CSEs around low-to-intermediate mass stars. In the case of OH 231.8, it has been proposed that extra Si and S are released into the gas phase from the sputtering of dust grains by shocks. Shocks might also initiate (endothermic) reactions that trigger the N and S chemistry and could also be additional suppliers of free atoms and ions (Morris et al. 1987; Sánchez Contreras et al. 2000; Velilla Prieto et al. 2015).

We have recently completed a sensitive molecular line survey of this object in the mm-wavelength and far-IR range with the IRAM 30 m telescope and *Herschel* (Velilla Prieto et al. 2015; Sánchez Contreras et al. 2014; full survey data to be published by Velilla Prieto et al.; Sánchez Contreras et al., in prep.). We have detected hundreds of molecular transitions, discovered >30 new species (including isotopologues), and extended the rotational ladders for many others. This has led to very detailed information on the global physicochemical structure of this envelope. From a preliminary analysis of the survey data (Sánchez Contreras et al. 2014), we find two main temperature components: a) a predominantly cold (∼10−40 K) component mainly traced by CO (but also by, e.g., HCN, HNC, HNCO, and HCO^+) and b) a warm (≈100 K) molecular component that is selectively traced by certain molecules, such as H_2O, amongst a few others (e.g., CS, H_2S, and SiS).

In this paper, we report the first detection of the molecular ions SO^+, N_2H^+, and (tentatively) H_3O^+ in OH 231.8 as part of our surveys. We also present and analyse several lines of HCO^+ and $H^{13}CO^+$, which are known to be present in OH 231.8 from earlier works (Morris et al. 1987; Sánchez Contreras et al. 1997, 2000). Molecular ions are believed to be significant contributors to the molecule formation process in circumstellar environments, which are active sites of molecular synthesis. In the interstellar medium (including molecular clouds, star-forming regions, PDRs, etc.) more than 30 molecular ions have been detected, however, in the envelopes around low-to-intermediate mass evolved stars detections still remain scarce and limited to HCO^+ in most cases (see, e.g., Sandford 2011). In only a few objects in the post-AGB or PN phase, other positive ions have been detected, namely, CO^+, N_2H^+, CH^+, OH^+, and (tentatively) HCS^+. Except for OH^+, so far these ions have been exclusively identified in C-rich objects, which show in general a richer chemistry than their O-rich analogues. In particular, toward the young PN NGC 7027, where HCO^+, $H^{13}CO^+$, CO^+, N_2H^+, CH^+, and, tentatively, HCS^+, are observed (Cernicharo et al. 1997; Hasegawa & Kwok 2001; Zhang et al. 2008, and references therein) and the pre-PN CRL618, where HCO^+ and N_2H^+ are detected (Bujarrabal et al. 1988; Pardo et al. 2007). Recently, the ion OH^+ has been detected with *Herschel* in five PNe (Etxaluze et al. 2014; Aleman et al. 2014). To our knowledge, in CSEs negatively charged molecular anions have been found to date only in the C-rich AGB star IRC+10216 (e.g., McCarthy et al. 2006; Cernicharo et al. 2007; Agúndez et al. 2010a).

2. Observations

These data are part of a spectral line survey in the mm/far-IR wavelength range carried out with the IRAM 30 m radio telescope (∼79−355 GHz; Sánchez Contreras et al. 2011; Velilla Prieto et al. 2013) and the *Herschel* space observatory

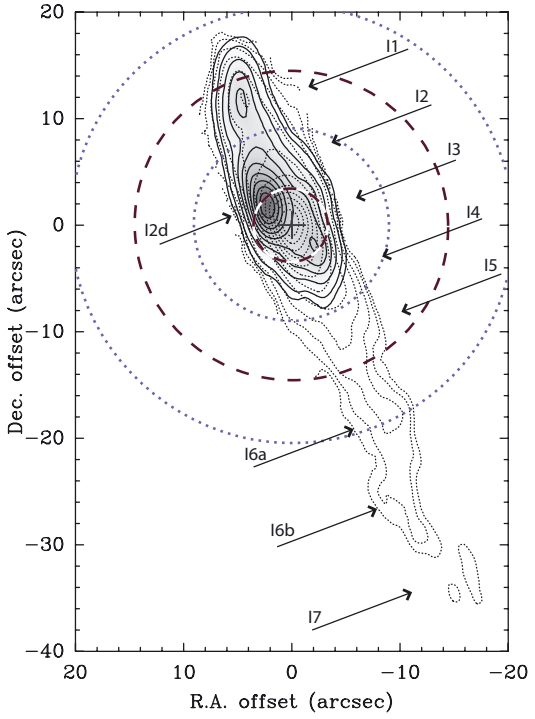

Fig. 1. Distribution of the HCO^+ (1–0) (gray scale and solid contours) and ^{12}CO (1–0) (dotted contours) velocity-integrated emission in OH 231.8 from previous interferometric observations; adapted from Fig. 2 of Sánchez Contreras et al. (2000). The smallest and largest HPBW of the IRAM 30 m (long dashed) and *Herschel* (dotted) telescopes in these observations are represented by the circumferences. We labeled the different regions/clumps in the molecular outflow as I1 to I7, as in Alcolea et al. (2001). Clump I2d corresponds to the region where the HCO^+ emission peaks. The V_{LSR} range (in km s^{-1}) of each clump is I1) [−80:−30], I2) [−30:+10], I2d) [−20:+60], I3) [+10:+55], I4) [+55:+80], I5) [+80:+150], I6a) [+150:+205], I6b) [+205:+230], and I7) [+230:+285]; see Table 2 in Alcolea et al. (2001), and also Sánchez Contreras et al. (1997, 2000), for more detail on the physical properties of the clumps.

(∼479−1244 GHz; Sánchez Contreras et al. 2014). The spectra are presented in units of antenna-temperature (T_A^*), which can be converted to a main-beam temperature (T_{MB}) scale via $T_{MB} = T_A^*/\eta_{eff}$, where η_{eff} is the frequency dependent ratio between the main-beam efficiency (η_{mb}) and the forward efficiency (η_l) of the telescope (values are provided in Sects. 2.1 and 2.2 for IRAM 30 m and *Herschel*, respectively).

In both surveys, we have observed one single position toward the center of OH 231.8 (with J2000 coordinates RA$\equiv^h42^m16^s.830$; Dec = −14°42′52.″10). Considering the half power beam width (HPBW) of the IRAM 30 m and *Herschel* telescopes at the observed frequencies ($HPBW_{30\,m} \sim 7''-29''$ and $HPBW_{HSO} \sim 18''-41''$), this pointing fully covers the slow central core at all frequencies and the fast bipolar lobes up to some extent depending on the frequency (Fig. 1).

2.1. Observations with IRAM 30 m/EMIR

Our mm/submm-wavelength survey was performed with the IRAM 30 m radio telescope (Pico Veleta, Granada, Spain) using the new generation heterodyne Eight MIxer Receiver (EMIR). Spectra were taken in several observational campaigns between years 2009 and 2013. We covered the whole accessible frequency range ∼79−355 GHz, using the four EMIR bands E090 = 3 mm, E150 = 2 mm, E230 = 1 mm, and E330 = 0.8 mm (Carter et al. 2012). The EMIR was operated in single sideband (SSB) mode for band E150, and in dual sideband (2SB) mode for bands E090, E230 and E330. In all cases, the image sideband was rejected with an average sideband rejection of ∼14 dB. Each receiver band was connected to different backends; here we report data observed with the WILMA autocorrelator, which provides a spectral resolution of 2 MHz, and the Fast Fourier Transform Spectrometer (FTS) in its 195 kHz spectral resolution mode. Observations were done in wobbler switching mode with a wobbler throw of 120″. Pointing and focus were checked regularly (every ∼1.5 and ∼4 h, respectively) on strong nearby sources. On-source integration times per tuning step were typically ∼1 h. Calibration scans on the standard two load system were taken every ∼18 min. Errors in the absolute flux calibration are expected to be ≲25%. The parameters of the beam of the IRAM 30 m telescope used in this work are described to a good accuracy as a function of the frequency (ν) by

$$\begin{cases} HPBW('') = \dfrac{2460}{\nu[\mathrm{GHz}]} \\ \eta_{eff} = 0.9\exp-\left(\dfrac{\nu[\mathrm{GHz}]}{399.7}\right)^2 \end{cases} \quad (1)$$

according to measurement updates performed in August 2013[2].

We reduced the data using CLASS[3] following the standard procedure, which includes killing bad channels, subtracting baseline, and averaging individual, good quality scans to produce final spectra.

2.2. Observations with Herschel/HIFI

Observations were carried out with the *Herschel* Space Observatory (Pilbratt et al. 2010) and its HIFI's wideband spectrometer (WBS de Graauw et al. 2010) in several runs in November 2011 and April-May 2012. Our survey, executed in spectral scan mode, covers the frequency range ∼479−1244 GHz (bands 1a−5a) with an average spectral resolution of $\Delta\nu$ = 1.1 MHz. Observations were performed in the dual beam switching (DBS) mode with a 3′ chop throw. The two orthogonal receivers of HIFI (horizontal H, and vertical V) were used simultaneously.

We reprocessed raw *Herschel*/HIFI data from level 0 to level 2 running the `hifiPipeline` task of HIPE[4] (versions 9.0−11.0; Ott 2010). Afterward, level 2 spectra were saved to FITS format and then imported by CLASS where standard data reduction routines were applied: blanking bad-quality data,

[2] http://www.iram.es/IRAMES/mainWiki/EmirforAstronomers

[3] CLASS is a worldwide software to process, reduce, and analyze heterodyne line observations maintained by the Institut de Radioastronomie Millimetrique (IRAM) and distributed with the GILDAS software, see http://www.iram.fr/IRAMFR/GILDAS

[4] HIPE is a joint development by the Herschel Science Ground Segment Consortium, consisting of ESA, the NASA Herschel Science Center, and the HIFI, PACS, and SPIRE consortia.

A&A 577, A52 (2015)

removing spurs, fitting and subtracting baselines, stitching of the spectrometer subbands, and combining individual spectra. We averaged the spectra from both V and H polarisations (with equal weights), reducing the noise in the final product.

HIFI is a double-sideband (DSB) heterodyne instrument and, therefore, every spectrum contains the upper and lower sideband data folded together. We performed the deconvolution of the DSB data into single-sideband (SSB) format in CLASS using the task `deconv`. We assumed a side-band gain ratio of one. We performed the DSB-convolution using all bands simultaneously, which takes advantage of redundant observations in the frequency overlap regions between bands and optimizes the rms of the final SSB spectra. The absolute flux calibration uncertainty of the full, deconvolved SSB spectrum is estimated to be ∼10% (HIFI Observers − Manual, version 2.4, Sect. 5.7). Here we adopt a more conservative value of ∼20%.

We adopted the values of HPBW and $\eta_{\rm eff}$ most recently updated and reported by Mueller et al. (2014)[5], which supersede previous estimates in Roelfsema et al. (2012). HIFI has 14 mixers (7 frequency bands in 2 polarizations), each of which has a frequency-dependent antenna pattern (beam). Detailed models of the beam have been obtained independently for each mixer and separately for polarizations H and V (i.e., a total of $7 \times 2 \times 2 = 28$ beam models). The HPBW of HIFI for one spot frequency per mixer and the adopted values for the Ruze-like scaling of the main-beam efficiency ($\eta_{\rm mb}$) within the frequency range of each mixer are provided in Table 3 and Table 2, respectively, of Mueller et al. (2014). For convenience, we reproduce the values of these beam-model parameters in Table A.1 of our Appendix A. Taking these values into account, the HPBW and $\eta_{\rm eff}$ can be described by

$$\begin{cases} HPBW('') = \dfrac{20\,950}{\nu[\mathrm{GHz}]} \\ \eta_{\rm eff} = \dfrac{\eta_{\rm mb}}{\eta_{\rm l}} = \dfrac{\eta_{\rm mb,0}}{\eta_{\rm l}} \exp\left[-\left(\dfrac{4\pi\sigma_{\rm mb}}{\lambda}\right)^2\right] \end{cases} \quad (2)$$

with the forward efficiency, $\eta_{\rm l}$, being 0.96 at all frequencies (Mueller et al. 2014; Roelfsema et al. 2012), and where λ and $\sigma_{\rm mb}$ are both expressed in μm. As shown in Table A.1, $\eta_{\rm mb,0}$ and $\sigma_{\rm mb}$ are different for the different mixers of HIFI.

3. Results

We detected emission from the molecular ions HCO^+, $H^{13}CO^+$, SO^+, N_2H^+, and (tentatively) H_3O^+ toward OH 231.8 (Table 1 and Figs. 2–5). Except for HCO^+ $J = 1$–0 (Morris et al. 1987; Sánchez Contreras et al. 1997), HCO^+ $J = 3$–2, and $H^{13}CO^+$ $J = 1$–0 (Sánchez Contreras et al. 1997), all transitions reported here are first detections in this source. SO^+ and H_3O^+ have not been detected before in CSEs around evolved stars (either oxygen- or carbon-rich). Quintana-Lacaci et al. (2013) recently reported the discovery of N_2H^+ emission toward the massive yellow hypergiant IRC+10420, but no detection of this molecule in O-rich low-to-intermediate mass evolved stars (AGB or post-AGB) has been published to date. Detection of N_2H^+ has been reported in two C-rich objects, the young PN NGC7027 and the pre-PN CRL618 (see Sect. 1).

In Table 1 we list the main parameters of the molecular transitions observed, which are all in the ground vibrational state.

[5] The HIFI Beam: Release #1. Release Note for Astronomers at http://herschel.esac.esa.int/twiki/bin/view/Public/Hifi\discretionary-CalibrationWeb#HIFI_performance_and_calibration

Table 1. Parameters of the transitions used in this research.

Rest Freq. (MHz)	Transition QNs	$E_{\rm u}$ (K)	$A_{\rm ul}$ (s^{-1})	$\int T_A^* d\upsilon$ (K km s^{-1})
$H^{12}CO^+$	μ = 3.888 Debyes			
89 188.5	1–0	4.3	4.161E-05	4.56 (0.05)
267 557.6	3–2	25.7	1.444E-03	9.1 (0.30)*
535 061.6	6–5	89.9	1.244E-02	0.15† (0.05)
624 208.4	7–6	119.8	1.997E-02	<0.11
$H^{13}CO^+$	μ = 3.888 Debyes			
86 754.3	1–0	4.2	3.829E-05	0.50 (0.05)
260 255.3	3–2	25.0	1.329E-03	1.85 (0.11)
346 998.3	4–3	41.6	3.267E-03	0.76 (0.10)
520 459.9	6–5	87.4	1.145E-02	<0.11
SO^+	μ = 2.3 Debyes			
162 198.6	7/2–5/2(e)	16.7	1.108E-04	0.64 (0.04)
208 965.4	9/2–7/2(f)	26.8	2.457E-04	0.50 (0.08)
254 977.9	11/2–9/2(e)	38.9	4.566E-04	0.55 (0.15)
301 361.5	13/2–11/2(e)	53.4	7.655E-04	<0.15
301 736.8	13/2–11/2(f)	53.5	7.684E-04	<0.15
347 740.0	15/2–13/2(e)	70.1	1.189E-03	0.25† (0.15)
348 115.2	15/2–13/2(f)	70.2	1.193E-03	<0.17
486 837.2	20/2–18/2(f)	133.5	3.330E-03	<0.11
487 212.1	20/2–18/2(e)	133.7	3.338E-03	<0.11
N_2H^+	μ = 3.4 Debyes			
93 173.1	1–0	4.5	3.628E-05	0.54 (0.04)
279 510.8	3–2	26.8	1.259E-03	1.17 (0.10)
558 965.1	6–5	93.9	1.085E-02	<0.12
652 094.2	7–6	125.2	1.741E-02	<0.14
H_3O^+	μ = 1.44 Debyes			
30 7192.4	$1_1^- - 2_1^+$	79.5	3.498E-04	0.28 (0.09)
984 708.7	$0_0^- - 1_0^+$	54.6	2.305E-02	0.40† (0.20)
1 031 299.5	$4_3^+ - 3_3^-$	232.2	5.148E-03	<0.31
1 069 827.6	$4_2^+ - 3_2^-$	268.8	9.850E-03	<0.23

Notes. The table includes: 1) rest frequency (MHz); 2) rotational quantum numbers; 3) upper level energy ($E_{\rm u}$); 4) spontaneous emission Einstein's coefficient ($A_{\rm ul}$); and 5) integrated intensity or line flux ($\int T_A^* d\upsilon$) and its error (within parenthesis); for nondetections, we provide 3σ-upper limits to the line flux adopting a spectral window of 30 km s^{-1}, except for H_3O^+ for which we use 12 km s^{-1} (see Sect. 3.4). The permanent dipole moment (μ) of the ions are also indicated. (*) Flux after removing the contribution of the SO_2 line (∼50%, see Sect. 3.1). (†) Tentative detection.

The flux is computed by integrating the area under the line profile. The corresponding formal errors of the flux are given in parenthesis in the last column of the table and have been calculated according to the error propagation theory as

$$\sigma = \mathrm{rms}\sqrt{FWZI \times \Delta\upsilon},$$

where FWZI is the spectral window (in km s^{-1}) over which the line is integrated and rms is the root mean square statistical noise (in kelvins) of the spectrum near the line for a spectral resolution of $\Delta\upsilon$ (in km s^{-1}). This estimate of the flux error does not include additional uncertainties that may result from baseline subtraction and absolute flux calibration. Typically, we binned our original spectra to match a common velocity resolution of $\Delta\upsilon \sim 2$ km s^{-1}, except for the 2 MHz-resolution WILMA data at frequencies lower than ∼300 GHz, for which $\Delta\upsilon$ is already larger than 2 km s^{-1} (Sect. 2).

We obtained the line frequencies and other spectroscopic parameters discussed here from the Cologne Database for Molecular Spectroscopy (CDMS; Müller et al. 2005), the Jet Propulsion Laboratory (JPL) molecular spectroscopy database

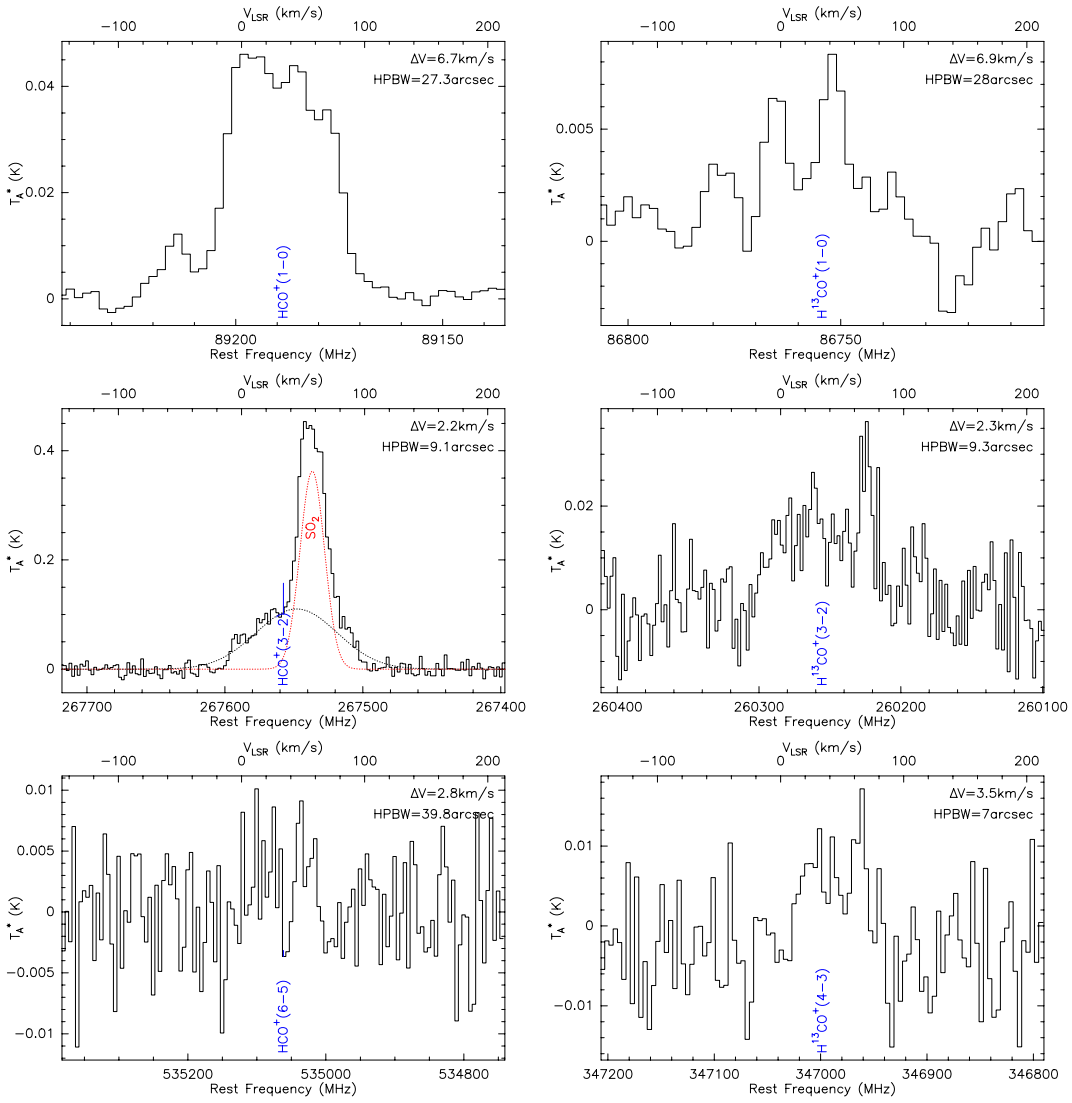

Fig. 2. Spectra of HCO^+ (*left*) and $H^{13}CO^+$ (*right*) emission lines in OH 231.8. The velocity resolution (ΔV) and half power beam width (HPBW) are indicated inside the boxes at the top-right corner. A two Gaussian fit to the blend of the HCO^+ $J = 3{-}2$ and SO_2 lines is shown (dotted lines).

(Pickett et al. 1998), and the MADEX catalogue (Cernicharo 2012).

3.1. $H^{12}CO^+$ and $H^{13}CO^+$

The three HCO^+ lines we observed toward OH 231.8 are shown in Fig. 2. The single-dish profiles of the $J = 1{-}0$ and $J = 3{-}2$ transitions were already known from previous observations (Sánchez Contreras et al. 1997, 2000). As expected, we find similar shapes and absolute intensities (within the calibration uncertainties). The HCO^+ $J = 1{-}0$ transition, observed over a full velocity range of ~200 km s^{-1} ($V_{\rm LSR}$ = [−80:+120] km s^{-1}), is characterized by a broad flattened profile centered around $V_{\rm LSR} \sim 30$ km s^{-1} with a full width at half maximum of $FWHM \sim 90$ km s^{-1} and a weaker, blue-shifted component centered at $V_{\rm LSR} \sim -53$ km s^{-1} with $FWHM \sim 25$ km s^{-1}.

The HCO^+ $J = 3{-}2$ line is also broad, covering the velocity range $V_{\rm LSR}$ = [−20:+105] km s^{-1}. There is a prominent feature centered at $V_{\rm LSR} \sim 55$ km s^{-1} with $FWHM \sim 24$ km s^{-1}, which represents roughly half of the total flux measured in the profile. This feature, observed but not discussed in previous works, is a blend of HCO^+ $J = 3{-}2$ with the SO_2 $J_{K,k} = 13_{3,11}{-}13_{2,12}$ line at 267.5 GHz ($E_{\rm u} = 105$ K). SO_2 shows a wealth of intense transitions that dominate the mm/far-IR spectrum of OH 231.8. We have used these other SO_2 transitions to estimate the total column density and excitation temperature of this molecule

A&A 577, A52 (2015)

with the classic population diagram method (to be published in Sánchez Contreras et al., in prep.). Using this technique, we confirm the identification of the SO_2 line as the main contributor to the $V_{LSR} \sim 55$ km s^{-1} feature and remove its emission from the total flux measured. We find that the expected intensity of this SO_2 transition accounts for 50% of the total flux measured in the blend at 267 GHz ($\int T_A^* d\upsilon \sim 18$ K km s^{-1}) and, thus, the remaining ∼50% is due to HCO^+ $J = 3-2$ (Table 1). A two Gaussian fit to the blended profile is consistent with the HCO^+ line being centered at $V_{LSR} \sim 40$ km s^{-1} and having $FWHM \sim 80$ km s^{-1} (although these figures are rather uncertain).

Regarding HCO^+ $J = 6-5$, although the low S/N ratio prevents an accurate characterization of the profile, the shape of this weak line is also consistent with a broad profile ($FWZI \sim 60$ km s^{-1}) with two peaks around $V_{LSR} \sim 20$ and 50 km s^{-1}, similar to the profile of the $H^{13}CO^+$ $J = 4-3$ (also in Fig. 2, right column).

As already noted and discussed by, e.g., Morris et al. (1987) and Sánchez Contreras et al. (1997), the broad HCO^+ profiles are notably different from those of most molecules, including ^{12}CO and ^{13}CO. The latter display an intense narrow emission core (in the range $V_{LSR} = [+10{:}+55]$ km s^{-1}) that arises at the low-velocity, low-latitude parts of the nebula (clump I3), which contain ∼2/3 of the total nebular mass, plus much weaker broad wings produced by the less massive but faster bipolar lobes. (Profiles of ^{13}CO transitions from our survey are included as additional material in Appendix B, Fig. B.2).

The spatio-kinematic distribution of HCO^+ $J = 1-0$ is known with $\sim 4'' \times 2''$-resolution from interferometric maps by Sánchez Contreras et al. (2000) – see Fig. 1. These data show that, indeed, the different line profiles of HCO^+ and CO come from significant differences between the spatial distribution of these molecules. In contrast to CO, the HCO^+ $J = 1-0$ emission is enhanced in the bipolar lobes and it shows a deficit of emission from the massive slow central region; this explains the broad flattened HCO^+ profiles. The HCO^+ emission peaks at a compact region (referred to as clump $I2_d$) at ∼3−4″ along PA ∼ 50° from the center. There is a large velocity dispersion, of ∼80 km s^{-1}, within this clump that, indeed, produces the bulk of the HCO^+ $J = 1-0$ emission in the velocity range $V_{LSR} = [-20{:}+60]$ km s^{-1}. The extent of the HCO^+ emission in the outflow is smaller than that of CO (in the southern lobe, the HCO^+ emission abruptly falls beyond clump I5) although the axial velocity gradient is similar in both cases.

The single-dish profile of the $J = 1-0$ transition (Fig. 2) is consistent with the whole HCO^+ emission completely filling the telescope beam at 89 GHz, $HPBW = 27''.3$: the bluest HCO^+ $J = 1-0$ spectral feature at $V_{LSR} = -53$ km s^{-1} traces the tip of the approaching North lobe (clump I1), while the reddest wing emission (up to $V_{LSR} = +120$ km s^{-1}) originates in the South lobe (mainly from clump I4 and partially from clump I5).

The smaller full width of the HCO^+ $J = 3-2$ transition (∼120 km s^{-1}), compared with the $J = 1-0$ line, is consistent with the smaller beam size of the IRAM 30 m telescope at 267 GHz ($HPWB = 9''.1$) and, thus, the smaller fraction of the axial outflow lying within the beam. Given the velocity range over which the HCO^+ $J = 3-2$ emission is observed in our single-dish data, most of the emission must arise at the nebular center, the bright clump $I2_d$ and, partially, at the base of the South lobe.

The full width of the HCO^+ $J = 6-5$ line is ∼60 km s^{-1}. At this frequency, the beam of *Herschel* is sufficiently large ($HPBW = 39''.8$, i.e., larger than the IRAM 30 m beam at 89 GHz) as to include the bipolar HCO^+-flow in its full extent. Therefore, one would expect to observe HCO^+ $J = 6-5$ emission over a velocity range comparable to that of the $J = 1-0$ line (∼200 km s^{-1}). The narrower $J = 6-5$ profile could indicate that the emission from this higher excitation transition, which has $E_u = 89$ K, is restricted to regions closer to the nebula center, with smaller expansion velocities. In particular, the emission could mainly be associated with the bright emission clump $I2_d$. However, these conclusions are very tentative because of the low S/N of this transition.

The $H^{13}CO^+$ line profiles are shown in Fig. 2 (right column). As expected, these transitions are weaker than their main isotope analogues. The spectra are broad, with a full width that ranges from ∼190 km s^{-1} in the $J = 1-0$ transition to ∼70 km s^{-1} in the $J = 4-3$. They lack a dominant narrow core component but, instead, show broad, multiple-peaked shapes. For the $J = 1-0$ transition, we clearly detect emisson at $V_{LSR} = -50$ km s^{-1} from the tip of the North lobe (clump I1). In all transitions, we detect emission from a velocity range that is consistent with emission produced at the bright clump $I2_d$ and at the base of the South lobe (clump I4). The emission contribution of the latter, clump I4, concentrates in the range $V_{LSR} \sim [60{:}80]$ km s^{-1}, this spectral feature being rather prominent and sharp in the $J = 3-2$ and 4−3 lines.

3.2. SO^+

SO^+ is a reactive radical with a $^2\Pi$-electronic state. The energy levels of a $^2\Pi$-molecule exhibit the additional splittings due to the electron spin and orbital angular momentum interactions (Ω- and Λ-doublets). The rotational levels are defined with three quantum numbers, Ω, J, l, which represent the absolute value of the projection of the total electronic angular momentum on the molecular axis, the total angular momentum from rotation and electronic motion, and the parity, respectively (Amano et al. 1991).

A total of twenty SO^+ transitions (five Λ-doublets in each of the $\Omega = 1/2$ and $\Omega = 3/2$ states) lie within the frequency range covered in our mm-wave survey with IRAM 30 m. The SO^+ transitions detected toward OH 231.8 are listed in Table 1 and their profiles are shown in Fig. 3. The lines detected correspond to the lowest rotational levels of the $^2\Pi_{1/2}$ ladder of SO^+, which require low- excitation temperatures, between $E_u = 17$ and 70 K. The nondetection of the $^2\Pi_{3/2}$ transitions is in very good agreement with the expectations given that the lowest levels are at $E_u \gtrsim 500$ K above the ground, much higher than the average temperature ($T_{kin} \sim 10-40$ K) of the molecular outflow of OH 231.8 (Sects. 1 and 4.1). In Table 1 we have not included additional SO^+ transitions that may be tentatively detected but that appear partially or fully blended with other stronger lines or in particularly noisy spectral regions (the spectra over the full range of frequencies covering the five SO^+ doublets observed are shown in Fig. B.1 of the Appendix).

The SO^+ line profiles are broad, with $FWHM \sim 60 \pm 10$ km s^{-1} and centered around $V_{LSR} \sim 40$ km s^{-1} (Fig. 3). The moderate S/N of the spectra does not justify an accurate analysis of the profiles, however, it is sufficient to establish that, as for HCO^+, the SO^+ lines lack a prominent, narrow central core, but instead are dominated by a broad spectral component. This suggests a similar distribution for SO^+ and HCO^+ and, therefore, it is likely that the emission from both molecules arises mainly at the fast outflow.

3.3. N_2H^+

N_2H^+ is a linear, triatomic molecule. Its spectral lines show hyperfine structure due to the electric quadrupole moment of the

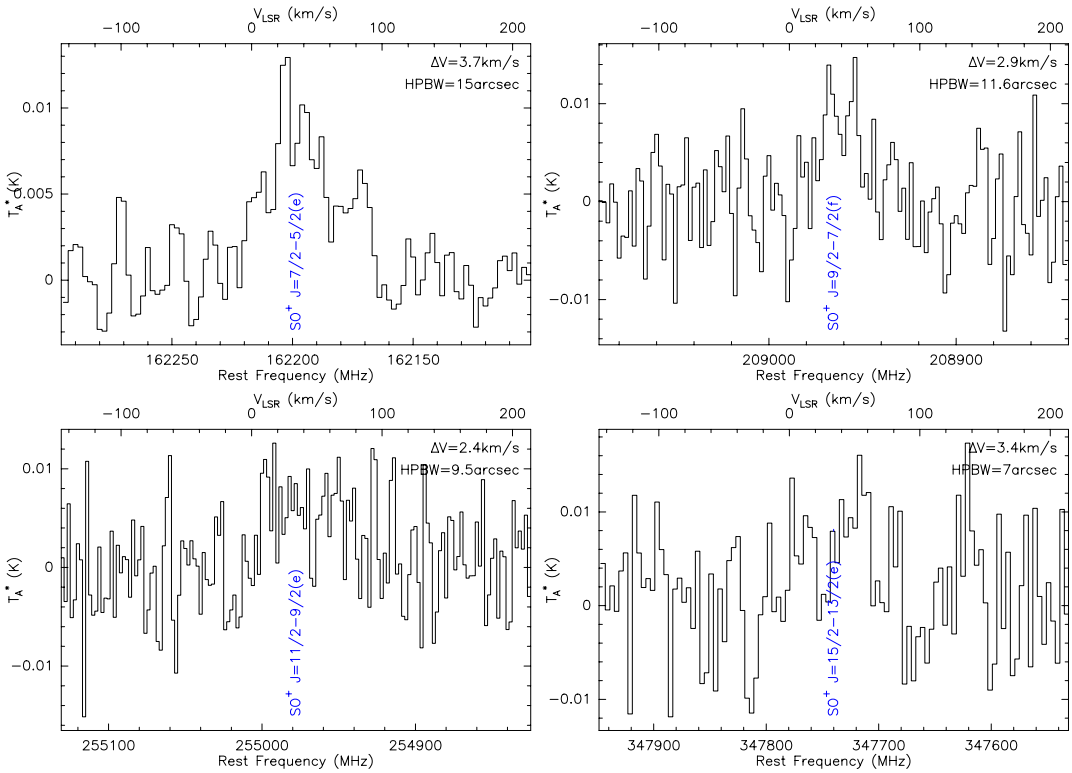

Fig. 3. Same as in Fig. 2 except for SO^+. See also Fig. B.1 in Appendix.

nitrogen nucleus. The line widths of the individual hyperfine components, which are separated by a few km s^{-1}, are expected to blend because of the large expansion velocities of OH 231.8's molecular outflow. In Table 1 we list the N_2H^+ J = 1−0 and 3−2 transitions detected in the mm-wavelength range and also provide flux upper limits for nondetections from our far-IR survey with *Herschel* up to upper level energies of $E_u \sim 125$ K.

The spectra of the two N_2H^+ transitions detected are shown in Fig. 4. Both lines have rather broad, somewhat structured profiles: the J = 1−0 line is centered at 45 ± 4 km s^{-1} and has $FWHM$ = 85 ± 10 km s^{-1} and the J = 3−2 line is centered at 39 ± 4 km s^{-1} and has $FWHM$ = 70 ± 10 km s^{-1}. The smaller line width of the N_2H^+ J = 3−2 transition is consistent with the smaller beam size at this frequency ($HPBW \sim 8\farcs7$), which implies that a smaller fraction of the outflow is probed.

The deconvolved width of the lines at half maximum, taking the hyperfine structure and the spectral resolution of the data into account, is ∼70 km s^{-1}, indicating that most of the N_2H^+ emission arises in the fast outflow. As for HCO^+ and SO^+, N_2H^+ lines present broad profiles, lacking of a prominent, narrow core component.

3.4. H_3O^+

The molecular ion H_3O^+, hydronium, is isoelectronic with ammonia (NH_3) and has a similar physical structure: H_3O^+ is a trigonal pyramid with the oxygen atom at the apex and the hydrogen atoms at the base. Like ammonia, H_3O^+ undergoes inversions as the oxygen atom tunnels through the plane of the hydrogen atoms leading to the characteristic inversion splitting of its rotational levels. An energy level diagram of this molecule for the lowest four rotational levels is shown by, e.g., Mamon et al. (1987). The rotation-inversions transitions are described by three quantum numbers J_K^p, where the parity number p takes a + or − value (see, e.g., Kozlov & Levshakov 2011). H_3O^+ has both ortho- and para- modifications: transitions with $K = 3n$, where n is an integer ≥0, are from the *ortho* and the rest are *para* variety.

The spectrum of the p-H_3O^+ $J_K^p = 1_1^- - 2_1^+$ line at 307 GHz is shown in Fig. 5. A weak emission line is observed centered at V_{LSR} = 34 ± 3 km s^{-1} and with a width of $FWHM \sim 14 \pm 6$ km s^{-1}. This profile is significantly narrower that those of the other molecular ions described here, but consistent with the low expansion velocities found in the central regions of OH 231.8 (Sect. 1). Although the H_3O^+ emission is weak, it satisfies a simple objective detection criterion: more than three adjacent channels of width 3.9 km s^{-1}, corresponding to an anticipated line-FWHM of ≳12 km s^{-1}, are above 1.5σ (this is adopting a gaussian profile with a ≳3σ level at the peak). Moreover, the line centroid coincides with the systemic velocity of the source within errors, which reinforces the detection case.

We observed the o-H_3O^+ $J_K^p = 0_0^- - 1_1^+$ line at 985 GHz and other transitions of this molecular ion at higher frequencies in our survey with *Herschel* toward OH 231.8. The spectrum at 985 GHz (shown in Fig. 5) is consistent with weak emission centered at V_{LSR} = 37 ± 3 km s^{-1} and $FWHM$ = 8 ± 5 km s^{-1}. The line flux measured over a 14 km s^{-1}-wide window

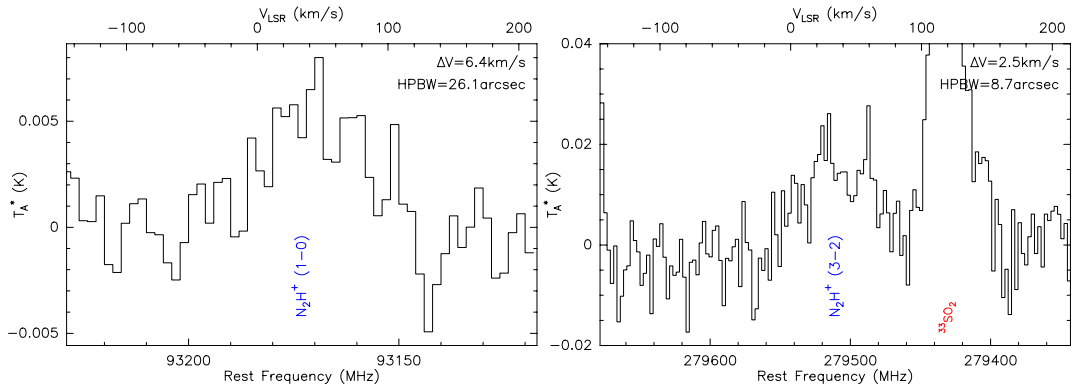

Fig. 4. Same as in Fig. 2 except for N_2H^+.

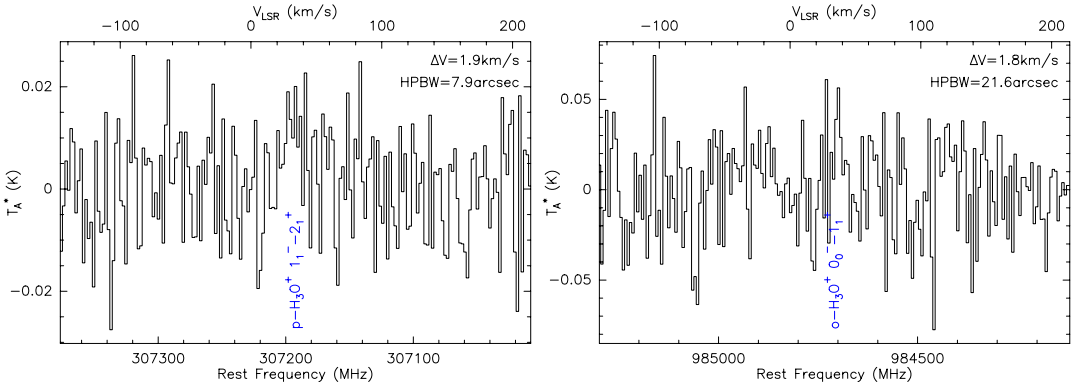

Fig. 5. As in Fig. 2 except for H_3O^+. Detection of the o-H_3O^+ $J^p_K = 0^-_0 - 1^+_1$ line at 985 GHz is tentative.

is $0.4(\pm0.2)$ K km s^{-1}, so we take a conservative position and consider this as a tentative detection. Nevertheless, it is worth noting that very weak emission from this transition is indeed expected if H_3O^+ arises in the warm ($\approx$100 K) envelope component that we recently discovered in our *Herschel* survey (see Sect. 1 and also Sect. 4.1). This warm component is found to be selectively traced by certain molecules, in particular, by H_2O (as well as by CS, H_2S, and SiS). Since the chemistry of H_3O^+ and H_2O are expected to be intimately related to each other, we consider the relatively high temperature suspected from the weakness of the H_3O^+ 985 GHz transition (compared to the H_3O^+ line at 307 GHz) consistent with both species being produced in similar regions.

4. Analysis

4.1. Column densities and excitation temperatures

We have obtained beam-averaged column densities ($N_{\rm tot}$) and excitation temperatures ($T_{\rm ex}$) for the different ions observed using the standard population diagram technique (e.g., Goldsmith & Langer 1999). In this method, the natural logarithm of the column density per statistical weight ($N_{\rm u}/g_{\rm u}$) is plotted against the energy of the upper level above the ground state ($E_{\rm u}$) for a number of transitions of the same molecule. Assuming that the lines are optically thin and thermalized, i.e., all levels are under local thermodynamic equilibrium (LTE) conditions at a given unique temperature, $N_{\rm u}/g_{\rm u}$ and $E_{\rm u}$ are related by the following formula:

$$\ln\frac{N_{\rm u}}{g_{\rm u}} = \ln\frac{3kW_{\rm ul}}{8\pi^3\nu_{\rm ul}\,S_{\rm ul}\mu^2} = \ln\frac{N_{\rm tot}}{Z(T_{\rm ex})} - \frac{E_{\rm u}}{kT_{\rm ex}}, \quad (3)$$

where k is the Boltzmann constant; $W_{\rm ul}$ is the source brightness temperature integrated over velocity; $\nu_{\rm ul}$ and $S_{\rm ul}$ are the frequency and line strength of the transition, respectively; μ is the appropriate component of the permanent dipole moment of the molecule; $Z(T_{\rm ex})$ its partition function; and u and l refer to the upper and lower levels involved in the transitions. According to Eq. (3), for a given molecule a straight-line fit to the points in the population diagram provides $N_{\rm tot}/Z(T_{\rm ex})$ from the y-axis intercept and $T_{\rm ex}$ from the slope of the fit. The line flux W is given by

$$W = f_{\rm d}^{-1}\eta_{\rm eff}^{-1}\int T_{\rm A}^{*}{\rm d}\upsilon, \quad (4)$$

where $\eta_{\rm eff}$ is the ratio between the main-beam efficiency and the forward efficiency of the telescope at a given frequency (values are given in Sect. 2) and $f_{\rm d}$ is the dilution correction factor. The latter is estimated as

$$f_{\rm d} = 1 - \exp\left\{-\frac{\Omega_{\rm src}}{\Omega_{\rm MB}}\right\}, \qquad \begin{cases}\Omega_{\rm src} = \frac{\pi}{4}\theta_{\rm a}\theta_{\rm b}\\ \Omega_{\rm MB} = \frac{\pi}{4\ln 2}HPBW^2\end{cases}$$

where $\Omega_{\rm src}$ and $\Omega_{\rm MB}$ are the solid angular extent of the source and the telescope main beam, respectively. These solid angles

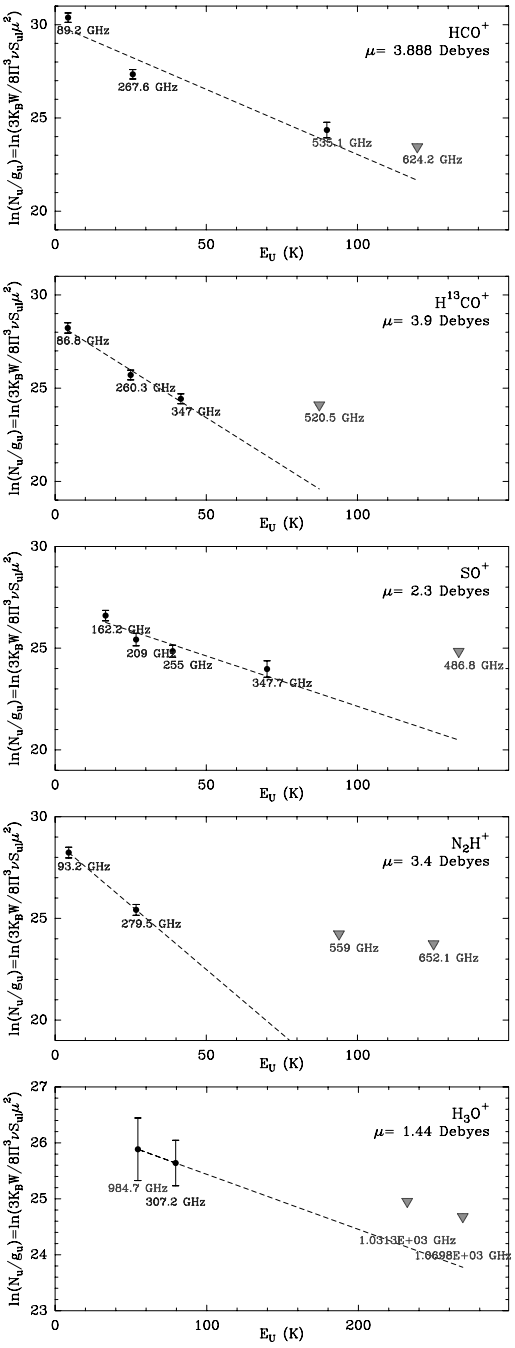

Fig. 6. Population diagrams. Line fluxes (circles) and upper limits (triangles) are from Table 1. The error bars include the rms of the spectra and absolute flux calibration uncertainties, up to ~25%. The frequencies of the transitions used are indicated in GHz. The column density and excitation temperature obtained from the linear fit to the data (dashed line) are given in Table 2.

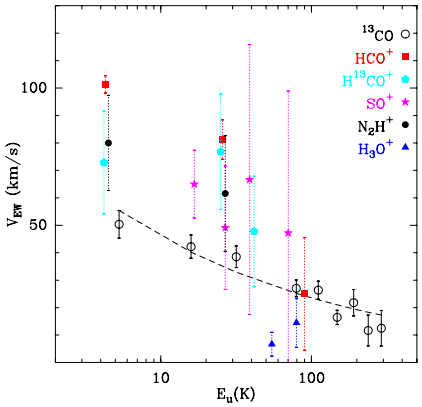

Fig. 7. Equivalent-width velocity (V_{EW}) versus upper-level energy (E_u) for HCO^+, $H^{13}CO^+$, SO^+, N_2H^+, and H_3O^+ transitions (filled symbols) and ^{13}CO, for comparison (empty circles; ^{13}CO profiles and line parameters are given in the Appendix). The dashed line is a fit to the V_{EW} of the ^{13}CO lines. For all ions, except for H_3O^+, the values of V_{EW} are systematically larger than for ^{13}CO, indicating a larger wing-to-core emission contribution to the observed profile; the H_3O^+ emission, in contrast, is dominated by the narrow, core emission component as indicated by the small V_{EW}.

are expressed above as a function of the telescope beam (HPBW) and the angular major (θ_a) and minor (θ_b) axes of a uniform elliptical source (see, e.g., Kramer 1997), which has been taken to roughly represent the elongated molecular outflow of OH 231.8.

Based on the angular extent of the $HCO^+ J = 1–0$ emission in OH 231.8 deduced from interferometric mapping (Sánchez Contreras et al. 2000); see discussion in Sect. 3.1, we adopt a characteristic angular size of $\theta_a \times \theta_b \sim 4'' \times 12''$ for all the species discussed here. Although the spatial distribution of $H^{13}CO^+$, SO^+, and N_2H^+ is unknown, their relatively broad emission profiles and similar excitation requirements justifies our assumption. In the case of H_3O^+, the narrower line profile and possibly higher T_{ex} inferred (see below) may suggest a more compact distribution. We have also considered a smaller size of the H_3O^+-emitting area of $\theta_a \times \theta_b \sim 4'' \times 4''$, which leads to a lower T_{ex} but a comparable value for N_{tot}. We note that the adopted angular size affects both N_u/g_u and T_{ex}: on the one hand, the smaller the size, the larger the value of N_u/g_u obtained from the fit; on the other hand, f_d changes by a different factor for different transitions, which translates into a modification of the slope of the straight-line fit to the points in the population diagram and, thus, into a different T_{ex}. In the particular case of H_3O^+, both effects compensate to yield a similar value of N_{tot} when adopting a smaller size of ~$4'' \times 4''$.

In Fig. 6 we plot the population diagrams for the molecular ions detected in OH 231.8. The partition function, $Z(T_{ex})$, has been computed for each molecule by explicit summation of a finite number of rotational energy levels from the ground vibrational state using MADEX (Cernicharo 2012). For H_3O^+ we have adopted an ortho-to-para ratio of 1, which is the expected value in statistical equilibrium conditions at $T \geq 50$ K (Phillips et al. 1992). The values of N_{tot} and T_{ex} obtained for the different species are given in Table 2. In this table, we also include results for ^{13}CO obtained in Velilla Prieto et al. (2015) using the same technique and assumptions. As discussed by these and other authors, ^{13}CO transitions are optically thin, or only

A&A 577, A52 (2015)

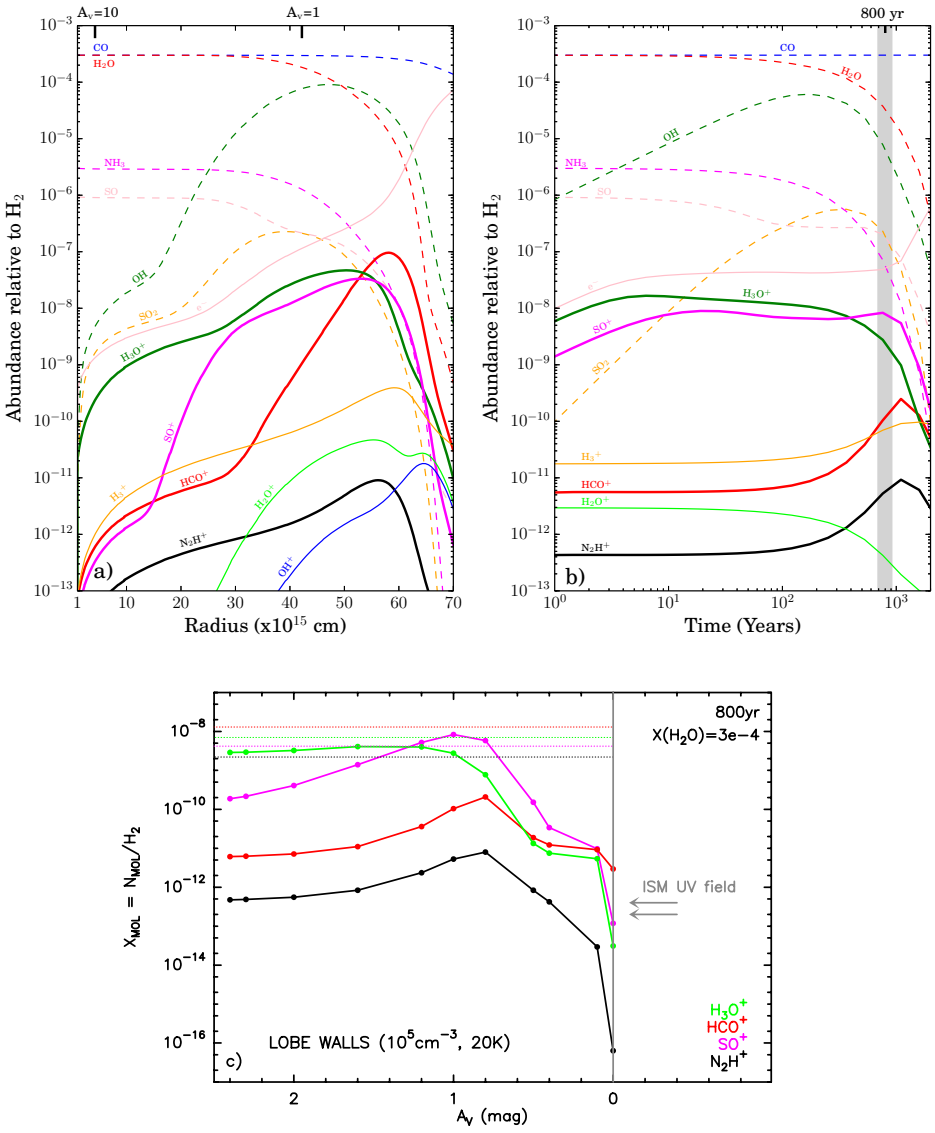

Fig. 8. Results from our chemical kinetics model adopting a fractional water abundance of $X(H_2O) = 3 \times 10^{-4}$ (Sect. 5.1). **a)** Spatial distribution of the model fractional abundances in the slow central core of the envelope (fossil remnant of the AGB CSE); **b)** evolution with time of the model fractional abundances in a representative gas slab or cell within the lobe walls (approximately in the midpoint between the outer and inner end of the wall) where the extinction is $A_V \sim 1$ mag; **c)** model fractional abundances as a function of the depth (expressed as A_V) into the lobe walls, at ~800 yr. Dotted horizontal lines in panel **c**)) represent the observed beam-averaged values of our estimated fractional abundances.

moderately opaque at the line peak toward the densest central parts, and are expected to be thermalized over the bulk of the nebula, with high average densities of $\sim 10^5$–10^6 cm^{-3}, and even larger in low-latitude regions closer to the nebular nucleus.

For HCO^+, $H^{13}CO^+$, SO^+, and N_2H^+, the values of T_{ex} obtained are low, ~8–20 K, in agreement with previous estimates of the kinetic temperature in the outflow, which is ~10–20 K in the fast lobes and, somewhat larger, ~10–40 K in the low-velocity, low-latitude component[6] (see Sect. 1). The excitation temperature inferred for H_3O^+, ≈100 K, is significantly larger than for the rest of the molecular ions (Fig. 6). This value of T_{ex} is very uncertain, however, the upper limit to the flux ratio

[6] These temperatures are derived from low-J transitions and, thus, correspond to the external layers of the central component, deeper regions are expected to be progressively warmer closer to the central star.

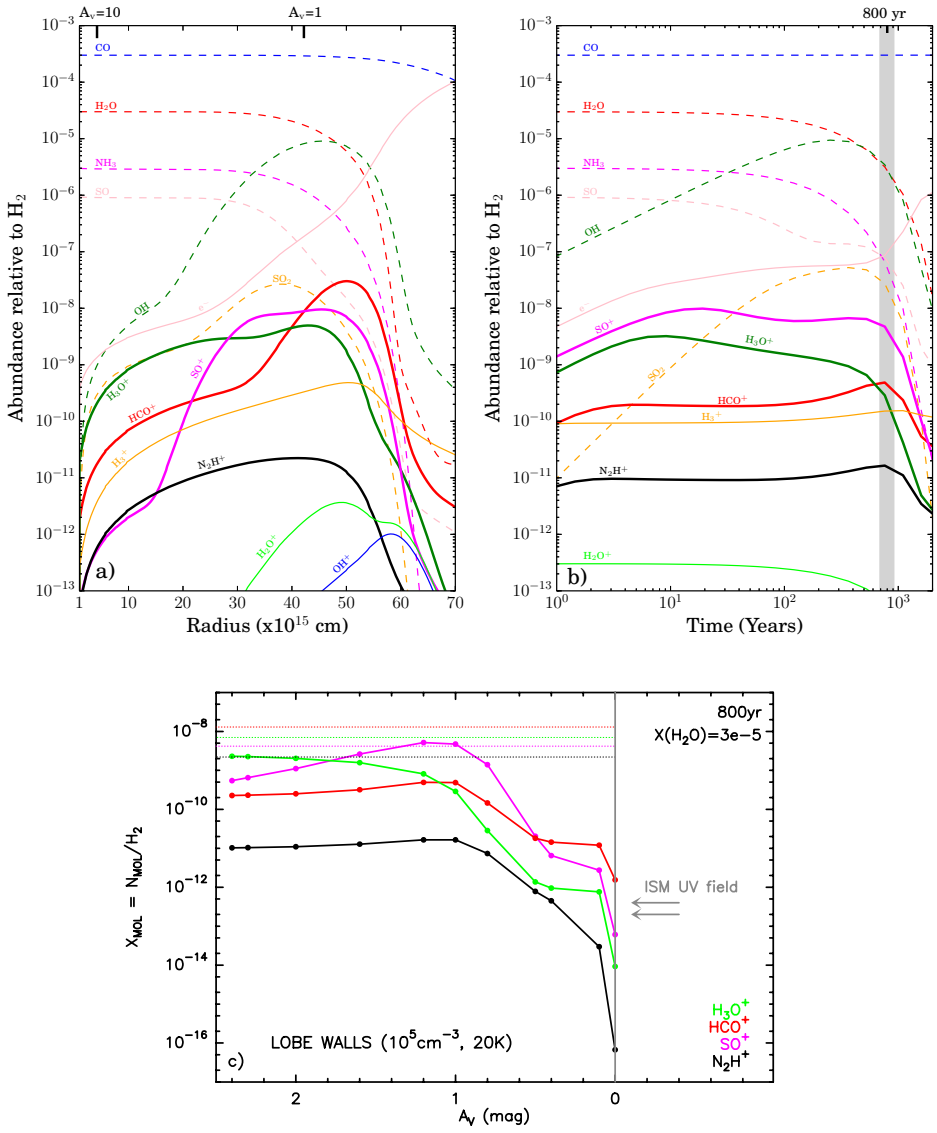

Fig. 9. Same as in Fig. 8 except for a lower abundance of water, $X(H_2O) = 3 \times 10^{-5}$ – see Sect. 5.1.1.

between the 985 GHz and the 307 GHz transitions indicates temperatures certainy larger than 40 K for the emitting region; otherwise, the 985 GHz line should have been much stronger, and thus well detected, given the relatively low energy of the upper state level of this transition ($E_u \sim 55$ K) compared to that of the 307 GHz line ($E_u \sim 80$ K). Moreover, it is suggestive that the excitation temperature guessed for H_3O^+ matches very well that deduced for H_2O and its main isotopologues, $H_2{}^{18}O$ and $H_2{}^{17}O$, from our recent survey with *Herschel* (Sánchez Contreras et al. 2014). Considering that the chemistry of H_3O^+ is expected to be closely linked to that of H_2O, the obtained result is probably more than an unlucky coincidence.

On top of that, the narrow profile of the $H_3O^+ J^p_K = 1^-_1 - 2^+_1$ line at 307 GHz suggests that the emission arises in the dense central parts of the nebula where the expansion velocities are smaller and the temperatures are presumably higher. Support for this comes from the fact that the narrow line width and lowish LSR velocity we find for H_3O^+ is, remarkably, also observed for the $(J, K) = (2, 2)$ and $(3, 3)$ lines of NH_3 by Menten & Alcolea (1995). According to these authors, these lines' profiles are "characterized by a narrow line width of $\leq$15 km s^{-1} (FWHM) and a centroid velocity around 30 km s^{-1}", which is in excellent agreement with the values we find for H_3O^+ (see Sect. 3.4). This gives, first, credence to the reality of our H_3O^+ detection.

A&A 577, A52 (2015)

Secondly, the NH_3 (2, 2) and (3, 3) lines arise from levels that are at energies 64 and 123 K above the ground state, respectively, and from their ratio Menten & Alcolea calculate a rotation temperature of ≈50 K from which they conclude that "the narrow component is emitted from a relatively warm region". By association, this supports our conjecture that the H_3O^+ emission arises from a warm environment. In contrast, the lower excitation NH_3 (1, 1) line, which arises from the molecule's inversion-split para-ground state, shows broader emission than the (2, 2) and (3, 3) lines over a 73 km s^{-1} (FWZI) velocity range with a (higher) centroid of 41 km s^{-1}.

For the values of T_{ex} and N_{tot} implied by the population diagrams, all the transitions detected are optically thin ($\tau < 0.1$). The largest optical depth (at the line peak) is found for the HCO^+ $J = 3-2$ transition, for which $\tau \sim 0.20$. In this case, we applied a small opactity correction factor of $\tau/(1-e^{-\tau})\sim1.1$, resulting in an insignificant effect on the T_{ex} and N_{tot} deduced from the fit. The optical depth of the HCO^+ $J = 1-0$ and 3−2 lines is only expected to be larger than 1 for column densities $\gtrsim 4 \times 10^{14}$ cm^{-2}; for the rest of the molecular ions under discussion even larger column densities, $\gtrsim 10^{15}$ cm^{-2}, would be necessary to produce optically thick emission.

In the previous work by Sánchez Contreras et al. (2000), a large opacity for the HCO^+ $J = 1-0$ transition is also ruled out based on the $HCO^+/H^{13}CO^+$($J = 1-0$) intensity ratio, which agrees well with the low $^{12}C/^{13}C$ isotopic ratio estimated from CO and other molecules in the fast outflow, where the emission is known to be optically thin (see also Sect. 4.2).

4.1.1. Non-LTE excitation effects

When the local density of molecular hydrogen (n_{H_2}) is insufficient to thermalize the transitions of a given molecule, departures from a linear relation in the population diagram are expected. We have performed a non-LTE excitation analysis of the HCO^+ and N_2H^+ emission. We have considered radiative and collisional processes and solved the statistical equilibrium equations under the large velocity gradient (LVG) approximation using the code MADEX (Cernicharo 2012, and references therein). We have adopted collisional coefficients for HCO^+ and N_2H^+ from Flower (1999) and Daniel et al. (2005), respectively. For SO^+ and H_3O^+ there are no collisional coefficients available in the literature, and thus non-LTE calculations cannot be done.

The critical densities of the mm-wave transitions of HCO^+, $H^{13}CO^+$, and N_2H^+ observed by us are in the range $n_{crit} \approx 10^5-10^6$ cm^{-3}. These values are comparable to the mean densities in the central core component ($\gtrsim 10^6-10^7$ cm^{-3}) and moderately larger that the typical densities of the high-velocity clumps where the bulk of the wing emission arises ($n_{H_2} \sim 10^5$ cm^{-3}). Note that the lowest H_2 densities in the molecular outflow of OH 231.8, $n_{H_2} \sim 10^4-10^3$ cm^{-3} are only found at very large distances from the star in the south lobe (clumps I5 and beyond; see Alcolea et al. 2001), but these distant, most tenuous and rapidly expanding regions (at $V_{LSR} \gtrsim 120$ km s^{-1}) do not contribute to the emission profiles of the molecular ions under discussion, as shown in Figs. 2–5.

For our non-LTE excitation calculations, we have adopted a representative density of $n_{H_2} = 10^5$ cm^{-3}. We find that for both HCO^+ and N_2H^+, only mild LTE deviations are expected at this density, which result in values of T_{ex} and N_{tot} (as deduced from the population diagram) slightly lower than the real T_{kin} and N_{tot}. This means that the temperatures and abundances quoted in Table 2 could be lower limits. We have explored the range of input T_{kin} and N_{tot} that would still be consistent with the observations if the characteristic density of the emitting regions is $n_{H_2} \sim 10^5$ cm^{-3}. For both HCO^+ and N_2H^+, we find that the population diagram could also be reproduced with a temperature of $T_{kin} \sim 30-40$ K; for these temperatures, the total column densities would be $N_{tot}(HCO^+) \sim 9 \times 10^{13}$ cm^{-2} and $N_{tot}(N_2H^+) \sim 1.5 \times 10^{13}$ cm^{-2}. Therefore, the column densities deduced under non-LTE and LTE conditions do not differ significantly (less than about 15%).

4.2. Fractional abundances

We computed the fractional abundances of the ions relative to H_2, $X = N_{tot}/N_{H_2}$ as $X = X(^{13}CO) \times N_{tot}/N_{tot}(^{13}CO)$ and adopted $X(^{13}CO) = 5 \times 10^{-5}$, as estimated by Morris et al. (1987). This value of the ^{13}CO abundance is in the high end of the typical range for O-rich stars; in the case of OH 231.8, this is consistent with the particularly low $^{12}C/^{13}C$ isotopic ratio, ∼5−10, measured in this object (and other O-rich CSEs; Sánchez Contreras et al. 2000; Milam et al. 2009; Ramstedt & Olofsson 2014, and references therein). We cannot exclude a lower value of $X(^{13}CO)$, by a factor ∼2−3, in which case the abundances derived for the rest of the species should be scaled down in the same proportion. The fractional abundances obtained from the rotational-diagram method are listed in Table 2. As shown in Sect. 4.1.1, the true values of $X(HCO^+)$ and $X(N_2H^+)$ could be slightly larger than those given in the table if mild non-LTE excitation effects are present (discrepancies ≳15% are unlikely).

The average fractional abundance of HCO^+ in OH 231.8 we derived, $X(HCO^+) \approx 10^{-8}$, is in good agreement with previous estimates (Morris et al. 1987; Sánchez Contreras et al. 1997, 2000). Small differences are expected due to data calibration uncertainties and the slightly different $X(^{13}CO)$ abundance and excitation temperature adopted in different works. The average abundance of HCO^+ in OH 231.8 is also within the range of values observationally determined on a small sample of O-rich envelopes, $\sim 0.15-1.3 \times 10^{-7}$ (Pulliam et al. 2011). The abundance of $H^{13}CO^+$, and its comparison with that of HCO^+, is consistent with a low $^{12}C/^{13}C$ isotope ratio of ∼7, in agreement with previous estimates for this object (see above).

The abundances of the other ions we presented have not been previously reported in O-rich CSEs. The fractional abundance of SO^+ in OH 231.8 implies an abundance relative to SO of $X(SO^+)/X(SO) \approx 2 \times 10^{-3}$; this is taking into account the fractional abundance of SO in OH 231.8 computed in other works, $X(SO) \sim [1-3] \times 10^{-6}$ (Guilloteau et al. 1986, Morris et al. 1987, Sánchez Contreras et al. 2000, and this survey, in prep.). For N_2H^+, our abundance estimate is consistent with the upper limit provided by Morris et al. (1987) based on the nondetection of the N_2H^+ $J = 1-0$ line by these authors ($X(N_2H^+) < 1.6 \times 10^{-8}$). We deduce an average HCO^+ abundance relative to N_2H^+ of $X(HCO^+)/X(N_2H^+) \sim 6$; as we will see in Sect. 5.1, the previous ratio may represent an upper limit to the [CO]/[N_2] proportion in OH 231.8. For H_3O^+, we obtain a fractional abundance of $\approx 7 \times 10^{-9}$, although we caution that this value is particularly uncertain given the low S/N of the H_3O^+ spectra. Our estimate is consistent with the range of values measured in interstellar clouds, $X(H_3O^+) \approx 10^{-10}-10^{-9}$ (Wootten et al. 1991; Phillips et al. 1992; Goicoechea & Cernicharo 2001). In these interstellar regions, the fractional abundance of H_3O^+ is expected to relate to that of water by a factor ≈1/1000−1/6000, based on gas-phase model predictions and observations. If this proportion also holds in OH 231.8, then one would infer an order-of-magnitude water content of $X(H_2O) \approx 10^{-5}-10^{-6}$. This value is at the low edge of the water abundance range deduced for a sample of six evolved

Table 2. Results from the rotational diagram analysis (Sect. 4.1) and molecular fractional abundances, X, i.e., relative to H_2, derived (Sect. 4.2).

Species	$\theta_a \times \theta_b$ ($''$) × ($''$)	N_{tot} (cm^{-2})	T_{ex} (K)	X
^{13}CO	4 × 12	3.0×10^{17}	20	5.0×10^{-5}
$H^{12}CO^+$	4 × 12	8.0×10^{13}	14	1.3×10^{-8}
$H^{13}CO^+$	4 × 12	1.2×10^{13}	10	2.0×10^{-9}
SO^+	4 × 12	2.2×10^{13}	20	3.7×10^{-9}
N_2H^+	4 × 12	1.3×10^{13}	8	2.2×10^{-9}
H_3O^+	4 × 12	$\sim 4 \times 10^{13}$	$\approx$100	$\sim 7 \times 10^{-9}$
	4 × 4	$\sim 5 \times 10^{13}$	~55	

Notes. We have adopted $X(^{13}CO) = 5 \times 10^{-5}$ (Morris et al. 1987).

Table 3. Upper limits to the column densities and fractional abundances of other ions in OH 231.8 adopting a 4$''$ × 12$''$-sized outflow, T_{ex} = 15 K, and $FWHM$ = 40 km s^{-1}.

Ion	N(cm^{-2})	X	Ion	N(cm^{-2})	X
OH^+	$<3 \times 10^{13}$	$<5 \times 10^{-9}$	HOC^+	$<1 \times 10^{12}$	$<2 \times 10^{-10}$
H_2O^+	$<2 \times 10^{13}$	$<3 \times 10^{-9}$	H_2COH^+	$<1 \times 10^{13}$	$<2 \times 10^{-9}$
CO^+	$<2 \times 10^{12}$	$<3 \times 10^{-10}$	H_2NCO^+	$<5 \times 10^{12}$	$<8 \times 10^{-10}$
HCS^+	$<8 \times 10^{12}$	$<1 \times 10^{-9}$	$HSCO^+$	$<7 \times 10^{13}$	$<1 \times 10^{-8}$
SH^+	$<2 \times 10^{13}$	$<3 \times 10^{-9}$	$HOCS^+$	$<4 \times 10^{13}$	$<7 \times 10^{-9}$
CS^+	$<5 \times 10^{13}$	$<8 \times 10^{-9}$	HC_3NH^+	$<4 \times 10^{13}$	$<7 \times 10^{-9}$
CH^+	$<1 \times 10^{13}$	$<2 \times 10^{-9}$	$HOCO^+$	$<7 \times 10^{12}$	$<1 \times 10^{-9}$
$HCNH^+$	$<6 \times 10^{13}$	$<1 \times 10^{-8}$	H_2Cl^+	$<4 \times 10^{13}$	$<8 \times 10^{-9}$
NO^+	$<4 \times 10^{13}$	$<7 \times 10^{-9}$	NeH^+	$<1 \times 10^{13}$	$<2 \times 10^{-9}$
CF^+	$<8 \times 10^{12}$	$<1 \times 10^{-9}$	H_2F^+	$<2 \times 10^{13}$	$<3 \times 10^{-9}$
C_3H^+	$<2 \times 10^{13}$	$<3 \times 10^{-9}$	ArH^+	$<5 \times 10^{12}$	$<8 \times 10^{-10}$
OH^-	$<3 \times 10^{13}$	$<5 \times 10^{-9}$	NCO^-	$<2 \times 10^{13}$	$<3 \times 10^{-9}$
C_2H^-	$<1 \times 10^{12}$	$<2 \times 10^{-10}$	C_4H^-	$<2 \times 10^{12}$	$<3 \times 10^{-10}$
CN^-	$<1 \times 10^{13}$	$<2 \times 10^{-9}$	C_3N^-	$<1 \times 10^{13}$	$<2 \times 10^{-9}$
SH^-	$<3 \times 10^{14}$	$<5 \times 10^{-8}$			

O-rich stars, $X(H_2O) \sim [10^{-3}-2\times10^{-6}]$, with the majority of the stars having $X(H_2O) \sim 6 \times 10^{-4}$ (Maercker et al. 2008).

We recall that the abundances given in Table 2 represent average values within the emitting regions covered by the telescope beam, that is, the central core and (partially) the fast lobes. The large wing-to-core intensity ratio of the HCO^+ profiles is known to reflect an abundance contrast of a factor ~3–4 between the fast lobes and the slow central clump I3, as determined by Sánchez Contreras et al. (1997) from their analysis by individual spectral and spatial components of the HCO^+ $J = 1-0$ emission maps; see their Table 2. This result is also corroborated by the interferometric observations of this transition (Fig. 1), which show that, in contrast to ^{12}CO, ^{13}CO, and most molecules, HCO^+ is found in abundance in the lobes of OH 231.8, but it is scarce at the nebula center (Sánchez Contreras et al. 2000).

The broad profiles of $H^{13}CO^+$, SO^+, and N_2H^+ suggest analogous lobe-to-core abundance enhancements for these ions. Unfortunately, except for the HCO^+ $J = 1-0$ transition, obtaining column densities separately for the different velocity ranges corresponding to the slow core and the fast lobes is hampered by the weakness of the molecular lines. However, a straightforward argument in support of a lobe-to-core abundance ratio >1 for $H^{13}CO^+$, SO^+, and N_2H^+ (as well as, of course, for HCO^+) is provided by the large equivalent-width velocity (V_{EW}) of these lines; the equivalent-width velocity is given by the ratio of the line flux, $\int T_A^* d\upsilon$, to the peak intensity, T_A^* (see, e.g., Sánchez Contreras & Sahai 2012). As can be seen in Fig. 7, the V_{EW} of the emission lines by these species are systematically larger than those of ^{13}CO. The ^{13}CO profiles are dominated by the most massive component, that is, the slow central core (clump I3). The larger V_{EW} of the $H^{13}CO^+$, SO^+, and N_2H^+ profiles indicates that the contribution to the emitting profile from the less massive fast lobes is larger for these ions than for ^{13}CO, implying that their fractional abundances in the fast lobes are higher than in the slow massive clump I3. This also indicates that the true abundances of HCO^+, $H^{13}CO^+$, SO^+, and N_2H^+ in the lobes and in the slow central clump are higher and lower, respectively, than the beam-averaged values given in Table 2.

In the case of H_3O^+, the narrow profile of the weak $J_K^p = 1_1^- - 2_1^+$ transition at 307 GHz suggests that the bulk of the emission is produced in the slow central clump I3. The V_{EW} of this transition is very uncertain but if it is confirmed to be lower than that of ^{13}CO (by higher S/N observations), as suggested by our data (Fig. 7), then one would infer a larger abundance of this ion in the slow core than in the fast lobes (i.e., a lobe-to-core abundance ratio <1). Moreover, since the higher T_{ex} suspected for H_3O^+ compared to that deduced for ^{13}CO favors the origin of the H_3O^+ emission in envelope layers closer to the center, the average abundance in Table 2 could represent a lower limit to the true value in the central, compact emitting regions.

4.2.1. Upper limits to nondetections

We provide upper limits to the column densities and fractional abundances of other ions that are not detected in OH 231.8 and that may be of interest (Table 3). We have adopted common values for the source emitting size, $\theta_a \times \theta_b$ ~4$''$ × 12$''$, T_{ex} = 15 K, and $FWHM$ = 40 km s^{-1} and LTE conditions. For the ions considered, adopting a smaller size, larger excitation temperatures, and narrower profiles (as may be the case of H_3O^+) normally results in slightly smaller values of N and X than those given in the Table. For the different ions, the upper limits to N_{tot} are derived from the rms noise around the transition that is expected to have the largest S/N in our data (adopting T_{ex} = 15 K); we have always checked that the upper limits obtained are also consistent with the nondetections of the rest of the transitions in the frequency range of our observations.

5. Formation of HCO^+, SO^+, N_2H^+, and H_3O^+

5.1. Chemical model

We performed chemical kinetics models to investigate the formation of the observed ions in OH 231.8. Our model is based on that by Agúndez & Cernicharo (2006) and we have used it recently to study the new N-bearing species detected in OH 231.8 by Velilla Prieto et al. (2015). The code has also been employed to model the chemistry in different astrophysical environments, including the prototypical C-rich star IRC+10216 (see, e.g., Agúndez et al. 2007, 2008, 2010b, 2012; Cernicharo et al. 2010, 2013), and the O-rich yellow hypergiant IRC+10420 (Quintana-Lacaci et al. 2013). The chemical network in our code includes gas-phase reactions, cosmic rays, and photoreactions with interstellar UV photons; it does not incorporate reactions involving dust grains, X-rays or shocks. Our code does not explicitly consider the chemistry of isotopologues, that is, does not include isotopic fractionation, such as selective photodissociation or isotope-exchange reactions; as a consequence, predictions for the $H^{13}CO^+$ abundance distribution are not made.

A&A 577, A52 (2015)

As input we adopt the same physical model for the envelope used in Velilla Prieto et al. (2015), which consists of two main components: a) a dense, spherically symmetric wind expanding at low velocity, which represents the slow, central nebular component of OH 231.8 (clump I3); and b) a rectangular slab of gas (plane-parallel geometry) with characteristics similar to those of the walls of the hollow bipolar lobes. We modeled separately these two components, which are externally illuminated by the interstellar UV field.

The main parameters of the simple physical model for OH 231.8 used as input in our chemical code are summarized in Table 4; additional details justifying the temperature, density, and velocity laws adopted are given in Sect. 6.1 of Velilla Prieto et al. (2015). The region of the envelope modeled in case *a* goes from $R_{\rm in} \sim 10^{15}$ cm ($\sim 20\,R_\star$) to its end, at $R_{\rm out} \sim 7 \times 10^{16}$ cm (we refer to this region as the intermediate/outer envelope). The outer radius is observationally determined (Sánchez Contreras et al. 1997; Alcolea et al. 2001) and the inner radius has been chosen to be well beyond the dust condensation radius so that the full expansion velocity of the gas has been reached. In these intermediate/outer regions of the envelope, the chemistry is driven by chemical kinetics. Another major input of our chemistry model is the set of initial abundances of the "parent" species. These are formed in deeper layers and are injected to the intermediate/outer envelope. The parent species, typical of O-rich environments, and the initial abundances adopted in our model are as in Velilla Prieto et al. (2015) and are reproduced again in Table 5.

As in Velilla Prieto et al. (2015), the sources of ionization and dissociation adopted in our model are cosmic-rays and the interstellar ultraviolet radiation field. The cosmic ray ionization rate adopted is 1.2×10^{-17} s^{-1} (Dalgarno 2006). The intensity of the UV field assumed is the Draine field or $G_0 = 1.7$ in units of the Habing field ($G_0 = 1.6 \times 10^{-3}$ erg s^{-1} cm^{-2}; Habing 1968; Draine & Salpeter 1978). We computed the dust optical extinction, A_V, across the envelope layers adopting the standard conversion from H_2 column density $N_{\rm H_2} = 9.3 \times 10^{20} \times A_V$ cm^{-2}, derived by Bohlin et al. (1978). The gas-to-dust mass ratio implicit in this conversion, ~100, is comparable within errors to the average value measured in nearby O-rich AGB stars and, in particular, in OH 231.8 (e.g., Knapp 1985; Kastner & Weintraub 1995; Sánchez Contreras et al. 1998).

The slow, central component. We used our chemical kinetics model first to investigate the formation of HCO^+, SO^+, N_2H^+, and H_3O^+ in an O-rich AGB CSE similar to the slow, core component of OH 231.8 (model a, Table 4). The fractional abundances predicted by the model as a function of the distance to the center are shown in Fig. 8. For HCO^+, N_2H^+, and H_3O^+, we checked that there is good agreement between our predictions and those obtained from analogous photochemistry simulations by Mamon et al. (1987); these authors modeled the chemistry of these three ions for O-rich CSEs with standard properties and a set of different mass-loss rates, including $\dot{M} = 10^{-4}\,M_\odot$ yr^{-1}. We found no previous modeling attempts for SO^+ in CSEs in the literature.

As the gas in the envelope expands, parent molecules start to be exposed to the interstellar UV radiation and photochemistry drives the formation of new species in the outer layers. Penetration of photons through the envelope is gradually blocked by dust and also by self-shielding of abundant gas species (mainly H_2, H_2O and CO). At the deepest layers of the intermediate/outer envelope inaccessible to the UV radiation, cosmic rays are major drivers of the chemistry. Cosmic rays ionize molecular hydrogen (H_2^+) , which combines with neutral H_2 to form H_3^+. The latter is a fundamental ion for breaking down parent molecules leading to the formation of new ions in the inner layers of the envelope.

It is well known that the radical OH is an important product of the photodissociation of H_2O in the external regions of O-rich CSEs. Our model predicts that OH reaches maximum abundance at $\sim 5 \times 10^{16}$ cm, in good agreement with the characteristic radius of the OH maser toroidal shell observed at the center of OH 231.8 (Morris et al. 1982; Zijlstra et al. 2001). Our model indicates that, as the radical OH, molecular ions should be most efficiently formed in the outermost layers of the envelope, showing a shell-like distribution with maximum abundances at typical distances from the star of $\sim [5-7] \times 10^{16}$ cm. Farther out, there is an abrupt fall of the ions' abundances due to their destruction by dissociative recombination with electrons (e^-) and to photodissociation of their main progenitors.

According to our model, HCO^+ forms in the outer layers of O-rich envelopes mainly as a photodissociation product of CO

Table 4. Parameters of the central Mira star and molecular envelope of OH 231.8 used for the chemical kinetics models (Sect. 5.1).

Parameter	Value	Reference
Distance (d)	1500 pc	b
Stellar radius (R_*)	4.4×10^{13} cm	g
Stellar effective temperature (T_*)	2300 K	g
Stellar luminosity (L_*)	$10^4\,L_\odot$	g
Stellar mass (M_*)	$1\,M_\odot$	g
Model a: slow, core		
AGB CSE expansion velocity ($V_{\rm exp}$)	20 km s^{-1}	a, e, f, g, i
AGB mass loss rate ($\dot{M}$)	$10^{-4}\,M_\odot$ yr^{-1}	e, a, f
Kinetic temperature ($T_{\rm kin}$)	$T_*(r/R_*)^{-0.70}$ K	i
Model b: lobe walls		
Wall thickness	1″	a
H_2 number density ($n_{\rm H_2}$)	10^5 cm^{-3}	a
Kinetic temperature ($T_{\rm kin}$)	20 K	a

References. a) Alcolea et al. (2001); b) Choi et al. (2012); c) Cohen (1981); d) Kastner et al. (1992); e) Morris et al. (1987); f) Sánchez Contreras et al. (1997); g) Sánchez Contreras et al. (2002); h) Sánchez Contreras et al. (2004); i) Velilla Prieto et al. (2015).

Table 5. Initial abundances relative to H_2 for representative elements and parent molecules used as input for the chemical kinetic models.

Species	Abundance	Reference
He	0.17	a
H_2O	3.0×10^{-4}	b, TE
CO	3.0×10^{-4}	c, TE
CO_2	3.0×10^{-7}	d
NH_3	4.0×10^{-6}	e
N_2	4.0×10^{-5}	TE
HCN	2.0×10^{-7}	f, g
H_2S	7.0×10^{-8}	h
SO	9.3×10^{-7}	f
SiO	1.0×10^{-6}	i
SiS	2.7×10^{-7}	j

References. a) Asplund et al. (2009); b) Maercker et al. (2008); c) Teyssier et al. (2006); d) Tsuji et al. (1997); e) Menten & Alcolea (1995); f) Bujarrabal et al. (1994); g) Schöier et al. (2013); h) Ziurys et al. (2007); i) González Delgado et al. (2003); j) Schöier et al. (2007) TE) From LTE chemical calculations by Velilla Prieto et al. (2015).

and H_2O (in order of importance):

$$\begin{array}{l} HOC^+ + H_2 \rightarrow HCO^+ + H_2 \\ CO^+ + H_2 \rightarrow HCO^+ + H \\ C^+ + H_2O \rightarrow HCO^+ + H, \end{array} \quad (5)$$

where the C^+ ion is predominantly produced in the CO photoionization chain, and the molecular ions HOC^+ and CO^+ are formed through

$$\begin{array}{l} C^+ + OH \rightarrow CO^+ + H \\ CO^+ + H_2 \rightarrow HOC^+ + H. \end{array} \quad (6)$$

An additional, but nondominant pathway to HCO^+ production is by proton transfer from N_2H^+ to CO ($N_2H^+ + CO \rightarrow HCO^+ + N_2$). The model predicts that HCO^+ reaches highest abundances in a very thin outer shell with a characteristic radius of $\sim 6 \times 10^{16}$ cm. HCO^+ has, together with N_2H^+, the most sharply peaked distribution amongst the ions modeled. The model peak abundance in the shell is $X(HCO^+) \approx 10^{-7}$, that is larger than the average value derived in OH 231.8 from these observations. Deeper into the envelope, i.e., in the $\sim[10^{15}-3 \times 10^{16}]$ cm region before the inner rim of the peak abundance shell, HCO^+ is formed in much lower amounts ($X(HCO^+) < 10^{-11}$) directly from CO and H_3^+, which is a product of cosmic-ray ionization ($H_3^+ + CO \rightarrow HCO^+ + H_2$).

The SO^+ shell-like abundance distribution predicted by the model is broader than that of HCO^+: for SO^+ the inner rim of the shell is located deeper in the envelope than for HCO^+. Within the SO^+ peak abundance shell, the fractional abundance varies between $X(SO^+) \sim 2 \times 10^{-12}$ and $\sim[3-4] \times 10^{-8}$, the maximum value being reached at a distance of $\sim 5 \times 10^{16}$ cm. The SO^+ abundance distribution shows a "hump" or secondary peak at $\sim 3 \times 10^{16}$ cm where the abundance is $X(SO^+) \sim 7 \times 10^{-9}$. The values of the SO^+ model abundance inside the shell seem, in principle, compatible with the beam-averaged value deduced in OH 231.8 from our observations. The main formation paths of SO^+ in the outer shell are

$$\begin{array}{l} S^+ + OH \rightarrow SO^+ + H \\ SO + h\nu \rightarrow SO^+ + e^- \\ C^+ + SO_2 \rightarrow SO^+ + CO. \end{array} \quad (7)$$

The reaction of S^+ with OH is the dominant formation route near the peak abundance radius; the hump or secondary peak of the SO^+ abundance distribution results from direct photoionization of SO by UV photons and the reaction of C^+ with SO_2 (Eq. (7)). In regions deeper into the envelope, cosmic rays are the fundamental source of direct ionization of SO leading to the production of SO^+ (although in much lower amounts, $<10^{-12}$, than within the shell) and free electrons.

The spatial distribution of N_2H^+ predicted by the model is sharply peaked, similar to that of HCO^+, but with a very low peak abundance of $X(N_2H^+) \sim [0.9-1.0] \times 10^{-11}$ that is reached at $\sim[5-6] \times 10^{16}$ cm. This maximum abundance is more than two orders of magnitude lower than the mean value measured in OH 231.8. Based on our model, N_2H^+ is formed mainly via

$$\begin{array}{l} H_3^+ + N_2 \rightarrow N_2H^+ + H_2 \\ N_2^+ + H_2 \rightarrow N_2H^+ + H \\ HCO^+ + N_2 \rightarrow N_2H^+ + CO, \end{array} \quad (8)$$

where the first reaction above plays a major role all the way throughout the different layers of the intermediate/outer envelope, whereas the second and third reactions become an important factor in N_2H^+ production only in the outermost parts near the peak abundance radius. In these outer envelope layers, the ion N_2^+ is mainly produced by the proton transfer reaction of He^+, which is produced by direct ionization of He by UV photons, with N_2.

Regarding H_3O^+, our model predicts efficient formation of this ion in the outer envelope mainly as a product of the photodissociation chain of H_2O and CO. The model peak abundance, $X(H_3O^+) \sim 5 \times 10^{-8}$, which is larger than the observed value, is reached at $\sim 5 \times 10^{16}$ cm. Near the peak abundance radius, the distribution of H_3O^+ is relatively broad and similar in shape and values to that of SO^+. In these outer regions, the main reactions involved in the production of H_3O^+ are

$$\begin{array}{l} H_2O^+ + H_2 \rightarrow H_3O^+ + H \\ HCO^+ + H_2O \rightarrow CO + H_3O^+. \end{array} \quad (9)$$

In contrast to the other ions, H_3O^+ is rather abundant not only within the peak abundance shell but also deeper into the envelope, with a fractional abundance that varies from $X(H_3O^+) \sim 2 \times 10^{-11}$ at 10^{15} cm to $X(H_3O^+) \sim 4 \times 10^{-9}$ at the inner rim of the shell (at $\sim 2 \times 10^{16}$ cm). In these inner envelope regions, H_3O^+ is by far the most abundant of the ions modeled and is produced by protonation of water ($H_2O + H_3^+ \rightarrow H_3O^+ + H_2$) after cosmic-ray ionization of H_2 leading to H_3^+.

In the outer layers of the envelope, dissociative recombination with electrons is the major mode of destruction of all the ions, except for N_2H^+, which instead is most rapidly destroyed by reactions with H_2O and CO. Dissociative recombination with electrons ceases to be the main destruction mechanism for all ions deeper into the envelope, where the electron abundance is low ($<$few $\times 10^{-9}$). In these inner regions, molecular ions are quickly disassembled primarily by reactions with H_2O and NH_3 (and, in the case of N_2H^+, also with CO), i.e.,

$$\begin{array}{l} HCO^+ + H_2O \rightarrow CO + H_3O^+ \\ N_2H^+ + H_2O \rightarrow N_2 + H_3O^+ \\ SO^+ + NH_3 \rightarrow SO + NH_3^+ \\ H_3O^+ + NH_3 \rightarrow NH_4^+ + H_2O. \end{array} \quad (10)$$

The lobes. We have also modeled the chemistry in the walls of the lobes (model b), which are on average more tenuous than the central regions and, thus, enable deep penetration of the ionizing interstellar UV radiation. The main input parameters of the simple physical model adopted for the lobe walls (a rectangular gas slab externally illuminated by one side by the interstellar UV field) are given in Table 4. Our chemical kinetics code computes the evolution with time of the molecular fractional abundances inside a series of individual gas cells at different depths into the lobe walls. An example is given in Fig. 8b for a representative cell midway between the inner and outer edge of the walls (i.e., at $\sim 0\farcs5$ through the lobe wall). The depth of the cell into the wall is expressed as a function of the dust optical extinction, A_V. For the cell whose abundances are represented in Fig. 8b, the optical extinction is $A_V \sim 1$ mag.

The spatial distribution of the model fractional abundances across the lobe walls attained at ~800 yr, which is the dynamical age of the outflow (Sect. 1), is shown in Fig. 8c. As a result of photodissociation, the abundances of all molecular ions rapidly increase inward across the lobe walls, reaching maximum values near $A_V \sim 1$ mag; at larger depths, the ions' abundances gently decrease as destruction processes by reactions with H_2O, NH_3, and CO start prevailing over formation routes. The peak abundances predicted by the model are comparable to the observed beam-averaged values in the case of SO^+, and possibly in the case of H_3O^+. In the latter case, the model value is lower

than the observational value but the model-data discrepancy, of a factor ∼2, is probably within the total uncertainties in the abundance calculation. According to the model, these two ions are the only ones that would form in detectable amounts[7] in the fast lobes of OH 231.8. In fact, in clear disagreement with the observations, our model predicts H_3O^+ to be the second most abundant ion (after SO^+) in the fast lobes of OH 231.8. For HCO^+ and N_2H^+, the model predicts fractional abundances two orders of magnitude lower than observed. We have checked that the model abundances for these ions never reach values comparable to the observed values for a reasonable range of outflow ages, ∼500−1000 yr.

For all the ions discussed in this research, the maximum abundances reached within the lobes (model b) are smaller than the maximum abundances reached in the slow, central component (model a). The largest core-to-lobe peak abundance ratio (∼500) is found for HCO^+. The ion N_2H^+ is predicted to be almost equally deficient in the lobes and in the central, peak abundance shell. SO^+ and H_3O^+ are intermediate cases, with core-to-lobe peak abundance ratios of ∼4 and 13, respectively.

It may appear a priori somewhat surprising that HCO^+, which is predicted by the model to be efficiently produced in the outer regions of the slow, central component (with a peak abundance of $X(HCO^+) \approx 10^{-7}$), is so scarce across the lobe walls, where the maximum abundance reached is only $X(HCO^+) \lesssim 10^{-10}$. This is because the HCO^+ formation and destruction processes in the lobes are similar to those prevailing in the deepest regions of the central component, where HCO^+ is indeed not very abundant because of the rapid destruction of this ion by reactions with the abundant H_2O molecule. In the peak abundance shell of the central component, however, the balance between photochemical formation processes and dissociative recombination with e^- results in an efficient net production of HCO^+.

5.1.1. Initial abundance of H_2O

We have investigated how the abundances of the molecular ions under discussion depend on the initial abundance of H_2O, which is a prime parent molecule tied up to the chemistry of these and other species. We ran our code using the same input parameters as in the previous section but with a relative abundance of water of $X(H_2O) = 3 \times 10^{-5}$ that is ten times lower (Fig. 9). For a given ion, the final role of H_2O either as a net builder or a net destroyer, after the balance of formation and destruction reactions with water, varies throughout the envelope and, of course, is different for the different ions considered.

We find that, within the peak abundance shell in model *a*, a decrease of the initial abundance of H_2O results in a decrease of the peak abundances for all ions except for N_2H^+. The peak abundances of HCO^+ and SO^+ are lowered by a factor ∼1/3−1/4 and the abundance of H_3O^+ (and also that of the radical OH) by a factor ∼1/10. In contrast, the peak abundance of N_2H^+ increases by a factor ∼2−3. Moreover, in the low H_2O abundance case, N_2H^+ no longer presents a sharply peaked, shell-like distribution, but rather its abundance progressively increases from the inner layers up to a radius of ∼[4−5] × 10^{16} cm; beyond this point, the abundance falls abruptly as for the rest of the species. The markedly different reaction of N_2H^+ to a decline in the H_2O abundance with respect to the other ions is because, in the case of N_2H^+, H_2O provides the main mode of destruction of this ion but is not a required formation ingredient in any of the regions of the envelope (see Sect. 5.1). In contrast, in the outer shell, for HCO^+, H_3O^+, and SO^+, water acts only as a main production agent (directly or indirectly via H_2O^+ and OH).

Deeper into the envelope, HCO^+ and N_2H^+ are the two ions whose abundances are most sensitive to $X(H_2O)$: our model predicts HCO^+ and N_2H^+ enhancements of one order of magnitude for a similar decrease of the water abundance. In contrast to N_2H^+, the response of $X(HCO^+)$ to a change in the water abundance is different in the outer peak abundance shell and in regions deeper into the envelope. This is because, as explained earlier, in the inner envelope regions the formation of HCO^+ is principally the result of protonation of CO from H_3^+, with H_2O acting almost exclusively as a main destroyer. We also find that the model abundances of SO^+ and H_3O^+ vary only marginally in the inner regions when the H_2O abundance is lowered. For SO^+ this result is readily expected since neither the main formation nor destruction processes in the inner envelope involve water in this case (as discussed in Sect. 5.1). The marginal response of H_3O^+ to a decrease of $X(H_2O)$, which a priori seems less predictable than for SO^+, is a direct consequence of the enhanced production of HCO^+ in the inner envelope when $X(H_2O)$ is lowered. In the low-water case, because of the $X(HCO^+)$ increase, the dominant formation route of H_3O^+ in the inner envelope is by $HCO^+ + H_2O \rightarrow CO + H_3O^+$ (instead of water protonation by H_3^+). Therefore, the lower H_2O abundance is compensated by the higher abundance of HCO^+, which translates to an unaffected H_3O^+ abundance.

In the lobes (model *b*), lowering the initial H_2O abundance to $X(H_2O) = 3 \times 10^{-5}$ produces a different effect at different depths into the lobe walls for HCO^+, SO^+, and N_2H^+. In the outer edge of the walls, fully exposed to the ISM UV radiation field (A_V = 0 mag), the fractional abundances of these ions remain almost equal or slightly smaller than in the high water abundance case ($X(H_2O) = 3 \times 10^{-4}$), whereas in the shadowed ($A_V \sim 2.3$ mag) inner rim of the lobe walls the predicted abundances are higher, with the largest enhancements (of a factor ∼20−40) being for HCO^+ and N_2H^+. In the case of H_3O^+, a lower water abundance results in a lower abundance of this ion in all regions throughout the lobe walls; at the shadowed inner edge of the lobe walls only, both the high and low water abundance models predict a similar value of the H_3O^+ abundance of $X(H_3O^+) \sim 2 \times 10^{-9}$.

For all ions modeled, it appears that lowering the water abundance results in the maximum abundance zone moving deeper into the lobe walls. As seen above, another effect is an increase of $X(HCO^+)$ and $X(N_2H^+)$ in the lobes, however, the model predictions are still significantly lower (∼2 orders of magnitude) than the abundances observationally deduced. Moreover, the core-to-lobe abundance contrast for HCO^+ and SO^+ in the low water abundance case (∼60 and 20, respectively) is still irreconcilable with the broad profiles observed for these species. As in the high water abundance case, N_2H^+ is equally deficient in the core and in the lobes. In the case of H_3O^+, the core-to-lobe abundance ratio diminishes to ∼2−3 for a low H_2O abundance.

Finally, by pushing the water abundance to the low end of the range of observed values in O-rich stars, $X(H_2O) \approx 10^{-6}$, the abundances predicted by our chemistry model in all cases, except maybe for SO^+, become much smaller than the observed values both in the slow core component and in the fast lobes.

5.1.2. Enhanced elemental abundance of nitrogen

In this section we examine the behavior of the ions discussed here against an overabundance of the elemental nitrogen (up to

[7] For the sensitivity limit reached by our observations.

a factor ×40)[8] and whether such an N-enhancement can explain the large fractional abundance of N_2H^+ observed in OH 231.8. As in Velilla Prieto et al. (2015), we ran our chemistry code again modifying the initial abundances of those parent species that are most sensitive to the elemental abundance of nitrogen, namely, N_2, NH_3, and HCN: N_2 is increased by a factor 40 and NH_3 and HCN by a factor 7 relative to the values in Table 5. We find that the N_2H^+ peak abundance increases to $\sim 2 \times 10^{-10}$ in the slowing expanding shell and to $\sim 10^{-10}$ in the fast lobes. Therefore, despite the substantial N-enhancement, the model still predicts N_2H^+ to be underabundant (by one order of magnitude). Moreover, as in the case of a standard N abundance, the model fails to reproduce the enrichment of N_2H^+ in the fast lobes relative to the slow core deduced from the observations. This was, in fact, expected since changing the elemental abundance of nitrogen comparably affects both the fast and slow outflow components.

The elemental nitrogen enhancement has only a minor effect on the other ions discussed in this research, except for H_3O^+ and SO^+ but only in the deepest layers of the slow central component. In these inner regions, the abundances of H_3O^+ and SO^+ decrease (by a factor ∼6 and ∼10, respectively) as these ions are destroyed at larger rates through their interaction with more NH_3 molecules (Eq. (10)).

Given the set of chemical reactions involved in the production and destruction of HCO^+ and N_2H^+, the abundance ratio between these two ions provides an upper limit to the CO to N_2 abundance ratio. In OH 231.8, we deduce $X(HCO^+)/X(N_2H^+) \sim 6$ from the observations and, therefore, one could conclude that $[CO]/[N_2] \lesssim 6$. This value, which is slightly smaller than, but comparable to, the $[CO]/[N_2] = 7.5$ ratio in O-rich sources (adopted in our model, Table 5), does not rule out some N enrichment but it also does not clearly point to a significant nitrogen excess. Based on observations and modeling of the [N II]$\lambda\lambda$6548, 6584 Å emission (and other optical lines) from the shock-excited regions at the tips of the lobes of OH 231.8, Cohen et al. (1985) suggest that N may be overabundant in these regions by a factor ∼5 relative to the solar value. This factor is much smaller than that used here to test this effect (×40), and that has been proven to be unable to bring the model N_2H^+ abundance close enough to the observed value.

We also recall that an enhancement of the elemental nitrogen is not able to reproduce satisfactorily the observed abundances of HNCO, HNCS, HC_3N, and NO recently discovered in OH 231.8 (Velilla Prieto et al. 2015): on the one hand, HNCO, HNCS, and HC_3N would be underestimated and, on the other hand, NO (and maybe others, such as NH_3) would be significantly overestimated. Moreover, there are other N-bearing molecules that, in contrast to N_2H^+, are not particularly abundant in OH 231.8. One example is HCN: while the average abundance of this molecule in O-rich CSEs is relatively large $X(HCN) \approx 10^{-7}$ (Bujarrabal et al. 1994; Schöier et al. 2013), and actually larger than predicted by standard chemistry models (e.g., Nercessian et al. 1989), the value found in OH 231.8 is $X(HCN) \sim$ few $\times\ 10^{-8}$ (Sánchez Contreras et al. 1997, 2014).

In any case, an enhancement of the elemental N abundance would at most be able to reduce the model-data discrepancies for N-bearing species, but it is unlikely to help improve the model predictions for all the other molecules that are not chemical daughter products of N_2, such as the ions HCO^+, SO^+, and H_3O^+ reported in this work.

[8] Elemental N-enrichment can result from hot bottom burning (HBB) processes in the nucleus of $\gtrsim 3\ M_\odot$ stars.

6. Discussion and conclusions

Based on single-dish observations with the IRAM 30 m and *Herschel* telescopes, we have detected HCO^+, $H^{13}CO^+$, SO^+, N_2H^+, and (tentatively) H_3O^+ in OH 231.8. The broad line profiles (with FWHM of up to ∼90 km s^{-1}) and low-excitation temperature (∼10−20 K) deduced for HCO^+, $H^{13}CO^+$, SO^+, and N_2H^+, support the location of these ions preferentially in the base of the cold high-velocity lobes of OH 231.8. The fact that the narrow emission component from the massive central parts of the nebula (clump I3) is minimal in the profiles of these ions, clearly points to an abundance enhancement in the fast lobes relative to the slow core. Although uncertain, the much narrower profile (*FWHM* ∼ 14 km s^{-1}) and higher excitation conditions (≈100 K) suspected for H_3O^+ suggest a different spatial distribution for this ion, which may be more concentrated toward the central parts of the slow, central core.

Our chemical kinetics model predicts that HCO^+, SO^+, and H_3O^+ can form profusely (with peak abundances of $\approx 10^{-8}$) in the external layers of the slow central regions of OH 231.8 and thus, most generally, in similar O-rich CSEs. A moderate production of H_3O^+ (with fractional abundances of up to $\sim 10^{-9}$) is also expected in regions deeper into the envelope. The production of N_2H^+ is, however, rather inefficient, leading to very low fractional abundances of $X(N_2H^+) \lesssim 10^{-11}$.

In the fast lobes of OH 231.8, our standard chemistry model predicts relatively high abundances for SO^+ and H_3O^+ (of up to $\approx 10^{-9}$); however, we predict that HCO^+ and N_2H^+ are very scarce, with abundances of $\lesssim 10^{-10}$ and $\lesssim 10^{-12}$, respectively.

There are various observational results that our chemistry model fails to reproduce satisfactorily. In particular, the high HCO^+ and N_2H^+ abundances in the fast lobes deduced from the observed profiles. If these ions were present in the lobes in the low amounts predicted by the model, their emission would have remained undetected in our survey. Another model prediction that is inconsistent with the observations is that all ions should be more abundant in the slow core than in the fast lobes, however, the broad profiles of HCO^+, N_2H^+, and SO^+, reflect exactly the opposite. One of the most extreme cases is HCO^+, for which the model predicts a core-to-lobe abundance ratio of ∼500 versus the measured value of ∼1/3−1/4; the latter value is deduced from the broad, flattened profiles we report, and from accurate characterization of the HCO^+ spatio-kinematic distribution obtained from previous single-dish and interferometric mapping (Sect. 1).

Regarding H_3O^+, the model predicts a spatial distribution analogous to those of the other ions, i.e., peaking at the external layers of the slow central core due to photodissociation processes. This distribution is not easily reconcilable with the suspected origin for the H_3O^+ emission in the deep (slow and warm) regions of the central core. The model predicts a detectable amount of H_3O^+, of $\approx 10^{-9}$, in the fast lobes that is not consistent with our observations. The tentative H_3O^+ abundance distribution in OH 231.8 deduced from our observations needs, however, to be confirmed by higher quality data.

The large core-to-lobe abundance ratio of HCO^+, SO^+, and N_2H^+ predicted by the model can be reduced (but not suppressed) by adopting a lower initial H_2O abundance of 3×10^{-5} (instead of 3×10^{-4} used in our standard model). Also, lowering the water content injected to the intermediate/outer envelope would produce somewhat lower values of the peak abundances of H_3O^+, which is probably overabundant in the external envelope layers in our standard model.

We also find that an elemental nitrogen overabundance in OH 231.8 (by a factor of up to ∼40) is not able to produce

sufficient N_2H^+, which remains one order of magnitude less abundant than observed. We believe that the model's inability to explain the large abundance of N_2H^+ is not mainly a problem caused by an assumed nitrogen abundance that is too low. A similar problem also resides in NH_3 in the majority of O-rich CSEs, which contain ammonia in amounts that exceed predictions from conventional chemical models by many orders of magnitude (e.g., Menten et al. 2010; Menten & Alcolea 1995).

6.1. Molecule reformation after the passage of fast dissociative shocks?

Taking into consideration the various important model-data discrepancies deduced from our analysis, we must conclude that the standard molecular formation scenario adopted (triggered by ionization by UV photons and cosmic rays of gas whose initial state is predominantly molecular) is too simple and/or does not correctly depict the recent molecular formation history of OH 231.8. The adopted scenario, however, may represent the chemistry of most molecules in the intermediate/outer layers of normal AGB CSEs reasonably well (see, e.g., Nejad & Millar 1988; Glassgold 1996; Millar et al. 2000; Agúndez et al. 2008).

The notable chemical differences between OH 231.8 and most O-rich AGB CSEs are widely recognized and are not restricted to the ions discussed here but affect most of the species identified in this object (Sect. 1). Since the earliest studies on the molecular composition of OH 231.8, the remarkable molecular richness of this source has been related to shocks. Indeed, the main difference between OH 231.8 and "normal" O-rich AGB CSEs is the presence of a fast ($\sim$400 km s^{-1}) outflow in OH 231.8. If the acceleration of the bipolar lobes resulted from the violent collision between underlying fast jets on the pre-existing slow AGB wind, as proposed by many authors, then shocks *must* have necessarily played a major role in defining the current chemical composition of the outflow.

In particular, given the high velocities observed in the fast outflow of OH 231.8, it is unlikely that molecules survived this kind of acceleration process but rather they were probably dissociated. Molecules are indeed expected to be destroyed by shocks with speeds larger than $\gtrsim$50 km s^{-1} (e.g., Hollenbach & McKee 1980). After the shocked gas has cooled below $\sim 10^4$ K, atoms begin to associate and form molecules again; if the post-shock gas is moderately dense (e.g., $\approx 10^5$–10^6 cm^{-3}), molecule reformation can happen indeed rather quickly, within a few years from the shock (e.g., Glassgold et al. 1989, Neufeld & Dalgarno 1989). We believe that most molecules observed in the fast outflow of OH 231.8, if shock accelerated, must have dissociated and reformed in the post-shock gas. A similar scenario has been proposed to explain the chemistry in the high-velocity molecular outflow of the C-rich PPN CRL 618 (Neri et al. 1992).

At present, the shocks that accelerated the outflow $\sim$800 yr ago are not active, therefore, the bulk of the molecular outflow in OH 231.8 is probably swept-up AGB wind material that has cooled down sufficiently to allow molecule reformation. Note that the lobe axial acceleration took place in less than $\approx$150 yr, which may have been the duration of, e.g., a pulsed fast wind.

The physical properties (density and temperature) of the fast post-shock gas, which could have been fully dissociated and fully ionized $\sim$800 yr ago, must have evolved as a function of time. In particular, the temperature in the lobes has certainly decreased to its current value of $\sim$10–20 K. The assembly of new molecules would have happened progressively while the shock-heated material was cooling down. The ionized, atomic, and molecular fractions in the post-shock gas must have also evolved with time in a way that is not easy to predict, over the course of the cooling and molecular regeneration. (In particular, a transition from an H^+-dominated regime to an H_2-dominated regime, passing through an intermediate H-dominated phase, has probably happened.) Since these are the basic ingredients for putting together new molecules, their evolution with time must have dictated the set of chemical reactions that were dominant at each precise moment over the course of molecular regeneration leading to the final molecular content observed at present.

We increase the number of observational studies and chemistry modeling of molecular ions, which is needed to make progress in determining the role of ion-molecule reactions in the chemistry scheme of O-rich CSEs. Taking the presence of fast outflows and the probable shock-acceleration history of the envelope of OH 231.8 into account, the observations reported here may contribute to the emergence of an observational picture of the effects of shocks on the molecular chemistry of circumstellar envelopes. In the future, it would be desirable to attempt new chemical kinetics models adopting the molecule reformation scenario proposed here for OH 231.8. This is a difficult task since determining the time dependence of the relevant physical parameters of the cooling gas, where second-generation species have formed, is a challenging theoretical problem. Undoubtedly, it would also be advantageous to enlarge the reaction network used in most standard chemistry models by including additional chemical reactions that may affect the predicted abundances of certain species (e.g., grain-surface reactions, X-rays, etc.).

Acknowledgements. *Herschel* is an ESA space observatory with science instruments provided by European-led Principal Investigator consortia and with important participation from NASA. HIFI is the Herschel Heterodyne Instrument for the Far Infrared. HIFI has been designed and built by a consortium of institutes and university departments from across Europe, Canada and the United States under the leadership of SRON Netherlands Institute for Space Research, Groningen, The Netherlands and with major contributions from Germany, France and the US. Consortium members are: Canada: CSA, U. Waterloo; France: CESR, LAB, LERMA, IRAM; Germany: KOSMA, MPIfR, MPS; Ireland, NUI Maynooth; Italy: ASI, IFSI-INAF, Osservatorio Astrofisico di Arcetri- INAF; Netherlands: SRON, TUD; Poland: CAMK, CBK; Spain: Observatorio Astronómico Nacional (IGN), Centro de Astrobiología (CSIC-INTA); Sweden: Chalmers University of Technology – MC2, RSS & GARD; Onsala Space Observatory; Swedish National Space Board, Stockholm University – Stockholm Observatory; Switzerland: ETH Zurich, FHNW; USA: Caltech, JPL, NHSC. HCSS/HSpot/HIPE is a joint development by the *Herschel* Science Ground Segment Consortium, consisting of ESA, the NASA *Herschel* Science Center, and the HIFI, PACS and SPIRE consortia. This work has been partially supported by the Spanish MINECO through grants CSD2009-00038, AYA2009-07304, and AYA2012-32032. This research has made use of the SIMBAD database, operated at CDS, Strasbourg, France, the NASA's Astrophysics Data System, and Aladin.

References

Agúndez, M., & Cernicharo, J. 2006, ApJ, 650, 374
Agúndez, M., Cernicharo, J., & Guélin, M. 2007, ApJ, 662, L91
Agúndez, M., Fonfría, J. P., Cernicharo, J., Pardo, J. R., & Guélin, M. 2008, A&A, 479, 493
Agúndez, M., Cernicharo, J., Guélin, M., et al. 2010a, A&A, 517, L2
Agúndez, M., Cernicharo, J., & Guélin, M. 2010b, ApJ, 724, L133
Agúndez, M., Fonfría, J. P., Cernicharo, J., et al. 2012, A&A, 543, A48
Alcolea, J., Bujarrabal, V., Sánchez Contreras, C., Neri, R., & Zweigle, J. 2001, A&A, 373, 932
Aleman, I., Ueta, T., Ladjal, D., et al. 2014, A&A, 566, A79
Amano, T., Amano, T., & Warner, H. E. 1991, J. Mol. Spectr., 146, 519
Asplund, M., Grevesse, N., Sauval, A. J., & Scott, P. 2009, ARA&A, 47, 481
Balick, B., & Frank, A. 2002, ARA&A, 40, 439
Bohlin, R. C., Savage, B. D., & Drake, J. F. 1978, ApJ, 224, 132
Bowers, P. F., & Morris, M. 1984, ApJ, 276, 646
Bujarrabal, V., Gomez-Gonzalez, J., Bachiller, R., & Martin-Pintado, J. 1988, A&A, 204, 242
Bujarrabal, V., Fuente, A., & Omont, A. 1994, A&A, 285, 247

Bujarrabal, V., Castro-Carrizo, A., Alcolea, J., & Sánchez Contreras, C. 2001, A&A, 377, 868
Bujarrabal, V., Alcolea, J., Sánchez Contreras, C., & Sahai, R. 2002, A&A, 389, 271
Carter, M., Lazareff, B., Maier, D., et al. 2012, A&A, 538, A89
Castro-Carrizo, A., Quintana-Lacaci, G., Neri, R., et al. 2010, A&A, 523, A59
Cernicharo, J. 2012, EAS Publ. Ser., 58, 251
Cernicharo, J., Liu, X.-W., González-Alfonso, E., et al. 1997, ApJ, 483, L65
Cernicharo, J., Guélin, M., Agúndez, M., et al. 2007, A&A, 467, L37
Cernicharo, J., Waters, L. B. F. M., Decin, L., et al. 2010, A&A, 521, L8
Cernicharo, J., Daniel, F., Castro-Carrizo, A., et al. 2013, ApJ, 778, L25
Choi, Y. K., Brunthaler, A., Menten, K. M., & Reid, M. J. 2012, IAU Symp., 287, 407
Cohen, M. 1981, PASP, 93, 288
Cohen, M., Dopita, M. A., Schwartz, R. D., & Tielens, A. G. G. M. 1985, ApJ, 297, 702
Dalgarno, A. 2006, Proc. Nat. Acad. Sci., 103, 12269
Daniel, F., Dubernet, M.-L., Meuwly, M., Cernicharo, J., & Pagani, L. 2005, MNRAS, 363,1083
Desmurs, J.-F., Alcolea, J., Bujarrabal, V., Sánchez Contreras, C., & Colomer, F. 2007, A&A, 468, 189
Draine, B. T., & Salpeter, E. E. 1978, Nature, 271, 730
Etxaluze, M., Cernicharo, J., Goicoechea, J. R., et al. 2014, A&A, 566, A78
Feast, M. W., Catchpole, R. M., Whitelock, P. A., et al. 1983, MNRAS, 203, 1207
Flower, D. R. 1999, MNRAS, 305, 651
de Graauw, T., Helmich, F. P., Phillips, T. G., et al. 2010, A&A, 518, L6
Glassgold, A. E. 1996, ARA&A, 34, 241
Glassgold, A. E., Mamon, G. A., & Huggins, P. J. 1989, ApJ, 336, L29
Goicoechea, J. R., & Cernicharo, J. 2001, ApJ, 554, L213
Goldsmith, P. F., & Langer, W. D. 1999, ApJ, 517, 209
González Delgado, D., Olofsson, H., Kerschbaum, F., et al. 2003, A&A, 411, 123
Guilloteau, S., Lucas, R., Omont, A., & Nguyen-Q-Rieu 1986, A&A, 165, L1
Habing, H. J. 1968, Bull. Astron. Inst. Netherlands, 19, 421
Hasegawa, T. I., & Kwok, S. 2001, ApJ, 562, 824
Hollenbach, D., & McKee, C. F. 1980, ApJ, 241, L47
Jura, M., & Morris, M. 1985, ApJ, 292, 487
Kastner, J. H., & Weintraub, D. A. 1995, AJ, 109, 1211
Kastner, J. H., Weintraub, D. A., Zuckerman, B., et al. 1992, ApJ, 398, 552
Knapp, G. R. 1985, ApJ, 293, 273
Kozlov, M. G., & Levshakov, S. A. 2011, ApJ, 726, 65
Kramer, C. 1997, Calibration of spectral line data at the IRAM 30 m radio telescope, IRAM report
Maercker, M., Schöier, F. L., Olofsson, H., Bergman, P., & Ramstedt, S. 2008, A&A, 479, 779
Mamon, G. A., Glassgold, A. E., & Omont, A. 1987, ApJ, 323, 306
McCarthy, M. C., Gottlieb, C. A., Gupta, H., & Thaddeus, P. 2006, ApJ, 652, L141
Menten, K. M., & Alcolea, J. 1995, ApJ, 448, 416
Menten, K. M., Wyrowski, F., Alcolea, J., et al. 2010, A&A, 521, L7
Milam, S. N., Woolf, N. J., & Ziurys, L. M. 2009, ApJ, 690, 837
Millar, T. J., Herbst, E., & Bettens, R. P. A. 2000, MNRAS, 316, 195
Morris, M., Bowers, P. F., & Turner, B. E. 1982, ApJ, 259, 625
Morris, M., Guilloteau, S., Lucas, R., & Omont, A. 1987, ApJ, 321, 888
Müller, H. S. P., Schlöder, F., Stutzki, J., & Winnewisser, G. 2005, J. Mol. Struct., 742, 215
Nejad, L. A. M., & Millar, T. J. 1988, MNRAS, 230, 79
Nercessian, E., Omont, A., Benayoun, J. J., & Guilloteau, S. 1989, A&A, 210, 225
Neri, R., Garcia-Burillo, S., Guelin, M., et al. 1992, A&A, 262, 544
Neri, R., Kahane, C., Lucas, R., Bujarrabal, V., & Loup, C. 1998, A&AS, 130, 1
Neufeld, D. A., & Dalgarno, A. 1989, ApJ, 340, 869
Ott, S. 2010, Astronomical Data Analysis Software and Systems XIX, 434, 139
Pardo, J. R., Cernicharo, J., Goicoechea, J. R., Guélin, M., & Asensio Ramos, A. 2007, ApJ, 661, 250
Phillips, T. G., van Dishoeck, E. F., & Keene, J. 1992, ApJ, 399, 533
Pickett, H. M., Poynter, R. L., Cohen, E. A., et al. 1998, J. Quant. Spectr. Rad. Transf., 60, 883
Pilbratt, G. L., Riedinger, J. R., Passvogel, T., et al. 2010, A&A, 518, L1
Pulliam, R. L., Edwards, J. L., & Ziurys, L. M. 2011, ApJ, 743, 36
Quintana-Lacaci, G., Agúndez, M., Cernicharo, J., et al. 2013, A&A, 560, L2
Ramstedt, S., & Olofsson, H. 2014, A&A, 566, A145
Roelfsema, P. R., Helmich, F. P., Teyssier, D., et al. 2012, A&A, 537, A17
Sabin, L., Zhang, Q., Zijlstra, A. A., et al. 2014, MNRAS, 438, 1794
Sahai, R., & Trauger, J. T. 1998, AJ, 116, 1357
Sánchez Contreras, C., & Sahai, R. 2012, ApJS, 203, 16
Sánchez Contreras, C., Bujarrabal, V., & Alcolea, J. 1997, A&A, 327, 689
Sánchez Contreras, C., Alcolea, J., Bujarrabal, V., & Neri, R. 1998, A&A, 337, 233
Sánchez Contreras, C., Bujarrabal, V., Neri, R., & Alcolea, J. 2000, A&A, 357, 651
Sánchez Contreras, C., Desmurs, J. F., Bujarrabal, V., Alcolea, J., & Colomer, F. 2002, A&A, 385, L1
Sánchez Contreras, C., Gil de Paz, A., & Sahai, R. 2004, ApJ, 616, 519
Sánchez Contreras, C., Velilla Prieto, L., Cernicharo, J., et al. 2011, IAU Symp., 280, 327
Sánchez Contreras, C., Velilla, L., Alcolea, J., et al. 2014, Asymmetrical Planetary Nebulae VI conference, Proc. Conf. held 4–8 November, 2013, eds. C. Morisset, G. Delgado-Inglada, S. Torres-Peimbert, 88, http://www.astroscu.unam.mx/apn6/PROCEEDINGS/
Sandford, S. A. 2011, in The Molecular Universe, eds. J. Cernicharo, & R. Bachiller, Proc. IAU Symp., 280, 275
Schöier, F. L., Bast, J., Olofsson, H., & Lindqvist, M. 2007, A&A, 473, 871
Schöier, F. L., Ramstedt, S., Olofsson, H., et al. 2013, A&A, 550, A78
Soker, N., & Kashi, A. 2012, ApJ, 746, 100
Teyssier, D., Hernandez, R., Bujarrabal, V., Yoshida, H., & Phillips, T. G. 2006, A&A, 450, 167
Tsuji, T., Ohnaka, K., Aoki, W., & Yamamura, I. 1997, A&A, 320, L1
Velilla Prieto, L., Sánchez Contreras, C., Cernicharo, J., et al. 2013, Highlights Spanish Astrophys. VII, 676
Velilla Prieto, L., Sánchez Contreras, C., Cernicharo, et al. 2015, A&A, 575, A84
Wootten, A., Mangum, J. G., Turner, B. E., et al. 1991, ApJ, 380, L79
Zhang, Y., Kwok, S., & Dinh-V-Trung 2008, ApJ, 678, 328
Zijlstra, A. A., Chapman, J. M., te Lintel Hekkert, P., et al. 2001, MNRAS, 322, 280
Ziurys, L. M., Milam, S. N., Apponi, A. J., & Woolf, N. J. 2007, Nature, 447, 1094

Pages 20 to 22 are available in the electronic edition of the journal at http://www.aanda.org

Table A.1. Adopted values for HPBW, η_{mb}, and Ruze-like scaling factors $\eta_{mb,0}$ and σ_{mb} (see Eq. (2) in Sect. 2.2) for one spot frequency per mixer and per polarizations (H and V) of the HIFI instrument.

Mixer	f (GHz)	*HPBW* ($''$)	η_{mb}	$\eta_{mb,0}$	σ_{mb} (μm)
1H	480	43.1	0.62	0.624 ± 0.007	2.278 ± 0.004
1V	480	43.5	0.62	0.618 ± 0.007	2.248 ± 0.004
2H	640	32.9	0.64	0.643 ± 0.009	2.219 ± 0.003
2V	640	32.8	0.66	0.662 ± 0.009	2.224 ± 0.002
3H	800	26.3	0.62	0.626 ± 0.008	2.227 ± 0.004
3V	800	25.8	0.63	0.639 ± 0.008	2.287 ± 0.010
4H	960	21.9	0.63	0.639 ± 0.008	2.227 ± 0.004
4V	960	21.7	0.64	0.643 ± 0.008	2.252 ± 0.006
5H	1120	19.6	0.59	0.595 ± 0.006	2.068 ± 0.005
5V	1120	19.4	0.59	0.597 ± 0.006	2.114 ± 0.005

Notes. Adapted from Tables 2 and 3 of Mueller et al. (2014).

Appendix A: The HIFI beam pattern

The HIFI beam pattern (size, efficiency, etc.) is described by Roelfsema et al. (2012). In October 2014, a release note was issued by the HIFI calibration team (Mueller et al. 2014[9]) reporting improved measures of the half-power beam width (HPBW) and main-beam efficiency (η_{mb}) that supersede previous estimates in Roelfsema et al. (2012). The new efficiency estimates are systematically lower than previous values by typically 15−20% for η_{mb}.

For convenience, we reproduce again in this appendix the updated values of the relevant beam-model parameters provided by Mueller et al. (2014) in Tables 2 and 3 of their release note. These values, given in Table A.1, are used to obtain the formulae (Eq. (2) in Sect. 2.2) that describe the frequency/wavelength dependence of HPBW and η_{eff} for the HIFI bands (1 through 5) used in this work. Since we average the H and V polarization data to obtain final spectra, we use the average of η_{mb} for H and V at a given frequency in order to convert antenna temperatures (T_A^*) to a main-beam scale (T_{MB}) at that frequency. We recall that, as stated in Sect. 2:

$$T_{MB} = T_A^* / \eta_{eff} = T_A^* \frac{\eta_l}{\eta_{mb}}.$$

Appendix B: Additional material

In this Appendix, we include additional material for the ion SO^+ and the molecule ^{13}CO in OH 231.8.

In Fig. B.1, we show all the SO^+ transitions (detected and nondetected) observed within the frequency range covered in our survey with the IRAM 30 m telescope. Some of the SO^+ lines are blended with transitions of other molecules and/or are in particularly noisy regions and have not been considered for the rotational diagram analysis presented in Sect. 4.1.

A total of nine ^{13}CO transitions have been detected in OH 231.8 from our surveys with IRAM 30 m and *Herschel* (Fig. B.2 and Table B.1). The ^{13}CO lines, which are good tracers of the density and kinematics of the nebula, show structured

Table B.1. Same as Table 1 except for ^{13}CO lines observed with IRAM 30 m and *Herschel*.

Rest Freq. (MHz)	Transition QNs	E_u (K)	A_{ul} (s^{-1})	$\int T_A^* d\upsilon$ (K km s^{-1})
^{13}CO	μ = 0.11 Debyes			
110 201.4	1−0	5.3	6.336E-08	13.45 (0.06)
220 398.7	2−1	15.9	6.082E-07	51.50 (0.13)
330 588.0	3−2	31.7	2.199E-06	42.00 (0.30)
550 926.3	5−4	79.3	1.079E-05	3.33 (0.07)
661 067.3	6−5	111.1	1.894E-05	3.03 (0.09)
771 184.1	7−6	148.1	3.040E-05	2.30 (0.13)
881 272.8	8−7	190.4	4.574E-05	2.00 (0.15)
991 329.3	9−8	237.9	6.554E-05	0.65 (0.15)
1 101 349.6	10−9	290.8	9.034E-05	0.70 (0.15)

profiles with two main components: (1) a prominent, relatively narrow core (centered around the systemic velocity of the source, $V_{sys}^{LSR} \sim 33-34$ km s^{-1}) plus weaker, broad wings. The line core arises at the slow, dense central (low-latitude) parts of the nebula, which expand at relatively low velocities of ∼10−35 km s^{-1} (clump I3), whereas the wing emission mainly arises at the fast, bipolar lobes (see Sect. 1 and Fig. 1). (As explained in the Introduction, the spatio-kinematic structure of the molecular outflow of OH 231.8 is well known from previous single-dish and interferemtric maps of ^{12}CO). The large core-to-wing intensity ratio of the ^{13}CO profiles is consistent with most (∼70%) of the mass in the molecular outflow being in the slow central regions (Sánchez Contreras et al. 1997; Alcolea et al. 2001).

The ^{13}CO wing emission progressively weakens, relative to the core, at higher frequencies. For transitions observed with the same telescope (i.e., for the three $J_u \leq 3$ lines observed with IRAM 30 m or for the six $J_u \geq 5$ lines observed with *Herschel*), this trend is partially explained by the smaller beam and, thus, the smaller fraction of the fast outflow sampled by the observations at higher frequencies. However, this is not the only reason, since at all frequencies the *Herschel* beam is comparable to, or larger than, the IRAM 30 m beam, with a maximum size of *HPBW* = 22.″1 at 110 GHz for the observations reported here.

Both the full width of the wings and the full width at half maximum of the ^{13}CO profiles decrease as the upper energy level increases. The full width of the wings is largest for the ^{13}CO (J = 1−0) transition, which is observed over a velocity range of V_{LSR} = [−80:+140] km s^{-1} with a beam *HPBW* = 22.1″, and decreases for higher-J transitions down to V_{LSR} = [+15:+55] km s^{-1} for the J = 7−6 line, observed with a comparable beam of *HPBW* = 27.6″; for transitions with $J > 7$, we do not detect wing emission. The FWHM of the ^{13}CO lines ranges between ∼36 to ∼14 km s^{-1} for the J = 1−0 and the 10−9 transitions, respectively. An analogous behavior is observed in most molecules observed in our surveys with IRAM 30 m and *Herschel*, including ^{12}CO (Sánchez Contreras et al. 2014; Sánchez Conteras et al., in prep.). The observed trend suggests that the envelope layers with higher excitation conditions (i.e., warmer and, thus, presumably closer to the central star) are characterized by lower expansion velocities.

[9] The HIFI Beam: Release #1. Release Note for Astronomers, http://herschel.esac.esa.int/twiki/bin/view/Public/Hifi\discretionary-CalibrationWeb#HIFI_performance_and_calibration

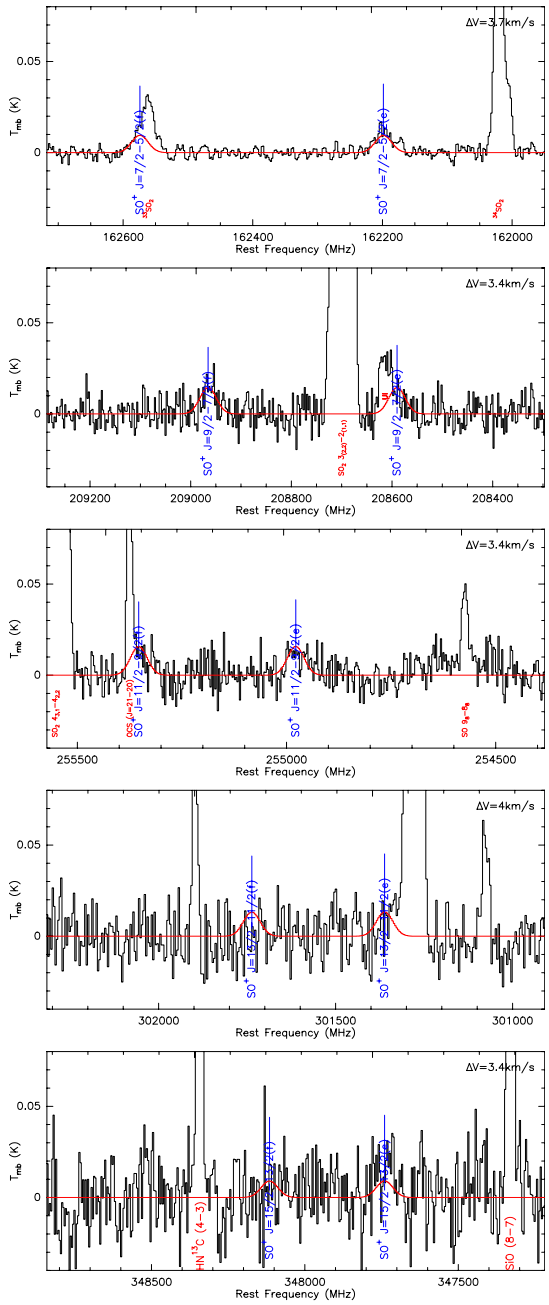

Fig. B.1. IRAM 30 m spectra toward OH 231.8 near the five mm-wave doublets of SO^+ (see Table 1). An LTE model compatible with values in Table 2 and adopting an average *FWHM* = 55 km s^{-1} for the lines is overplot (red line).

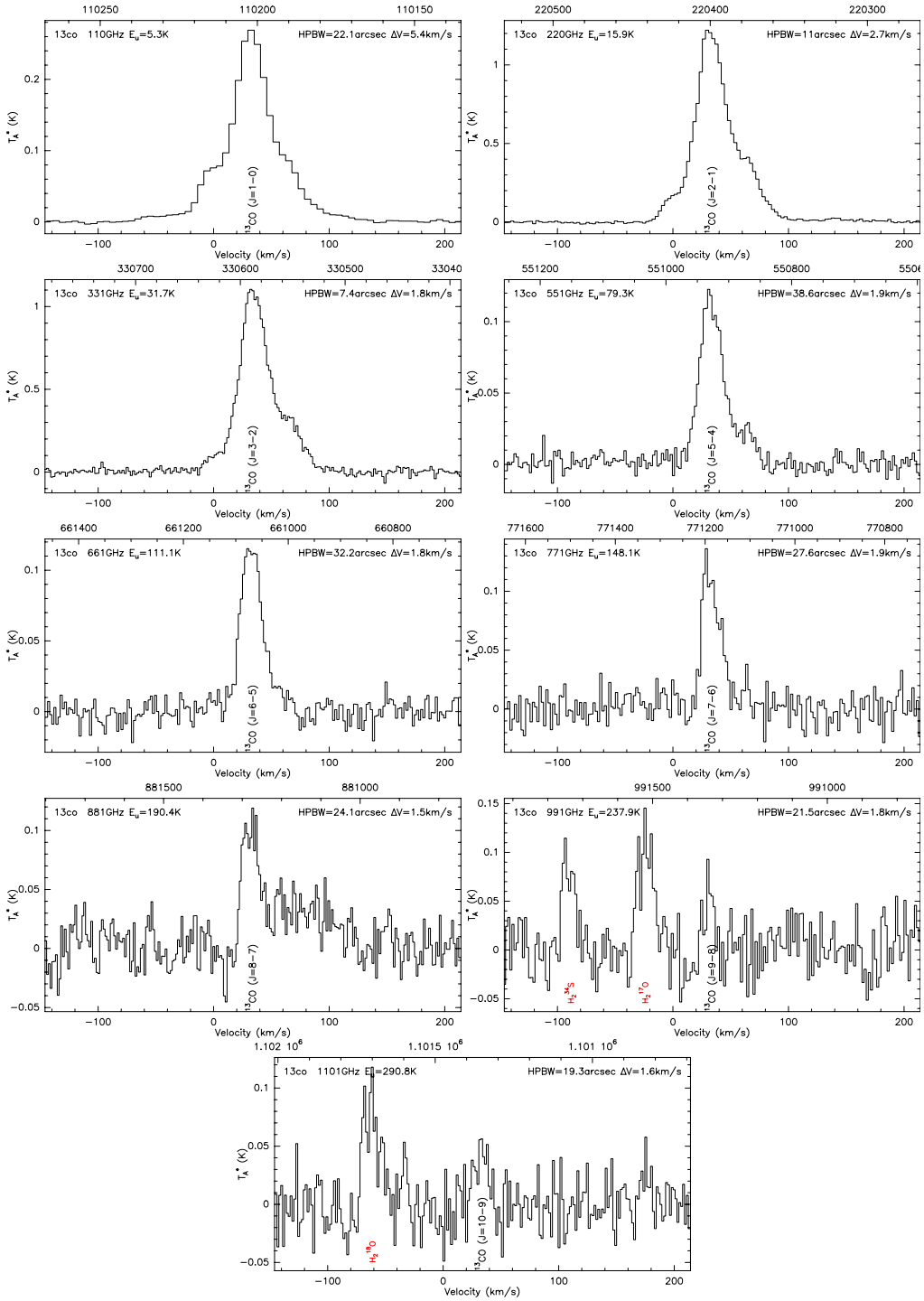

Fig. B.2. ^{13}CO transitions detected in OH 231.8+4.2 with IRAM 30 m and *Herschel*. The red broad shoulder observed in the ^{13}CO (J = 8−7) line is probably an artificial feature due to residual baseline distorsion.

CHAPTER

6

SI-BEARING MOLECULES TOWARD IRC+10216

In this chapter the first sub-arcsecond spatial resolution ALMA maps of several Si-bearing molecules toward IRC+10216 are presented. Si-bearing molecules are closely related to the formation and growth of dust grains in circumstellar envelopes, and particularly, Si-C bond bearing molecules in carbon rich envelopes. IRC+10216 is considered as the referent object for C-rich objects and the most studied envelope. Hence, IRC+10216 is an excellent target for these ALMA studies. This work has been published in Velilla Prieto et al. (2015b).

6.1 Summary

SiO, SiS, and SiC_2 molecules are efficiently formed in the inner regions of C-rich CSEs (Tsuji, 1973). Then, in the dust growth region, which extends up to a few stellar radii ($\lesssim 20 R_*$), these molecules are likely to condense onto dust grains owing to the temperatures and the refractory nature of these species, thus, their gas phase abundance is expected to decrease. Previous observations toward IRC+10216, and chemical models predictions seem to be consistent with this scenario (Olofsson et al., 1982, Lucas et al., 1995, Schöier et al., 2006, Agúndez et al., 2012, Fonfría et al., 2014). The maps obtained by Lucas et al. (1995), Schöier et al. (2006) and Fonfría et al. (2014), show the brightness distribution of several emission lines of SiO, SiS and SiC_2, which display spherically symmetric distributions centred at the source, and with different sizes, with diameters of $\sim 6''$[1] for the SiO J=5–4 (v=0) line, or $\sim 2''$ for SiS J=14–13 (v=0) line. Additionally, SiC_2 emission can be seen in the innermost regions of the CSE,and also in an outer hollow spherical shell at a distance of $\sim 15''$ from the star. The formation mechanism that explains the outermost shell of SiC_2 was proposed by Cernicharo et al. (2010), where the authors propose that SiC_2 is efficiently formed through the reaction between Si and C_2H_2.

In this paper, we present the first observations obtained with the ALMA interferometer during its Cycle 0, which represent the first subarcsecond spatial resolution maps for several lines toward the reference object IRC+10216. IRC+10216 is the most studied C-rich CSE, where ∼80 different molecules have been detected (see Sect. 1.4.1.3). We detected lines of SiS J=15–14 in the ground vibrational state up to v=7 (and tentatively up to v=10), ^{29}SiS (up to v=5) lines, ^{30}SiS (up to v=4) lines, Si^{33}S (up to v=3), Si^{34}S (up to v=4), ^{29}Si^{33}S (in the ground vibrational level), and ^{29}Si^{34}S (in the ground vibrational level). Also, we detected SiO J=6–5 lines up to the excited vibrational level v=2, the J=6–5 v=0 ^{29}SiO line, and several lines in the ground vibrational level of SiC_2.

[1] At the distance of IRC+10216 (∼130 pc) $1''$ corresponds to $\sim 1.9\times10^{15}$ cm.

➢ We have done the following analysis:

- study of the observed brightness distributions,
- analysis of the variation of the SiS linewidths as a function of the upper energy level, for all the detected isotopologues and vibrationally excited levels,
- vibrational diagram (which is equivalent to the rotational diagram described in Sect. 2.1 applied to the lines with equal J but different v) of the detected lines of SiS (its main isotopologue), in order to determine the excitation conditions and the column density of the molecule,
- radiative transfer analysis under the LVG approximation and considering a multishell structure of the CSE, to model the SiS (its main isotopologue) emission (see Sect. B.2.1) using MADEX (Sect. 2.2). For this model we included energy levels up to v=12, thus, we computed the spectroscopy and the vibrational dipole moment of this molecule.

➢ From the analysis we derive the following main results:

- we obtained the first high-resolution maps ($\sim$0.″6, which corresponds to a size of $\sim10^{15}$ cm or $\sim40R_*$) with ALMA, of several emission lines of SiO, SiS, and SiC_2 toward the CSE of IRC+10216. The SiC_2 $J_{K_a,K_c}=11_{6,6}$–$10_{6,5}$ line displays a central component with a size of $\sim4''$ elongated in the NE-SW direction, as well as a spherical shell-like component surrounding the star at a distance of $\sim11''$, which corresponds to $\sim2\times10^{16}$ cm. The ^{29}SiO J=6–5 line shows a clumpy extended component with a size of $\sim6''$ and also an elongation along the NE-SW direction. The SiS J=15–14 lines of the vibrational states v=0 up to the v=7 display a very compact distribution,
- the lines of the different SiS isotopologues display a decrease of their linewidths as a function of the upper energy level (e.g. v=2 line is narrower than v=1 and so on),
- two different trends can be seen in the vibrational diagram of SiS: *i*) one trend for the lines with $v \leq 2$, which indicates a vibrational temperature of $\sim$500 K, and, *ii*) a second trend for the lines with $v > 2$, which indicates a temperature of $\sim$1700 K. The column densities derived are $\sim1\times10^{18}$ cm^{-2} for the $v \leq 2$ fit, and one order of magnitude lower for the fit of the $v > 2$ lines,
- the LVG model predicts temperatures similar to those we derive from observations. For the column densities we obtain moderate discrepancies between the model and the vibrational diagram, i.e. the LVG model underestimates the column density by a factor $\sim$2,
- no SiC lines (in the ground vibrational state) lie in the frequency range covered by these observations. Nevertheless, we did detect emission of neither SiC v=1 nor ^{29}SiC v=1 (several lines of these species lie in the frequency range observed), thus, we were able to derive an upper limit of the column density of SiC $\lesssim4\times10^{14}$ cm^{-2}.

➢ After the analysis, we conclude that:

- the brightness distribution observed for the vibrationally excited lines of SiS is compatible with emission arising from the innermost regions of the CSE. The brightness distribution observed for SiC_2 can be interpreted as the SiC_2 is formed in regions close to the star ($r<20R_*$), then it condenses onto the dust grains, and eventually it reappears at the outer shells of the

CSE (r∼1000R_*), as a hollow shell, as the consequence of the interaction between the UV Galactic radiation field and the CSE. The elongation seen in the distributions of SiC_2 and ^{29}SiO may indicate the presence of a bipolar outflow as a consequence of a binary companion (Cernicharo et al., 2015a),

- vibrationally excited SiS linewidths, together with the excitation temperatures derived from the vibrational diagram, indicates that the SiS emission arises from the innermost regions of the CSE (<20R_*), which is also consistent to the expansion velocities derived from the linewidths compared to the terminal expansion velocity of the gas. Moreover, the analysis indicates that the emission of high vibrationally excited lines arises from inner and hotter regions than the emission of low excited lines, i.e. the closer to the star the lower the expansion velocity (and also the higher temperature). Hence, those lines involving higher vibrational states are narrower,

- differences between the radiative transfer model and the vibrational diagram, can be explained as a result of the optical depth of the observed lines (mainly for the lowest vibrationally excited levels), and the maser nature of the SiS J=15–14 v=0 line,

- SiC_2 is the main gas phase carrier of Si-C bond in the dust formation region of IRC+10216, which is consistent with SiC as one of the main building blocks of dust grains in C-rich stars.

6.2 Resumen

Las moléculas SiO, SiS y SiC_2, se forman de manera eficiente en las regiones más internas de las envolturas circunestelares ricas en carbono (Tsuji, 1973). Tras su formación, estas moléculas parecen incorporarse en los granos de polvo en la zona donde crecen estos granos ($\lesssim 20 R_*$) debido a las temperaturas que experimentan y su carácter refractario, por lo que sus abundancias en fase gas tienden a disminuir. Las observaciones realizadas previamente en IRC+10216, así como las predicciones de los modelos químicos parecen apoyar este escenario (Olofsson et al., 1982, Lucas et al., 1995, Schöier et al., 2006, Agúndez et al., 2012, Fonfría et al., 2014). Los mapas obtenidos por Lucas et al. (1995), Schöier et al. (2006) y Fonfría et al. (2014), muestran las distribuciones de brillo de diversas líneas de emisión de SiO, SiS y SiC_2, que se observan como distribuciones con simetría esférica, centradas en la fuente, y con distinto tamaño, con un diámetro de $\sim 6''$ para la línea SiO J=5–4 (v=0), o un diámetro de $\sim 2''$ para la línea SiS J=14–13 (v=0). Adicionalmente, se observa que el SiC_2 además de una componente compacta central, muestra una capa esférica externa a una distancia de $\sim 15''$ de la estrella, cuyo mecanismo de formación ha sido explicado por Cernicharo et al. (2010) como el producto de la reacción del Si con la molécula C_2H_2.

En este trabajo, se presentan las primeras observaciones obtenidas con el interferómetro ALMA durante el Ciclo 0, y que suponen los primeros mapas de resolución espacial inferior al segundo de arco del objeto de referencia IRC+10216 para alguna de las líneas detectadas. IRC+10216 es la envoltura circunestelar más estudiada, es rica en carbono y en ella se han detectado aproximadamente unas 80 moléculas (ver Sec. 1.4.1.3). Se presenta la detección de las líneas de SiS J=15–14 desde el nivel v=0 hasta el nivel vibracional excitado v=7 (y tentativamente hasta el v=10), así como otros de sus isotopólogos ^{29}SiS (hasta v=5), ^{30}SiS (hasta v=4), Si^{33}S (hasta v=3), Si^{34}S (hasta v=4), ^{29}Si^{33}S (en el nivel vibracional fundamental), y ^{29}Si^{34}S (en el nivel vibracional fundamental). Detectamos además las líneas de SiO J=6–5 hasta el nivel vibracional excitado v=2, la línea J=6–5 en el nivel vibracional fundamental de ^{29}SiO y varias líneas en el nivel vibracional fundamental de SiC_2.

➢ El análisis realizado consta de:

- el estudio de las distribuciones de brillo observadas,
- estudio de la variación de las anchuras de las líneas detectadas de los distintos isotopólogos de SiS, en función de la energía del nivel superior para los distintos niveles vibracionales,
- ajuste del diagrama de vibración (equivalente al diagrama de poblaciones rotacionales que se describe en la Sec. 2.1, aplicado a las líneas de igual J pero distinto v) de las líneas del isotopólogo principal del SiS hasta la línea v=7 (al considerar las líneas con v >7 como tentativas) para determinar las condiciones de excitación y la densidad de columna de la molécula,
- aplicación de modelo de transferencia radiativa en aproximación LVG y multicapa (Sec. B.2.1) para estudiar la emisión del isotopólogo principal de SiS usando MADEX (Sec. 2.2). Para este análisis se ha estimado el momento dipolar vibracional y la espectroscopía (energías de los niveles, frecuencia de las transiciones...) de la molécula (incluyendo transiciones ro-vibracionales) hasta el nivel v=12.

➢ Del análisis realizado, se obtienen los siguientes resultados principales:

- obtención de los primeros mapas de alta resolución ($\sim$0.6″, que correspondería a un tamaño de $\sim10^{15}$ cm o $\sim40R_*$) con ALMA, de la emisión de varias líneas de las moléculas SiO, SiS y SiC_2, en la envoltura circunestelar de IRC+10216. La línea de SiC_2 J_{K_a,K_c}=$11_{6,6}$–$10_{6,5}$ muestra una componente central con un tamaño de $\sim$4″ elongada en la dirección Noreste–Sudoeste, además de una componente de tipo capa esférica hueca que rodea a la estrella a una distancia de $\sim$11″, que correspondería a $\sim2\times10^{16}$ cm. En el caso de la línea de ^{29}SiO J=6–5, se observa una componente extendida y grumosa con un tamaño de $\sim$6″ y se observa también una elongación en la dirección Noreste–Sudoeste. Las líneas de SiS J=15–14 desde v=0 hasta v=7, muestran una distribución muy compacta centrada en la estrella,

- las líneas de los distintos isotopólogos de SiS muestran una tendencia a disminuir su anchura conforme incrementamos la energía del nivel considerado,

- el diagrama vibracional muestra dos tendencias distintas: *i*) para las líneas de $v \leq2$, el ajuste indica una temperatura de vibración (o de excitación) de $\sim$500 K, y *ii*) las líneas de $v >2$ se ajustan a una temperatura de $\sim$1700 K. Las densidades de columna que se obtienen son de $\sim1\times10^{18}$ cm^{-2} para las líneas de $v \leq2$, y un orden de magnitud menor para el ajuste de las líneas con $v >2$,

- el modelo LVG predice temperaturas de excitación parecidas a las que derivamos de las observaciones, mientras que para las densidades de columna obtenemos discrepancias moderadas, siendo la densidad del modelo un factor $\sim$2 más baja comparada con la obtenida del diagrama,

- nuestras observaciones no cubrieron un rango en frecuencia que permitiera observar alguna línea de SiC en el nivel vibracional fundamental, no obstante, si cubríamos varias líneas del estado v=1 de SiC y ^{29}SiC de las cuales no registramos emisión en el espectro de IRC+10216, estableciendo un límite superior para la densidad de columna de SiC de $\lesssim4\times10^{14}$ cm^{-2}.

➢ De la interpretación de los resultados, concluimos que:

- la distribución de brillo observada para las líneas vibracionalmente excitadas de SiS es compatible con emisión que emerge de las zonas más internas de la envoltura. La distribución espacial observada para SiC_2 es compatible con que esta molécula se forme en las zonas más internas de la envoltura (r<$20R_*$), luego se incorporaría en los granos de polvo, hasta que finalmente reaparece en fase gas en las zonas más externas de la envoltura ($r\sim1000R_*$) como consecuencia de la interacción de la envoltura con el UV ISRF. La elongación que se observa para el caso de las componentes centrales de SiC_2 y ^{29}SiO podría indicar la presencia de un flujo de material bipolar como consecuencia de la presencia de una estrella compañera (Cernicharo et al., 2015a),

- las anchuras de las líneas, junto con las temperaturas de excitación derivadas del diagrama vibracional, parecen indicar que provienen de una región interna de la envoltura circunestelar ($<20R_*$) dado que no alcanzan la velocidad terminal de expansión (FWHM$< v_\infty$), y además es compatible con que las líneas de más alta excitación se formen en regiones más internas (y calientes) que aquellas de más baja excitación (v bajo), ya que las de alto v requieren mayor energía (temperatura) para excitarse, y la velocidad de expansión será menor (líneas más estrechas) cuanto más cerca de la estrella se encuentre el gas,

- las diferencias entre el modelo LVG y el diagrama vibracional, pueden explicarse como resultado de la profundidad óptica de las líneas observadas, sobre todo para aquellas de baja excitación (v bajo), y dada la naturaleza máser de la línea J=15–14 v=0 de SiS,

- SiC_2 es la molécula portadora de enlaces Si-C más abundante (en fase gas) en la región de formación de polvo de IRC+10216, lo que es compatible con que el SiC sea uno de los principales componentes en fase sólida de los granos de polvo en las estrellas ricas en carbono.

6.3 Velilla Prieto et al. 2015b[2]

The Astrophysical Journal Letters, 805:L13 (7pp), 2015 June 1 doi:10.1088/2041-8205/805/2/L13
© 2015. The American Astronomical Society. All rights reserved.

Si-BEARING MOLECULES TOWARD IRC+10216: ALMA UNVEILS THE MOLECULAR ENVELOPE OF CWLeo

L. Velilla Prieto[1,2], J. Cernicharo[1], G. Quintana-Lacaci[1], M. Agúndez[1], A. Castro-Carrizo[3], J. P. Fonfría[4], N. Marcelino[5], J. Zúñiga[6], A. Requena[6], A. Bastida[6], F. Lique[7], and M. Guélin[3,8]
[1] Group of Molecular Astrophysics, ICMM, CSIC, C/ Sor Juana Inés de la Cruz 3, E-28049 Cantoblanco, Madrid, Spain
[2] Centro de Astrobiología, INTA–CSIC, E-28691 Villanueva de la Cañada, Madrid, Spain
[3] Institut de Radioastronomie Millimétrique, 300 rue de la la Piscine, F-38406 Saint Martin d'Hères, France
[4] Departamento de Estrellas y Medio Interestelar, Instituto de Astronomía, Universidad Nacional Autónoma de México (UNAM), Ciudad Universitaria, 04510, Mexico City, México
[5] Istituto di Radiastronomia, INAF–CNR, via Gobetti 101, I-40129 Bologna, Italy
[6] Departamento de Química Física, Facultad de Química, Universidad de Murcia, Campus Espinardo, E-30100 Murcia, Spain
[7] LOMC–UMR 6294, CNRS–Université du Havre, 25 rue Philippe Lebon, BP 1123, F-76063 Le Havre cedex, France
[8] LERMA, Observatoire de Paris, PSL Research University, CNRS, UMR 8112, F-75014 Paris, France
Received 2015 April 8; accepted 2015 May 4; published 2015 May 27

ABSTRACT

We report the detection of SiS rotational lines in high-vibrational states as well as SiO and SiC_2 lines in their ground vibrational state toward IRC+10216 during the Atacama Large Millimeter Array Cycle 0. The spatial distribution of these molecules shows compact emission for SiS and a more extended emission for SiO and SiC_2 and also proves the existence of an increase in the SiC_2 emission at the outer shells of the circumstellar envelope (CSE). We analyze the excitation conditions of the vibrationally excited SiS using the population diagram technique, and we use a large velocity gradient model to compare with the observations. We found moderate discrepancies between the observations and the models that could be explained if SiS lines detected are optically thick. Additionally, the line profiles of the detected rotational lines in the high-energy vibrational states show a decreasing linewidth with increasing energy levels. This may be evidence that these lines could be excited only in the inner shells, i.e., the densest and hottest, of the CSE of IRC+10216.

Key words: astrochemistry – circumstellar matter – line: identification – molecular processes – stars: AGB and post-AGB – stars: individual (IRC+10216)

1. INTRODUCTION

Silicon is mostly locked in SiS, SiO, and SiC_2 in the circumstellar envelope (CSE) of the carbon-rich star IRC +10216, as evidenced observationally and predicted by models (Olofsson et al. 1982; Lucas et al. 1995; Agúndez et al. 2012). These molecules are efficiently formed in the gas phase, close to the stellar photosphere as a consequence of chemical processes enabled under thermodynamical equilibrium (Tsuji 1973). In the dust formation region ($\sim$5–20 $R_\star$), the Si-bearing molecules are likely to condense onto the dust grains due to their highly refractory nature. The silicon contained in the dust grains can form molecules through grain-surface reactions. Also, the interaction of shocks produced by the pulsation of the star with the dust grains can extract certain amounts of silicon from the grains and incorporate that silicon into the gas phase to react and form other species (see, e.g., Castro-Carrizo et al. 2001). Beyond this region, the abundances of Si-bearing molecules are expected to decrease up to the outermost shells of the envelope, where the interstellar ultraviolet (UV) radiation field dissociates all the remaining molecules.

Previous interferometer observations showed the spatial distribution of these molecules in IRC+10216. The SiS $J = 5-4$, $J = 6-5$, $J = 8-7$, $J = 9-8$, and $J = 12-11$ brightness distributions display a quasi-circular shape with a diameter of $\sim$20″ elongated along the nebular axis (P.A.$\sim$20°; Bieging & Tafalla 1993; Lucas et al. 1995). Recent observations with the Combined Array for Research in Millimeter-wave Astronomy (CARMA) of the SiS $J = 14-13$ $v = 0$ and $v = 1$ lines have been reported by Fonfría et al. (2014), where the $v = 0$ line shows a circular and compact brightness distribution of $\sim$2″ and displays maser emission. The $v = 1$ brightness distribution shows a compact source centered at the star position.

SiO $J = 5-4$ $v = 0$ brightness distribution maps carried out with the Submillimeter Array were reported in Schöier et al. (2006). They show circular symmetry with a diameter of $\sim$6″ at the systemic velocity of the source, which is -26.5 km s^{-1} (e.g., Cernicharo et al. 2000). The $J = 6-5$ $v = 0$ brightness distribution reported in Fonfría et al. (2014) displays a quasi-circular symmetry centered at the position of the star, with a diameter of $\sim$3″ elongated along the nebular direction (NE–SW).

SiC_2 observations carried out with the Plateau de Bure Interferometer and CARMA show a brightness distribution composed of (i) an elongated compact component located at the innermost regions of the CSE (Fonfría et al. 2014) and (ii) a hollow shell structure located $\sim$15″ from the star (Lucas et al. 1995). The formation mechanism for this outer component was suggested in Cernicharo et al. (2010), where the reaction between Si and C_2H_2 yielding SiC_2 could be responsible for the SiC_2 enhancement in the outer envelope.

In this work, we present the Cycle 0 observations carried out with the Atacama Large Millimeter Array (ALMA) toward IRC+10216. We detected emission of SiS $J = 15-14$ lines of vibrationally excited states, from $v = 0$ up to $v = 7$, and tentatively of $v = 8$, 9, and 10. $J = 15-14$ lines of different isotopologues are also detected: ^{29}SiS (v = 0–5), ^{30}SiS (v = 0–4), Si^{33}S (v = 0–3), Si^{34}S (v = 0–4), ^{29}Si^{33}S ($v = 0$), and ^{29}Si^{34}S ($v = 0$). We also detected emission of SiO

[2] ApJL, 805, L13, 2015, reproduced with permission (AAS)

Table 1
Observational Parameters

Setup #	Frequency Range (GHz)	rms (mJy beam^{-1})	Synthetic Beam ($''\times''$)	FOV[a] ($''$)
3	269.9–274.8	6	0.61 × 0.47	23.2–22.9
4	265.0–269.9	10	0.86 × 0.47	23.7–23.2
5	260.2–265.0	17	0.96 × 0.47	24.2–23.7
6	255.3–260.2	6	0.77 × 0.60	24.6–24.2

[a] Field of view calculated as $\theta(\mathrm{rad}) = 1.22\lambda(\mathrm{mm})/D(\mathrm{mm})$, where D is the diameter of a single antenna (12 m) and λ is the observed wavelength.

$J = 6-5$ ($v = 0$–2), ^{29}SiO $J = 6-5$ ($v = 0$), and several lines of SiC_2 in the ground vibrational state.

2. OBSERVATIONS

The observations were carried out with ALMA[9] between 2012 April 8 and 23 during Cycle 0. IRC+10216 was observed in the frequency range 255.3–274.8 GHz (band 6) covered by four different setups, with a bandwidth of ∼5 GHz, a channel spacing of 0.49 MHz, and an effective resolution of 0.98 MHz. Detailed information of each setup is summarized in Table 1. The observations were performed using 16 antennas covering baselines up to 402 m that allowed us to obtain an angular resolution of ∼0.″6. The shortest baselines used were ∼20 m, which allows us to recover structures with a size up to $\lesssim$12″. Two runs of 72 minutes each were performed, of which 26 minutes correspond to correlations on source. Further details about calibration and imaging restoration can be found in Cernicharo et al. (2013). The coverage of the uv plane achieved with setup 6 provides low contributions of the sidelobes ($\leqslant$10% of the primary beam) to the dirty beam. For the rest of the setups, the uv coverage is worse, and large contributions of the sidelobes (up to 20%–30% of the primary beam) appear in the dirty beam.

The continuum comes from a point-like source located at $\alpha = 9^{\mathrm{h}}47^{\mathrm{m}}57\overset{\mathrm{s}}{.}446$ and $\delta = 13°16'43\overset{''}{.}86$(J2000), which is in good agreement with the position of IRC+10216 measured with the Very Large Array with 40 mas resolution (Menten et al. 2012). We measured an intensity peak of 650 mJy beam^{-1} with an uncertainty of ∼8 %.

The calibration of the data was performed using CASA[10] and data analysis with GILDAS.[11]

3. RESULTS

3.1. Spatial Distribution of Si-bearing Molecules

In Figures 1 and 2, we show maps of the emission of the lines SiC_2 $J_{K_a,K_c}=11_{6,6}-10_{6,5}$, ^{29}SiO $J = 6-5$, and ^{29}SiS $J = 15-14$ in their ground vibrational state at different offset velocities with respect to the systemic velocity of the source.

SiC_2 (Figure 1) displays a central component elongated in the NE–SW direction with a size of ∼4–5″ along the nebular axis and ∼3–4″ in the perpendicular direction. The elongation is also observed in the ^{29}SiO emission (see below) and in the SiO and SiC_2 maps by Fonfría et al. (2014), where the authors invoke a possible bipolar outflow to explain it. At the systemic velocity of the source and at +6 km s^{-1} offset, a ringlike, clumpy, and weak component is seen ∼10–11″ from the central star. The angular distance between the position of the star and the ring structure, considering a distance of ∼130 pc to the star from us (Groenewegen et al. 2012), corresponds to a linear distance of $\sim 2\times10^{16}$ cm. This ringlike component is consistent with the peak abundance of SiC_2 in the outer envelope of IRC +10216 reported in Lucas et al. (1995) and the chemical model of Cernicharo et al. (2010). Although, this ringlike structure is probably filtered in our data given the shortest baselines used. Between the central and the ringlike structure, emission of SiC_2 is either very low or absent (Lucas et al. 1995). Finally, the redshifted emission (+12 km s^{-1}) displays a quasi-circular distribution with a diameter of ∼5–6″. These brightness distributions could be interpreted as the SiC_2 is formed in regions close to the star, then it condenses onto the dust grains, and eventually it reappears at the outer shells of the CSE, perhaps as a hollow shell, as the consequence of the interaction between the UV Galactic radiation field and the CSE (Lucas et al. 1995; Fonfría et al. 2014).

For ^{29}SiO (Figures 1 and 2), the bulk of the emission arises from a compact central component with a size of 2″. This line also displays an extended and clumpy distribution, elongated in the NE–SW and with a size of ∼6–7″. At velocities close to the terminal expansion velocity, ∼14.5 km s^{-1}(Cernicharo et al. 2000), the brightness distribution is elongated in the NE–SW direction with a size of ∼3–4″. The blueshifted emission at −13 km s^{-1} displays a decrease just in front of the star, which can be interpreted as self-absorption and probably absorption of the continuum emission mostly coming from the star. There is no conclusive explanation for the elongation; nevertheless, some authors pointed out that it could evidence the presence of a bipolar outflow in the CSE (Fonfría et al. 2014). The possible presence of a binary companion to CWLeo could also play a decisive role in this scenario (Guelin et al. 1993; Cernicharo et al. 2015).

The observed brightness distributions of the vibrationally excited SiS lines are expected to be compact and centered on the star since the involved levels are excited at the high temperatures prevailing close to the star. The SiS $J = 15-14$ $v = 0$ line, which displays maser emission (Fonfría Expósito et al. 2006), shows a circular brightness distribution with a diameter of ∼2″ at the systemic velocity of the source. For the SiS $J = 15-14$ $v \geqslant 1$ lines, the observed distributions are not spatially resolved. Figure 1 shows the emission of the ^{29}SiS $J = 15-14$ $v = 0$ line, which displays a brightness distribution of a compact source surrounding the central star with a diameter of ∼2″. A large-scale artificial modulation can be seen below the 25σ level. Since it is related to the visibilities at short baselines, we do not expect it to modify the shape and flux of the compact central component of the brightness distribution. Also, the quality of the SiS and ^{29}SiS maps is affected owing to the low uv coverage and non-neglible contribution of the sidelobes for setups 3–5 (see Table 1). The lines that lie in the

[9] This paper makes use of the following ALMA data: ADS/JAO. ALMA#2011.0.00229.S. ALMA is a partnership of ESO (representing its member states), NSF (USA) and NINS (Japan), together with NRC (Canada), NSC and ASIAA (Taiwan), and KASI (Republic of Korea), in cooperation with the Republic of Chile. The Joint ALMA Observatory is operated by ESO, AUI/NRAO, and NAOJ.

[10] CASA (Common Astronomy Software Applications) is a comprehensive software package used to calibrate, image, and analyze radioastronomical data from interferometers. See http://casa.nrao.edu.

[11] GILDAS is a worldwide software mainly used to process, reduce, and analyze astronomical single-dish and interferometric observations. It is maintained by the Institut de Radioastronomie Millimétrique (IRAM). See http://www.iram.fr/IRAMFR/GILDAS.

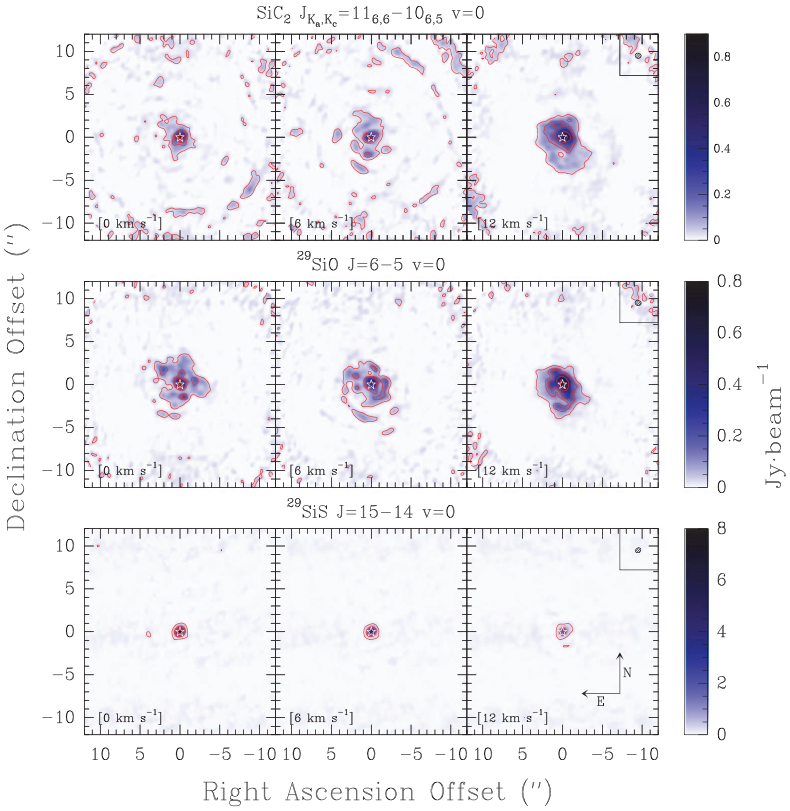

Figure 1. From top to bottom: SiC_2 $J_{K_a,K_c} = 11_{6,6} - 10_{6,5}$ $v = 0$, ^{29}SiO $J = 6 - 5$ $v = 0$, and ^{29}SiS $J = 15 - 14$ $v = 0$. Three velocity offsets with respect to the V_{LSR} of the source are shown: +0, +6, and +12 km s^{-1}. The position of the star is shown as a white star. The first contour corresponds to 5σ (see Table 1), and the rest correspond to 15%, 25%, 50%, 75%, and 90% of the maximum intensity, except for ^{29}SiS $J = 15 - 14$, where the first contour is at the 25σ level (a large-scale artificial modulation appears below that level). The synthetic beam is represented in the top right corner of each of the three map series. The intensity scale in Jy beam^{-1} is shown at the right edge of the figure. The orientation is explicitly shown in the bottom right box.

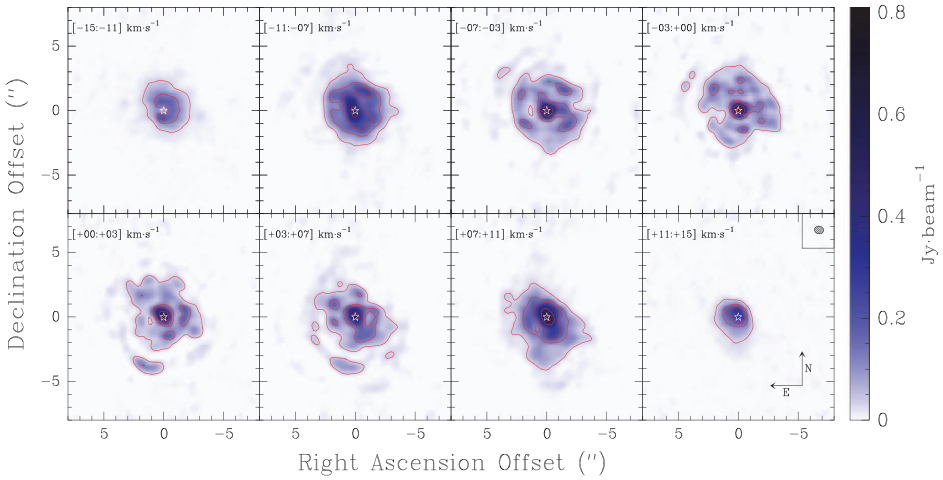

Figure 2. ^{29}SiO $J = 6 - 5$ $v = 0$ velocity interval averaged maps. The velocity averaged interval is shown at the top left corner of each box. These velocities are offset velocities with respect to the V_{LSR} of the source (−26.5 km s^{-1}). The position of the star is shown as a white star. The first contour corresponds to 5σ (see Table 1), and the rest correspond to 15%, 25%, 50%, 75%, and 90% of the maximum intensity. The intensity scale in Jy beam^{-1} is shown at the right edge of the figure. The synthetic beam is represented in the top right corner of the bottom right box. The orientation is explicitly shown in the bottom right box.

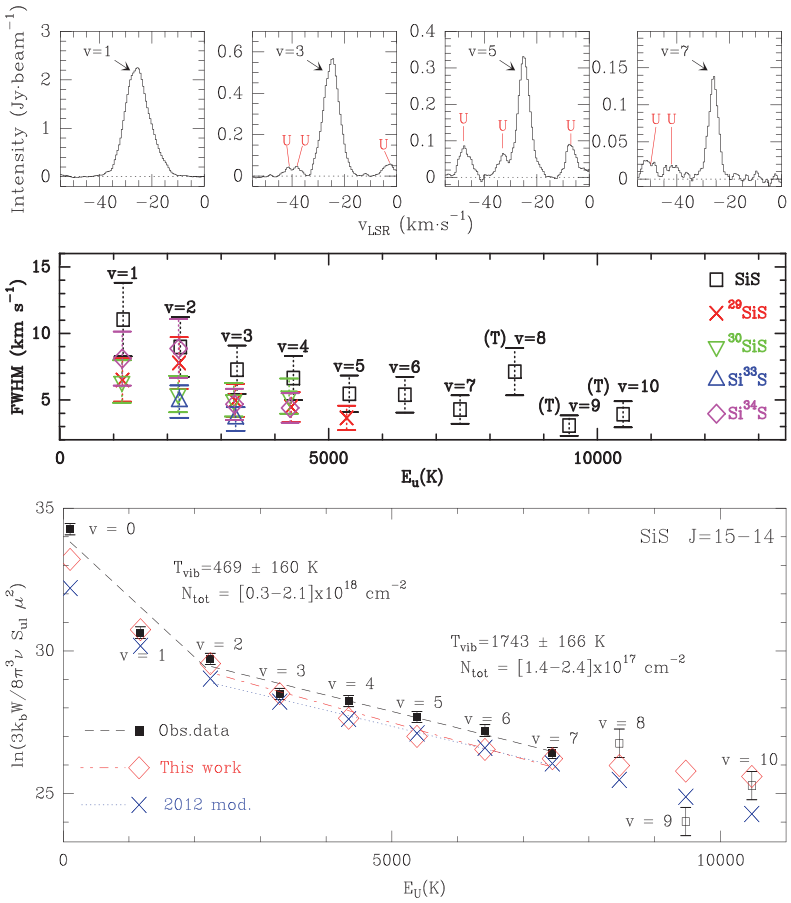

Figure 3. (Top) Central pixel spectra of the SiS $J = 15 - 14$ $v = 1$, 3, 5, and 7 lines. Unidentified lines are marked with a U. Baselines are indicated in each box with a dashed line. (Middle) FWHM of the $v \geqslant 1$ detected lines of SiS isotopologues in the central pixel vs. the upper energy of the transition. The tentative lines are marked with a (T). We adopted a 25% value of the total measure for the uncertainties, which takes into account uncertainties of the calibration, statistical errors, and the contribution of the sidelobes of the dirty beam. (Bottom) Vibrational diagram of the SiS $J = 15 - 14$ lines. The vibrational quantum number of each line is shown. The error bars represent 20% of the integrated intensity of the line and 50% for the $v = 8$, 9, and 10 lines. The values derived for the vibrational temperature and column density are shown with their formal errors for two fits: $v = 0$–2 and $v = 3$–7. The LVG models (see Section 3.2) are plotted with a rhombus and a cross.

range covered by setup 6 are those of high vibrationally excited states (e.g., SiS $J = 15 - 14$ $v \geqslant 10$; ^{29}SiS $J = 15 - 14$ $v \geqslant 6$), which are tentative and spatially unresolved.

3.2. Vibrationally Excited SiS

The Cycle 0 observations with ALMA allowed us to detect several $J = 15 - 14$ lines of high vibrationally excited states of SiS isotopologues, in particular, up to $v = 7$ for the main isotopologue (see Figure 3). The SiS $J = 15 - 14$ $v = 8$ and $v = 10$ lines are probably blended with unidentified lines, so we consider them to be tentative. Additionally, the SiS $J = 15 - 14$ $v = 9$ line is considered tentatively detected because even though its FWHM measured seems to follow the trend shown in Figure 3, its measured integrated intensity is underestimated considering the population diagram of Figure 3. All these lines display a compact unresolved emission peaking at the central star. The FWHM of the lines measured from the spectra at the stellar position decreases with increasing upper level energy (see Figure 3). We verified this behavior for SiS, ^{29}SiS, ^{30}SiS, Si^{33}S, and Si^{34}S. In the dust formation region, the gas displays a velocity gradient as a function of the radial distance to the star, i.e., the closer to the star the lower the expansion velocity (Agúndez et al. 2012 and references therein). Hence, those lines involving higher vibrational states, which are excited in inner and warmer regions, are narrower. Thermal broadening for the SiS lines excited in the dust formation region is $\sim$1 km s^{-1}, and thus this mechanism could only account partially for the FWHM variation of the lines.

We analyzed the excitation conditions of SiS with the rotational diagram technique (Goldsmith & Langer 1999) using the spectra at the stellar position (see Figure 3). We considered two different linear trends for the observational data: one for the transitions with $E_{up} \lesssim 2500$ K (i.e., $v = 0$, 1, and 2) and a different trend for the rest (i.e., $v = 3$–7). The $v \geqslant 8$ lines are excluded from the fit. The values derived from the $v = 0$ to $v = 2$ fit are uncertain owing to the maser nature of the SiS $J = 15 - 14$ $v = 0$ line and also to possible optically thick emission. Both data series show a linear behavior consistent

Table 2
Calculated Vibrational Dipole Moment Matrix Elements (D) for $^{28}Si^{32}S$

v'/v''	0	1	2	3	4	5	6	7	8	9	10	11	12
0	1.7420	…	…	…	…	…	…	…	…	…	…	…	…
1	−0.1348	1.7658	…	…	…	…	…	…	…	…	…	…	…
2	-0.6333×10^{-2}	−0.1907	1.7896	…	…	…	…	…	…	…	…	…	…
3	0.4068×10^{-3}	0.1101×10^{-1}	0.2336	1.8135	…	…	…	…	…	…	…	…	…
4	-0.3379×10^{-4}	-0.8184×10^{-3}	-0.1564×10^{-1}	0.2697	1.8375	…	…	…	…	…	…	…	…
5	-0.3359×10^{-5}	-0.7613×10^{-4}	-0.1302×10^{-2}	0.2027×10^{-1}	−0.3016	1.8615	…	…	…	…	…	…	…
6	0.3804×10^{-6}	-0.8306×10^{-5}	0.1329×10^{-3}	-0.1852×10^{-2}	-0.2493×10^{-1}	0.3304	1.8857	…	…	…	…	…	…
7	0.4752×10^{-7}	0.1018×10^{-5}	0.1569×10^{-4}	-0.2046×10^{-3}	0.2465×10^{-2}	0.2961×10^{-1}	−0.3568	1.9100	…	…	…	…	…
8	-0.6394×10^{-8}	-0.1363×10^{-6}	-0.2061×10^{-5}	0.2587×10^{-4}	-0.2916×10^{-3}	-0.3137×10^{-2}	0.3433×10^{-1}	0.3814	1.9343	…	…	…	…
9	-0.9087×10^{-9}	-0.1952×10^{-7}	-0.2934×10^{-6}	0.3612×10^{-5}	-0.3918×10^{-4}	-0.3943×10^{-3}	0.3866×10^{-2}	0.3909×10^{-1}	−0.4045	1.9587	…	…	…
10	0.1339×10^{-9}	0.2936×10^{-8}	0.4441×10^{-7}	-0.5435×10^{-6}	0.5779×10^{-5}	0.5594×10^{-4}	-0.5130×10^{-3}	-0.4649×10^{-2}	0.4388×10^{-1}	0.4262	1.9833	…	…
11	0.2005×10^{-10}	0.4562×10^{-9}	0.7033×10^{-8}	-0.8654×10^{-7}	0.9143×10^{-6}	0.8674×10^{-5}	-0.7649×10^{-4}	-0.6482×10^{-3}	0.5485×10^{-2}	0.4871×10^{-1}	−0.4469	2.0079	…
12	-0.2954×10^{-11}	-0.7182×10^{-10}	-0.1147×10^{-8}	0.1437×10^{-7}	-0.1525×10^{-6}	-0.1437×10^{-5}	0.1241×10^{-4}	0.1011×10^{-3}	-0.8003×10^{-3}	-0.6373×10^{-2}	0.5358×10^{-1}	0.4667	2.0326

Note. Internuclear potential energy parameters for the SiS molecule: $D_e = 51993.7274\ \mathrm{cm}^{-1}$, $r_e = 1.929260274$ Å, $\beta_0 = 5.9671641$, $\beta_1 = 5.8793706$, $\beta_2 = 9.3200373$, $\beta_3 = 18.402479$, $\beta_4 = 18.451287$, $u_1^{Si} = -749.1309\ \mathrm{cm}^{-1}$ amu, $u_2^{Si} = 6844.274\ \mathrm{cm}^{-1}$ amu, $u_1^{S} = -1003.321\ \mathrm{cm}^{-1}$ amu, $u_2^{S} = 7128.960\ \mathrm{cm}^{-1}$ amu.

with a single vibrational (excitation) temperature for each of the fits. The vibrational temperature derived from the fit involving the transitions in high-energy vibrational states is higher than the temperature derived for the low vibrational levels. Therefore, the emission produced by SiS transitions in high-energy vibrational states can only arise from regions close to the photosphere. This result is similar to the one obtained by Cernicharo et al. (2011) for HCN.

We used a large velocity gradient (LVG) code to model the SiS emission (Cernicharo 2012). Further details about the spectroscopic data used in the calculations are given in Section 3.2.1. The SiS collisional data were taken from Toboła et al. (2008) and extrapolated to high rovibrational levels. We adopted a distance to the star of ∼130 pc, an effective temperature of ∼2330 K, and a stellar radius of $\sim 4 \times 10^{13}$ cm as input for our model (Cernicharo et al. 2000; Monnier et al. 2000; Groenewegen et al. 2012). We used two different models: (i) the model of Agúndez et al. (2012), which was used to reproduce the molecular abundances in the inner layers of IRC+10216, which we call the "2012 model," and (ii) this work, which is a modification of model (i). We modified the H_2 density, decreasing it by a factor ∼2, as described in Cernicharo et al. (2013; this was used to reproduce the dust nucleation zone, 1–10 $R_\star$, of IRC+10216). Additionally, the SiS abundance in the dust nucleation zone needs to be balanced with a similar increase (factor of ∼2) to avoid an underestimation of the SiS emission. From these models (see Figure 3), we obtain a good agreement with the vibrational temperature derived from the vibrational diagram and moderate discrepancies with the total column density within a factor of ∼2. These discrepancies in the column density may be explained by the dilution due to the size of the emitting region compared to the half power beam width of the synthetic beam, which would increase the optical depth of the lines. The size of the emitting region should decrease with the vibrational state owing to the energies needed to excite those lines. With our models, we found moderate to high optical depths $\tau(v = 1) \sim 10$ to $\tau(v = 4) \sim 0.8$ for abundance profile (i) and $\tau(v = 1) \sim 47$ to $\tau(v = 8) \sim 1.0$ for abundance profile (ii).

3.2.1. SiS Potential Energy Function and Vibrational Dipole Moment

The potential energy function used to describe the internuclear motions of the SiS isotopologues is a Born–Oppenheimer (BO) potential properly extended to accommodate Born–Oppenheimer breakdown (BOB) corrections. The effective potential has the form (Campbell et al. 1993; Ram et al. 1997; Dulick et al. 1998; Coxon & Hajigeorgiou 2000)

$$V^{\rm eff}(r) = V^{\rm BO}(r) + \frac{V_A(r)}{M_A} + \frac{V_B(r)}{M_B} - \frac{\hbar^2}{2\mu}[1 + q(r)]\frac{J(J+1)}{r^2}, \quad (1)$$

where M_A and M_B are the silicon and sulfur atomic masses and μ is the reduced mass. The BO potential is given by

$$V^{\rm BO}(r) = D_e\left[\frac{1 - e^{-\beta(r)}}{1 - e^{-\beta(\infty)}}\right]^2, \quad (2)$$

where

$$\beta(r) = z\sum_{i=0}^{4}\beta_i z^i, \quad (3)$$

$$\beta(\infty) = \sum_{i=0}^{4}\beta_i, \quad (4)$$

and

$$z = \frac{r - r_e}{r + r_e}, \quad (5)$$

and the BOB potential and centrifugal correction terms are represented by the power expansions

$$V_A(r) = \sum_{i=1} {u_i}^A z^i, \quad (6)$$

$$V_B(r) = \sum_{i=1} {u_i}^B z^i, \quad (7)$$

$$q(r) = M_A^{-1}\sum_{i=1} {q_i}^A z^i + M_B^{-1}\sum_{i=1} {q_i}^B z^i. \quad (8)$$

The potential parameters were obtained by nonlinear least squares fitting to the observed infrared and microwave line positions of the SiS isotopologues up to $v = 12$. The final data set included a total of 2863 lines, 414 rotational transitions (Tiemann et al. 1972; Sanz et al. 2003; Müller et al. 2007), and 2449 rovibrational transitions (Birk & Jones 1972; Frum et al. 1990). Mass-independent Dunham coefficients, U_{ij}, have been derived by Müller et al. (2007). The fit to the potential energy function was performed using the Levenberg–Marquardt algorithm (Levenberg 1944; Marquardt 1963) to minimize the χ^2 function, with the line positions weighted by the square of the experimental uncertainties. The rovibrational energy levels of the isotopologues needed to calculate the line positions were computed by solving the radial Schrödinger equation using the variational method of Harris et al. (1965) along with harmonic-type basis functions. The potential parameters obtained in the fit are given in the comments of Table 2. The final χ^2 value was 1.767. The unweighted standard deviations for the rotational and vibrational–rotational line positions were 0.0229 MHz and 0.000657 $\rm cm^{-1}$, respectively.

The dipole moment function used for SiS was determined semiempirically by Piñeiro et al. (1987), and the dipole moment matrix elements were computed up to $v = 4$. In Table 2, we provide them up to $v = 12$. The agreement between our calculations and those of Piñeiro et al. (1987) for $v \leqslant 4$ is excellent.

3.3. Other Si-bearing Species

SiC was detected in IRC+10216 by Cernicharo et al. (1989) with line profiles indicating that the molecule was produced in an external shell, probably as a product of the photodissociation of SiC_2. Our observations did not cover any frequency range where SiC lines could arise; however, lines of ^{29}SiC and SiC $v = 1$ lie in this range, but they were not detected. For a temperature in the photosphere of 2300 K, a significant number of SiC molecules could be in the $v = 1$ state ($E_{\rm up} \sim$ 1400 K) and higher vibrational levels. We derived an upper limit to the SiC column density of 4.4×10^{14} $\rm cm^{-2}$ from the ^{29}SiC upper limit, where we used an isotopic ^{28}Si/^{29}Si ratio of 20

(Cernicharo et al. 1989, 1991). Hence, SiC_2 is the main carrier of SiC bonds in the gas phase in the dust formation zone of IRC +10216.

4. CONCLUSION

ALMA has proved to be an outstanding tool to study the molecular emission from CSEs of evolved stars, even at the early stages of its development. In particular, ALMA allowed us to detect SiS rotational lines in high-energy vibrational states that have been analyzed to constrain the physical conditions of the innermost shells of IRC+10216. We found that these lines should be excited in regions close to the photosphere of IRC +10216. It also has served to unveil the different brightness distributions of Si-bearing molecules. We expect that future ALMA science, with its full suite of capabilities ready for the next observation cycle, would give us the chance to map the brightness distributions of these Si-bearing molecules in greater detail, allowing us to understand their formation mechanisms.

We thank the Spanish MINECO/MICINN for funding support through grants AYA2009-07304 and AYA2012-32032, the ASTROMOL Consolider project CSD2009-00038, and the European Research Council (ERC grant 610256: NANOCOSMOS).

REFERENCES

Agúndez, M., Fonfría, J. P., Cernicharo, J., et al. 2012, A&A, 543, AA48
Bieging, J. H., & Tafalla, M. 1993, AJ, 105, 576
Birk, H., & Jones, H. 1972, CPL, 175, 536
Campbell, J. M., Dulick, M., Klapstein, D., et al. 1993, JChPh, 99, 8379
Castro-Carrizo, A., Lucas, R., Bujarrabal, V., Colomer, F., & Alcolea, J. 2001, A&A, 368, L34
Cernicharo, J. 2012, in EAS Publications Ser. 58, European Conference on Laboratory Astrophysics, ed. C. Stehlé, C. Joblin, & L. d'Hendecourt (Les Ulis: EDP Sciences), 251
Cernicharo, J., Agúndez, M., Kahane, C., et al. 2011, A&A, 529, LL3
Cernicharo, J., Daniel, F., Castro-Carrizo, A., et al. 2013, ApJL, 778, LL25
Cernicharo, J., Gottlieb, C. A., Guelin, M., Thaddeus, P., & Vrtilek, J. M. 1989, ApJL, 341, L25
Cernicharo, J., Guélin, M., & Kahane, C. 2000, A&AS, 142, 181
Cernicharo, J., Guélin, M., Kahane, C., Bogey, M., & Demuynck, C. 1991, A&A, 246, 213
Cernicharo, J., Marcelino, N., Agúndez, M., & Guélin, M. 2015, A&A, 575, AA91
Cernicharo, J., Waters, L. B. F. M., Decin, L., et al. 2010, A&A, 521, LL8
Coxon, J. A., & Hajigeorgiou, P. G. 2000, JMoSp, 203, 49
Dulick, M., Zhang, K. Q., Guo, B., & Bernath, P. F. 1998, JMoSp, 188, 14
Fonfría Expósito, J. P., Agúndez, M., Tercero, B., Pardo, J. R., & Cernicharo, J. 2006, ApJL, 646, L127
Fonfría, J. P., Fernández-López, M., Agúndez, M., et al. 2014, MNRAS, 445, 3289
Frum, C. I., Engleman, R., Jr., & Bernath, P. F. 1990, JChPh, 93, 5457
Goldsmith, P. F., & Langer, W. D. 1999, ApJ, 517, 209
Groenewegen, M. A. T., Barlow, M. J., Blommaert, J. A. D. L., et al. 2012, A&A, 543, LL8
Guelin, M., Lucas, R., & Cernicharo, J. 1993, A&A, 280, L19
Harris, D. O., Engerholm, G. G., & Gwinn, W. D. 1965, JChPh, 43, 1515
Levenberg, K. 1944, QJMAM, 2, 164
Lucas, R., Guélin, M., Kahane, C., Audinos, P., & Cernicharo, J. 1995, Ap&SS, 224, 293
Marquardt, D. W. 1963, J. Soc. Ind. Appl. Math, 11, 431
Menten, K. M., Reid, M. J., Kamiński, T., & Claussen, M. J. 2012, A&A, 543, AA73
Monnier, J. D., Danchi, W. C., Hale, D. S., et al. 2000, ApJ, 543, 861
Müller, H. S. P., McCarthy, M. C., Bozzocchi, L., et al. 2007, PCCP, 9, 1579
Olofsson, H., Johansson, L. E. B., Hjalmarson, A., & Nguyen-Quang-Rieu 1982, A&A, 107, 128
Piñeiro, A. L. L., Tipping, R. H., & Chackerian, J. C. 1987, JMoSp, 125, 184
Ram, R. S., Dulick, M., Guo, B., et al. 1997, JMoSp, 183, 360
Sanz, M. E., McCarthy, M. C., & Thaddeus, P. 2003, JChPh, 119, 11715
Schöier, F. L., Fong, D., Olofsson, H., Zhang, Q., & Patel, N. 2006, ApJ, 649, 965
Tiemann, E., Renwanz, E., Hoeft, J., & Torring, T. 1972, ZNatA, 27a, 1566
Toboła, R., Lique, F., Kłos, J., & Chałasiński, G. 2008, JPhB, 41, 155702
Tsuji, T. 1973, A&A, 23, 411

CHAPTER

7

IRC+10216: FURTHER STUDIES

In this chapter, other relevant publications in which I participated as co-author are presented. These publications address several research works concerning the molecular emission of the circumstellar envelope of IRC+10216. A brief summary of each work is presented as well as the first page of the articles.

7.1 Time variability of the spectral line emission

In Cernicharo et al. (2014) we reported strong intensity variations of the high energy rotational lines of several abundant molecular species toward IRC+10216. These lines have been observed with the IRAM-30 m telescope and with the Herschel Space Observatory-HIFI instrument in several observational campaigns which cover a time period of ∼3 years between 2010 and 2013. The observations evidence that the effect of intensity variation can be seen for some species (e.g. lines of H_2O, high-J transitions of HNC, HCN, CO, CS, SiO, and SiS) while others species display no significant intensity variations, such as the SiC_2 lines or low-J transitions of abundant species like CO, CS, SiO or SiS (see Fig. 7.1). Our observations prove that the intensity variation is more noticeable for the rotational lines that lie in the sub-millimeter and fIR wavelength ranges, and specially for the high-J lines. The intensity variations seem to be correlated with the stellar phase, and it also displays a phase delay for each layer of the CSE. Therefore, molecules that are located closer to the star, such as HCN, interact with the stellar radiation before than the molecules located in the outermost parts, such as CCH, and a phase delay in their intensity variations is seen. We concluded that sub-mm and far-IR molecular emission of AGB CSEs cannot be considered as reliable flux calibrators, and radiative transfer analysis including these lines must consider IR flux variations and IR pumping throughout the envelope.

7.2 Detection of SiCSi toward IRC+10216

In Cernicharo et al. (2015b) we reported the detection of SiCSi in space, toward the CSE IRC+10216 based on IRAM-30 m observations and laboratory work. We detected 112 rotational lines of SiCSi, where 9 of them where also observed with the SMA. Laboratory work by McCarthy et al. (2015) allowed us to accurately predict frequencies that lie in the 3 mm wavelength domain, and also obtain spectroscopic constants (up to sixth order centrifugal distortion constants for a Watson Hamiltonian in the A and S reductions) to derive accurate rotational

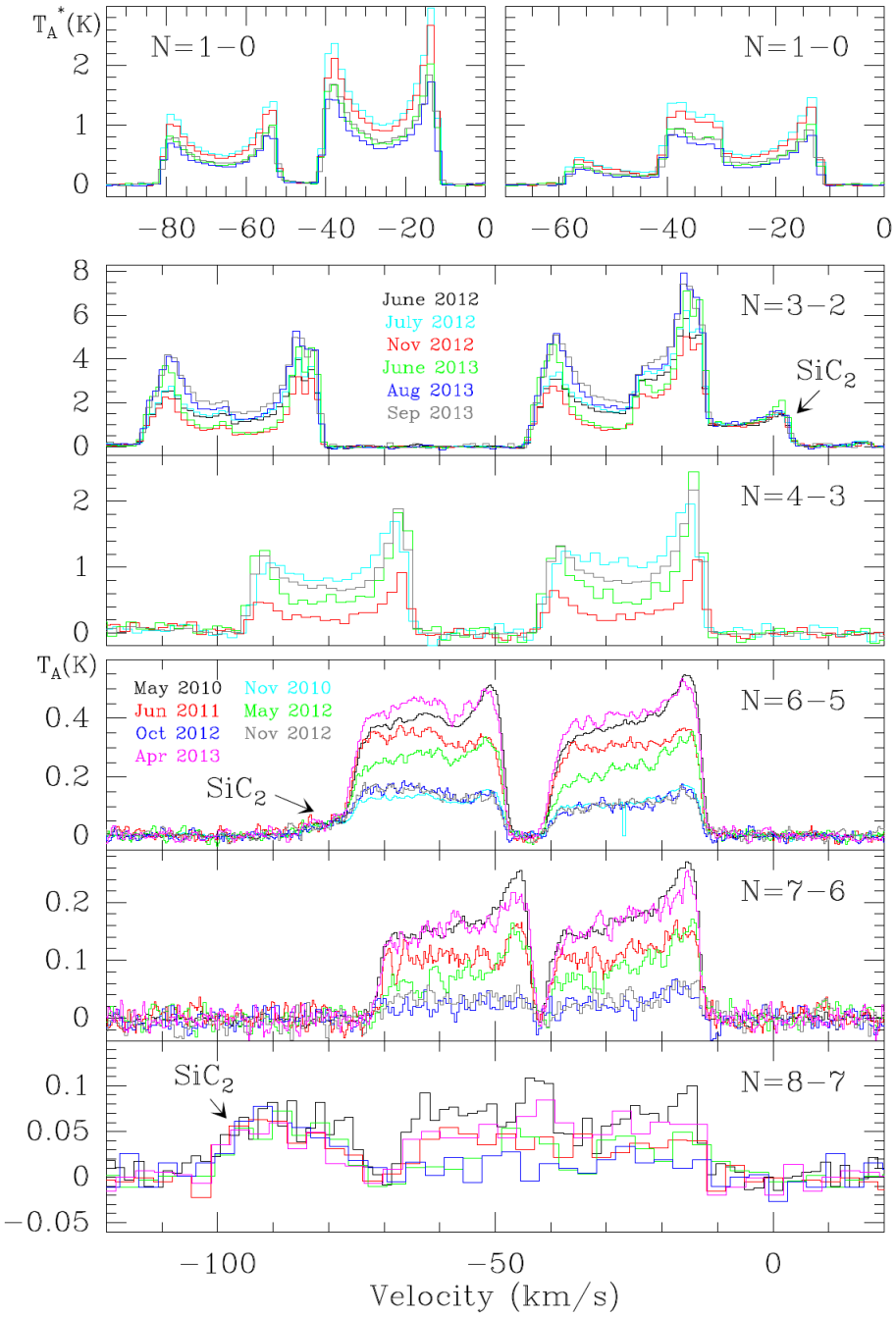

Figure 7.1: CCH lines observed with the IRAM-30 m telescope (N=1–0, 3–2, and 4–3) and with HIFI (N=6–5, 7–6, and 8–7) presented in Cernicharo et al. (2014). Spectra observed at different epochs are shown in different colours. The velocity scale in km s^{-1} is referred respect to the frequency of each strongest hyperfine component. The intensity scale is in antenna temperature in K. Note that several SiC_2 lines are shown which do not display strong intensity variations at different epochs.

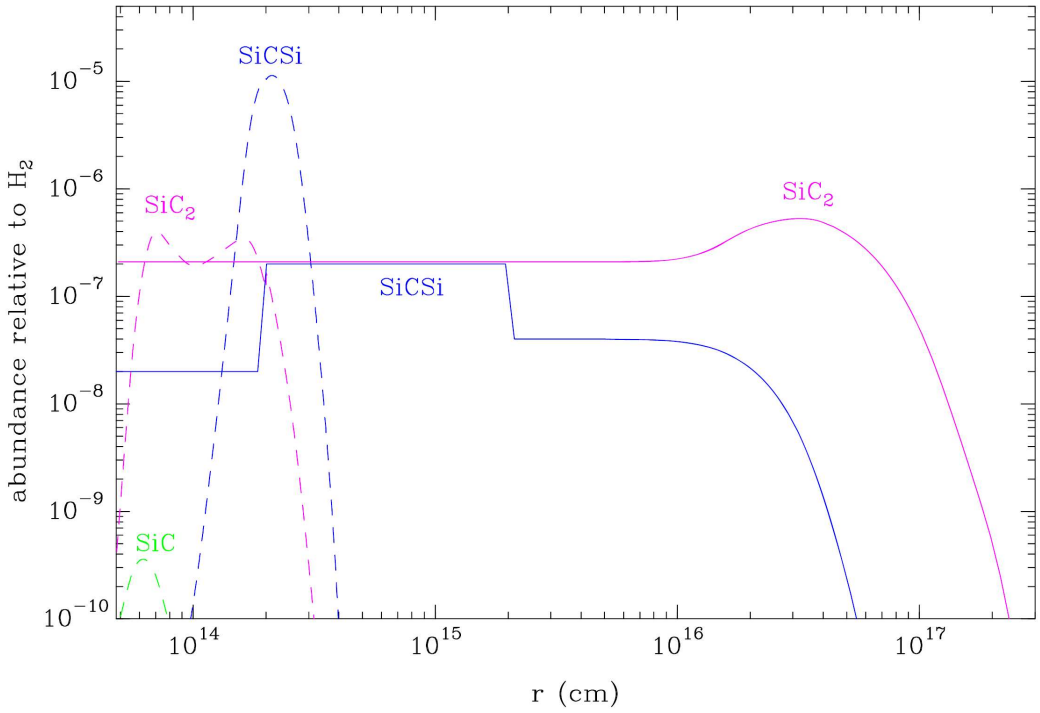

Figure 7.2: Radial abundance distribution of SiCSi, SiC_2, and SiC as calculated by chemical equilibrium (dashed lines) and as derived from the observations of IRC+10216 (solid lines). The derived abundance profile of SiC_2 is taken from Cernicharo et al. (2010). This model has been published in Cernicharo et al. (2015b).

constants and predict lines in the 2 and 1 mm wavelength range. The rotational diagram of the lines detected displays three different temperature regions: a cold (∼30 K) component, a second component with ∼120 K, and a warm (∼280 K) component. This temperature stratification and the profiles observed indicate that this molecules is concentrated around the star but with a relatively extended distribution. After a radiative transfer analysis of the molecular emission, we concluded that SiCSi lines are well reproduced by assuming a radial abundance profile as seen in Fig. 7.2. We are currently analysing high angular resolution observations of Si-C bond bearing species toward IRC+10216 as explained in Chapter 9. Molecular precursors of SiC dust grains are still unknown, thus, it is important to study Si-C bond bearing molecules in gas phase, which could be the nucleation seeds of dust grains and participate in the growth of the grains.

7.3 Mid-IR observations of SiS isotopologues

In Fonfría et al. (2015) we reported mid-IR (720-790 cm^{-1}) high spectral resolution observations of SiS isotopologues toward IRC+10216. We detected 204 ro-vibrational lines of SiS isotopologues (i.e. $^{28}Si^{32}S$, $^{29}Si^{32}S$, $^{28}Si^{34}S$, and $^{30}Si^{32}S$) with the Texas Echelon-cross-Echelle Spectrograph mounted on the NASA Infrared Telescope Facility. We used the radiative transfer code by Fonfría et al. (2008, 2014) to model the line profiles observed. We found that $^{28}Si^{32}S$ has a fractional abundance (reltaive to H_2) of $\sim 5\times10^{-6}$ for $r<5R_*$, and decreases linearly down to $\sim 2\times10^{-6}$ in the region comprised between 5-20R_*. Beyond that region, up to 50R_*, the

abundance of ^{28}Si^{32}S is $\sim 1\times10^{-6}$, which is probably explained by the depletion of SiS onto the dust grains due to its refractory nature. We have also found that ^{28}Si/^{29}Si and ^{32}S/^{34}S have isotopic ratios of 17 and 14, respectively. These ratios are compatible with previous estimations on the source. We derived the expansion velocity profile of the gas in the CSE from the radiative transfer model, and we obtained the following values: $v_{\rm exp}(1R_*\leq r <5R_*)=1+2.5(r/R_*-1)$ km s^{-1}, $v_{\rm exp}(5R_*\leq r <20R_*)=11$ km s^{-1}, and $v_{\rm exp}(r \geq 20R_*)=14.5$ km s^{-1}.

7.4 The ALMA view of IRC+10216: CH_3CN and metals

• In **Agúndez et al. (2015)** we reported the first ALMA maps of CH_3CN toward the C-rich CSE of IRC+10216. The observations were carried out during the Cycle 0 of ALMA, with an angular resolution of $\sim$0.″6. CH_3CN is distributed in a hollow shell located at $\sim$2″ from the star, where the inner edge of the shell is located at a distance of $\sim$1″ from the star (see Fig 7.3). This distribution is somewhat unexpected given that previous observations of other molecules

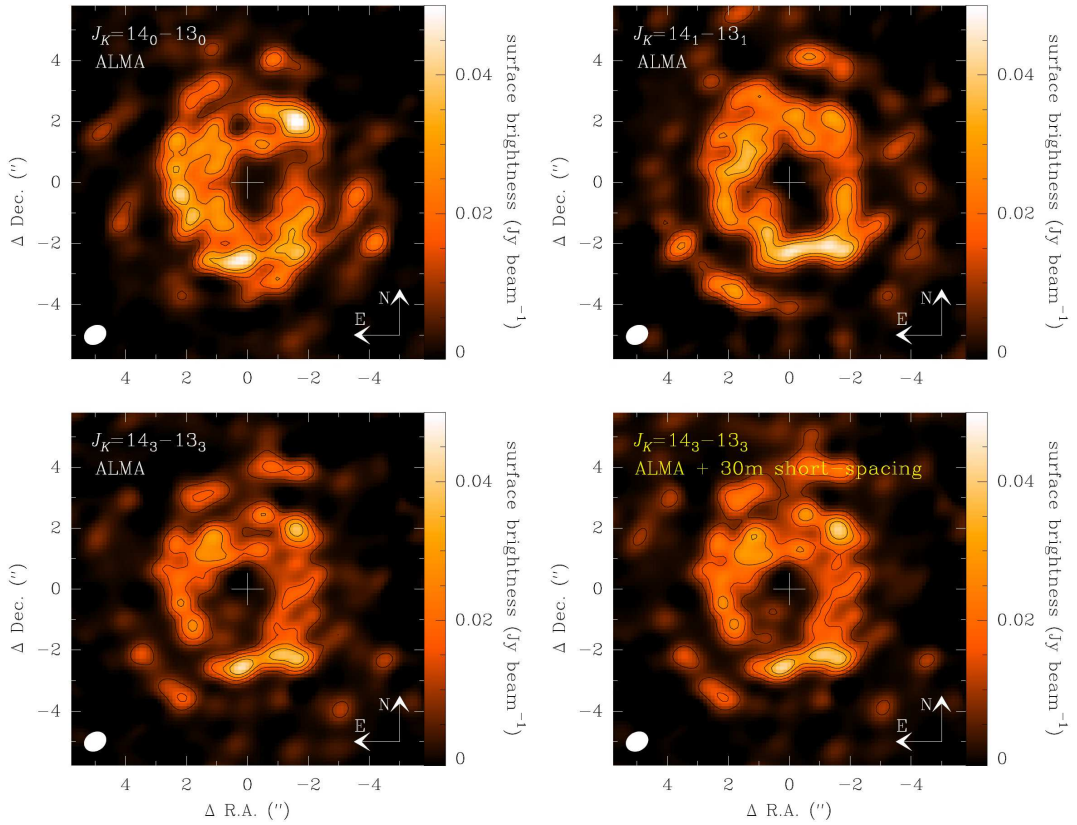

Figure 7.3: Observed brightness distribution for the K=0, 1, 2, and 3 components of CH_3CN J=14–13, averaged over a velocity range of 2.8 km s^{-1} wide, and centred at $v_{\rm LSR}$=$v_{\rm sys}$. K=0 and 1 components are partially blended, thus, their maps are partially contaminated by emission of the other component. The K=3 map is a merge of ALMA observations with IRAM-30 m short-spacing (bottom-right panel). The rms per 2.8 km s^{-1} channel is 1.6 mJy beam^{-1}. The contour levels correspond to 5, 10, 15, and 20 times the rms. The size (0.″76 × 0.″61) and shape of the synthesised beam is shown in the bottom-left corner of each box. These maps have been published in Agúndez et al. (2015).

displayed brightness distributions compatible with either a compact uniform distribution or a hollow shell but located at 15″ from the star. We computed LVG multishell radiative transfer calculations, and we also created a chemical model to constrain the abundance, distribution, and excitation of this molecule in IRC+10216. We were able to reproduce CH_3CN emission adopting a Gaussian-like abundance profile with an average fractional abundance of $\sim 10^{-8}$. Our chemical model predicts that CH_3CN is formed through the dissociative recombination of CH_3CNH^+ after the radiative association between CH_3^+ and HCN, although it predicts that CH_3CN is formed at a distance of ∼15″ with an abundance two orders of magnitude lower than that obtained from the radiative transfer analysis. These discrepancies are probably related to the uncertain reaction rate constants used in the model, and the cosmic-ray ionization rate of H_2, which could enhance the formation of CH_3CN in the innermost regions of the CSE if we take a higher rate than the one adopted of $1.2\times10^{-17}\,s^{-1}$. The formation of CH_3CN in the innermost regions of the CSE could be also enhanced if the envelope had a clumpy structure.

• In **Quintana-Lacaci et al. (2016)** we reported the first ALMA maps of several metal bearing species toward the CSE of IRC+10216. In particular, we mapped the brightness distribution of NaCl (both in the ground and v=1 vibrational states), $Na^{37}Cl$, KCl, $K^{37}Cl$, AlCl, $Al^{37}Cl$, and AlF (all in the ground vibrational state). The Al-bearing species show an emission peak close to the star, while the KCl and NaCl emission maps display a central minimum surrounded by two peaks (see Fig. 7.4). It could be possible that due to the low dipole moment of the Al-bearing species, the same structure is not seen given that these species would be thermalised in both dense and diffuse regions, while NaCl and KCl would be thermalised only in dense regions. We interpreted these observations as NaCl and KCl distributed in a spiral structure with a mass of $\sim 0.08\,M_\odot$, or distributed in a torus-like structure with r_{in}∼27 AU and r_{out}∼73 AU, and $m\sim1.1\times10^{-4}\,M_\odot$. We compared our observations to simulations obtained with the GILDAS ALMA simulator. The simulations suggest that the most likely scenario is a spiral distribution for NaCl and KCl as also seen for other species like CO (Cernicharo et al.,

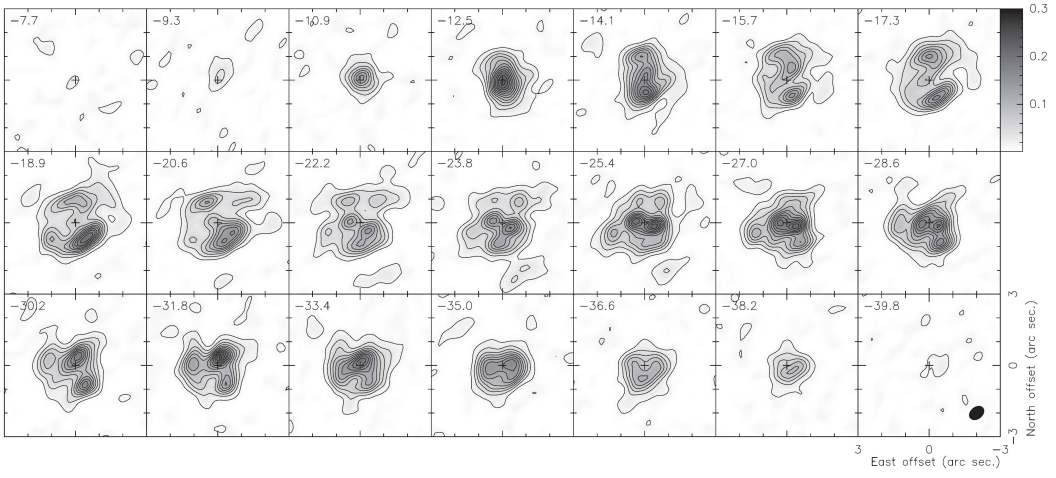

Figure 7.4: Interferometric map of the NaCl J=21–20 emission, which has been published in Quintana-Lacaci et al. (2016). The HPBW of the synthesised beam is $0\farcs70\times0\farcs52$ with a position angle of -52°, which is shown in the bottom-right corner of the last panel. The corresponding v_{LSR} is shown in the upper-left corner of each box. The rms of the map is 3.85 mJy beam^{-1}. The first contour correspond to 3σ and the rest are equally spaced in jumps of 5σ with respect to the first contour. The flux density scale is in Jy beam^{-1}.

2015a). Nevertheless, we cannot totally rule out the possibility of a torus-like structure for both molecules, but this scenario is less plausible considering that this structure is not seen for other molecules (e.g. HCN or SiC_2). We computed an LVG multishell radiative transfer model of NaCl including levels up to J=100 and v=5 to fit the observed emission, obtaining a good agreement (see Table 3 and Figs. 19 and 21 in Quintana-Lacaci et al. (2016)).

• In **Cabezas et al. (2016)** we reported high-resolution spectroscopy of the J=1–0 and J=2–1 lines of $Na^{35}Cl$ and $Na^{37}Cl$ in several vibrational states based on a laboratory study. We also obtained Dunham coefficients and the potential energy function of NaCl. This is a complementary work to Quintana-Lacaci et al. (2016).

7.5 First page of publications

Europe PMC Funders Group
Author Manuscript
Astrophys J Lett. Author manuscript; available in PMC 2015 December 29.

Published in final edited form as:
Astrophys J Lett. 2014 October 20; 796(1): . doi:10.1088/2041-8205/796/1/L21.

Discovery of Time Variation of the Intensity of Molecular Lines in IRC+10216 in The Submillimeter and Far Infrared Domains

J. Cernicharo[1], **D. Teyssier**[2], **G. Quintana-Lacaci**[1], **F. Daniel**[3], **M. Agúndez**[1], **L. Velilla Prieto**[1], **L. Decin**[4], **M. Guélin**[5], **P. Encrenaz**[6], **P. García-Lario**[2], **E. de Beck**[7], **M.J. Barlow**[8], **M.A.T. Groenewegen**[9], **D. Neufeld**[10], and **J. Pearson**[11]

[1]Group of Molecular Astrophysics. ICMM. CSIC. C/Sor Juana Inés de La Cruz N3. E-28049, Madrid. Spain

[2]ESA. ESAC. P.O. Box 78, Villanueva de la Cañada E-28691 Madrid. Spain

[3]Univ. Grenoble Alpes, IPAG, F-38000 Grenoble, France CNRS, IPAG, F-38000 Grenoble, France

[4]Instituut voor Sterrenkunde, Katholieke Universiteit Leuven, Celestijnenlaan 200D, B-3001 Leuven, Belgium

[5]Institut de Radioastronomie Millimétrique, 300 rue de la Piscine, F-38406, St-Martin d'Hères, France

[6]LERMA, Observatoire de Paris, 61 Av. de l'Observatoire, F-75014 Paris, France

[7]Department of Earth and Space Sciences, Chalmers University of Technology, Onsala Space Observatory, SE 43992 Onsala, Sweden

[8]Department of Physics and Astronomy, University College London, Gower Street, London WC1E 6BT, UK

[9]Koninklijke Sterrenwacht van België, Ringlaan 3, B-1180, Brussel, Belgium

[10]Department of Physics and Astronomy, Johns Hopkins University, 3400 North Charles Street, Baltimore, MD 21218, USA

[11]Jet Propulsion Laboratory, California Institute of Technology, Pasadena, CA, 91109, USA

Abstract

We report on the discovery of strong intensity variations in the high rotational lines of abundant molecular species towards the archetypical circumstellar envelope of IRC+10216. The observations have been carried out with the HIFI instrument on board *Herschel*[1] and with the IRAM[2] 30-m telescope. They cover several observing periods spreading over 3 years. The line intensity variations for molecules produced in the external layers of the envelope most probably result from time variations in the infrared pumping rates. We analyze the main implications this

[1]*Herschel* is an ESA space observatory with science instruments provided by European-led Principal Investigator consortia and with important participation from NASA

[2]This work was based on observations carried out with the IRAM 30-meter telescope. IRAM is supported by INSU/CNRS (France), MPG (Germany) and IGN (Spain)

Europe PMC Funders Author Manuscripts

Europe PMC Funders Author Manuscripts

Europe PMC Funders Group
Author Manuscript
Astrophys J Lett. Author manuscript; available in PMC 2015 December 29.

Published in final edited form as:
Astrophys J Lett. 2015 June 10; 806(1): . doi:10.1088/2041-8205/806/1/L3.

Discovery of SiCSi in IRC +10216: A missing link between gas and dust carriers of Si–C bonds

J. Cernicharo[1], **M. C. McCarthy**[2], **C. A. Gottlieb**[2], **M. Agúndez**[1], **L. Velilla Prieto**[1], **J. H. Baraban**[3], **P. B. Changala**[4], **M. Guélin**[5], **C. Kahane**[6], **M. A. Martin-Drumel**[2], **N. A. Patel**[2], **N. J. Reilly**[2,7], **J. F. Stanton**[8], **G. Quintana-Lacaci**[1], **S. Thorwirth**[9], and **K. H. Young**[2]

[1]Group of Molecular Astrophysics. ICMM. CSIC. C/Sor Juana Inés de La Cruz N3. E-28049, Madrid. Spain

[2]Harvard-Smithsonian Center for Astrophysics, Cambridge, MA 02138, and School of Engineering & Applied Sciences, Harvard University, Cambridge, MA 02138

[3]Department of Chemistry and Biochemistry, University of Colorado, Boulder, CO 80309

[4]JILA, National Institute of Standards and Technology and University of Colorado, and Department of Physics, University of Colorado, Boulder, CO 80309

[5]Institut de Radioastronomie Millimétrique, 300 rue de la Piscine, F-38406, St-Martin d'Hères, France

[6]Universit Grenoble Alpes, IPAG, F-38000 Grenoble, France; CNRS, IPAG, F-38000 Grenoble, France

[8]Institute for Theoretical Chemistry, Department of Chemistry, The University of Texas at Austin, Austin, TX 78712

[9]I. Physikalisches Institut, Universität zu Köln, Zülpicher Str. 77, 50937 Köln, Germany

Abstract

We report the discovery in space of a disilicon species, SiCSi, from observations between 80 and 350 GHz with the IRAM[10] 30m radio telescope. Owing to the close coordination between laboratory experiments and astrophysics, 112 lines have now been detected in the carbon-rich star CW Leo. The derived frequencies yield improved rotational and centrifugal distortion constants up to sixth order. From the line profiles and interferometric maps with the Submillimeter Array[11], the bulk of the SiCSi emission arises from a region of 6″ in radius. The derived abundance is comparable to that of SiC_2. As expected from chemical equilibrium calculations, SiCSi and SiC_2 are the most abundant species harboring a Si–C bond in the dust formation zone and certainly both play a key role in the formation of SiC dust grains.

[10]This work was based on observations carried out with the IRAM 30-meter telescope. IRAM is supported by INSU/CNRS (France), MPG (Germany) and IGN (Spain)

[11]The Submillimeter Array is a joint project between the Smithsonian Astrophysical Observatory and the Academia Sinica Institute of Astronomy and Astrophysics, and is funded by the Smithsonian Institution and the Academia Sinica.

[7]Present address: Department of Chemistry, Marquette University, Milwaukee, WI 53233

Europe PMC Funders Author Manuscripts

Europe PMC Funders Group
Author Manuscript
Mon Not R Astron Soc. Author manuscript; available in PMC 2016 March 18.

Published in final edited form as:
Mon Not R Astron Soc. ; 453: 439–449. doi:10.1093/mnras/stv1634.

The abundance of $^{28}Si^{32}S$, $^{29}Si^{32}S$, $^{28}Si^{34}S$, and $^{30}Si^{32}S$ in the inner layers of the envelope of IRC+10216

J. P. Fonfría[1,*], **J. Cernicharo**[2], **M. J. Richter**[3,†], **M. Fernández-López**[4], **L. Velilla Prieto**[2], and **J. H. Lacy**[5,†]

[1]Departamento de Estrellas y Medio Interestelar, Instituto de Astronomía, UNAM, Ciudad Universitaria, 04510, Mexico City (Mexico)

[2]Grupo de Astrofísica Molecular, Instituto de Ciencia de Materiales de Madrid, CSIC, C/ Sor Juana Inés de la Cruz 3, 28049, Cantoblanco, Madrid (Spain)

[3]Physics Dept. - UC Davis, One Shields Ave., Davis, CA 95616 (USA)

[4]Instituto Argentino de Radioastronomía, CCT-La Plata (CONICET), C.C.5, 1894, Villa Elisa (Argentina)

[5]Astronomy Dept., University of Texas, Austin, TX 78712 (USA)

Abstract

We present high spectral resolution mid-IR observations of SiS towards the C-rich AGB star IRC +10216 carried out with the Texas Echelon-cross-Echelle Spectrograph mounted on the NASA Infrared Telescope Facility. We have identified 204 ro-vibrational lines of $^{28}Si^{32}S$, 26 of $^{29}Si^{32}S$, 20 of $^{28}Si^{34}S$, and 15 of $^{30}Si^{32}S$ in the frequency range 720 – 790 cm^{-1}. These lines belong to bands $v = 1 - 0$, 2 – 1, 3 – 2, 4–3, and 5–4, and involve rotational levels with $J_{low} \lesssim 90$. About 30 per cent of these lines are unblended or weakly blended and can be partially or entirely fitted with a code developed to model the mid-IR emission of a spherically symmetric circumstellar envelope composed of expanding gas and dust. The observed lines trace the envelope at distances to the star $\lesssim 35R_\star (\simeq 0''.7)$. The fits are compatible with an expansion velocity of $1+2.5(r/R_\star - 1)$ km s^{-1} between 1 and $5R_\star$, 11 km s^{-1} between 5 and $20R_\star$, and 14.5 km s^{-1} outwards. The derived abundance profile of $^{28}Si^{32}S$ with respect to H_2 is 4.9×10^{-6} between the stellar photosphere and $5R_\star$, decreasing linearly down to 1.6×10^{-6} at $20R_\star$ and to 1.3×10^{-6} at $50R_\star$. $^{28}Si^{32}S$ seems to be rotationally under LTE in the region of the envelope probed with our observations and vibrationally out of LTE in most of it. There is a red-shifted emission excess in the $^{28}Si^{32}S$ lines of band $v = 1 - 0$ that cannot be found in the lines of bands $v = 2 - 1$, 3 – 2, 4 – 3, and 5 – 4. This excess could be explained by an enhancement of the vibrational temperature around $20R_\star$ behind the star. The derived isotopic ratios $^{28}Si/^{29}Si$, and $^{32}S/^{34}S$ are 17 and 14, compatible with previous estimates.

* fonfria@astro.unam.mx.
† Visiting Astronomer at the Infrared Telescope Facility, which is operated by the University of Hawaii under contract from the National Aeronautics and Space Administration.

Europe PMC Funders Author Manuscripts

Europe PMC Funders Group
Author Manuscript
Astrophys J. Author manuscript; available in PMC 2015 December 23.

Published in final edited form as:
Astrophys J. 2015 December 1; 814(2): . doi:10.1088/0004-637X/814/2/143.

THE PECULIAR DISTRIBUTION OF CH_3CN IN IRC +10216 SEEN BY ALMA

M. Agúndez[1], **J. Cernicharo**[1], **G. Quintana-Lacaci**[1], **L. Velilla Prieto**[1], **A. Castro-Carrizo**[2], **N. Marcelino**[3], and **M. Guélin**[2]

[1]Instituto de Ciencia de Materiales de Madrid, CSIC, C/ Sor Juana Inés de la Cruz 3, 28049 Cantoblanco, Spain

[2]Institut de Radioastronomie Millimétrique, 300 rue de la Piscine, 38406 St. Martin d'Héres, France

[3]INAF, Istituto di Radioastronomia, via Gobetti 101, 40129 Bologna, Italy

Abstract

IRC +10216 is a circumstellar envelope around a carbon-rich evolved star which contains a large variety of molecules. According to interferometric observations, molecules are distributed either concentrated around the central star or as a hollow shell with a radius of ~15″. We present ALMA Cycle 0 band 6 observations of the $J = 14 - 13$ rotational transition of CH_3CN in IRC +10216, obtained with an angular resolution of $0\overset{''}{.}76 \times 0\overset{''}{.}61$. The bulk of the emission is distributed as a hollow shell located at just ~2″ from the star, with a void of emission in the central region up to a radius of ~1″. This spatial distribution is markedly different from those found to date in this source for other molecules. Our analysis indicate that methyl cyanide is not formed neither in the stellar photosphere nor far in the outer envelope, but at radial distances as short as 1-2″, reaching a maximum abundance of ~ 0.02 molecules cm^{-3} at 2″ from the star. Standard chemical models of IRC +10216 predict that the bulk of CH_3CN molecules should be present at a radius of ~ 15″, where other species such as polyyne radicals and cyanopolyynes are observed, with an additional inner component within 1″ from the star. The non-uniform structure of the circumstellar envelope and grain surface processes are discussed as possible causes of the peculiar distribution of methyl cyanide in IRC +10216.

Keywords

astrochemistry; line: identification; molecular processes; stars: AGB and post-AGB; circumstellar matter; stars: individual (IRC +10216)

1. INTRODUCTION

The chemical structure of the well known carbon-rich envelope IRC +10216 and, in general, of circumstellar envelopes around asymptotic giant branch (AGB) stars is in general terms well described by an scenario in which stable molecules are formed in the warm and dense

Europe PMC Funders Author Manuscripts

Europe PMC Funders Author Manuscripts

Europe PMC Funders Group
Author Manuscript
Astrophys J. Author manuscript; available in PMC 2016 March 18.

Published in final edited form as:
Astrophys J. 2016 February 20; 818(2): . doi:10.3847/0004-637X/818/2/192.

Hints of a rotating spiral structure in the innermost regions around IRC +10216

G. Quintana-Lacaci[1], **J. Cernicharo**[1], **M. Agúndez**[1], **L. Velilla Prieto**[1,2], **A. Castro-Carrizo**[3], **N. Marcelino**[4], **C. Cabezas**[5], **I. Peña**[5], **J.L. Alonso**[5], **J. Zúñiga**[6], **A. Requena**[6], **A. Bastida**[6], **Y. Kalugina**[7,8], **F. Lique**[7], and **M. Guélin**[3,9]

[1]Group of Molecular Astrophysics. ICMM, CSIC. C/ Sor Juana Inés de la Cruz 3, 28049 Cantoblanco, Madrid, Spain

[2]Centro de Astrobiología, INTA-CSIC. E-28691 Villanueva de la Cañada, Madrid, Spain

[3]Institut de Radioastronomie Millimétrique. 300 rue de la la Piscine, F-38406, Saint Martin d'Hères, France

[4]INAF, Istituto di Radioastronomia, via P. Gobetti 101, 40129, Bologna, Italy

[5]Grupo de Espectroscopía Molecular, Edificio Quifima, Laboratorios de Espectroscopía y Bioespectroscopía. Unidad asociada CSIC, Parque científico Uva, Universidad de Valladolid, Paseo de Belén 5, E-47011, Valladolid, Spain.

[6]Universidad de Murcia. Faculdad de Química. Dpto. de Química-Física. Campus Espinardo E-30100, Murcia, Spain

[7]LOMC-UMR 6294, CNRS-Université du Havre, 25 rue Philippe Lebon, BP. 1123, 76063 Le Havre cedex, France

[8]Department of Optics and Spectroscopy, Tomsk State University, 36 Lenin av., Tomsk 634050, Russia

[9]LERMA, Observatoire de Paris, PSL Research University, CNRS, UMR 8112, F-75014, Paris, France

Abstract

The Atacama Large Millimeter/submillimeter Array (ALMA) is allowing us to study the innermost regions of the circumstellar envelopes of evolved stars with **un-precedented** precision and sensitivity. Key processes in the ejection of matter and dust from these objects occur in their inner zones. In this work, we present sub-arcsecond interferometric maps of transitions of metal-bearing molecules towards the prototypical C-rich evolved star IRC +10216. While Al-bearing molecules seem to be present as a roughly spherical shell, the molecular emission from the salts NaCl and KCl presents an elongation in the inner regions, with a central minimum. In order to accurately analyze the emission **from** the NaCl rotational lines, we present new calculations of the collisional rates for this molecule based on new spectroscopic constants. The most plausible interpretation for the spatial distribution of the salts is a spiral with a NaCl mass of $0.08 M_{\odot}$. Alternatively, a torus of gas and dust would result in similar structures as those observed. **From**

Europe PMC Funders Author Manuscripts

Europe PMC Funders Group
Author Manuscript
Astrophys J. Author manuscript; available in PMC 2016 October 10.

Published in final edited form as:
Astrophys J. 2016 July 13; 825: .

High-Resolution Rotational Spectrum, Dunham Coefficients, and Potential Energy Function of NaCl

C. Cabezas[1], **J. Cernicharo**[2], **G. Quintana-Lacaci**[2], **I. Peña**[1], **M. Agundez**[2], **L. Velilla Prieto**[2], **A. Castro-Carrizo**[3], **J. Zuñiga**[4], **A. Bastida**[4], **J. L. Alonso**[1], and **A. Requena**[4]

[1]Grupo de Espectroscopía Molecular, Edificio Quifima, Laboratorios de Espectroscopía y Bioespectroscopía, Unidad asociada CSIC, Parque científico Uva, Universidad de Valladolid, Paseo de Belén 5, E-47011, Valladolid, Spain

[2]Group of Molecular Astrophysics, ICMM, CSIC. C/Sor Juana Inés de la Cruz 3, E-28049 Cantoblanco, Madrid, Spain

[3]Institut de Radioastronomie Millimétrique, 300 rue de la la Piscine, F-38406, Saint Martin d'Hères, France

[4]Universidad de Murcia. Faculdad de Química, Dpto. de Química-Física, Campus Espinardo E-30100, Murcia, Spain

Abstract

We report laboratory spectroscopy for the first time of the $J = 1–0$ and $J = 2–1$ lines of $Na^{35}Cl$ and $Na^{37}Cl$ in several vibrational states. The hyperfine structure has been resolved in both transitions for all vibrational levels, which permit us to predict with high accuracy the hyperfine splitting of the rotational transitions of the two isotopologues at higher frequencies. The new data have been merged with all previous works at microwave, millimeter, and infrared wavelengths and fitted to a series of mass-independent Dunham parameters and to a potential energy function. The obtained parameters have been used to compute a new dipole moment function, from which the dipole moment for infrared transitions up to $\Delta v = 8$ has been derived. Frequency and intensity predictions are provided for all rovibrational transitions up to $J = 150$ and $v = 8$, from which the ALMA data of evolved stars can be modeled and interpreted.

Keywords

astrochemistry; molecular data; molecular processes; radiative transfer; stars: AGB and post-AGB

1 Introduction

Metal halides were found in the circumstellar envelope of IRC+10216 by Cernicharo & Guelin (1987). Recently, the spatial distribution of some of these species has been analyzed using the ALMA interferometer (Cernicharo et al. 2013; Agúndez et al. 2015; Quintana-Lacaci et al. 2016). The increase of sensitivity provided by ALMA allows us to characterize the excitation mechanisms of the transitions of metal-bearing species in different vibrational states (Quintana-Lacaci et al. 2016). Most of the metal halides found in IRC +10216 have low values for their vibrational frequencies. Hence, vibrational levels could be excited by

Europe PMC Funders Author Manuscripts
Europe PMC Funders Author Manuscripts

CHAPTER

8

GENERAL DISCUSSION AND CONCLUSIONS

Circumstellar envelopes of evolved stars are crucial objects for the chemical evolution of the Universe, since they are major contributors to ISM enrichment. Thanks to our work, we have added several essential components to that evolutive picture, and we also have answered some of the open questions about chemical complexity in one of the most important stages of this evolution. In this chapter, we present a consolidating in which we comment on several topics that have been briefly described previously, and the main conclusions of this thesis.

8.1 General discussion

In this PhD thesis we have done a detailed study of the molecular content toward the CSEs of three evolved stars: IKTau, OH231.8+4.2, and IRC+10216. The study is based on the analysis of the spectral emission lines detected in the millimeter wavelength spectra of these sources, which have been observed with the instruments IRAM-30 m, Herschel Space Observatory-HIFI, and ALMA. Our work proves the value of observations of CSEs in the millimeter wavelength range, which have allowed us to determine their molecular content, their abundances, their spatial distribution, their excitation conditions, and the mechanisms that form these species.

Spectral line surveys

Spectral line surveys in the millimeter wavelength range are the best suited observational strategy for these molecular characterisation studies. Thanks to spectral line surveys we can consistently cover a wide spectral range of the spectrum of the source, which maximises the chances of detecting new species (Chapter 3). Additionally, line surveys foster the detection of an elevated number of lines arising from the same species, which would lead to the characterisation of different excitation conditions in different shells of the CSE.

Thanks to the spectral line surveys carried out with the IRAM-30 m radiotelescope we have updated the molecular inventory of IKTau (see Table 8.1) and OH231.8+4.2 (see Table 8.2). We have detected 19 different species toward IKTau and 23 toward OH231, excluding isotopologues in both cases. We have discovered more than 40% of all the species detected in IKTau (see Table 8.1), and approximately 60% of all the species detected in OH231 (see Table 8.2). We have observed different transitions for most of the species detected, which allowed us to characterise

Table 8.1: Molecular inventory of IKTau after our work

2-atoms		3-atoms		4 or more atoms
CO	^{13}CO	HCN	H_2S	NH_3
SiO	^{29}SiO	SO_2	H_2O	HC_3N
^{30}SiO	SiS	$H_2{}^{17}O$	$H_2{}^{18}O$	H_2CO
SO	NaCl	HNC	HCO^+	
CS	CN	H^{13}CN	$H_2{}^{34}S$	
PO	PN	$^{34}SO_2$		
OH	AlO			
NS	NO			
C^{18}O	Si^{17}O			
Si^{18}O	^{29}SiS			
^{30}SiS	Si^{34}S			
^{13}CS	C^{34}S			
^{34}SO				

Notes. Molecules in black were detected for the first time before our work (see Sect. 1.4.1.1), while molecules in red have been discovered thanks to our work.

exhaustively and unprecedentedly the excitation conditions and the circumstellar chemistry of these objects across the different envelope layers. We computed radiative transfer models with MADEX to determine the excitation conditions of the species observed, in particular for those molecules that are first detections. We also modelled the circumstellar chemistry under TE conditions and considering chemical kinetics for a standard O-rich CSE, as well as for the fast lobes of OH231. Additionally, we studied the impact on the chemistry that would have an enhancement of the initial nitrogen abundance, as well as how the chemistry of the ions depends on the initial H_2O abundance, and how the presence of a T_{eff} ∼10000 K companion star may alter the photoinduced chemistry. Our work has evidenced the main differences between a standard O-rich AGB CSE such as the CSE of IKTau with respect to a more evolved object (from the nebular point of view) like OH231 (see below). This work proves that the chemistry of O-rich CSEs is more active than previously thought, and it will serve as a future reference for circumstellar chemistry studies, in particular for O-rich objects.

Line surveys are very expensive in terms of observing time, which requires to plan the observations along different epochs. In our case, the spectral line surveys of IKTau and OH231 were carried out during more than five different observational runs between 2009 and 2014. This may have an impact on our results if the emission varies with time. Therefore, we have been able to investigate, and we continue investigating the time variability of the emission lines of the rotational transitions of molecules in CSEs of evolved stars. Our conclusion is that the results obtained are not compromised due to this variability and the uncertainties in the column densities and abundances derived are well below the uncertainties expected due to calibration.

Molecular complexity: C-rich versus O-rich

It is clearly evident that the molecular content of IKTau and OH231, in terms of molecular complexity and richness, cannot be compared to that of IRC+10216. Nevertheless, our results prove that the chemistry toward O-rich CSEs is more active than it was previously

Table 8.2: Molecular inventory of OH231.8+4.2 after our work

2-atoms		3-atoms		4 or more atoms
CO	^{13}CO	SO_2	H_2O	H_2CO
SO	OH	H_2S	HCN	NH_3
SiO	NS	H^{13}CN	HNC	$H_2{}^{13}CO$
CS	C^{18}O	HCO$^+$	H^{13}CO$^+$	HNCO
C^{17}O	^{29}SiO	OCS	HN^{13}C	HNCS
^{30}SiO	Si^{17}O	$H_2{}^{34}S$	$H_2{}^{33}S$	HC_3N
SiS	N^{34}S	O^{13}CS	OC^{34}S	H_3O^+
^{13}CS	C^{34}S	$^{34}SO_2$	$^{33}SO_2$	
C^{33}S	CN	N_2H^+		
^{34}SO	^{33}SO			
S^{18}O	NO			
SO$^+$				

Notes. Molecules in black were detected for the first time before our work (see Sect. 1.4.1.2), while molecules in red have been discovered thanks to our work.

thought (Velilla Prieto et al., 2015a, Sánchez Contreras et al., 2015, Velilla Prieto et al., 2017, and references therein). 22 different species are detected toward IKTau (excluding isotopologues, but including our detections and the AlO detection by De Beck et al. (2015)), and 24 species toward OH231 (including our detections), against the 79 species detected toward IRC+10216 (Cernicharo et al., 2000, Anderson & Ziurys, 2014, Cernicharo et al., 2015b, and references therein). There are also 12 different species detected in the C-rich CSE of CIT6 (Zhang et al., 2009a), 11 species toward the C-rich CSE of CRL 3068 (Zhang et al., 2009b), 19 species toward the C-rich pPN AFGL 2688 (Zhang et al., 2013), 27 toward the C-rich pPN CRL 618 (Pardo et al., 2007), or six species toward the CSE of the S-type star χ Cyg detected with Herschel (Schöier et al., 2011), or five species toward the CSE of the S-type star W Aql (Danilovich et al., 2014). Considering the number of species detected toward IKTau and OH231, both objects should be considered relatively rich among the aforementioned list of objects, close to CRL 618. IRC+10216 stands out among the rest of objects, trebling the number of species detected in its envelope compared to the second most rich object, CRL 618. This difference is partially explained as a result of an observational bias of IRC+10216, which has been and continues being the most observed CSE of the Universe. This in turn is justified due to the remarkable characteristics of this object, i.e. it is the most brilliant object of the IR sky ($\lambda \sim 5\mu$m), it is very close to us, and it has an intense mass loss rate (e.g. Cernicharo et al., 2015a, and references therein). Our work add more information and reduce this observational bias.

Stellar evolution and shocks: IKTau versus OH231

On the other hand, we analysed the differences between IKTau and OH231, which we have interpreted in terms of the evolutionary stage of both objects. It has been described the steps in the evolution of AGB CSEs toward the planetary nebula stage (see Sect. A.2). There are two main processes in this evolution: *i*) the mass loss cease, and *ii*) the rupture of the spherical symmetry due to the formation of fast winds. The cease of the mass loss results in the formation

of a cavity in the innermost part of the envelope, which will grow as the last ejected AGB wind expands out. This turns into a decrease of the density in this region, and also a decrease of the abundances of the molecules that are formed or excited efficiently in that region. This is the case of molecules like NaCl, PO, or the vibrationally excited states of species such as SiO. The emission of these species seems to arise from the innermost, densest and hottest regions of standard AGB CSEs like that of IKTau, as it is shown in Velilla Prieto et al. (2017). There is not emission of NaCl or PO toward OH231, and the analysis of the emission of SiS indicates a lower abundance compared to that of IKTau. Additionally, we have not detected emission lines of the different SiS isotopologues, and the rotational lines of vibrationally excited states of SiO are scarce and less intense than that of IKTau. These results evidence that there is a density decrease in the innermost region of OH231, that could be explained as the result of a decrease of its mass loss rate recently. This scenarios is consistent to the results presented by Sánchez Contreras et al. (2002), which indicate an attenuation of the SiO maser emission arising from a few stellar radii.

Interferometric maps of OH231 (e.g. Alcolea et al., 2001) show a dominant elongated distribution of the molecular material, deviating from the characteristic spherical symmetry of standard AGB CSEs. Our analysis proves that OH231 is, from the nebular point of view, in an intermediate evolutionary stage between the AGB and the PN phases.

The molecules that we have detected for the first time toward OH231, which have not been detected toward IKTau (Velilla Prieto et al., 2015a, Sánchez Contreras et al., 2015), are formed as a consequence of the changes that this object has experienced. The presence and formation of these molecules cannot be explained as a result of standard chemical processes or as a consequence of the chemistry of dust grains, as we deduced from our study including chemical models. Both objects are O-rich AGB CSEs, which should have a similar standard chemistry during the AGB stage. If the progenitor star of the CSE would have a mass of $\gtrsim 3 M_{\odot}$, it would be expected an enrichment in HBB products (such as the ^{14}N). However, such an enrichment due to HBB would not be enough to reproduce the observed abundances according to the results of our chemical models. We have also considered the presence of hotter stellar binary companion, which would produce an UV radiation field more intense than the UV ISRF, resulting in a different photoinduced chemistry in OH231 (Velilla Prieto et al., 2015a). Nevertheless, we ruled out this scenario considering that the inclusion of an extra source of ionisating/dissociating UV radiation in the chemical models is also unable to reproduce the observed abundances The chemical differences concerning to these N-bearing molecules and molecular ions, as well as the differences observed in other cases such as for S-bearing molecules, are a consequence of the shock processes experienced by the CSE of OH231.

Interferometric studies of IRC+10216

In the case of IRC+10216, we carried out observation with ALMA of the molecular emission in the innermost regions of IRC+10216 with an angular resolution below one arcsecond ($\lesssim 50 R_{*}$). Our work will serve as a future reference to understand the processes given in the region of the formation and condensation of dust grains in circumstellar envelopes. Interferometric maps provide the high angular resolution information that single-dish radiotelescopes lack in certain situations, and they also allow us to determine the radial abundance profiles of the molecules present in the CSEs. In particular, the observations with ALMA and NOEMA (see Chapter 7) toward IRC+10216 prove the spatial distribution of SiC_2, which is found to be the

most abundant Si-C bond bearing molecule in the innermost region of the CSE. The SiC_2 also reappears at a distance of $\sim$15″ from the star as a spherical hollow shell, which is the result of the photochemistry given in the outermost region of the CSE. These observations prove also that the rotational lines of vibrationally excited states of SiS (Velilla Prieto et al., 2015b) trace the excitation conditions of the innermost part of the CSE.

The high angular resolution that can be achieved with actual interferometers like ALMA, let us to tackle the problem of emission dilution if the emitting region is very small. As it is shown in Chapter 9 (see Fig. 9.1), we detected spectral emission lines in the millimeter spectrum of IRC+10216 as observed by NOEMA and ALMA, which were not detected with the IRAM-30 m telescope despite its sensitivity and the amount of time spent observing this source. Most of these lines remain unidentified, but they will probably arise from very compact regions ($\theta_s \ll \theta_{b,single-dish}$) of the CSE, which would explain why these lines cannot be detected with current single-dish telescopes. In the near future, it will be important to carry out spectral line surveys with interferometers and increase the instantaneous observable bandwidth of the receivers, as it is being prepared for future upgrades in NOEMA and the SMA.

8.2 Conclusions

➢ The main conclusions of this thesis from the study of IKTau are the following:

- we have obtained the most complete molecular census up to date of IKTau with a total of 19 different species detected, excluding isotopologues,

- we have detected for the first time toward this CSE emission lines of H_2CO, NS, NO, and HCO^+ (Velilla Prieto et al., 2017). We also detected for the first time emission lines of several isotopologues such as $C^{17}O$, $Si^{34}S$, or $C^{34}S$, among others,

- the lines of most of the species detected in IKTau have linewidths that indicate bulk gas expansion velocities consistent with the terminal expansion velocity of the CSE (v_∞=18.5 km s^{-1}). However, the lines of NaCl, PO, H_2O, the high-E_u SO_2 lines, and the lines of vibrationally excited species (e.g. SiO ν=1) display line profiles consistent with $v_{exp}<v_\infty$. These narrow profiles indicate emission of gas arising from the acceleration region ($\lesssim 8R_*$),

- the results from the rotational diagrams show that most of the molecules display rotational temperatures in the range between 15 and 40 K. CN has the lowest rotational temperature (i.e. 9 K) and the warm component of SO_2 displays the highest rotational temperature (i.e. 290 K),

- the total column densities of each species averaged in the emitting region range between $\gtrsim 1.3\times10^{17}$ cm^{-2} (in the case of ^{12}CO), and 2.6×10^{13} cm^{-2} (in the case of NS),

- we have detected emission lines of SO_2 that seem to arise from the innermost regions of the CSE (Velilla Prieto et al., 2017). In particular, we have detected 30 emission lines with E_u>160 K. Our analysis indicates that this emission must arise from the dust condensation region ($r < 8R_*$), which is in disagreement with the predictions made by chemical models, even for those that take into account the effect of shocks. These models must be revised in order to explain our results,

- among the species detected, we highlight the detection of H_2CO and NS for the first time in this source with abundances of f(H_2CO)$\sim$[10^{-7}–10^{-8}] and f(NS)$\sim10^{-8}$. We also estimated fractional abundances for the first time detected (in IK Tau) molecules HCO^+ and NO obtaining f(HCO^+)$\sim10^{-8}$ and f(NO)$\sim10^{-6}$,
- the detection of several C-bearing species like HCN, CS, H_2CO or CN with abundances of $\sim10^{-7}$ indicates an active carbon chemistry which is not expected given that most of the available carbon should be locked up into CO,
- current chemical models are unable to predict the abundances derived from our work in several cases such as NaCl or SO_2 (Velilla Prieto et al., 2017, and references therein),
- the study of the time variability of the intensity of the emission lines in the millimeter wavelength range shows that the intensity variations are limited. The variations are not significant for most of the lines detected in the spectral survey of IKTau (Velilla Prieto et al., 2017). The intensity variations registered for the rotational lines in the ground vibrational state are below the level of the calibration uncertainty. We only registered significant intensity variations for the vibrationally excited lines.

➢ The main conclusions of this thesis from the study of OH231.8+4.2 are the following:

- we have obtained the most complete molecular census up to date of OH231 with a total of 23 different species detected, excluding isotopologues,
- we have detected for the first time emission lines of HNCO, HNCS, HC_3N, NO, SO^+, N_2H^+, and tentatively H_3O^+ (Velilla Prieto et al., 2015a, Sánchez Contreras et al., 2015). This object shows a particularly rich chemistry of N-bearing species and ions,
- the line profiles of OH231 are varied. Some species display lines compatible with emission that arises from the central slow region of the CSE and also from the fast lobes (such as CO or SO_2), lines of other species (such as SiS) are consistent with emission arising only from the central component. There is also emission of some molecules that seems to be enhanced toward the fast lobes (e.g. HCO^+),
- the rotational temperatures of most of the molecules are in the range between 15 and 40 K,
- the total column densities of each species averaged in the emitting region range between $\gtrsim6.6\times10^{17}$ cm^{-2} (in the case of ^{12}CO), and 2.3×10^{12} cm^{-2} (in the case of $Si^{17}O$),
- the detection of N-bearing species and molecular ions toward OH231, together with the non-detection of these species toward IKTau and our analysis, indicates that these species are neither efficiently formed through standard chemical processes (chemical equilibrium, photochemistry, or gas-phase chemistry) nor as a consequence of dust grains chemistry (Velilla Prieto et al., 2015a, Sánchez Contreras et al., 2015, Velilla Prieto et al., 2017). Additionally, the abundances of these species cannot be explained as a consequence of a N-enrichment or as a result of the photochemistry induced by a hotter stellar companion. The main difference between IKTau and OH231 is the passage of shocks in OH231 $\sim$800 years ago, as a result of the interaction between the high velocity bipolar jets and the standard AGB CSE. The shocks should have dissociated the material of the CSE. After the dissociation, the chemistry should have evolved under different conditions compared to the initial conditions given during the formation of the AGB CSE, which should explain the presence of these species.

➢ The main conclusions of this thesis from the ALMA high spatial resolution study of IRC+10216 are the following:

- the rotational lines of vibrationally excited states of SiS (up to v=7 and tentatively up to v=10) detected toward IRC+10216 with ALMA, arise from the innermost, densest, and hottest regions of its CSE (Velilla Prieto et al., 2015b). These observations prove the excitation conditions of the dust condensation region (r <20R_*), with an excitation temperature of ∼1700 K for the SiS lines in with v=2–7,

- the ALMA Cycle 0 maps of the ^{29}SiO J=6–5 emission line toward IRC+10216 show a clumpy extended distribution, which is elongated in the NE-SW direction (Velilla Prieto et al., 2015b). This elongation indicates a preferential direction of the emission, which may evidence the presence of a bipolar outflow as a result of the presence of a binary companion (Cernicharo et al., 2015a). The elongation is also seen in the central component of the emission of SiC_2,

- the studies carried out with the IRAM-30 m telescope, NOEMA, and ALMA toward IRC+10216, prove that the SiC_2 is the most abundant Si-C bond bearing molecule in the innermost region of the CSE (Velilla Prieto et al., 2015b). This scenario is consistent with the lack of SiC in the gas-phase, which may condense onto the dust grains as a major constituent of them in the CSE of IRC+10216, and C-rich CSEs in general.

CAPÍTULO

8

DISCUSIÓN GENERAL Y CONCLUSIONES

Las envolturas circunestelares de estrellas evolucionadas son objetos cruciales para entender la evolución química del Universo, pues son los principales responsables del enriquecimiento del medio interestelar. Con nuestro trabajo hemos dado respuesta a algunas de las cuestiones abiertas sobre la complejidad química en una de las fases más importantes dentro de dicho esquema evolutivo. En este capítulo se presenta una discusión integradora en la que se comentan algunos aspectos que han sido descritos anteriormente de manera breve, junto con las principales conclusiones extraídas en esta tesis.

8.1 Discusión general

En esta tesis se ha llevado a cabo un análisis detallado del contenido molecular de las envolturas circunestelares de tres estrellas evolucionadas: IKTau, OH231.8+4.2 e IRC+10216. Este estudio se basa en el análisis de las líneas espectrales de emisión que se detectan en el espectro milimétrico de estas fuentes, y que ha sido observado principalmente con los instrumentos IRAM-30 m, HIFI de Herschel y ALMA. Nuestro trabajo demuestra el valor que aportan las observaciones de envolturas circunestelares en el rango de longitud de onda milimétrico, que nos ha permitido determinar su contenido molecular, las abundancias de dichas especies y su distribución espacial, las características de su excitación, y los mecanismos que forman estas especies.

Barridos espectrales de líneas

Los barridos espectrales de líneas de emisión en el rango de longitud de onda milimétrico son la estrategia observacional adecuada para este tipo de estudios de caracterización molecular. Esta estrategia de observación nos permite cubrir de manera consistente un amplio rango espectral, lo que maximiza las posibilidades de detección de nuevas especies (Capítulo 3). Adicionalmente, los barridos espectrales permiten detectar un mayor número de líneas de una misma especie, lo que produce resultados detallados que abarcan las distintas condiciones de excitación que se dan en diferentes capas de la envoltura.

Gracias a los barridos espectrales llevados a cabo con el radiotelescopio de IRAM-30 m hemos actualizado el inventario molecular en IKTau (ver Tabla 8.1) y en OH231.8+4.2 (ver Tabla 8.2).

En total hemos detectado 19 especies distintas en IKTau y 23 en OH231, sin tener en cuenta isotopólogos en ambos casos. Hemos descubierto más del 40 % de todas las especies que han sido detectadas en IKTau (ver Tabla 8.1), y aproximadamente el 60 % en el caso de OH231 (ver Tabla 8.1). Para todas las especies detectadas se han observado diferentes transiciones, lo que nos ha permitido caracterizar las condiciones de excitación y la química circunestelar, a lo largo de las distintas capas de la envoltura, de ambos objetos de manera exhaustiva y sin precedentes. Hemos llevado a cabo modelos de transferencia radiativa con MADEX para determinar las condiciones de excitación de dichas especies, en especial para las moléculas que representan nuevas detecciones. También hemos modelizado la química circunestelar en condiciones de equilibrio termodinámico y teniendo en cuenta la cinética química, para una envoltura estándar rica en oxígeno y también para la química que se daría en los lóbulos rápidos de OH231. Además, hemos estudiado como afectaría el enriquecimiento de nitrógeno a esta química, cómo depende la química de los iones de la abundancia inicial de H_2O y cómo influye la fotoquímica inducida por la presencia de una estrella binaria más caliente (T_{eff} ∼10000 K) que el objeto central de las envolturas. Nuestro trabajo nos ha permitido determinar las principales diferencias entre una envoltura estándar rica en oxígeno como la de IKTau con respecto a un objeto más evolucionado (al menos desde el punto de vista nebular) como OH231 (ver más adelante). Nuestro trabajo demuestra que la química de envolturas ricas en oxígeno es bastante más activa de lo que se pensaba con anterioridad, y servirá de referencia para futuros estudios de química circunestelar, en particular para estos objetos ricos en oxígeno.

Tabla 8.1: Inventario molecular en IKTau tras nuestro trabajo

2-átomos		3-átomos		4 o más átomos
CO	^{13}CO	HCN	H_2S	NH_3
SiO	^{29}SiO	SO_2	H_2O	HC_3N
^{30}SiO	SiS	$H_2{}^{17}O$	$H_2{}^{18}O$	H_2CO
SO	NaCl	HNC	HCO^+	
CS	CN	$H^{13}CN$	$H_2{}^{34}S$	
PO	PN	$^{34}SO_2$		
OH	AlO			
NS	NO			
C^{18}O	Si^{17}O			
Si^{18}O	^{29}SiS			
^{30}SiS	Si^{34}S			
^{13}CS	C^{34}S			
^{34}SO				

Notes. Se muestran en negro las moléculas detectadas por primera vez previamente a nuestro trabajo (ver Sec. 1.4.1.1) y en rojo aquellas que se han descubierto gracias a nuestro trabajo.

Los barridos espectrales de líneas son costosos en términos de tiempo de observación, por lo que se requiere realizar observaciones en distintas épocas. En nuestro caso, las observaciones correspondientes a los barridos espectrales de IKTau y OH231 se han realizado durante más de cinco campañas distintas entre 2009 y 2014. Por esta razón hemos podido investigar, y continuamos investigando, la variabilidad temporal de la emisión de líneas rotacionales de moléculas en las envolturas circunestelares de estrellas evolucionadas. Nuestra conclusión es que los resul-

Tabla 8.2: Inventario molecular en OH231.8+4.2 tras nuestro trabajo

2-átomos		3-átomos		4 o más átomos
CO	^{13}CO	SO_2	H_2O	H_2CO
SO	OH	H_2S	HCN	NH_3
SiO	NS	H^{13}CN	HNC	$H_2{}^{13}CO$
CS	C^{18}O	HCO$^+$	H^{13}CO$^+$	HNCO
C^{17}O	^{29}SiO	OCS	HN^{13}C	HNCS
^{30}SiO	Si^{17}O	$H_2{}^{34}S$	$H_2{}^{33}S$	HC_3N
SiS	N^{34}S	O^{13}CS	OC^{34}S	H_3O^+
^{13}CS	C^{34}S	$^{34}SO_2$	$^{33}SO_2$	
C^{33}S	CN	N_2H^+		
^{34}SO	^{33}SO			
S^{18}O	NO			
SO$^+$				

Notes. Se muestran en negro las moléculas detectadas por primera vez previamente a nuestro trabajo (ver Sec. 1.4.1.2) y en rojo aquellas que se han descubierto gracias a nuestro trabajo.

tados obtenidos no están comprometidos por dicha variabilidad y que las incertidumbres que se obtienen en las densidades de columna y las abundancias, están dentro de las incertidumbres que se esperan por la calibración de los datos.

Complejidad molecular: carbono frente a oxígeno

Es evidente que la emisión en IKTau y OH231 en términos de complejidad y riqueza molecular es incomparable con la emisión molecular en IRC+10216. No obstante, nuestros resultados demuestran que la química en objetos ricos en oxígeno es más activa de lo que se especulaba en los primeros trabajos de caracterización molecular en envolturas circunestelares de estrellas AGB (Velilla Prieto et al., 2015a, Sánchez Contreras et al., 2015, Velilla Prieto et al., 2017, y referencias ahí). En IKTau se detectan 22 especies distintas (excluyendo isotopólogos, contando nuestras detecciones y el AlO por De Beck et al. (2015)) y 24 especies en OH231 (contando nuestras detecciones), frente a las 79 detectadas en IRC+10216 (Cernicharo et al., 2000, Anderson & Ziurys, 2014, Cernicharo et al., 2015b, y referencias ahí), las 12 que se detectan en la envoltura rica en carbono de CIT6 (Zhang et al., 2009a), las 11 de la envoltura rica en carbono CRL 3068 (Zhang et al., 2009b), o las 19 especies de la pPN rica en carbono AFGL 2688 (Zhang et al., 2013), las 27 de la pPN rica en carbono CRL 618 (Pardo et al., 2007), o las que 6 se detectan en la estrella tipo S χ Cyg mediante observaciones con Herschel (Schöier et al., 2011), o las 5 detectadas en la estrella tipo S W Aql también gracias a Herschel (Danilovich et al., 2014). En la comparación de la cantidad de especies detectadas en todos estos objetos, observamos que las envolturas de IKTau y OH231 serían consideradas relativamente ricas en especies, cerca del número de CRL 618. IRC+10216 se distingue claramente del resto de objetos, triplicando el número de especies que se detectan en su envoltura con respecto de la segunda fuente más rica, CRL 618. Esta diferencia se explica parcialmente por un sesgo observacional de IRC+10216, que ha sido y continúa siendo la envoltura circunestelar más observada del Universo. A su vez este sesgo observacional esta justificado por las

características del objeto, i.e. es el objeto más brillante del cielo IR ($\lambda \sim 5\mu$m), se encuentra muy cerca de nosotros, y tiene una tasa de pérdida de masa intensa (e.g. Cernicharo et al., 2015a, y referencias en el artículo). Nuestras observaciones añaden más información y permiten continuar reduciendo este sesgo observacional.

Evolución estelar y choques: IKTau frente a OH231

Por otro lado encontramos las diferencias entre IKTau y OH231, que interpretamos en un sentido evolutivo de ambos objetos. En la Sección A.2 se detallan los cambios que experimentan las envolturas circunestelares de estrellas AGB, en su evolución a la etapa de nebulosa planetaria. Principalmente son dos: *i*) el cese del proceso de pérdida de masa, y *ii*) la ruptura de la simetría esférica por la aparición de vientos rápidos. La detención de la pérdida de masa provoca que se cree una cavidad en el interior de la envoltura, que irá creciendo a medida que el gas expulsado en el último viento AGB se expanda. Esto supone que la densidad en esa zona disminuirá, y que la abundancia de las moléculas que antes se formaban allí (o se ven excitadas en esas regiones) de manera eficiente disminuya. Este es el caso de moléculas como NaCl, PO, o las líneas vibracionalmente excitadas de especies como SiO, que como se muestra en Velilla Prieto et al. (2017) provienen de esas regiones densas, calientes e internas de las envolturas estándar de estrellas AGB como IKTau. En OH231, no hay presencia de emisión de NaCl o de PO, las líneas de SiS indicarían una abundancia no muy elevada y además no se detectan sus isotopólogos. Las líneas rotacionales de niveles vibracionalmente excitados de SiO son también escasas en OH231. Estos resultados evidencian que en la zona interna de OH231 existe un decremento de densidad, que podría explicarse como consecuencia de una disminución importante de su ritmo de pérdida de masa en épocas recientes. Este escenario es consistente además con las observaciones realizadas por Sánchez Contreras et al. (2002), que indican un debilitamiento de la emisión de los máseres de SiO que proceden de unos pocos radios estelares.

Los mapas interferométricos de OH231 (e.g. Alcolea et al., 2001) muestran claramente una distribución elongada para la componente molecular, desviándose así de la simetría esférica característica de las estrellas AGB estándar. Nuestro análisis demuestra por tanto que OH231 se encuentra, desde el punto de vista nebular, en una fase evolutiva intermedia entre la etapa AGB y la etapa de nebulosa planetaria.

Las moléculas que detectamos por primera vez en OH231 pero que no han sido detectadas en IKTau (i.e. los iones moleculares y las moléculas HNCO, HNCS y HC_3N, Velilla Prieto et al., 2015a, Sánchez Contreras et al., 2015) se forman probablemente como consecuencia de los cambios que ha experimentado este objeto. La presencia de estas moléculas no se puede explicar como un efecto de la química estándar o como consecuencia de la química de granos de polvo tal y como hemos deducido de nuestro estudio incluyendo modelos químicos. De ser así, no existe una razón que diferencie ambos objetos dado que ambos son envolturas circunestelares de estrellas AGB ricas en oxígeno. Si la estrella progenitora de OH231 tuviera una masa $\gtrsim 3M_{\odot}$ cabría esperar un enriquecimiento en productos de HBB (como el ^{14}N). Sin embargo, este enriquecimiento debido al HBB no sería suficiente para explicar las abundancias observadas de estas moléculas, a la vista de los resultados de nuestros modelos químicos. También hemos considerado la presencia de una estrella binaria más caliente que pudiera producir un campo UV más intenso que el UV ISRF, modificando la fotoquímica en la envoltura de OH231 (Velilla Prieto et al., 2015a). La inclusión de este aumento de radiación ionizante/disociante en nuestros modelos tampoco puede explicar la presencia de dichas moléculas con abundancias

como las observadas. Las diferencias químicas, en relación a estas moléculas ricas en nitrógeno y los iones, como también se observan en otros casos como las moléculas que contienen azufre, se deben por tanto al proceso de choque que ha sufrido la envoltura de OH231.

Estudios interferométricos de IRC+10216

En el caso de IRC+10216, hemos llevado a cabo observaciones con ALMA de la emisión molecular en regiones muy cercanas a la estrella IRC+10216 con una resolución angular inferior al segundo de arco ($\lesssim 50 R_*$). Nuestro trabajo servirá de futura referencia para comprender los procesos que se dan lugar en la región de formación y condensación del polvo en envolturas circunestelares. Los mapas interferométricos, nos dan la información espacial de alta resolución que los radiotelescopios de antena única no pueden alcanzar, y nos permiten determinar los perfiles radiales de abundancias de las moléculas presentes en envolturas circunestelares. En particular, las observaciones con ALMA y NOEMA (ver Capítulo 7) de IRC+10216, prueban por ejemplo la distribución de SiC_2, que resulta ser la molécula portadora de enlaces Si-C más abundante en la zona interna de la envoltura, y que además reaparece en forma de capa esférica hueca a unos $\sim 15''$ de la estrella, como producto de la fotoquímica que se da en la región externa. Estas observaciones prueban también que las líneas rotacionales de niveles vibracionales excitados como las observadas en Velilla Prieto et al. (2015b) trazan las condiciones de excitación de las regiones más internas.

La alta resolución angular que se puede alcanzar actualmente con estos instrumentos permite evitar el problema de la dilución de la emisión cuando la región emisora es muy pequeña. Como se ha mostrado en el Capítulo 9 (ver Fig. 9.1), a pesar de la gran sensibilidad de los receptores instalados en los radiotelescopios de antena única, se detectan líneas de emisión en el espectro milimétrico de IRC+10216 obtenido con NOEMA y ALMA que no se han detectado previamente con IRAM-30 m. A pesar de que la mayor parte de estas líneas permanezcan sin identificar, es muy probable que la emisión provenga de regiones muy compactas ($\theta_s \ll \theta_{b,single-dish}$) y por esta razón la señal de estas líneas no sea detectable actualmente con radiotelescopios de antena única. En el futuro, será importante realizar barridos espectrales con interferómetros, a medida que los receptores de estos instrumentos incrementen el ancho de banda instantáneo registrable, como actualmente se está preparando para NOEMA y SMA.

8.2 Conclusiones

➢ Las principales conclusiones obtenidas en esta tesis a partir del estudio de IKTau son las siguientes:

- hemos obtenido el censo de moléculas más completo hasta la fecha de IKTau con un total de 19 especies distintas, excluyendo isotopólogos,
- hemos descubierto por primera vez en esta envoltura líneas de emisión de las moléculas H_2CO, NS, NO y HCO^+, en la envoltura circunestelar de IKTau (Velilla Prieto et al., 2017). Hemos detectado por primera vez líneas de algunos isotopólogos, como $C^{17}O$, $Si^{34}S$, o $C^{34}S$ entre otros,
- las líneas de la mayor parte de especies detectadas en IKTau tienen anchuras que indicarían velocidades de expansión compatibles con la velocidad terminal de expansión (v_∞=18.5 km s^{-1}). Sin embargo, las líneas de NaCl, PO, H_2O, las líneas de SO_2 con alta-E_u, y las líneas de especies

vibracionalmente excitadas (e.g. SiO ν=1) mostrarían perfiles compatibles con $v_{\rm exp}<v_{\infty}$. Estos perfiles estrechos indicarían emisión de gas que vendría de la región de aceleración ($\lesssim 8R_*$),

- los resultados de los diagramas rotacionales muestran que la mayoría de las moléculas tienen temperaturas rotacionales comprendidas entre 15 y 40 K. CN tiene la temperatura rotacional más baja (i.e. 9 K) y la componente caliente de SO_2 la más alta (i.e. 290 K),

- las densidades de columna promediadas para la región emisora que estimamos varían entre $\gtrsim 1.3\times10^{17}$ cm^{-2} para ^{12}CO y 2.6×10^{13} cm^{-2} para NS,

- hemos detectado líneas de emisión de SO_2 en la envoltura circunestelar que se producirían en sus regiones más internas (Velilla Prieto et al., 2017). En particular, hemos detectado 30 líneas de emisión con $E_{\rm u}>160$ K. Nuestro análisis indica que esta emisión debe provenir de la región de condensación de polvo ($r<8R_*$), lo que está en desacuerdo con las predicciones de los modelos de química, incluso aquellos que tienen en cuenta los efectos de los choques. Estos modelos deben revisarse para poder explicar los resultados de nuestras observaciones,

- entre las especies detectadas, reseñamos la detección del H_2CO y el NS por primera vez en este objecto con abundancias de f(H_2CO)$\sim$[10^{-7}–10^{-8}] y f(NS)$\sim10^{-8}$. Hemos estimado también abundancias fraccionales de las moléculas detectadas por primera vez en esta fuente HCO^+ y NO, obteniendo f(HCO^+)$\sim10^{-8}$ y f(NO)$\sim10^{-6}$,

- la detección de varias moléculas que contienen carbono como el HCN, CS, H_2CO o el CN, con abundancias de $\sim10^{-7}$ indica una química de carbono activa, lo que no es esperable considerando que la mayor parte de carbono disponible debería estar en forma de CO,

- los modelos químicos actuales no son capaces de predecir las abundancias derivadas de nuestro trabajo en algunos casos como el NaCl o el SO_2 (Velilla Prieto et al., 2017, y referencias en el artículo),

- el estudio de la variabilidad de las intensidades de las líneas de emisión en el rango milimétrico muestra que dichas variaciones son limitadas. Estas variaciones no son significativas en el caso de la mayor parte de líneas estudiadas en el barrido espectral de IKTau (Velilla Prieto et al., 2017). Las variaciones de intensidad registradas para líneas rotacionales del nivel vibracional fundamental están por debajo del nivel considerado como incertidumbre de calibración. Sólo en el caso de líneas de niveles vibracionales excitados hemos registrado variaciones de intensidad significativas.

➢ Las principales conclusiones obtenidas en esta tesis a partir del estudio de OH231 son las siguientes:

- hemos obtenido el censo de moléculas más completo hasta la fecha de OH231 con un total de 23 especies distintas, excluyendo isotopólogos,

- hemos detectado por primera vez líneas de emisión de las moléculas HNCO, HNCS, HC_3N, NO, SO^+, N_2H^+ y tentativamente H_3O^+ (Velilla Prieto et al., 2015a, Sánchez Contreras et al., 2015). Este objeto muestra una química particularmente activa de especies que contienen nitrógeno e iones,

- las líneas observadas en OH231 muestran perfiles de diversos tipos. Algunas especies muestran líneas de emisión que proviene de la zona central de expansión lenta de la envoltura circunestelar y también de los lóbulos rápidos (como CO o SO_2), la emisión de otras especies (como la del SiS) parece provenir sólo de la zona central. Existe también emisión de algunas moléculas que parece estar favorecida en los lóbulos de la nebulosa (e.g. HCO^+),

- las temperaturas rotacionales de la mayor parte de las moléculas se encuentran comprendidas entre 15 y 40 K,

- las densidades de columna promediadas para la región emisora que estimamos varían entre $\gtrsim 6.6\times10^{17}\,cm^{-2}$ para ^{12}CO y $2.3\times10^{12}\,cm^{-2}$ para el $Si^{17}O$,

- la detección de líneas con nitrógeno e iones moleculares en OH231, y su no detección en IKTau, junto con nuestro análisis, indica que estas especies no se forman de manera eficiente por procesos de química estándar (química en equilibrio, fotoquímica, o reacciones estándar en fase gas), y tampoco como consecuencia de la química de granos de polvo (Velilla Prieto et al., 2015a, Sánchez Contreras et al., 2015, Velilla Prieto et al., 2017). No se puede tampoco explicar mediante un enriquecimiento de nitrógeno, ni como resultado de la fotoquímica inducida por la presencia de una estrella binaria más caliente. La diferencia principal entre IKTau y OH231 es la presencia de procesos de choques en este último, hace unos 800 años, debidos a la interacción de chorros bipolares de alta velocidad con la envoltura AGB estándar. Estos choques disociaron el material de la envoltura, y con el tiempo la evolución de la química en condiciones distintas a las iniciales han dado lugar a la reformación de nuevas especies como las que se detectan.

➢ Las principales conclusiones obtenidas en esta tesis sobre el estudio de alta resolución espacial con ALMA en el objeto IRC+10216 son las siguientes:

- las líneas rotacionales de niveles vibracionalmente excitados de SiS (hasta v=7 y tentativamente hasta v=10) detectadas en IRC+10216 gracias a la resolución angular y sensibilidad de ALMA, provienen de las regiones más internas, calientes, y densas de la envoltura (Velilla Prieto et al., 2015b). Estas observaciones prueban las condiciones de excitación en la zona de condensación del polvo (r <20R_*), determinando una temperatura de excitación de ∼1700 K para las líneas J=15–14 de SiS en los niveles vibracionales v=2–7,

- los mapas obtenidos con ALMA durante el Ciclo 0 de la emisión de la línea J=6–5 de ^{29}SiO en IRC+10216 muestran una distribución extensa, grumosa, y elongada en la dirección noreste-sudoeste (Velilla Prieto et al., 2015b). Esta elongación indica una dirección preferente de dicha emisión, que podría evidenciar la presencia de un flujo bipolar como consecuencia de la presencia de una estrella binaria (Cernicharo et al., 2015a). La elongación se observa también en la componente central de emisión de SiC_2,

- los estudios realizados con IRAM-30 m, NOEMA y ALMA, demuestran que el SiC_2 es la molécula mas abundante portadora de enlaces Si-C en la región interna de IRC+10216, por encima del SiC y del SiCSi (Velilla Prieto et al., 2015b). Este escenario es consistente con que el SiC prácticamente desaparezca de la fase gas en esa región interna para condensar como uno de los principales constituyentes de los granos de polvo en la envoltura de IRC+10216, y en envolturas ricas en carbono en general.

CHAPTER

9

CURRENT AND FUTURE WORK

Our work will serve as a reference for future studies of the molecular emission in CSEs of evolved stars, in particular toward the two O-rich CSEs IK Tau and OH231.8+4.2, and toward the most studied C-rich object, IRC+10216. However, these CSEs are far from being completely understood. In this section I describe my current work and my perspective about how to tackle some of the unsolved enigmas in the field of the CSEs of evolved stars.

9.1 Current work

SO_2 in the innermost regions of IK Tau

The millimeter surveys that we carried out with the IRAM-30 m antenna (Chapter 3) have motivated subsequent studies of both IK Tau and OH231.8+4.2 CSEs. For example, the presence of SO_2 with abundances of $\sim 10^{-6}$ in the innermost regions of O-rich CSEs is not reproduced by TE or shock models. Consequently, chemical kinetic models include SO_2 as a parent molecule and adopt an ad hoc input SO_2 abundance. None of the chemical models proposed explained how SO_2 can be found close to the stellar surface with such high abundances in O-rich stars (Gobrecht et al., 2016, Li et al., 2016). Thanks to the sensitivity and spatial resolution provided by ALMA, interferometric observations of SO_2 toward IK Tau will provide additional information to characterise the emission of SO_2, and discover how SO_2 is distributed and formed in the innermost regions of the CSE. Our group requested high spatial resolution observations with ALMA to confirm the presence of SO_2 close to the stellar surface of IK Tau which should be considered for future investigation of the main formation channels of S-bearing parent species in the inner winds of O-rich AGB stars. This project, for which I am the principal investigator, has been graded A and it is going to be observed during the current ALMA Cycle 4.

Si-C bond bearing molecules toward IRC+10216

Concerning the C-rich CSE of IRC+10216, the work presented in Chapter 6 and our recent discoveries about Si-C bearing molecules have motivated a subsequent study with NOEMA and ALMA. Si-C bearing molecules (SiC, Si_2C, and SiC_2) are closely related to the dust formation processes in the envelopes of C-rich stars given that grains are mainly composed of silicon carbide and also carbonaceous material. These molecules are efficiently formed in gas phase, close to the stellar photosphere as a consequence of different chemical processes. Then, in

the dust formation region, which extends up to a few stellar radii from the photosphere (∼5-20 $R_\star$), these molecules are likely to condense onto dust grains due to their highly refractory nature. Beyond this region, the abundances of Si-C bearing molecules are expected to decrease until they are eventually reformed in the outer shells of the circumstellar envelope due to the interaction between the gas and the UV ISRF. We proposed to map the emission of several lines of Si_2C, SiC, and SiC_2 toward IRC+10216. The proposed observations will allow us to characterise their spatial distribution, and study their radial abundance profiles as well as the chemical processes that form these molecules at intermediate and large spatial scales, and the time-dependent chemical evolution of Si-C bonds carriers through the circumstellar envelope of IRC+10216. This project has been recently observed with NOEMA, and complemented with short-spacing observations with the IRAM-30 m telescope. Additionally, this project has been graded B for ALMA Cycle 4 observations and it is currently being observed. I am the principal investigator of these proposals.

Other studies

I am also involved in other different studies and proposals, for example to study the variability of the emission of rotational lines in the millimeter wavelength range toward AGB CSEs, or to explore the chemical richness of the Ring Nebula, among others.

9.2 Future approach to several unsolved problems

Chemical differentiation and observational bias

Sensitive millimeter wavelength surveys are excellent observational strategies to provide exhaustive information about physical and chemical processes in AGB CSEs. However, only a limited number of these studies have been carried out, which may result in a relative bias on the conclusions derived for particular objects. For example, IK Tau is often taken as a reference for O-rich CSE, or IRC+10216 as the archetype of C-rich CSE, but some of their properties, or the molecules found in their CSEs, could be different for other C- and O-rich objects. Thus, additional observational efforts should be carried out in order to reduce that bias.

Concerning to the chemical evolution of AGB stars, some authors have recently proposed that young AGB stars display an O-rich chemistry while late AGB stars display a C-rich chemistry (Kwon & Suh, 2014, and references therein). In this scenario, CSEs surrounding S-type stars could represent a transition stage between O- and C-rich CSEs. This theory could motivate subsequent studies of S-type objects. It would be interesting to carry out a sensitive millimeter wavelength survey toward the CSE of a S-type star, such as χ Cygni, with the IRAM-30 m telescope.

Spectral line surveys with interferometers

Aperture synthesis will play a key role in the future discoveries toward AGB CSEs, in particular with the fully development of the SMA, NOEMA, and ALMA. Sensitive high angular resolution observations of AGB CSEs with interferometers are revealing how molecules are distributed toward IRC+10216 (e.g. Agúndez et al., 2015, Velilla Prieto et al., 2015b, Quintana-Lacaci et al., 2016). Furthermore, these observations surprisingly revealed hundreds of unidentified lines

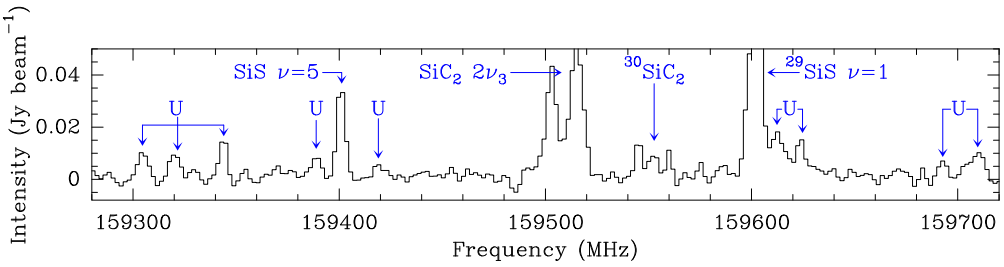

Figure 9.1: Spectrum of IRC+10216 in the millimeter wavelength range observed with NOEMA, where several unidentified (U) lines are shown. The spectral resolution is ∼2 MHz and the synthesised beam is ∼2.″5.

which were not observed with single-dish telescopes despite the increasing number of observations made in recent years (see Fig. 9.1). In this context, further observational and laboratory efforts must be carried out to detect more emission lines and be able to identify these lines. From the technical point of view, it would be interesting to improve the bandwidth and sensitivity of the receivers currently installed on antenna arrays in order to make feasible (in terms of observing time) very high-spatial resolution spectral line surveys in the (sub)millimeter wavelength range.

The launching mechanism of pPN outflows

Additionally, ALMA may offer the opportunity to extend previous research works concerning the launching mechanisms in pPN objects. One of the most interesting stages of stellar evolution of low-mass stars, is the transition phase between the AGB and the PN phase, that is the post-AGB or pre-PN stage. During this stage, the mass-loss experienced by the AGB star decreases dramatically, and the circumstellar envelope, composed of gas and dust, begins to detach from the central star. The nebular evolution is complex. From the spherical symmetry usually seen toward the CSEs of AGB stars, they shift to bipolar, multipolar, ring, spiral or irregular structures, with the presence of discs and/or toroids, as a consequence of the shock interaction between the dense, slow AGB envelope and the fast post-AGB wind (see Fig. A.4). The mechanisms that feeds this interaction are not well understood, despite the large number of studies performed toward several pPNs (e.g. Bujarrabal et al., 2001, Sahai et al., 2008). The presence of binary systems and magnetic driven jets has been proposed to explain the formation of these outflows that depict some of the most beautiful objects of the Universe (Zijlstra, 2007, Sahai et al., 2011). High spatial resolution observations of molecular shock tracers such as SiO, SO or HCO^+ (Pineau des Forets et al., 1993, Bachiller & Pérez Gutiérrez, 1997) may prove the regions where this interaction between the fast jets and the slow AGB wind occurs. Moreover, polarisation studies can be carried out in these objects in order to understand the role of magnetic fields in the launching mechanism of pPN outflows by studying paramagnetic molecules such as SO, or highly polarised emission lines (e.g. masers) (e.g. Vlemmings, 2014).

Complete chemical modelling: dust grains chemistry

The presence of C-bearing molecules in O-rich CSEs and vice versa is one of the unsolved problems of AGB CSEs. The current chemical models cannot reproduce the abundances observed of these molecules. One of the the paths that should be followed in order to investigate

this problem would be to create a complete chemical model that comprises TE and chemical kinetics with non equilibrium processes (e.g. shocks) and incorporate the gas-grain chemistry. This would require not only further observational efforts but also laboratory characterisation of different processes, e.g. gas-dust interaction. J. Cernicharo, J. A. Martín-Gago, and C. Joblin are PIs of the NANOCOSMOS ERC project which is finishing the construction of the so-called *Stardust* machine. This machine will be able to simulate the physical conditions given in the CSE of an AGB star, and will create typical AGB dust grains that can be used in different experiments (e.g. involving interaction with different gases). Therefore, some of the most non-studied physical processes may be reproduced in the laboratory, resulting in input for AGB CSEs chemical models.

APPENDIX

A

CIRCUMSTELLAR ENVELOPES: BASIC CONCEPTS

In this appendix we summarised the basic concepts about circumstellar envelopes, that is, stellar evolution, evolution of circumstellar envelopes, and their physico-chemical properties. A complete discussion on this topic can be found in the revision text by Habing & Olofsson (2003).

A.1 Brief description of stellar evolution

Main sequence stars with masses between 0.8 to $8M_{\odot}$ go through the AGB phase at the late stages of their lives (Iben & Renzini, 1983, Habing & Olofsson, 2003). An example of their evolutionary track can be seen in Fig. A.1. These stars, which are mainly composed of H, transform this H into He during the main sequence by nuclear reactions, i.e. the proton-proton chain. At the end of the main sequence, the H in the core is exhausted, leaving an inert He core and a H envelope. When the fusion reactions stop in the core, the balance between hydrostatic pressure and gravitational force becomes unbalanced in favour of the gravitational force. Therefore, the core begins to contract. At this point the star enters the so-called RGB phase.

During the red giant stage, the core of the star continues its contraction, which increases progressively its temperature. H-shell nuclear fusion into He is active in the innermost regions of the H envelope, which causes the expansion of the envelope due to the pressure of this H-shell fusion layer acting on the outermost layers of the star. The effect of this expansion is a decrease of the surface temperature, which together with the increasing radius, lead to an increase of the brightness of the star. Thus, these objects will move up in the HR diagram and will enter in the E-AGB stage. The end of the RGB stage and the beginning of the E-AGB phase will be determined by the mass of the star.

The stars that have reached the end of the RGB stage with masses lower than 1.8-2.2$M_{\odot}$ will experience a He flash in their nucleus. This means that the triple alpha fusion processes (which transform He into C and O) have started in an explosive way. The violent ignition in the nucleus is due to the degeneracy pressure of electrons. The energy generated is absorbed in a controlled way by the outer layers of the star, and the degenerate state of the nucleus disappears. If the star has a mass greater than 1.8-2.2$M_{\odot}$, the nuclear fusion of He into C and O, will not start explosively and the core will not reach a degenerate state. At this point of their evolution, stars will experience a kind of second main sequence stage, where its main fuel is the nuclear fusion of He in the core. This phase is known as HB.

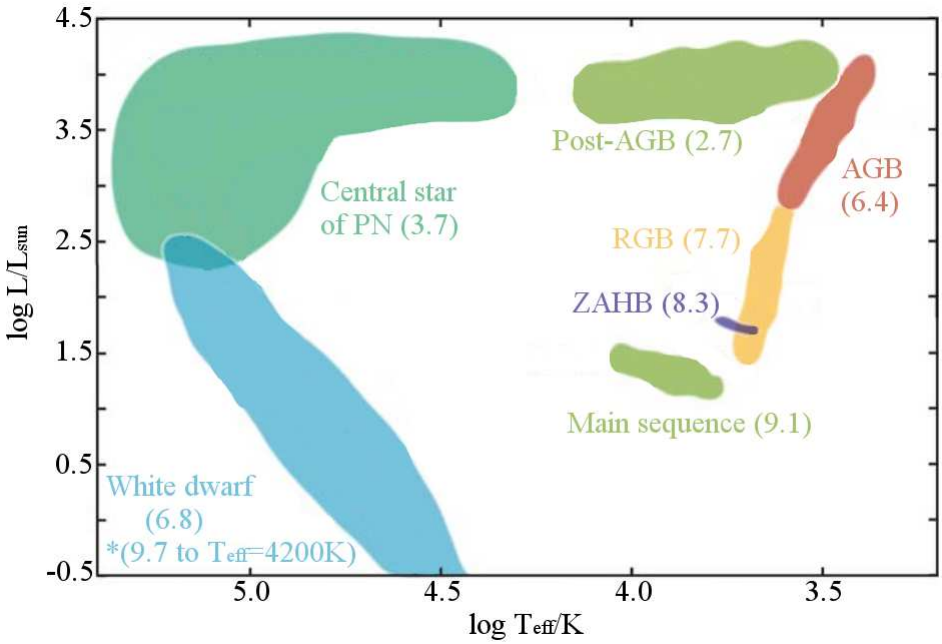

Figure A.1: Herztsprung–Russell diagram of a $2\,M_{\odot}$ star with solar metallicity, from the main sequence to the white dwarf phase. The numbers shown in each stage correspond to the logarithm of time (in years) that each stage will last. *(Credits: Adapted from Herwig (2005))*

While this nuclear fusion of He into C and O occurs in the core of the star, the surrounding envelope also experience changes. During the RGB phase, the star has a He inert core, immediately after a H-burning shell, and the outermost part is a convective envelope composed mainly of H. If the convective envelope penetrates more deep toward the H-burning shell, the material processed in this shell may be transported to the external layers of the star, this is known as the first dredge-up. The elements that will be mixed into the outermost layers are mainly the products of the proton-proton chain and the CNO cycle, which may occur if the star is more massive than $1M_{\odot}$. In the case of stars with masses greater than 3.5-4$M_{\odot}$ a second dredge-up will occur owing to the convective transport of the elements produced in a He-burning shell around the core to the outermost layers of the star (see Fig. A.2). This material is then essentially composed of ^{4}He and ^{14}N (Busso et al., 1999, and references therein).

The changes of the envelope, explained before, occur during the so-called E-AGB stage. The He-burning region has started to move toward more external zones of the star, in a similar way that H-burning shell moved during the end of main sequence phase (and start of the RGB phase). The star will have a radius of $\sim 10^{13}$ cm and an effective temperature of 2000-3000 K. The structure of the star, similar to that observed in Fig. A.2 (right), will begin to vary in the H-burning and He-burning layers. This phase is known as TP-AGB phase. At this stage thermal pulses will occur, causing changes to the brightness of the star, its temperature, and its size. The He-burning shell lead to an expansion of the outer layers. This expansion implies that the outer shells will cool down, deactivating the H-burning shell. The expansion will continue until the deactivation of the He-burning shell (due to the same cool down), then, the gravitational collapse of the outermost shells will start, and the temperature of these layers will progressively increase. The temperature increase will reactivate the H-burning, and the resulting material of this nuclear fusion will fall in the He shell. Eventually, the He shell will have enough density and temperature to reactivate the He-burning, and the process will

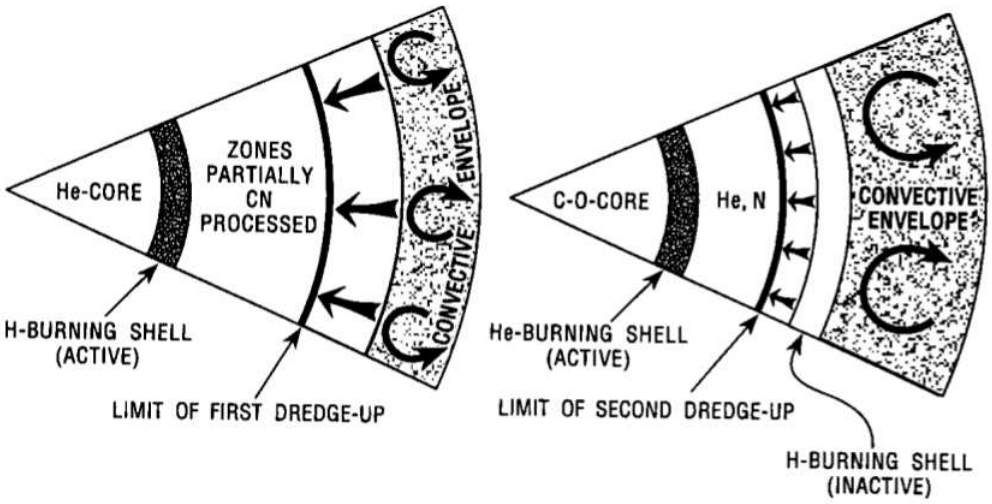

Figure A.2: Sketch of the stellar interior of RGB (left) and E-AGB (right) star, where the dredge-up processes are shown. *(Credits: Busso et al. (1999))*

complete one cycle or thermal-pulse. The time between thermal pulses is estimated to be 1 or 2 years.

During the pulsation of the star, due to nuclear fusion in alternating layers of He and H, two important processes occur: the third dredge-up, and the mass loss, which will create a CSE. The third [1] dredge-up occurs causing the mix of material between the He- and H-burning shells. These thermal pulses may cause that the convective envelope penetrates beyond the H-burning shell, thus, the fusion products of the He-burning shell may be transported to the outermost layers of the star (mainly ^{12}C). If this phenomenon is repeated in successive thermal pulses, the atmosphere of the star will become C-rich (instead of O-rich). This will be critical for the CSE chemistry, as discussed in Sect. A.3. For more massive stars ($\gtrsim 3 M_{\odot}$, although this value may vary with the star metallicity), carbon nuclear fusion may occur at the bottom region of the convective envelope, which will enrich the atmosphere of the star with C-burning products. This process is known as HBB (e.g. Sackmann & Boothroyd, 1992).

The other important effect of thermal pulsation, which is key in the context of this PhD thesis, is the mass loss that AGB stars experience, and which will create a CSE composed mainly of molecular gas and dust. The mass loss rates of AGB stars can reach values up to 10 $^{-4}\,M_{\odot}$ year^{-1}, and it can last up to 10^5 years. After the AGB stage, the mass loss will cease, the stellar envelope[2] will become optically transparent and the photosphere will retract back quickly to the C and O core. The star has left the AGB phase and becomes a blue dwarf, with a surface temperature of $\sim$50000 K and a radius of $\sim$10 ^{11} cm, which will dissociate and ionise the circumstellar material, creating a PN. Meanwhile, the star will continue its contraction which leads to an increase of the surface temperature, but it will not produce enough heating up in the core to activate the nuclear fusion of the triple alpha products. The star has reached the beginning of the end of its life, the white dwarf stage.

[1] In the case of stars with masses lower than 3.5-4$M_{\odot}$ this is actually the second dredge-up.

[2] This term refers to the stellar envelope, i.e. the He- and H-burning shells plus the H convective envelope. Do not mislead this term with the term circumstellar envelope.

A.2 Formation, evolution, and properties

A.2.1 Formation

During the TP-AGB phase, AGB stars experience a mass loss, i.e. an outflow of gas and dust expelled from the surface of the star as a stellar wind. The most accepted mechanism for the formation of this stellar wind in the AGB phase, which leads to the formation of a CSE, relies on the stellar pulsation (e.g. Morris, 1987b, Sedlmayr & Dominik, 1995, Gail & Sedlmayr, 2014, and references therein). Pulsation in the TP-AGB phase generates waves which propagates through the outermost shells, i.e. shockwaves which drive a stellar wind that reaches average mass loss rates of $10^{-6}\,M_{\odot}$ year^{-1} for long-period variable stars (Mira-type) (e.g. Loup et al., 1993). The physical conditions given in these winds (high densities and low temperatures) allow the formation of molecules and dust grains. In particular, the star would develop a circumstellar shell of dust. In the case of irregular or semi-irregular variable stars, the mass loss rate can reach values of 10^{-8}-$10^{-6}\,M_{\odot}$ year^{-1}, and consequently it generates little amounts of dust grains. At the time that the dust shell is created in the atmosphere of the star, the radiation pressure exerted on the dust grains overcomes the gravitational force acting on the material, since these objects have large luminosities ($10^{4}\,L_{\odot}$). Thus, the material is ejected from the surface of the star (dragging also the gas), with mass loss rates that can reach values as high as $10^{-4}\,M_{\odot}$ year^{-1}. Therefore, CSEs of evolved stars are the main source of ISM enrichment.

This formation mechanism of CSEs is probably the most accepted. Although, there are alternative processes that have been proposed to explain the mass loss mechanism, which could at least partially account for it. For example, it has been investigated, the influence of radiation pressure on molecules (Maciel, 1977, Jorgensen & Johnson, 1992), which could explain the formation of a levitating shell near the photosphere. Pijpers & Hearn (1989) investigated the effect of sound waves as the wind driving mechanism, resulting in mass losses of 10^{-7} to $10^{-4}\,M_{\odot}$ year^{-1}. However, these models have not been fully accepted since several authors pointed out that sound waves should be blocked and reflected by the shock front, and therefore, shock waves should be unable to drive the stellar wind (e.g Wood, 1990). Finally, Alfven waves could explain mass loss rates of up to $10^{-7}\ M_{\odot}$ year^{-1}, although these magnetohydrodynamical models are highly parametrized, so this theory is considered somewhat uncertain and should be further investigated (Holzer & MacGregor, 1985, Airapetian et al., 2000).

A.2.2 Evolution

As the central star evolves, so does the circumstellar envelope. The mass loss occurs during the TP-AGB phase, and it seems to occur episodically, as observed in the IR and the millimeter wavelength ranges (e.g. Olofsson et al., 1996a, 2000, Marengo et al., 2001). AGB CSEs are highly symmetric, displaying spherical shapes, more or less extended depending on the amount of ejected mass (Fig. A.3). At the end of the AGB phase, the mass loss ceases, and the CSE begins to detach from its progenitor star. Additionally, deviations from spherical symmetry are observed in more evolved transitional (between the AGB and PN stages) objects with different shapes (e.g. bipolar, multipolar or elliptical, see Fig. A.4). The mechanism for the spherical symmetry breakdown is still not well known, and there are various theories that point to the emergence of strong and fast highly collimated bipolar winds, during the pPN phase which may occur due to the presence of a companion star or the presence of magnetic fields (e.g. Balick & Frank, 2002, De Marco, 2009, Vlemmings et al., 2012).

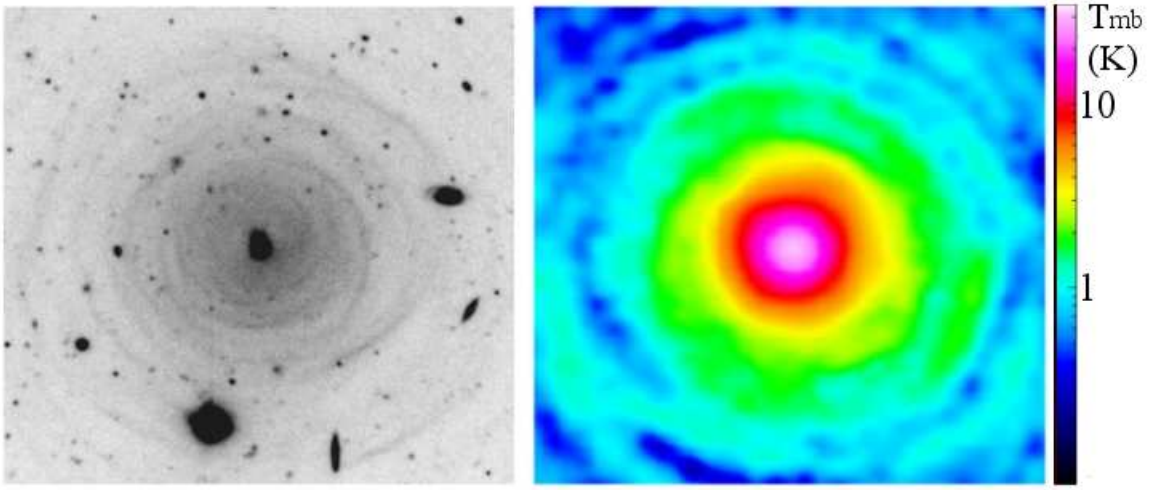

Figure A.3: Left, V-band image (550 nm) centred toward the C-rich CSE IRC+10216, in a 90″×90″field (North is up and East to the left). The CSE is observed as a set of circular arcs owing to the dust scattering of the Galactic light. Right, the CO J=2–1 line emission is shown for the systemic velocity of the source, as observed by the IRAM-30 m radiotelescope for the same field on the sky. *(Credits: Mauron & Huggins (2010) and Cernicharo et al. (2015a))*

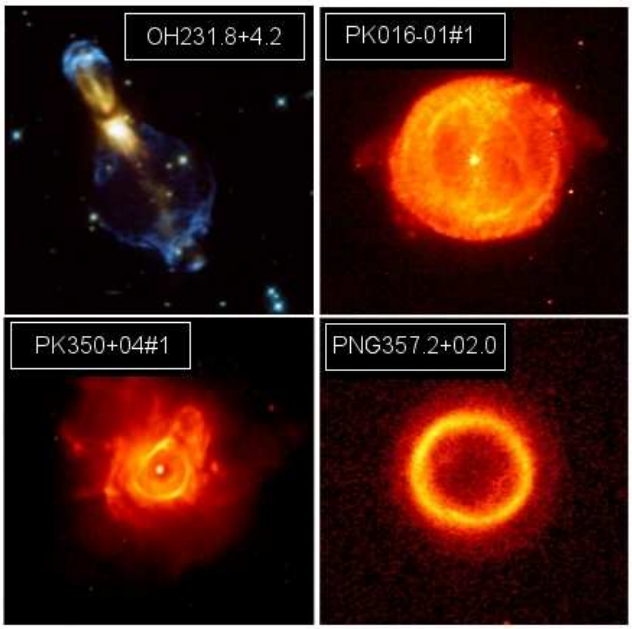

Figure A.4: Top-left, false colour image of OH231.8+4.2 (see Sect. 1.4.1.2) (Sánchez Contreras et al., 2004). The rest of the images are false colour images of young planetary nebulae observed with the HST (Sahai et al., 2011). *(Credits: Sahai et al. (2011) and HST/ESA V. Bujarrabal)*

A.2.3 Observations

The first observations of variable stars were reported in the sixteenth and seventeenth centuries, in particular toward the Mira star in the constellation Cetus (see e.g. the introduction of Habing & Olofsson, 2003). Concerning CSEs, the birth of a whole observational discipline occurred in the twentieth century, in the IR wavelength range, thanks to the California Institute of Technology K-band (2.0-2.4 μm) and I-band (0.7-0.9 μm) sky survey, which gave rise to the 2.2 μm IRC sky survey (Neugebauer & Leighton, 1969). And also thanks to the IRAS satellite, which took spectra in the range of 8-23 μm and photometry at 12, 25, 60 and 100 μm.

As already indicated, AGB stars have low surface temperatures of 2000-3000 K, therefore, the spectral energy distribution of an AGB star displays an emission maximum at wavelengths of $\sim$1 μm, according to Wien's Law (as discussed in Sect. B.2.1). However, it must be considered the composition of the CSE (mainly molecular gas and dust) so that EM radiation emitted by the star will be blocked by dust (i.e. dust extinction). Therefore, the star light may be impossible to observe in the visible wavelength range (except for partial reflection into dust grains in certain directions), and the emission maximum should be redshifted (up to 10 μm). The CSEs can be also observed in the IR wavelength range where bands produced by solid constituents of dust particles, like SiC at 11.3 μm, and also the bands and lines corresponding to molecular vibrational and ro-vibrational transitions, lie (e.g. Speck et al., 2000, Zijlstra et al., 2006, Fonfría et al., 2008, and references therein). This wavelength range, has been observed with excellent results by the ISO and Herschel satellites.

Nevertheless, concerning to the millimeter wavelength range and molecular emission, which is the main objective in the analysis of this thesis, we can observe spectral lines produced due to the change of rotational state of molecules (in the fundamental or ground vibrational state as well as in excited vibrational states). For example CO, which is the most abundant molecule (after H_2) in CSEs, presents rotational transitions of its ground vibrational level that produce lines at 2.6 mm ($\sim$ 115 GHz), 1.3 mm ($\sim$230 GHz), and 0.9 mm ($\sim$345 GHz). In particular, the first detected molecule in a CSE was CO, its J=1–0 line at 2.6 mm with the NRAO Kitt Peak antenna toward IRC+10216 (Solomon et al., 1971). New molecular detections in the millimeter wavelength range toward CSEs have occurred thanks to the development of better receivers and new radio telescopes. As it will be shown throughout this thesis, we can obtain a lot of information about the chemical composition and the physical conditions (densities, temperatures, mass loss rate, ...) of the CSEs through the study of the molecular rotational lines that arise from these objects.

Note that CSEs are generally named accordingly to the central object of the CSE (i.e. the star), and correspond mainly to the mentioned catalogues. For example:

- the IRAS objects, which are followed by two numbers that correspond to their right ascension (hours, minutes and tenths of minutes) and declination (degrees and minutes with its sign) in abbreviated J1950.0 coordinates, such as IRAS09425-6040,

- the IRC objects, which are followed by the declination in degrees rounded to a multiple of 10 (e.g. +10 if the declination is in the range between +5° and +15°) with its sign, and then followed by an ordinal number indicating its order within that declination band, e.g. IRC+10216, which is the 216$^{\text{th}}$ object in the +10° declination band,

- the OH objects, because they display maser emission of OH. They are often followed by their galactic coordinates (OH231.8+4.2) or their abbreviated right ascension and declination

(OH739-14),

- the CRL or AFCRL objects (Walker, 1975), which were renamed AFGL or RAFGL after the rename of the Cambridge Research Laboratory to the Air Force Geophysics Laboratory. The revised catalogue (Price & Murdock, 1983), originally comprised the objects 1 to 3000 for the objects detected in northern hemisphere flights (rockets launched by the American Air Forces with initial military purposes), and the objects 4001 to 4036 for the southern hemisphere flights, such as RAFGL2688,

- objects named according to the GCVS (e.g. Samus et al., 2004), whose names correspond to the constellation in where they are located, preceded by a letter code which refers to the number in the catalogue, such as CW Leo,

- or named according to their shape (Calabash Nebula), or the discoverer (Westbrook Nebula) or other characteristics.

A.2.4 Physical properties of CSEs

As described above, an AGB CSE, is a cloud composed of gas and dust, expanding into the ISM, and with spherical symmetry, that surrounds the AGB star. The radial dependence of the most important physical properties of a CSE, which are decribed below, are shown in Fig. A.5.

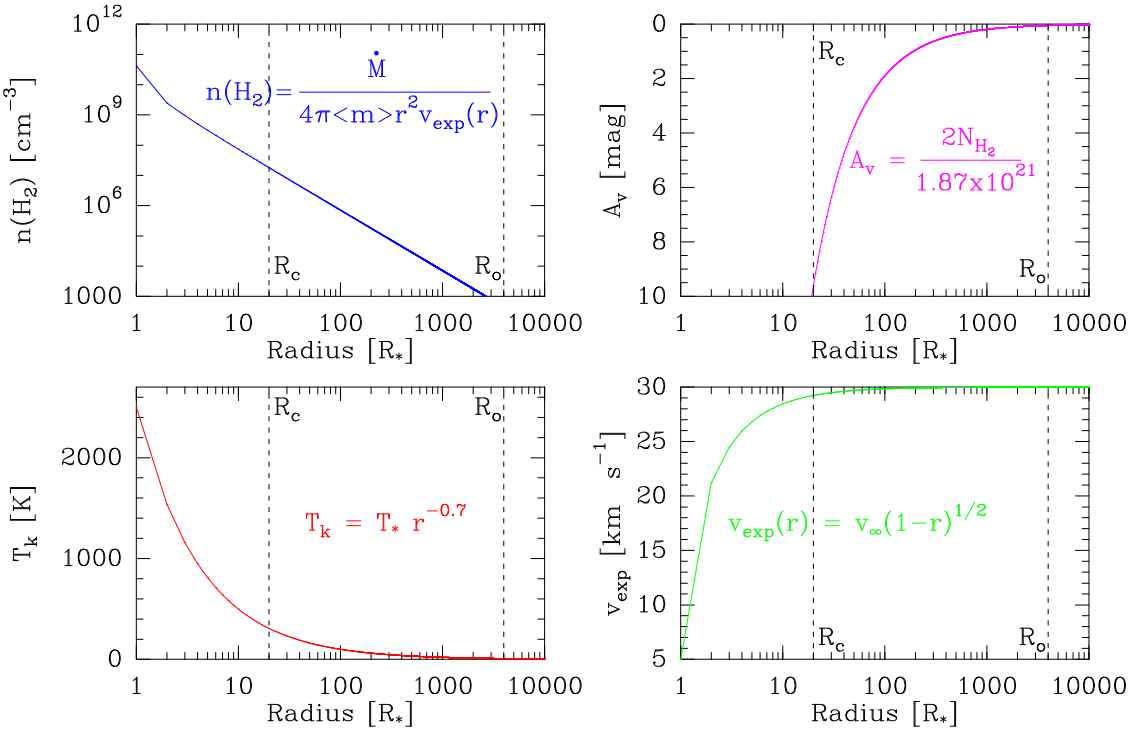

Figure A.5: Physical properties of the CSE of a star with a radius of $2.5{\times}10^{13}$ cm, a mass loss rate of $10^{-5}\,M_{\odot}$ year^{-1}, an effective temperature of 2500 K, and a terminal expansion velocity (v_{∞}) of 30 km s^{-1}. The represented physical laws are given by Eqs.(A.1), (A.9), (A.12) and (A.15), where it has been considered that the CSE is composed of H_2. The dashed lines marked with a "R_c" and "R_o" indicate an approximated radius for the dust condensation region ($20R_*$) and the outer radius of the CSE ($\sim 10^{17}$ cm$\equiv 4000R_*$)

The density of an expanding (at constant velocity) CSE is given, in general, by the continuity equation:

$$n(r) = \frac{\dot{M}}{4\pi r^2 \langle m \rangle v_{exp}(r)} \quad [cm^{-3}] \tag{A.1}$$

where $\dot{M}$ is the mass loss rate of the star, r is the distance to the star, $\langle m \rangle$ is the average mass of the particles forming the gas (which is usually considered mainly H and He, so that is equal to 2.3 amu), and $v_{\rm exp}$ the expansion velocity of the envelope. This equation explains quite accurately most observations of CSEs (e.g. Bujarrabal & Alcolea, 1991, Olofsson, 1996b, and references therein), although, there are deviations from this equation in the regions where the gas has not reached the terminal expansion velocity, particularly in the regions closest to the stellar photosphere, where the presence of shocks due to the pulsation of the star can modify the density. In the region of the stellar photosphere, the density is determined by the hydrostatic equilibrium (balance between pressure which tends to expand the star, and gravity which tends to collapse it):

$$\frac{\partial P}{\partial r} = -\rho(r) g(r) \tag{A.2}$$

where g is the gravitational field (GM_*/r^2), ρ the density, and P the pressure. Therefore, for a temperature law like $T(r) \propto r^{-\alpha}$ (as we will see below), we obtain:

$$\rho(r) = \rho(R_*) \exp\left\{ -\frac{R_*}{H_o(R_*)(1-\alpha)} \left[1 - \left(\frac{r}{R_*} \right)^{(\alpha-1)} \right] \right\} \tag{A.3}$$

where R_* is the radius of the star, α is the exponent of the temperature dependence discussed below, and $H_{\rm o}$ is the *height scale* or *height increase*:

$$H_o(r) = \frac{kT(r)}{\langle m \rangle g(r)} \tag{A.4}$$

with k the Boltzmann's constant. Eq.(A.3) should be valid in the static atmosphere, which extends from the photosphere to the region of shocks formation (1-1.2R_*) (see e.g. Cherchneff et al., 1992). Beyond this region, and up to the dust condensation region (∼5-8R_*), also called dynamic atmosphere, the density radial dependence, i.e. Eq.(A.3), must be corrected of the effect of the shocks due to the stellar pulsation (e.g Bowen, 1988). This correction is applied introducing average values of the physical quantities in the momentum equation:

$$\frac{Dv}{Dt} = \frac{\partial v}{\partial t} + v \frac{\partial v}{\partial r} = -\frac{GM_*}{r^2} - \frac{1}{\rho} \frac{\partial P}{\partial r} \tag{A.5}$$

where Dv/Dt denotes the *material derivative* also called *Lagrangian derivative*, which results in the following expression for the density (see e.g. Wilson & Bowen, 1984, Cherchneff et al., 1992):

$$\rho(r) = \rho(r_o) \exp\left\{ -\frac{r_o(1-\gamma^2)}{H_o(r_o)(1-\alpha)} \left[1 - \left(\frac{r}{r_o} \right)^{(\alpha-1)} \right] \right\} \tag{A.6}$$

where $r_{\rm o}$ is the radius where shocks are formed (1-1.2R_*), and γ a dimensionless parameter used to scale the fluid velocity in the shock ($v = \gamma\, v_{\rm exp}$).

The kinetic temperature of the gas (T_k) will be determined by solving the first law of thermodynamics, applied to the gas in the CSE:

$$\frac{du}{dt} = \frac{P}{\rho^2}\frac{d\rho}{dt} + \frac{dq}{dt} \tag{A.7}$$

where du/dt is the internal energy variation (per unit mass) over time, and dq/dt is the variation of heat (also per unit mass). Eq.(A.7) expresses the energy balance between the work done by the gas due to expansion, and the amount of heat exchanged in the interaction of the gas particles. With the continuity equation (Eq.(A.1)), the ideal gas law ($P = \rho RT$), and Eq(A.7), we obtain:

$$\frac{1}{T}\frac{dT}{dr} = \frac{-4}{3r}\left(1 + \frac{\epsilon}{2}\right) + \frac{8\pi r^2}{3kT\dot{M}}(H - C) \tag{A.8}$$

where ϵ is the logarithmic velocity gradient with respect to the radius logarithm (i.e. $\epsilon = d\ln(v)/d\ln(r) = \frac{r}{v}dv/dr$), H is the gas heating rate (per unit mass), C is the gas cooling rate (also per unit mass), and where it is assumed that the adiabatic coefficient is γ= 5/3 (Goldreich & Scoville, 1976). In the case of an adiabatic expansion (the cooling of the CSE occurs due to expansion without any heat exchange) and for ϵ=1, we would have a dependency $T(r) \propto r^{-4/3}$. However, there are several heat exchanging processes between the gas in the CSE and the medium, therefore, Eq.(A.8) is only an approximated solution to the real situation.

Heating will occur primarily by collisional processes between gas and dust caused indirectly by radiation pressure on the dust grains, which will drag in its movement gas particles, causing collisions and friction between gas and dust. The cooling of the envelope, occurs owing to the emission of photons produced in de-excitation processes (either radiative or collisional) that are produced by the rotational and vibrational state changes of the most abundant molecules in the CSE, such as CO or HCN in the case of C-rich CSEs, and H_2O in O-rich CSEs. Cooling by H_2 would be only important for regions with high kinetic temperatures (Groenewegen, 1994, and references therein). Other heating and cooling processes considered by different authors, are often considered insignificant (though they may dominate in specific regions of the envelope), like heating due to photoelectric effect by UV ISRF ionisation of molecules, or photodissociation of molecules, or photoionisation of atomic carbon (see e.g. Goldreich & Scoville, 1976, Huggins et al., 1988, Groenewegen, 1994).

Finally, considering as main heating sources the gas-dust shocks, and as sources of cooling, the expansion of the envelope and molecular emission lines, the solution of Eq.(A.8) results in the following expression for the kinetic gas temperature of a CSE:

$$T_k(r) = T_k(r_0)\left(\frac{r}{r_0}\right)^{-\alpha} \tag{A.9}$$

where $T_k(R_0)$ is the kinetic temperature at a point R_0 which is usually taken as the effective temperature of the star (T_*), and α the parameter that describes the temperature variation, which usually has values of 0.5-1 (e.g. Goldreich & Scoville, 1976, Bujarrabal et al., 1989, Groenewegen, 1994, Decin et al., 2010b, and references therein).

Another important parameter of CSEs is the expansion velocity. As it has been said before, the most accepted mechanism to explain the formation and expansion of a CSE is the radiation pressure on dust grains which causes an acceleration of the dust grains, that also drag the gas particles in their expansion (see e.g. Kwok, 1975). The equation of motion of a dust grain

located at a distance r from the centre of the star can be written (in scalar form on a given radial direction) as (Kwok, 1975):

$$m_d \frac{dv_d}{dt} = F_{rad} - F_{grav} - F_{dr} = \frac{\bar{Q}\pi a^2 L_*}{4\pi c r^2} - m_d \frac{GM_*}{r^2} - \alpha\pi\rho_d a^2 v_{dr}(c_s^2 + v_{dr}^2)^{1/2} \tag{A.10}$$

where m_d is the mass of a dust grain, v_d the speed of a dust grain, F_{rad} is radiation force, F_{grav} the gravitational force, F_{dr} the drag force, $\bar{Q}$ the ratio between the radiation pressure cross section and the geometric cross section of the dust grains (i.e. a cross section efficiency), a the dust grain size, L_* the luminosity of the star, c the speed of light, G the gravitational constant, M_* the mass of the star, α is a parameter that defines the elasticity of the collision between a gas particle and a dust grain (it would be equal to 1 if the collision is elastic), ρ_d is the density of a dust grain, v_{dr} is the drag speed (the speed that a dust grain has when it moves through a space region occupied by gas particles that are moving with a Maxwellian velocity distribution), and c_s is the speed of sound through the medium (c_s=$\sqrt{\gamma kT/m_g}$, where γ is the adiabatic coefficient of the gas and m_g the mass of the particles in gas phase).

In the case of gas particles, the equation of motion is slightly different. The transfer of momentum by radiation pressure is not efficient for molecules, and would only be able to explain a levitating shell of material close to the photosphere of the star (Jorgensen & Johnson, 1992). Thus, their movement is mainly driven by the drag forces of the expanding dust grains. The equation of motion for gas particles is:

$$m_g \frac{dv_d}{dt} = F_p - F_{grav} + F_{dr} = -\frac{m_g}{\rho_g}\frac{dP}{dr} - m_g \frac{GM_*}{r^2} - \alpha m_g n_g \sigma_d v_{dr}(c_s^2 + v_{dr}^2)^{1/2} \tag{A.11}$$

where m_g is the mass of a gas particle, F_p is the force exerted due to gas pressure, dP/dr is the radial pressure gradient (which is negative), ρ is the gas volume density, n_g the number density of gas particles, and σ_d the geometric cross section of dust grains. For gas particles, the most efficient way to gain momentum is by collisions with dust grains (Gilman, 1972, Tielens, 1983).

It is possible to find an analytical solution for Eqs.(A.10)-(A.11) under certain approximations. It is assumed a constant dust grain density ($v_T \ll c_s$), and perfect gas-grain coupling ($F_{rad} = F_{dr}$). These approximations and the expansion condition ($F_{rad} \gg F_{grav}$), lead to the following expression:

$$v(r) = v_\infty \sqrt{1 - \frac{r}{R_0}} \tag{A.12}$$

where v_∞ is the terminal expansion velocity, and R_0 the starting point (the radius of the star or the condensation radius, for example). Eq.(A.12) shows that the terminal expansion velocity is reached quickly (in terms of r) because the forces describing the equation of motion have a radial dependence $\propto r^{-2}$. Computationally, Eqs (A.10)-(A.11) can be solved (Kwok, 1975, Goldreich & Scoville, 1976, Justtanont et al., 1994), obtaining values that range between 5-30 km s^{-1}, which are consistent with the linewidths of the rotational molecular lines observed toward CSEs, although, some discrepancies have been found for the regions between the photosphere of the star and the dust condensation region ($\sim$5-20 R_*, e.g. Decin et al., 2010d).

Finally, it is important to set the size of CSEs, i.e. which is their outer radius. The size depends mainly on two factors, the mass loss rate and the intensity of the UV ISRF. The size is also different for each of the molecules considered, being the H_2 and CO envelopes the largest ones ($\gtrsim 10^{17}$ cm), and also for the dust envelope, which can be even larger than gaseous envelopes, reaching sizes of $\sim$0.1 pc (e.g. Bujarrabal & Alcolea, 1991, Loup et al., 1993, Ladjal et al., 2010,

Cox et al., 2012, and references therein). The size may be used to estimate the age of the CSE, if the expansion velocity is known, through observations of molecular lines (e.g. Young et al., 1993, and references therein). As it has been previously mentioned, mass loss rates are estimated between 10^{-8} up to $10^{-4}\,M_{\odot}$ year^{-1}, and may occur episodically throughout the AGB phase (e.g. Olofsson et al., 1996a, Olofsson, 1996b, Olofsson et al., 2000). For molecules, the size of the CSEs is determined by their resistance to UV photodissociation by ISRF, which depends on shielding and extinction, mainly by dust, H_2, and CO. Photodissociation and photoionisation energies of most of the molecules of interest in astrophysics, lie in the UV range between 912 Å (13.6 eV which is the ionisation energy of H), and 2000-2500 Å (∼5 eV, being 4.5 eV the dissociation energy of H_2), and it is often taken the range between 912-2400 Å as in Habing (1968), for which the average integrated intensity for the whole sky is 5.6×10^{-14} erg cm $^{-3}$ (Habing, 1968, Le Petit et al., 2006). The photodissociation rate for continuous radiation can be written as follows:

$$k_{pd} = \int_{\lambda_i}^{\lambda_f} \sigma(\lambda) I(\lambda)\, d\lambda \tag{A.13}$$

where $\sigma(\lambda)$ is the cross section for the studied molecule, and $I(\lambda)$ is the specific intensity of the photodissociating radiation (in this case the UV ISRF produced mainly by O, B, A, and F stars of the Galaxy), which is usually fitted to an exponential law:

$$k_{pd} = \alpha \exp\left(-\gamma A_v\right) \tag{A.14}$$

which depends on the extinction in a certain wavelength range (in this particular case in the visible), which is also described in Sect. B.1.1 (where α and γ are parameters). The dust causes a radiation extinction which depends on the wavelength, the amount of dust, and its physical properties (see e.g. Suh, 1999, and references therein). Extinction in the visible wavelength range (for the Solar vicinity), is given by:

$$A_V = \frac{N_H}{1.87 \times 10^{21}} \quad [mag] \tag{A.15}$$

where $A_{\rm V}$ is the visual extinction measured in magnitudes, and $N_{\rm H}$ is the H column density in cm^{-2} (Bohlin et al., 1978). In general, extinction laws for other wavelength ranges different than visible are usually approximated with the expression $A_\lambda = \lambda^{-1}$. There are also several empirical relations between different extinctions for certain wavelengths and the visible extinction such as Cardelli et al. (1989), Fitzpatrick (1999), Schöier et al. (2011) and references in these articles, where the expression $A_\lambda = \lambda^{-1.3}$ is found to be more accurate. These works also derive extinction laws for different wavelength ranges parametrized as a function of $R = A(V)/E(B-V)$, where $A(V)$ is the extinction in the V-band (∼550 nm), and $E(B-V)$ the colour excess between the bands B (∼445 nm) and V.

Concerning molecules, it has to be considered the *self-shielding*, which is mainly produced for H_2 and CO (Glassgold & Huggins, 1983, Mamon et al., 1988). The self-shielding is the ability of a given molecule, located in a cloud (or envelope), to protect itself from photodissociating radiation, i.e. the outermost shells of a molecular CSE (where photodissociation occurs) protect its inner shells. In particular, H_2 is photodissociated through Lyman bands (1298 to 1444 Å), and CO through lines in the range of ∼912-960 Å (see e.g. Morris & Jura, 1983). As we penetrate in the cloud or CSE, the line of the shielded molecule will start to become optically thick, therefore, the photodissociation rate decreases rapidly, and inside the interior of the cloud is protected. It has been also evaluated recently the importance of N_2 self-shielding and its influence on CSE chemistry (Li et al., 2014, 2016).

A.3 Circumstellar chemistry

A.3.1 Elemental composition: carbon vs oxygen

CSEs are mainly composed of molecules and dust. As it is shown in Sect. B.1.2, dust grains and molecules are formed in the atmosphere of the star where the physical conditions (high densities and low temperatures) are favourable for their formation. Nevertheless, the stellar atmosphere is not the only region of the CSE where molecules can be formed. Molecules can be formed in different regions of the CSE through gas reactions, or shock-induced processes, or photo-induced processes (e.g. ISM radiation or cosmic rays), and also due to the interaction between gas and dust. The type of dust and molecules found in CSEs depend on how the stellar envelope has evolved during the dredge-up processes. There are O-rich CSEs ([C]/[O]<1), C-rich ([C]/[O]>1), and CSEs of S-type stars ([C]/[O]$\sim$1). Molecules such as SiO or SO are more abundant in O-rich CSEs, while molecules like SiC_2 or C_2H are more abundant in C-rich CSEs, although, as discussed throughout this thesis, C-bearing molecules can be found in O-rich CSEs and vice versa. Concerning dust, there is also a chemical differentiation between different type stars that produce different types of dust. For example, amorphous carbon dust grains are observed toward C-rich stars, and silicates or metal oxides are found toward O-rich stars (see e.g. Habing & Olofsson, 2003).

A.3.2 Molecular formation

Circumstellar chemistry depends on the elemental composition of the considered star, i.e. O-rich, C-rich, or S-type star. Additionally, circumstellar chemistry may be divided or classified according to the dominant chemical processes at work, therefore, classified according to the different regions of the CSE (see Fig. B.1).

Several molecules are efficiently formed in the gas phase, close to the stellar photosphere as a consequence of chemical processes enabled under thermodynamical equilibrium conditions (e.g. Tsuji, 1973). Carbon and oxygen are (after H and He) the most abundant elements in the atmosphere. In the case of O-rich CSEs, carbon plays the role of "limiting reactant" and it is supposed to be almost fully locked up in CO, which is a very abundant and stable species, while the remaining oxygen is free to react with other atoms, thus, forming additional O-bearing molecules. This is why in general, O-rich envelopes are relatively poor in C-bearing molecules other than CO, while C-rich ones show low abundances of O-bearing species (e.g. Bujarrabal et al., 1994). An example of the expected chemistry in the innermost regions of O-rich and C-rich CSEs is shown in Fig. A.6.

From the stellar atmosphere to the dust condensation radius ($\sim$20 R_*), several ingredients must be taken into account in order to evaluate the formation of new molecules: the presence of shocks, the interaction between gas and dust, and the gas phase processes. As explained before, AGB stars experience thermal pulses that generate shock waves that may affect the innermost regions of the CSEs (e.g. Cherchneff, 2006, and references therein). Temperature and density increase caused by shocks can trigger the formation of molecules in non-LTE conditions. Shock models try to explain the presence of C-bearing molecules in O-rich CSEs and vice versa (e.g. Duari et al., 1999, Cherchneff, 2006, Gobrecht et al., 2016). However, these models are not able to reproduce some of the observational abundances found as discussed in Chapters 3 and 8. Shocks are also relevant in extracting material from grains and incorporate this material into the gas phase.

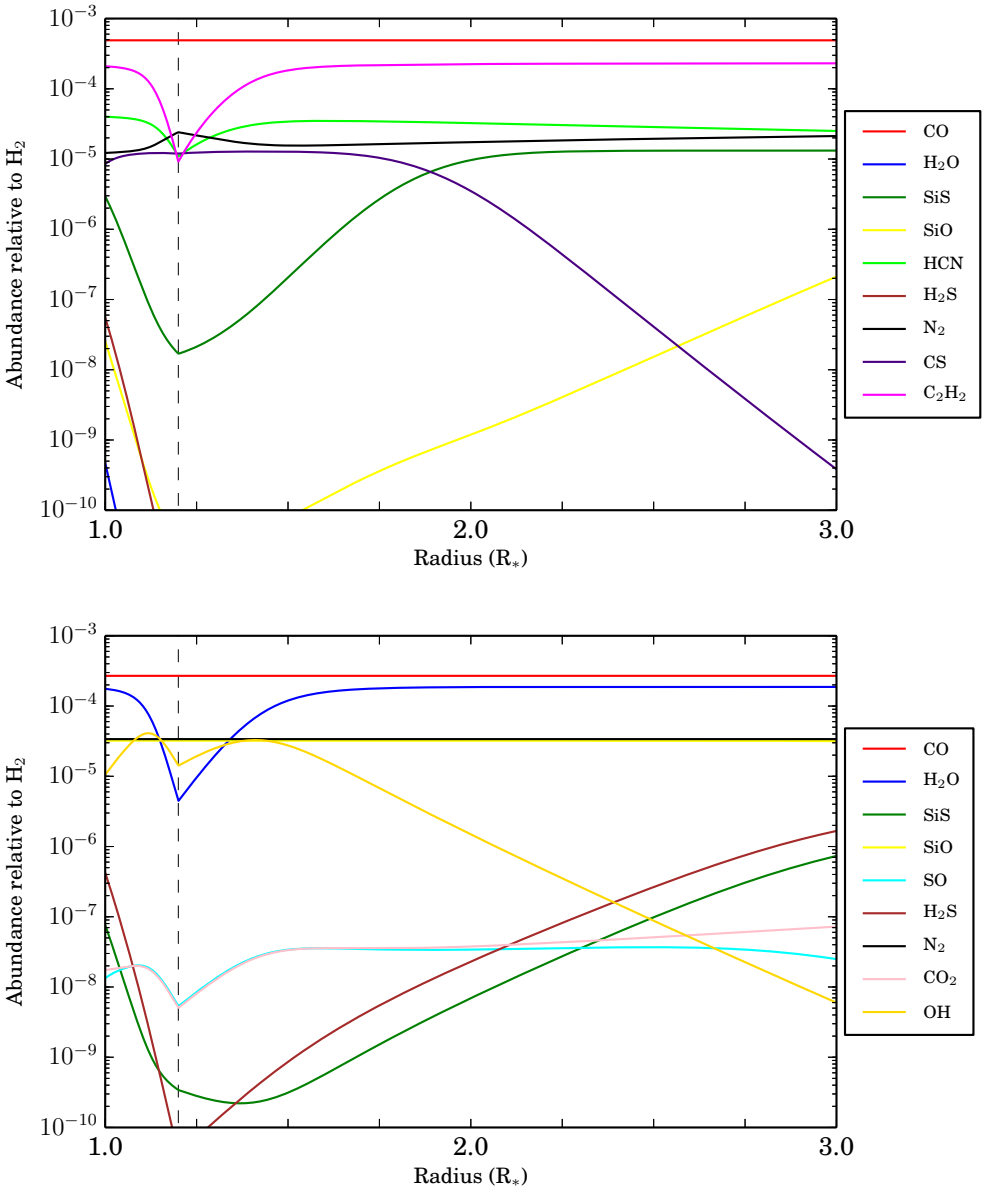

Figure A.6: TE models for a C-rich (top) and an O-rich (bottom) CSE. The input elemental abundances correspond to those of Asplund et al. (2009) for the O-rich CSE (see Table 2.1), while for the C-rich model the carbon elemental abundance was corrected to the value $log(\epsilon_C)$=8.99. Both models were calculated for a star with 1 $M_\odot$, R_*=3×10^{13} cm, T_*=2500 K, an expansion velocity of 5 km s^{-1}, and a temperature of $T(r) = T_* (r/R_*)^{-0.65}$ (see Sect. 2.3 for more details about the model). The dashed line marks the separation between the static atmosphere and the dynamic atmosphere (see Sect. A.2).

Concerning dust grains, their formation occurs inside the dust condensation radius ($\sim 20 R_*$) by the condensation of refractory elements and subsequent growth of the nucleation seed by accretion and coagulation of molecules, like SiO in the case of O-rich CSEs or SiC in the case of C-rich CSEs (see e.g. Gail & Sedlmayr, 2014). This mechanism may explain the spatial distribution of certain molecules in the regions of dust condensation (Lucas et al., 1992, González Delgado et al., 2003, Velilla Prieto et al., 2015b).

Beyond the region where abundances are determined by TE processes, chemistry will be determined by gas phase reactions, gas-grain interaction, and other processes as photodissociation (caused directly by UV ISRF or indirectly by cosmic rays), or cosmic rays collisions. Therefore, chemical kinetics determines which processes are relevant to the formation of molecules, according to reaction and dynamical times (see Sect. B.1.1). In the region comprised between the dust condensation radius and the photodissociation region, the abundances are commonly said frozen (see Fig. B.1), since the expansion of the envelope is faster than the characteristic time of chemical reactions, thus, chemical abundances cannot re-adapt to the physical conditions encountered with the expansion. These frozen abundances are therefore similar to TE abundances (excepts for molecules involved in dust formation and growth). Among these molecules, which expand from the TE region, the most abundant molecules are known as *parent* molecules, which will determine the chemistry in the outermost regions of the envelope. Parent molecules react between them in gas phase (neutral-neutral reactions), and may participate in the formation of molecules on the surface of dust-grains (grain-gas interaction) or react with molecules evaporated from their surface. Dust grains may act as catalysts in the formation of molecules in CSEs, for example in the formation of H_2 (Glassgold & Huggins, 1983). These processes related to dust grains are still poorly known and they have not been well characterised in the laboratory. Although, some efforts have been done recently in creating models of gas-grain chemistry (e.g. Quan et al., 2010, Reboussin et al., 2014, Ruaud et al., 2015).

Finally, in the outermost regions of the CSEs, chemistry is dominated by photoionisation and photodissociation processes due to the interaction with the UV ISRF. These chemical processes are described in the Section B.1.1. But photo-induced processes may also occur in the inner regions of the CSEs, due to indirect production of UV photons by cosmic rays, or due to the presence of a companion star with non-negligible UV emission, or they may occur if the CSE is clumpy enough to allow penetration of UV ISRF photons (e.g. Agúndez et al., 2010b, Velilla Prieto et al., 2015a, Sánchez Contreras et al., 2015). Thus, the formation of radicals and ions is enhanced in these regions, such as CN, which is a photodissociation product of HCN in IRC+10216. The emission of CN arises from a shell immediately external to the HCN (Lucas et al., 1995).

A.3.3 Isotopologues

In the Section A.1 it has been shown that nucleosynthesis, dredge-ups, and also neutron capture processes, will determine the evolution of the chemistry of AGB CSEs. These processes can alter the isotopic ratios of elements that react to form molecules in the atmosphere of the star (e.g. $^{12}C/^{13}C$, $^{14}N/^{15}N$, or $^{16}O/^{18}O$). For example, carbon monoxide can be found in the form of $^{12}C^{16}O$ and also in the form of $^{13}C^{16}O$. These isotopologues are also excellent tracers of the physical properties of CSEs, as discussed throughout this thesis. Following the same example, $^{13}C^{16}O$ can be used to estimate the mass loss rate of an AGB star given that it is usually optically thin, while $^{12}C^{16}O$ is optically thick. A detailed review on this topic can be consulted in e.g. Busso et al. (1999).

APPENDIX

B

THEORY AND METHODS

In this appendix we summarised the fundamental concepts required to describe and understand how electromagnetic radiation is produced due to the changes in the rotational state of molecules found in circumstellar envelopes, as well as the theory that describes the interaction between matter and radiation, chemical processes, basic concepts about observations and the use of radiotelescopes and interferometers. Nevertheless, it is recommended to consult Habing & Olofsson (2003), Atkins & de Paula (2006) for a complete description of topics related to chemistry. Concerning molecular spectroscopy, texts by Herzberg (1950), Townes & Schawlow (1975) can be consulted. In the case of the interaction between matter and radiation the text by Rybicki & Lightman (1979) can be consulted. For the topics related to radioastronomy, interferometers, and observational methods, the texts by Kraus (1966), Thompson et al. (2001), Rohlfs & Wilson (2004) can be consulted. Additionally, we recommend the texts by Kwok (2007), Draine (2011) and the PhD thesis by Agúndez (2009) for some specific topics (e.g. LVG approximation or dust opacity), as well as the references provided throughout the chapter.

In astrophysics, the information about different objects in the Universe, such as their chemical composition, temperature or densities, is mainly obtained through the study of EM radiation produced by them. Therefore, it is important to study their spectrum at different wavelengths. In the case of this present PhD thesis, we analysed the EM radiation in the millimeter wavelength range (in particular between ∼80-360 GHz), produced by the molecules that form the circumstellar envelopes of evolved stars. Particularly, the spectral lines formed due to the change of the rotational state of the molecules. Therefore, in this Chapter we describe the processes that explain the formation of spectral lines of rotational transitions, their most relevant properties, the related methods, and basic concepts related to observations with radiotelescopes in this wavelength range.

B.1 Circumstellar chemistry

As presented in Sect. A.3, molecules and dust grains that form the CSEs are produced in the atmosphere of AGB stars under TE conditions, with high densities ($n \gtrsim 10^{12}\,\mathrm{cm}^{-3}$) and temperatures ($T \sim 2500\,\mathrm{K}$) that favour their formation (Tsuji, 1973). The type of species formed will depend on the initial abundances of the elements in the atmosphere of the star. Thus,

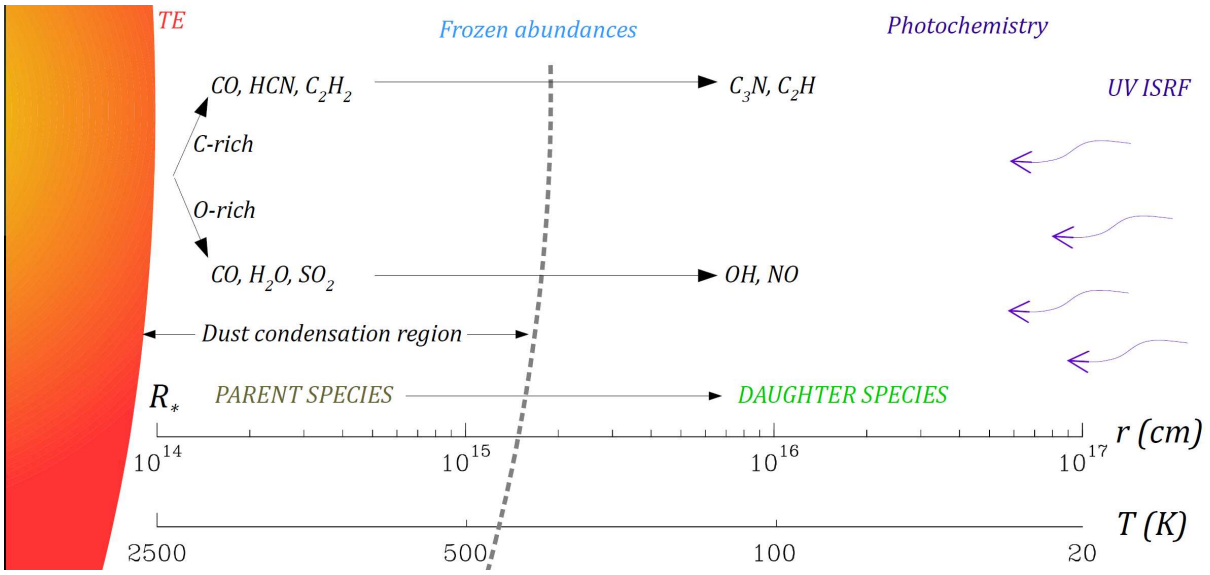

Figure B.1: Sketch of the chemistry in a circumstellar envelope of an evolved star, where the regions of thermodynamical equilibrium (TE), frozen abundances, and photochemistry are indicated. The scale of the radius (in cm) and temperature (in K) are shown.

dredge-up processes, which are described in Sect. A.1, will determine the chemical composition of the CSE. Once molecules have been formed, they will travel outwards from the atmosphere driven by the AGB wind. Therefore, physical conditions will change during this expansion. In particular, density will decrease down to $10^3\,\mathrm{cm}^{-3}$, and temperature will decrease down to $\sim$10 K in the outermost layers of the CSE.

Beyond the atmosphere of the AGB star, the circumstellar chemistry will be determined by chemical kinetics. In the innermost regions of the CSE, up to the condensation region ($r\sim$5–20 R_*), shocks due to the pulsation of the star and gas-grain interaction processes will play a determining role in the circumstellar chemistry (e.g. Cherchneff, 2006, Garrod, 2008, Gobrecht et al., 2016). As the expansion of the gas in the envelope continues, chemical reactions will not be fast enough to re-adapt the abundances to the physical conditions encountered, and the abundances are said to be "frozen".

In the outermost part of the CSE, density is so low that UV ISRF penetrates into the CSE and UV photons can dissociate molecules. This process will occur gradually depending on photodissociation rates of each molecule. The photodissociation of some species can enhance the formation of other molecules (e.g. CN in Lucas et al., 1995). Fig. B.1 shows a general sketch of the chemistry in the CSE of AGB stars.

B.1.1 Types of reactions

There are different types of chemical reactions that can occur in a CSE, which in general depend on the nature and the amount of the reactants. We can find two-body reactions, three-body, ion-neutral reactions, neutral-neutral, recombination... However, some types are more relevant in certain regions of the CSE than other types of reactions. In general, the effect of a particular chemical reaction in a particular region of the CSE will be negligible if the reaction time (t_r) is greater than the dynamical time of expansion ($t_{din} = r/v_{\mathrm{exp}}$, where r is the distance between the star and the region considered, and v_{exp} the expansion velocity of that region), thus, the

abundances of the species involved will not re-adapt to the physical conditions encountered during the expansion (i.e. lower temperatures and densities).

If we consider a simple gas phase reaction like:

$$A + B \rightarrow C, \tag{B.1}$$

the velocity of the reaction is defined according to the variations of the concentrations of the reactants and products as follows:

$$v = -\frac{d[A]}{dt} = -\frac{d[B]}{dt} = \frac{d[C]}{dt} = k[A][B], \tag{B.2}$$

where $[A]$, $[B]$, and $[C]$ are the concentrations, and k is the *reaction rate constant or coefficient* of the reaction, which depends on temperature and it is usually estimated experimentally in the laboratory, and:

$$k = \langle v\sigma \rangle, \tag{B.3}$$

where v is the velocity of the reactants, and σ the collisional cross-section, which is calculated with the analysis and study of the PES (see Sect. B.2.2). In the context of CSEs, reaction rates are extrapolated to the low temperatures given in the outermost parts of the CSE, and occasionally reaction rates have to be roughly guessed given the difficulties that can be found to synthesise a molecule or reproduce the physical conditions in the laboratory.

The reaction rates follow, in general, the *Arrhenius equation*:

$$k = A \exp\left(-E_a/kT\right), \tag{B.4}$$

where A is the so-called *pre-exponential factor* or *frequency factor*, and E_a is the *activation energy* of the reaction. For the collision of two molecules described by Eq.(B.1), the activation energy is the minimum kinetic energy that reactants should have to react and form the products. The pre-exponential factor corresponds to the Boltzmann distribution, that is, the fraction of collisions that have energies greater than the activation energy. Therefore, the pre-exponential factor can be interpreted as the fraction of collisions that have enough energy to form the products.

The Arrhenius equation can be parametrised in a way that the temperature dependence of the reactions rates is shown explicitly as follows:

$$k(T) = \alpha(T/300)^{\beta} \exp\left(-\gamma/T\right), \tag{B.5}$$

where α, β, and γ are parameters.

The most important types reactions found in CSEs, which have been used in our chemical kinetic code (Sect. 2.3)), are given in Table B.1. In general, all of these reactions can be expressed according to Eq.(B.5), although, in reactions involving cosmic rays and photons, there are particular expressions of the reaction rates, which are described below.

For ion-neutral reactions in which the neutral species has no permanent electric dipole moment, the kinetic rate constant can be expressed with the Langevin expression as:

$$k_L = 2\pi e(\alpha_p/\mu)^{1/2}, \tag{B.6}$$

where e is the electron charge, α_p is the polizaribility, and μ the reduced mass of the reactants. If the neutral species is polar, the capture theories that describe the electrostatic interaction between the ion and the neutral are more complex, and the reaction constant is temperature dependent (in general $k(T) \propto T^{-1/2}$), with typical values of $10^{-7}\,\mathrm{cm^3\,s^{-1}}$ for T $\sim$10 K (see e.g. Herbst, 1995, Wakelam et al., 2010, 2012).

Table B.1: Types of reactions that can be found in CSEs

Type	Example	Units of k
CR direct processes	$H_2 + \zeta \rightarrow H_2^+ + e^-$	s^{-1}
Neutral-neutral	$H_2 + OH \rightarrow H + H_2O$	$cm^3\ s^{-1}$
Ion-neutral	$CH^+ + H_2O \rightarrow HCO^+ + H_2$	$cm^3 s^{-1}$
Radiative association	$Si + O \rightarrow SiO + \gamma$	$cm^3\ s^{-1}$
Dissociative recombination	$HCO^+ + e^- \rightarrow CO + H$	$cm^3\ s^{-1}$
Mutual neutralisation	$H_2CO^+ + e^- \rightarrow H_2CO + \gamma$	$cm^3\ s^{-1}$
3-body reactions	$H + H + H_2 \rightarrow H_2 + H_2$	$cm^6\ s^{-1}$
Thermal dissociation	$CH + H \rightarrow C + H + H$	$cm^3\ s^{-1}$
γ-induced reactions	$HCN + \gamma \rightarrow CN + H$	s^{-1}

Notes. ζ: Cosmic ray. γ: Photon. Among the most used databases we have: UDfA-UMIST (*http://udfa.ajmarkwick.net/*) and KIDA (*http://kida.obs.u-bordeaux1.fr/*)

Photodissociation

UV photons of the ISM radiation field are the main responsible for the photodissociation processes in CSEs. The energy and intensity distribution of the ISRF has been studied by Habing (1968) and Draine (1978), among others. These photons have enough energy to dissociate molecules, in particular molecules with dissociation energies lower than 13.6 eV (e.g. the dissociation energy for the ground state of CO is ∼11.1 eV and that of H_2 is ∼4.5 eV). As it was shown in Sect. A.2, the extinction will determine the amount of photons that can penetrate into the CSE. Therefore, the reaction rate constants of photodissociation reactions are expressed as:

$$k_{pd} = \alpha \exp\left(-\gamma A_v\right),$$

where α and γ are specific parameters for each species, and A_v is the visual extinction. Occasionally, photodissociation rates are approximated to second order functions of the extinction. These parameters depend on the type of dust responsible for the extinction and the geometry of the cloud. The photodissociation rates have typical values of 10^{-9}-$10^{-10}\,s^{-1}$, and can be consulted, for example, in the UDfA-UMIST (Woodall et al., 2007).

Cosmic rays

There are direct and indirect reactions caused by cosmic rays. Cosmic rays are highly energetic (with MeV up to GeV) particles (protons or He nuclei) that can dissociate and ionise different species, through direct processes but also through indirect processes caused by the electronic excitation of the gas (Prasad & Tarafdar, 1983). The ionisation and dissociation rate by cosmic rays for a particular species (ζ_X) is scaled in terms of the ionisation and dissociation rate for hydrogen, which has a value of 1-5$\times 10^{-17}\,s^{-1}$ (Dalgarno, 2006).

Rimmer et al. (2012) have studied the cosmic ray ionisation rate dependence with the column density toward the Horse-head nebula, although, this factor is usually not taken into account.

B.1.2 Equilibrium chemistry

The appropriated conditions to favour the formation of molecules under TE are given in the innermost regions of CSEs, close to the photosphere of AGB stars between 1-5R_*. In order to have a system under equilibrium, its free energy must be minimum. The energy of a system can be estimated with the *Gibbs free energy*:

$$G = \sum_i \mu_i x_i, \tag{B.7}$$

where x_i is the number of moles of the species i, and μ_i is the *chemical potential* of that species:

$$\mu = \left(\frac{G}{RT}\right)_i + \ln P + \ln\left(\frac{x_i}{\bar{x}}\right), \tag{B.8}$$

where $(G/RT)_i$ is the Gibbs free energy of the species i, P is the total pressure of the system, R is the gas constant, and $\bar{x}$ is the total sum of the moles of all the species in the system. The Gibbs free energies of molecules (as well as other thermodynamical properties) are tabulated, for example, in NIST-JANAF[1] (Chase, 1998). Thus, we can find the abundances that minimise the Gibbs free energy of each molecule in a given system under TE by using the equilibrium constants of the formation/dissociation reactions expressed as a function of the partial pressures of reactants and products (e.g. Russell, 1934, Tsuji, 1973). Given the formation and dissociation reactions of molecules from its constituents (i.e. elements) such as:

$$aX + bY + cZ \rightleftarrows X_aY_bZ_c, \tag{B.9}$$

the *equilibrium constant* (K_p) of a reaction is defined as follows:

$$K_p = \frac{P_X^a P_Y^b P_Z^c}{P_{X_aY_bZ_c}}, \tag{B.10}$$

where all the P represent the partial pressures of the species involved in the reaction Eq.(B.9). The equilibrium dissociation constants can be calculated using macroscopical properties (Gibbs free energies, standard formation enthalpies and entropies) that are tabulated (e.g. Chase, 1998). We also need to consider the mass conservation law for all the elements that form the system. For example, the total amount of initial oxygen must be conserved and must be distributed among all the O-bearing species. We can write a system of equations, one per each considered element that form the system, as follows:

$$n_{o,X} = n_X + a\, n_{AX} + b\, n_{BX} + \ldots, \tag{B.11}$$

where $n_{o,X}$ is the total density of the element X (which is an input of the calculation), n_X is the density of neutral atoms of X, n_{AX} is the density of AX molecules (in the case of oxygen the molecules will be CO, SiO...), a is the number of atoms of X that compose the molecule AX, and including all the molecules that the element X can form with the elements considered. These conservation equations can be expressed as a function of the partial pressures of the elements and species of the system. This is the method used by Tsuji (1973), where the authors make use of the *fictitious pressures*, that is, the pressure of an element (e.g. oxygen) is equal to the

[1] *http://kinetics.nist.gov/janaf/*

total density of that element considering all the different forms in which the element can be found in the system (e.g. O, O^+, ...) multiplied by kT. Thus, the pressures for all the elements in the system are:

$$\begin{aligned} P(H) &= n_{o,H}\, kT, \\ P(O) &= \epsilon_O\, n_{0,H} kT, \\ P(C) &= \epsilon_C\, n_{0,H} kT, \\ P(N) &= \epsilon_N\, n_{0,H} kT, \\ &\dots \end{aligned} \tag{B.12}$$

where $n_{0,H}$ is the total density of H atoms, and ϵ_X is the abundance (with respect to H) of the element X (see Table 2.1). This set of equations along with some stellar parameters (such as T_{eff}, R_*, $\dot{M}$, v_{exp} and the radial dependence of the temperature expressed as $T(r) \sim T_{eff}(r/R_*)^{-\alpha}$), which will determine the physical conditions of the system, and the initial abundances of the elements, allow to estimate the radial abundance profiles of the species considered. A first guess can be obtained if we simplify the calculation by assuming that the gas is mainly composed of H and He. This is the method applied in our chemical code LTEINNER (see Sect. 2.3).

B.1.3 Chemical kinetics

The abundances of species found in the CSEs are determined by the kinetics of the reactions occurring in it (except for the innermost regions where, as we have seen, we can apply the TE). At the beginning of Sect. B.1.1, we have seen how the kinetic constants of these reactions are described, and which types of reactions are given in CSEs. For a given system, we can calculate the abundances of the species considered by solving a system of differential equations like Eq.(B.2), for a network of reactions that involve all the species in the system. Therefore, for each species, there will be a differential equation describing the variation of the abundance of that species i over time, which will depend on the kinetic constants of the reactions that form and destroy that species, and the abundances of the reactants involved in these reactions, for example:

$$\frac{dn_i}{dt} = -k_i\, n_i \;\rightarrow\; n_i = n_{0,i} e^{-k_i t}, \tag{B.13}$$

for the simple case of a first order reaction. There must be a destruction chemical route for each species, which can be calculated using thermodynamical properties (equilibrium constants K_{eq}) as follows:

$$K_{eq}(T) = k_{direct}/k_{inverse}, \tag{B.14}$$

where the different k correspond to the direct and inverse reaction rates (e.g. $a + b \rightleftarrows c + d$). We must solve a system of differential equations that includes all the species involved in the considered chemical network, using some initial abundances for parent species (e.g. the abundances resulting from a TE calculation or observationally measured abundances), and a physical model for the CSE. The physical model is described by the T_{eff}, the R_*, the $\dot{M}$, the v_{exp}, the radial dependence of the temperature ($T(r) \sim T_{eff}(r/R_*)^{-\alpha}$), the H_2 ionisation/dissociation rate induced by cosmic rays, and the UV ISRF intensity. With this model, we can evaluate the physical conditions given at each layer of the CSE and solve the system of equations (such as Eq.(B.2) or Eq.(B.13) or more complex differential equations in case of second order reactions), to obtain the radial abundance profile of each considered species.

B.2 Formation of rotational lines

The spectral lines in the millimeter wavelength range analysed in this thesis, arise as a result of the changes in the rotational state of the molecules in the CSEs studied. These changes are caused by the interaction of the molecules with radiation (radiative processes) or by the interaction with other abundant molecules, mainly H_2 (collisional processes). Thus, the analysis of the millimeter wavelength range spectrum of the CSEs allows to characterise the processes at work which form the spectral lines, and also allows to determine several physical properties such as temperatures, densities or abundances.

B.2.1 Radiation-matter interaction

Radiation

The *specific intensity* (I_ν) of the EM radiation is defined as the amount of energy that passes through a differential element of area per unit time at a certain solid angle, and within a differential frequency range, expressed mathematically as follows:

$$I_\nu(\theta,\phi) = \frac{dE}{dS\,dt\,d\Omega\,d\nu} \quad [erg\,cm^{-2}\,s^{-1}\,sr^{-1}\,Hz^{-1}]. \tag{B.15}$$

The specific intensity is also simply called intensity or *brightness*. From the specific intensity, we define the *flux density*[2] as the total energy emitted by an object and received on a given area per unit frequency and time:

$$S_\nu = \int_{\Omega_s} I_\nu(\theta,\phi)\cos\theta\,d\Omega \quad [erg\,cm^{-2}\,s^{-1}\,Hz^{-1}], \tag{B.16}$$

where the commonly used unit of flux density in radio astronomy is the Jansky (Jy). Note that the flux density depends on the distance to the source (as r^{-2}) while specific intensity does not depend on the distance. If the angular size of the source is small ($\theta_s \ll 1$), the flux density is simply the integrated specific intensity over the size of the source. In practice, if we observe a source that is not spatially resolved ($\theta_s \ll$PSF of the observing telescope), the flux density is measured directly from the observations with a radiotelescope. However, if the source is spatially resolved, the radiotelescope measures the specific intensity toward the observed position, thus, we must integrate over the size of the source to obtain the flux density. It is often considered as an approximation that the specific intensity is constant over the the source, then:

$$S_\nu = I_\nu \Delta\Omega, \tag{B.17}$$

where $\Delta\Omega$ is the area subtended by an object located at a distance r.

Under TE at a temperature T, the radiation intensity emitted by a black body is given by the *Planck's function*:

$$I_\nu = B_\nu(T) = \frac{h\nu^3}{c^2}\frac{1}{e^{h\nu/kT}-1}, \tag{B.18}$$

[2]The flux density is usually designated with the following notation S_ν, which is also used in some texts to designate the source function. To avoid such confusion I have used the notation S_ν for the flux density and $\mathcal{S}_\nu$ to designate the source function.

which depends on the temperature of the system and the frequency, and whose maximum is given by the *Wien's displacement law*:

$$\lambda_{max}[mm] = \frac{2.898}{T[K]}. \tag{B.19}$$

Generally speaking, the radiation-matter system may be out of TE, but we can describe the radiation intensity at each frequency by a Planck-type function with a specific temperature called *brightness temperature* ($I_\nu = B_\nu(T_B)$). That is, the brightness temperature is the temperature that a black body that emits the same amount of radiation would have at a specific frequency.

The Planck's function can be approximated for two different regimes called *Wien* regime ($h\nu \gg KT$) and *Rayleigh-Jeans* regime ($h\nu \ll KT$), the latter being particularly interesting at long wavelengths. Under the Rayleigh-Jeans approximation, the specific intensity may be expressed as follows:

$$I_\nu = B_{RJ}(\nu, T_B) \simeq \frac{2\nu^2}{c^2} k T_B. \tag{B.20}$$

The validity range of the Rayleigh-Jeans approximation can be expressed (in practical units) as:

$$\nu[GHz] \ll 20.84\, T[K]. \tag{B.21}$$

Additionally, under the Rayleigh-Jeans approximation, the Eq.(B.17) is written as:

$$S_\nu = \frac{2k\nu^2}{c^2} T_B \Delta\Omega, \tag{B.22}$$

which is particularly interesting to convert the observed intensities with a single-dish, to flux density (e.g. to observe with an interferometer).

It is worth noting that the definition of brightness temperature is just a convention (completely accepted in the field of radioastronomy), which could not have any physical significance. This scale is commonly used even when the Rayleigh-Jeans approximation is not valid. In that case, the brightness temperature is called *radiation temperature* ($J(T)$ or T_R):

$$T_R \equiv J(T) = \frac{c^2}{2k\nu^2} I_\nu = \frac{h\nu}{k} \frac{1}{e^{h\nu/kT} - 1}. \tag{B.23}$$

Radiative transfer

The EM radiation that arises from the studied source, must travel through the space until it reaches our telescope and detectors. Therefore, it will interact with the matter found in the CSE, in the ISM, or in the Earth's atmosphere. Energy can be added or subtracted to the radiation beam through radiative and collisional processes. The equation that describes the changes of energy within the radiation beam along the path it travels is called *radiative transfer equation*:

$$\frac{dI_\nu}{ds} = -\alpha_\nu I_\nu + j_\nu, \tag{B.24}$$

where α_ν is the *absorption coefficient* (in units of cm^{-1}, and it is positive if the energy is subtracted from the beam, which explains the minus symbol in Eq.(B.24)) and j_ν is the emission

coefficient (in units of $\mathrm{erg\,cm^{-3}\,s^{-1}\,sr^{-1}\,Hz^{-1}}$). The absorption coefficient can be written also as follows:

$$\alpha_\nu = \rho\kappa_\nu, \quad [cm^{-1}] \tag{B.25}$$

where ρ is the *density* (in $\mathrm{g\,cm^{-3}}$), and κ_ν is the *opacity coefficient* (in $\mathrm{cm^2\,g^{-1}}$). Eq.(B.24) can be written in a simpler way by using the *optical depth*, which is defined as follows:

$$\tau_\nu(s) = \int_{s_0}^{s} \alpha_\nu(s')ds', \tag{B.26}$$

and the medium is considered as *optically thin or transparent* if τ_ν<1, and *optically thick or opaque* if τ_ν>1. The physical interpretation of an optically thick medium, is that a photon will not be able to go through that medium without being absorbed by the material. With Eq.(B.26), we can re-write the Eq.(B.24) as follows:

$$\frac{dI_\nu}{d\tau_\nu} = -I_\nu + \mathcal{S}_\nu, \tag{B.27}$$

where $\mathcal{S}_\nu$ is the *source function*, which is equal to:

$$\mathcal{S}_\nu = j_\nu/\alpha_\nu. \tag{B.28}$$

The solution of Eq.(B.27) is:

$$I_\nu(\tau_\nu) = I_\nu(0)e^{-\tau_\nu} + \int_0^{\tau_\nu} \mathcal{S}_\nu(\tau'_\nu)e^{-(\tau_\nu-\tau'_\nu)}d\tau'_\nu, \tag{B.29}$$

where we defined the intensity at a point where τ_ν=0 as $I_\nu(0)$ (for example the CMBR). In the case of a homogeneous medium (see Fig. B.2), the source function is constant, and the solution to the radiative transfer equation is:

$$I_\nu(\tau_\nu) = I_\nu(0)e^{-\tau_\nu} + \mathcal{S}_\nu(1 - e^{-\tau_\nu}), \tag{B.30}$$

thus, if $\tau_\nu \to \infty$ then $I_\nu \to \mathcal{S}_\nu$, and the information about the background radiation is lost.

Einstein coefficients and statistical equilibrium

The Einstein coefficients describe the transition probabilities that have radiative processes between two given energy levels. In the case of a two energy levels system (u and l, where the energies are E_u>E_l, see Fig. B.3), we have:

- A_{ul} (*spontaneous emission coefficient*), which is the probability (in units of $\mathrm{s^{-1}}$) that a molecule in the energy state u, emits spontaneously a photon and decays to the energy state l,
- $B_{lu}\bar{J}$ is the probability that a molecule in the energy state l absorbs a photon (with an energy equal to $E_u - E_l$=$h\nu$) and excites to the energy state u. B_{lu} is the *absorption coefficient*, which has units of $\mathrm{erg^{-1}\,cm^3\,s^{-2}}$, and $\bar{J}$=$4\pi\bar{I}/c$ is the average density of the radiation field (also written as $\bar{U}$), where:

$$\bar{I} = \int_0^\infty I_\nu\,\phi(\nu)\,d\nu, \tag{B.31}$$

where $\phi(\nu)$ is the function that describes the line profile (see below), which follows the normalisation condition:

$$\int_0^\infty \phi(\nu)\,d\nu = 1 \tag{B.32}$$

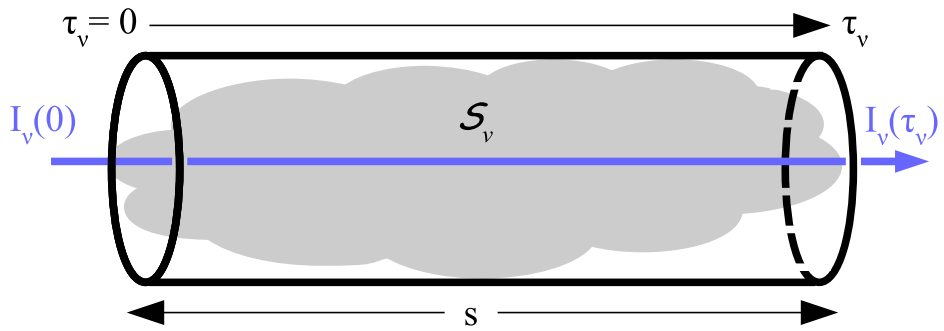

Figure B.2: Radiative transport along a gas cloud of length s, whose source function is $\mathcal{S}_\nu$. The radiation that goes through the cloud has an initial intensity $I_\nu(0)$ (and $\tau = 0$), and the optical depth (τ_ν). The specific intensity (I_ν) can be calculated by using the Eq.(B.27).

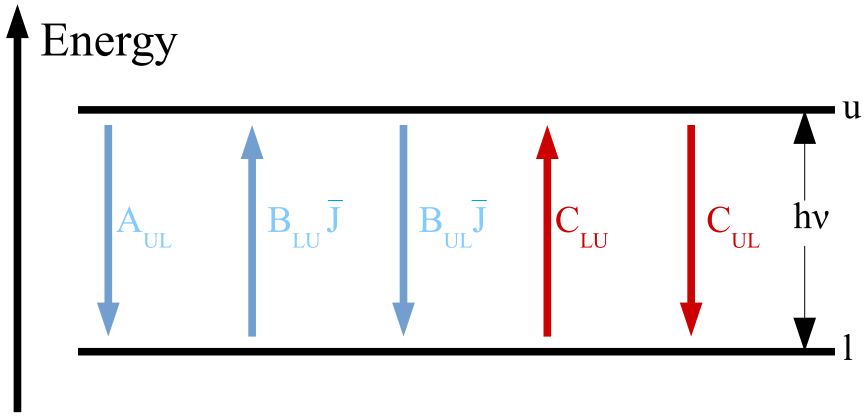

Figure B.3: Diagram of a two energy levels system, u and l, with E_u>E_l, and ΔE=$h\nu$. The radiative processes are shown in blue, and the collisional processes are shown in red, together with their transition probabilities.

- $B_{ul}\bar{J}$, is the probability that a molecule in the energy state u emits a photon and decays to the energy state l, in a stimulated process (not spontaneous). B_{ul} is the stimulated absorption coefficient, which has units of $\mathrm{erg}^{-1}\,\mathrm{cm}^3\,\mathrm{s}^{-2}$.

Under TE conditions, the number of emitted photons of a system must be equal to the number of absorbed photons. This defines the *statistical equilibrium equation* for radiative processes:

$$N_u A_{ul} + N_u B_{ul} \bar{J} = N_l B_{lu} \bar{J}, \tag{B.33}$$

where N_u and N_l are the populations (number density of molecules), that are in states u and l, respectively. These populations are described by the *Boltzmann distribution* in the case of TE:

$$\frac{N_u}{N_l} = \frac{g_u}{g_l} \exp\left(-\frac{h\nu}{kT}\right), \tag{B.34}$$

where g_u and g_l are the *statistical weights or degenerations* of the levels u and l, respectively, and ν is the frequency of the transition. In this simple case of a two level system in TE conditions, the energy distribution of the radiation is given by Planck's function. If we solve the Eq.(B.33) for a certain $\bar{J}$, we obtain the following expressions:

$$g_l B_{lu} = g_u B_{ul} \qquad A_{ul} = \frac{8\pi h\nu^3}{c^3} B_{ul}. \tag{B.35}$$

We define the *the partition function* (Z or Q) as the fraction of particles (or molecules) that occupy a certain energy state given a specific temperature (considering TE). The partition function is expressed as follows:

$$Z = \sum_i g_i e^{-E_i/kT}, \tag{B.36}$$

where i represents the energy levels (or states) that the system can have. In the context of this PhD thesis, the partition function is sometimes evaluated for low energies. In that case, we can consider only the rotational energy levels according to the Born-Oppenheimer approximation (see Sect. B.2.2).

We have seen the equation of radiative transport (Eq.(B.24)) written as a function of the absorption and emission coefficients from a macroscopic point of view, although these coefficients can be expressed as a function of the Einstein coefficients (microscopical description). Then, the source function can be expressed as follows:

$$j_\nu = \frac{h\nu}{4\pi} N_u A_{ul} \phi(\nu), \tag{B.37}$$

$$\alpha_\nu = \frac{c^2 A_{ul} g_u}{8\pi\nu^2} \left(\frac{N_l}{g_l} - \frac{N_u}{g_u} \right) \phi(\nu), \tag{B.38}$$

$$\mathcal{S}_\nu = \frac{2h\nu^3}{c^2} \left(\frac{N_l/g_l}{N_u/g_u} - 1 \right)^{-1}, \tag{B.39}$$

We can define an *excitation temperature* from Boltzmann equation that can be used under non-LTE conditions:

$$T_{ex} = \frac{E_{ul}/k}{ln\left(\frac{N_l/g_l}{N_u/g_u}\right)}, \tag{B.40}$$

where $E_{ul}{=}E_u - E_l{=}h\nu$. The excitation temperature describes the relative populations between the considered energy levels. Under TE conditions with a kinetic temperature T_{kin}, we have that $T_{ex}{=}T_{kin}$. Under non-LTE conditions, a system with $T_{ex}{<}T_{kin}$ is said to be *subthermally excited*. There are two different values for the excitation temperature:

(i) *normal state*, if $T_{ex}{>}0$, thus $N_l/g_l{>}N_u/g_u$,

(ii) *population inversion*, if $T_{ex}{<}0$, thus $N_l/g_l{<}N_u/g_u$. This would imply that the absorption coefficient is negative (see Eq. B.38), and the radiation intensity is amplified when it pass through the medium. This phenomenon is called *MASER*.

Collisional processes and detailed balance

We described several situations that are valid under TE or LTE conditions. In general, we must evaluate the physical conditions of the system for each of the molecular species considered.

Under LTE conditions, we can use the Boltzmann distribution, the Maxwell distribution of velocities (which will be shown below), and the approximation $\mathcal{S}_\nu{=}B_\nu(T_{ex})$. However, we must compare collisional and radiative processes in order to determine if LTE conditions can be applied for a certain species in a CSE.

The collisional processes considered are the collisional *excitation* and *de-excitation*, whose probabilities are given by the collisional coefficients γ_{ul} and γ_{lu}, respectively. These coefficients have units of $\mathrm{cm^3\,s^{-1}}$, and they give us the collisional probabilities or rates (C_{ul} o C_{lu}, in $\mathrm{s^{-1}}$) if we multiply these coefficients by the number density of the collisional partner (see Fig. B.3). A collisional transition occurs when a molecule in a specific energy state, collides with a collisional partner (in general H_2, which is the most abundant gas in the CSE, although sometimes these coefficients are given with respect to He), in such a way that the molecule can absorb part of the kinetic energy of the collisional partner, or transfer part of its own energy. Collisional transitions have their own selection rules (allowed transitions between two energy levels), which depend on the geometry of the molecule, and in general they are less restrictive than selection rules for dipolar electric transitions (see Sect. B.2.2). In the case of a diatomic molecule or a linear molecule, whose rotational state is described by the quantum number J, the selection rule for dipolar electric transitions is $\Delta J{=}\pm1$, while collisional transitions may occur between any pair of levels.

Collisional coefficients can be understood as the cross sections of the transition process $u \to l$ or $l \to u$, convolved with the Maxwellian velocity distribution, that is, the average of the collisional cross sections over a Maxwellian distribution of velocities:

$$f(v) = 4\pi \left(\frac{m}{2\pi kT}\right)^{3/2} v^2 \exp\left(\frac{-mv^2}{2kT}\right), \tag{B.41}$$

and the collisional coefficients as a function of the kinetic energy (with respect to the collisional centre of mass) are written as follows:

$$\begin{aligned} \gamma_{ul} &= \int_0^\infty \sigma_{ul} v f(v) dv, \\ \gamma_{ul} &= \left(\frac{8}{\pi\mu k^3 T^3}\right)^{1/2} \int_0^\infty \sigma_{ul} E_{kin} e^{-E_{kin}/kT} dE_{kin}, \end{aligned} \tag{B.42}$$

where the mass (m) has been substituted by the reduced mass of the system (μ), and σ is the collisional cross section. This cross section can be calculated experimentally or theoretically by determining the PES (see below) (e.g. Lique et al., 2014). The expression of the collisional coefficients is obtained by using the detailed balance of the populations (for the levels u and l):

$$\gamma_{lu} = \gamma_{ul} \frac{g_u}{g_l} e^{-h\nu/kT}, \tag{B.43}$$

where g are the corresponding statistical weights, and ν the frequency that corresponds to the transition ($E_u - E_l{=}h\nu$).

There are several collisional coefficients databases such as LAMDA (Schöier et al., 2005), BASECOL (Dubernet et al., 2013), or MADEX (Cernicharo, 2012, see Sect. 2.2). In the case that collisional coefficients for a particular species are not available, we may use a set of collisional coefficients of a similar species correcting them by the reduced mass. This approximation

is commonly used when collisional coefficients of a molecular species with He are available, and we need collisional coefficients with H_2:

$$\gamma_{X-H_2} = \gamma_{X-He} \left(\frac{\mu_{X-He}}{\mu_{X-H_2}} \right)^{1/2}. \tag{B.44}$$

Once we have the collisional coefficients of a particular transition, we can estimate which processes (radiative or collisional) dominate for a specific case, by calculating the *critical density*:

$$n_{crit} = \frac{A_{ul}}{\gamma_{ul}}, \quad [cm^{-3}] \tag{B.45}$$

and the system will be dominated by collisions (close to LTE) if the density of particles of the system is higher than the critical density ($n(H_2)>n_{crit}$), or radiatively dominated if the density is lower than the critical density ($n(H_2)<n_{crit}$).

We can rewrite the detailed balance equation for a system in a stationary state (dN/dt=0) in a more general form by including the collisional probabilities, as follows:

$$N_j \left[\sum_{j \neq i} \left(B_{ij}\bar{J} + C_{ij} \right) + \sum_{j<i} A_{ij} \right] = N_j \left[\sum_{j \neq i} \left(B_{ji}\bar{J} + C_{ji} \right) + \sum_{j>i} A_{ji} \right], \tag{B.46}$$

where the left-side of the equation corresponds to the processes that de-populate the level i, and the right-side of the equation corresponds to the processes that populate the level i, which depend on the radiation field, $\bar{J}$ (see Eq.(B.31). Considering all the energy levels of the molecule, we will have a system of equations (i.e. the detailed balance for each level), which depends on the radiation field. Thus, we need to solve the radiative transfer equation, which depends on the Einstein coefficients. Therefore, both problems are coupled. Under LTE conditions, the problem is easily solved given that the populations are described by the Boltzmann equation Eq.(B.34). But in case of non-LTE conditions, the problem is not so easily solved. In particular, we need to know the value of the radiation field at each of the single points of the system, which in general depends on the processes that occur at the different points (*radiative trapping*). Additionally, in the case of a CSE there is a temperature gradient in the radial direction, which implies that the system cannot be described by a source function with a single excitation temperature. It is shown below how these problems can be treated and solved in the case of an spherically radially expanding CSE.

The radiative transfer problem coupled to the detailed balance can be solved iteratively assuming an initial solution for the populations (for example the populations given by the Boltzmann equation). With this initial solution we can calculate the value of the radiation field, and recalculate the populations until a convergence criteria is reached (e.g. tolerance value for the populations). Therefore, the radiative transfer problem can be solved computationally by using different methods. Some of these methods are described below. The typical difficulties for these computational methods are the convergence problems found for low densities or complex systems (e.g. molecules with a complex structure of energy levels).

Radiative trapping and LVG approximation

In many astrophysical systems, including CSEs, a photon emitted due to the transition between two energy levels, u and l, of a molecule or an atom (X_1) has a high probability of being absorbed

by a molecule/atom (X_2) of the same species. This effect would reduce the observed emission of that transition. Additionally, this problem is non-local, given that a photon emitted in a certain region of the CSE (or cloud) may be absorbed by a molecule located in a different region, which complicates the resolution of the radiative transfer problem coupled with the calculation of the populations. This problem can be solved by using the LVG approximation, which is based on the *scape probability* (Sobolev, 1960, Castor, 1970). The LVG consists in considering that the velocity gradient of the CSE varies with the distance. In general, the velocity gradient is usually approximated by the expression $dln(v)/dln(r)$=1. This implies that the emitted photons will be absorbed in a very close region, given that at distant locations the lines (i.e. transitions) are shifted due to Doppler effect. Therefore, these distant regions are transparent to the radiation emitted from a region with different velocity. We can estimate locally the radiation field by using the *escape probability* (β) (for a radial expanding spherical CSE):

$$\bar{J}(r) = (1 - \beta(r))\mathcal{S}_\nu(r) + \beta_c(r) I_{\nu,c}(r), \tag{B.47}$$

where r is the distance to the star, β describes the probability that an emitted photon can escape, $I_{\nu,c}$ is the background radiation (e.g. the CMBR and the radiation from the star), and β_c is the probability that a background photon could penetrate in the region where the problem is evaluated. The escape probability has the following expression:

$$\beta(r) = \int_0^1 \frac{1 - e^{-\tau(r)}}{\tau(r)} d\mu, \tag{B.48}$$

where μ is the cosine of the angle defined by the radial direction and the direction of the propagation of rays. The probability β_c has the following expression:

$$\beta_c(r) = \frac{1}{2}\left[1 - \left(1 - \frac{r_c^2}{r^2}\right)^{1/2}\right]^{1/2} \beta = W\beta(r), \tag{B.49}$$

where W is the *geometric dilution factor*, which is the ratio between the angle subtended by an object at a distance r and the total solid angle, and r_c the radius of the background source. In the case of the CMBR, which is isotropic, we have β_c=β and $I_{\nu,c}$=$B_\nu(2.7\,\mathrm{K})$.

The optical depth ($\tau(r)$), which depends on the radial position of the point at where we evaluate the problem, has the following expression:

$$\tau(r) = \frac{\tau_0}{1 + \mu^2}\left(\frac{d\ln v(r)}{d\ln r} - 1\right), \tag{B.50}$$

where $\frac{d\ln v(r)}{d\ln r}$ is the value of the velocity gradient. If this fraction is equal to 1, i.e. $v(r) \propto r$, we obtain:

$$\beta = (1 - e^{-\tau_0})/\tau_0, \tag{B.51}$$

and for the optical depth at the line centre (τ_0) we obtain:

$$\tau_0 = \frac{c^2 A_{ul} g_u}{8\pi\nu^2}\left(\frac{N_l}{g_l} - \frac{N_u}{g_u}\right)\frac{r}{\nu\, v(r)/c}. \tag{B.52}$$

In the simple case of the system with two energy levels, we can rewrite the detailed balance considering the escape probability by multiplying by β the probability of radiative transition:

$$\frac{dN_u}{dt} = -\beta A_{ul}\frac{N_u}{g_u} - 4\pi B_{ul}\beta_c(r) I_c(r)\left(\frac{N_u}{g_u} - \frac{N_l}{g_l}\right), \tag{B.53}$$

where the radiative trapping problem has been eliminated by using the LVG approximation.

Temperature gradient

Circumstellar envelopes have radial temperature gradients, from ∼2500 K in the photosphere of the star down to 10 K in the outermost parts. This temperature gradient has to be considered in the case that we solve the excitation problem of a molecule that is spatially distributed through the whole envelope, such as CO. Thus, a cloud with homogeneous T_{ex}, as well as density, would be a rough approximation for a CSE.

In the particular case of molecules that are spatially distributed in regions where these physical conditions may have varied significantly, we can divide the CSE in different shells. For each shell, the physical conditions can be considered homogeneous, and we can solve the radiative transfer problem by solving it first for the innermost shell, and then subsequently up to the outermost shell. The method will be explained below.

Numerical methods to solve the radiative transfer problem

In practice, the resolution of the radiative transfer equation (Eq.(B.24)) is an iterative process. We start from an initial guess for the populations or the radiation field. The LTE populations of each level are often used as initial guesses. Then, with these populations, we estimate the absorption coefficients and the source function (Eq.(B.38) and (B.39)), which allow us to solve the radiative transfer equation (Eq.(B.47)) and obtain the average value of the intensity of the radiation. With these values we solve the detailed balance (Eq.(B.46)), obtaining new values for the populations. Then, the previous process is done iteratively until a convergence criteria is reached. This method is applied for the total number of energy levels of the system (i.e. the molecule) and solved by linearasing the system of equations and applying a standard elimination. A more sophisticated formalism for this linearisation is the *lambda iteration* (LI) method, which is easily computationally implemented by using the formal solution of the radiative transfer equation $J_\nu = \Lambda_\nu \mathcal{S}_\nu$. However, it may have convergence issues for optically thick regions, and the method is more complicated to implement for a 3D model or for complex geometries.

Another frequently used method is Monte Carlo (MC) simulations, which simulates the physics of the radiative transport by modelling the emitted photons, and calculating which of them are absorbed, and adding photons that are incorporated as a part of an external radiation field. The studied system is divided in cells (gridding), for which the physical conditions (temperature and/or density) are given. The photons of the simulation are generated by stochastic processes, and each of the photons in the model represent a group or a package of photons that are re-counted at different steps. Thus, we can estimate the number of photons that have been absorbed or emitted trough the medium or cloud. MC methods require an initial guess of the solution (i.e. the populations), and the computational code proceeds iteratively until it reaches a convergence state. MC simulations are easily implemented in 3D models, compared to LI models. The execution time of a MC simulation will depend on the number of cells (i.e. the gridding) used, and also on the signal-to-noise ratio we want to obtain. However, this method has also convergence problems for optically thick regions.

There are also accelerated versions of both methods (ALI and AMC). All these methods are described in van Zadelhoff et al. (2002).

Emission lines of molecular rotational transitions

The transitions between rotational states of molecules (see Sect. B.2.2) produce lines in the spectra of EM radiation received from a CSE, according to the processes described before. The profile of the lines depends on the physical conditions and the dynamical properties of the regions where the molecules are located.

The lines produced by a gas whose molecules are distributed according to a Maxwellian velocity distribution, will have a shaped de-projected velocity component along the line of sight:

$$f(v)dv = \frac{1}{\sqrt{\pi}} \left(\frac{m}{2\pi T_k} \right)^{1/2} \exp \left(\frac{-mv^2}{2kT_k} \right) dv, \tag{B.54}$$

where T_k is the kinetic temperature of the gas, v is the average velocity of the molecules, and m their mass. Thus, line profiles are described by a -like profile:

$$\phi(v) = \frac{1}{\sqrt{\pi}} \frac{1}{\Delta\nu} \exp \left[- \left(\frac{\nu - \nu_0}{\Delta\nu} \right)^2 \right], \tag{B.55}$$

where ν_0 is the rest frequency of the line, and $\Delta\nu$ is the linewidth. The line profile function satisfies the following normalisation condition:

$$\int_0^\infty \phi(v)dv = 1. \tag{B.56}$$

The physical conditions (temperature, velocity ...) of the region where a spectral line arises from determine its linewidth:

$$\Delta\nu = \frac{\nu_0}{c} \sqrt{\Delta v_{turb}^2 + \Delta v_{th}^2} = \frac{\mathrm{FWHM}}{2\sqrt{\ln 2}}, \tag{B.57}$$

where Δv_{turb} is the *turbulence broadening*, and Δv_{th} is the thermal broadening. The turbulence broadening accounts for the non-thermal effects that occur at microscopic scales, which in the case of CSEs has typical values of $\sim$3 km s^{-1}. The thermal broadening is produced by the macroscopic movement of the molecules (in this particular case), which has the following expression as a function of velocity:

$$\Delta v_{th} = 2\sqrt{\ln 2} \sqrt{\frac{2kT_k}{m}}. \tag{B.58}$$

Besides these two broadening mechanisms, spectral lines may be broadened by opacity effects. The opacity broadening can be described as follows (e.g. Phillips et al., 1979):

$$\Delta v = \frac{\Delta v_i}{\sqrt{\ln 2}} \left[\ln \left(\frac{\tau_0}{\ln \left(\frac{2}{e^{-\tau_0}+1} \right)} \right) \right]^{1/2}, \tag{B.59}$$

where Δv_i is the intrinsic width of the line (Eq.(B.57)), and τ_0 is the optical depth at the line centre. $\Delta v \to \Delta v_i$ in the particular case that $\tau_0 \to 0$.

Additionally, the ratio between the spatial response of the telescope or power pattern (discussed in Sect. B.3.1) and the size of the observed source must be considered. Hence, for a

spherically expanding (at constant velocity) CSE, the typical line profiles observed can be described by the following expression:

$$S(v_z) = S(v_*)\left[1 - \frac{(v_z - v_*)^2}{v_e^2}\right]^{\alpha}, \tag{B.60}$$

where α is a parameter, v_z is the line of sight component of the velocity, v_* is the systemic velocity of the source, v_e is the terminal expansion velocity of the gas, and $S(v_z)$ and $S(v_*)$ are the flux densities for v_z and v_*, respectively (see Sect. 7.2.6.2 in Habing & Olofsson, 2003). The different line profiles are:

- *double horn*, if α<0, which corresponds to spatially resolved emission (i.e. the beam of the telescope is smaller than the size of the source, $\theta_b > \theta_s$), and optically thin emission (τ <1),
- *flat-topped*, if 0< α <1, which corresponds to spatially unresolved emission, and optically thin emission (τ <1),
- *parabolic*, if α=1, which occurs for optically thick emission (τ >1).

In addition to these profiles, the lines may display a triangular or Gaussian-shaped profile in the case that the emission arises from a region where the gas in the CSE is still being accelerated (i.e. inside the dust condensation region). Finally, lines of maser emission display very narrow and intense profiles due to the amplification effect (with an exponential growth) and velocity coherence, which occurs at very specific regions of the CSE (see e.g. Elitzur, 1992). An example of these line profiles is shown in Sect.4.1 in Velilla Prieto et al. (2017) (see Chapter 3).

Radiative transfer solution for a spherical multi-shell CSE

As it has been aforementioned, the resolution of the radiative transfer problem for a molecule that is distributed throughout the whole CSE, requires to divide the envelope into shells to take into account the temperature gradient. Thus, in the case of a radially expanding spherical CSE we will make the following approximations: (*i*) the velocity gradient will be $d\ln v/d\ln r$=1, which will allow us to use the LVG formalism, and (*ii*) the physical conditions for each shell are considered homogeneous, thus, we can consider that $\mathcal{S}_\nu$ is constant for each shell, and the solution will be Eq.(B.47).

The iterative method explained before must be applied for each shell, from the innermost shell up to the outermost shell. The method starts from the following expression:

$$\bar{J} = (1-\beta)\mathcal{S}_\nu + \beta(B_{\nu,cmb} + I_{\nu,*} + I_{\nu,dust}), \tag{B.61}$$

where the background radiation is composed of three different components: (*i*) the CMBR ($B_{\nu,cmb}$(T=2.7 K)), (*ii*) the radiation emitted by the central star ($I_{\nu,*}$), and (*iii*) the radiation emitted by the dust ($I_{\nu,dust}$). The dust and gas of the envelope will have a contribution to the emission and absorption coefficients:

$$j_\nu = j_{\nu,gas} + j_{\nu,dust} \qquad \alpha_\nu = \alpha_{\nu,gas} + \alpha_{\nu,dust}, \tag{B.62}$$

where $j_{\nu,gas}$ and $\alpha_{\nu,gas}$ are described according to Eqs.(B.37)-(B.38), and $j_{\nu,dust}$ and $\alpha_{\nu,dust}$ can be described by the following expressions:

$$j_{\nu,dust} = \alpha_{\nu,dust}B_\nu(T_{dust}), \qquad \alpha_{\nu,dust} = \kappa_{dust}\frac{\langle m_{gas}\rangle}{\rho_{gas}/\rho_{dust}}, \tag{B.63}$$

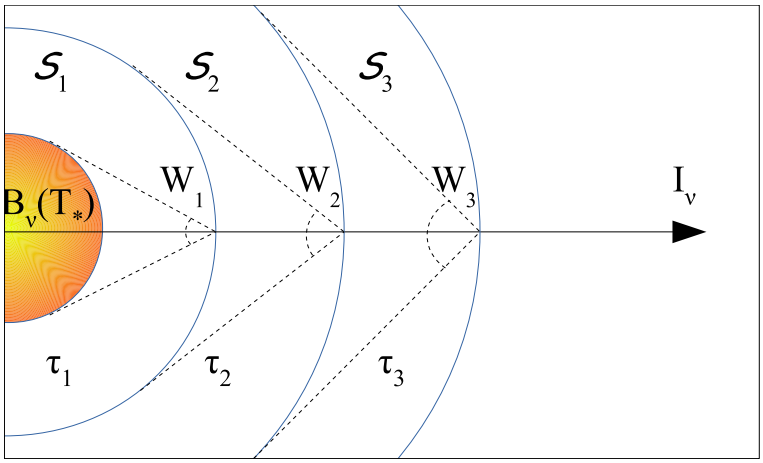

Figure B.4: Sketch of the radiative transfer through a CSE divided in multiple shells. Each shell is described by its source function ($\mathcal{S}_i$) and its optical depth (τ_i). The geometrical dilution of each shell at a point over the radial direction is represented by W_i. The initial specific intensity, which in this case corresponds to the blackbody radiation with a temperature T_*, is transported from shell to shell, until it goes through the whole envelope. The emergent specific intensity can be estimated by using Eq.(B.67).

where κ_{dust} is the *mass absorption coefficient* of the dust (this coefficient is sometimes expressed multiplying it by the density, i.e. the volume absorption coefficient), which is given by the collisional cross section of the grain per unit mass in $\mathrm{cm}^2\,\mathrm{g}^{-1}$ (see e.g. Suh, 1999), $\langle m_{gas}\rangle$ is the average mass of a gas particle (∼2.3 uma considering that the gas is mainly composed of H and He), and ρ_{gas}/ρ_{dust} the gas to dust ratio, which is observationally estimated (e.g. Bergeat & Chevallier, 2005).

The dust emission corresponds to the emission of a blackbody with the temperature of the dust ($B_\nu(T_{dust})$), corrected by the absorption coefficient. This temperature can be estimated by fitting the SED of the object to a power law expression such as $T_{dust} \propto r^{-\alpha}$. The absorption coefficient depends on the collisional cross section of the dust grains, the number density of dust particles (n_{dust} in units of cm^{-3}), and the *extinction efficiency* (Q_ν). The extinction efficiency depends, in general, on the frequency. The dust absorption coefficients can be estimated by using the optical properties of the considered dust, which can be found tabulated in some cases (e.g. Suh, 1999, Draine, 2003).

The optical depth must be calculated for each shell, and it corresponds to the sum of the gas (Eq.(B.38)) and dust contributions. The contribution of dust is:

$$\tau_{\nu,dust} = \int_{s_0}^{s} \alpha_{\nu,dust} ds = \kappa_{\nu,dust} \frac{\langle m_{gas}\rangle}{\rho_{gas}/\rho_{dust}} \frac{n}{N}. \tag{B.64}$$

The background radiation, as it was mentioned before, has three contributions. The CMBR is considered isotropic and equal to a blackbody at 2.7 K. The radiation from the star is diluted from shell to shell as it travels from the innermost shell to the outermost shell. Thus, for the N-th shell we have the following contributions:

- first shell, with a background intensity equal to $B_\nu(T_{eff})$ diluted according to the angle subtended by the star at the point r_1 (W_1), and its optical depth ($\tau_{\nu,1}$):

$$I_{\nu,1} = B_\nu(T_{eff}) W_1 e^{-\tau_{\nu,1}} + \mathcal{S}_{\nu,1}(1 - e^{-\tau_{\nu,1}}) \tag{B.65}$$

- second shell, with a background intensity equal to $I_{\nu,1}$ diluted according to the angle subtended by the first shell at the point r_2 (W_2), and its optical depth ($\tau_{\nu,2}$):

$$I_{\nu,2} = I_{\nu,1} W_2 e^{-\tau_{\nu,2}} + \mathcal{S}_{\nu,2}(1 - e^{-\tau_{\nu,2}}) \tag{B.66}$$

...

- N-th shell, with a background intensity equal to $I_{\nu,N-1}$ diluted according to the angle subtended by the N-1-th shell at the point r_N (W_N), and its optical depth ($\tau_{\nu,N}$):

$$I_{\nu,N} = I_{\nu,N-1} W_N e^{-\tau_{\nu,N}} + \mathcal{S}_{\nu,N}(1 - e^{-\tau_{\nu,N}}) \tag{B.67}$$

The radiation emitted by the dust must be transported from the outermost shell down to the immediately external shell to the shell considered, i.e. from the outermost shell down to the N+1-th shell, given that the contribution of the inner shells has been implicitly considered in the source function as well as in the emission coefficient in the Eq.(B.61).

With all the equations and approximations described before, we can solve the radiative transfer problem iteratively, adopting an initial guess for the populations (i.e. Boltzmann populations), from shell to shell, until we obtain all the populations in each shell. Once we have determined these populations, we can calculate the emergent intensity from the CSE according to the *ray-tracing* technique. This technique consists in solving the radiative transfer equation along different paths traced by the rays that pass through the circumstellar medium, and are collected by the detection device, i.e. the telescope. The intensity distribution is estimated as a function of the velocity component in the line of sight of the expanding gas, and the *impact parameter* (p), which is defined by the separation distance between a given ray and the line of sight to the centre of the source. It has to be considered which specific shells are crossed by each of the rays, in order to estimate the optical depth, and also which is the background intensity that must be taken into account. We must evaluate the integral over the line profile function Eq.(B.55)) as a function of the velocity, the impact parameter, and the distance (z) defined from the perpendicular to the position of the star. Thus, the line profile function has the following expression:

$$\phi(p, v, z) = \frac{c}{\sqrt{\pi}\nu_0 \Delta v} \exp\left\{ - \left[\frac{v + \frac{z}{(z^2+p^2)^{1/2}} v_{exp}}{\Delta v} \right]^2 \right\}, \tag{B.68}$$

where Δv is the linewidth (Eq.(B.57)), ν_0 is the rest frequency of the transition, and v_{exp} is the terminal expansion velocity of the gas in the CSE. We also consider a large number of shells:

$$r_{shell} \approx r_{in,shell} + \frac{r_{out,shell} - r_{in,shell}}{2} \approx cte. = \sqrt{z^2 + p^2}, \tag{B.69}$$

where $r_{out,shell}$ is the outer radius of a certain shell, and $r_{in,shell}$ is the inner radius of that shell. Now we can estimate the optical depth for each ray (and for a specific transition between the levels u and l):

$$\tau_{z_i,z_j}(p, v) = \frac{c^2 A_{ul} g_u}{8\pi\nu^2} \left(\frac{N_l}{g_l} - \frac{N_u}{g_u} \right) \int_{z_i}^{z_j} \phi(p, v, z) dz + \int_{z_i}^{z_j} \alpha_{\nu,dust} dz. \tag{B.70}$$

Finally, the radiative transfer equation can be solved for each of the rays following their path from shell to shell in the case of a radially expanding spherical CSE with a temperature gradient, obtaining the emergent intensity $I_\nu(p, v)$. In Sect. B.3 it is shown how to convolve this intensity with the power pattern of the telescope.

B.2.2 Molecular rotational spectroscopy

The rotational spectroscopy of molecules studies the transitions between the different energy levels of molecules due to the change of their rotational state. In general, molecules experience changes in their electronic configuration, in their vibrational state, and also in their rotational state. Electronic transitions occur at the visible and ultraviolet wavelength range, i.e. the same wavelength range in which transitions between levels of neutral atoms lie. Vibrational transitions lie in the infrared wavelength range. Pure rotational transitions lie between the radio wavelength range (for poliatomic molecules) down to the far infrared (for light H-bearing diatomic molecules), including the microwave wavelength range. Thus, the arrangement of the different types of transitions depends on their characteristic energies:

$$\Delta E = h\nu = hc/\lambda, \quad [K] \text{ or } [\mathrm{cm}^{-1}] \tag{B.71}$$

where ν is the frequency of the transition, and λ its wavelength. For the rotational transitions of the molecules considered in this PhD thesis, the energies are in general $\lesssim$20 K (e.g. $\sim$17 K for the transition J=3–2 of CO),[3] and the transitions lie in the millimeter wavelength range.

Consider a given diatomic molecule as a rigid rotor with a reduced mass (μ) as a first approximation. The rotational energy levels for a rigid rotor can be obtained by solving the time independent Schrödinger equation:

$$H\psi = -\frac{\hbar^2}{2\mu}\nabla^2\psi = E\psi, \tag{B.72}$$

where H is the Hamiltonian of the system, ψ is the wave function of the system, and μ the reduced mass. We make use of the *Born-Oppenheimer approximation*, which states that the nuclei can be considered fixed with respect to the electrons (which move faster and can re-adapt instantaneously to the overall movement) due to the difference between the masses of the nuclei and that of the electrons. Hence, the wave function can be separated into a nuclear contribution and an electronic contribution. Moreover, the nuclear wave function can be divided into a rotational contribution and a vibrational contribution given the large difference between energies of each type of transitions, then:

$$\psi_{tot} = \psi_{ele}\,\psi_{vib}\,\psi_{rot}, \tag{B.73}$$

$$E_{tot} = E_{ele} + E_{vib} + E_{rot}, \tag{B.74}$$

with $E_{ele} \gg E_{vib} \gg E_{rot}$, and the rotational part of the Schrödinger equation can be solved under the approximation of a rigid rotor. The solutions to this eigenvalues problem are:

$$E_J = \frac{\hbar^2}{2I}J(J+1), \tag{B.75}$$

where I is the *moment of inertia* of the molecule (I=μr^2), J is the *rotational angular momentum quantum number* (which represents the total angular momentum of the molecule), and r the *internuclear distance*. In the case of diatomic molecules, the principal moment of inertia is the moment with respect to the perpendicular axis to the line that links both nuclei, which intersects the mass centre of the molecule. Although, for the sake of simplicity, the two atoms

[3] Throughout the manuscript I have used temperature units for the energies, which makes easier their interpretation. However, energies are usually expressed by spectroscopists in units of cm^{-1}.

system is treated as the equivalent reduced system of a single mass equal to the reduced mass of the system.

The energy of a rotational level is quantized according to Eq.(B.75), and the emission of a photon will occur, for example, if a transition between a high energy state to a low energy state occurs according to Eq.(B.71). Therefore, the transition between two energy levels u and l, with $E_l<E_u$, is expressed as follows:

$$\nu = \frac{E_u - E_l}{hc} = F(J_u) - F(J_l), \tag{B.76}$$

where $F(J)$ is the *rotational term*, and has units of cm^{-1}. The rotational term is:

$$F(J) = E/hc = \frac{h}{8\pi^2 cI} J(J+1) = BJ(J+1), \tag{B.77}$$

where B is the *rotational constant*, and has also units of cm^{-1}. From the determination of the rotational constant, we determine the internuclear distance.

Molecules will have rotational transitions if they have a *permanent electric dipole moment*, μ, which has CGS units of statC cm, although it is commonly used the *Debye*. From a semi-classical point of view, an electric dipole moment is present if the charge distribution is not symmetrical. This situation occurs for all heteronuclear diatomic molecules, such as CO or SO, while homonuclear molecules such as H_2 have no electric dipole moment due to the symmetrical arrangement of their charges. Homonuclear molecules can be detected by observing their electric quadrupole transitions or magnetic transitions (e.g. Timmermann et al., 1996). In the case of rotational transitions for diatomic or linear molecules, the selection rule $\Delta J=\pm 1$ must be fulfilled.

The energy states have a *degeneration*, that is, there are several available energy levels with the same energy. In the case of a diatomic molecule, there is only one principal rotation axis, given that the rotation around the axis that passes through both atoms is negligible. For a fixed orientation of the principal rotation axis of a molecule, which is usually called laboratory axis, and considering the projections of the total angular momentum over the laboratory axis, there are $2J+1$ equivalent orientations with the same J. These states are called degenerated states, and are differentiated by the quantum number M_J ($M_J=0,\pm 1,...,\pm J$).

Molecules with more than 2 atoms

We must consider how the previous concepts change when considering non-linear molecules. As a first consideration, those molecules that have an inversion centre do not have an electrical dipole moment (e.g. CO_2), and will not be discussed here. Non-linear molecules have three principal moments of inertia (I_a, I_b, and I_c), which are perpendicular between them and pass through the centre of mass of the molecule. The moment of inertia is minimum along the a axis, and maximum along the c axis, thus:

$$I_c \geq I_b \geq I_a. \tag{B.78}$$

Linear molecules such as HCN or diatomic molecules have $I_a=I_b$, and $I_c=0$. Spherical rotors such as SF_6 or CH_4 have $I_c=I_b=I_a\neq 0$. Asymmetrical rotors (see Fig. B.5) such as H_2CO have $I_c\neq I_b\neq I_a$. Symmetrical prolate tops such as NH_3 have $I_c=I_b>I_a\neq 0$, while oblate tops such as benzene have $I_c>I_b=I_a\neq 0$. The formalism that has been previously shown for diatomic

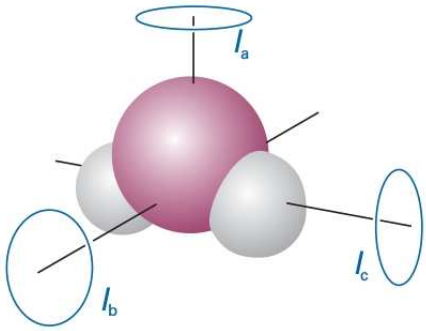

Figure B.5: Asymmetric rotor with its three rotation axes and its three moments of inertia (I_a, I_b and I_c). *(Credits:Atkins & de Paula (2006))*

molecules is also valid for poliatomic linear molecules. However, for the rest of geometries, the solution to the Schrödinger equation will not be equal, in general, to that of Eq.(B.75). In these cases, the angular momentum of a molecule may be oriented along any direction in space, thus, we must use additional quantum numbers to describe its rotational state, such as the quantum numbers K_a or K_c which describe the projection of the total angular momentum over these axes. In the case of a symmetrical prolate rotor, for example, the rotational term is:

$$F(J,K) = BJ(J+1) + (A-B)K^2 \tag{B.79}$$

where A and B are the rotational constants that correspond to the axes a and b, respectively. K corresponds to the quantum number that represents the projection of the total angular momentum over the a-axis, which has the values K=0, 1, 2,. . . ,J.

The selection rules depend on the geometry of the molecule. In the particular case of an asymmetrical rotor, the rotation is described by three different electric dipole moments (μ_a, μ_b and μ_c) with respect to the three principal axes, and it will have a-, b-, and c-type transitions. Each type of transition has its own selection rules, which depend on the quantum numbers J, K_a, and K_c. Energy levels of non-linear molecules will also have a degeneration, and its expression depends on the geometry of the molecule.

Deviations of the rigid rotor model

For the sake of simplicity, we will consider a diatomic molecule. The rigid rotor model states that both nuclei stay at a fixed distance, but it is more accurate to describe the bond between the nuclei as a spring instead of a rod. From a classical point of view, it is clearly seen that the rotation of a molecule will lead to a change of the internuclear distance. The distance between nuclei will increase with the energy of the rotational state. This is called *centrifugal distortion*, and it has to be considered in the rotational term as:

$$F(J) = BJ(J+1) - DJ^2(J+1)^2, \tag{B.80}$$

where D is the *centrifugal distortion constant*, which is always positive for a diatomic molecule.

Additionally, we have only considered the rotational movement of molecules, but molecules may also vibrate and modify their internuclear distance. The formalism described in Eqs.(B.75)-(B.77) describes the energies and transitions of the ground vibrational state. However, in the

innermost regions of CSEs temperatures are high enough to vibrationally excite molecules through collisional processes (E∼1000-2000 K) for example. The vibration of a molecule modifies the rotational term, the rotational constant, and the centrifugal distortion constant. In the case of a linear molecule, we obtain:

$$F_v(J) = B_v J(J+1) - D_v J^2 (J+1)^2, \tag{B.81}$$

and the centrifugal distortion constant, under the harmonic oscillator approximation, has the following expression:

$$D = 4B^3/\omega^2, \tag{B.82}$$

where B is the rotational constant and ω is the vibrational wave number (see e.g. Herzberg, 1950).

Nuclear spin effect in the rotational spectrum

We omitted the effect of the nuclear spin in the wave functions, and this must be included as an additional term (ψ_{sn}) in Eq.(B.73). The rotational spectrum of molecules is modified by the nuclear spin due to the magnetic moment, which produces a separation between levels or *hyperfine structure*. This occurs, for example, for HCN given that ^{14}N has a non-zero nuclear spin.

Moreover, in the case of symmetric molecules, the nuclear spin will determine if rotational levels can be occupied according to the Pauli exclusion principle. This principle states that the total wave function must be anti-symmetric for systems of fermions (half-integer spin), and symmetric for bosons (integer spin) with respect to the exchange of two identical fermions or bosons, respectively. Consider for simplicity the H_2. Both nuclei are fermions (s=1/2), therefore, the wave function that describes the system must be anti-symmetric with respect to the exchange of both nuclei, with a total of four different possibilities to combine them (m_s=±1/2 for each nucleus). There are three symmetrical combinations and only one anti-symmetrical combination with respect to the exchange of nuclei. The electronic and vibrational wave functions are symmetric. The rotational wave function is symmetric if J is an even number, and anti-symmetric if J is an odd number. Then, the energy levels for which J is an odd number, must be combined with a symmetric nuclear wave function in order to not violate the Pauli exclusion principle, and vice versa. Given that there are three symmetric nuclear spin wave functions and just one anti-symmetric (with respect to permutation of nuclei), the degeneration of symmetric states is three (*ortho*, for odd J with g_N=3), and is one for anti-symmetric states (*para*, for even J with g_N=1).

Potential energy surfaces (PES)

The potential energy surfaces of a system (e.g. a molecule) describes the energy of the system in terms of the relative positions of the components of the system (e.g. the atoms of the molecule). The energetic analysis of system can be studied through experimental techniques and theoretical models, such as the study of the collisions between atoms to form a molecule. For example, the reaction rate constant (see Eq.(B.3)) of a given process can be determined by averaging all the possible successful interactions of reactants (in different initial energy states), i.e. the processes for which the products are formed. Furthermore, if the PES is characterised

we can determine the distribution of the energy levels of the molecule formed, and its collisional coefficients.

Some examples of experimental characterisation methods of the PES and reaction rates are the CRESU, the IR chemiluminiscence, or the laser induced fluorescence techniques (e.g. Chastaing et al., 2001, Antiñolo et al., 2016). Theoretical ab initio methods, such as MOLPRO[4], are based on the Hartree-Fock equations and density functional theory (e.g. Parr, 1983, Amusia et al., 2003).

Aditional considerations

Basic concepts of molecular rotational spectroscopy have been presented in this section. As it has been shown, there are deviations from the rigid rotor approximation, such as the coupling between rotation and vibration, and deviations from the harmonic oscillator approximation with respect to Eqs.(B.81)-(B.82). In particular, the anharmonic oscillator would be a better approximation. Additionally, hyperfine separation of levels can occur due to different couplings such as the Λ-*doubling*. A rigorous explanation of these considerations is out of the scope of this PhD manuscript, thus, I suggest to consult Herzberg (1950) for further details.

The main problem of molecular rotational spectroscopy lies in the complexity of the Hamiltonian of the systems (e.g. the molecules) studied. More sophisticated methods simplify the problem by using a reduced Hamiltonian and a set of reduced parameters to describe it, such as the S-type reduced Hamiltonian, which includes high order terms of the centrifugal distortion constants (Dunham, 1932, Watson, 1967, 1977). This problem can be solved through different approaches, with the aim of obtaining the PES and determine the structure of the energy levels of the studied molecule. As mentioned above, PES and the spectroscopy of a molecule can be determined through ab initio calculations. Inversely, we can determine the PES of a molecule from its calculated or observed spectrum. Therefore, laboratory and theoretical studies as well as observational astronomical studies are important to determine the spectroscopy of molecules. The latter are particularly important, given that some species or physical conditions are not easily synthesised or reproduced in the laboratories.

B.3 Line detection: radiotelescopes

The next step is to describe how to register or receive the EM radiation produced in the observed source, which is carried out by observing with telescopes, mainly by ground-based telescopes. The Earth's atmosphere is the principal handicap of ground-based observations, given that gases and particles that form the atmosphere would scatter and absorb EM radiation. Water vapour and oxygen (O_2) are the main contributors to the atmospheric opacity in the millimeter wavelength range, while for frequencies above 350 GHz other molecules such as N_2 or CO_2 contribute to this opacity. According to this, radiotelescopes are built at high altitude locations, in order to reduce the amount of the atmospheric O_2, and also in dry locations, to avoid large amounts of water vapour.

[4] `https://www.molpro.net/`

Figure B.6: Image of ALMA, located at the "Llano de Chajnantor" in Chile, at an altitude of 5000 m. The atmospheric conditions at this location are excellent to carry out astronomical observations in the millimeter wavelength range. *(Credits: R. Hills, ESO/NAOJ/NRAO ALMA)*

B.3.1 Single dish observations

Radiotelescopes are large antennas with a (in general) parabolic dish that focus the radiation on its paraboloid toward its primary focus. Depending on the design of the antenna, a feed-horn (or wave guide) could be located at the primary focus to collect the EM radiation, or it could be reflected by a sub-reflecting system and sent through a hole at the centre of the dish, where a feed-horn collects the radiation or an optical system redirects this radiation toward the receiver system. The signals collected by our telescope are very weak, and they must be amplified. The receiver system makes a previous down conversion of the signal (i.e. transforms the signal to a low frequency), which is better to avoid cable transmission losses and better for amplification. This low frequency signal is obtained by mixing the signal collected by the telescope with a reference signal called *LO frequency*, inside a low-noise superconducting mixer. This mixing process is known as *heterodining* process, and the resulting signal is called *IF* or intermediate frequency. The IF is amplified first by a cryogenic amplifier and then by subsequent amplifiers before being sent to the spectrometers. The IF signal is analysed in the spectrometers, filter banks, or correlators, which are commonly known as *backends*. Finally, the signal is transmitted to a computer, which records the data in a proper format.

Radiotelescope response and main parameters

Radiotelescopes have their own response to the intensity of the EM radiation collected from a non-resolved source, which is known as *beam pattern*, *power pattern*, or *PSF*(see Fig. B.7). The normalised power pattern as a function of the azimuthal and elevation angles is expressed as follow:

$$P_n(\theta,\phi) = \frac{P(\theta,\phi)}{P_{max}}, \tag{B.83}$$

which is specific for a given telescope, is dimensionless, and where P_{max} is the maximum power received by the telescope. If we observe a given brightness distribution ($I_\nu(\theta,\phi)$), the received power is equal to:

$$P_{rec,\nu} = \frac{1}{2}A_e \int_\Omega I_\nu(\theta,\phi)P_n(\theta,\phi)d\Omega, \tag{B.84}$$

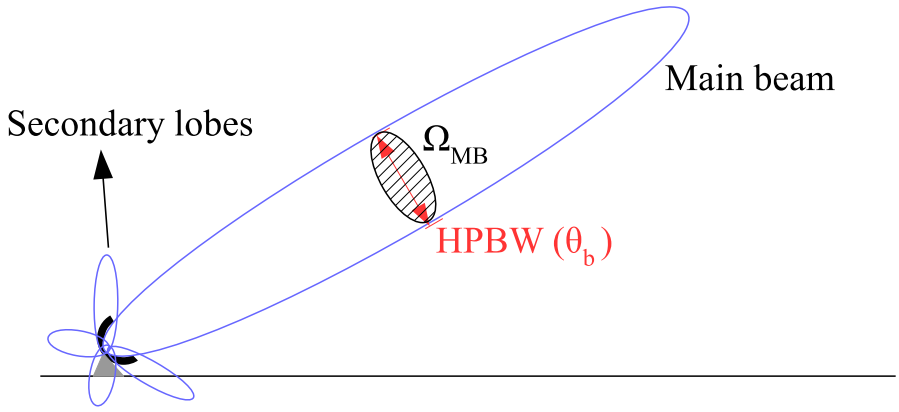

Figure B.7: Sketch of the power pattern or beam pattern of an antenna. The main beam, the secondary lobes, the half power beamwidth (HPBW$\equiv \theta_b$), and the subtended angle by the main beam (Ω_{mb}), are explicitly shown.

where A_e is the *effective aperture* of the antenna (in units of cm^2), which is intuitively interpreted as the cross section of the antenna.

The *solid angle of the beam* is defined as follows:

$$\Omega_A = \iint_{4\pi} P_n(\theta,\phi)d\Omega, \tag{B.85}$$

which is measured in units of rad^2 or arcsec^2, and where $d\Omega$=$sin\theta d\theta d\phi$, integrated over the whole sky (4π). The solid angle of the beam and the effective aperture of an antenna satisfy the following relation:

$$A_e\Omega_A = \lambda^2 \tag{B.86}$$

The integration of the solid angle over the main lobe of the power pattern gives the *main beam* of the telescope:

$$\Omega_{mb} = \iint_{mb} P_n(\theta,\phi)d\Omega, \tag{B.87}$$

from which the *half power beam width* (θ_b) is defined by the angle subtended by the main lobe at the half of its maximum value. The HPBW represents the spatial resolving power of the telescope, which depends on the observed frequency. Additionally, the *main beam efficiency* is defined as follows:

$$B_{eff} = \eta_b = \frac{\Omega_{mb}}{\Omega_A} \leq 1, \tag{B.88}$$

which describes the fraction of the received radiation that comes from the main beam.

According to the Nyquist theorem, a given resistor at a temperature T, produces a thermal noise whose power is equal to $P = \Delta\nu kT$, where $\Delta\nu$ is the bandwidth. Analogously, the power received when a telescope is pointed toward a source can be related to a temperature scale using the Nyquist theorem, where the radiotelescope plays the role of the resistor. This magnitude is called *antenna temperature*, and is equal to:

$$T_A(\theta,\phi) = \frac{1}{\Omega_A}\int_{source} T_R(\theta,\phi)P_n(\theta,\phi)d\Omega, \quad [K] \tag{B.89}$$

which depends on the radiotelescope used, so it must be conveniently converted to a temperature scale that does not depend on the parameters of the antenna. Thus, we define the *main beam temperature* (T_{mb}) as:

$$T_{mb} = \frac{F_{eff}}{B_{eff}} T_A^* = \eta_{mb} T_A^*, \quad [K] \tag{B.90}$$

where T_A^* is the *corrected antenna temperature*, i.e. the temperature that the observed source would have measured outside the Earth's atmosphere and corrected from radiative losses and other factors such as the spillover, η_{mb} is the *efficiency of the telescope*, and F_{eff} is the forward efficiency, which is defined as follows:

$$F_{eff} = \eta_f = \frac{\iint_{2\pi} P_n(\theta, \phi) d\Omega}{\Omega_A} \leq 1. \tag{B.91}$$

The forward efficiency stands for the fraction of the collected power that comes from the forward part of the telescope. Finally, making use of Eqs.(B.23), (B.89), and (B.90), we can obtain the expression of the corrected antenna temperature for the observed intensity distribution:

$$T_A^* = \frac{1}{F_{eff}} \int_{source} T_R(\theta, \phi) P_n(\theta, \phi), \quad [K] \tag{B.92}$$

and correct this scale to T_{mb} by using Eq.(B.90).

Calibration

The calibration of observations in the millimeter wavelength range is applied to correct the effects produced mainly by the atmosphere and the receiving system. The goal is to obtain the net astronomical signal in units of a physical scale of the intensity of the received power. In practice, the goal is to convert the output voltage from the receiver into a temperature scale, corrected of the atmospheric contribution, and the electronic currents produced by the electronics of the receiving system. The Earth's atmosphere absorbs the EM radiation that passes through it. The atmospheric impact on the observed signal can be minimised by creating models of the atmospheric transmission (see Fig. B.8) to constrain the effects on the opacity, radiance, phase-delay, and polarisation produced by the atmosphere (e.g. Cernicharo et al., 1985, Pardo et al., 2002). These models are in general simplified by considering a one dimensional plane parallel atmosphere under LTE conditions.

The calibration method in the millimeter wavelength range is based on the *chopper wheel*[5] (Jewell, 2002, and references therein). With this method the electric response (i.e. voltages) of the receiver is measured when a hot or a cold load (which act as reference blackbody emitters) or the blank sky and the sky including the source are observed. The power output is linearly related to the temperature of the receiving system, according to the Nyquist theorem. This standard method is described in Ulich & Haas (1976). The corrected antenna temperature obtained when observing an spectral emission line arising from a source with an excitation temperature T_{ex}, with a background radiation described by T_{bg}, and an optical depth equal to τ_ν, is:

$$T_A^* = \eta_f (1 - e^{-\tau_\nu})(J_\nu(T_{ex}) - J_\nu(T_{bg})), \tag{B.93}$$

[5]This name is given because the wheel that spins to alternate between the different calibration loads is similar to a boat screw or a chopper wheel.

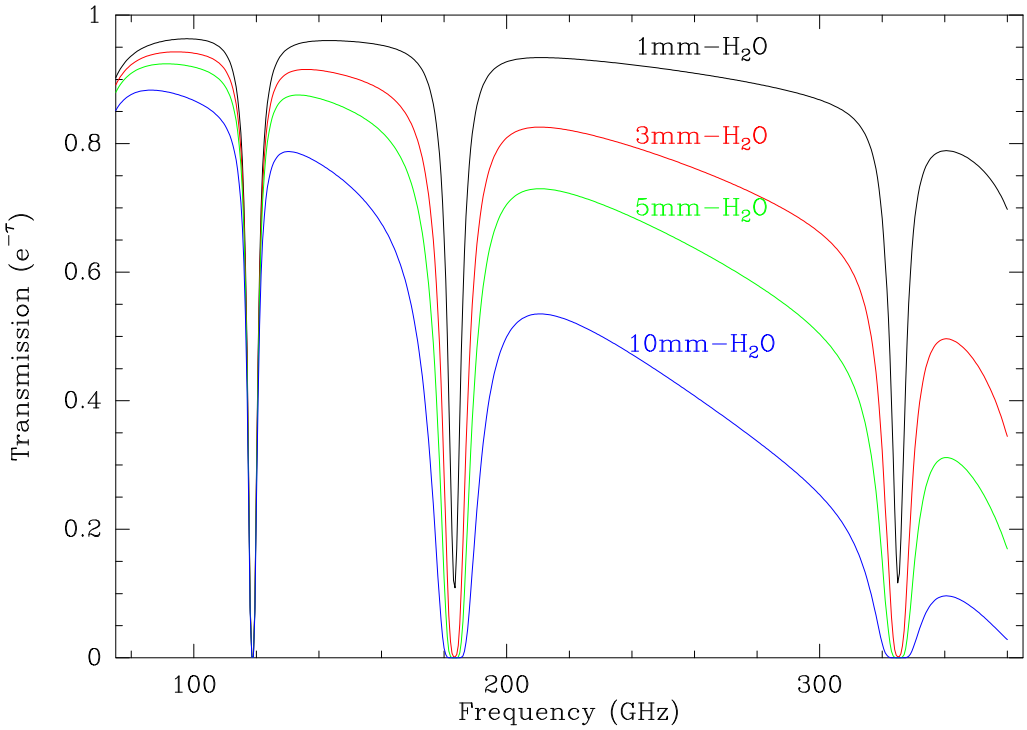

Figure B.8: Atmospheric transmission model for different contents of precipitable power vapour, for a ground-based telescope at an altitude of 2560 m, computed with the task ATMOSPHERE of the ASTRO software of GILDAS, which makes use of the ATM85 model (Cernicharo et al., 1985).

where the radiation temperatures $J_\nu(T_{ex})$ and $J_\nu(T_{bg})$, are described by Eq.(B.23). This method requires to observe the source (i.e. the "on" position) and the blank sky (i.e. the "off" position) alternately, which allow us to subtract the contributions that do not correspond to the radiation arising from the source.

The rms of the noise of the signal observed is given by the *radiometer equation*:

$$\sigma = \frac{T_{sys}}{\eta_{spec}\sqrt{\Delta\nu\, t}}, \quad [K] \tag{B.94}$$

where σ is the rms of the noise obtained by integrating during the time t with a spectral resolution equal to $\Delta\nu$, T_{sys} is the *system temperature*, and η_{spec} the efficiency of the spectrometer. The system temperature accounts for the different sources of noise that are added to the signal due to the optics of the system, the receiver system, the emission of the sky, and the emission from the secondary lobes of the radiotelescope. In the case of heterodyne receivers, it must be taken into account an additional factor due to the number of polarisations:

$$\sigma = \frac{T_{sys}}{\eta_{spec}\sqrt{\Delta\nu n_{pol} t}}. \quad [K] \tag{B.95}$$

The total integration time t as a function of the times spent at the on and off position is expressed as follows:

$$t = \frac{t_{on} t_{off}}{t_{on} + t_{off}} \tag{B.96}$$

Observing modes for single dish and data reduction methods

As mentioned before, on-source and off-source positions are observed in standard observational procedures. Both positions can be observed by doing *position switching* or *frequency switching*. Position switching consists in pointing the antenna toward a region of the sky that is free of emission arising from the scientific target, but close enough to avoid large atmospheric variations. This can be done by moving the dish of the telescope or by *wobbler switching*, in which the antenna stays fixed and the sub-reflector is moved by throws of $\lesssim 1'$. Wobbler switching produces very flat and stable baselines, given that the atmospheric variation between the on and off positions is minimal. However, it is not suited to observe extended sources.

Frequency switching refers to the strategy in which the off-source integration is obtained by switching the observed frequency, thus, the antenna keeps the pointing toward the scientific target. The off-source integration must correspond to a wavelength range in which the source does not present emission or absorption in its spectrum. Therefore, this method is particularly good for line-poor sources. The rms of the noise for the position switching method is a factor $\sqrt{2}$ larger than the rms obtained by frequency switching.

Previous to the observation of the scientific target, in the case of millimeter radiotelescopes, the *pointing* and *focus* of the antenna must be calibrated. Both parameters are calibrated by observing an intense source, like a planet or a quasar, with a diameter smaller than the HPBW of the radiotelescope. The antenna is initially pointed toward the pointing/focus calibrator. In the case of the pointing, the antenna collects the radiation arising from the calibrator while it sweeps the source in the azimuthal and elevation directions. In the case of the focus, the antenna collects the radiation while the optical path of the rays is modified. Then, these calibration observations are compared to pointing and focus models to determine the corrections that must be applied. Pointing corrections are made when the telescope has to move considerable distances, and also each 45–60 minutes, even it has been stopped, given that temperature variations, anomalous refraction and stress forces acting on the structure may off-centre the telescope. The calibration of the focus must be checked when significant variations of the air temperature (e.g. during the sunset or sunrise) occurs. Typical uncertainties of the pointing are in the order of a few arcseconds, and $\lesssim 1$ mm for the correction of the focus.

After the observations, we obtain our spectra calibrated in antenna temperature and frequency scale. The reduction process is done by using a specific software (e.g. GILDAS[6] for IRAM-30 m), and will depend on the observation. In the case of on-off wobbler switching observations, such as those analysed in this PhD thesis, bad spectra and bad channels must be flagged first. The remaining spectra must be corrected by applying an appropriated baseline. Then, image band contribution must be identified and removed. Finally, the resulting spectra are averaged to produce the final product, which will be analysed.

Image band

The heterodining process of the mixing of the LO signal with the sky signal, produces two different signals, which correspond to the frequencies $\nu_{LO} \pm \nu_{IF}$. Both signals are amplified and transmitted through the detection system. IRAM-30 m receivers are equipped with electronic devices that are able to attenuate one of these two signals up to -14 dB (Carter et al., 2012). This means that the lines lying in the upper sideband will appear attenuated in the lower sideband, and vice versa. These contributions are called *real* and *image* signals.

[6] `http://www.iram.fr/IRAMFR/GILDAS`

A typical observational strategy to easily identify the image band consists in observing the target frequency range and additionally the same range but shifted by +50 and -50 MHz. This frequency offset is enough considering the bandwidth and spectral resolution achieved with EMIR. If the standard and frequency shifted spectra are compared, it will be noticed that image lines shift their central frequencies, while real lines do not experience any shift.

Spatially unresolved and resolved sources

If the HPBW is larger than the size of the source (i.e. the angular diameter of the source), that is $\theta_s \ll \theta_b$, the integral of the power pattern over the solid angle subtended by the source can be considered equal to 1. Therefore, the antenna temperature (Eq.(B.89)) is:

$$T_A = \frac{A_e}{2k} \int\limits_{source} I_\nu \, d\Omega, \tag{B.97}$$

obtained by using Eq.(B.86), the Rayleigh-Jeans approximation, and the Nyquist theorem. The integral in Eq.(B.97) is equal to the flux density of the source (Eq.(B.16)). Therefore, under the point-source approximation, the antenna temperature gives a direct measure of the flux density of the source, then:

$$T_A = \frac{A_e}{2k} S_\nu, \tag{B.98}$$

where the inverse of the factor $A_e/2k$ determines the conversion factor between the antenna temperature and flux density in $\mathrm{K\,Jy^{-1}}$ for a given telescope. This conversion factor is usually tabulated as a function of frequency.

If the observed source is spatially resolved ($\theta_s > \theta_b$), it would be necessary to integrate the flux density of the object over the total solid angle subtended by the source. In this case, the antenna temperature (Eq.(B.89)) is expressed as follows:

$$T_A = \frac{A_e}{2k} I_\nu \, \Omega_{mb} = \frac{A_e}{2k} I_\nu \, \frac{\pi}{4 \ln 2} \theta_b^2, \tag{B.99}$$

where the main beam has been considered Gaussian. If the specific intensity is not constant for the whole brightness distribution of the source, we will be measuring the specific intensity averaged over the main beam, or flux density per main beam in units of $\mathrm{Jy\,beam^{-1}}$. The usage of these units for interferometric maps may be confusing, which are units of specific intensity or units of flux density per beam (both are equivalent), and only in the case of a non-spatially resolved source can be considered as a direct measure of the flux density.

Beam Filling Factor

It has to be considered the fraction of the main beam that the observed source occupies to correct the main beam temperature to the brightness temperature of the source. This fraction is called *beam filling factor* or *beam dilution factor* (η_{dil}). If the observed source is extended and it is spatially resolved ($\theta_s > \theta_b$, i.e. the source is larger than the HPBW), the main beam temperature is a measure of the average specific intensity of the source in the area delimited by the beam, i.e. $T_{mb} = J_\nu(T_B)$.

On the other hand, if the source is spatially unresolved ($\theta_b < \theta_s$), the dilution of the source must be considered:

$$T_B = \eta_{dil} T_{mb}, \tag{B.100}$$

where η_{dil} is the dilution factor. This factor depends on the geometry of the source. The dilution factor for a gaussian distribution is:

$$\eta_{dil} = \frac{\theta_s^2}{\theta_s^2 + \theta_b^2}, \tag{B.101}$$

where θ_s is the FWHM of the Gaussian and θ_b the HPBW of the main beam of the telescope. In the case of a uniform disc, we have:

$$\eta_{dil} = 1 - e^{\ln 2(\theta_s/\theta_b)^2}, \tag{B.102}$$

where θ_s is in this case the diameter of the disc.

B.3.2 Basic concepts of millimeter interferometry

The interferometry or aperture synthesis is the use of an array of antennas to measure the interference patterns received by each pair of antennas of the array, and obtain the brightness distribution of the source observed. The spatial resolution of a single-dish is limited due to its size (first null of an Airy disc):

$$\theta \approx 1.22\frac{\lambda}{D}, \tag{B.103}$$

where θ is the spatial (i.e. angular) resolution in radians, λ is the observed wavelength, and D the diameter of the antenna. According to Eq.(B.103), it would be needed an unrealistic huge radiotelescope to spatially resolve small regions at distant objects, such as the dust formation region of an AGB CSE. Interferometry solves this problem through the usage of several small antennas separated by large distances, which is approximately equivalent to observe with a virtual antenna with a diameter equal to the maximum *baseline* of the array. The baseline is the distance that separates two antennas of the array.

Consider the example of a two element interferometer separated by a distance b observing the same object, at the same time, and frequency. The signals collected by the antennas will have a certain time delay because the optical path travelled by the radiation is not equal for each antenna (see Fig. B.9). A single measure of the brightness distribution by each pair of antennas is called *visibility*. The *correlator* collects the signals (i.e. the output voltages) from each pair of antennas, multiplies these voltages, and makes their time-average. The mathematical expression for a visibility is:

$$V(u,v) = \iint\limits_{source} I(x,y)e^{2\pi i(ux+vy)}dxdy = Ae^{-i\varphi}, \tag{B.104}$$

which is also called *spatial autocorrelation function*, where u and v are the coordinates (baselines expressed as spatial frequencies, i.e. b/λ) in the uv-plane, x and u are the real coordinates (the direction cosines defined by the tangent plane to the source and relative to the reference position in the uv-plane), $I(x,y)$ is the brightness distribution of the source, A is the *amplitude*, and φ the *phase*. A sketch with the coordinates is shown in Fig. B.10.

The uv-plane (see Fig. B.10) is defined with respect to a reference antenna and baseline, where u is defined along the East-West direction, and v in the North-South direction. Visibilities (Eq.(B.104)) are the two-dimensional Fourier transform of the brightness distribution of the

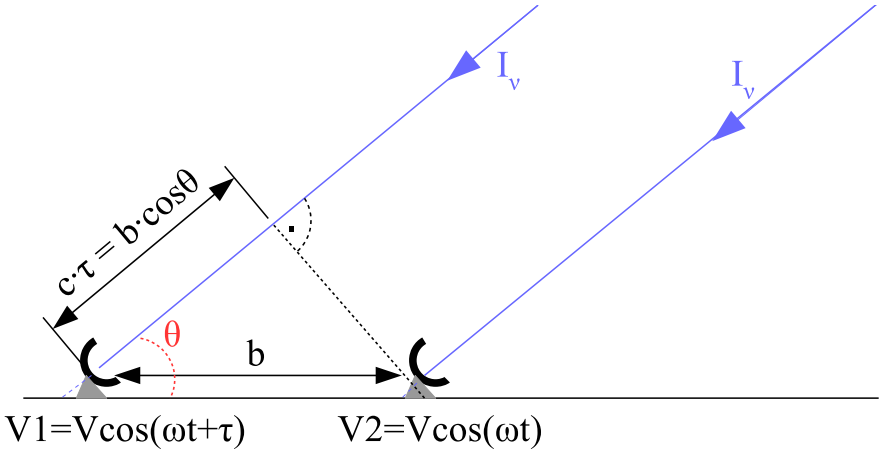

Figure B.9: Two-dimensional sketch of a two-element interferometer separated by a baseline b. The astronomical signal (I_ν) is collected by the antenna 2, for which the output voltage is V2, and the same signal is collected by the antenna 1 after a time delay (τ), for which the output voltage is V1. The correlation of both signals results in a signal with an amplitude proportional to the square of the voltage: $\frac{V^2}{2}\cos(\omega\tau)$.

source, and vice versa with the inverse Fourier transform. This is known as the *van Cittert-Zernike theorem*. Visibilities have complex values, which can be expressed in terms of an amplitude and a phase. The amplitude represents the intensity of each pair of spatial frequencies (u, v), and the phase will give us the spatial location with respect to the centre of phases, defined as (x,y)=(0,0). According to this method, the sampling of the real brightness distribution improves with the number of baselines observed. Additionally, each measure produced in the correlator (C) must be corrected (divided) by the primary beam response, thus:

$$C = \iint_{source} A(x,y)I(x,y)e^{2\pi i(ux+vy)}dxdy, \tag{B.105}$$

where $A(x,y)$ is the primary beam or normalised power pattern of the elements (i.e. antennas) in the array. The *field of view* (FOV) of the interferometer is given by the HPBW of the antennas.

In practice, the best way to improve the sampling of the uv-plane, that is, increase the number of observed spatial frequencies, is done by following these three actions:

1. increase the number of antennas in the array, which increases the number of the observed baselines to $(N(N-1))/2$, where N is the number of antennas,

2. arrange the antennas in different configurations,

3. use the Earth rotation, which increases the uv-plane coverage without moving the antennas from their positions.

Each particular baseline samples a specific pair of spatial frequencies. The longest baseline corresponds to the maximum angular resolution achievable (allow to spatially resolve small physical structures), while the shortest baseline corresponds to the minimum angular resolution achievable (large structures). The *maximum recoverable scale* (MRS) is the minimum angular

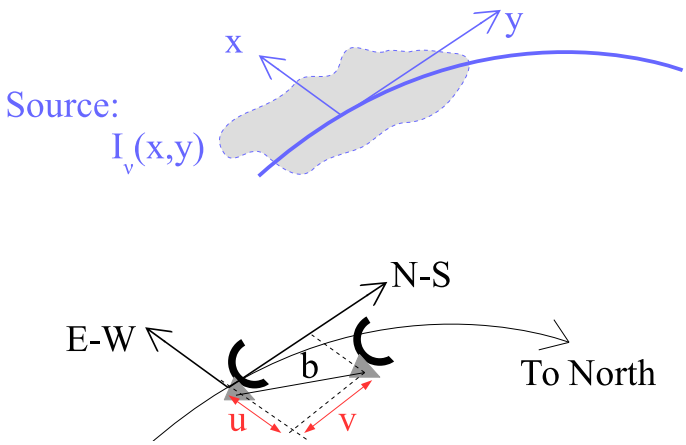

Figure B.10: Sketch of the systems of reference for a two-element interferometer observing a source with a brightness distribution $I_\nu(x, y)$. The spatial frequencies u and v are defined along the E-W and N-S directions, respectively.

resolution achieved, which is given by the minimum separation of the antennas (b_{min}) in a given configuration:

$$MRS \approx \frac{\lambda}{b_{min}}, \quad [rad] \text{ o [arcseg]} \tag{B.106}$$

The minimum separation between antennas is limited by their diameters, given that two antennas cannot be physically closer than that, or slightly closer when observing objects at low declinations. However, in the low declination case, the antennas may produce *shadowing*, that is, one dish blocks the incoming radiation to the shadowed antenna.

The lack of observed short spatial frequencies (see Fig. B.11) in extended objects can be corrected by single-dish observations, either through *total power* (also called *zero spacing*) observations, or by *on-the-fly* (also called *short spacing*) observations, which consists in observe the extended object while the antenna moves covering the observed region of the sky. In the case of ALMA, there is a second compact interferometer composed of smaller antennas called ACA, which allows to recover the flux filtered by ALMA due to the lack of observed short spatial frequencies in certain scientific cases.

Calibration

In the case of aperture synthesis the calibration is slightly complex than that of single-dish observations. There are instrumental and atmospheric contribution for each antenna, which in general will be different. These contributions are taken into account by defining a complex *gain*. Each gain is different for each antenna and baseline, and depends on frequency and time. As seen in Sect. (B.3.1), the following factors must be calibrated:

- the opacity and atmospheric water vapour, by using radiometers installed on each antenna and atmospheric transmission models,
- pointing and focus calibration,
- absolute flux calibration, by observing a calibrator (e.g. a quasar) with a known flux density,

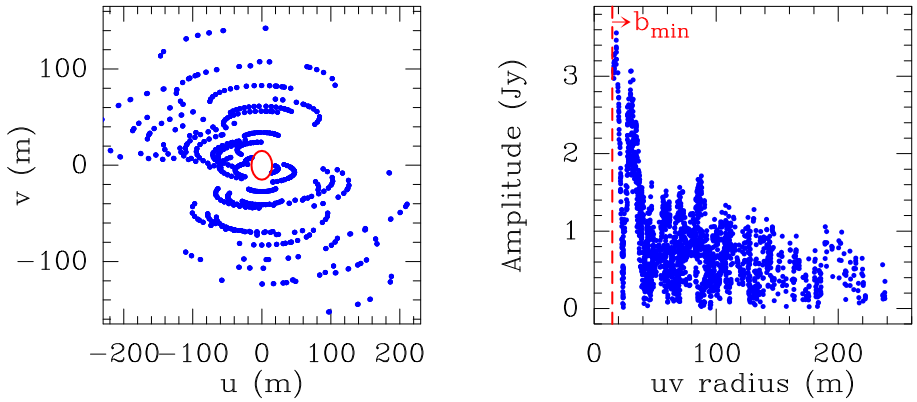

Figure B.11: Left, *uv*-plane coverage for observations carried out with NOEMA in a single configuration toward IRC+10216 in 2016. The red circle delimits the area where the antennas cannot get closer (∼15 m, which is the diameter of the antennas). Right, representation of the amplitudes of the visibilities as a function of the *uv* distances. The red line marks the shortest observed baseline (b_{min}), given by the size of the antennas. Therefore, smaller spatial frequencies than b_{min} cannot be observed, and emission from structures larger than $\sim\lambda/b_{min}$ is filtered out.

- phase calibration, by observing calibrators that must be point-like sources with flat emission spectra close to the target source. This corrects the phase variations of the visibilities due to the electronics of the receivers and the atmospheric fluctuations.

Sensitivity

Eqs.(B.94)-(B.95) give a mathematical expression for the rms of the noise (or sensitivity). In the case of aperture synthesis, the sensitivity is:

$$\sigma \propto \frac{T_{sys}}{\eta_{spec}\sqrt{\Delta\nu N(N-1)n_{pol}t}}, \quad [Jy] \tag{B.107}$$

where T_{sys} is the system temperature, η_{spec} is the efficiency of the spectrometer, $\Delta\nu$ is the bandwidth, N is the number of the antennas, n_{pol} is the number of polarisations, and t is the on-source integration time. This values is usually given in the user's manual of each interferometer.

Imaging

The process that results in the obtention of an image is divided in two main stages, the Fourier transform of the visibilities (to obtain the *dirty image*), and the deconvolution of this image to obtain the brightness distribution of the source. The sampling of the *uv*-plane during a typical interferometric observing run, which is a discrete collection of visibilities, can be mathematically expressed as follows:

$$B(u,v) = \sum_{i,j} \delta_{ij}(u,v), \tag{B.108}$$

thus:

$$I^D(x,y) = \mathfrak{F}^{-1}\left\{B(u,v)V(u,v)\right\}, \tag{B.109}$$

where $I^D(x,y)$ is the dirty image, $\mathfrak{F}^{-1}$ is the inverse Fourier transform, and:

$$b(x,y) = \mathfrak{F}^{-1}\left\{B(u,v)\right\}, \tag{B.110}$$

where $b(x,y)$ is the PSF or *dirty beam* of the interferometer. The inverse Fourier transform of the visibilities results in the brightness distribution of the sky convolved with the PSF, which is called dirty image. The definition of the dirty beam includes a *weighting function* as follows:

$$b(x,y) = \mathfrak{F}^{-1}\left\{W(u,v)B(u,v)\right\}, \tag{B.111}$$

where $W(u,v)$ is the weight function. This weighting function acts on the secondary lobes of the dirty beam and can take different values depending on the aim of the science proposed. The typical weighting functions are:

- *natural weighting*. In this case the visibilities are weighted by the inverse of the noise variance $(1/\sigma^2)$, which gives more weight to the shortest baselines. This weighting produces the best overall rms of the noise for the image,
- *uniform weighting*. This weighting produces a maximum resolution by giving more weight to the longest baselines. The result is a better spatial resolution, but increases the noise of the image,
- *robust weighting*, which is parametrised by the robustness parameter R. This parameter is defined by the user, and controls which visibilities have more weight,
- *tapering*, which is the apodization (i.e. smoothing) of the uv coverage by a Gaussian function. This increases the sensitivity to extended structures by removing the visibilities corresponding to the largest spatial frequencies. However, it is recommended to use compact configurations of the interferometer instead of removing visibilities.

The FOV of an interferometer is given by the HPBW of the antennas. Thus, if the source is larger than approximately half of the FOV, it is necessary to carry out a *mosaic* to map the brightness distribution of the source. A mosaic consists in different pointings toward the source which cover its total distribution. The spatial sampling of the mosaic will depend on the positions of the mosaic. In the case of a rectangular mosaic, the recommended separation between pointings, according to the Nyquist sampling theorem, is $\lambda/2D$, where D is the diameter of an antenna. In the case of an hexagonal mosaic, the separation should be equal to $\frac{2}{\sqrt{3}}\lambda/2D$.

After the obtention of the dirty image, this has to be deconvolved to obtain the brightness distribution of the source. The deconvolution techniques are based on the use of non-linear algorithms, which require an a priori model of the expected brightness distribution of the source. The most used algorithm for this task is the *CLEAN* algorithm (Högbom, 1974). The CLEAN algorithm is an iterative process, for which it is assumed that the observed image is composed of a sum of point-like sources. Starting from the dirty image, we identify an intensity peak on the image as a real component (i.e. a component that is not produced by the PSF of the interferometer). At the position of that component, we subtract a fraction g of the PSF (called the *iteration gain*, which has typical values between 0.05-0.1) to the dirty image. This process (i.e. the identification of real components and their subtraction from the dirty image) is done iteratively, until a convergence criteria is fulfilled, such as a number of iterations or a specific value for the rms of the noise. Once the convergence is reached, the clean (or real) components

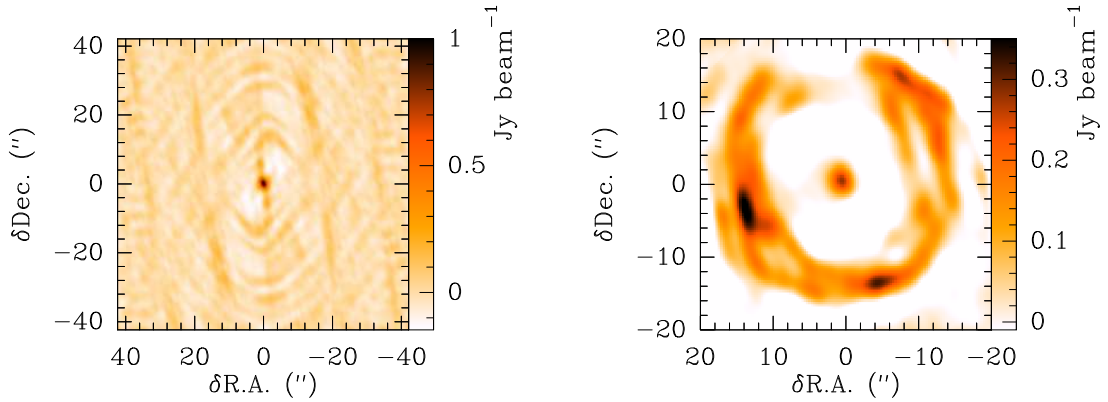

Figure B.12: Left panel, image of the dirty beam of NOEMA for a single configuration during observations of IRC+10216, at ∼158 GHz, in 2016. Right panel, clean image of the $7_{0,7}$–$6_{0,6}$ emission line of the ground vibrational state of SiC_2, at the systemic velocity of the source. The image has been obtained by using the CLEAN algorithm.

are recovered and convolved with a clean beam (gaussian), which are added to the residual map that left after the iterative process, which should be only random noise. The resulting image is the clean image of the source. There are several variants of the CLEAN algorithm, each of them designed for a specific goal (e.g. Clark, 1980, Steer et al., 1984, Wakker & Schwarz, 1988).

APPENDIX

C

CONTRIBUTION AND LIST OF PUBLICATIONS

I hereby detail my labour and tasks carried out during this PhD thesis, as well as the list of my publications and conference contributions.

C.1 Personal contribution

I actively participated in different observational campaigns, mainly for the IRAM-30 m telescope (>100 hours), including the observational runs for the millimeter wavelength range surveys presented in this manuscript. I also produced the final data set used for the analysis of the surveys by reducing all the spectra observed that correspond to IK Tau and OH231.8+4.2. I did the identification, measure, and analysis of each of the lines detected in these spectra. I also interpreted and analysed the ALMA maps presented in Velilla Prieto et al. (2015b). I have participated, either as first author or co-author, in a total of 10 publications in peer-reviewed journals, which are listed in Sect. C.2.

For the analysis, I have used the MADEX radiative transfer code and spectroscopic catalogue, which was written and maintained by Prof. Cernicharo (Cernicharo, 2012), as well as the TE chemical code written by J. Tejero and Prof. Cernicharo (Tejero & Cernicharo, 1991). The chemical kinetics code was also written by Prof. Cernicharo and Dr. Agúndez (Cernicharo, 2004). Dr. Agúndez has also modified and mantained these three codes. I used them in the context of this PhD thesis adapting them to our scientific case. For example, I updated the reaction network to include the rates for several HNCO reactions (Chapter 4). The corresponding training and work with these codes was partially carried out during a short stay in Bordeaux (Laboratoire d'Astrophysique de Bordeaux). I also created several tasks and scripts written in Python and the computational language used by GILDAS (which is mainly based on FORTRAN), to handle and analyse our datasets.

During my PhD, I have submitted proposals as principal investigator for several telescopes and interferometers: the IRAM-30 m, CARMA, NOEMA, and ALMA. Thanks to these proposals, we obtained observing time for all of these telescopes, in particular, I am the principal investigator of two ALMA projects that will be observed during 2016-17. These projects will allow our group to keep state-of-the-art research in the field of the circumstellar medium, and also motivate collaboration with other researchers from different institutions. Additionally, I had the opportunity to assist to several meetings, workshops, seminars, and conferences, where I presented the results of our work. Some of these contributions are listed in Sect. C.3. I also collaborated in the tasks related with outreach of our results, which have been communicated through Spanish media by N. Ruiz Zelmanovich.

C.2 Publications in peer-reviewed journals

C.2.1 Pillar papers of this thesis

1. "The millimeter IRAM-30 m line survey toward IK Tau"
Velilla Prieto, L.; Sánchez Contreras, C.; Cernicharo, J.; Agúndez, M.; Quintana-Lacaci, G.; Bujarrabal, V.; Alcolea, J.; Balança, C.; Herpin, F.; Menten, K.M.; Wyrowski, F.
Astronomy & Astrophysics, Volume 597, id.A25 (2017)

2. "Si-bearing molecules toward IRC+10216: ALMA unveils the molecular envelope of CWLeo"
Velilla Prieto, L.; Cernicharo, J.; Quintana-Lacaci, G.; Agúndez, M.; Castro-Carrizo, A.; Fonfría, J.P.; Marcelino, N.; Zúñiga, J.; Requena, A.; Bastida, A.; Lique, F.; Guélin, M.
The Astrophysical Journal Letters, Volume 805, Issue 2, article id. L73, 7pp. (2015)

3. "Molecular ions in the O-rich evolved star OH 231.8+4.2: HCO^+, $H_{13}CO^+$ and first detection of SO^+, N_2H^+, and H_3O^+"
Sánchez Contreras, C.; **Velilla Prieto, L.**; Agúndez, M.; Cernicharo, J.; Quintana-Lacaci, G.; Bujarrabal, V.; Alcolea, J.; Goicoechea, J. R.; Herpin, F.; Menten, K. M.; Wyrowski, F.
Astronomy & Astrophysics, Volume 577, id.A52, 22 pp. (2015)

4. "New N-bearing species towards OH 231.8+4.2. HNCO, HNCS, HC_3N and NO"
Velilla Prieto, L.; Sánchez Contreras, C.; Cernicharo, J.; Agúndez, M.; Quintana-Lacaci, G.; Alcolea, J.; Bujarrabal, V.; Herpin, F.; Menten, K.M.; Wyrowski, F.
Astronomy & Astrophysics, Volume 575, id.A84, 22 pp.(2015)

C.2.2 Co-author papers

1. "High-resolution rotational spectrum, dunham coefficients, and potential energy function of NaCl"
Cabezas, C.; Cernicharo, J.; Quintana-Lacaci, G.; Peña, I.; Agúndez, M.; **Velilla Prieto, L.**; Castro-Carrizo, A.; Zúñiga, J.; Bastida, A.; Alonso, J.L.; Requena, A.
The Astrophysical Journal, Volume 825, Issue 2, article id. 150, 20 pp. (2016)

2. "Hints of a rotating spiral structure in the innermost regions around IRC+10216"
Quintana-Lacaci, G.; Cernicharo, J.; Agúndez, M.; **Velilla Prieto, L.**; Castro-Carrizo, A.; Marcelino, N.; Cabezas, C.; Peña, I.; Alonso, J.L.; Zúñiga, J.; Requena, A.; Bastida, A.; Kalugina, Y.; Lique, F.; Guélin, M.
The Astrophysical Journal, Volume 818, Issue 2, article id. 192, 20 pp. (2016)

3. "The peculiar distribution of CH_3CN in IRC+10216 seen by ALMA"
Agúndez, M.; Cernicharo, J.; Quintana-Lacaci, G.; **Velilla Prieto, L.**; Castro-Carrizo, A.; Marcelino, N.; Guélin, M.
The Astrophysical Journal, Volume 814, Issue 2, article id. 143, 7 pp. (2015)

4. "The abundance of $^{28}Si^{32}S$, $^{29}Si^{32}S$, $^{28}Si^{34}S$, and $^{30}Si^{32}S$ in the inner layers of the envelope of IRC+10216"

Fonfría, J.P.; Cernicharo, J.; Richter, M.J.; Fernández-López, M.; **Velilla Prieto, L.**; Lacy, J.H.
Monthly Notices of the Royal Astronomical Society, Volume 453, Issue 1, p.439-449 (2015)

5. "Discovery of SiCSi in IRC+10216: a missing link between gas and dust carriers of Si–C bonds"
Cernicharo, J.; McCarthy, M. C.; Gottlieb, C. A.; Agúndez, M.; **Velilla Prieto, L.**; Baraban, J. H.; Changala, P. B.; Guélin, M.; Kahane, C.; Martin-Drumel, M. A.; Patel, N. A.; Reilly, N. J.; Stanton, J. F.; Quintana-Lacaci, G.; Thorwirth, S.; Young, K. H.
The Astrophysical Journal Letters, Volume 806, Issue 1, article id. L3, 6 pp. (2015)

6. "Discovery of time variation of the intensity of molecular lines in IRC+10216 in the submillimeter and far-infrared domains"
Cernicharo, J.; Teyssier, D.; Quintana-Lacaci, G.; Daniel, F.; Agúndez, M.; Decin, L.; **Velilla Prieto, L.**; Guélin, M.; Encrenaz, P.; García-Lario, P.; de Beck, E.; Barlow, M. J.; Groenewegen, M. A. T.; Neufeld, D.; Pearson, J.
The Astrophysical Journal Letters, Volume 796, Issue 1, article id. L21, 6 pp. (2014)

C.3 Non-refereed publications and conference contributions

1. "Circumstellar chemistry of Si-C bearing molecules toward IRC+10216"
Velilla Prieto, L.; Cernicharo, J.; Agúndez, M.; Castro-Carrizo, A.; Quintana-Lacaci, G.; Marcelino, N.; McCarthy, M.C.; Gottlieb, C.A.; Sánchez-Contreras, C.; Fonfría, J.P.; Young, K.H.; Patel, N.A.; Joblin, C.; Martín-Gago, J.A.
European Conference on Laboratory Astrophysics, held in Madrid 21-25 November, 2016.
Poster contribution

2. "The depletion of the refractory molecules SiS, SiO, SiC_2, and C_2H_4 in the innermost envelope of the AGB star IRC+10216"
Fonfría, J.P.; Cernicharo, J.; Fernández-López, M.; Hinkle, K.H.; Richter, M.J.; Agúndez, M.; **Velilla Prieto, L.**; Lacy, J.H.; Curiel, S.; Wallace, L.
European Conference on Laboratory Astrophysics, held in Madrid 21-25 November, 2016.
Poster contribution

3. "Gas phase chemical models and observations of AGBs"
Agúndez, M.; Quintana-Lacaci, G.; **Velilla Prieto, L.**; Castro-Carrizo, A.; Cernicharo, J.
European Conference on Laboratory Astrophysics, held in Madrid 21-25 November, 2016.
Oral contribution

4. "Silicon bearing molecules towards IRC+10216: Herschel and ALMA unveil the molecular envelope of CWLeo"
Velilla Prieto, L.; Cernicharo, J.; Quintana-Lacaci, G.; Agúndez, M.; Castro-Carrizo, A.; Fonfría, J.P.; Zúñiga, J.; Requena, A.; Lique, F.; Guélin, M. *ALMA/Herschel archival workshop. ESO-Garching (Germany), April 15-17, 2015.*
Oral contribution

5. "Mm-wave and far-IR Molecular line survey of OH 231.8+4.2: Hard-boiled rotten eggs"
Sánchez Contreras, C.; **Velilla Prieto, L.**; Alcolea, J.; Quintana-Lacaci, G.; Cernicharo, J.; Agúndez, M.; Teyssier, D.; Bujarrabal, V.; Castro-Carrizo, A.; Daniel, F.; and 24 coauthors
Asymmetrical PNe VI conference, Proceedings of the conference held 4-8 November, 2013. Edited by C. Morisset, G. Delgado-Inglada and S. Torres-Peimbert.
Online at http://www.astroscu.unam.mx/apn6/PROCEEDINGS/, id.88
Oral contribution

6. "Molecular variety in O-rich envelopes around evolved stars: new detections towards OH231.8+4.2 and IKTau"
Velilla Prieto, L.; Sánchez Contreras, C.; Cernicharo, J.; Alcolea, J.; Agúndez, M.; Pardo, J. R.; Bujarrabal, V.; Herpin, F.; Menten, K. M.; Wyrowsky, F. *Second national conference on laboratory and molecular astrophysics, held in the UPO, Sevilla (Spain). November 14-16, 2012.*
Poster contribution

7. "Molecular complexity in envelopes of evolved Oxygen-rich stars: IK Tauri and OH 231.8+4.2"
Velilla Prieto, L.; Sánchez Contreras, C.; Cernicharo, J.; Alcolea, J.; Agúndez, M.; Pardo, J. R.; Bujarrabal, V.; Herpin, F.; Menten, K. M.; Wyrowsky, F.
Highlights of Spanish Astrophysics VII, Proceedings of the X Scientific Meeting of the Spanish Astronomical Society (SEA), held in Valencia, July 9 - 13, 2012, Eds.: J.C. Guirado, L.M. Lara, V. Quilis, and J. Gorgas., pp.676-676
Poster contribution

8. "Complex non-equilibrium chemistry in the shock accelerated outflow of the pre-planetary nebula OH231.8+4.2"
Velilla Prieto, L.; Sánchez Contreras, C.; Cernicharo, J.; Alcolea, J.; Agúndez, M.; Pardo, J. R.; Bujarrabal, V.; Herpin, F.; Menten, K. M.; Wyrowsky, F. *NRAO-NASSC 2012 "Outflows, winds and jets: from young stars to supermassive black holes". Charlottesville (Virginia), USA. March 4, 2012.*
Oral contribution

9. "Molecular complexity in O-rich circumstellar envelopes around evolved stars: IK TAU and OH 231.8+4.2"
Sanchez Contreras, C.; **Velilla Prieto, L.**; Cernicharo, J.; Alcolea, J.; Pardo, J. R.; Agúndez, M.; Bujarrabal, V.; Herpin, F.; Menten, K. M.; Wyroswky, F.
The Molecular Universe, Posters from the proceedings of the 280th Symposium of the International Astronomical Union held in Toledo, Spain, May 30-June 3, 2011, #327
Poster contribution

BIBLIOGRAPHY

Adande, G. R., Halfen, D. T., Ziurys, L. M., Quan, D., & Herbst, E. 2010, ApJ, 725, 561

Agúndez, M. 2009, Ph.D. Thesis

Agúndez, M., Cernicharo, J., Guélin, M., et al. 2010, A&A, 517, L2

Agúndez, M., Cernicharo, J., & Guélin, M. 2010, ApJ, 724, L133

Agúndez, M., Fonfría, J. P., Cernicharo, J., et al. 2012, A&A, 543, A48

Agúndez, M., Cernicharo, J., Quintana-Lacaci, G., et al. 2015, ApJ, 814, 143

Airapetian, V. S., Ofman, L., Robinson, R. D., Carpenter, K., & Davila, J. 2000, ApJ, 528, 965

Akyilmaz, M., Flower, D. R., Hily-Blant, P., Pineau Des Forêts, G., & Walmsley, C. M. 2007, A&A, 462, 221

Alcolea, J., & Bujarrabal, V. 1992, A&A, 253, 475

Alcolea, J., Pardo, J. R., Bujarrabal, V., et al. 1999, A&AS, 139, 461

Alcolea, J., Bujarrabal, V., Sánchez Contreras, C., Neri, R., & Zweigle, J. 2001, A&A, 373, 932

Aleman, I., Ueta, T., Ladjal, D., et al. 2014, A&A, 566, A79

ALMA Partnership, Brogan, C. L., Pérez, L. M., et al. 2015, ApJ, 808, L3

Amusia, M. Y., Msezane, A. Z., & Shaginyan, V. R. 2003, PhSSc, 68, C133

Anderson, J. K., & Ziurys, L. M. 2014, ApJ, 795, L1

Antiñolo, M., Agundez, M., Jimenez, E., et al. 2016, arXiv:1603.04244

Asplund, M., Grevesse, N., Sauval, A. J., & Scott, P. 2009, ARA&A, 47, 481

Atkins, P. & de Paula, J. 2006, Physical Chemistry 8th Ed.. Oxford University Press

Audinos, P., Kahane, C., & Lucas, R. 1994, A&A, 287, L5

Bachiller, R., & Pérez Gutiérrez, M. 1997, ApJ, 487, L93

Balick, B., & Frank, A. 2002, ARA&A, 40, 439

Becklin, E. E., Frogel, J. A., Hyland, A. R., Kristian, J., & Neugebauer, G. 1969, ApJ, 158, L133

Bergeat, J., & Chevallier, L. 2005, A&A, 429, 235

Bohlin, R. C., Savage, B. D., & Drake, J. F. 1978, ApJ, 224, 132

Bowen, G. H. 1988, ApJ, 329, 299

Bowers, P. F., & Morris, M. 1984, ApJ, 276, 646

Bowers, P. F., Johnston, K. J., & de Vegt, C. 1989, ApJ, 340, 479

Brittain, J. E. 1984, IEEE Proceedings, 72, 709

Brown, R. L. 1981, ApJ, 248, L119

Bujarrabal, V., Gomez-Gonzalez, J., Bachiller, R., & Martin-Pintado, J. 1988, A&A, 204, 242

Bujarrabal, V., Gomez-Gonzalez, J., & Planesas, P. 1989, A&A, 219, 256

Bujarrabal, V., & Alcolea, J. 1991, A&A, 251, 536

Bujarrabal, V., Fuente, A., & Omont, A. 1994, A&A, 285, 247

Bujarrabal, V., Castro-Carrizo, A., Alcolea, J., & Sánchez Contreras, C. 2001, A&A, 377, 868

Bujarrabal, V., Alcolea, J., Sánchez Contreras, C., & Sahai, R. 2002, A&A, 389, 271

Burbidge, E. M., Burbidge, G. R., Fowler, W. A., & Hoyle, F. 1957, Reviews of Modern Physics, 29, 547

Busso, M., Gallino, R., & Wasserburg, G. J. 1999, ARA&A, 37, 239

Cabezas, C., Cernicharo, J., Quintana-Lacaci, G., et al. 2016, ApJ, 825, 150

Cardelli, J. A., Clayton, G. C., & Mathis, J. S. 1989, ApJ, 345, 245

Carter, M., Lazareff, B., Maier, D., et al. 2012, A&A, 538, A89

Castor, J. I. 1970, MNRAS, 149, 111

Castro-Carrizo, A., Quintana-Lacaci, G., Neri, R., et al. 2010, A&A, 523, A59

Chase, M. W. 1998, 'NIST-JANAF Thermochemical Tables', J. Phys. Chem. Ref. Data, Monograph. 9, 4th ed., Melville: AIP

Chastaing, D., Le Picard, S. D., Sims, I. R., & Smith, I. W. M. 2001, A&A, 365, 241

Cherchneff, I. 2006, A&A, 456, 1001

Cernicharo, J., Guelin, M., & Askne, J. 1984, A&A, 138, 371

Cernicharo, J. 1985, Internal IRAM report (Granada:IRAM)

Cernicharo, J., Kahane, C., Gomez-Gonzalez, J., & Guelin, M. 1986, A&A, 167, L9

Cernicharo, J., Kahane, C., Guelin, M., & Hein, H. 1987, A&A, 181, L9

Cernicharo, J., & Guelin, M. 1987, A&A, 183, L10

Cernicharo, J., Liu, X.-W., González-Alfonso, E., et al. 1997, ApJ, 483, L65

Cernicharo, J., Guélin, M., & Kahane, C. 2000, A&AS, 142, 181

Cernicharo, J. 2004, ApJ, 608, L41

Cernicharo, J., Guélin, M., Agündez, M., et al. 2007, A&A, 467, L37

Cernicharo, J., Waters, L. B. F. M., Decin, L., et al. 2010, A&A, 521, L8

Cernicharo, J. 2012, EAS Publications Series, 58, 251

Cernicharo, J., Daniel, F., Castro-Carrizo, A., et al. 2013, ApJ, 778, L25

Cernicharo, J., Teyssier, D., Quintana-Lacaci, G., et al. 2014, ApJ, 796, L21

Cernicharo, J., Marcelino, N., Agúndez, M., & Guélin, M. 2015, A&A, 575, A91

Cernicharo, J., McCarthy, M. C., Gottlieb, C. A., et al. 2015, ApJ, 806, L3

Cherchneff, I., Barker, J. R., & Tielens, A. G. G. M. 1992, ApJ, 401, 269

Cherchneff, I. 2006, A&A, 456, 1001

Cheung, A. C., Rank, D. M., Townes, C. H., Thornton, D. D., & Welch, W. J. 1969, Nat, 221, 626

Choi, Y. K., Brunthaler, A., Menten, K. M., & Reid, M. J. 2012, Cosmic Masers - from OH to H0, 287, 407

Clark, B. G. 1980, A&A, 89, 377

Cohen, M. 1979, MNRAS, 186, 837

Cohen, M. 1981, PASP, 93, 288

Cox, N. L. J., Kerschbaum, F., van Marle, A. J., et al. 2012, A&A, 543, C1

Crowther, P. A., Schnurr, O., Hirschi, R., et al. 2010, MNRAS, 408, 731

Cutri, R. M., Skrutskie, M. F., van Dyk, S., et al. 2003, VizieR Online Data Catalog, 2246, 0

Cutri, R. M., & et al. 2012, VizieR Online Data Catalog, 2311,

Dalgarno, A. 2006, Proceedings of the National Academy of Science, 103, 12269

Daniel, F., Agúndez, M., Cernicharo, J., et al. 2012, A&A, 542, A37

Danilovich, T., Bergman, P., Justtanont, K., et al. 2014, A&A, 569, A76

Danilovich, T., De Beck, E., Black, J. H., Olofsson, H., & Justtanont, K. 2016, A&A, 588, A119

De Beck, E., Kamiński, T., Patel, N. A., et al. 2013, A&A, 558, A132

De Beck, E., Kamiński, T., Menten, K. M., et al. 2015, Why Galaxies Care about AGB Stars III: A Closer Look in Space and Time, 497, 73

Decin, L., De Beck, E., Brünken, S., et al. 2010a, A&A, 516, A69

Decin, L., Cernicharo, J., Barlow, M. J., et al. 2010b, A&A, 518, L143

Decin, L., Agúndez, M., Barlow, M. J., et al. 2010c, Nat, 467, 64

Decin, L., Justtanont, K., De Beck, E., et al. 2010d, A&A, 521, L4

De Marco, O. 2009, PASP, 121, 316

Desmurs, J.-F., Alcolea, J., Bujarrabal, V., Sánchez Contreras, C., & Colomer, F. 2007, A&A, 468, 189

Dickman, R. L., Snell, R. L., & Schloerb, F. P. 1986, ApJ, 309, 326

Donati, G. B. 1864, Astronomische Nachrichten, 62, 375

Douglas, A. E., & Herzberg, G. 1941, ApJ, 94, 381

Duari, D., Cherchneff, I., & Willacy, K. 1999, A&A, 341, L47

Dubernet, M.-L., Alexander, M. H., Ba, Y. A., et al. 2013, A&A, 553, A50

Dunham, J. L. 1932, Physical Review, 41, 721

Draine, B. T. 1978, ApJS, 36, 595

Draine, B. T. 2003, ARA&A, 41, 241

Draine, B. T. 2011, Physics of the Interstellar and Intergalactic Medium by Bruce T. Draine. Princeton University Press, 2011. ISBN: 978-0-691-12214-4

Duari, D., Cherchneff, I., & Willacy, K. 1999, A&A, 341, L47

Elitzur, M. 1992, ARA&A, 30, 75

Etxaluze, M., Cernicharo, J., Goicoechea, J. R., et al. 2014, A&A, 566, A78

Ewen, H. I., & Purcell, E. M. 1951, Nat, 168, 356

Feast, M. W., Catchpole, R. M., Whitelock, P. A., et al. 1983, MNRAS, 203, 1207

Fitzpatrick, E. L. 1999, PASP, 111, 63

Fonfría, J. P., Cernicharo, J., Richter, M. J., & Lacy, J. H. 2008, ApJ, 673, 445-469

Fonfría, J. P., Fernández-López, M., Agúndez, M., et al. 2014, MNRAS, 445, 3289

Fonfría, J. P., Cernicharo, J., Richter, M. J., et al. 2015, MNRAS, 453, 439

Frerking, M. A., Linke, R. A., & Thaddeus, P. 1979, ApJ, 234, L143

Gail, H.-P., & Sedlmayr, E. 2014, Physics and Chemistry of Circumstellar Dust Shells, by Hans-Peter Gail , Erwin Sedlmayr, Cambridge, UK: Cambridge University Press, 2014

Garrod, R. T. 2008, A&A, 491, 239

Gehrz, R. 1989, Interstellar Dust, 135, 445

Gerin, M., Viala, Y., Pauzat, F., & Ellinger, Y. 1992, A&A, 266, 463

Gilman, R. C. 1972, ApJ, 178, 423

Glassgold, A. E., & Huggins, P. J. 1983, MNRAS, 203, 517

Glassgold, A. E., Mamon, G. A., & Huggins, P. J. 1989, ApJ, 336, L29

Gobrecht, D., Cherchneff, I., Sarangi, A., Plane, J. M. C., & Bromley, S. T. 2016, A&A, 585, A6

Goldreich, P., & Kwan, J. 1974, ApJ, 189, 441

Goldreich, P., & Scoville, N. 1976, ApJ, 205, 144

Goldsmith, P. F., & Langer, W. D. 1999, ApJ, 517, 209

González-Alfonso, E., & Cernicharo, J. 1999, The Universe as Seen by ISO, 427, 325

González Delgado, D., Olofsson, H., Kerschbaum, F., et al. 2003, A&A, 411, 123

Groenewegen, M. A. T. 1994, A&A, 290,

Groenewegen, M. A. T., & Ludwig, H.-G. 1998, A&A, 339, 489

Guilloteau, S., Lucas, R., Omont, A., & Nguyen-Q-Rieu 1986, A&A, 165, L1

Habing, H. J. 1968, BAIN, 19, 421

Habing, H. J. 1996, A&AR, 7, 97

Habing, H. J., & Olofsson, H. 2003, Asymptotic giant branch stars, by Harm J. Habing and Hans Olofsson. Astronomy and astrophysics library, New York, Berlin: Springer, 2003

Hale, D. D. S., Bester, M., Danchi, W. C., et al. 1997, ApJ, 490, 407

Halfen, D. T., Apponi, A. J., & Ziurys, L. M. 2001, ApJ, 561, 244

Hasegawa, T. I., & Kwok, S. 2001, ApJ, 562, 824

Herbst, E. 1995, Annual Review of Physical Chemistry, 46, 27

Herbst, E., & van Dishoeck, E. F. 2009, ARA&A, 47, 427

Herwig, F. 2005, ARA&A, 43, 435

Herzberg, G. 1939, Molecular spectra and molecular structure. Vol.1: Diatomic Molecules, by G. Herzberg. New York: Prentice Hall Inc., 1939, 1

Herzberg, G. 1945, Molecular spectra and molecular structure. Vol.2: Infrared and Raman spectra of polyatomic molecules, by G. Herzberg. New York: Van Nostrand, Reinhold, 1945, 2

Herzberg, G. 1950, New York: Van Nostrand Reinhold, 1950, 2nd ed.

Herzberg, G. 1966, Molecular spectra and molecular structure. Vol.3: Electronic spectra and electronic structure of polyatomic molecules, by G. Herzberg. New York: Van Nostrand, Reinhold, 1966, 3

Heyer, M., & Dame, T. M. 2015, ARA&A, 53, 583

Högbom, J. A. 1974, A&AS, 15, 417

Hollenbach, D., & McKee, C. F. 1980, ApJ, 241, L47

Holzer, T. E., & MacGregor, K. B. 1985, Mass Loss from Red Giants, 117, 229

Bladh, S., Höfner, S. 2012, A&A, 546, A76

Huggins, W. 1881, Proceedings of the Royal Society of London Series I, 33, 1

Huggins, P. J., Olofsson, H., & Johansson, L. E. B. 1988, ApJ, 332, 1009

Iben, I., Jr., & Renzini, A. 1983, ARA&A, 21, 271

Jackson, J. M., Armstrong, J. T., & Barrett, A. H. 1984, ApJ, 280, 608

Jansky, K. G. 1933, Popular Astronomy, 41, 548

Jewell, P. R. 2002, Single-Dish Radio Astronomy: Techniques and Applications, 278, 313

Jorgensen, U. G., & Johnson, H. R. 1992, A&A, 265, 168

Jura, M., & Morris, M. 1985, ApJ, 292, 487

Jura, M. 1986, ApJ, 303, 327

Justtanont, K., Skinner, C. J., & Tielens, A. G. G. M. 1994, ApJ, 435, 852

Karovicova, I., Wittkowski, M., Ohnaka, K., et al. 2013, A&A, 560, A75

Kastner, J. H., Weintraub, D. A., Zuckerman, B., et al. 1992, ApJ, 398, 552

Kim, H., Wyrowski, F., Menten, K. M., & Decin, L. 2010, A&A, 516, A68

Kramer, C. 1997, Internal IRAM report (Granada:IRAM)

Kraus, J. D. 1966, Radio astronomy. New York: McGraw-Hill, 1966

Küppers, M., O'Rourke, L., Bockelée-Morvan, D., et al. 2014, Nat, 505, 525

Kwok, S. 1975, ApJ, 198, 583

Kwok, S. 2007, Physics and Chemistry of the Interstellar Medium by Sun Kwok. University Science Books, 2007.

Kwon, Y.-J., & Suh, K.-W. 2014, Journal of Korean Astronomical Society, 47, 123

Ladjal, D., Barlow, M. J., Groenewegen, M. A. T., et al. 2010, A&A, 518, L141

Lane, A. P., Johnston, K. J., Bowers, P. F., Spencer, J. H., & Diamond, P. J. 1987, ApJ, 323, 756

Le Bertre, T. 1992, A&AS, 94, 377

Le Petit, F., Nehmé, C., Le Bourlot, J., & Roueff, E. 2006, ApJS, 164, 506

Li, X., Millar, T. J., Walsh, C., Heays, A. N., & van Dishoeck, E. F. 2014, A&A, 568, A111

Li, X., Millar, T. J., Heays, A. N., et al. 2016, A&A, 588, A4

Lindqvist, M., Nyman, L.-A., Olofsson, H., & Winnberg, A. 1988, A&A, 205, L15

Lindqvist, M., Olofsson, H., Winnberg, A., & Nyman, L. A. 1992, A&A, 263, 183

Lique, F., Kalugina, Y., Chefdeville, S., et al. 2014, A&A, 567, A22

Loup, C., Forveille, T., Omont, A., & Paul, J. F. 1993, A&AS, 99, 291

Lucas, R., Bujarrabal, V., Guilloteau, S., et al. 1992, A&A, 262, 491

Lucas, R., Guélin, M., Kahane, C., Audinos, P., & Cernicharo, J. 1995, Ap&SS, 224, 293

Maciel, W. J. 1977, A&A, 57, 273

Maercker, M., Mohamed, S., Vlemmings, W. H. T., et al. 2012, Nat, 490, 232

Malphrus, B. K. 1996, The history of radio astronomy and the National Radio Astronomy Observatory : evolution toward big science Malabar, Fla. : Krieger, 1996.

Mamon, G. A., Glassgold, A. E., & Omont, A. 1987, ApJ, 323, 306

Mamon, G. A., Glassgold, A. E., & Huggins, P. J. 1988, ApJ, 328, 797

Marengo, M., Ivezić, Ž., & Knapp, G. R. 2001, MNRAS, 324, 1117

Martín, S., Requena-Torres, M. A., Martín-Pintado, J., & Mauersberger, R. 2008, ApJ, 678, 245

Marvel, K. B. 2005, AJ, 130, 261

Mauron, N., & Huggins, P. J. 2010, A&A, 513, A31

McCarthy, M. C., Gottlieb, C. A., Gupta, H., & Thaddeus, P. 2006, ApJ, 652, L141

McCarthy, M. C., Baraban, J. H., Changala, B., et al. 2015, 70th International Symposium on Molecular Spectroscopy

McKellar, A. 1940, PASP, 52, 187

Men'shchikov, A. B., Balega, Y., Blöcker, T., Osterbart, R., & Weigelt, G. 2001, A&A, 368, 497

Menten, K. M., Wyrowski, F., Alcolea, J., et al. 2010, A&A, 521, L7

Menten, K. M., Reid, M. J., Kamiński, T., & Claussen, M. J. 2012, A&A, 543, A73

Milam, S. N., Apponi, A. J., Woolf, N. J., & Ziurys, L. M. 2007, ApJ, 668, L131

Milam, S. N., Woolf, N. J., & Ziurys, L. M. 2009, ApJ, 690, 837

Mohr, P. J., Newell, D. B., & Taylor, B. N. 2015, arXiv:1507.07956

Morris, M., Turner, B. E., Palmer, P., & Zuckerman, B. 1976, ApJ, 205, 82

Morris, M., & Jura, M. 1983, ApJ, 264, 546

Morris, M., Guilloteau, S., Lucas, R., & Omont, A. 1987, ApJ, 321, 888

Morris, M. 1987, PASP, 99, 1115

Müller, H. S. P., Schlöder, F., Stutzki, J., & Winnewisser, G. 2005, Journal of Molecular Structure, 742, 215

Neri, R., Kahane, C., Lucas, R., Bujarrabal, V., & Loup, C. 1998, A&AS, 130, 1

Neufeld, D. A., & Dalgarno, A. 1989, ApJ, 340, 869

Neugebauer, G., Martz, D. E., & Leighton, R. B. 1965, ApJ, 142, 399

Neugebauer, G., & Leighton, R. B. 1969, NASA SP, Washington: NASA, 1969,

Olofsson, H., Johansson, L. E. B., Hjalmarson, A., & Nguyen-Quang-Rieu 1982, A&A, 107, 128

Olofsson, H., Bergman, P., Eriksson, K., & Gustafsson, B. 1996, A&A, 311, 587

Olofsson, H. 1996, Ap&SS, 245, 169

Olofsson, H., Lindqvist, M., Nyman, L.-A., & Winnberg, A. 1998, A&A, 329, 1059

Olofsson, H., Bergman, P., Lucas, R., et al. 2000, A&A, 353, 583

Omont, A., Lucas, R., Morris, M., & Guilloteau, S. 1993, A&A, 267, 490

Pardo, J., Cernicharo, J., & Serabyn, E. 2002, Astronomical Site Evaluation in the Visible and Radio Range, 266, 188

Pardo, J. R., Cernicharo, J., Goicoechea, J. R., Guélin, M., & Asensio Ramos, A. 2007, ApJ, 661, 250

Parr, R. G. 1983, Annual Review of Physical Chemistry, 34, 631

Penzias, A. A., & Wilson, R. W. 1965, ApJ, 142, 419

Penzias, A. A., & Burrus, C. A. 1973, ARA&A, 11, 51

Pesch, P. 1967, ApJ, 147, 381

Phillips, T. G., Huggins, P. J., Wannier, P. G., & Scoville, N. Z. 1979, ApJ, 231, 720

Pickett, H. M., Poynter, R. L., Cohen, E. A., Delitsky, M. L., Pearson, J. C., & Muller, H. S. P. 1998, Journal of Quantitative Spectroscopy and Radiative Transfer 60, 883-890

Pijpers, F. P., & Hearn, A. G. 1989, A&A, 209, 198

Pineau des Forets, G., Roueff, E., Schilke, P., & Flower, D. R. 1993, MNRAS, 262, 915

Prasad, S. S., & Tarafdar, S. P. 1983, ApJ, 267, 603

Price, S. D., & Murdock, T. L. 1983, AFGL-TR-0208 Environemental Research papers, 161

Quan, D., Herbst, E., Osamura, Y., & Roueff, E. 2010, ApJ, 725, 2101

Quintana-Lacaci, G., Agúndez, M., Cernicharo, J., et al. 2013, A&A, 560, L2

Quintana-Lacaci, G., Cernicharo, J., Agúndez, M., et al. 2016, ApJ, 818, 192

Ramstedt, S., & Olofsson, H. 2014, A&A, 566, A145

Reber, G. 1940, ApJ, 91, 621

Reber, G. 1944, ApJ, 100, 279

Reboussin, L., Wakelam, V., Guilloteau, S., & Hersant, F. 2014, MNRAS, 440, 3557

Reipurth, B. 1987, Nat, 325, 787

Ridgway, S., & Keady, J. J. 1988, ApJ, 326, 843

Rimmer, P. B., Herbst, E., Morata, O., & Roueff, E. 2012, A&A, 537, A7

Rodríguez-Fernández, N. J., Tafalla, M., Gueth, F., & Bachiller, R. 2010, A&A, 516, A98

Rohlfs, K., & Wilson, T. L. 2004, Tools of radio astronomy, 4th rev. and enl. ed., by K. Rohlfs and T.L. Wilson. Berlin: Springer, 2004,

Ruaud, M., Loison, J. C., Hickson, K. M., et al. 2015, MNRAS, 447, 4004

Russell, H. N. 1934, ApJ, 79, 317

Rybicki, G. B., & Lightman, A. P. 1979, Radiative processes in astrophysics, New York, Wiley-Interscience, 1979. 393 p.

Sabin, L., Zhang, Q., Zijlstra, A. A., et al. 2014, MNRAS, 438, 1794

Sackmann, I.-J., & Boothroyd, A. I. 1992, ApJ, 392, L71

Sahai, R., & Trauger, J. T. 1998, AJ, 116, 1357

Sahai, R., Findeisen, K., Gil de Paz, A., & Sánchez Contreras, C. 2008, ApJ, 689, 1274-1278

Sahai, R., & Chronopoulos, C. K. 2010, ApJ, 711, L53

Sahai, R., Morris, M. R., & Villar, G. G. 2011, AJ, 141, 134

Samus, N. N., Durlevich, O. V., & et al. 2004, VizieR Online Data Catalog, 2250

Sánchez Contreras, C., Bujarrabal, V., & Alcolea, J. 1997, A&A, 327, 689

Sánchez Contreras, C., Bujarrabal, V., Neri, R., & Alcolea, J. 2000, A&A, 357, 651

Sánchez Contreras, C., Desmurs, J. F., Bujarrabal, V., Alcolea, J., & Colomer, F. 2002, A&A, 385, L1

Sánchez Contreras, C., Gil de Paz, A., & Sahai, R. 2004, ApJ, 616, 519

Sánchez Contreras, C., Velilla, L., Alcolea, J., et al. 2014, Asymmetrical Planetary Nebulae VI Conference, 88

Sánchez Contreras, C., Velilla Prieto, L., Agúndez, M., et al. 2015, A&A, 577, A52

Sanchez Contreras, C., Velilla Prieto, L., Cernicharo, J., et al. 2011, The Molecular Universe, 280, 327

Sánchez Contreras, C., & Sahai, R. 2012, ApJS, 203, 16

Schlafly, E. F., & Finkbeiner, D. P. 2011, ApJ, 737, 103

Schöier, F. L., & Olofsson, H. 2001, A&A, 368, 969

Schöier, F. L., van der Tak, F. F. S., van Dishoeck, E. F., & Black, J. H. 2005, A&A, 432, 369

Schöier, F. L., Fong, D., Olofsson, H., Zhang, Q., & Patel, N. 2006, ApJ, 649, 965

Schöier, F. L., Maercker, M., Justtanont, K., et al. 2011, A&A, 530, A83

Schöier, F. L., Ramstedt, S., Olofsson, H., et al. 2013, A&A, 550, A78

Sedlmayr, E., & Dominik, C. 1995, SSR, 73, 211

Skinner, C. J., Justtanont, K., Tielens, A. G. G. M., et al. 1999, MNRAS, 302, 293

Snyder, L. E., & Buhl, D. 1972, ApJ, 177, 619

Sobolev, V. V. 1960, Cambridge: Harvard University Press, 1960,

Solomon, P., Jefferts, K. B., Penzias, A. A., & Wilson, R. W. 1971, ApJ, 163, L53

Speck, A. K., Barlow, M. J., Sylvester, R. J., & Hofmeister, A. M. 2000, A&AS, 146, 437

Steer, D. G., Dewdney, P. E., & Ito, M. R. 1984, A&A, 137, 159

Suh, K.-W. 1999, MNRAS, 304, 389

Swings, P., & Rosenfeld, L. 1937, ApJ, 86, 483

Tarduno, J. A., Blackman, E. G., & Mamajek, E. E. 2014, Physics of the Earth and Planetary Interiors, 233, 68

Tejero, M., Cernicharo, J., 1991, Modelos de equilibrio termodinámico aplicados a envolturas circunestelares de estrellas evolucionadas (Madrid:IGN)

Teyssier, D., Hernandez, R., Bujarrabal, V., Yoshida, H., & Phillips, T. G. 2006, A&A, 450, 167

Thompson, A. R., Moran, J. M., & Swenson, G. W., Jr. 2001, "Interferometry and synthesis in radio astronomy by A. Richard Thompson, James M. Moran, and George W. Swenson, Jr. 2nd ed. New York : Wiley, c2001, 692p.

Tielens, A. G. G. M. 1983, ApJ, 271, 702

Timmermann, R., Bertoldi, F., Wright, C. M., et al. 1996, A&A, 315, L281

Townes, C. H., & Schawlow, A. L. 1975, Microwave spectroscopy., by Townes, C. H.; Schawlow, A. L.. New York, NY (USA): Dover Publications, 698 p.,

Townes, C. H. 1977, The Observatory, 97, 52

Tsuji, T. 1973, A&A, 23, 411

Turner, B. E. 1971, ApJ, 163, L35

Turner, B. E. 1971, APL, 8, 73

Ukita, N., & Morris, M. 1983, A&A, 121, 15

Ulich, B. L., & Haas, R. W. 1976, ApJS, 30, 247

Ulrich, B. T., Neugebauer, G., McCammon, D., et al. 1966, ApJ, 146, 288

van Dishoeck, E. F., Kristensen, L. E., Benz, A. O., et al. 2011, PASP, 123, 138

van Zadelhoff, G.-J., Dullemond, C. P., van der Tak, F. F. S., et al. 2002, A&A, 395, 373

Velilla Prieto, L., Sánchez Contreras, C., Cernicharo, J., et al. 2013, Highlights of Spanish Astrophysics VII, 676

Velilla Prieto, L., Sánchez Contreras, C., Cernicharo, J., et al. 2015, A&A, 575, A84

Velilla Prieto, L., Cernicharo, J., Quintana-Lacaci, G., et al. 2015, ApJ, 805, L13

Velilla Prieto, L., Sánchez-Contreras, C., Cernicharo, J., et al. 2017, A&A, 597, A25

Velilla Prieto, L., Sánchez-Contreras, C., Cernicharo, J., et al. 2017, A&A, in prep.

Vlemmings, W. H. T., Ramstedt, S., Rao, R., & Maercker, M. 2012, A&A, 540, L3

Vlemmings, W. H. T. 2014, Magnetic Fields throughout Stellar Evolution, 302, 389

Wakelam, V., Smith, I. W. M., Herbst, E., et al. 2010, SSR, 156, 13

Wakelam, V., Herbst, E., Loison, J.-C., et al. 2012, ApJS, 199, 21

Wakker, B. P., & Schwarz, U. J. 1988, A&A, 200, 312

Walker, R. G. 1975, Environmental Research Papers Air Force Cambridge Research Labs

Wallerstein, G., & Knapp, G. R. 1998, ARA&A, 36, 369

Watson, J. K. G. 1967, JCP, 46, 1935

Watson, J. K. G. 1977, Journal of Molecular Spectroscopy, 65, 123

Weinreb, S., Barrett, A. H., Meeks, M. L., & Henry, J. C. 1963, Nat, 200, 829

Wilkins, G. A. 1989, The IAU Style Manual

Willacy, K., & Millar, T. J. 1997, A&A, 324, 237

Willacy, K., & Cherchneff, I. 1998, A&A, 330, 676

Wilson, R. W., Jefferts, K. B., & Penzias, A. A. 1970, ApJ, 161, L43

Wilson, R. W., Penzias, A. A., Jefferts, K. B., Kutner, M., & Thaddeus, P. 1971, ApJ, 167, L97

Wilson, L. A., & Bowen, G. H. 1984, Nat, 312, 429

Wing, R. F., & Lockwood, G. W. 1973, ApJ, 184, 873

Wood, P. R. 1990, Confrontation Between Stellar Pulsation and Evolution, 11, 355

Woodall, J., Agúndez, M., Markwick-Kemper, A. J., & Millar, T. J. 2007, A&A, 466, 1197

Young, K., Phillips, T. G., & Knapp, G. R. 1993, ApJ, 409, 725

Zhang, Y., Kwok, S., & Trung, D.-V.- 2008, Organic Matter in Space, 251, 169

Zhang, Y., Kwok, S., & Dinh-V-Trung 2009, ApJ, 691, 1660

Zhang, Y., Kwok, S., & Nakashima, J.-i. 2009, ApJ, 700, 1262

Zhang, Y., Kwok, S., Nakashima, J.-i., Chau, W., & Dinh-V-Trung 2013, ApJ, 773, 71

Zijlstra, A. A., Chapman, J. M., te Lintel Hekkert, P., et al. 2001, MNRAS, 322, 280

Zijlstra, A. A., Matsuura, M., Wood, P. R., et al. 2006, MNRAS, 370, 1961

Zijlstra, A. A. 2007, Baltic Astronomy, 16, 79

Ziurys, L. M., Tenenbaum, E. D., Pulliam, R. L., Woolf, N. J., & Milam, S. N. 2009, ApJ, 695, 1604